The *MYCN* oncogene

as a minimal residual disease marker

and therapeutic target in neuroblastoma

Inaugural-Dissertation
to obtain the academic degree
Doctor rerum naturalium (Dr. rer. nat.)

submitted to the Department of Biology, Chemistry, Pharmacy
of Freie Universität Berlin

by

Annabell Krienelke-Szymansky

2020

Die folgende Arbeit wurde von Dezember 2015 bis November 2020
unter der Leitung von Herrn Prof. Dr. Johannes H. Schulte an der Klinik für Pädiatrie mit Schwerpunkt Onkologie, Hämatologie und SZT der Charité - Universitätsmedizin Berlin angefertigt.

1. Gutachter:	Prof. Dr. med. Johannes Hubertus Schulte
2. Gutachter:	Prof. Dr. rer. nat. Peter Robin Hiesinger

Disputation am 14.06.2021

Acknowledgements

First of all, I would like to thank my advisor Prof. Johannes H. Schulte for the opportunity to be part of his neuroblastoma research group at the Charité University Medicine Berlin and to write my dissertation under his supervision. I have always been fascinated by how many different professions and projects he is able to unite in one person. He always had an open ear for me and supported and advised me in pursuing all of my ideas. Any project or experiment was possible and feasible while working with him – we were always able to discuss how to proceed. He is a role model for me, especially as a medical student, and without him there is no way I would have had the opportunity to become a physician.

I also would like to thank Prof. Peter R. Hiesinger for his external supervision and for agreeing to be a referee for my thesis.

I am very grateful to Prof. Angelika Eggert for convincing me to move from Heidelberg to Berlin to thus continue my research on pediatric cancer. “Shoot for the moon. Even if you miss, you'll land among the stars.” (Norman Vincent Peale)

At this point I would also like to thank PD Cornelia Eckert for always being there for me. I am really happy about all the experiences we shared: our intense MRD conversations, setting up new and innovative projects, – and dancing in Wilsede.

Special thanks to Falk Hertwig and Jörn Tödling. I am very glad that they accompanied me on my way to the doctorate. As a biologist I always looked up to them, and they both taught me a great deal. We had wonderful discussions, and I acquired valuable science skills through their training, in both the dry lab and the wet lab world. In addition, I thank them very much for their contributions and comments on my dissertation.

I would also like to thank Nicole. As everyone knows, it is not a lie when I say: without her, many projects and experiments could not have been possible! I would also like to thank Steffen for his support with the clinical data of the MRD project and for every wake-up coffee we had in the lab in the evening. I would also like to thank Steffi and Filippos for their support and the helpful conversations we had.

Furthermore, I would like to thank my colleagues of the pediatric clinic and research for outstanding and fruitful collaboration. Many thanks to Anton, Hedi, Marco, Theresa, Kathy, Patrick, Karin, Annette, Helia and Renate. Moreover, I especially want to thank the other cooperation partners from research and industry who were involved in the realization of the projects. Thank you Lukas, Roopika and Bettina from Hämatopathologie Hamburg/NEO New Oncology; Thank you Matthias, Jessica, Nadine, Witali, Roswitha and Martina from the University Hospital Cologne; Thanks to Hoffmann-La Roche for providing the TEN-010 inhibitor; Thanks to Dennis Gürgen, Jens Hoffmann and Wolfgang Walther from the Experimental Pharmacology & Oncology Berlin-Buch GmbH; Thanks to the whole research group under Angela M. Kaindl.

I would also like to express my special thanks to the two students whose thesis work I had the chance to supervise during my time at Schulte group, Max D. Overath and Katharina A. Firle. I would like to thank Max for the great support I received from him in the ASPM project and especially for the assistance in performing the CRISPR/Cas9 ASPM-FLAG tagging experiments. I would further like to thank Kathi for her valuable contribution to the TEN-010 project, especially in the evaluation of possible combination therapies.

At this point I would like to thank a very special person, and your name has already become a legend in our pediatric research group. I would really like to thank dear Awi very much for her support. She has been a great help to me in many laboratory experiments and also gave me so much emotional support. But I would also like to thank Mella and Aleix, who have always supported me and my projects, be it in my professional or private life.

I would also like to take this opportunity to thank other assistants from the pediatric clinic and research for their daily support, Georg, Belgin, Constanze, Nadine, Helena and Jutta, Yvonne, Katharina, Madlen, Anke, Susanne, Katarzyna, Marion, Claudia, Ute, Aki, Silke, Daniela and Jasmin.

Of course I would also like to thank my PhD fellow students for the wonderful time we shared, we were always a great community and have been through a great deal together. Many thanks to Kerstin, Mareike, Louisa, Sinduja, Malwine, Birte, Sabine, Laura, Lena, Heathcliff, Konstantin, Rocío and Yi.

Dear Frauke, Susan, Kathy, Sabine and Steffen, thanks so much for proofreading my doctoral thesis, thanks for your time and effort!

At this point I would also like to thank the sponsors of the projects presented here, who offered me so many possibilities for personal training. My special thanks therefore go to the German Cancer Aid, the Berlin Cancer Society, the DKFZ/DKTK, the GlaxoSmithKline foundation and the EMBL Corporate Partnership Programme. Furthermore, I would like to take this opportunity to thank the patients and their guardians for their participation in the neuroblastoma studies.

To my best friends I would like to express my special thanks for their strong backing, thanks a lot Jennifer, Sophie and Annika. I am deeply thankful to my loving family, Brigitte, Paul and especially my parents Sabine and Jürgen, thank you for your unlimited support every day of my life. I would also like to personally thank the whole Krienelke family for their very kind support, thank you Christa, Karl-Heinz, Eva, Burkhard, Tabea, Sascha and of course little Simon.

However, I am deeply thankful to my love Dominik for all the sacrifices he has made on my behalf the last years. Without him, this thesis would not have been possible!

Statement of authorship

I hereby certify that this dissertation has been composed by myself, and describes my own work, unless otherwise acknowledged in the text. All references and verbatim extracts have been quoted, and all sources of information have been specifically acknowledged. I also declare that I have not applied to be examined at any other institution, nor have I used the dissertation in this or any other form at any other institution as an examination paper, nor submitted it to any other faculty as a dissertation. This thesis has not been accepted in a previous doctoral procedure, nor has it been judged insufficient or was rejected.

Hiermit erkläre ich, dass ich diese Dissertation selbständig verfasst habe und keine anderen als die angegebenen Quellen und Hilfsmittel benutzt habe. Alle Stellen der Arbeit, die wörtlich oder sinngemäß aus Veröffentlichungen oder aus anderweitigen fremden Äußerungen entnommen wurden, sind als solche kenntlich gemacht. Ferner erkläre ich, dass ich weder einen Antrag auf Prüfung an einer anderen Institution gestellt habe, noch die Dissertation in dieser oder einer anderen Form an einer anderen Institution als Prüfungsarbeit verwendet oder an einer anderen Fakultät als Dissertation eingereicht habe. Diese Arbeit wurde nicht schon einmal in einem früheren Promotionsverfahren angenommen, noch wurde diese als ungenügend beurteilt oder abgelehnt.

Berlin, den 29.11.2020

Annabell Krienelke-Szymansky

"It is perfectly true, as the philosophers say, that life must be understood backwards.

But they forget the other proposition, that it must be lived forwards."

Søren Kierkegaard (1843)

The *MYCN* oncogene as a minimal residual disease marker and therapeutic target in neuroblastoma

Table of content

ACKNOWLEDGEMENTS **3**

STATEMENT OF AUTHORSHIP **5**

TABLE OF CONTENT **7**

LIST OF ACRONYMS **10**

1 INTRODUCTION **18**

1.1 NEUROBLASTOMA 18

1.1.1 The origin of the adrenal gland and rise of neuroblastomas *19*

1.1.2 Clinical presentation of neuroblastomas. *20*

1.1.3 Genetic characteristics of neuroblastomas *21*

1.1.4 The MYCN oncogene *22*

1.2 DIAGNOSTICS OF NEUROBLASTOMA 25

1.2.1 Current standard of diagnostics *25*

1.2.2 Risk stratification *27*

1.3 TARGETED SEQUENCING FOR NEUROBLASTOMA DIAGNOSTICS 30

1.3.1 Next generation sequencing for cancer diagnostics *30*

1.3.2 Targeted NGS panel sequencing for neuroblastoma diagnostics *32*

1.4 MINIMAL RESIDUAL DISEASE DETECTION OF NEUROBLASTOMA CELLS 33

1.4.1 An example of established MRD diagnostics: Leukemia *33*

1.4.2 Investigation of MRD occurrence in neuroblastoma *36*

1.5 TREATMENT OF NEUROBLASTOMA 37

1.5.1 Standard first-line multimodal therapy in neuroblastoma study protocols and treatment of relapsed neuroblastoma *37*

1.5.2 Conventional pharmacotherapy of high-risk neuroblastoma *39*

1.5.3 Clinically implemented targeted therapies for high-risk neuroblastomas *40*

1.6 NOVEL MOLECULARLY TREATMENTS AGAINST MYCN 41

1.6.1 Inhibition of MYCN transcription *43*

1.6.2 Targeting MYCN mRNA translation *46*

1.6.3 Preventing the oncogenic stabilization of the MYCN protein *47*

1.6.4 Blocking MYCN dimerization and transcriptional activity *51*

1.6.5 Targeting MYCN-driven cell proliferation through inhibition of mitotic spindle assembly *51*

1.7 MOTIVATION AND AIM OF THE THESIS 55

2 METHODS 57

2.1 ORIGIN OF BIOMATERIAL AND DATA 57
2.2 PATIENT MATERIAL PROCESSING 59
2.3 ANIMAL EXPERIMENTATION 60
2.4 GENERAL CELL CULTURE METHODS 61
2.5 CELL BIOLOGY METHODS 63
2.6 MOLECULAR BIOLOGY METHODS 84
2.7 BIOCHEMICAL METHODS 106
2.8 DNA SEQUENCING 109
2.9 ANALYSES OF WGS, TARGETED NGS AND MICROARRAY DATA 109
2.10 DATA PROCESSING AND ANALYSIS 114

3 RESULTS 122

3.1 DETECTION OF NEUROBLASTOMA-SPECIFIC MUTATIONS USING HYBRID CAPTURE-BASED PANEL NGS AND SENSITIVE MONITORING OF MINIMAL RESIDUAL TUMOR CELLS 122

3.1.1 Evaluation of a neuroblastoma hybrid capture-based NGS panel for risk assessment, treatment stratification and detection of MYCN amplicon breakpoints 122

3.1.2 Detection of minimal residual disease based on MYCN amplicon breakpoints and other neuroblastoma-relevant mutations 137

3.2 INFLUENCE OF THE MYCN REGULATORY NETWORK AND ITS TARGETED THERAPY 164

3.2.1 Monotherapy with BET inhibitors reduce neuroblastoma cell viability in vitro 164

3.2.2 PLK1 and PI3K dual inhibition shows therapeutic potential in high-risk neuroblastoma models 175

3.2.3 Combination of BRD4 and PLK1 inhibition has synergistic anti-tumoral effects in neuroblastoma cell lines 192

3.2.4 High expression of ASPM is related to an aggressive neuroblastoma 195

4 DISCUSSION 230

4.1 DETECTION OF NEUROBLASTOMA RELEVANT MUTATIONS USING A CUSTOMIZED HYBRID CAPTURE-BASED NGS PANEL AND SENSITIVE MONITORING OF MINIMAL RESIDUAL TUMOR CELLS 230

4.1.1 Mapping of the complex MYCN amplicon structure and its unique breakpoints using a neuroblastoma hybrid capture-based NGS panel 230

4.1.2 Quantitative and highly sensitive detection of neuroblastoma minimal residual disease based on MYCN amplicon breakpoints 237

4.1.3 Detection of other neuroblastoma-associated mutations using the NB targeted NGS assay and recovery with the neuroblastoma breakpoint PCR or ASQ-PCR MRD assay 242

4.1.4 The NB targeted NGS assay is preferred to WGS or WES sequencing and applicable for routine diagnostics of neuroblastoma 248

4.1.5 Utilizing latest MRD techniques to improve the detection of the neuroblastoma cells with the NB MYCN breakpoint MRD assay 251

4.1.6 Clinical implementation of the NB targeted NGS assay and the NB MYCN breakpoint assay into the routine diagnostics of the HR-NBL2/SIOPEN study ... 256

4.2 AIMING NEUROBLASTOMA AT THE "UNTARGETABLE" MYCN ONCOGENIC DRIVER ... 257

4.2.1 Targeting the transcription of MYCN using BET inhibitors ... 258

4.2.2 Preventing the oncogenic stabilization of the MYCN protein using kinase inhibitors ... 271

4.2.3 ASPM is a regulator of neuroblastoma cell proliferation and differentiation ... 279

5 CONCLUDING REMARKS ... 287

6 SUMMARIES ... 288

6.1 ZUSAMMENFASSUNG ... 288

6.2 ABSTRACT ... 290

7 LIST OF REFERENCES ... 291

8 PUBLICATIONS AND CONGRESS CONTRIBUTIONS ... 353

8.1 PUBLICATIONS ... 353

8.2 CONGRESS CONTRIBUTIONS ... 354

8.3 AWARDS AND SCHOLARSHIPS ... 357

9 CURRICULUM VITAE ... 358

10 APPENDIX ... 359

10.1 ADDITIONAL MATERIAL ... 359

10.2 LIST OF FIGURES ... 402

10.3 LIST OF TABLES ... 406

10.4 LIST OF MATERIALS ... 407

10.5 BUFFERS AND SOLUTIONS RECIPES ... 426

List of acronyms

For gene and protein names, the guidelines of the HGNC Guidelines | HUGO Gene Nomenclature Committee were followed (http://www.genenames.org/about/guidelines/).

°C	degree Celsius
%	percentage
♀	female
♂	male
α	alpha
β	beta
γ	gamma
Δ	delta, difference operator
λ	lambda, wavelength
µl	microliter
µg	microgram
µm	micrometer
µm²	square micrometer
µM	micromolar
^{99m}TC	technetium 99m
^{123}I-mIBG	^{123}-iodine-meta-iodobenzylguanidine scintigraphy
^{131}I-mIBG	^{131}-iodine-meta-iodobenzylguanidine therapy
7-AAD	7-amino-actinomycin D
A	adenine base
A	ampere
AB	antibody
ABTS	2,2'-azinobis [3-ethylbenzothiazoline-6-sulfonic acid]-diammonium salt
AG	adrenal gland
ALL	acute lymphoblastic leukemia
ALT	alternative telomere lengthening
alt-EJ	alternative end joining mechanism
AML	acute myeloid leukemia
ANOVA	analysis of variance
APC	allophycocyanin
ASCO	American Society of Clinical Oncology
ASCT	autologous stem cell transplantation
ASQ-PCR	allele-specific quantitative polymerase chain reaction
ATG	DNA translation initiation codon
ATP	adenosine triphosphate
ATRA	all-trans retinoic acid

ATRT	atypical teratoid rhabdoid tumors
AU	relative tumor volume
BAM	binary alignment map
BC	“buffy coat”, mononuclear cells of peripheral neuroblastoma-free blood pooled from at least ten healthy individuals
BCA	bicinchoninic acid
BD	bromodomain
BET	bromodomain and extraterminal domain proteins
BHQ1	Black Hole Quencher®-1
bit	binary digit
BM	bone marrow
bp	base pair
BR/HLH/LZ	basic region helix-loop-helix leucine zipper motif
BrdU	5-BrdU, 5-Bromo-1-(2-deoxy-β-D-ribofuranosyl)uracil
BSA	bovine serum album
BuMel	melphalan and buthionine sulfoximine
C	cytosine base
$CaCl_2$	calcium dichloride
CAM	chloramphenicol
CCD	charge-coupled device camera
cDNA	complimentary DNA
cen	centromeric direction
cfDNA	cell-free DNA
chr	chromosome
cm	centimeter
cm^3	cubic centimeter
CNS	central nervous system
CNV	copy number variation
CO_2	carbon dioxide
CR	clinical remission
CRISPR/Cas9	clustered regularly interspaced short palindromic repeats/ CRISPR-associated nuclease 9
C_T	threshold cycle
CT	computed tomography scan
CTC	circulating tumor cells
ctDNA	circulating tumor DNA
CTX	chemotherapy
DAPI	4′,6-diamidino-2-phenylindole
DEPC	diethyl dicarbonate
dH_2O	distilled water

ddH_2O	double-distilled water
ddPCR	droplet digital PCR
DM	DNA double minutes
DMEM	Dulbecco's Modified Eagle Medium
DMSO	dimethyl sulfoxide
dNTPs	deoxy-nucleoside triphosphates
DNA	deoxyribonucleic acid
DOD	death of disease
dpi	dots per inch
DPBS	Dulbecco's Phosphate-Buffered Saline
dsDNA	double stranded DNA
DTC	disseminated tumor cell
dUTP	2´-deoxyuridine, 5´-triphosphate
E1000	inhibition by the drug at a concentration of 1000nM in %
E-box	enhancer box element
EBRT	external photon beam radiation therapy
ecDNA	extrachromosomal DNA
EC50	half maximal effective concentration
E.coli	*Escherichia coli*
EDTA	ethylenediaminetetraacetic acid
EdU	5-ethynyl-2´-deoxyuridine
e.g.	exempli gratia (for example)
EGFP	enhanced green fluorescent protein
ELISA	enzyme-linked immunosorbent assay
Emax	maximal effect
EMT	epithelial-to-mesenchymal transition
et al.	et alii (and others)
EtOH	ethanol
FACS	fluorescence-activated cell sorting
FAM	6-carboxyfluorescein amidite
FCS	fetal calf serum
FFPE	formaldehyde-fixed paraffin-embedded tissue
FISH	fluorescence in situ hybridization
FITC	fluorescein isothiocyanate
FPN	FLAG-tag
FRA2C	common fragile site (chromosome 2)
g	gravity of earth = 9,807 m/s^2
g	gram
G	guanine base
G4	G-quadruplex

G418	Geneticin®
gDNA	genomic deoxyribonucleic acid
GD2	disialoganglioside
GFP	green fluorescent protein
GO	Gene Ontology
G-protein	GTP (guanosine triphosphate)-binding proteins
GPOH	Gesellschaft für pädiatrische Onkologie und Hämatologie
GRCh37/hg19 or 38	Genome Reference Consortium Human Build 37 or 38
Gy	gray
H3K27ac	acetylation of histone marker H3 lysine 27
h	hour
HA	homology arms
HCl	hydrochloric acid
HCV	hepatitis C virus
HDAC	histone deacetylases
HDR	homology-directed repair
H&E	hematoxylin and eosin stain
HeBS	HEPES-buffered saline
HEX	6-hexachloro-fluorescein
HR	high-risk
HPR	horseradish peroxidase
HSCT	hematopoietic stem cell transplantation
HSR	homogenously staining regions
HUGO	Human Genome Organisation
HVA	catecholamine homovanilic acid
IC50	half maximal inhibitory concentration
i.e.	id est (that is)
IF	immunofluorescence
Ig	immunoglobulin
IGV	Integrative Genomics Viewer
InDel	insertion or deletion of a base
INPC	International Neuroblastoma Pathology Classification System
INSS	International Neuroblastoma Staging System
INRG(SS)	International Neuroblastoma Risk Group (Staging System)
i.p.	intraperitoneal injection
kb	kilobase
kDa	kilodaltons
kg	kilogram
kV	kilovolt
l	liters

LB	lysogeny broth medium
LINE	long interspersed nuclear elements
LN	lymph node
log_{10}	decadic logarithm
LTR	long terminal repeat
M	month
M	mole
Mb	megabase
MCPH	autosomal recessive primary microcephaly
mCR	molecular complete remission
MEM	non-essential amino acid solution
mer	meros (part)
mg	milligram
$MgCl_2$	magnesium chloride
min	minute
miRNA	microRNA
ml	milliliter
mM	millimolar
MMBIR	microhomology-mediated break-induced replication
MMEJ	microhomology-mediated end joining
MNA	*MYCN*-amplified
MOI	multiplicity of infection
MP-PCR	mediator probe polymerase chain reaction
MRD	minimal residual disease
MRI	magnetic resonance imaging
mRNA	messenger RNA
ms	millisecond
MTOC	microtubule-organizing center
MW	molecular weight
NaOH	sodium hydroxide
NeoR	neomycin resistance
NB	neuroblastoma
NBL	neuroblastoma
NC	neural crest
NFQMGB	non-fluorescent quencher minor groove binder channel
NGS	next generation sequencing
NLS	nucleus localization sequence
nm	nanometer
nM	nanomolar
no	number

nonMNA	non-*MYCN*-amplified
NS3	viral nonstructural protein
NT	neural tube
NTC	no template control
NUT-midline carcinoma	nuclear protein in testis (NUT) midline carcinoma
OD	optical density
p	chromosome arm p (short)
P2A	2A self-cleaving peptide
PAM	protospacer adjacent motif
PBD	polo-box domain
PBMC	peripheral blood mononuclear cell
p.b.n.q.	positive, but not quantifiable
PBS	phosphate-buffered saline
PCM	pericentriolar material
PCR	polymerase chain reaction
PDX	patient derived xenograft
PFA	paraformaldehyde
pg	picogram
pH	negative decadic logarithm of the hydrogen ion concentration
PI	propidium iodide
pixel	physical point
pmol	picomole
PMT	photomultiplier tube
pN	piconewton
PROTAC	PROteolysis TArgeting Chimeras
P/S	penicillin/streptomycin
PVDF	polyvinylidene difluoride
q	chromosome arm q (long)
qPCR	quantitative polymerase chain reaction
R^2	coefficient of determination
RBD	RAS-binding domain
RLU	relative light units
Rn	fluorescence emission intensity of the reporter dye
RNA	ribonucleic acid
rpm	revolutions per minute
RPMI	Roswell Park Memorial Institute 1640 media
RQ-PCR	real-time quantitative polymerase chain reaction
RSS	recombination signal sequences
RT	room temperature (~22°C)
RT-qPCR	reverse transcription quantitative polymerase chain reaction

RTK	receptor tyrosine kinase
s	second
SDS-PAGE	sodium dodecyl sulfate polyacrylamide gel electrophoresis
SEQC	Sequencing Quality Control consortium
sgRNA	single guide RNA
SINE	short interspersed nuclear elements
siRNA	small interfering RNA
SIOPEN	European association involved in the research and care of children with neuroblastoma
shRNA	short hairpin RNA
SMASh	small-molecule-associated shutoff Tag
SNP	single-nucleotide polymorphism
SNV	single-nucleotide variations
SOB	Super Optimal broth
SOC	Super Optimal broth with catabolites repression
SPECT	single-photon emission computed tomography scan
STR	short tandem repeat
t	translocation
T	thymidine base
T_a	annealing temperature
T_m	Melting temperature
Taq (pol)	*Thermus aquaticus* (polymerase)
TAG	DNA translation termination codon
TaqMAMA	allele-specific polymerase chain reaction-based and mismatch amplification mutation assay
TBS(-T)	phosphate-buffered saline (with Tween)
TCR	T-cell receptor
TE	tris-EDTA buffer
tel	telomeric direction
TREC	T-cell receptor excision circles
TRITC	tetramethylrhodamine
TU	transduction units
U	unit
U	uracil base
UAG	RNA translation termination codon
UHR	ultra-high-risk patients with a neuroblastoma
USD ($)	US-Dollar
UTR	untranslated region
UV	ultraviolet
V	volt

VDJ	V (variable), D (diversity) and J (joining) segments
VMA	catecholamine vanillylmandelic acid
VOD	veno-occlusive disease
WES	whole-exome sequencing
WGS	whole-genome sequencing
wt	wildtype
X-ray	X-radiation
Y	year

1 Introduction

1.1 Neuroblastoma

Neuroblastoma (NB) is the most common extracranial and deadliest solid childhood tumor, which arises from the embryonic neural crest and affects the entire developing sympathetic nervous system. Most neuroblastoma cells accumulate in the abdomen along the sympathetic nerve cord and in the medullary region of the adrenal glands, which are located on the upper pole of the kidney (Figure 1)[1–3]. The primary tumor can also appear in other parts of the body, including the chest, head and neck, and the pelvis[4]. The first description of a tumor mass in the adrenal gland found in a child can be attributed to the German physician Rudolf Virchow in 1864[5]. In 1910, the pathologist James Homer Wright introduced the term neuroblastoma[6,7]. The tumor occurs predominantly in younger children, with a median age of 18 months at diagnosis[8]. According to the German Childhood Cancer Registry, about 166 children under 15 years are newly diagnosed with neuroblastoma in Germany every year (based on data from 1980-2017)[9]. Neuroblastoma accounts for 6-10% of all childhood cancers worldwide[10,11], with a 6.6% relative frequency in Germany[9]. Moreover, neuroblastoma is a very deadly tumor, which is responsible for 12-15% of the deaths of children with cancer[10,11]. The current classification divides the patients with a neuroblastoma into low, medium and high risk group. Neuroblastoma is charatarized by a clinical dichotomy. While about half the newly diagnosed cases require little to no treatment including cases with spontaneous regression, the other half are diagnosed with a high-risk disease with cure rates under 40% despite aggressive multimodal therapy[1,12]. A patient subgroup with particularly poor outcome was also identified among the high-risk group with only 10-15% five-year event-free survival, which represents the group of ultra-high-risk (UHR) patients[13]. Approximately 50% of patients with high-risk disease relapse, and 80% of relapses occur within two years of the initial diagnosis[14].

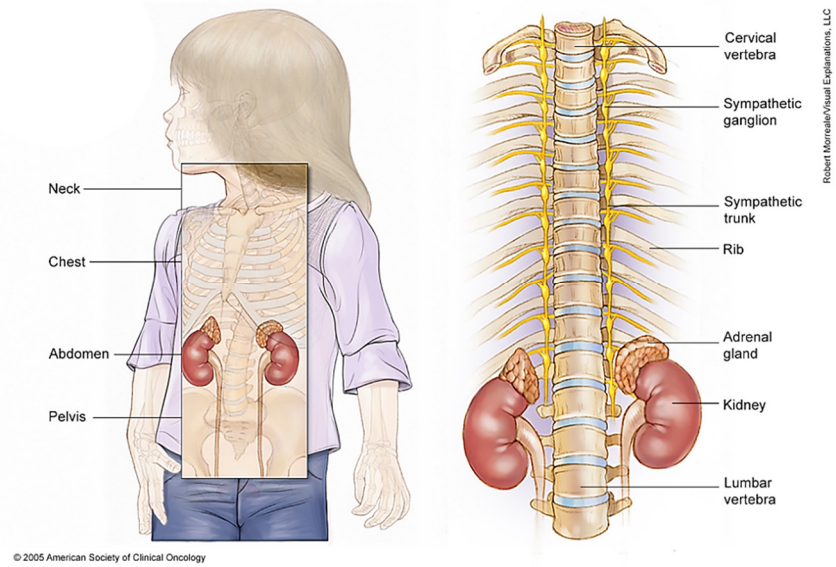

Figure 1: The primary distribution of neuroblastomas in children.
Childhood neuroblastoma affects the sympathetic nervous system and primary tumors mostly appear in the medullary region of the adrenal glands. (Figure taken from the American Society of Clinical Oncology (ASCO)[15].)

1.1.1 The origin of the adrenal gland and rise of neuroblastomas

Neuroblastoma originates from a pathogenesis of the embryonic neural crest. After gastrulation of the embryo, the neural tube emerges from the ectoderm (the outer cotyledon) tissue[16]. A part of the ectoderm differentiates into the neuroectoderm (neural plate), forming a fold (neural groove) and leading to a fusion of the two neural folds at the edge of the neural plate (neural crest)[16]. After the closure of the neural tube is completed, the neural crest separates from the epidermis and the neural crest cells undergo an epithelial-to-mesenchymal transition (EMT)[17]. This complex transformation is driven by external (homing) signals, changes in intracellular transcriptional programs and epigenetic processes[18]. The cellular maturation causes the neural crest cells to delaminate from its origin, to migrate and to differentiate in different distant locations in groups or individually on predetermined pathways (Figure 2). Neural crest cells of the body trunk area of the embryo migrate ventrolateral towards the dorsal aorta initiated by transcription factor expression of SOX10 and FOXD3[17,19]. Here, most of the neural crest cells differentiate into sympathetic progenitor cells following the development into the sympathetic neurons. A small group of neural crest cells migrate further ventrally towards the midline and represent the adrenal chromaffin progenitors which then differentiate into chromaffin cells of the medulla of the adrenal gland[17,20]. The neural programming of the crest cells is caused by expression of ASCL1 or PHOX2B in the beginning, and later by HAND2 or GATA3[19]. A recent study further highlights that neural crest cell derived peripheral glial stem cells, called Schwann cell precursor cells, can also develop into chromaffin cells[21]. These Schwann cells precursors migrate from the dorsal root ganglion on the preganglionic nerve which innervates the adrenal medulla and give rise to a large majority of chromaffin cells. Neuroendocrine chromaffin cells express specific enzymes for catecholamine biosynthesis (tyrosine hydroxylase (TH), dopamine-beta-hydroxylase (DBH) and phenylethanolamine N-methyltransferase (PNMT)), which enable the release of the hormones adrenaline, noradrenaline and dopamine[19,22–25]. The ventral migration and further expansion of neural crest cells is controlled by the expression of the proto-oncogene *MYCN* (V-MYC Avian Myelocytomatosis viral-related oncogene, neuroblastoma-derived)[22,26,27]. Protein levels of MYCN are decreasing with progressive differentiation of the cells. However, defective neural crest cells can give rise to a neuroblastoma. Mutations of the transcription factors and other key players in the neuronal programming networks can contribute to uncontrolled proliferation, inhibition of differentiation and drive tumorigenesis in general. A possible crucial initial event is an amplification of the *MYCN* gene[22]. In addition, the distinctive origin of neuroblastoma cells, developing from neural crest cells or Schwann cell progenitors, indicates the emergence of a heterogeneous disease. Recent reports could already demonstrate that a neuroblastoma can be composed of two different tumor cell types with different traits (adrenergic-like and mesenchymal-like differentiation state)[28,29]. However, there are still many unknown aspects of the cellular origin of neuroblastomas that need to be clarified.

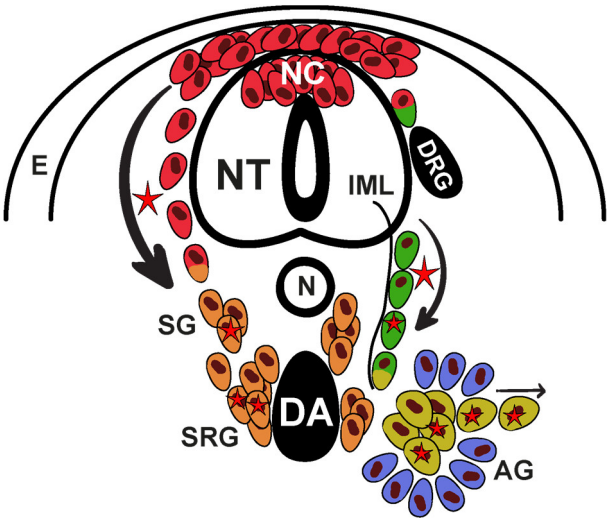

Figure 2: Embryonic development of the sympathoadrenal system and model of neuroblastoma initiation.
Two precursor cell types generate the sympathoadrenal system. First, neural crest (NC) cells (red) are delaminating from the neural tube (NT) and are migrating ventrally passing the notocord (N) towards the dorsal aorta (DA) to become sympathoblasts and glial cells (orange). Second, multipotent Schwann cell precursors (green) migrate from the dorsal root ganglion (DRG) to the adrenal gland (AG) and develop into chromaffin cells (yellow). During the migration, proliferation and maturation of the cells, genetic mutations can trigger the pathogenesis of the neuroblasts and can lead to the development of a neuroblastoma. (E: ectoderm; IML: intermediolateral nucleus, SG: sympathetic ganglion, SRG: suprarenal ganglion; figure modified from Kastriti et al. 2020[19]).

1.1.2 Clinical presentation of neuroblastomas

Neuroblastomas show a broad spectrum of symptoms and varied tumor spread, which is why the disease can progress very differently. In general it was found that 26% of the patients had a poor overall condition, 28% suffered from pain, 22% had a fever and 18% had swelling at the primary tumor site (German NB97 trial)[30]. The cancer can roughly be divided into three different groups based on their contrasting biology: First, a regressive subtype which can occur at different (distant) sites in the patient, lacking molecular tumor markers, but demonstrating a rapid progression and a fast regression within hours or days[31]. The survival outcome for these patients is about 80-85%. Second, a maturative subtype exists, which may show tumor markers. The disease is localized in the abdomen and absent of metastases. It matures on its own, is usually detected retrospectively and demonstrates a very good survival outcome[31]. Finally, there is the progressive subtype, which can exhibit tumor markers and exhibit a worsening progression of the disease. In addition, metastases may be present in especially severe (high-risk) cases. These patients receive extensive therapy, but the survival outcome is still very low at around 20-30%[31]. The symptoms of neuroblastoma indicate the primary tumor localization and possible metastases. Primary sites for the occurrence are the sympathetic ganglia or paraganglia along the sympathetic paravertebral chain[32]. The site of origin is predominantly the adrenal gland. In 90% of the patients with metastases the primary site is located in the abdomen. In high-risk patients, metastases are often found in the bone marrow (BM), bone or lymph nodes. These patients are already severely ill at the time of diagnosis, presenting with pallor, belly pain, fever and weight loss[33]. They show various symptoms in connection with an extended primary tumor mass or (several) metastases (e.g. bilateral

periorbital ecchymosis, spinal cord compression, disorders of neurological functions, opsomyoclonus-ataxia syndrome, Horner's syndrome, treatment resistant diarrhea, hypertension, enlarged lymph nodes, bone pain, limping or bone marrow failure)[1].

1.1.3 Genetic characteristics of neuroblastomas

In addition to the very heterogeneous phenotype, neuroblastoma also displays heterogeneous genetics, which has a major influence on the survival of the patient. The consensus opinion is that neuroblastomas being caused less by the inheritance of a single gene mutation than by sporadic development of somatic mutations. Only about 1-2% of all cases of neuroblastoma diseases are based on a familial inheritance of genetic predispositions[33]. However, these mutations show an incomplete penetrance, which is why there do exist carriers of mutations that are not affected by the disease[34,35]. Germline mutations are present in neuronal developmental genes, such as single-nucleotide variations (SNV) in the *PHOX2B* or the anaplastic lymphoma kinase (*ALK*) gene[36,37]. *ALK* encodes for a cell-surface receptor tyrosine kinase (RTK). The most frequently found *ALK* mutation is a change in a amino acid (R1275Q)[34,37]. The majority of neuroblastomas are not inherited by the patients family, but are associated with somatic, acquired mutations. The sporadically developing neuroblastoma is characterized by extensive genetic aberrations, such as gains or amplifications or by hemizygous deletions. It was found that the ploidy state (tumor-cell DNA, deoxyribonucleic acid, index) in particular is connected to the clinical presentation of the heterogeneity of neuroblastomas[38]. Low or intermediate risk neuroblastomas have been shown to be prone to defects in the mitosis process, which leads to entire chromosome (chr.) gains or losses[8]. High-risk neuroblastomas, on the other hand, have rather fundamental defects in genome stability which can then lead to chromosomal rearrangements[8]. This is why the occurrence of large structural chromosomal aberrations is a common finding in neuroblastoma, including losses of the chromosome arms 1p, 3p, 4p, 6p 11q and gains of 1q, 2p, 7q, 11p and 17q[25,39,40]. A gain of the large 17q chromosome arm is the most frequent type of chromosomal abnormalities, which occurs in approximately 47% of all neuroblastomas[41]. Losses of 1p and 11q are the second most common abnormality and are identified in 20-30% of all cases. Furthermore, large rearrangements within specific chromosomal regions are critical for the development of neuroblastoma. Particularly recurrent genomic rearrangements that occur within the chr.2p arm (where the *MYCN* and *ALK* genes are located), the chr.5p arm (location of the *TERT* gene) and the chr.Xq arm (location of the *ATRX* gene) are the involved in tumorigenesis of neuroblastoma. Accordingly, the most frequent chromsomal aberration involving a particular gene is an amplification of the *MYCN* gene, occurring in approximately 25% of all neuroblastomas (see for details 1.1.4)[6,18,42]. The appearance of genomic rearrangements in *TERT,* (which encodes for the telomerase reverse transcriptase), is the second most common mutation in neuroblastoma, found in about 12.9% of all cases[43,44]. Similarly with regard to *MYCN* and *TERT*, it can be shown that a rearrangement event frequently occurs in the *ATRX* gene in neuroblastomas (focal deletions are in around 7.1% of all cases detected)[45]. Prognostically, especially tumors with an advanced

disease exhibit comparable patterns of chromosomal segmentations. For example, the combination of a 17q gain with a 1p loss or a solitary 11q loss correlates with *MYCN* amplification, which is connected with a poor prognosis[46]. Somatic mutations, which are limited only to single genes (e.g. caused by an SNV), are a rather rare find in primary neuroblastoma deep-sequencing studies. They are located in the genes *ALK* (~9.2% of all cases; displaying three major mutations within this group: R1275 (43%), F1174 (30%), and F1245 (12%))[47–52], *PTPN11* (~2.9%, 7 variants)[45], *ATRX* (~2.5%, 6 variants)[45], *MYCN* (~1.7%, P44L)[45], *TP53* (tumor suppressor, ~2%, P219S)[53] and *NRAS* (0.83%, 2 variants)[45]. Mutations that are restrained to individual genes become more frequent in the event of a recurrence. These include, for example, mutations in the *TP53*, *CHD5*, *DOCK8*, *PTPN14* and *YAP* gene and for RAS-MAP kinase pathway mutations, e.g. in the associated *ALK* gene[54–57]. Neuroblastoma tumorigenesis is therefore most likely triggered by broad chromosomal rearrangements and does usually not involve single mutations in common oncogenes. While several pathogenic alterations can be detected in one neuroblastoma tumor, whereby *MYCN* amplifications, *TERT* rearrangements and *ATRX* mutations have been found mutually exclusive at a tumor site[43,45,58]. However, apart from an amplification in the *MYCN* gene, the driver genes for the majority of neuroblastomas are unknown at present. It is currently assumed that a combination of *MYCN/TERT/ATRX* alterations, segmental chromosomal aberrations, telomere lengthening, RAS/p53 pathway alterations and changed gene expressions result in an unfavorable tumor biology[44].

1.1.4 The *MYCN* oncogene

MYCN, a gene of the *MYC* family of cellular oncogenes, is the most commonly amplified gene found in pediatric cancer[59]. Approximately 25% of all neuroblastomas show an amplification of the *MYCN* oncogene on chromosome band 2p24-25, and this alteration is also stable over the course of the disease and in relapse[6,18,42,60]. An amplification of *MYCN* is associated with a high-risk disease and a poor outcome, which is further reflected by an accumulation of *MYCN* amplifications by up to 40-50% among the high-risk neuroblastoma group[18,61,62]. The *MYCN* gene and its amplification was first discovered and described in 1983[63,64]. A correlation of the *MYCN* gene amplification with an advanced disease stage was stated by Brodeur et al a year later.[65] *MYCN* is located on the p arm of chromosome 2 in the region of the chromosome band 2p24.3 (exact genomic location: chr2:16,080,683-16,087,129 (genome version GRCh37/hg19)[66], see Figure 3). The non-amplified gene is 6,447 bp (base pair) long and consists of 3 exons, of which 2 exons code for the MYCN protein[67]. An amplification of the *MYCN* gene copy number is defined as a > 4-fold increase of *MYCN* signals (in relation to the number of reference signals on chromosome 2; for example detected using the DNA fluorescence in situ hybridization technique (FISH)), whereas a 1.5- to 4-fold higher signal is defined as a *MYCN* copy number gain[68–70]. Pathological amplifications of the *MYCN* gene in tumor samples were reported with a copy number of up to 700 times higher than normal[64,65,71]. The *MYCN* amplicon in neuroblastoma can be present on 2p in chromosomal homogenously staining regions (HSR) as a “self-repeating array”, as well as in circular extrachromosomal DNA double minutes (ecDNA, alias DM) as a “rolling circle amplification”[72–74].

The structure of these DMs can be highly variable, with few to complex differences compared to the reference chromosome sequence[75,76]. DMs can promote oncogenic remodeling by reintegration into the linear genome, and can also reassemble carried enhancers into the *MYCN* amplicon to the proximity of the promotor (enhancer hijacking)[74,77]. Further, it was found that neuroblastoma-specific noradrenergic core regulatory circuit enhancers contribute to the formation of the *MYCN* amplicon structure and lead to MYCN overexpression[28]. The DNA sequence pattern of the *MYCN* amplicon is modelled by chromosomal rearrangements and reintegrated extrachromosomal material which can result from mitotic segregation errors. One mechanism following such a catastrophic event is chromothripsis, which is characterized by massive clustered chromosomal rearrangements, occurring in multiple chromosomes or in specific chromosomal regions[78]. Several research groups have already demonstrated that neuroblastoma genomes show traces of chromothripsis[79–81]. In addition, chromosome bridges (as an event which promotes rearrangements) can emerge from DNA breakage, telomere crisis, incomplete DNA replication or failed chromosome condenstation[82,83]. Several cycles of breakage-fusion-bridges during subsequent mitoses than initiate gene amplification[83,84]. The resulting double strand breaks are rejoined by repair mechanisms of the cell. However, the exact type of repair mechanism is not exactly clarified so far. It is supposed that the alternative end joining mechanism (alt-EJ), also known as microhomology-mediated end joining (MMEJ)[85,86], plays a role in the repair of *MYCN* double strand breaks[87,88]. A different assumption is based on the microhomology-mediated break-induced replication (MMBIR) mechanism[89]. Both repair mechanisms create nucleotide "scars" at the junction site of the DNA strands in the chromosome, so-called (junctional) microhomologies[79]. These short DNA sequences are identical in each of the genomic segments involved in the rearrangement, therefore it is not possible to assign the exact breakpoint location within the junction site or the origin of nucleotides to a specific segment[85]. These mechanisms give rise to a very high intertumoral variability of the DNA sequence and the copy number of the *MYCN* amplicon. Thus, the size of the *MYCN* amplicon can be variable starting from 350kb (kilobase) up to 8Mb (megabase)[90,91]. In 1996, Reiter and Brodeur identified a common 130kb core region of the *MYCN* amplicon found in 32 neuroblastoma samples[92]. A co-amplification of *MYCN* and the upstream located *DDX1* gene was found in 50-70% of neuroblastomas, but not in all *MYCN*-amplified neuroblastomas[93–98]. The *DDX1* gene was therefore defined as an extension of the *MYCN* amplification, which is situated 340-400kb upstream of the 5' region of *MYCN* and external of the core amplification domain or located on DMs[97,99–106]. Like *DDX1*, the *NBAS* gene is also involved in the *MYCN* amplicon and rearrangements of the oncogene[101,107,108]. Even the neuroblastoma-relevant *ALK* gene, which is located 13.2Mb downstream of the *MYCN* gene, can be co-amplified with the *MYCN* amplicon in around 2% of all cases[109,110]. However, it is assumed that the *MYCN* gene is the primary target of genomic amplification, since all investigated amplicons containing other genes always contain *MYCN*[101]. It is therefore believed that the growth advantage of the *MYCN*-amplified cells constitutes a clonal selection benefit of chr.2p amplifications.

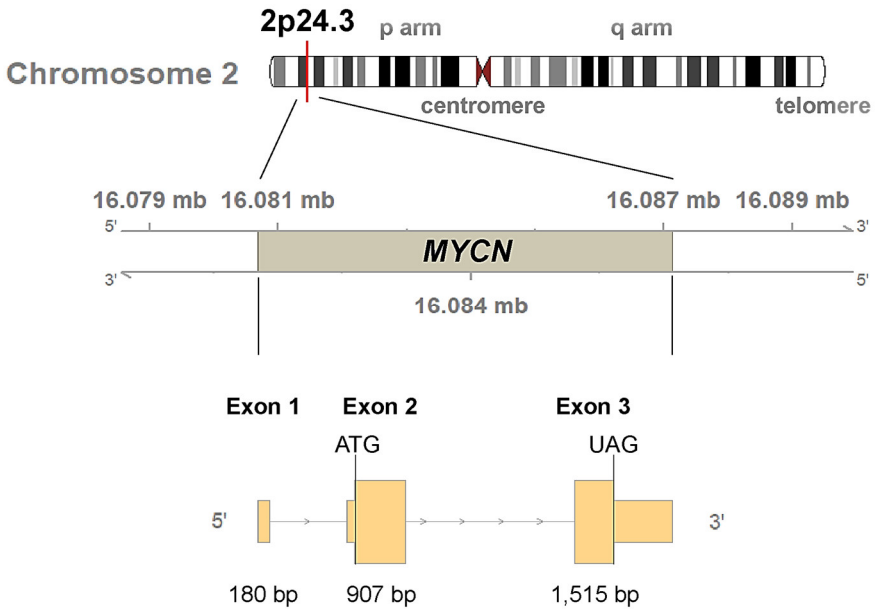

Figure 3: Genomic location and transcript structure of the *MYCN* oncogene.
The *MYCN* oncogene is located on the p-arm of chromosome 2 within the 24.3 chromosomal band. The 6,447bp long gene is positioned on the plus strand at chr2:16,080,683-16,087,129 (genome version GRCh37/hg19) and consists of 3 exons, of which exon 2 and 3 encode for the MYCN protein. The nucleotide codon ATG represents the translation initiation site, whereas UAG is the translation termination site.

The regular, undamaged *MYCN* gene transcript has a length of 2.602bp, the encoded protein has a size of 464 amino acids. MYCN functions as a transcription factor that promotes cell proliferation, cell growth, vasculogenesis, metastasis, genomic instability and inhibits cell differentiation and cell adhesion[111]. The protein is localized in the cell nucleus and has two different regions: an amino-terminal transactivation domain, and a carboxyl-terminal basic region helix-loop-helix leucine zipper motif (BR/HLH/LZ)[112].To regulate the transcriptional activity of it's downstream targets, MYCN requires the binding to the MAX protein, the MYC-associated factor X. MYCN and MAX establish a connection via their BR/HLH/LZ domains[113,114]. A MYCN-MAX protein heterodimer activates the transcription by binding to strong canonical DNA E-box elements (enhancer box, CACGTG)[111]. MYCN-MAX complexes are increasingly found in proliferating cells[115], whereas a loss of MYCN leads to a global reduction of transcription[116]. In combination with the transcription factors TWIST1, PHOX2B GATA3 and HAND2, MYCN is co-occupying enhancer, defining a sympathetic noradrenergic cell identity[28,116–119]. Finally, the orchestration of the enhancer dysregulation leads to pathogenic "MYC target gene signatures"[116]. A genomic alteration and/or overexpression of the MYCN protein therefore already drives neuroblastoma development in the early stages of the sympathetic nervous system and leads to a poorer prognosis for the patient's outcome[28]. Moreover, MYCN promotes the emergence of metastases by enhancing cell adhesion, motility and invasion and supports the degradation of surrounding matrices[6]. Interestingly, elevated MYCN protein levels are not absolutely correlated with the copy numbers of the amplified *MYCN* gene[120–122]. An increased *MYCN* expression promoting tumorigenesis was also found e.g. in other pediatric tumors of the nervous system, e.g. in medulloblastoma or retinoblastoma[123]. In contrast, non-*MYCN*-amplified neuroblastomas (as well as other cancers entities) can compensate a lack

of high *MYCN* gene expression by a high *c-MYC* expression, which is found in ~0.05-8% of all cases[124]. Similar to *MYCN*, genomic rearrangement events modify the structure of the genomic neighborhood of the *c-MYC* gene, including enhancer hijacking or upregulation by focal enhancer amplification[74,124,125].

1.2 Diagnostics of neuroblastoma

For the diagnosis of a neuroblastoma, clinical criteria are important, but also molecular genetic analyses of relevant mutations, have been implemented for years. Risk assessment and therapy stratification are currently only evaluated at the single time point of initial and relapse diagnosis. An amplification of the *MYCN* gene being an independent prognostic indicator of high-risk disease was already recognized decades ago[63,126]. As genetic investigation methods and sequencing techniques have improved, additional mutations related to neuroblastoma have recently been discovered in comprehensive research studies[43,44].

1.2.1 Current standard of diagnostics

Children with serious symptoms can be presented by their parents to a pediatrician, an internist or an emergency room. After a physical examination, multiple techniques are applied to diagnose a neuroblastoma and its spread. The neck, mediastinum and abdomen are inspected with ultrasound imaging[30]. Further, an X-ray examination of the chest and more advanced methods such as contrast-enhanced magnetic resonance imaging (MRI, see Figure 4A) and ^{123}-iodine-meta-iodobenzylguanidine scintigraphy (^{123}I-mIBG) with or without single-photon emission computed tomography (SPECT), are usually performed. Neuroblastomas can produce catecholamine and the radioactive tracer mIBG is chemically related to the body's own catecholamine. Therefore, the mIBG typically accumulates in tumors that produce catecholamine. Particular attention within imaging is paid to the lymph nodes for possible metastasis, as well as the head and neck, which may show a tumor manifestation or skull-based metastases. A neurological examination is performed to identify for example paraspinal masses and other neurological impairments. Blood tests are conducted to detect elevated levels of neuron-specific enolase (NSE) and lactate dehydrogenase (LDH) levels as clinical tumor markers. A urine sample will also be taken to detect an increase in catecholamine vanillylmandelic and homovanilic acids (VMA and HVA). In addition, a mandatory open tumor biopsy is performed at the time of diagnosis. However, in many high-risk neuroblastoma cases this biopsy has to be delayed, as an unfavorable tumor location prevents surgery. After surgery, tumor touch preparations are produced, which are used to detect a *MYCN* amplification utilizing cytology and FISH methods (see Figure 4B)[68–70]. The results of the FISH analysis must be confirmed by an independent method (usually qPCR, quantitative polymerase chain reaction). If a patient with neuroblastoma relapses, the *MYCN* status is re-checked. The tumor pieces are preserved in formalin and are histologically examined (using the International Neuroblastoma Pathology Classification System (INPC)). It is highly recommended that the tumor be subjected to an in-depth

molecular genetic analysis. These analyses are implemented in the new upcoming High-Risk Neuroblastoma Study 2 of SIOP-Europa-Neuroblastoma (SIOPEN) protocol (HR-NBL2)[52]. Genomes and expression profiles of DNA and RNA (ribonucleic acid) isolated from formalin-fixed tumor material or snap-frozen material taken at diagnosis will be tested. In addition, the bone marrow is examined for tumor cell infiltration. The distribution and severity of neuroblastoma cells within the bone marrow is roughly estimated using ^{123}I-mIBG. Imaging-based localization of the cells can reveal spotty marrow involvement or substitute bone marrow biopsies in non-accessible areas. A bone marrow sampling must be performed at several puncture sites. Either four bone marrow aspirates or two aspirates and two needle biopsies are required to assess bone marrow involvement[127]. Bone marrow aspirates are obtained with an aspirate needle, which is advanced through the bony cortex to the bone cavity of the iliac crest. The aspirate is withdrawn and collected directly into EDTA-anticoagulated (ethylenediaminetetraacetic acid) tubes. The bone marrow is then smeared on glass slides and subjected to a transmitted light microscopic cytological examination (see Figure 4C). In this analysis, the total number of cells examined is compared to the number of suspicious cells. Moreover, the bone marrow is screened for neuroblastoma cells using an anti-GD2 (disialoganglioside) immunocytology stain. Neuroblastoma cells are found single or accumulated in so-called "nests" in the bone marrow. The tumor cells are usually situated in a rosette ring around a nucleus of neuropil, a neuron felt consisting of dendrites, axons and glial extensions. In the new HR-NBL2 study, the prognostic and predictive value of DNA, mRNA (messenger RNA) and miRNAs (microRNA) in bone marrow and blood samples will be investigated at diagnosis and throughout the disease course respectively[52].

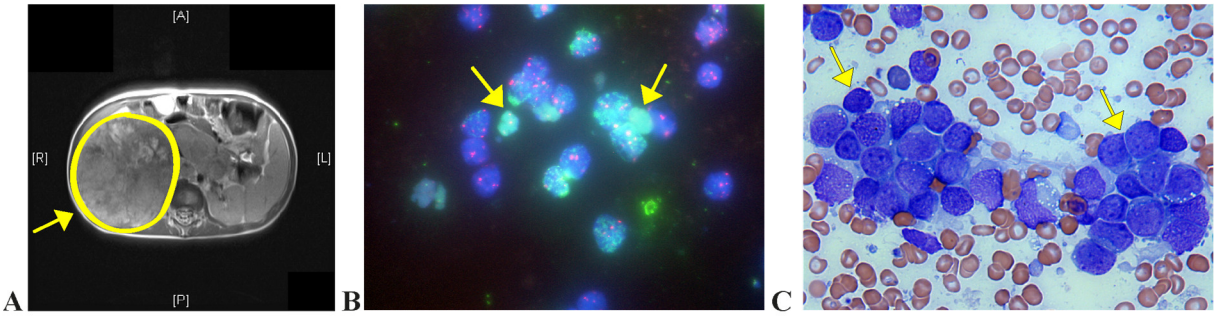

Figure 4: Diagnostic identification of a neuroblastoma.
Exemplary results of diagnostic examination according to current neuroblastoma study standards (GPOH guidelines Simon et al. 2017[30]) prior therapeutic intervention. **(A)** MRI cross section of a 1.4-year-old patient. The image is showing a large encapsulated neuroblastoma mass in the right upper abdomen that exceeds almost the middle line (indicated by yellow arrow and circle; R = right, L = left, A = anterior, P = posterior). **(B)** Microscopic image of FISH method detected tumor cells with positive *MYCN* amplification (green color, indicated by yellow arrows; CEP2 chromosome enumeration control is confirmed by red color). **(C)** Microscopic detection of neuroblastoma cells in smear of bone marrow aspirate. The tumor cells are clustered in two nests (indicated by yellow arrows) connected by neuropil, which indicates a possible feature of cellular differentiation.

1.2.2 Risk stratification

The current classification of neuroblastomas is based on the International Neuroblastoma Stagging System (INSS), which was first proposed in 1988 by Brodeur et al.[128]. This system is applied for diagnoses that are carried out in Germany. It divides patients into low, intermediate and high risk groups by clinical and biological appearance. The criteria include the age of the patient at diagnosis, the spread of the disease, the resectability of the tumor and the aggressiveness of the tumor. The risk groups are divided numerically into 1-4, whereby stage 4 represents the group of high-risk neuroblastomas (see Table 1). Neuroblastomas that show a regressive biology are categorized in a separate group, the 4S (S = special). This group is defined by the age at diagnosis under one year with a localized tumor and metastases limited to the organs liver, skin and bone marrow (with < 10% infiltration of bone marrow). These tumors disappear spontaneously, if at all require minimal therapy, and have a very good prognosis[129]. In about 10.6% of neuroblastomas, a 4S type tumor is found and usually only needs to be observed[42]. Low-risk neuroblastomas, which are classified as stage 1 according to the INSS, have no bone marrow involvement or affected lymph nodes, they are large resected and localized, and exhibit a good outcome[130]. The findings of Zhang et al. show that a stage 1 type is found in about 24.3% of all neuroblastomas[42]. Patients with low-risk stage 2 (A+B) neuroblastomas represent about 15.7% of all cases and have a localized tumor without metastases[42]. Intermediate-risk patients with stage 3 neuroblastoma have a localized tumor that can also be extended to lymph nodes, as the INSS reports. These cases represent about 12.7% of all neuroblastomas[42]. The stage 4 high-risk group of neuroblastomas show advanced tumor progression and distant metastases. These represent the largest group of the INSS-classified types with 36.7% of all attributed cases[42]. In contrast to other tumor entities, low-risk stage 1 neuroblastomas (and relapsed low-risk neuroblastomas) do not exhibit a progression into stage 4 high-risk neuroblastomas[123].

However, the specification of INSS staging is limited, mainly because it focuses on clinical appearances and is based on the surgical removal of the tumor to define stages 1-3. The extent of tumor removal depends strongly on the individual surgeon, and low-risk tumors in particular are rarely removed surgically[30]. Therefore, the International Neuroblastoma Risk Group (INRG) has developed a new staging system in 2009, which translates these surgical evaluations into image-defined risk factors[131–133]. The INRG stating distinguishes between localized tumors without (L1) and with (L2) additional image-defined risk factors, a stage M for metastatic disease and stage MS for metastases restricted to skin, liver and limited bone marrow infiltration (in children with less than 18 months at diagnosis; see Table 1). Moreover, the INRG takes into account other criteria such as tumor histology, grade of cell differentiation and molecular genetic markers. Molecular critera of hazard risk are deletions of chromosome arms 1p, 3p, 4p and 11q, or gains of 1q, 2p or 17q, *MYCN* amplification, *TERT* aberration, *ATRX* deletion or *ALK* SNVs.

Table 1: International Neuroblastoma Staging System (INSS)[129] and International Neuroblastoma Risk Group Staging System (INRGSS)[131].

INSS		INRGSS	
Stage	**Description**	**Stage**	**Description**
1	Localised tumor with complete gross excision, with or without microscopic residual disease; representative ipsilateral lymph nodes negative for tumour microscopically (nodes attached to and removed with the primary tumor could be positive)	**L1**	Localised tumor not involving vital structures as defined by the list of image-defined risk factors and confined to one body compartment
2A	Localised tumor with incomplete gross excision; representative ipsilateral non-adherent lymph nodes negative for tumor microscopically	**L2**	Locoregional tumor with presence of one or more image defined risk factors
2B	Localised tumor with or without complete gross excision, with ipsilateral non-adherent lymph nodes positive for tumor. Enlarged contralateral lymph nodes should be negative microscopically		
3	Unresectable unilateral tumor infiltrating across the midline, with or without regional lymph node involvement; or localised unilateral tumor with contralateral regional lymph node involvement; or midline tumor with bilateral extension by infiltration (unresectable) or by lymph node involvement		
4	Any primary tumor with dissemination to distant lymph nodes, bone, bone marrow, liver, skin, or other organs (except as defined by stage 4S)	**M**	Distant metastatic disease (except MS)
4S	Localised primary tumor in infants younger than 1 year (as defined for stage 1, 2A, or 2B), with dissemination limited to skin, liver, or bone marrow (<10% malignant cells)	**MS**	Metastatic disease in a child under 18 moths, with metastases confined to skin, liver and/or bone marrow

The table is modified after Simon et al. 2017 [30]

In current German study protocols, the GPOH Guidelines for Diagnosis and Treatment of Patients with Neuroblastic tumors (2017) and the associated neuroblastoma registry study (NB Registry 2016), as well as in the previous NB2004 study (Trial Protocol for Risk Adapted Treatment of Children with Neuroblastoma), a stratification of the risk groups into low-risk, intermediate-risk and high-risk was defined (see Figure 6)[30,134,135].

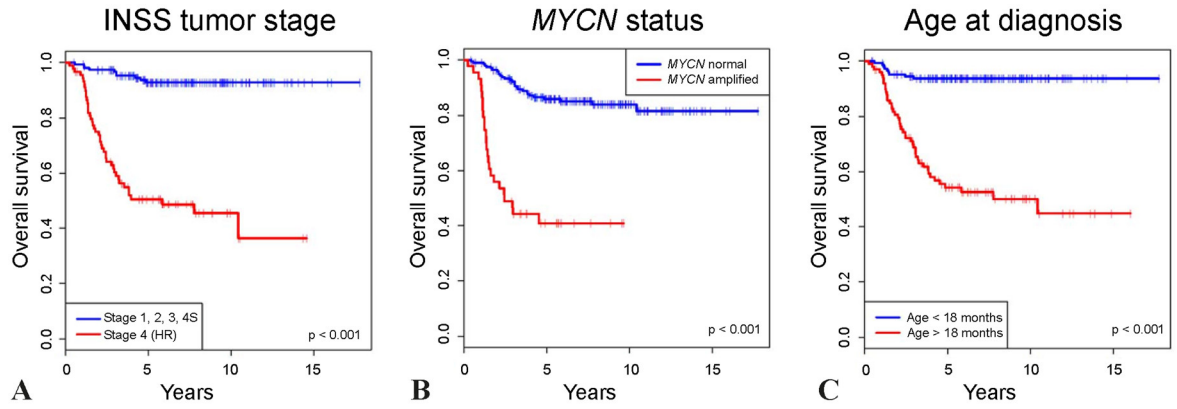

Figure 5: Kaplan-Meier overall survival estimates of patients with neuroblastoma according to INSS stage, *MYCN* status and age.
Classification of high-risk neuroblastomas according to clinical risk factors. Assignment of the patient with neuroblastoma to the INSS stage 4, a *MYCN* amplification and an age above 18 months correlates with a lower overall survival probability. Survival curves according to the **(A)** INSS tumor stage (blue, stages 1, 2, 3, 4S; red, stage 4), the **(B)** *MYCN* status (blue, tumors without *MYCN* amplification; red, *MYCN*-amplified tumors) and the **(C)** Age at diagnosis (blue, <18 months; red, >18 months). (RNA-sequencing data of the SEQC study[42], figure modified from Zhang et al. 2015[42]).

As proposed by Simon et al 2017, a genetic analysis of copy number profiles, telomere and ALT status (alternative telomere lengthening, associated with *ATRX* deletion or loss) and the performance of a panel sequencing at diagnosis is recommended by SIOPEN. Within the upcoming HR-NBL2 protocol, a patient with a high-risk neuroblastoma, by definition, has a stage M disease and is over the age of 12 months, displaying any *MYCN* status[52]. Moreover, patients with a neuroblastoma at stage L2, M or MS with an additional *MYCN* amplification at any age are assigned to the high-risk group. A possible involvement of other genetic aberrations (e.g. *TERT*, *ATRX*) in the pathogenesis of a high-risk neuroblastoma was also mentioned, but not defined as an inclusion criterion for the study as a high-risk non-*MYCN*-amplified neuroblastoma. Optimization of the current diagnostic standard could lead to improved investigation of the different biological subgroups and to more effective risk stratification of neuroblastoma, according to its heterogeneity. Attempts have already been made to define a biological subgroup of high-risk patients (stage 4/M) with extremely bad outcome under the available therapeutic interventions, the UHR patient group[136]. Although there is no universal consensus definition of UHR neuroblastoma established so far, clinical criteria of UHR neuroblastomas refer to a metastatic disease, a refractory disease, death from disease within 18 months of diagnosis or to patients with a five-year event-free survival of about 10-15%[13,136]. A recent publication by Ackermann et al. focused on the molecular definition of a very-high-risk group, which can be divided from the high-risk group by the presence of the following mutations: *MYCN* amplification, *TERT* rearrangement (associated with telomere maintenance), high *TERT* expression or ALT and additional acquisition of RAS/p53 pathway alterations[44].

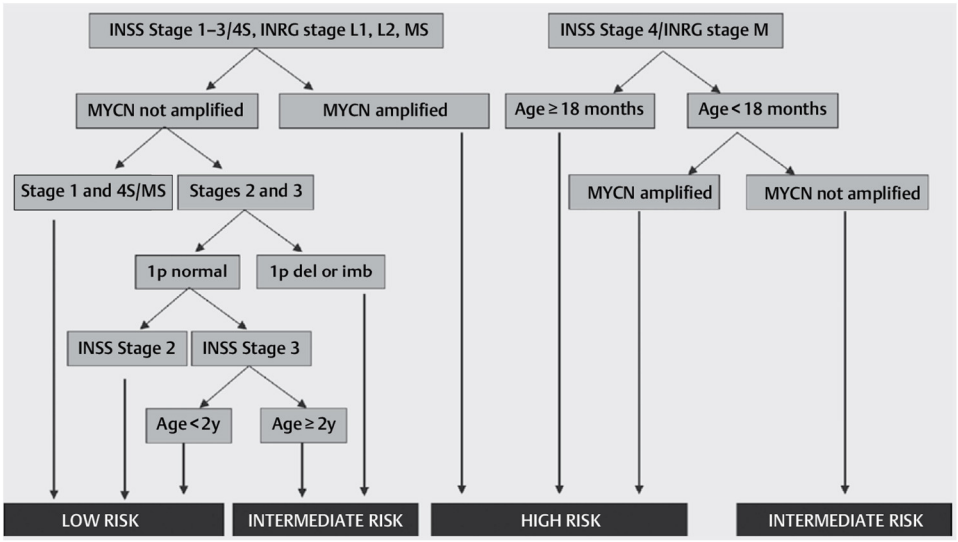

Figure 6: Treatment stratification of patients with a neuroblastoma.
For the stratification of neuroblastomas, the patients are classified into the low-risk, intermediate-risk and high-risk groups based on clinical and molecular characteristics. The current risk stratification according to the GPOH Guidelines (2017) is shown. (Figure taken from Simon et al. 2017[30]).

1.3 Targeted sequencing for neuroblastoma diagnostics

The development of next generation sequencing (NGS) has improved the precise diagnosis of tumors and thus the therapy and outcome of patients with cancer. High- coverage whole-genome sequencing still is too expensive for use in routine diagnostics, so for many adult cancer entities specific panels of relevant genes for targeted sequencing have been developed. Since neuroblastoma is a rare cancer, there are no specific NGS panels commercially available, which especially include a coverage of the entire *MYCN* gene amplicon. However, it is assumed in two reports that approximately 29% of the patients with a neuroblastoma enrolled in registered studies have an unknown or undetected *MYCN* status[137]. The establishment of a targeted panel NGS assay covering the oncogenic *MYCN* could therefore contribute to the reliable and precise determination of high-risk disease factors.

1.3.1 Next generation sequencing for cancer diagnostics

In the field of cancer research, NGS assays are used to decipher the specific tumor genome and to understand the biology of the disease. Regions of interest include genomic deletions and insertions, inversions, duplications, translocations and integrations of pathogens[138]. On application of the recent techniques, large chromosomal aberration events (e.g. chromothripsis, interchromosomal translocations) or even small base substitutions (e.g. SNV) can be detected[138]. The three most frequently used DNA sequencing methods are whole-genome sequencing (WGS), whole-exome sequencing (WES) and targeted sequencing (Figure 7). The sequencing method WGS covers the entire genome to be investigated[138]. The method detects genes (introns and exons), but also non-coding regions, repetitive regions and regulatory elements. Therefore, WGS is suitable for the identification of genomic alterations and to explore the landscape of mutations in cancer[139]. With a sequencing depth of about 30x and costs

of about $1000-3000 USD per array, the WGS is a high throughput screening assay[138,140]. WES is limited to exomes of genes (protein-coding region), which represent approximately 1% of the total genome[141]. Therefore, WES allows the detection of mutations that have already been known or which are of unknown clinical relevance. This sequencing method achieves a depth of about 100x and costs of about $500-2000 USD per array, and therefore represents a detection tool for mutations in functional gene regions[138,142]. A targeted NGS covers only the genomic regions of interest by the selection of probes chosen in advance. In this way, genes and non-gene regions can be detected (inter- and intergenic) similar to the WGS method. With a sequencing depth of 200 to over 1000x and costs of about $300-1000 USD per array, the panel sequencing represents a method for the precise analysis of already known genomic locations[140,142]. However, the cost of sequencing is growing with the genomic coverage extension and numbers of genes included in the targeted NGS panel (number of probes required).

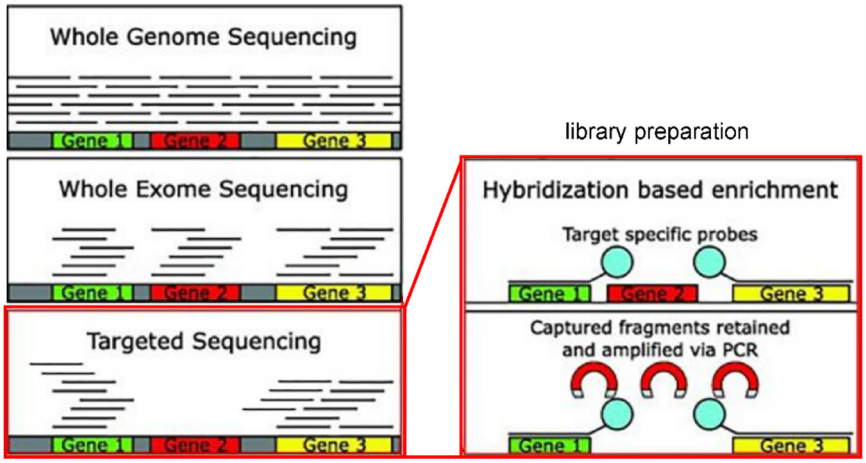

Figure 7: Comparison of DNA sequencing methods, focusing on the targeted sequencing method.
WGS, WES and targeted sequencing are visualized in the left panel. Applying the WGS method, the whole genome is covered with probes for detection of genetic information (top left panel). When using the WES method, only the exons of genes are covered and detected (middle left panel). In targeted sequencing, only genome regions of interest (exons and introns) are covered using sequence specific probes (bottom left panel). The hybridization based enrichment library preparation method for targeted sequencing is shown in the right panel, which uses the hybridization between DNA libraries and short DNA/RNA baits to enrich the desired DNA fragments in the sample (right panels). (Figure modified from Bewicke-Copley et al. 2019[142]).

The targeted NGS has the major advantage that only specific gene segments and a limited number of genes are detected, which have been defined beforehand[142]. Targeted NGS gene panels can provide a higher sequencing depth, but the specificity and the selection of the genes influence the success of the sequencing or diagnosis[139]. A high sequencing depth is essential, especially in a clinical setting, if e.g. heterozygous sub-clonal variants should be identified[143]. Hybrid-capture approaches in particular minimize false negative calls by reduction of genetic noise and have a uniform coverage in the sequencing among samples[143–145]. The processing time of the sequencing as well as analysis of the results is another aspect which will be shortened considerably by usage of targeted sequencing, e.g. with pre-made bioinformatics analysis pipelines or scripts[142]. In a comparison of the different sequencing

techniques targeted NGS, WES and WGS in other clinical questions[139,143,144], the targeted NGS was also found to be the most cost-efficient application due to these properties. The detection of genomic regions that have no known disease associations further provide little clinical value for the respective patient. Their impact must be further evaluated in research settings[143]. NGS panels also avoid ethical questions in terms of sequencing genomic regions that are not primarily associated with the disease (e.g. detection of germline mutations), which is why NGS panels are best suited for patients who already have received an initial diagnosis based on other criteria (e.g. the clinical appearance)[143]. Furthermore, a reduction in the detection of genetic variants also means that the complexity of clinical reports is reduced, which makes them more understandable for non-bioinformaticians, focusing on the essential disease causing mutations[143]. Panel sequencing is thus an ideal method for examining tumor samples quickly, cost-effectively, with a limited number of targets and a fixed analysis pipeline. This approach allows for easier screening of patient samples for tumor-specific mutations and enables the results to be used in terms of drug target evaluation. Additional WES or WGS should be considered if a genetic diagnosis was infeasible using panel sequencing. This might be the case, if the mutations for the development of the disease are located outside the genomic regions covered by the targeted NGS panel assay or the disease is dependent on multiple, possibly novel, genetic factors[143].

1.3.2 Targeted NGS panel sequencing for neuroblastoma diagnostics

With regard to neuroblastoma diagnostics, NGS of tumor material, (especially as targeted NGS panel), is recommended in existing and upcoming neuroblastoma study protocols[30,134,135]. So far there is no targeted NGS panel available which covers all neuroblastoma-specific chromosomal aberrations and mutations of interest, let alone a panel that is uniformly accessible across all study centers in Europe. Individual clinical centers and their diagnostic laboratories often intent to develop their own targeted NGS assay and establish their own analysis pipelines[142]. As a result, the findings are difficult to compare with one another, creating an urgent need for a standardized NGS assay and downstream data processing methods. Most published targeted cancer panels are gene-centric, meaning chromosomal aberrations are not included (e.g. chr.1p36), genomic rearrangements and breakpoint regions (e.g. *MYCN*)[146,147]. However, two specific panel NGS approaches exist for the sequencing of neuroblastoma tumors. First, a large NGS panel which detects 53 genes, 3 chromosomal regions (chr.1p36, chr.11q and chr.1p36), has already been published[148], but is not suitable for neuroblastoma diagnostics. The panel was made up of half a general cancer NGS panel (containing e.g. BRCA1, a gene which is most important for breast cancer diagnostics) and the other half was compiled with neuroblastoma-specific mutations. The panel focused on the detection of non-*MYCN*-amplified neuroblastomas and deliberately left out the detection of *TERT* or *MYC*, which are of relevance for the diagnosis and biology of neuroblastoma. Another interesting approach highlights an NGS panel including probes for 134 neuroblastoma-relevant genes. The target genes were found in an investigation of several neuroblastoma WES data sets, which were sequenced using a whole exome or a deep-targeted approach on tumor material[149]. The study focused

solely on the detection of gene mutations and not on large chromosomal aberrations or on the base exact detection of genomic rearrangements or breakpoints. These first attemptions are showing, that due to the genetic heterogeneity of neuroblastoma, a cancer specific panel NGS assay has to cover several chromosomal aberrations and many target genes. In particular, emphasis should be placed on the detection of the driving oncogene *MYCN*, as this gene unites the majority of patients via a highly destructed amplicon. Therefore, the *MYCN* gene and its chromosomal expansion should be covered extensively by sequencing probes. Furthermore, the detailed mapping of *MYCN* is not only important for the diagnosis of neuroblastoma, but also for the investigation of the disease and its development.

1.4 Minimal residual disease detection of neuroblastoma cells

Approximately 50% of all patients with a neuroblastoma show metastases already at the time point of diagnosis. These metastases are most frequently found in the bone marrow (~70%), followed by bone (~55%), lymph node (~30%) and liver (~30%)[150]. Within the group of high-risk neuroblastomas, about 80-90% of the patients show an infiltration of the bone marrow[151]. It is assumed that the migration of the tumor cells into the bone marrow is related to the neural crest origin of the cells[152]. More than half the patients with high-risk neuroblastoma relapse and succumb to their disease despite initial remission in response to intensive treatment, implying the survival of neuroblastoma cells as minimal residual disease (MRD)[14,153]. *MYCN* amplification is a major driver of high-risk neuroblastoma and is only evaluated in tumor material taken at initial diagnosis. High expression levels of the MYCN protein were found to correlate with invasive and metastic behavior of neuroblastoma[154–156]. Based on these observations, it can be assumed that *MYCN*-amplified neuroblastoma cells migrate and accumulate in the bone marrow, which can favor a recurrence. Although bone marrow aspirates of patients with a neuroblastoma are visually examined for infiltration, advanced molecular biology techniques are needed for the precise detection of MRD within a patient sample[30]. MRD is therefore originally defined by Foroni as the "lowest level of disease detectable in patients in continuous complete remission by methods available"[157]. Extending risk assessment of neuroblastomas to multiple time points during treatment and/or follow-up by evaluating MRD would expose dynamic changes associated with response or non-response to therapy and allow dynamic risk re-assessment and adjustment of therapy intensity in a personalized approach. The development of curative therapeutic strategies (eliminating MRD following treatment) would also be assisted by robust MRD markers and thus MRD detection could be incorporated in clinical trial protocols.

1.4.1 An example of established MRD diagnostics: Leukemia

The concept of MRD and sensitive detection methods were initially developed and are currently refined for therapy management in patients with hematological malignancies[158]. The ability to detect residual tumor cells depends on the sensitivity limitation of the applied method. For risk stratification in case of a high tumor burden it is possible to quantitatively detect malignant lymphoblasts with light microcopy

up to a sensitivity level of $5x10^{-2}$. If the patients with leukemia do not show any visual evidence of leukemic cells, they are in (morphological) complete remission (CR, < 5% blasts in the bone marrow[159], Figure 8). Below the cytological evaluation, it is necessary to apply more sensitive molecular biology techniques, which cover a sensitivity of at least 10^{-3} [160]. For measurement of a very low number of leukemic residual cells in a sample (from 10^{-2} up to 10^{-5}), specified as MRD, the sensitive real-time quantitative polymerase chain reaction (RQ-PCR) technique is preferred. In nearly all cases, the quantification limit of the available techniques is reached at 10^{-4}, whereas the detection sensitivity can achieve a level below 10^{-4} (commonly at 10^{-5}), expressed as "positive but not quantifiable"[161]. When no leukemic cells are identified below this limit, the patient is considered to be in molecular complete remission (mCR[162]).

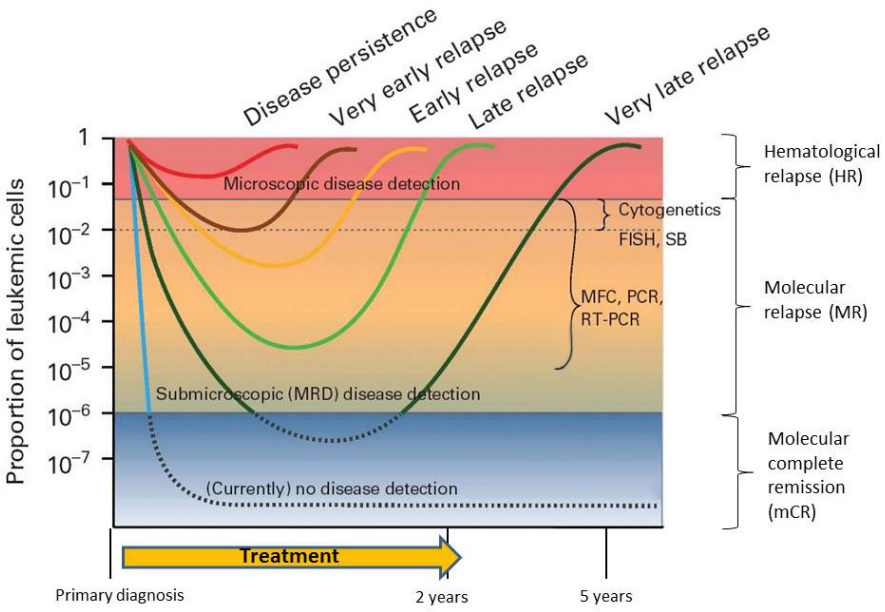

Figure 8: Schematic of the MRD concept within cell burden changes of leukemia progression and following relapses. MRD as a diagnostic tool is the likelihood of tumor recurrence related to the amount of residual tumor cells. Within the red area, patients suffer a hematological relapse, which is detectable via light microscopy. Down to a cell level of 10^{-2}, the cell burden is detectable via cytogenetics, FISH and SB (Southern blotting). Below that level only specialized techniques like MFC (multiparameter flow cytometry), PCR or RQ-PCR identify a molecular relapse (MR). Below a level of 10^{-5} only a sensitivity based positive, but not quantifiable statement can be achieved. In an even higher dilution, no leukemic cells can be measured (negative MRD). (Figure modified after Buckley et al. 2013[163]).

The first molecular marker used to detect MRD was the Philadelphia chromosome (*BCR-ABL*) in patients with chronic myelogenous leukemia (CML), and was followed by expression of recurrent fusion genes, such as *AML1-ETO8* and *TEL-AML1*, used to classify and monitor hematological malignancies[164–167]. Today, genomic breakpoints of the de novo fusion genes are used as stable and reliable MRD markers instead of fusion gene transcripts, for example for *ETV6-RUNX1*, *BCR-ABL* or T-cell receptor (TCR; -α, -β, -γ) and immunoglobulin (Ig) gene rearrangements[168,169]. The biological benefit for those somatic DNA-rearrangements in healthy cells is the generation of a wide repertoire of antibodies as well as antigen receptors during lymphoid development and differentiation, to improve

the defense against diseases. RAG enzyme-mediated (recombination-activating gene product complex) antibody generation promotes the rearrangement of V (variable), D (diversity) and J (joining) segments in the heavy and light chain antibody locus by recognizing recombination signal sequences (RSS). Via this antibody somatic (VDJ) recombination and subsequently variable addition and subtraction of random nucleotides, a unique genetic repertoire is created[170]. Similarly to the healthy development of lymphocyte antibodies and receptors, leukemic clones show specific TCR/Ig rearrangements that represent a "fingerprint-like sequence" for each leukemic clone (clonospecific junctional regions)[160,171]. This region can be used as a specific cancer marker to detect and to quantify the proportion of leukemic cells among normal bone marrow cells via MRD techniques during the follow-up of ALL (acute lymphoblastic leukemia)[172]. The applicability of TCR rearrangements for MRD detection with regard to different recurrences of ALL was demonstrated by Szczepanski[173]. They disclose clonal stability of TCR rearrangement MRD markers at diagnosis and relapse (of T-ALL), which reveal the occurrence of a second ALL. Moreover, within the study of Guggemos, a clonal stability of TCR/Ig markers between relapses was observed[174]. These molecular markers are detected with high sensitivity in standardized protocols using the clinically implemented diagnostic RQ-PCR technique[175]. This method can sensitively detect as few as 1 leukemic cell in a pool of 100,000 non-malignant cells. By means of continuous improvement of MRD related RQ-PCR diagnostic methods e.g. by employing TaqMan probes, the biological knowledge about leukemia was increased and the treatment adapted[176,177]. The most important finding of numerous studies was the high prognostic relevance of sensitive measurements of treatment responses in ALL. At first, this was demonstrated by studies on ALL initial diseases, followed by studies on ALL relapses[178,179]. Reports of Eckert et al. and others showed that an early response after induction therapy (MRD level $\geq 10^{-3}$) of intermediate-risk patients with relapsed ALL to the treatment is one of the most important prognostic factors, which predict independently a long-term outcome[172,180]. Additional studies on ALL primary diseases underpinned the prognostic relevance of treatment response via MRD detection[178,179]. Several subsequent studies demonstrated the prognostic value of MRD before hematopoietic stem cell transplantation (HSCT) as a prognostic factor of the quality of remission after an HSCT in relapsed ALL patients[181–183]. The pioneering MRD approaches in leukemia paved the way for further successful MRD exploration in solid tumors, including breast[184], prostate[185], small cell lung[186] and gastrointestinal[187] cancers. In addition, MRD for hematological malignancies is a leading model for new diagnostic technologies and their analysis methods. Currently, the clinically implemented MRD technique of RQ-PCR is in the process of being replaced by state-of-the-art and even more sensitive droplet digital PCR[158,188,189]. DdPCR has been demonstrated to be more precise[190] and more reproducible[191] than RQ-PCR and enables the use of very small sample quantities[191].

1.4.2 Investigation of MRD occurrence in neuroblastoma

In as early as the 1970s, the potential of neuroblastoma cells to migrate into bone marrow was recognized with the diagnostic exploration of skeletal scans and bone marrow biopsies[192,193]. While the detection of neuroblastoma cells was initially carried out using skeletal radiography, ^{99m}TC pyrophosphate bone scintigraphy and bone marrow histocytology[192,193], the understanding of the spread of neuroblastoma cells within the body and its detection methods continued to develop[194]. Bone marrow cytology was complemented by immunohistochemically detection of e.g. the GD2 ganglioside on the tumor cell surface[195–200], which is still a diagnostic standard today. The occurrence of MRD in bone marrow was first demonstrated immunocytologically in patients with neuroblastoma in 1991[201]. Moss et al. showed that the appearance of disseminated neuroblastoma cells in the bone marrow following induction therapy correlated with increased risk of tumor recurrence. Residual neuroblastoma cells have even been detected as well in the products used for autologous transplantation after high-dose chemotherapy (CTX), but their significance remains controversial[62,202]. But this cytology and immunocytology based techniques lack the sensitivity required to accurately and reproducibly detect MRD. In addition, flow cytometry has been used to detect tumor cells in bone marrow samples, however the detection sensitivity was limited[203]. Employing semi-quantitative PCRs and RT-qPCRs (reverse transcription quantitative PCR) for neuroblastoma diagnostics, several tumor cell traits (*PHOX2B, TH* or *DCX*) have been proposed to serve as mRNA transcript markers to monitor neuroblastoma MRD[203–218]. A pathogenic PHOX2B overexpression in selected cohorts of neuroblastoma correlated with high MRD load at different times during treatment and predicted a poor prognosis[203]. In particular, the detection of *MYCN* mRNA transcripts was extensively performed[219–222], but no such assay has yet reached clinical routine diagnostics. The detection of neuroblastoma-specific gene expression using RT-qPCR was not sufficiently reproducible because target gene expression can vary under therapy, RNA transcripts proved less stable and these test systems only allowed a semi-quantitative MRD estimation[204,223–228]. While MRD was demonstrated to have prognostic value for patients with neuroblastoma, technical difficulties prevented the application of these first assays in large prospective studies and their transfer into routine diagnostics. More recently, some approaches have therefore focused on the use of genomic DNA and gene targets similar to the well-established leukemia MRD. Even though recurrent genomic aberrations are seldom in neuroblastoma cells, some mutations can be employed as targets for MRD assessment. A large proportion of neuroblastomas harbor an amplification of the *MYCN* oncogene, and this genomic alteration is also stable over the course of the disease and in relapse[60]. *MYCN* amplicon breakpoints present an ideal biological marker which is connected to pathological cell function. These breakpoints will most likely not occur in healthy cells but are connected to preliminary cancerous rearrangement events[6]. Early in the history of neuroblastoma diagnostics, the detection of a *MYCN* amplification in tumor cells utilizing the FISH or PCR method (in combination with Southern blotting) was established[229–234]. These methods are still recommended in diagnostic research and neuroblastoma study protocols for the determination of the *MYCN*

status[30,229,231,235–238]. More advanced concepts implemented "qPCR" assays utilizing SYBR green dyes or TaqMan probes to increase the detection sensitivity of *MYCN* gene segments or CNVs (copy number variation) in patient-derived material[98,235,239–242]. Other attempts were made to use the specific genomic breakpoints of the *MYCN* amplicon rearrangements to develop even more sensitive PCR test systems[89,243]. The use of specific recurrent segmental chromosomal aberrations (e.g. in the *MYCN* amplicon) as prognostic biomarkers for neuroblastoma diagnostics was proposed over a decade ago, but the development of such assays has taken several years[244]. Five studies have demonstrated the application of genomic breakpoints to detect neuroblastoma MRD in patient samples[60,89,245–247], including four assays which are employing *MYCN* amplicon breakpoints. In particular, Weber et al. stated that individual patient-specific PCR assays based on *MYCN* amplicon breakpoints (which they called amplicon fusion sites) can be used for MRD detection[247]. However, technical difficulties and the complexity of the patient-individual mapping and analysis of genomic *MYCN* breakpoints have, as yet, prevented application in clinical trials and translation into clinical practice.

1.5 Treatment of neuroblastoma

The therapy of neuroblastoma depends on the severity of the disease which is determined by risk stratification. Patients with biologically favorable neuroblastomas, e.g. INSS stage 4S, without severe symptoms and without the evidence of negative prognostic markers, usually do not require therapy but are merely observed. Other neuroblastoma grades, by contrast, require a local treatment up to a comprehensive high-dose therapy. Because of its biological and clinical heterogeneity, special care must be taken to ensure that patients with a neuroblastoma are administered neither undertreated nor overtreated medical care.

1.5.1 Standard first-line multimodal therapy in neuroblastoma study protocols and treatment of relapsed neuroblastoma

The treatment of neuroblastoma is very diverse and depends on the degree of the disease. Patients with a local low-risk neuroblastoma are treated according to a watch and wait principle, as most of them undergo spontaneous regression[248]. Intermediate risk staged neuroblastomas receive an initial open biopsy up to a partial removal of the tumor to collect cancer material for improved (molecular) diagnostics and for adjustment of the risk stratification if necessary[30]. Subsequently, the patients receive intensified chemotherapy. The therapy schedule is similar to the treatment protocol of the high-risk group, but does not include stem cell transplantation, for example[30]. A reduced tumor size as a result of the chemotherapy enables the complete surgical resection of the residual tumor. The high-risk group of patients with a neuroblastoma receives the most intensive, neoadjuvant therapy (Figure 9). Similar to the intermediate risk group, an open biopsy of the primary tumor is performed first for detailed diagnotics[249]. An initial complete removal of the tumor is not executed because the patients are often in poor general condition or the tumor has invasively grown into adjacent tissues. The patients then receive

a comprehensive chemotherapy, in which several cytotoxic drugs are combined (Figure 9). The primary tumor surgery is performed during or after the induction chemotherapy. If the tumor can only be partially removed due to its location, external photon beam radiation therapy (EBRT, 36-40Gy (gray) total dose) can be added[30]. Patients who show residual tumor cells in bone and bone marrow in the ^{123}I-mIBG scintigraphy can be treated with ^{131}I-mIBG (^{131}-iodine-mIBG) therapy (2Gy daily dose)[30]. ^{131}I-mIBG is administered intravenously and incorporated by the neuroblastoma cells via norepinephrine transporters. After induction therapy, myeloablative chemotherapy is followed by autologous stem cell transplantation (ASCT)[30]. Subsequently EBRT is performed within the first-line therapy, especially in the presence of residual tumor tissue[30]. Immunotherapy is administered as post consolidation therapy, using an anti-GD2 antibody (dinutuximab beta)[30].

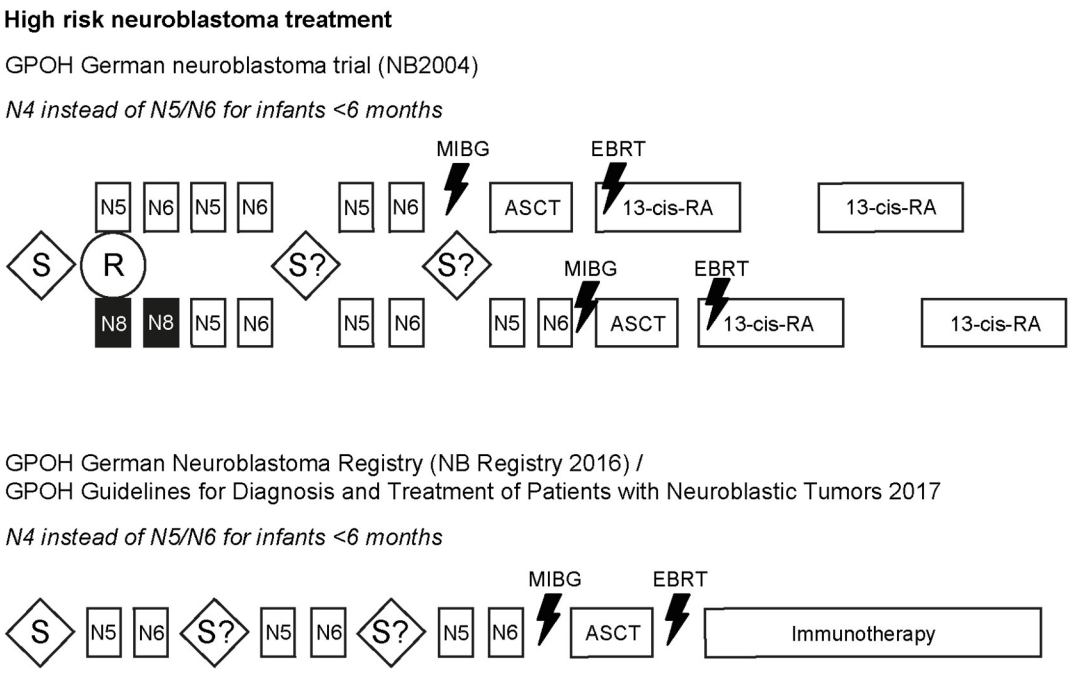

Figure 9: Time course of high-risk neuroblastoma treatment protocols.
Schematic overview of the previous first-line treatment protocol NB2004 and current recommendations of the NB Registry 2016 and the GPOH guidelines from 2017. The chemotherapy cycles include the following therapies: cycle N4 (doxorubicin, vincristine, cyclophosphamide, MESNA, hydration), cycle N5 (cisplatin, etoposide, vindesine, hydration, G-CSF), cycle N6 (vincristine, dacarbacine, ifosfamide, doxorubicin, hydration MESNA, G-CSF) and cycle N8 (topotecan, cyclophosphamide and etoposide). Other forms of treatment are S = surgery, MIBG, EBRT, ASCT and 13-cis-RA = 13-cis-retinoic acid. Trial randomization is indicated by the letter R. (Figure modified from NB2004 protocol, NB Registry 2016 and GPOH guidelines 2017[30,134,135]).

A treatment with isotretinoin (13-cis retinoic acid) is not performed based on the current GPOH Guidelines 2017. In case of a relapse, progressive neuroblastoma tumors are resistant to standard therapy in about 10-15%[248]. Depending on the severity and time of the relapse, the therapy is adjusted accordingly[30]. In the event of an early relapsed neuroblastoma, the induction therapy is prolonged[248]. In addition, doses are intensified or other chemotherapeutic agents are added that have a different mechanism of action from the drugs used in the induction or targeted radiotherapy is applied. This is followed by myeloablative high-dose therapy and an haploidentical HSCT. In addition, an anti-GD2

antibody and targeted therapies may also be administered, especially in case of a late relapse after previous myeloablative therapy. If a multiple relapsed neuroblastoma arises, the patient can usually only be treated palliative or with phase-I study medication, but a cure has never been reported.

1.5.2 Conventional pharmacotherapy of high-risk neuroblastoma

The treatment of high-risk neuroblastomas usually begins with the chemotherapeutic induction therapy to reduce the tumor growth and to ideally shrink the size of the tumor. The medication in current (NB Registry 2016 and GPOH Guidelines 2017) and future (HR-NBL2) induction protocols include the substance classes of alkylating agents, topoisomerase II inhibitors and mitosis inhibitors[30,52,135]. The substances administered to the patients with neuroblastoma are cyclophosphamides, tubulin interactive agents (e.g. vincristine, vindesine), anthracyclines and platinum compounds (e.g. carboplatin, cisplatin; see Figure 10)[250]. However, the beneficial role of anthracyclines is not fully established yet[251,252].

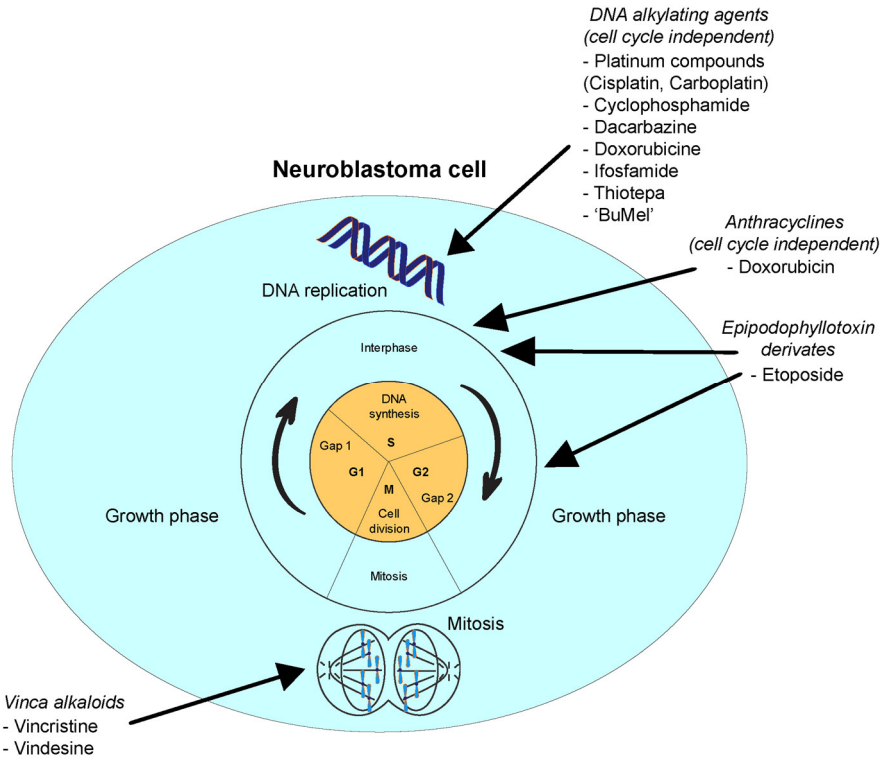

Figure 10: Chemotherapeutics applied in neuroblastoma therapy act on different phases of the cell cycle.
The activity of some classes of chemotherapeutic agents is related to defined phases of the cell cycle (epipodophyllotoxin and vinca alkaloids). Other drugs function non-phase specific and cell cycle independent (DNA alkylating agents and anthracyclines).

Cisplatin, carboplantin, cyclophosphamide, dacarbazine, ifosfamide, thiotepa, melphalan and buthionine sulfoximine ("BuMel") are mainly used in neuroblastoma first line therapy and are classified as DNA alkylating and DNA cross-linking agents[253,254]. These drugs form covalent bonds or cause a methylation of N_7 nitrogen of the nucleotide guanine in the DNA. Cell division is inhibited by intra- and interstrand cross-linking of DNA strands, leading to DNA damage repair arrest, cell cycle arrest and finally cell death. Vinca alkaloids such as vincristine and vindesine bind to the tubulin molecules of the

cell, and thus preventing the polymerization of microtubules and subsequent mitosis by leading to apoptosis. Further inhibitory regimes are directed against DNA-topoisomerases, such as the antibiotic drug doxorubicin, which also proofs antitumoral efficacy. Epipodophyllotoxins, like doxorubicin, inhibit the function of the topoisomerase. Anthracyclines intercalate between the DNA, thereby inhibiting DNA topoisomerases I and II. Both, anthracyclines and epipodophyllotoxins inhibit *de novo* DNA synthesis during the cell cycle, ultimately resulting in cell death. Etoposide, which is used in several neuroblastoma trials, is harming the DNA topoisomerase II enzyme as well. The conventional chemotherapy is not specifically acting on neuroblastoma cells, but also has an impact on healthy somatic cells, especially on rapidly dividing cells[248]. These high-dose chemotherapies therefore cause clinical short-term side effects in patients with neuroblastomas, e.g. neutropenia, anemia, muscositis, diarrhea, nausea, alopecia, cardiotoxicity, CNS (central nervous system) toxicity and nephrotoxicity, which can persist over the duration of medication[248]. Moreover, it was demonstrated that long-term complications of the treatment are reported in 89% of high-risk neuroblastoma survivors[255]. The most common late effects are permanent hearing loss (ototoxicity) due to the administration of platinum compounds and ovarian failure (sterility/infertility) caused mainly by alkylating agents. It is therefore of major importance to develop new therapeutic strategies and drugs that specifically target the neuroblastoma tumor cells, thereby enhancing survival rates and improving the patient's quality of life.

1.5.3 Clinically implemented targeted therapies for high-risk neuroblastomas

At present, targeted therapies are only marginally implemented in neuroblastoma therapy trials. According to the German NB Registry 2016 study and the GPOH guidelines from 2017, the targeted anti-GD2 antibody dinutuximab beta is used in the first-line maintenance therapy of the high-risk group[30,135,256,257]. Membrane situated GD2 seem to play an important biological role in the attachment of neuroblastoma cells to the extracellular matrix. The majority of neuroblastoma cells express high levels of GD2 relative to other body cells. Therefore, a human/mouse chimeric antibody ch14.18 was designed as a targeted therapy against GD2-exposing tumor cells. Unfortunately not all patients can be helped with this treatment, as about one third of the neuroblastomas do not respond to the therapy, because not all neuroblastoma cells express GD2 or only at minor levels[258]. Furthermore, dinutuximab also binds to peripheral neurons expressing GD2 and free circulating GD2, thus limiting its anti-tumor availability. In addition, the treatment of dinutuximab triggers opioid-resistant neuropathic pain and vision impairment[52]. Current research aims to modify the chemical structure to make it more effective against neuroblastoma and reduce side effects. Beyond an administration of anti-GD2 antibodies within first-line therapies, targeted small-molecules for the treatment of (high-risk) neuroblastoma are applied to relapsed or refractory neuroblastomas[248]. Ideally, improved diagnostics indicate actionable targets of the specific tumor (for example, evaluated by WES). Patients with a neuroblastoma are then enrolled in pharmaceutical-clinical studies or receive a targeted treatment as part of an (off-label) experimental treatment. As an example, recent studies are focused on compounds targeting the ALK receptor, which

can be altered in neuroblastoma by a gain-of-function SNV. The most interesting pharmacological candidates for targeting of mutated ALK are certitinib[259] or lorlatinib[260]. However, despite a change to a targeted medication, the chances of a successful cure of relapsed (high-risk) neuroblastoma are poor.

1.6 Novel molecularly treatments against MYCN

Conventional cytotoxic chemotherapy attacks essential cellular processes. It therefore also exhibits non-specific toxicity against non-cancerous cells and severe clinical side effects. The advanced understanding of molecular mechanisms in the (tumor) cell is the basis for research and development of targeted compounds. Targeted therapy refers to a new generation of cancer drugs designed to interfere with a specific molecular target (typically a protein) that is believed to have a critical role in tumor growth or progression[261]. The identification of suitable molecular targets is therefore the preliminary step towards a personalized therapy, meaning it will be tailored to the individual biology of the patient's tumor. The most prominent target in neuroblastoma is MYCN, which genetic sequence is amplified in about 25% of all cases and is correlated to an unfavorable outcome[42]. Similar to MYCN, c-MYC deregulation is involved in the development of a high-risk neuroblastoma and thus the MYC family proteins MYCN and c-MYC together represent 35% of the driver mutations in high-risk cases[60,124,262]. For high-risk neuroblastomas, cure rates are under 40% using conventional chemotherapeutics[12]. This makes the family of MYC proteins, especially MYCN, attractive targets for cancer therapy (Figure 11). However, MYC proteins are challenging therapeutic targets. First of all, approximately 75% of all patients with a neuroblastoma will not benefit from anti-MYCN treatment, because the tumors do not show a *MYCN* amplification. In addition, many modern inhibitors are designed for instance to interfere with active protein pockets of the target protein, but the transcription factor MYCN is not an enzyme[263]. The surfaces of the MYCN protein-protein interaction sites (e.g. to MAX) are featureless, i.e. large, flat and special motifs or clefts are missing[263,264]. Chemically, an inhibitor must therefore be able to overcome the large free energy of the protein-protein interaction at the coupling sites of MYCN and its partners[263]. The inhibition of MYCN also does not specifically only target a mutated protein or neuroblastoma cells. Unlike for example the treatment of fusion protein BCR-ABL1 positive chronic myeloid leukemia with the inhibitor imatinib, the expression of MYC(N) is almost universally found in all proliferating cells and could therefore trigger undesired side effects[263,265]. However, the expression of MYCN is strongly increased in *MYCN*-amplified neuroblastoma tumors, suggesting a drug dose adjustment. Because the (ongoing) development of direct MYCN inhibitors is currently still in an experimental research stage, the inhibition of the MYCN regulatory network is of particular importance[266]. Indirect MYCN targeting, in particular involving the protein products of recently discovered neuroblastoma oncogenes (e.g. ALK), is thus an important therapeutic option to combat *MYCN*-amplified neuroblastomas[264,267]. In addition, a combination of the indirectly targeting MYCN therapeutics should also be considered. Administration of only one drug harbors a high risk of resistance

development and treatment failure. Drug resistance manifests itself as diminished activity of the small molecule and reduces event-free treatment outcome of patients[268]. Biologically, there are several mechanisms that can trigger resistance, such as increased activity of efflux pumps or decreased activity of influx pumps, increased activity of detoxifying proteins, repair of induced DNA damage, enhanced proliferation and disrupted apoptotic signaling pathways[268]. Drug resistance is either primarily present before treatment or acquired through the course of treatment[268]. Combinatorial therapies take advantage of the possibility that a sensitive tumor cell cannot become resistant to two drugs at the same time, because it requires at least two discrete events to adapt its sensitivity[269]. Therefore, an early administration of combination therapies should also be considered for the treatment of *MYCN*-amplified neuroblastomas in order to prevent the risk of resistance development. This is particularly possible with the implementation of targeted therapies, which could attack different sites in the MYCN regulatory network simultaneously. In the following, the various connections of MYCN to cell physiology that are suitable for employing a pharmaceutical treatment will be discussed: Transcription of *MYCN*, mRNA translation of *MYCN*, MYCN protein stabilization, preventing the protein-protein interactions involving MYCN and targeting of MYCN-driven cell proliferation. Moreover, approaches to combination therapy will be introduced, especially with regard to different MYCN physiological processes, which are also employed practically in this thesis.

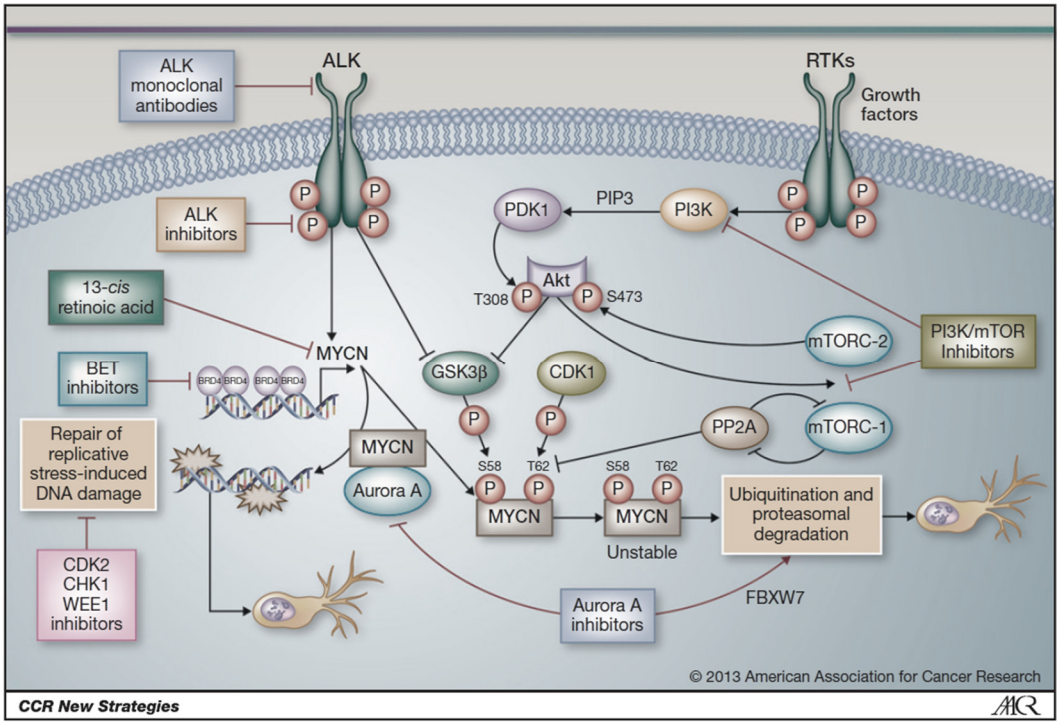

Figure 11: Therapeutic strategies targeting the MYCN oncoprotein in neuroblastoma.
This scheme shows some selected approaches for the targeted therapy of *MYCN*-amplified high-risk neuroblastoma. The MYCN protein is a difficult molecular drug target, which is why many approaches focus on indirect therapies within the cellular network of MYCN. A number of these small molecules are already being tested in clinical trials or are still in the experimental stage. (Figure taken from Barone et al. 2013[267]).

1.6.1 Inhibition of *MYCN* transcription

In many human tumors, the increased expression of oncogenes is caused by the pathological acquisition of enhancer elements driving oncogene expression. Enhancers are regulatory gene elements that activate promoter transcription over large distances, independently of the transcriptional orientation[270]. These elements control gene expression according to the corresponding cell type and interact with cell type-specific transcription factors. Large clusters of enhancer elements are known as super-enhancers, which show a stronger transcriptional activation and are more frequently located adjacent to genes that impact the cell identity[271]. In neuroblastoma, genomic rearrangements modify the structure of the *MYCN* amplicon and the genomic neighborhood of the *c-MYC* gene, including (distal) enhancer hijacking or upregulation by focal enhancer amplification[74,124,125]. These changes lead to an increased translation of *MYCN* and *c-MYC*. Moreover, it was found that proximal enhancers to *MYCN* drive the neuroblastoma development into a sympathetic noradrenergic cell identity through specific regulatory transcription factors[28,74,272]. In this context, super-enhancers were discovered to be active in neuroblastoma and other tumor entities. Hematological malignancies show an acetylation of histone marker H3 lysine 27, which is indicative of an open chromatin and transcriptional activity (H3K27ac)[273–275]. Histone proteins form a chromatin complex with the DNA and thus the histones function as epigenetic regulators of DNA transcription and modulators of nucleosome dynamics[276]. The chromatin can be either packed and is therefore functionally inactive (heterochromatin), or the chromatin is relaxed and thus has a transcriptionally active status (eurchromatin)[277]. In this regard, for example histone lysine residue marks indicate the state of transcriptional activity and inactivity of chromatin. The acetylation of the lysine residues causes a release of the condensed heterochromatin and makes the genomic region accessible for enhancer activation, binding of transcription factors, and the transcription machinery itself[278]. In turn, deacetylation of the lysine residues initiates the formation of packaged chromatin following gene repression[279]. Bromodomain and extraterminal domain (BET) proteins function as epigenetic readers of acetylated histone signals in the genome and regulate the transcriptional activity of MYCN[74,279–282]. The BET protein family consists of BRD2, BRD3, BRD4 and BRDT, whereas the BRD4 protein has a prominent role in embryogenesis and cancer development[279,283,284]. The transcriptional regulation of the *MYCN* expression is directly regulated by BET proteins, especially by BRD4[285]. The BRD4 protein as well promotes the retention of transcriptional factors at the promotor sites of *MYCN*, which then ensure the (increased) transcription of *MYCN*[279]. Moreover, it has been reported that BRD4 plays an important role in connection with MYCN in the epigenetic regulation of super-enhancer-directed genes, such as the rearranged TERT[123]. The BET proteins are composed of two tandem bromodomains (BD1 and BD2) for the detection of acetylated lysine tails of histones, an extraterminal domain (ET) involved in protein-protein interactions, and a C-terminal domain which binds to proteins of the transcription machinery and is only possessed by BRD4 and BRDT[286,287]. The bromodomains of the BET proteins are composed of four α-helices, which are connected via two loop structures (ZA and BA loop) forming a hydrophobic

cavity that allows the binding of aminoacetyl groups[288]. The ability to bind to both histones and other proteins enables BET molecules to act as a connector between active gene promotors and enhancers and proteins of transcriptional initiation and elongation. The binding affinity of BET proteins to acetylated histone marks increases with the occurrence of multiple adjacent acetylated sites ("hyper-acetylated regions") compared to solitary acetylated lysine residues[289]. The involvement of the BRD4 protein in the transcription process is the most studied. BRD4 that is bound to acetylated lysine residues of the histones has been found to interact with the positive transcription elongation factor (P-TEFb) kinase (Figure 12)[290,291]. As a result, pTEFb is unable to associate with the 7SK/HEXIM complex, which otherwise inactivates the kinase. Thus, P-TEFb can recruit and phosphorylate the RNA polymerase II[290,291]. The RNA polymerase II becomes activated and transcriptional elongation is induced[279]. In addition, BRD4 itself can phosphorylate the RNA polymerase II, can acetylate histone lysine marks and enables the RNA polymerase II to be passed along the acetylated histones in the elongation process[292–294].

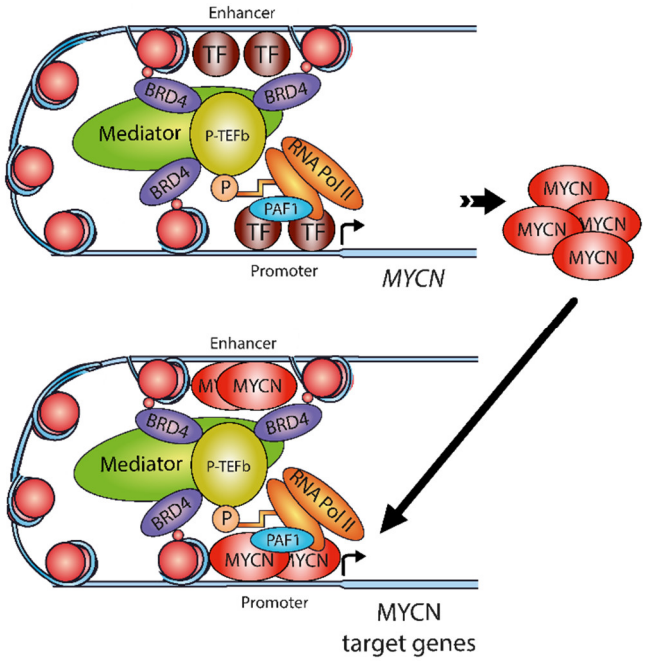

Figure 12: The BET protein BRD4 binds to acetylated histone residues in open chromatin regions and promotes the transcription of *MYCN*.
BRD4 is recruited to open chromatin in the genome, especially to enhancer complexes of the *MYCN* gene, and regulates the transcription of *MYCN* (top). MYCN is a transcription factor which binds to genomic target gene promotors and enhancer sites. Thus, the MYCN protein fosters gene expression in cooperation with the BRD4 protein (bottom). (Figure modified from Henssen et al. 2016[282]).

The first application of a BET inhibitor was directed against NUT-midline carcinoma (nuclear protein in testis), using the tool compound JQ1[295,296]. JQ1 is a thieno-triazolo-1,4-diazepine and has two enantiomers, whereby only (+)-JQ1 shows an effect against BET proteins (Figure 13A)[297]. The (tool) compound displays chemical affinity for the bromodomain recognition site for acetyl lysine tails and prevents the BET proteins from binding to the histones, which especially causes a reduction of BRD4 proteins bound to enhancers and promoters[297–299]. Treatment with the inhibitor JQ1 resulted in cancer

cell differentiation and cellular growth arrest, and was reported to demonstrate the potency to downregulate *MYC* gene expression[298]. The small molecule JQ1 has also displayed anti-tumoral activity against neuroblastoma *in vitro* and *in vivo*, resulting in reduced growth, increased apoptotic signals and downregulation of MYCN protein-regulated transcription[285,300]. Thus, JQ1 proved to be an efficient BET inhibitor, but due to its short half-life in mice blood plasma the drug could not be applied in clinical studies[301]. Therefore, the chemical structure of JQ1 was modified to develop a clinically applicable BET inhibitor[297]. OTX015 (Birabresib), a JQ1 analog, is a BRD2/3/4 inhibitor which is orally bioavailable and has shown clinical efficacy in hematologic malignancies and advanced solid tumors (Figure 13B)[297,302,303]. Using OTX015, it was also discovered that the HEXIM1 protein is a suitable and robust pharmacodynamic biomarker for monitoring the target engagement of BET inhibitors[304]. MYCN-driven neuroblastoma models have demonstrated the efficacy of OTX015, downregulating genome wide transcription of the tumor cells[282]. However, only JQ1 and second generation JQ1 lead structure BET inhibitors such as OTX015 have been considered for the treatment of neuroblastoma so far. The small molecule TEN-010 (RO6870810) is a newly developed substance structurally related to JQ1, but has preferable chemical and biological properties (Figure 13C)[305]. The pharmaceutical formulation and the solvent attributes of TEN-010 facilitate its subcutaneous administration. This form of application is advantageous in the field of pediatric oncology, as tablets do not need to be swallowed or infusions laid. In addition, it aids the autonomous use at home. TEN-010 is currently being investigated in clinical studies against adult tumors such as acute myloid leukemia, myelodysplatic syndrome, lymphoma, advanced ovarian cancer and triple negative breast cancer[306]. This inhibitor has not yet been tested in preclinical neuroblastoma models or in clinical neuroblastoma studies, but TEN-010 could be a very promising drug based on previous reports of other tumor entities.

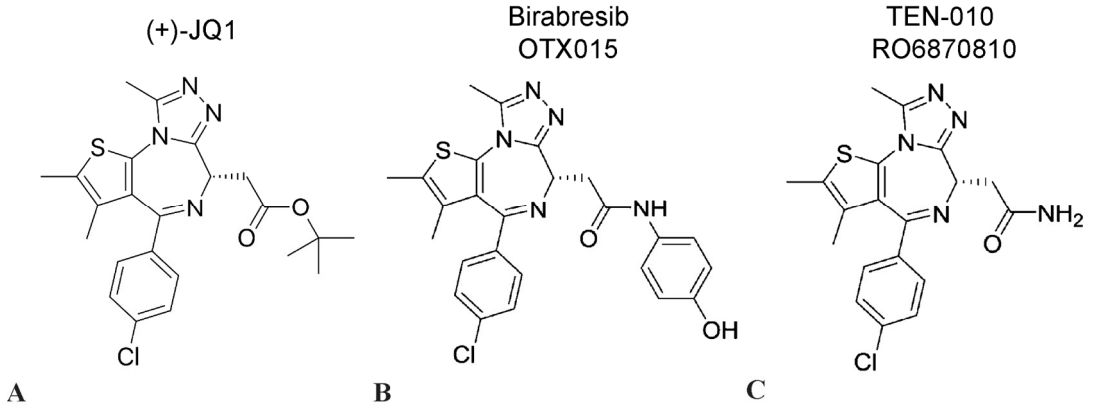

Figure 13: Chemical structures of the BET inhibitors JQ1, OTX015 and TEN-010.
Small-molecule BET inhibitors JQ1 and inhibitors based on the JQ1 lead structure acting as acetyl lysine mimics which occupy one of the two bromodomain sites of the BRD4 protein. **(A)** The first (tool) compound JQ1, discovered by J. Bradner and J. Qi, which showed anti-BET activity. At the carboxyl moiety, an ester bond was introduced at the carbon position C6 to obtain a carboxylate ester. **(B)** A second generation small molecule against BET proteins, OTX015, which was designed by Oncoethix. A change in the chemical structure was achieved by modifying the carboxyl moiety to an amide. **(C)** A latest third generation BET inhibitor TEN-010, which was created by Tensha Therapeutics. The chemical structure was modified to introduce two hydrogen atoms as substituents at the carboxyl site. (Figure modified from Li et al. 2017 [307]).

In addition to these three BET inhibitors (BETi), alternative BETi are available which have already been examined in preclinical neuroblastoma models: I-BET 151 (GSK1210151A, GlaxoSmithKline plc)[308], I-BET 762 (GSK525762, GlaxoSmithKline plc)[309] or BAY1238097 (Bayer)[310,311]. Overall, 24 clinical studies are registered at the NIH (National Institutes of Health, Bethesda, Maryland, USA) to date, which evaluate the application of different BET inhibitors in patients with cancer[312]. Although several experimental and clinical studies applying BET inhibitors are being conducted, their anti-tumoral activity has not been compared to each other so far. In addition, no specific small molecule exists which targets the BRD4 protein alone. All proteins of the BET family have similar structural binding sites, which are targeted by BET inhibitors to a similar extent[313]. This may create the impression that the BET inhibitors are not specific enough, although the proteins BRD2, BRD3 and BRD4 partly have the same cellular roles[314]. These findings are based on the application of different first and second generation BET inhibitors. A direct comparison of the activity of the older JQ1 and OTX015 compounds has only been carried out using preclinical models such as triple negative breast cancer or T-cell lymphomas[315,316]. Thus, it is difficult to predict whether the effects of the latest BET inhibitors (e.g. TEN-010) is similar to already validated BET inhibitors and especially whether these new drugs also have an effect on pediatric, *MYCN*-driven models. Moreover, (neuro)pediatric cancer studies lack the concept of indirect combinatorial approaches against MYCN, including BET inhibitors and other molecule classes, to achieve synergistic effects against tumor cells.

1.6.2 Targeting *MYCN* mRNA translation

Another possibility for an indirect therapy of MYCN-driven neuroblastomas can be aimed at reducing the translation of *MYCN* mRNA transcripts into functional proteins. Previous research has shown that MDM2 regulates *MYCN* mRNA stabilization and translation in human neuroblastoma cells[317]. The inhibition of MDM2 is therefore an option for treatment of high-risk neuroblastomas, which further promotes the reactivation of the p53 transcription factor, which in turn regulates e.g. cell cycle arrest, apoptosis and DNA repair[318–320]. A high *MYCN* mRNA expression in neuroblastoma not only ensures a high protein level, but also serves as a "sponge" to capture highly expressed tumor suppressor miRNA[321]. For instance, a report showed that the LIN28B protein induced murine neuroblastoma and enhanced *MYCN* expression via let-7 suppression[322]. A possible therapy for *MYCN*-amplified tumors would therefore be the application of miRNA mimics, e.g. of let-7[323], miR-17-5p antagomiRs[324] or miR-34a GD2-coated nanoparticles[325]. Other forms of therapy utilizing siRNA oligonucleotides (small interfering RNA), which can trigger a targeted knockdown of the *MYCN* mRNA (see method 2.5.7)[326,327]. Since a delivery to the target location inside the cell is also difficult in this context, liposome-*MYCN* siRNA-folic acid complexes have already been designed for improved uptake[328]. Other systems make use of viruses (e.g. adenoviruses) as tools for the transport of siRNA as shRNA (short hairpin RNA, see method 2.5.8)[329]. The major obstacles for the use of miRNA, siRNA or shRNA for targeting *MYCN* is the reduced stability of the RNAs, the administration of an RNA drug, the RNA

delivery into the cell target component and the achievement of an effective dose. However, in 2018 the first siRNA was approved as a medical intervention, known as Patisiran, against rare polyneuropathy[330]. Overall, studies and reports on other cancer entities suggest a promising future for RNA drugs in neuroblastoma against *MYCN* mRNA translation[331,332].

1.6.3 Preventing the oncogenic stabilization of the MYCN protein

Targeted inhibition of the MYCN protein is difficult because the protein is required for normal cell development in humans and drives cell proliferation and cell growth in many different parts of the body[333]. However, the pathogenic amplification of the *MYCN* oncogene and increased MYCN protein levels lead to excessive proliferation and a degenerated cell cycle of neuronal progenitor cells[334]. Various cellular proteins are responsible for the stabilization of the MYCN protein. They are central players in the control of the proliferation and cell cycle of neuronal progenitor cells and may serve as an indirect MYCN target.

Upon initial stimulation of the cell by growth factors, the dimerization and autophosphorylaton of RTK, as for example ALK or EGFR leads to phosphorylation of the PI3K/AKT/mTOR pathway or the RAS-RAF-MEK-ERK proliferation pathway[335] (Figure 15). These intracellular signaling pathways are important for the transmission of information involved in the regulation of many cellular processes, such as growth, proliferation, differentiation and metabolism. Common SNVs in *ALK* (e.g. F1174) found in neuroblastomas provide constitutive activity of the kinase, which leads to permanent activation of key pathways and subsequent growth of neuroblasts[336–338]. The downstream located phosphoinositide 3-kinase (PI3K) binds to the phosphorylated ALK protein and gets activated through phosphorylation. PI3K transduces signals from activated RTK, G protein-coupled receptors or from activated RAS protein[339]. Thus, PI3K is a stabilizer of the MYCN protein and is an essential node for cellular signal transduction, cell survival and cell metabolism[340]. The activation of PI3K through the stimulation of RTKs promotes cell growth and survival and conveys resistance to chemotherapy or chemosensitvy[341]. In neuroblastoma, *PIK3CA* gene mutations are infrequent (in about 2.9% of all cases) and do not occur together with a *MYCN* amplification[342]. This further indicates that PI3K signaling is not dependent on *MYCN* amplification[343]. Thus, it can be deduced that a PI3K inhibitor can be administered against all high-risk neuroblastomas, not only in cases harboring a *MYCN* amplification. The small molecule (NVP)-BYL719 alias alpelisib, a drug which showed promising results for the therapy of breast cancer, could be considered for the treatment of neuroblastoma (Figure 14A)[344]. Alpelisib specifically targets the catalytic subunit PI3Kα by competitively binding to the ATP (adenosine triphosphate) pocket in the kinase domain[345]. In contrast to earlier pan-PI3K inhibitors, alpelisib represents less off-target effects and toxicities[346]. However, the significance of a treatment using alpelisib has not yet been evaluated on neuroblastomas. PI3K inhibitor-based treatments against neuroblastoma were conducted in research settings using the small molecule inhibitor LY294002[343], PI-103[347] and the mycotoxin wortmannin[876]. Moreover, first findings highlight possible PI3Ki combinatorial treatments together with conventional

chemotherapy[348]. In addition, PI3K inhibition was found to downregulate the MYCN protein level, increase apoptosis and showed *in vivo* efficacy in TH-MYCN mice[347,349]. In the murine TH-MYCN model, MYCN overexpression is induced in neural crest cells, which solely leads to the development of tumors that are very similar to a human neuroblastoma[350]. Furthermore, it was reported that activation of GSK3β is responsible for the phosphorylation of MYCN after inhibition of PI3K[343]. After MYCN is phosphorylated by GSK3β, the protein gets ubiquitinated and subsequently degrades[343]. Due to the close biological relationship between the PI3K protein and the MYCN protein, an improved effect of PI3K inhibition in *MYCN*-amplified *in vitro* neuroblastoma models has been reported, but was not compared to non-*MYCN*-amplified models so far[343]. However, PI3K inhibitors applied in neuroblastoma *in vitro* models, so far, are generally considered to be non-selective, and in the case of the drug wortmannin, the effects of inhibition are irreversible, unlike with apelisib[351]. These reports thus point towards of the use of alpelisib as an specific anti-tumor treatment, as this small molecule has already been successfully tested in clinical trials including breast cancer, renal cell cancer and pancreatic tumors[352,353].

Following the activated PI3K/AKT/mTOR pathway including the subsequent phosphorylation of PI3K, inositol-containing membrane lipids become activated though PI3K[354]. The product of this phosphorylation, PIP3 binds to AKT, whereupon AKT is translocated to the membrane. At this site AKT gets activated by PDK1. The AKT protein then phosphorylates and thereby activates several substrates, for example mTOR[354]. Many small molecules are available which have shown to target the mTOR protein (e.g. rapamycin, everolimus) and have been demonstrated to harbor anti-cancer activity[355,356]. Moreover, combinations of mTOR inhibitors with single agents or in dual or even triple hybrid compounds have been increasingly used in neuroblastoma research[341,355–367]. By initiating the activation of the cellular RAS-RAF-MEK-ERK pathway, the PI3K kinase is phosphorylated by the G-protein RAS (guanosine triphosphate-binding protein)[339]. The activated RAS communicates the signal to the RAF kinase, which in turn gets activated. RAF then phosphorylates and activates MEK, after which ERK/MAP kinase is phosphorylated. Novel dual PI3K and RAS inhibitors (BEZ-235 or rigosertib[368]) are reported to successfully aim at both signaling pathways, the PI3K/AKT/mTOR pathway and the RAS-RAF-MEK-ERK pathway[369]. Furthermore, those inhibitors are described as beneficial for dual application using additional Raf inhibitors (RAF265 or dabrafenib)[363,370] or employing an inhibitor targeting the downstream located MEK proteins[370–372]. Earlier studies highlighted the combined PI3K/AKT and RAF/MEK/ERK pathway inhibition in Hodgkin lymphoma[373] and colorectal cancer[374], applying effective PI3K/ERK dual inhibitors (e.g. AEZS-136 or DPS-2). Besides PI3K, other kinases like PLK1 (polo-like-kinase 1) also play an important role in the stabilization of the MYCN protein. PLK1 belongs to the serine/theronine protein kinases and has a central role in the cell cycle and cell division. For example, PLK1 is involved in the onset of mitosis, regulation of the G2/M checkpoint, control of the centrosome, centrosome maturation, mitotic spindle assembly and chromosome segregation[375,376]. The deregulation of the PLK1 protein in neuroblastoma is initiated from several starting points. First, PLK1 is highly expressed in unfavorable neuroblastomas

and associated with high-risk criteria (including *MYCN*-amplified tumors)[377]. Second, PLK1 indirectly stabilizes the MYCN protein[378]. The stabilization is achieved by autopolyubiquitination and proteasomal degradation of ubiquitin ligases via PLK1 which prevents degradation of MYCN and other proteins such as cyclin E and MCL-1. And third, stabilized MYCN activates PLK1 transcription[378]. Various inhibitors targeting PLK1 in neuroblastoma models have already been tested successfully, including the small molecule BI 2536[377,379,380], GW-843682X[379] and GSK461364[381]. Moreover, Pajtler et al. highlights the inhibition of neuroblastoma cell growth though GSK461364 regardless of the *MYCN* copy number status[887]. The inhibitor BI 6727 (volasertib), a dihydropteridine derivative, showed significant anti-tumor potential and high selectivity upon single drug application in neuroblastoma and rhabdomyosarcoma models[382,383] (Figure 14B). Volasertib is competitively targeting the ATP-binding pocket of PLK1, similar to the PI3K inhibitor alpelisib[384]. Although the efficacy of PLK1 inhibition against neuroblastoma could be shown experimentally *in vivo*, initial clinical testing has so far been unable to demonstrate comprehensive clinical applicability[381–383]. Beyond a singular treatment against the PLK1 protein, successful combinations of PLK1 inhibitors in addition with vinca alkaloids, BET inhibitors and HDAC (Histone deacetylases) inhibitors were described[383,385–388]. However, single PLK1 drugs such as volasertib not only inhibit PLK1 but are also effective against the kinase PLK2 and the PLK3 tumor suppressor[389–391]. PLK3 in particular activates and stabilizes other tumor suppressor proteins such as p53[392]. This has fostered the need for specific PLK1 inhibitors, such as rigosertib, a RAS-mimetic[368] (Figure 14C).

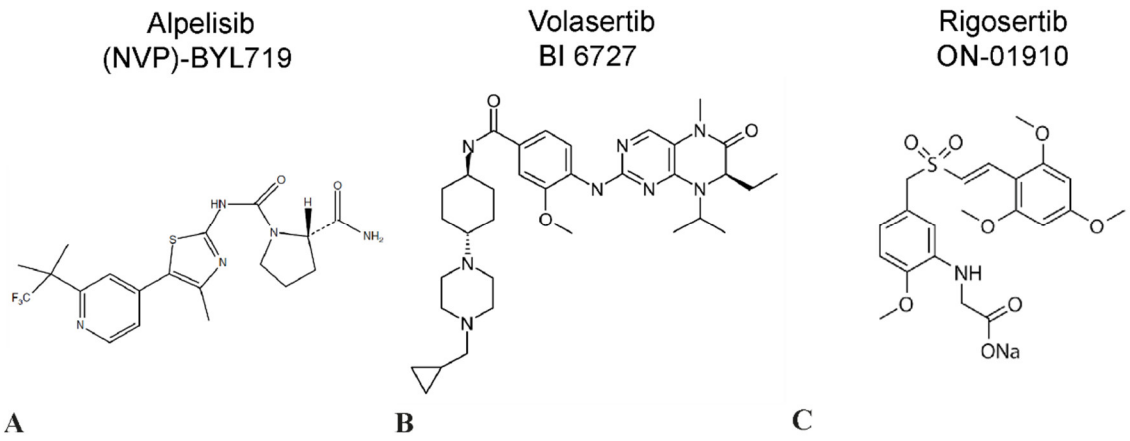

Figure 14: Chemical structures of the PLK1/PI3K inhibitors alpelisib, volasertib and rigosertib.
A selection of small-molecule PLK1/PI3K inhibitors which prevent the stabilization of the MYCN protein. **(A)** Alpelisib, an ATP competitor, targets the PI3K kinase. **(B)** Volasertib as well represents an ATP competitor, which acts against the PLK1 kinase. **(C)** Rigosertib, a dual kinase inhibitor, attracts the RBD of kinases, for instance as found in PI3K and RAF kinases. (Figure modified from Markham 2019 (alpelisib)[344], Gjertsen & Schöffski 2014 (volasertib)[393] and Selleck Chemicals 2013 (rigosertib sodium)[394].)

Rigosertib (ON-01910) is a multi-kinase inhibitor, which suppresses the activity of the cell cycle regulator PLK1 and the PI3K signaling pathway activation (Figure 15).[395,396]. Both PLK1 and PI3K are expressed at elevated levels in high-risk neuroblastomas and correlate with an unfavorable disease outcome[361,397]**.** Rigosertib attacks the RAS-binding domain (RBD) of kinases (e.g. PI3K and RAF),

leading to the inability for the kinase to bind its native substrate RAS. The inhibitor was described in early publications as direct PLK1 inhibitor, but rigosertib does only indirectly suppresses the PLK1 kinase activity through inhibition of the CRAF^{Ser338}-mediated PLK1-activation via its polo-box domain (PBD)[398].

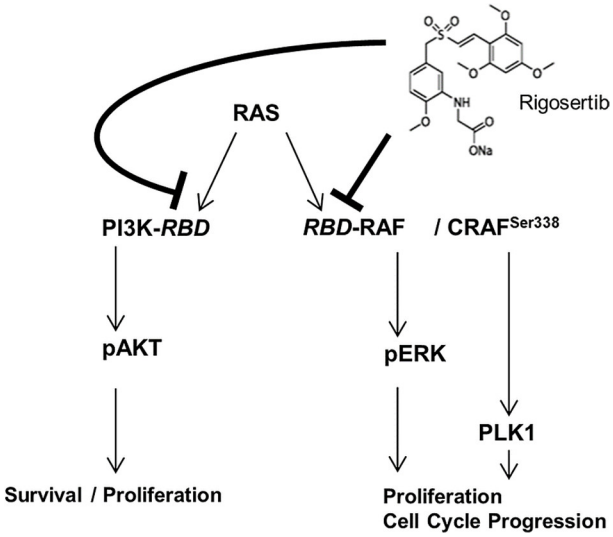

Figure 15: Kinase inhibitors like rigosertib prevent RAS-mediated ERK- and AKT activation in cancer cells.
Rigosertib interacts with the RAS-binding domains of different kinases such as PI3K and RAF. Thereby downstream pathways such as RAS-RAF-ERK and PI3K-AKT are inhibited and thus the survival, the proliferation and the progression of the cell cycle of malignant cells. (Figure taken from Dietrich et al. 2017[398]).

Thus, is was shown that rigosertib treatment induced a mitotic arrest in tumor cells[399]. Rigosertib was tested successfully in several cancer entities, such as the myelodysplastic syndrome[400], leukemia[401], head and neck cancer[402], head and neck squamous cell carcinoma[403] and epidermolysis bullosa-associated squamous cell carcinoma-cell lines[404]. Based on these promising reports and due to the fact that the kinases PI3K and PLK1 contribute to the stabilization of the MYCN protein, rigosertib is considered to be a potential therapeutic option for neuroblastoma[343,378]. Findings in other tumor entities also demonstrated that rigosertib could be combined effectively with conventional chemotherapy and furthermore, a synergistic effect was archived[405,406]. These are first evidences that rigosertib could be well integrated into the standard neuroblastoma induction regimen. In addition, a combination of rigosertib with DNA methyltransferase inhibitors (e.g. azacitidine) was proposed[407,408].

In summary, it was demonstrated that the prevention of MYC(N) protein stabilization by small molecules is the most investigated therapy on targeting MYC(N). Especially the inhibition of the kinases with the PI3K/AKT/mTOR pathway or the RAS-RAF-MEK-ERK pathway have shown significant success. Moreover, targeted therapies inhibiting the stabilization of MYCN also demonstrate promising results regarding combinatorial treatment approaches. The destabilization of MYCN by indirect targeting is therefore an important treatment option for neuroblastoma. To date, there is only limited data published on the use of volasertib in neuroblastoma, and so far no studies are reported on alpelisib or rigosertib use in neuroblastoma. In future studies it has to be evaluated if these small molecules are also suitable for neuroblastoma treatment. Moreover, the mechanism of combination treatments adding

conventional chemotherapy and/or other targeted treatments must be better understood, as this provides the basis for implementation of the targeted therapies into clinics.

1.6.4 Blocking MYCN dimerization and transcriptional activity

MYCN binds to the MAX protein via their BR/HLH/LZ domains[113,114], which can be used as a target structure for MYCN-MAX dimer disruptors. Successful small molecules have already been described, e.g. the inhibitors 10058-F4 and 10074-G5, which induce differentiation and apoptosis of neuroblastoma cells upon application[409,410]. *In vivo,* the drug 10058-F4 has shown tumor growth inhibition in *MYCN*-amplified PDX (patient derived xenograft) mice and increased survival in treated TH-MYCN mice[411]. However, these inhibitors have a short half-life due to difficult solubility and rapid metabolization, which is in line with reports of the low uptake of 10058-F4 in solid adult tumors[412,413]. In this regard, small molecules with a broader efficacy that cause the reduction of all MYC family proteins (e.g. KI-MS2-008) might also effect normal cell proliferation[414]. Another drug candidate, MYCMI-6, demonstrated a good inhibitory activity against neuroblastoma models[415]. Nevertheless, the administration of MYCMI-6 does not lead to the degradation of the MYC(N) protein or the blockage of MYC(N) expression, but only to the inhibition of the MYC(N)-MAX interaction. It is therefore difficult to say whether MYCMI-6 is sufficient to inhibit high levels of overexpressed MYCN due to its enhanced transcription. An additional approach to MYCN-MAX inhibition is the use of a mutant HLH peptide (helix-loop-helix, dominant negative) that mimics a binding partner of MYCN, such as the omomyc peptide[416]. After the administration on cancer cells, the transcriptional activation of MYCN downstream targets is prevented[417]. Omomyc has already been shown to be effective against neuroblastoma *in vitro* models[418,419]. The inhibitor is currently in transition from pre-clinical research (and transgenic gene expression[420]) to clinical application (using an omomyc purified mini-protein[421]), but has shown safe and potent efficacy in *in vivo* experiments so far[422].

1.6.5 Targeting MYCN-driven cell proliferation through inhibition of mitotic spindle assembly

Disturbances in the homeostasis of cell proliferation are hallmarks of tumorigenesis as well as of the pathogenesis of developmental defects. While an increased proliferation of neuronal progenitor cells is central in the tumor biology of the embryonal tumors including neuroblastoma, a reduced proliferation of neuronal progenitor cells is a cause of congenital microcephaly[423–425]. The prototype of congenital microcephaly, primary autosomal recessive microcephaly (MCPH), is a rare and genetically heterogeneous neurodevelopmental disease. It is characterized by severely reduced brain volume at birth (defined by the occipitofrontal head circumference which is more than two standard deviations below the mean for age, sex and ethnicity[426]), mostly of the cerebral cortex, and the patients show an intellectual disability[427,428]. With a prevalence ranging from 1:30,000 to 1:250,000 live births, it is considered a rare

disorder[426,428,429]. So far, mutations in 23 genes have been shown to cause MCPH (see Table 28). The main etiological factor of MCPH is a proliferation defect of neural stem cells, causing a premature switch from symmetric (stem cell pool regenerating) to asymmetric (differentiation promoting) stem cell divisions[428]. Mutations in the gene coding for the abnormal spindle-like, microcephaly associated protein (ASPM or MCPH5, located on chr.1q31.3 (GrCh38)), are the most common cause of MCPH[430]. ASPM was found to have a main function in the orientation of the mitotic cleavage plane leading to a symmetric, proliferative division of neuroepithelial cells during brain development[431]. Moreover, ASPM takes part in cell migration, neuronal plasticity and neuronal signaling[432,433]. The absence of ASPM promotes asymmetric cell divisions and modified division planes, which can cause premature differentiation over proliferation[434]. The full length human ASPM protein contains a microtubules binding domain, two actin binding calponin homology domains and several calmodulin-binding IQ (isoleucine-glutamine) motifs which supports spindle rotation[435–437]. Phylogenic studies suggest that ASPM was an important factor in the expansion of the human brain size and the evolution of language promoted by gene insertion of roughly 900bp[438–440]. Mutations of the ASPM gene in MCPH can be manifold, ranging from a complete loss of the gene, to large partial deletions including several exons and different SNVs (often deletions and nonsense mutations)[426]. In particular, mutations are found frequently in the region which encodes for the microtubules binding site[426]. ASPM is a centrosomal protein that localizes at the spindle poles during mitotic cell division[441,442] and is required to maintain the structure of the centrosome, a microtubule-organizing center (MTOC), where the formation of microtubules is initiated (Figure 16)[443–453]. One MTOC is composed of the centrosome which consists of two centrioles and the surrounding pericentriolar material (PCM)[454]. The ASPM protein has a dual affinity for the components of MTOCs and functions as a connector anchoring the α-tubulin proteins of microtubule minus ends to the centrosomes[443,455–459]. For the assembly of the MTOC within mitosis, the PLK1 kinase plays an important role[375,376,449]. PLK1 can promote G2/M progression, centrosome maturation, the mitotic spindle assembly and chromosome segregation[375,376]. Moreover, PLK1 aims kinetochore to microtubule attachment to ensure chromosome stability against pulling forces during mitosis[460,461]. On average, a force of 750pN is applied to the centromeres of the chromosomes via 15 microtubules to perform cell division, whereas the tensile strength of the DNA is only around 250pN of force[462,463]. Interestingly, PLK1 stabilizes the MYCN protein[378] and in turn, its transcription is activated by stabilized MYCN[378]. The function of ASPM is modulated by the interaction with PLK1 supporting the maintenance of the pole structure of bipolar spindles[444]. During mitosis, ASPM is recruited to the PCM at the spindle poles[464], where the protein is involved in mitotic spindle stabilization[465], organization and positioning[464] through the recognition of growing microtubules in cells. As ASPM binds to microtubules, their growth is stopped, ensuring their stability[443,466,467]. Beside mitosis, stabilized microtubules improve a binding by the kinesin-13 family of proteins[459,466,468,469]. These motor proteins use the microtubules as intracellular “roads” to transport proteins, vesicles and organelles through the cytoplasm of the cell[470–472]. In developing neurons, blocked minus end microtubules get disassembled

by kinesin-13 proteins which further drives the microtubule and cell spindle flux[459,466,468,469]. The movement of microtubules is a crucial process in the development of mature neurons and their plasticity[457,458,467,471]. In the course of development, the microtubules are cut off from the centrosomes and parts of them are transported into the emerging axons and dendrites[473–476]. Some of these microtubules remain in the cell soma resulting in a mixture of plus/minus end directed microtubules in the entire neuron. In this process, minus end leading microtubules are always located to dendrites, where the neuron is electrochemically stimulated via synapses and thus, cellular information is transmitted[458]. The maturation of neurons is coupled with the migration of these cells to the respective brain target regions, which is mediated by microtubules[477]. For cell movement, the microtubules get shuttled to the centrosome building a fork- or cage like structure, pulling the cell soma in the direction of the leading edge[456,459,478]. Mouse experiments showed that *ASPM* is specifically expressed in the cerebral regions at embryonic day 14.5 during normal brain development[479]. Later, *ASPM* expression is diminished at embryonic day 16.5 and was greatly reduced at birth.

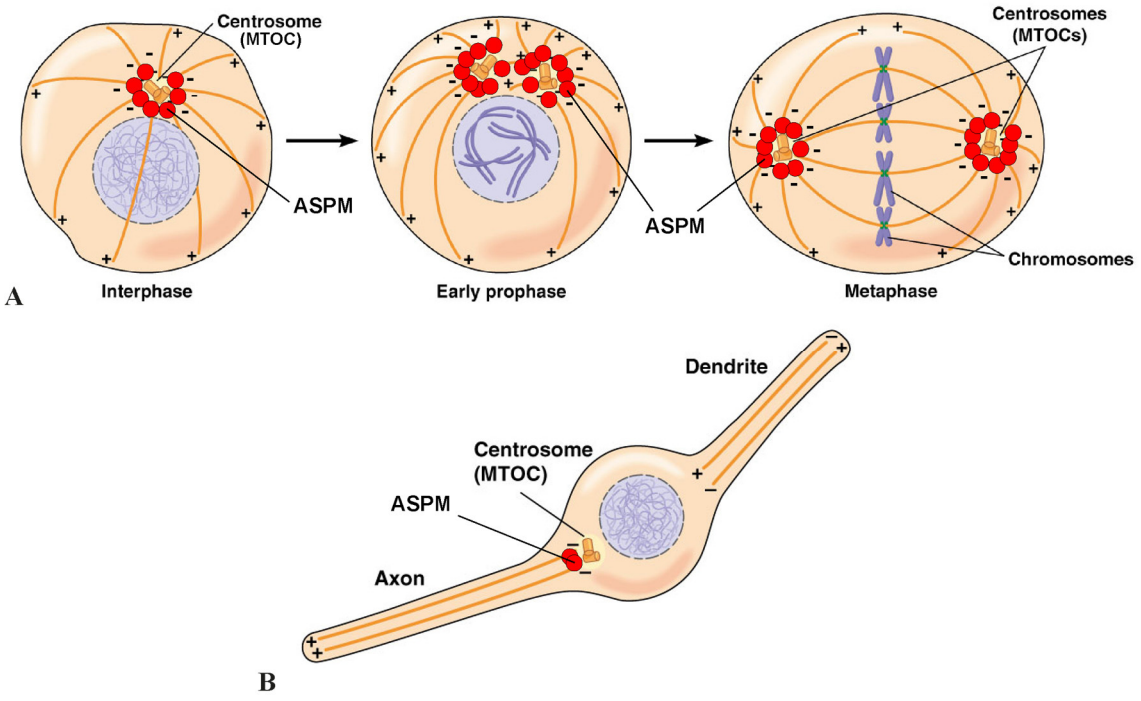

Figure 16: ASPM, a microtubule-binding protein, is associated with centrosomes (MTOCs).
ASPM is located at the cellular spindle poles and connects the microtubules to the centrosomes (MTOC). **(A)** At the onset of mitosis, the ASPM protein is recruited to the PCM (interphase), where ASPM anchors the α-tubulin proteins of microtubule minus ends to the centrosomes (early prophase). Later, ASPM stabilizes the mitotic spindle and is required for spindle organization and positioning (metaphase). **(B)** Since ASPM is associated with the minus ends of microtubules, this protein might also influence neurite (axon) establishment, growth guidance and neuronal maturation. ASPM is highlighted by red dots. (Figure modified from Hardin, Bertoni & Kleinsmith 2010[480]) .

These observations from animal experiments are consistent with the knowledge of human embryonic development, showing a change from symmetric to asymmetric cell division after about 30 days of gestation[481,482]. In summary, the assembly of microtubules is critical for a neuron in terms of

proliferation, differentiation, migration, intracellular transport, neuronal signaling, and plasticity, and their stability is controlled through ASPM[466]. Opposed to a dysfunctional or loss of the ASPM protein following the reduction of proliferation in MCPH microcephaly, *ASPM* overexpression showed an initiation of increasing cellular proliferation in cancer[483,484]. *ASPM* mRNA has been found upregulated in medulloblastoma[485,486], glioblastoma[487,488], ependymomas[489], hepatocellular carcinoma[490], prostate cancer[491], ovarian cancer[492] and bladder cancer.[493] Due to its role in regulating proliferation in neuronal progenitor cells, MCPH genes and in particular ASPM, might be driver of neuroblastoma. In addition, ASPM is functionally linked to PLK1 in the mechanism of cell division and stabilization of MYCN. A very recent review suggested that the stabilization of MYCN further results in symmetric cell divisions in MYCN-dependent neuroblastoma cells[494]. This implies that ASPM might be a new potential target for small molecules being developed for the treatment of high-risk neuroblastoma.

1.7 Motivation and aim of the thesis

The transcription factor *MYCN* is amplified in about 25% of all neuroblastoma cases and associated with a dismal prognosis. Although the extent of the amplified *MYCN* oncogene-spanning chromosome 2 in HSR or DM has been explored in several studies, little is known about the exact structure and the rearrangement breakpoints of the pathological amplicon. *MYCN* amplifications in patient material, especially in tumor samples, are detected with simple molecular biological methods as part of diagnostic investigations within current study protocols. Currently, there is no diagnostic panel available which is tailored to the in-depth detection of the *MYCN* oncogene or to other regions relevant for the diagnosis of neuroblastoma.

The objectives of the first part of this thesis are to evaluate a custom neuroblastoma hybrid-capture based NGS panel in order to provide improved risk stratification and to detect neuroblastoma residual disease based on *MYCN* amplicon breakpoints. The *NB targeted NGS assay* is intended for high coverage (>1000x) detection of gene mutations and large genomic structural changes, it also yields information about possible targets for indirect *MYCN* molecular therapies. The extensive coverage of the complex *MYCN* amplicon should provide further insight into the structure of the amplified gene and the distribution of its unique breakpoints. Previous attempts to use the specific genomic breakpoints sought to develop sensitive PCR test systems for neuroblastoma detection[89,247]. However, technical difficulties and the complexity of the mapping and analysis of genomic *MYCN* breakpoints for individual patients have, as yet, prevented the translation of PCR based neuroblast detection into clinical practice. Employing the *NB targeted NGS assay* on cell line and tumor material, the hypothesis is that the detection of unique *MYCN* breakpoints by RQ-PCR and ddPCR techniques may be suitable for sensitive quantification of MRD neuroblastoma cells. This work will further address and evaluate the applicability of these *NB breakpoint MRD assays* for longitudinal clinical samples (e.g. bone marrow aspirates). Additionally, those RQ-PCR and ddPCR MRD assays are to be compared with available gold standard techniques (e.g. FISH, immunocytology) of tumor cell infiltration on clinical specimens. Eventually, the findings will stipulate standardized sample processing and analysis guidelines, which may support therapy decisions on a personalized basis.

In addition to determining *MYCN* amplicon breakpoint information for application in clinical diagnostics, this thesis also includes preclinical investigation of the indirect targeting of *MYCN* in high-risk neuroblastoma models. As it is difficult to target small, surface inaccessible proteins like *MYCN* and other transcription factors, this thesis addresses *MYCN* inhibition via alternative drug targets. Small molecules against indirect target proteins already exist, which affect the molecular network of *MYCN* by focusing on the different biological roles of the protein in cellular function. One approach will be to inhibit *MYCN*-associated transcription by targeting BET proteins, which can be evaluated by dose

response assays of promising BETi drugs (JQ1, OTX015 and TEN-010) in *in vitro* experiments on neuroblastoma cells lines. The other approach focuses on *MYCN* biology with the aim of preventing *MYCN* protein stabilization, by inhibiting cell signaling transmission of several kinases. Small molecule inhibitors of either PI3K (alpelisib), PLK1 (volasertib) or both (rigosertib) have been shown to have specific antitumoral efficacy, which will be tested individually on neuroblastoma cell lines using dose response assays. Particular consideration is given to the *in vitro* investigation of rigosertib for neuroblastoma treatment, a dual PI3K/PLK1 inhibitor with additional anti-RAS activity, which is already under clinical investigation for leukemia. A first evaluation of the clinical applicability of rigosertib for neuroblastoma therapy will be attempted with *in vivo* administration in PDX mice. In addition, I seek to address a multidrug approach to treat *MYCN*-driven neuroblastomas by employing BETi plus protein kinase inhibitors. A third angle is to tackle the protein ASPM, a substrate of the PLK1 kinase, as a potential new indirect MYCN target. ASPM controls spindle assembly during cell division, and loss-of-function mutations in *ASPM* are a common cause of MCPH microcephaly, a disorder arising from defective neural stem cell proliferation. In contrast to the depletion of *ASPM* in MCPH microcephaly, it is questioned whether *ASPM* is overexpressed in neuro-pediatric tumors, especially neuroblastoma. A further question is whether a variation in the *ASPM* mRNA level affects clinical outcomes, especially if increased *ASPM* expression is indicative of a high-risk neuroblastoma. It will also be investigated whether an alteration of the *ASPM* level has a functional effect on the viability, proliferation, apoptosis and differentiation status of neuroblastoma cells. Finally, ASPM will be investigated as a biomarker and a new drug target for *MYCN*-driven neuroblastomas.

2 Methods

This section describes in detail the research methods used in this thesis. For more information, including the materials utilized, this can be found in the appendix section (10). All read-out assays were conducted in at least three biological replicates using three technical replicates each time, unless otherwise specified in the method and the results section. The generated data was exported to Excel 2016 (Microsoft Corporation, Redmond, WA, USA) and visualized with GraphPad Prism® version 7.0 (Graphpad Software, Inc., San Diego, CA, USA). See as well 2.10, unless otherwise specified in the method section.

2.1 Origin of biomaterial and data

2.1.1 Patients and biomaterial samples and data

Patients of the NB targeted assay and the NB-MRD project were enrolled in the German neuroblastoma trial (NB2004) or the German Neuroblastoma Registry (NB Registry 2016)[30,236,237,495]. Written informed consent from patients or parents/guardians is available within the trial and registry documentation. Tumor tissue samples were obtained from the German Neuroblastoma Biobank (Cologne, Germany) for initial biopsies (7 patients) and biopsies after relapse (2 of the 7 patients). Tumor tissue and bone marrow aspirates were obtained directly from 6 patients treated at the Department of Pediatric Oncology and Hematology (Charité – Universitätsmedizin Berlin, Berlin, Germany). Written informed consent was obtained from patients or parents/guardians within the ERA-NET (European Research Area Networks) LIQUIDHOPE consortium, which obtained ethics approval from the local Charité Ethics Committee (EA2/055/17). Clinical features of the patient cohort are listed in Table 11 within the appendix. Control DNA for *NB breakpoint MRD assays* sensitivity evaluation was obtained from mononuclear cells of peripheral neuroblastoma-free blood pooled from at least ten healthy individuals was available by the MRD molecular genetics laboratory of the ALL-REZ BFM trials (Protocol for the treatment of children with recurrence of acute lymphoblastic leukemia, Charité)[161]. This control was named “buffy coat” in this thesis. Whole-genome sequencing data from 14 primary *MYCN*-amplified neuroblastomas obtained within previous studies was used for breakpoint analysis[43,44,76]. For the investigation of MCPH genes in different tissues, preprocessed gene expression data from 25 data sets (n = 3,984 samples in total) were downloaded from the R2 Platform[496,497] (sources and details see Table 27 in appendix). Processed data from the SEQC dataset[42], which comprises data of 498 primary neuroblastomas profiled by RNA-Sequencing, were downloaded from the NCBI GEO (Gene Expression Omnibus) database (NCBI, NIH, Bethesda, MD, USA)[498,499].

2.1.2 Mice strains

To assess the anti-tumoral effectiveness of the PLK1/PI3K inhibitor rigosertib, a total of three different neuroblastoma PDX *in vivo studies* were carried out. Two studies using patient tumor engraftments were

performed using a highly immunocompromised NOG mice strain, or more precisely CIEA NOD.Cg-*Prkdc*^{scid} *Il2rg*^{tm1Sug}/JicTac. One study using IMR5/75 cell line engraftments was performed using a NMRI$^{nu/nu}$ nude mice strain, or more precisely BomTac:NMRI-*Foxn1*^{nu}. All mice were female animals and were obtained from Taconic Biosciences, Inc. (Rensselaer, NY, USA). The purchase and keeping of the mice was carried out by Experimental Pharmacology & Oncology Berlin-Buch GmbH (EPO, Berlin, Germany) as part of the rigosertib *in vivo* efficacy studies (study MV16240, study MV16158 and study MV16738). All experiments were performed according to local animal experimental ethics committee guidelines.

2.1.3 Cell lines

This section contains information on the origin of the cell lines used. The human neuroblastoma cell line BE(2)-C was obtained from European Collection of Authenticated Cell Cultures (ECACC) (Salisbury, UK) and the cell lines Kelly, SH-SY5Y, LAN-1 and LAN-5 were obtained from the German Collection of Microorganisms and Cell Cultures GmbH (DSMZ; Braunschweig, Germany). CHP-212 was obtained from the American Type Culture Collection (ATCC; Manassas, VA, USA). The cell lines SK-N-BE, SK-N-FI, SK-N-BE(2), NB-1634, Rh1 rhabdomyosarcoma (reclassified as Ewing family tumor based on molecular signature)[500] and HEK293 kidney epithelium cells were kindly provided by J.H. Schulte (Charité). CHLA-90 was kindly provided by H.L. Davidson (Children's Hospital of Philadelphia, Philadelphia, PA, USA). NGP was kindly provided by F. Speleman (Cancer Research Institute Ghent, Ghent, Belgium). TR-14 and N206 cell lines were kindly provided by J. J. Molenaar (Princess Máxima Center for Pediatric Oncology, Utrecht, Netherlands). IMR5/75 was kindly provided by F. Westermann (German Cancer Research Center, Heidelberg, Germany). SK-N-DZ was kindly provided by A. Künkele (Charité). IMR-5, IMR-32, CHP-134, SH-EP, NBL-S, SK-N-AS, SK-N-SH, GI-ME-N and HeLa cervix adenocarcinoma were kindly provided by A. Schramm (Medizinische Fakultät, Universitätsklinikum Essen, Essen, Germany). BJ1-hTERT foreskin fibroblasts and hTERT RPE-1 retinal pigment epithelial cells were kindly provided by A. G. Henssen (Experimental and Clinical Research Center, ECRC, of the Charité and Max-Delbrück-Center for Molecular Medicine, MDC, Berlin, Germany). Foreskin fibroblast cell line VH7 was kindly provided by H. E. Deubzer (Charité). HEK293T cell line (highly transfectable, contains SV40 T-antigen[501]) used in lentivirus experiments was kindly provided by K. Ahrens and F. Buttgereit (Charité). Primary human embryonic lung fibroblast cell line PLF (Fi301)[502] was kindly provided by C. Hagemeier (Charité). Master stocks for all cell lines were authenticated by short tandem repeat DNA typing (STR) by Idexx Bioresearch (Westbrook, ME, USA) or Multiplexion (Heidelberg, Germany) before conducting experiments. Cultures were routinely tested for the absence of *Mycoplasma sp.* contamination using MycoAlert™ Mycoplasma Detection Kit (Lonza Group Ltd., Basel, Switzerland). Established human cell lines used in this thesis are listed in Table 9: in the appendix.

2.2 Patient material processing

2.2.1 Mononuclear cell purification from bone marrow aspirates

The bone marrow aspirate was collected directly into EDTA-anticoagulated tubes (BD Vacutainer® blood collection tubes; BD Biosciences, Franklin Lanes, IN, USA). Samples taken were processed for Ficoll density gradient centrifugation[503,504] as published previously by Krentz/Eckert et al.[505] within 1-4h of collection. Aspirates were diluted 1:3 in Roswell Park Memorial Institute (RPMI) 1640 media, were carefully overlaid onto 4ml Biocoll® (Biochrom, Merck KGaA, Darmstadt, Germany) per 5ml diluted aspirate, then separated by centrifugation at 2400rpm for 20min at 20°C and decelerating without breaking. The mononuclear cell fraction (peripheral blood mononuclear cell, PBMCs) was aspirated out of the gradient and washed twice with equal volumes of RPMI 1640 followed by sedimentation at 1500rpm for 10min at 20°C. If samples were contaminated with erythrocytes, they were lysed with ammonium chloride (see buffer recipe 10.5.1), before washing mononuclear cells again twice with 1x PBS (phosphate-buffered saline) and centrifugations at 1500rpm for 10min at 20°C. Mononuclear cells were quantified using a Neubauer cell counting chamber (or Neubauer improved; BRAND GMBH + CO KG, Wertheim, Germany), and DNA was isolated (see 2.2.2) from 1 x 10^6 to 4 x 10^6 cell aliquots before storing at -20°C until use in *NB targeted NGS assay* (2.8.1), RQ-PCR (2.6.17) or ddPCR (2.6.19).

2.2.2 Isolation of genomic DNA from mononuclear cells, snap-frozen tumor material or FFPE tumor material (Charité or NEO New Oncology GmbH)

DNA for *NB targeted NGS assay* or *NB breakpoint MRD assay* was either isolated by A. Szymansky/ J. Proba (Charité) or by NEO New Oncology GmbH Cologne, Germany or Institute of Hematopathology Hamburg, Germany. For sample preparations conducted at Charité, DNA was isolated from mononuclear cell purification from bone marrow aspirates (2.2.1) or from surgery-obtained snap-frozen tumor material collected at Charité using the NucleoSpin® Tissue kit (Macherey-Nagel GmbH & Co. KG, Düren, Germany) according to the manufacturer's instructions. For tumor DNA isolations from formaldehyde-fixed paraffin-embedded tissue (FFPE) tissue sections obtained at Charité, DNA was isolated using the QiAamp DNA FFPE Tissue Kit (QIAGEN N.V., Hilden, Germany) according to the manufacturer's instructions. For sample preparations conducted at NEO New Oncology GmbH or Institute of Hematopathology Hamburg, DNA was isolated from macrodissected cells from 10-15 units of 10µm sections of FFPE or snap-frozen tumor material obtained from the German Neuroblastoma Biobank or Charité. The tumor material was histologically evaluated by an experienced pathologist, and only regions with at least 10% tumor cell content were accepted. If tumor content was reduced, tumor cells were accumulated by laser microdissection (Leica LMD 6500; Leica Microsystems) for cases with limited tumor cell content. DNA was automatically extracted using a Maxwell® Instrument and Maxwell® 16 FFPE Plus LEV DNA Purification Kit (Promega Corporation, Madison, WI, USA), then

sheared mechanically by ultrasonic acoustic energy (Covaris ultrasonicator (Covaris, Matthews, NC, USA).

2.2.3 Measurement of DNA concentration

DNA concentration (ng/µl) of isolated bone marrow, snap-frozen tumor or FFPE derived tumor DNA samples have been measured using a NanoDrop™ 2000 spectrophotometer (Thermo Fischer Scientific) according to the manufacturer's instructions. DNA (1.0µl volume) was measured applying dsDNA settings with a nucleic acid absorbance wavelength ratio of 260/280nm. An optical density OD_{260} of 1 corresponds to 50µg/ml double-stranded DNA. Baseline correction was applied with 340nm. The detected signal is used by the NanoDrop 2000 software to calculate the amount of DNA in a solution. Any Protein contamination was detected at 280nm.

2.2.4 Measurement of DNA size, concentration and integrity

The isolated tumor DNA for *NB targeted NGS assay* was tested for size, concentration and integrity using a 4200 TapeStation System (Agilent Technologies, Inc., Santa Clara, CA, USA). Genomic DNA ScreenTape analysis was performed according to the manufacturer's instructions and passed samples showed a DNA Integrity Number of at least 8.0 applying standard settings.

2.2.5 Whole genome amplification of patient derived DNA

Occasionally, the available amount of patient-derived tumor or bone marrow DNA was low, therefore it was necessary to amplify the DNA for classical PCR assay establishment. DNA was whole genome amplified using the REPLI-g® UltraFast Mini Kit (QIAGEN) applying the UltraFast protocol for 1.5h at 30°C and for 3min at 65°C.

2.3 Animal experimentation

2.3.1 *In vivo* rigosertib efficacy testing using patient-derived xenograft mice models

The efficacy of rigosertib was tested on its anti-tumor potential in neuroblastoma PDX mice models using female immunodeficent NOG or NMRI nude mice. The mouse experiments were carried out in three independent test series under sterile conditions. In the first series, a total of 10 NOG mice were subcutaneously engrafted with a high-risk *MYCN*-amplified neuroblastoma tumor (patient 11, internal no. CB1057, passage 5, for more information see Neuroblastoma MRD Table 16 in appendix). The mice were 47 days old at the time of fragment engraftment. The experiment was started when the tumor had grown to a size of 0.2 – 0.25cm³ (around 2-3 weeks after PDX transplantation) with a solid and firm to soft character. The group of 10 mice was then randomized into two groups of 5 mice each, a treatment group and a vehicle group. The mice were 66 days old at the time of treatment start. The treatment was conducted with rigosertib sodium (batch: 592542-60-4; Axon Medchem LLC, Reston, VA, USA).

The rigosertib sodium powder was solved in a concentration of 50mg/ml in PBS. The treatment was applied at a daily intraperitoneal injection (i.p.) dose of 250mg/kg body weight per mice of the first group for a total of 14 days. The treatment was administered daily (7 days/week and single dose of 250mg/kg weight). The treatment scheme for rigosertib *in vivo* experiments has already been published in detail by Gumireddy et al.[406]. Previously, the pharmacological safety profile of rigosertib was also determined in two standard toxicology animal studies using rats and dogs by Gumireddy et al[403,506,507]. As a vehicle control for the second group only the solvent PBS in a dose of 10ml/kg was applied. To determine the efficacy of rigosertib on neuroblastoma tumors, the parameters body weight and tumor volume were recorded twice a week (five times within two weeks). In addition, the parameter survival was recorded as well. At a tumor size of >1.5cm³, the experiment was terminated for the affected mouse (cause of death: tumor volume), as well as for both experimental groups overall on day 15 (cause of death: study end). At the end of the experiment, two snap-frozen tumor samples, one tumor sample for FFPE preparation and blood serum were collected per mouse. For the second test series administering rigosertib, a total of 10 NOG mice were subcutaneously engrafted with a high-risk non-*MYCN*-amplified neuroblastoma tumor (patient not enclosed in this thesis, internal no. CB1002; passage 7). The mice were 38 days old at the time of fragment engraftment and 63 days old at the time of treatment start. The treatment was applied in an i.p. dose of 250mg/kg body weight per mice of the first group for a total of 14 days. The treatment was administered on five consecutive days followed by a two-day break (5 days/weekend-off schedule and using a single dose of 250mg/kg weight). As a vehicle control for the second group only the solvent PBS in a dose of 10ml/kg was applied. The termination criteria applied were the same as in the first study. For a third test, a total of 18 NMRI nude mice were subcutaneously engrafted with a *MYCN*-amplified neuroblastoma cell line (IMR5/75). The implanted cell line is derived from the IMR-32 cell line which originates from an abdominal primary tumor of a 1Y1M old male patient, with a stage 4 disease (see Table 9 in appendix)[508]. The immundeficient NMRI nude female mice with subcutaneously engrafted neuroblastoma xenografts were randomized in two groups (n=8). Rigosertib sodium was applied in an i.p. dose of 250mg/kg body weight per mice of the first group for a total of 14 days. The treatment was administered on seven consecutive days (7 days/week schedule and using a single dose of 250mg/kg weight). As a vehicle control for the second group only the solvent PBS in a dose of 10ml/kg was applied. The termination criteria applied were the same as in the first study. *In vivo* rigosertib efficacy testing using PDX mice models was performed in cooperation with EPO Berlin-Buch GmbH.

2.4 General cell culture methods

2.4.1 Culturing of cells

Neuroblastoma cell lines were cultured in RPMI 1640 or Dulbecco's Modified Eagle Medium (DMEM) (Thermo Fisher Scientific Inc., Waltham, MA, USA) supplemented with 10% fetal calf serum (FCS Superior; Merck Millipore, Burlington, MA, USA), 1% penicillin (100U/ml) and 1% streptomycin

(100µg/ml; P/S; Thermo Fischer Scientific) at 37°C and 5% CO_2. Cells were grown on cell culture dishes or flasks (Costar™, Corning, Inc., Corning, NY, USA or CELLSTAR®, Greiner Bio-One International, Kremsmünster, Austria). Cell culture media and additives used in this thesis are listed in appendix Table 10. Cells were controlled every day for growth and for contaminations via transmitted light microscopy using Axio Vert.A1. with 5x and 40x objective lenses and supported by Zen 2.3 lite software (Carl Zeiss AG, Oberkochen, Germany; see in detail 2.4.2). Cell maintenance was preserved via separation of the cell population in a ratio of 1:2 to 1:15 at approximately 80% confluence depending on cell line for at least twice a week. For the performance of *in vitro* experiments, cell lines were cultured for no more than 18 passages. Cells were seeded in different numbers depending on their growth rate and size (see Table 22 in appendix). Cryopreservation of cells was performed in FCS Superior containing 10% (v/v) DMSO (dimethyl sulfoxide; Sigma-Aldrich, St.Louis, MO, USA) at -196°C to -80°C.

2.4.2 Visualization of cell morphology with transmitted light microscopy

Cells were controlled every day via transmitted light microscopy using the ZEISS Axio Vert.A1. To assess GFP (green fluorescent protein) emission of manipulated cells, the GFP filter was used in addition (EX BP 470/40, BS FT 495, EM BP 525/50). Within inhibitor experiments, every 0^{th} and 3^{rd} day pictures of the cultures were taken with Zen 2012 1.1.0.0 (blue edition) software adjusted to 5x and 20x objective lenses. Cells treated within the ASPM project were controlled every 4^{th} and 10^{rd} day and pictures of the cultures were taken adjusted to 5x, 10x, 20x and 40x objective lenses. Pictures were saved as Carl Zeiss Image .czi and as Tagged Image Files .tif.

2.4.3 Harvesting of cell material

From adherent cells, the media was discarded and the plate was washed once with sterile 1x PBS (see buffer recipes 10.5.1). Trypsin-EDTA (0.05%; Thermo Fischer Scientific) or Accutase® solution (in preparation for flow cytometry; Sigma-Aldrich) was added for cell dissociation and incubated on the plate for 3-5min at 37°C and 5% CO_2. The proteolytic and metal chelation process was stopped adding RPMI 1640 or DMEM containing FCS, using an amount of media 3 times the media of the trypsin-EDTA/Accutase® solution volume applied before. The cells were collected in a 15 or 50ml Falcon™ tube (Corning, Inc.) and centrifuged in a Centrifuge 5424 R (Eppendorf AG, Hamburg, Germany) at 1195rpm for 5min. If the cell pellet was used for DNA isolation or culturing afterwards, cells were centrifuged at RT (room temperature, ~22°C). If a downstream application was RNA isolation, protein lysis or native freeze storage, the cells were centrifuged at 4°C. After centrifugation, the medium supernatant was discarded and the pellet was solved in either fresh media for re-cultivation, in corresponding lysis buffer for cell component isolation or was washed twice with 1x PBS and was stored natively at -80°C for later applications.

2.4.4 Assessment of cell numbers

Cells were counted using the TC20™ Automated Cell Counter and related dual-chamber counting slides (Bio-Rad Laboratories, Inc., Hercules, CA, USA) following manufacturer instructions. To determine live cell counts, 0.4% trypan blue solution (Thermo Fischer Scientific) was added in a 1:1 ratio to cell suspension prior to cell counting.

2.5 Cell biology methods

2.5.1 Seeding a defined number of cells into 96-, 12-, 6-well or 10, 15cm cell culture plates

For seeding of cells, a defined number of cells was added to a volume of cell culture media suitable for the intended well size.

$$\frac{(desired\ number\ of\ cells\ \left[\frac{cells}{ml}\right] \times (desired\ total\ assay\ media\ volume\ [ml]))}{cell\ count\ of\ given\ suspension\ after\ harvest\ \left[\frac{cells}{ml}\right]}$$
$$= volume\ of\ suspension\ needed\ to\ achieve\ desired\ number\ of\ cells\ in\ assay\ media$$

The cell numbers were adjusted to not exceed 70-80% confluency (visual judgement) of the well surface at the end/read-out time point of the planned assay. Therefore, cells from the same cell line to be used in the intended assay were pre-seeded in different cell numbers without treatment to determine the correct number of cells for this well size/assay[509,510]. Cells were controlled every day for growth and pictures were taken via transmitted light microscopy using the Axio Vert.A1. (see 2.4.2). Estimated cell numbers for different cell culture plates and assay durations are listed in Table 22 in the appendix. For seeding, the medium with the added, defined number of cells for this assay was vigorously vortexed and a defined volume was applied into each well of the plate using the slowest level of a Multipette® Xstream (Eppendorf AG). In general, these volume quantities were used for cell seeding: 100-200µl for 96-well, 1-2ml for 12-well, 1-4ml for 6-well, 10-15ml for 10cm plates and 20-25ml for 15cm plates. Precise information for each individual assay is noted in the respective sections, as are planned media changes within the assays. The edges of a 96-well plate were always filled with 200µl 1x PBS to avoid edge effects with assay detection and drying out of cells.

2.5.2 Serum starvation and cell density

For serum starvation experiments at defined cell density, NGP, GI-ME-N and LAN-5 cells were grown with RPMI 1640 medium containing 1% penicillin/streptomycin and supplemented with either 10% or 2% FCS. Previously of a qPCR analysis, the cells were seeded in a 6-well plate format (CELLSTAR®), at a density of either $2x10^4$ cells/well, $1x10^5$ cells/well or $1x10^6$ cells/well using the 10% FCS RPMI 1640 medium and at a density of $4x10^4$ cells/well, $3x10^5$ cells/well or $2x10^6$ cells/well using the 2% FCS

RPMI 1640 medium. This was done to obtain different confluence levels, considering as well the different doubling times at different serum levels. Cells were incubated for four days at 37°C and 5% CO_2 and were photographed afterwards using a Axio Vert.A1. microscope, see 2.4.2 for details. Afterwards, cells were harvested for qPCR analysis (see 2.6.35) of *ASPM* expression. For Cell Proliferation ELISA BrdU assays (enzyme-linked immunosorbent assay, 5-BrdU, 5-Bromo-1-(2-deoxy-β- D -ribofuranosyl)uracil) neuroblastoma cells were seeded at different confluencies of either $6.25x10^2$ cells/well, $2.5x10^4$ cells/well or $1x10^5$ cells/well using the 10% FCS RPMI 1640 medium and $1.25x10^4$ cells/well, $5x10^4$ cells/well or $2x10^5$ cells/well using the 2% FCS RPMI 1640 medium in a 96-well plate. The cells were cultured for four days before performing the ELISA BrdU assays (see 2.5.14 for method).

2.5.3 Manual or automated monotherapy treatment of cells with single pharmaceutical substances

For treatment of cells with a BET-inhibitor, (+)-JQ1 and OTX015 were ordered at Selleckchem (Houston, TX, USA); TEN-010 was kindly provided by Hoffmann-La Roche. For PLK1/PI3K inhibition, rigosertib and volasertib were ordered at Selleckchem, and the PI3K inhibitor alpelisib was ordered at Hycultec GmbH, Beutelsbach, Germany. (+)-JQ1, OTX015, volasertib and alpelisib were solved in DMSO, whereas TEN-010 and rigosertib were solved in ddH_2O. The respective pharmaceutical substance or the powder was dissolved in a sterile volume of ddH_2O or DMSO under sterile conditions at RT. The mass [mg], molecular weight MW [gM] and desired concentration [mM] was taken into account for the volume [ml] in which the agent was dissolved, as specified by the manufacturer:

$$\frac{mass\ [mg]}{concentration\ [mM] \times molecular\ weight\ [g/mol]} = volume\ [ml]$$

The stock solution thus produced was aliquoted in small portions and frozen at -80°C. The cells to be tested were seeded the previous day before treatment and incubated at 37°C and 5% CO_2. For inhibitor application on the cells, either a manual "by hand" treatment was performed or a device supported, automated method (see below). A panel of cell lines was treated using different BET inhibitors TEN-010 (n=16), JQ1 (n=14) and OTX015 (n=14). In order to obtain an overview of the substance effect on the cells to the range of different concentrations, the cells were treated with an end concentration per well from 0nM – 50,000 or 100,000nM. Calculation of the concentration of a pharmaceutical agent within media was done using the formula:

$$final\ volume\ [ml] \times final\ concentration\ [nM] = stock\ volume\ [ml] \times stock\ concentration\ [nM]$$

For 96-well BET inhibitor experiments, every concentration was tested in at least three technical replicates (three wells) up to six technical replicates (six wells). The medium used was applied as a background control in 3-6 technical replicate wells. If the substance was dissolved in DMSO, a DMSO control was also applied in 3-6 technical replicate wells, which corresponded to the highest DMSO concentration used within the highest treatment concentration. This resulted in a test of approximately 10-18 different concentrations of the substance. Care was taken to ensure that high concentrations were not located next to low concentrations in order to prevent the signals from other wells from spilling over within readout assays. For manual treatment application, the media was aspirated very carefully. A volume of 100-200µl media with the respective end concentration of the substance per well was added to the cells slowly. In order to automate the *in vitro* treatment, the PLK1/PI3K inhibitors were administered to the cells using an electronically fluid dispenser system. The PLK1 and PI3K inhibitors volasertib (n=5), apelisib (n=5) and rigosertib (n=15) were applied to different cell lines using the Tecan HP Digital Dispenser D300E supported with D300eControl Tecan version 3.2.5 software (both Tecan Group AG, Männedorf, Switzerland). The cells were administered with an end concentration per well from 0nM - 100,000nM in a logarithmic scale. If the agent was dissolved in ddH_2O, Tween 20 was added with an end concentration of 0.3%, to create a greater viscosity of the solution which is necessary for dispensing. For PLK1/PI3K inhibitor application on 96-well experiments, every concentration was tested in at least three technical replicates (three wells) up to six technical replicates (six wells). A substance to be dispensed was created as an entry in the dispenser software with the parameters: *Name of the fluid*, *class* (*DMSO-based* or *aqueous + Tween 20*), *concentration* (of the stock in mM) and *dispense by concentration* and *no priority of dispense order*. Furthermore, the volume was set to an additional/starting volume of 100µl (seeded cells in media), a DMSO limit of 1% and a normalization of DMSO or ddH_2O with 0.3% Tween 20 to the highest volume of inhibitor was used. For starting the dispensing process, Digital Dispenser D300E D4+ or T8+ dispense heads cassettes were loaded with the pharmaceutical agent (*fluids*) or DMSO/Tween 20 as solvent controls (*normalization fluids*). The dispensing process was carried out as described by the manufacturers. Tecan HP D300 digital dispenser files were saved as .tdd data. Subsequently, the cells were incubated with the substance for three days at 37°C and 5% CO_2. Afterwards conducted cell culture readout methods or assays provide a means of quantitatively analyzing the change of presence, amount, or functional activity of a cell, reacting to a treatment. Readout was performed with CellTiter-Glo® Luminescent Cell Viability Assay or Cell Proliferation ELISA, BrdU assay (see method 2.5.13 or 2.5.14). For other readout assays, which were qPCR (2.6.35), Western blot (2.7.1) or analysis of apoptosis by flow cytometry (2.5.20), cells were seeded in a bigger scale (2.5.1) in 12- or 6-well plates and treated manually as explained in this section.

2.5.4 Automated, combinatorial treatment of cells with two pharmaceutical substances

Neuroblastoma and fibroblast cells were seeded (2.5.1) in 96-well white plates a day before treatment. The next day, the cells were treated using the Tecan Digital Dispenser D300E (see technique 2.5.3). The cells were administered with a "therapy combination" of two substances. Combination experiments were performed in two *MYCN*-amplified (CHP-134, IMR5/75), two non-*MYCN*-amplified (SK-N-AS, GI-ME-N) neuroblastoma or fibroblast cells (VH7). The BET inhibitor OTX015 and the PLK1 inhibitor volasertib were combined in non-constant ratios using a checkerboard titration pattern over 2 plates of 96-wells. Therefore, the following concentrations of the treatments were applied to the cells: IMR5/75 and CHP-134: OTX015: 5, 10, 25, 50, 100, 250, 500, 1000nM; volasertib: 1, 2.5, 5, 7.5, 10, 15, 50nM; SK-N-AS and GI-ME-N: OTX015: 5, 25, 50, 125, 500, 1250, 2500, 6250nM; volasertib: 2.5, 5, 7.5, 10, 15, 20, 50nM. To identify suitable concentration ranges, dose response curves for the respective chemotherapeutic agents were assessed for each cell line (IMR5/75, CHP-134, SK-N-AS and GI-ME-N) beforehand. Afterwards, the cells were incubated with the substance(s) for three days at 37°C and 5% CO_2, followed by a readout of the cell viability (see 2.5.13). The results were later evaluated with *SynergyFinder*[511] (CRAN) (see 2.10.3).

2.5.5 Treatment of neuroblastoma cells with all-trans-retinoic acid

All-trans retinoic acid (ATRA) and 13-cis-RA treatment has been shown to cause arrest of cell growth and induction of differentiation of neuroblastoma cells[512]. A treatment with ATRA was administered alongside a treatment of NGP cells with siRNA (see 2.5.7) in additionally seeded cells. This control experiment can determine whether cells are capable of undergoing differentiation and if the differentiation can not only be attributed to side effects of the siRNA treatment. The neuroblastoma cell line NGP was seeded in 10cm plates (Corning, Inc.; $6x10^5$ cells/plate; in preparation for qPCR) or on cover slips in 6-well plates (Corning, Inc.; $5.4x10^4$ cells/well; in preparation for immunofluorescence). After one day of incubation at 37°C and 5% CO_2, cells were treated with 1µM or 2µM ATRA (Sigma-Aldrich) by adding respective ATRA to the media. DMSO was applied as a control treatment. ATRA treatment was pulsed every 4th day after initiation of the experiment. After 4 and 10 days, cells were harvested utilizing Trypsin/EDTA (see 2.4.3). Cell material was analyzed for detection of *MAP2*, *TUBB3* and *DCX* mRNA expression, applying qPCR (2.6.35). Furthermore, cells were prepared for analysis of MAP2 and ßIII-TUBULIN using immunofluorescence (see section 2.5.22).

2.5.6 Depolymerizing microtubules and synchronizing NGP ASPM-FPN-sgRNA87 neuroblastoma cells by usage of nocodazole

Nocodazole, a synthetic compound, binds to free ß-tubulin dimers and preventing them from incorporation in microtubules, which are induced to depolymerize[513,514]. Cells which were treated with nocodazole arrest in G2/M-phase of mitosis and cannot form metaphase spindles[515]. Neuroblastoma

NGP cells and related NGP CRISPR/Cas9 *ASPM* 3x FLAG knockin clones (NGP ASPM-FPN) were treated with nocodazole to induce a cell cycle arrest for cell synchronization[516] and the accumulation of the ASPM protein[441]. NGP and NGP ASPM-FPN-sgRNA87 cell clones no. #1 and #7 were seeded in 10cm plates (Corning, Inc.; $6x10^5$ cells/plate; in preparation for qPCR or Western blotting) or on cover slips placed in 6-well plates (Corning, Inc.; $5.4x10^4$ cells/well; in preparation for immunofluorescence). For NGP cells, RPMI 1640 media supplemented with 10% FCS and 1% P/S was applied to the cells, for NGP-ASPM-FPN cells, 800µg/ml G418 for maintaining the selection pressure was further added to the media. After one day of incubation at 37°C and 5% CO_2, cells were treated with 20ng/ml, 30ng/ml or 50ng/ml nocodazole (0.25mg/ml stock; Sigma-Aldrich) by adding the respective nocodazole concentration to the cells. DMSO was applied as a control treatment. After 20h, cells were harvested in case of downstream qPCR or Western blot assays (see 2.4.3). The cell material was analyzed for detection of *ASPM*, *CCNB1* and *CDK1* mRNA expression, applying qPCR (2.6.35). Furthermore, ASPM-FLAG protein detection was performed with Western blotting (2.7.2). For simultaneous treatment of NGP and NGP ASPM-FPN cells with nocodazole and siASPM, cells were seeded and treated for siASPM using fast forward transfection method first (2.5.7). Three days after siASPM transfection, the cells were additionally treated with nocodazole as stated above and cells were harvested (2.4.3) four days after siASPM transfection/20h after nocodazole treatment. Subsequently, cell material was analyzed for detection of ASPM-FLAG protein with Western blotting (2.7.2) and immunofluorescence (2.5.22).

2.5.7 SiRNA mediated knockdown of *ASPM*: Fast-forward transfection of cells with siRNA

A siRNA is a 20-25bp long double-stranded non-coding RNA molecule, and is processed within the cellular RNA interference pathway. It interferes with the expression of a selected gene to be downregulated with its complementary nucleotide sequence. The mRNA of the selected gene will be degraded after transcription, preventing the translation to a protein[517]. The transfection of siRNAs is only transient and is not stable integrated into the genome. However, the high copy number of the transfected siRNA leads to a high knockdown efficacy of the mRNA of the selected target gene[518]. The siRNAs used in this work were designed according to specific structural rules and ordered as oligonucleotides (see for design molecular biology methods 2.6.20). Transfection of cells with siRNA was performed as fast-forward protocol, the transfection of the cells was performed shortly after the seeding procedure. Neuroblastoma or fibroblast cells were harvested and seeded in 96-well plates (clear plates from CELLSTAR®; if an ELISA assay was performed afterwards or white plates from Costar™; if CellTiter-Glo® Luminescent Cell Viability Assay was performed afterwards) or 6-well plates (from CELLSTAR®; if qPCR, Western blot or immunofluorescence staining was performed afterwards). RPMI 1640 or DMEM supplemented with 10% FCS and 1% P/S was used for this assay as standard seeding media. Afterwards, siRNA mixture was prepared in a precise order and all substances used were

pre-warmed to RT before. Transfection mixture of a 96-well plate was as follows: 0.2µl/well siRNA (stock concentration 20µM, end concentration 40nM) is added carefully into 20µl/well Opti-MEM™ (Thermo Fischer Scientific). To increase the cellular uptake of the siRNA, 0.2µl/well Lipofectamine RNAiMax (Thermo Fischer Scientific) is added slowly into the mixture. Subsequently, the reaction tube is inverted about 5 times and the transfection mixture is incubated at RT for 15min. After incubation, 20µl/well of the transfection solution dropped into a well and mixed thoroughly together with the pre-plated cell suspension. For transfection of a 12-well or 6-well plate, 200µl/well Opti-MEM™, 2µl/well siRNA and 2µl/well Lipofectamine RNAiMax are applied. The treated cells were incubated with siRNA at 37°C and 5% CO_2. Through the whole procedure, a random scrambled siRNA was carried which was used as negative control for normalization (see siRNA sequences in appendix Table 24). Four days after siRNA transfection, functional down-stream assays are performed (e.g. cell harvest for assessment of *ASPM* expression using qPCR; see 2.4.3 and 2.6.35).

2.5.8 ShRNA mediated knockdown of *ASPM*: Production of shASPM lentiviral particles from transfection of HEK293T cells

A shRNA is a double-stranded RNA with a hairpin turn (about 9 nucleotides long loop), and is used to silence the expression of target genes via the RNA interference pathway[519]. In contrast to synthetic siRNA (see 2.5.7 and 2.6.20), which is applied directly and manually to a cell culture, shRNA is a precursor which is intercellularly expressed from a viral vector and is subsequently processed in the cytoplasm to siRNA[520]. For achievement of a stable shRNA integration into the human host genome, the shRNA construct was brought in lentiviral particles, which transduced human cells for shRNA expression. Lentiviruses were generated using a highly transfectable HEK293T cell line as host / intermediate host, which were transfected which a mixture of plasmids ("2nd generation system") containing the shRNA target vector, a virus packaging vector (psPAX2) and a virus envelope vector (pMD2.G)[520]. Generated lentiviral particles in the supernatant of HEK293T cells were then used to transduce neuroblastoma cells, which started to express shRNA after genomic integration. The vector plasmids used in this work were cloned in advance of the transfection of the HEK293T cells (see for vector cloning: molecular biology methods 2.6.21). Transfection of HEK293T cells with shASPM target vector, envelope and packaging vector was performed applying the calcium phosphate co-precipitation method[521–523]. HEK293T cells were seeded to a confluence of 7.5x10^6 cells in a T75 cell culture flask (75cm²) using DMEM supplemented with 10% FCS 18-24h before transfection. Transfection procedure was started one day after cell seeding. Buffers used for transfection were always prepared fresh, sterilized twice using 0.22µM cellulose acetate filters (Carl Roth GmbH + Co. KG, Karlsruhe) and were not frozen (see 10.5.5, Buffers and solutions recipes). Plasmid DNA amount was diluted to a total of 40µg concentration using 2.5mM HEPES (Sigma-Aldrich) to a total volume of 540µl in a 1.5 reaction tube, resulting in a 1:1:2 plasmid mixture (20µg pLKO.1_shASPM_Puro-T2A-GFP target plasmid

including shASPM or shScramble, 10µg pMD2.G envelope plasmid and 10µg psPAX2 packaging plasmid). See plasmid used in Table 26 in the appendix section. A volume of 60µl $CaCl_2$ solution was added to the plasmid mixture then. The plasmid DNA/HEPES/$CaCl_2$ solution was transferred carefully and drop-wise into a 15ml Falcon™ tube filled with 600µl of 2x HeBS (HEPES-buffered saline) buffer while the Falcon™ tube was virgously vortexed. Afterwards, the solution was incubated on the bench top at RT for 30min. Old DMEM media was removed from HEK293T cells and 12ml transfection DMEM media (including 25µM chloroquine, see recipe 10.5.5) was added to the cells. The calcium phosphate DNA solution was administered to the HEK293T cells slowly and drop by drop. The calcium phosphate DNA solution was further distributed very carefully by tilting the cell culture flask from site to site. The flask was incubated at 37°C and 5% CO_2 for 16h to avoid double transfections of HEK293T cells. The next day, transfection media was removed carefully from HEK293T cells and cells were washed once with 5ml 1xHeBS buffer. To wash out the plasmids, 2ml glycerol solution was added to the cell culture flask and was incubated for exactly 2min. Afterwards, the cells were washed once again with 5ml 1xHeBS buffer. Fresh DMEM growth media (12ml of DMEM supplemented with 10-20% FCS) was filled into the cell culture flasks and HEK293T cells were incubated at 37°C and 5% CO_2 for another 24h. The next day, HEK293T were checked for a GFP expression by fluorescence microscopy using Axio Vert.A1. (see 2.4.2). If ≥70% of cells display a GFP expression estimated by eye, the transfection was considered successful. The supernatant DMEM media was collected from HEK293T cells and filled into pre-cooled 15ml Falcon™ tubes. Virus containing supernatant was filtered with 0.45µM cellulose acetate filters to remove floating HEK293T cells and debris. The tube was further kept on ice for the whole procedure. To concentrate the virus, supernatant was filled into Amicon® Ultra-15, PLHK Ultracel-PL Membran tubes (Merck Millipore) and centrifuged at 3,000x*g* using breaks and 4°C for 30min. The flow-through was discarded and the virus concentrate in the residue was aliquoted and frozen to -80°C immediately. Remaining HEK293T cells were harvested (see 2.4.3) and analyzed for expression rate of GFP using flow cytometry (2.5.17).

2.5.9 ShRNA mediated knockdown of *ASPM*: Titration of functional lentiviral titer

The virus concentrate obtained was first tested for the ability to transduce neuroblastoma cells. For this purpose, HEK293T cells and NGP neuroblastoma cells were transducted (see transduction protocol in 2.5.10) using the shASPM lentiviral concentrate (produced in 2.5.8). In preparation for assessment of transduction efficacy, HEK293T/neuroblastoma cells were seeded into a 96-well (Costar™) or 12-well (CELLSTAR®) cell culture plate containing DMEM (HEK293T cells) or RPMI 1640 (neuroblastoma cells) supplemented with 10%FCS (see section 2.5.1). After one day, the cells were transducted with a titration of virus concentrate in a dilution series format. For that, 3-5x 96-wells or 2x 12-wells were treated with one virus concentrate in different a ranges of 0.1µl – 10µl. The concentrate from each virus was tested individually. After one day of incubation, the media was replaced. The day after, the cell culture media was replaced with fresh RPMI 1640 supplemented with 10% FCS, 1% P/S and puromycin

dihydrochloride (Sigma-Aldrich; stock 10mg/ml) as selection antibiotics (see for concentration Table 10 in appendix; estimated by a antibiotic kill curve[524] beforehand). Subsequently, the media was replaced daily. Three days after starting the selection antibiotics treatment, the transduction efficacy was measured by applying at least one of these methods: 1) live and dead cells were counted in supernatant media and from attached cells to the well (after trypsinization), 2) cells were checked visually for a GFP expression signal using fluorescence microscopy (see method 2.4.2; for cells which were transducted with pLKO.1_shASPM_Puro-T2A-GFP target plasmid, see for details appendix Table 26), 3) supernatant media was collected, cells attached to plate were harvested (2.4.3), pooled with the supernatant and cells were analyzed for expression of GFP using flow cytometry (see section 2.5.17, only for 12-well plates; for cells which were transducted with pLKO.1_shASPM_Puro-T2A-GFP target plasmid, see for details appendix Table 26) or 4) the cell viability was detected using CellTiter-Glo® assay (see section 2.5.13, only for 96-well plates). For exact determination of the number of lentiviral particles needed to infect a certain number of neuroblastoma cells, the calculation of the multiplicity of infection (MOI) is required. The MOI is a parameter that predict viral infectivity in a population of target cells. An infectious unit refers to the smallest amount of virus capable of producing an infection in a susceptible cell[525]. The titer of lentiviral particles of the original suspension is usually given as transduction units (TU) per milliliter of the preparation[526]. To assess the MOI for transfection of neuroblastoma cells, the target cell line (NGP) was seeded in 12-well (CELLSTAR®) cell culture plates and transducted with the shASPM viral particels as explained above. Three days after transduction, the media was discarded and cells attached to the plate were stained with 1% crystal violet applying the 2D colony formation assay protocol (2.5.11). Viral titer was assessed by counting all stained colonies in each well and the MOI was calculated using the formula:

$$\frac{volume\ of\ viral\ concentrate\ [ml]\ x\ (dilution\ fold)}{number\ of\ colonies\ per\ well} = viral\ titer\ \left[\frac{TU}{ml}\right] = MOI$$

Based on the results, a virus concentration with the highest transduction rate was determined and a MOI of 1 per 1 neuroblastoma cell was used for further experiments with this virus preparation.

2.5.10 ShRNA mediated knockdown of ASPM: Lentiviral transduction of neuroblastoma cells with virus containing shASPM

Neuroblastoma NGP cells were seeded in 12-well plates (CELLSTAR®, see cell counts applied in appendix Table 22) using RPMI 1640 supplemented with 10% FCS, 1% MEM non-essential amino acid solution (Biozym Scientific GmbH, Hessisch Oldendorf, Germany) and 1%L-Glutamine (200mM; Thermo Fischer Scientific). The cells then were incubated at 37°C and 5% CO_2 for 24h. The next day, viral concentrate was slowly thaw on ice from -80°C, using one aliquot per transduction and left-overs were discarded afterwards. The virion concentrate was then allowed to adjust to RT. For transduction,

the virus (volume used depending on MOI, see 2.5.9) was mixed with 1ml RPMI 1640 media and 1.6µl polybrene per well (hexadimethrine bromide; Sigma-Aldrich; for concentration see Table 10 in appendix). Polybrene is used to neutralize the charge repulsion between the viral particles and sialic acid on the surface of the cell[527], therefore increasing the transduction efficacy. The virus/media/polybrene solution was mixed by inverting, the old RPMI 1640 media was removed from target cells and 1ml virus containing RPMI 1640 media was added per well. The cells then were incubated with the virus at 37°C and 5% CO_2 for 18-24h. Next day, the virus media was discarded and replaced with fresh RPMI 1640 supplemented with 10%FCS, 1%MEM (non-essential amino acid solution). Four days after viral transduction, functional assays were performed directly (e.g. cell harvest for assessment of ASPM expression using qPCR; see 2.6.35) or cell lines with a stable *ASPM* suppression were generated. To obtain a stable shRNA cell line, media was replaced with fresh RPMI 1640 supplemented with 10%FCS, 1%P/S and puromycin (see 2.5.9 for explanation).

2.5.11 Clonogenic 2D assay with crystal violet staining

Clonogenic assay or colony formation assay is a cell survival assay based on the ability of one cell to grow into a colony[528]. A colony is defined to consist of a minimum of 50 cells[529]. The clonogenic assay enables an evaluation of the variations in reproductive viability (capacity of cells to generate progeny) e.g. after chemotherapeutic treatment. Only a fraction of seeded cells, which did not die due to the treatment, retains the capability to produce colonies. To perform a clonogenic assay, neuroblastoma cells (IMR5/75, CHP-134, SK-N-AS, GI-ME-N and NGP) were harvested (2.4.3) and seeded (2.5.1) in RPMI 1640 (supplemented with 10%FCS and 1%P/S) in clear 6-well plates in case of rigosertib treatment or in 12-well plates (both CELLSTAR®) in case of viral transduction a day before treatment. Cells were seeded (see cell counts in appendix Table 22), and variations thereof were IMR5/75 ($5x10^3$ cells/well), SK-N-AS ($1x10^4$ cells/well) and GI-ME-N ($1x10^4$ cells/well). Next day, the cells were treated using rigosertib or viral shASPM particles by media change with RPMI 1640 media containing the inhibitor/virus. See for viral transduction 2.5.10. For rigosertib treatment, the cells were administered with the respective EC amount (effective concentration) EC10, EC20, EC30, EC40 and EC50 concentration for each cell line, which was determined beforehand using CellTiter-Glo® Luminescent Cell Viability Assay (2.5.13). Afterwards, the cells were incubated for 7 days at 37°C and 5%CO_2 and confluency was checked every day with transmitted light microscopy (see 2.4.2). After a week, the media was aspirated very carefully and cells were washed once with 1x PBS. In the following, the cells were fixed at RT with 4% paraformaldehyde (PFA)/PBS for 15 min. PFA was then discarded and cells were washed once with 1x PBS. To stain the cells, 2ml of a 1% crystal violet solution is applied to the wells and incubated at RT for 20min. Subsequently, the crystal violet solution was discarded and the cells are washed three times with 1ml dH_2O. The plates were then air-dried under a fume hood. Recipes for the buffers and solutions used are described in section 10.5.4. Pictures of the whole cell culture plate

was taken with computer Apple iMac 7,1 (Apple Inc., Cupertino, CA, USA) and scanner Epson Perfection V700 Photo (Seiko Epson K.K., Suwa, Prefecture Nagano, Japan). The scanning was done with the software Epson Scan Version 5.1.1f2 (Seiko Epson K.K.). These parameters were applied for scanning: *doc type: film*, *film type: positive film*, *1200 dpi resolution*, *24-bit color depth* and *unsharp mask*. The pictures were saved with the program in .tiff format.

2.5.12 Wound healing assay

The wound healing assay was used for the investigation of cell migration and cell-cell interaction under a pharmaceutical treatment. After induction of a wound in the surface monolayer of adherent cells, the generated gap closes by migration and proliferation of the cells into the gap area. Cell migration was visualized via microscopy and wound closure was measured[530]. To perform a wound healing assay, cell culture-inserts 2-well for self-insertion (ibidi GmbH, Martinsried, Germany) were sterilized in 70% ethanol (EtOH)/ddH_2O for 1h, following autoclavation. Afterwards, the insert was placed in one well of a 12-well plate (CELLSTAR®), using sterile forceps (Dumostar, Fine Science Tools (FST) Group, North Vancouver, B.C., Canada). The area around the insert within the well was filled immediately with 1ml media RPMI 1640 (with 10% FCS and 1% P/S), to prevent drying out of the insert. The neuroblastoma cell line IMR5/75 was harvested as described (2.4.3) and $1x10^4$ cells were seeded within 70µl media in per chamber of the insert. Cells within chambers were incubated at 37°C and 5% CO_2 for 24h. After appropriate cell attachment (after about 24 h) the insert was gently removed by using a sterile forceps and a first picture was taken with transmitted light microscopy operated with 5x objective lens (see 2.4.2 time point 0h). The medium was aspirated and either 1ml of standard media was applied as a control or rigosertib treatment was started with a concentration of 100nM in RPMI 1640 media.

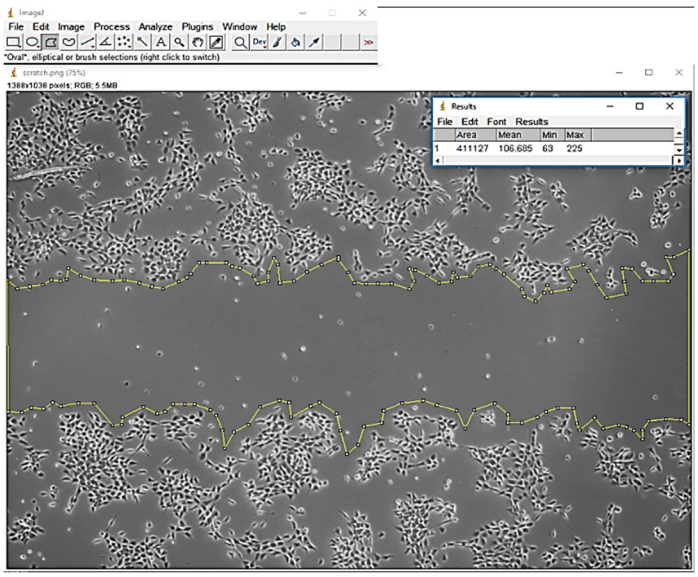

Figure 17: Analysis of wound healing assay using Image J.
After cell attachment the ibidi insert is gently removed and pictures are taken with transmitted light microscopy every day. Using the tool polygone selections, the gap of the picture was selected and measured in pixels (applying analyze).

Cells within chambers were incubated again at 37°C and 5% CO_2 and pictures from the wound closure were taken with a 5x magnification at 0h, 24h, 48h and 72h time points. For analysis, microscopy images were loaded as .jpg file into ImageJ version 1.8.0_112 (National Institutes of Health (NIH), Bethesda, MD, USA). Using the tool polygon selections, the whole area of the picture was selected and measured in pixels (applying analyze). Afterwards, the gaps of all pictures were measured in pixels for its area using the polygon selection tool manually. Area pixel values from ImageJ were converted into percentages, using setting the area of a whole picture as 100% filled (Figure 17).

2.5.13 Cell Viability Assay (CellTiter-Glo Luminescent Assay)

The CellTiter-Glo® Luminescent Cell Viability Assay (Promega Corporation) is based on cell lysis coupled with simultaneous ATP measurement by a luciferase reaction[531]. The relative luminescence of the reaction was measured and baseline correction was conducted with wells containing the control. ATP levels correlate with cell viability, why this assay is suitable to quantify the effect of a treatment (inhibitor, siRNA or shRNA) on the physiological status of cells[532]. CellTiter-Glo® Luminescent Cell Viability Assay was performed according to the manufacturer's instructions. In detail, cells were seeded in 96-well white plates (2.5.1, Costar™) to reduce over spilling of luminescence signals. The cells were either treated with pharmaceutical inhibitors (2.5.3 or 2.5.4) or siRNA or shRNA against *ASPM* (see section 2.5.7 or 2.5.10). After the respective treatment was performed, the cells were incubated at 37°C and 5% CO_2 in inhibitor experiments for three days, and within the ASPM project for four or 10 days. Following the incubation time, the 96-well plate was equilibrated to RT for 30min. Subsequently, the CellTiter-Glo reagent was added with a Multipette® Xstream (Eppendorf AG) in 1:10 ratio to the final volume in a well. After application of the reagent, the plate was kept in a dark environment and covered in aluminum foil, and put on an orbital shaker for 2min with agitation speed of 180rpm. After another 10min of incubation at RT, the luminescence was measured of the entire plate with a GloMax®-Multi+ Microplate Multimode Reader supported by GloMax-Multi+ Detection System with Instinct™ Software (both Promega Corporation). The method applied was CellTiter-Glo, luminescence, measurement per well in 0.5 s increments, reading whole 96-well plate, single well read mode, reading 1 and loop 1. Shortly before the measurement, the detector photomultiplier tube (PMT) was activated, and the luminescence was measured after activation. Raw data of the measurements were saved as .csv and .xml file and processed for dose response analyses (2.10.2 and 2.10.3). All assays were conducted using 3-6 technical replicates each time.

2.5.14 Colorimetric cell proliferation detection ELISA, BrdU

The Cell Proliferation ELISA, BrdU (colorimetric) kit (Hoffmann-La Roche) was used for relative quantification of cell proliferation based on the measurement of BrdU incorporation during DNA replication in proliferating cells. Prior to the assay, neuroblastoma NGP and GI-ME-N cells were seeded (see 2.5.1) on clear 96-well plates (CELLSTAR®) and treated with siRNA or shRNA viral particles

against *ASPM* (see section 2.5.7 and 2.5.10). Afterwards, the cells were incubated for four or 10 days at 37°C and 5% CO_2. Subsequently, BrdU labeling solution was added in a volume of 1:10 to the media volume and the plate was gently shaken and incubated at 37°C and 5% CO_2 for 2h. In the following, the medium with the labeling solution was removed by flicking off and tapping, 200µl/well FixDenat solution (denaturation of DNA) was added to the cells and incubated at RT for 30min. The FixDenat was removed by flicking off and tapping, 100µl/well anti-BrdU-peroxidase (POD) working solution (binding to BrdU incorporated in DNA) was added and incubated at RT for 90min. The anti-BrdU-POD working solution was removed by flicking off and tapping and wells were rinsed three times with 100µl/well washing solution. The washing solution was removed by flicking off and tapping and 100ml/well substrate solution (TMB chromogen) was added and incubated at RT for 10min. Detection of signals was performed using photometric detection via absorbance at wavelength 370/492 nm with Epoch™ Microplate Spectrophotometer supported by Gen5™ Data Analysis Software version 2.04.11.0 (both BioTek Instruments Inc., Winooski, VT, USA). Protocols were saved as Gen5 Protocol .prt file and measured assays were saved as Gen5 Experiment .xpt file. All assays were conducted using 5-6 technical replicates each time.

2.5.15 IncuCyte® Live-Cell Analysis Proliferation assay

The proliferation of neuroblastoma cells and the effects of a treatment were investigated in detail with the help of live cell imaging. The advantage of longitudinal live cell imaging is that there is no temporal endpoint of the measurement as in biochemical detection methods (see 2.5.14) where a change in proliferation cannot be shown over time. It is also possible that the neuroblastoma cells continue to metabolize ATP (see 2.5.13) or incooperate BrdU (see 2.5.14) after treatment, but still have altered cell growth and morphology. To evaluate the long-term effects and the dynamics of *ASPM* siRNA treatment on neuroblastoma cell proliferation, the NGP cells were observed in live cell imaging. Neuroblastoma NGP cells were first seeded in clear 96-well plates (2.5.1, Costar™) and treated with siRNA (see in detail 2.5.7). The plate was then left under the clean bench at RT for at least 15min to allow the cells to settle on the bottom. The cell plate was then carefully placed in the incubator of the analyzer and after another 30min placed in the IncuCyte® S3 Live-Cell Analysis System (no. of IncuCyte® device: 10.43.144.105; Essen BioScience, Ann Arbor, MI, USA). The cells were then monitored with the following settings: *scan on schedule*, *4 images per well*, *phase contrast*, no usage of fluorescence color1 or color2, *magnification of 10x*, scan type *adherent cell-by-cell*, schedule with *scans at intervals of 12h*, *scan indefinitely* (until the experiment was manually terminated by the user; the plates were tracked from 96-324h). The first scan (time point 0h) was performed approximately 30min after the plate was placed in the IncuCyte® S3 Live-Cell Analysis System. Subsequently to the experiment, the images were evaluated with the program IncuCyte® version 2019B Rev2 (Essen BioScience). For this purpose, an analysis mask was created, which could analyze either the occupied image area or the cell confluence (basic analyzer) or the cell number per image (cell-by-cell analyzer; see Figure 18). Using the basic

analyzer, the expansion of the cells and the use of the available space can be observed, as well as whether the cells reach an ideal end point of approximately 90% cell confluence in the control treatment. In order to determine cell proliferation, the cell-by-cell analyzer is required to determine the exact cell number based on cell morphology (boundary, nucleus and cell-by-cell adherence). When establishing the respective analysis masks, representative images from a) all biological replicates, b) different treatments (scramble siRNA and siASPM) and c) different times (e.g. 24h, 76h) were selected as training set for the analysis software. Based on these images, the following mask definitions for the detection of NGP cells were manually defined: For the basic analyzer a *segmentation* adjustment of 0,8 was used, with a shift towards the background. Furthermore, a *hole fill* (µm²) of 100,00 and no adjustment of size (pixels; 0) was used for the cleanup. As filter the *cell area* (µm²) was defined with a minimum of 400,00 and a *cell eccentricity* of at least 0,3 (see Figure 18 left panel). For the cell-by-cell analyzer, a cell boundary with a *segmentation* adjustment of 0,8 was used, with a shift towards the background.

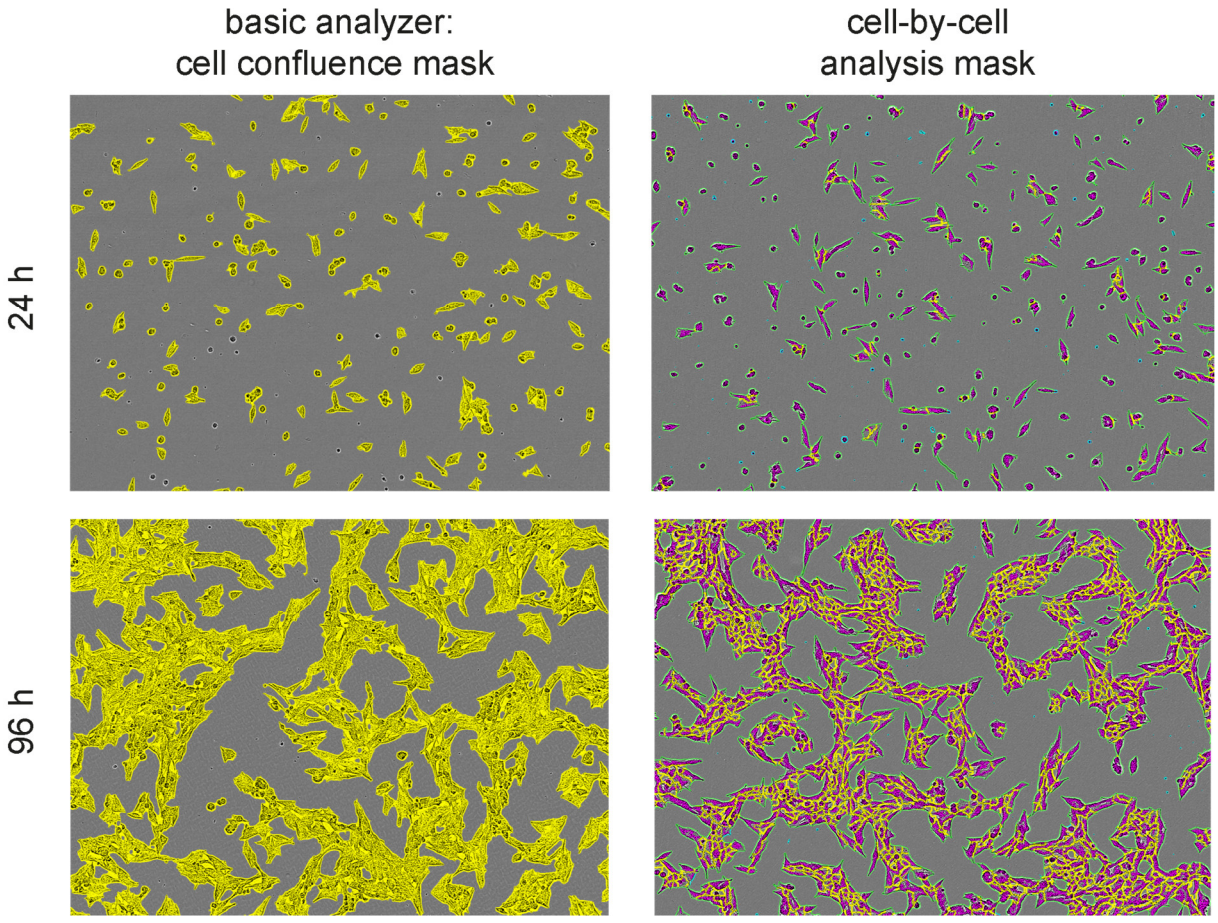

Figure 18: Basic and cell-by-cell analyzer masks for examination of cell proliferation in live cell analysis.
Cell confluence and cell counts of neuroblastoma NGP cells was detected through an IncuCyte® Live-Cell Analysis System. Left panel: analysis of cell confluence using the basic analyzer. The yellow areas represent cell expansion. Right panel: analysis of cell proliferation using the cell-by-cell analyzer. The yellow outline represents the cell boundary, the magenta color represents the cell seed and the green lines represent cell-by-cell expansion. Each image shows one of the four images which were taken per 1x96-well. The NGP cells displayed were non-treated.

Furthermore, a hole fill (µm²) of 450,00 and an adjustment of size of 1 pixel was utilized for the cleanup. The object seeding definition (cell nucleus definition) was performed with a cell detection sensitivity of 1,6, which was in the high range. The cell contrast was set to 1, which was in the lowest possible range. The cell morphology was also adjusted to 1, which corresponded to a rather round cell morphology. For the definition of the cell-by-cell analysis, the filter of the cell area (µm²) was defined with a minimum of 100,00 and with a maximum of 1E+06. The eccentricity was set to a minimum of 0,3 and with a maximum of 1,0 (see Figure 18 right panel). Mask measurement data was saved as .xml files and images were exported as .png files. For each experiment, 6 technical replicates equally to 6 wells (taking 4 images per well) per treatment were analyzed. Concerning the experimental duration of 0-96h, 7 biological replicates and for 108-324h 1-5 biological replicates are examined with their respective median and range. If the basic analyzer was used previously, the occupied area or cell confluence was displayed in %, if the cell-by-cell analyzer was used, the cell counts per image was shown in graphical results.

2.5.16 Colorimetric cell death detection ELISA^{PLUS}

The Cell Death Detection ELISA^{PLUS} kit (Hoffmann-La Roche) was used for relative quantification of histone-complexed DNA fragments, which are released into the cytoplasm of cells after induction of apoptosis. The assay was carried out according to the manufacturers recommendations. To perform the assay, NGP neuroblastoma cells were seeded (see 2.5.1) and treated with siASPM (see 2.5.7) in clear 96-well flat bottom plates (CELLSTAR®) and incubated for four or 10 days at 37°C and 5% CO_2. On day four or 10, the plate was centrifuged for 10min at 200*xg* and the supernatant was removed carefully. Afterwards, the cell pellets were lysed in assay buffer and centrifuged again. In the following, 20µl of the supernatant was collected and transferred into a streptavidin-coated microplate. A volume of 80µl of the immunoreagent, containing anti-histone-biotin (biotin-labeled monoclonal antibody from mouse; clone H11-4) and anti-DNA-peroxidase (monoclonal antibody from mouse; clone MCA-33), was added to the wells. This mixture was incubated under shaking at 300rpm at RT for 2h. Subsequently, the wells were washed with incubation buffer and 100µl ABTS solution was added and developed on a plate shaker for 10min. The reaction was stopped by adding 100µl ABTS stop solution to each well. Detection of signals was performed using photometric detection via absorbance at wavelength 405/490nm with Epoch™ Microplate Spectrophotometer supported by Gen5™ Data Analysis Software version 2.04.11.0. All assays were conducted using four technical replicates each time.

2.5.17 Analysis of Green Fluorescent Protein expressing cells by flow cytometry

The ability to transiently or steadily incorporate the GFP gene for an expressible fluorescent protein has become a critical method for the investigation of gene expression and protein localization[533,534]. The original wild type GFP derived from the coelenterate *Aequeora victoria*[535]. In this work, a flow cytometry-optimized enhanced green fluorescent protein (EGFP) expressed from shRNA lentiviral

transfer vectors (see Table 26 in appendix) was detected in HEK293T and neuroblastoma cell populations using flow cytometry[536]. For flow cytometry acquisition, a sample containing cells is suspended in a fluid, which is pressurized and then injected into a sheath liquid flow by the machine[537]. Instead of the term "cell" for a measured unit, the word "particle" is used as a general term for any of the objects flowing through a flow cytometer. The term "event" is used to indicate anything that has been interpreted by the instrument as a single particle[538]. Ideally, every particle of a suspension to be analyzed is passing a laser beam through a flow with one particle at a time. The light of the laser is scattered (forward scatter and side scatter) characteristic to the particles and their components. Furthermore, components of cells can be labeled with fluorescent markers beforehand which emit light when excited by a laser with the corresponding excitation wavelength[539]. Deflected or emitted light photons are detected, amplified and converted into an electric voltage signal[540]. For EGFP detection, the cells were transfected (HEK293T) or transducted (HEK293T and neuroblastoma cells) as described before (2.5.8 and 2.5.10). The cells were harvested using Accutase® solution (see 2.4.3). During the following procedure, the cells were kept cool. Cells were centrifuged within a 15ml Falcon™ tube at 300x*g* at 4°C for 5min, supernatant was discarded and cell pellet was resolved in cold FACS buffer (fluorescence-activated cell sorting).

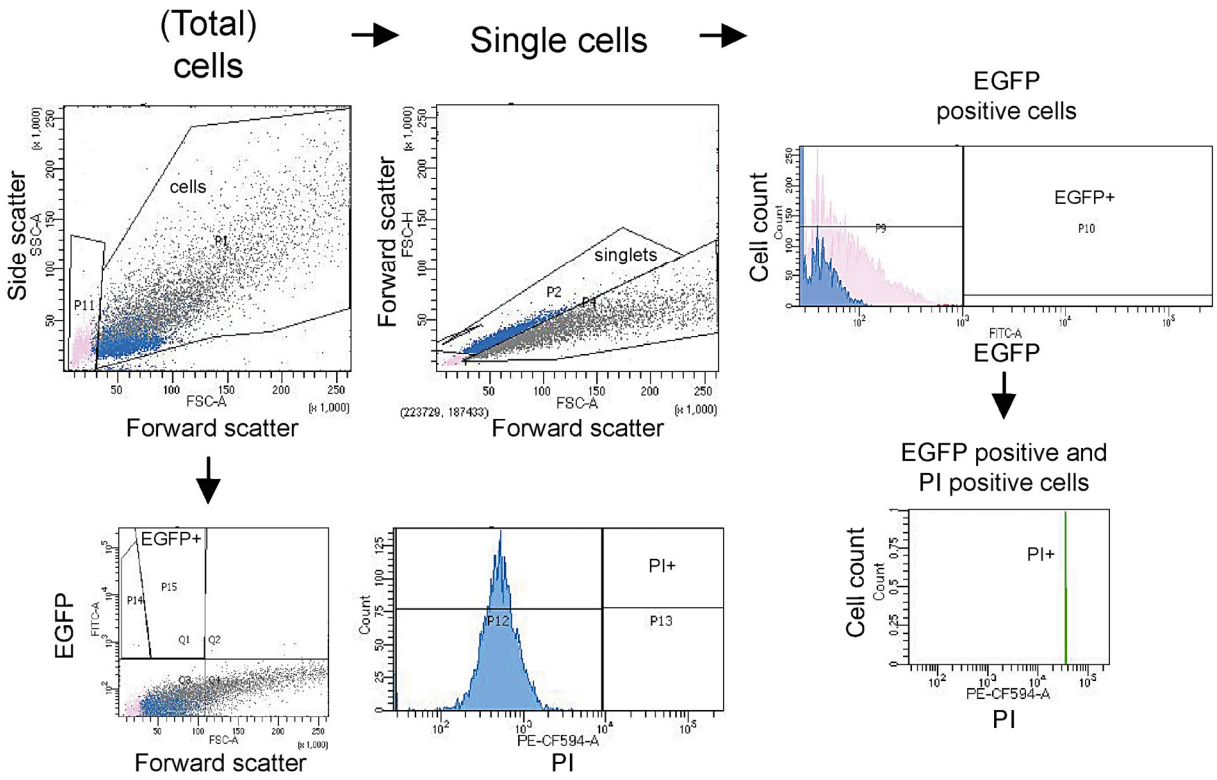

Figure 19: Gating strategy of EGFP detection and DNA content using PI staining.
Representative FACS dots plots displaying HEK293T cells without shASPM lentiviral vector transfection (transducted with non-EGFP control plasmid), harvested four days after experiment start. For an analysis of the cell cycle, all cells were first selected (total cells, without debris). The double cells ("doublets") were then excluded within the next step. For assessment of EGFP positive cells and EGFP / PI double positive cells, the cell count was plotted over the area of EGFP (FITC channel) or PI (PE-CF594 channel). Non-transfected, on-transducted and unstained cells served as negative controls.

Afterwards, the cells were washed two times using cold FACS buffer. Subsequently, the sample was centrifuged at 300g and 4°C for 5min, the supernatant was discarded and the cells were resuspended in 300µl FACS buffer. For DNA staining (see 2.5.18), aliquots of cells were administered with propidium iodide (PI, staining with 2x 4µg/ml in PBS; Sigma-Aldrich) and incubated at RT for 10min. Recipes for all buffers used are found in the supplement section 10.5.3**.** Samples were analyzed subsequently with a BD LSR Fortessa™ flow cytometer using BD FACSDiva™ Software v8.0.2 (both BD Biosciences)**.** Analysis of EGFP expression and DNA staining with PI was performed utilizing forward scatter vs. side scatter, pulse area vs. pulse width, cell count vs. FITC (fluorescein isothiocyanate channel) and cell count vs. PI plots. The raw data from BD LSR Fortessa™ flow cytometer device was saved as .fcs file using the BD FACSDiva™ Software. The data was further processed using BD FACSDiva™ (see Figure 19 for gating) and saved as a .wsp file. The EGFP expression and DNA staining data was visualized with BD FACSDiva™.

2.5.18 Analysis of cell cycle by DNA content using flow cytometry

The cell cycle was evaluated by measurement of the cellular DNA content. During this procedure, a fluorescent dye that binds to DNA was incubated with the cell suspension. PI intercalates into double-stranded nucleic acids. Since PI binds to DNA stoichiometrically, the amount of fluorescent signal is directly proportional to the amount of DNA[541]. The investigation of DNA content within cell cycle allows the detection of cell separation between G1, S, G2 and M phases[542]. Within the preparation, cells were fixed and permeabilized to allow PI to enter the cell and to prevent efflux of PI out of the cell. PI stains RNA as well in addition to DNA, so cells were treated with RNase to ensure only the DNA content is being estimated. General use of the flow cytometry technique is explained in more detail in section 2.5.20. Cell cycle analysis by flow cytometry was used to determine whether different serum concentrations and cell densities have an impact on the cell cycle of NGP neuroblastoma cells. NGP cells were supplemented with either 10% or 2% FCS and in different cell densities as described before (2.5.2). Subsequently of the treatments, the cells were harvested using Accutase® solution (see 2.4.3). During the following procedure, the cells were kept cool. Cells were centrifuged at 270g at 4°C for 5min, the supernatant was discarded and cell pellet was resolved in FACS buffer. Afterwards, the cells were centrifuged at 270 g at 4°C for 5min, the supernatant was discarded and the cell pellet was resolved in 300µl 0.15 M NaCl (Sigma-Aldrich). In the following, 700µl of -20° cold and absolute EtOH (99%; Sigma-Aldrich) was transferred carefully and drop-wise to the cell suspension in NaCl while the tube was vortexed virgously. The tube was then transferred to a -20°C freezer and incubated overnight in an upright position. The protocol continued within the next 7 days. Cells were thawed slowly on ice and washed twice with FACS buffer at 500g and 4°C for 5min each. Afterwards, the supernatant was discarded and the cells were resuspended in PI staining solution by adding 100µl per sample. The mixture was then incubated at 37°C and 5% CO_2 for 30min. Subsequently, the sample was centrifuged at 500g and 4°C for 5min, the supernatant was discarded and the cells were resuspend in 300µl FACS

buffer. Recipes for all buffers used are found in the supplement section 10.5.3. Samples were analyzed subsequently with a BD LSR Fortessa™ flow cytometer using BD FACSDiva™ Software v8.0.2. Application of the BD LSR Fortessa™ flow cytometer measurements for cell cycle analysis after serum starvation was performed in cooperation with K. Ahrens (Charité)[543,544]. Analysis of cell cycle by DNA content was carried out including forward scatter vs. side scatter, pulse area vs. pulse width, and cell count vs. PI. The raw data from BD LSR Fortessa™ flow cytometer was saved as .fcs file using the BD FACSDiva™ Software and loaded into the FlowJo™ v10.6.1 software (FlowJo LLC Becton Dickinson, Ashland, OR, USA). The data was further processed using FlowJo (see Figure 20 for gating) and saved as a .wsp file. Phases of the cell cycle were determined with the automatic detection, if this was not possible (e.g. due to higher deviations of the peaks when applying a high dose of inhibitor), the assignment was made manually. In each case, the assignment of the cell cycle phases was checked and readjusted manually if necessary. The Watson Pragmatic algorithm[545], was used to create a fit to cell cycle data based on DNA content. The Watson algorithm assumes that only the data within the G0/G1 and G2/M peaks follow a Gaussian distribution and that one of those two peaks is identifiable[546]. Cell cycle analysis was conducted in one biological replica using three technical replicates each time.

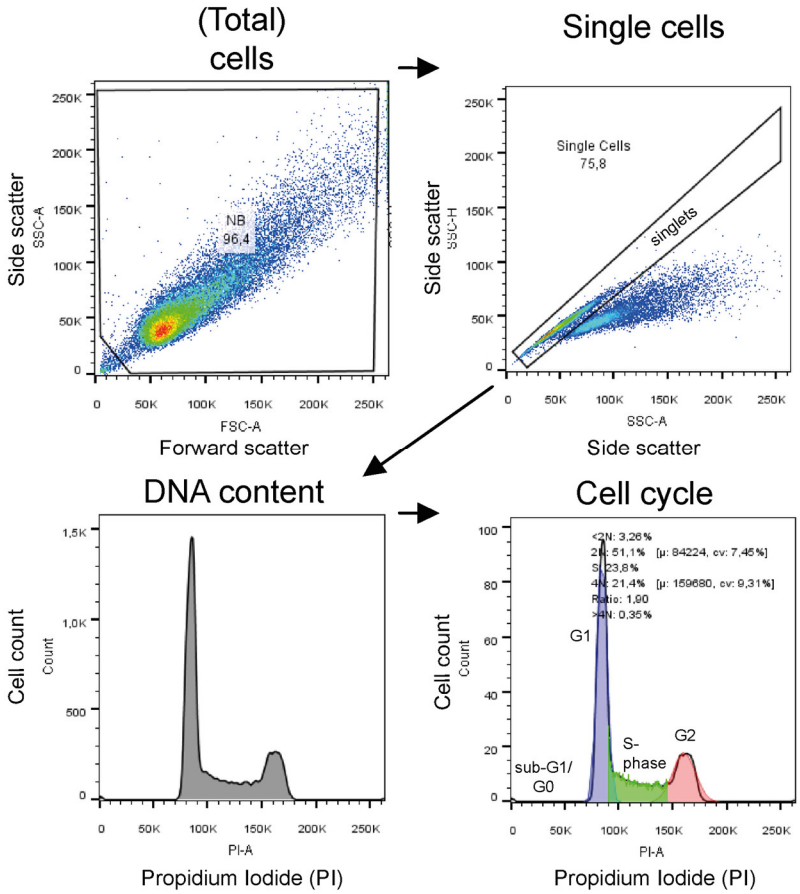

Figure 20: Gating strategy of cell cycle analysis by DNA content using PI.
Representative flow cytometry dots plots and histograms displaying gating strategy of cell cycle analysis. In serum starvation experiments, NGP cells were grown to 70% cell confluence and supplemented with 10% FCS. Cells were harvested 48h after experiment start. For an analysis of the cell cycle, all cells were first selected (total cells). Afterwards, only single cells were selected for further cell cycle calculations (doublets were excluded). For cell cycle assessment, the cell count was plotted over the area of the PI dye. Unstained cells served as negative control.

2.5.19 Click-iT™ Plus EdU Alexa Fluor™ 647 flow cytometry analysis of cell proliferation

EdU (5-ethynyl-2´-deoxyuridine) is an analogue to the nucleobase thymidine and is incorporated into DNA during DNA replication within the S-phase, allowing an estimation of cell proliferation through its detection. EdU incorporation is quantified by measuring fluorescence of chemically modified EdU. Using copper-catalyzed click chemistry, picolyl azide reacts with the ethynyl moiety of EdU to result in a fluorescent product. Applying the Click-iT Plus EdU Alexa Fluor™ 647 flow cytometry Assay (Thermo Fischer Scientific), the picolyl azide is coupled to an Alexa Fluor™ 647 dye, and fluorescence is measured at 647nm using flow cytometry[547]. In preparation for the Click-iT Assay, neuroblastoma NGP cells were seeded (see 2.5.1) and treated (see 2.5.7) with siASPM in clear 6-well flat bottom plates four days before. The Flow cytrometric assay was performed according to the manufacturers recommendations. NGP cells were labeled with EdU and incubated for 2h. After this time, the supernatant was collected. Cells were harvested using Accutase® solution (see 2.4.3), and the cells were pooled with the supernatant. The samples were centrifuged at 1195rpm for 5min and the cell pellet was washed with FACS Buffer.

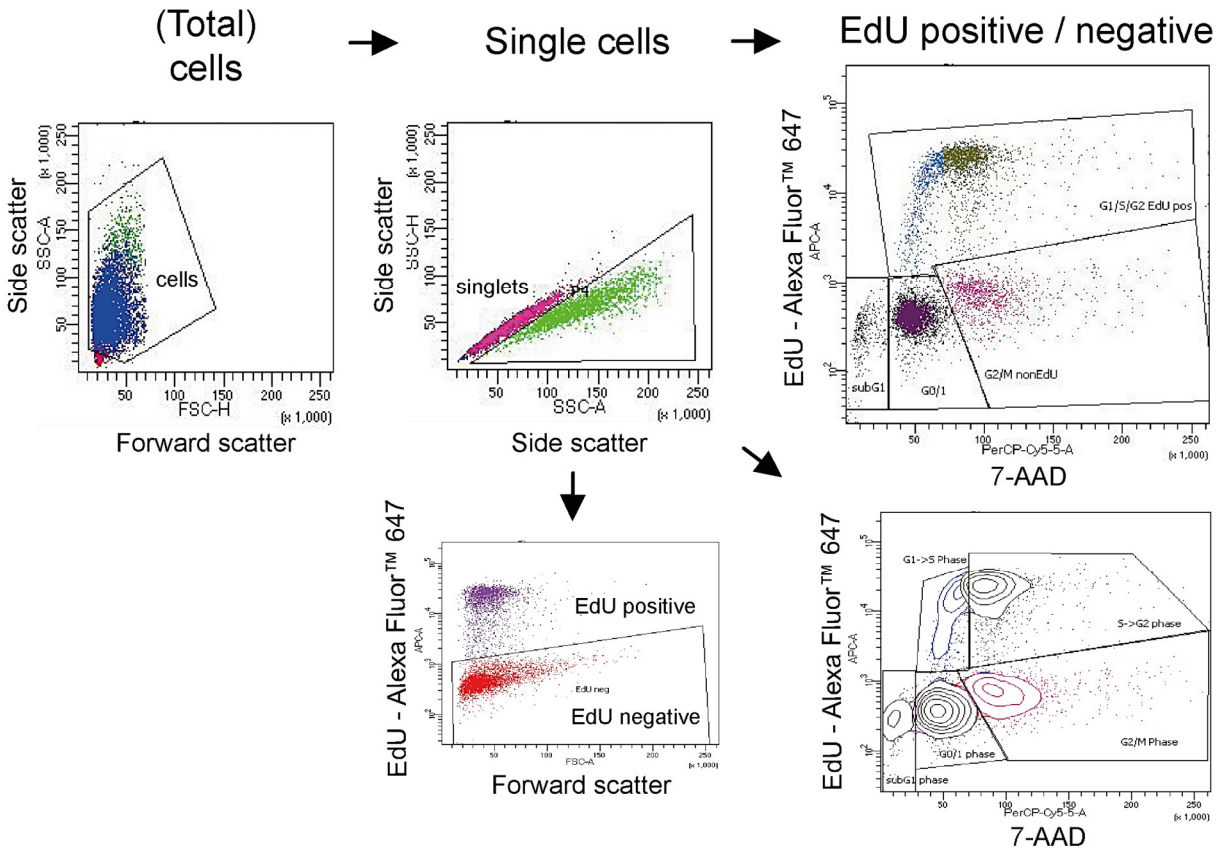

Figure 21: Gating strategy of EdU Alexa Fluor™ 647 and 7-AAD DNA staining using the Click-iT™ Plus Assay. Representative FACS dots plots displaying NGP cells treated with siScramble 1 and harvested four days after experiment start. For an analysis of EdU incorporation and proliferation, all cells were first selected (total cells, without debris). The double cells ("doublets") were then excluded within the next step. For assessment of EdU positive cells and 7-AAD positive cells, EdU (APC (allophycocyanin) channel) was plotted over the area of 7-AAD (PerCP-Cy5-5 channel). Non-siRNA transfected and unstained cells served as negative controls.

The cells were administered with Click-iT fixative containing 4% PFA in PBS for 15min and were washed with 1% BSA in PBS. Afterwards, saponin-based permeabilization and wash reagent was applied and incubated for 15min. The samples were centrifuged and the wash reagent was discarded. The cell pellet was solved in a cocktail of PBS, copper protectant as 100mM aqueous solution, Alexa Fluor™ 647 picolyl azide solved in DMSO and incubated for 30min. In the following, the cells were administered with wash reagent, centrifuged and the cell pellet was resuspended in 600µl wash reagent. For DNA staining, the cells were treated with 7-amino-actinomycin D (7-AAD; stock 1mg/ml in PBS; Sigma-Aldrich) due to the passage of 7-AAD into the nucleus where it binds to the DNA[548]. 7-AAD was incubated at RT for 10min. Recipes for all buffers used are found in the supplement section 10.5.3. Samples were analyzed subsequently with a BD LSR Fortessa™ flow cytometer using BD FACSDiva™ Software v8.0.2. Analysis of EdU incooperation and DNA staining with 7-AAD was performed using flow cytometry including forward scatter vs. side scatter, pulse area vs. pulse width, EdU vs. 7-AAD and EdU vs. forward scatter plots. The raw data from BD LSR Fortessa™ flow cytometer device was saved as a .fcs file using the BD FACSDiva™ Software. The data was further processed using BD FACSDiva™ Diva (see Figure 21 for gating) and saved as a .wsp file. The EdU incorporation and DNA staining with 7-AAD data was visualized with BD FACSDiva™.

2.5.20 Analysis of apoptosis by flow cytometry

The initiation of the programmed cell death after inhibitor application was detected using Flow cytometry. For identification of apoptosis signals after PLK1/PI3K inhibition, IMR5/75 neuroblastoma cells were treated with rigosertib using the relative IC50 (EC50): 33nM and IC80: 132nM for 24 and 72h (2.5.3) and were harvested subsequently using Accutase® solution (see 2.4.3). Cell staining with FITC labeled annexin V and 7-AAD was conducted applying the Dead Cell Apoptosis Kit with Annexin V FITC and PI (Thermo Fisher Scientific Inc). Annexin V is an intracellular protein that binds to phosphatidylserine, which is part of the plasma membrane and dissociates during early apoptosis. In the outer layer, phosphatidylserines attaches to FITC-fluorochrome-labeled annexin V and stains the cell surface. Therefore, FITC-labeled annexin V can then be used to specifically target and identify apoptotic cells. The distinction between late apoptotic or secondary necrotic cells can be archived by further usage of PI staining[549]. Living or early apoptotic cells will not show PI signals, while late stage apoptotic cells will stain positively. The Dead Cell Apoptosis Kit with Annexin V FITC and PI was applied following the manufacturer's instructions. Recipes for the buffers and solutions used are described in section 10.5.3. Samples were analyzed subsequently with a BD LSR Fortessa™ flow cytometer using BD FACSDiva™ Software v8.0.2. Analysis of annexin V cell apoptosis and DNA staining with PI was performed using flow cytometry including forward scatter vs. side scatter, pulse area vs. pulse width, PI vs. FITC, cell count vs. PI and cell count vs. FITC plots. In addition, the overspillings of the two channels PI and FITC-annexin V were compensated for using the BD FACSDiva™ software. The raw data from BD LSR Fortessa™ flow cytometer was saved as a .fcs file using the BD FACSDiva™ Software and

loaded into the FlowJo™ v10.6.1 software. The data was further processed and visualized using FlowJo™ (see Figure 22 for gating) and saved as a .wsp file. Detection of cell apoptosis was conducted in one biological replica using three technical replicates.

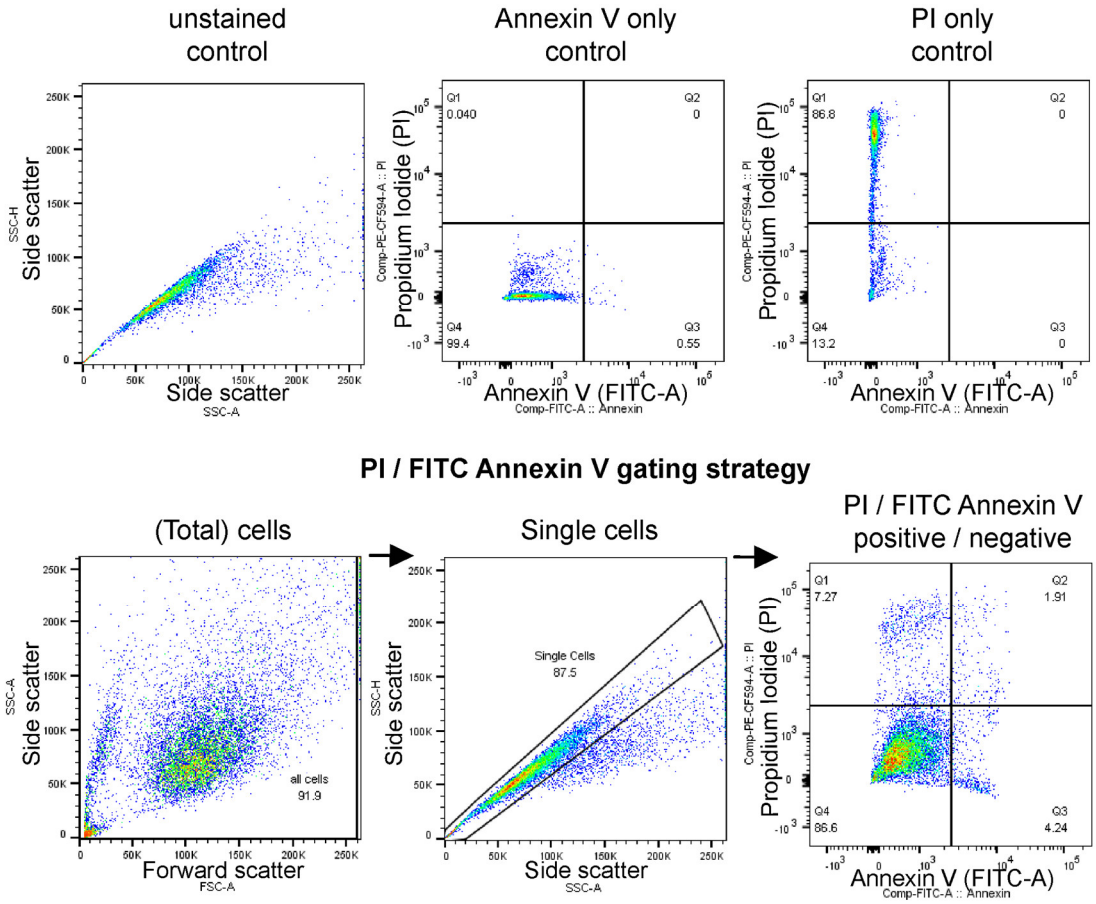

Figure 22: Gating strategy of FITC labeled annexin V cell apoptosis analysis combined with 7-AAD DNA staining. Representative flow cytometry dots plots displaying IMR5/75 cells without rigosertib treatment, harvested 24h after experiment start. For apoptosis analysis, all cells were first selected (total cells). The double cells ("doublets") were then excluded. For apoptosis assessment, the PI DNA staining was drawn over the area of the FITC annexin V dye. Unstained cells served as negative control.

2.5.21 DNA fluorescence *in situ* hybridization

Neuroblastoma cell lines were seeded (2.5.1) separately in a four chamber Nunc™ Lab-Tek™ II Chamber Slide™ system (Sigma-Aldrich) and cultured for at least 48h. Afterwards, the media was discarded and the plastic chambers were removed from the superfrost slides using a provided slide separator. The slides were washed once with 1x PBS and fixed in a 4% PFA (neoLab Migge GmbH, Heidelberg, Germany) for 10min. PFA was removed by immersing the slides once in 1x PBS and slides were air-dried in the following. The DNA FISH analysis was performed according to Theissen et al. 2009[68], the recommendations of the European Neuroblastoma Quality Assessment group[69] and the NB2004 trial protocol for Risk adapted Treatment of Children with Neuroblastoma[70]. For detection of a *MYCN* gene amplification, a DNA probe complementary to chr.2p24 (Vysis LSI N-MYC SG/CEP2 SO, start at chr2:15,957,690, stop at chr2:16,163,618; Vysis, Abbott Laboratories, Chicago, IL, USA)

was used. As a reference, a CEP2 probe (Vysis, Abbott Laboratories) which binds a repetitive sequence in the centrosomal area of chromosome 2, was added. The FISH technique was performed in a dual-color procedure following the manufacturers' instructions. Sections were covered using ProLong™ Gold Antifade Mountant (Thermo Fischer Scientific), including nuclear counterstaining with DAPI (4′,6-diamidino-2-phenylindole) blue-fluorescent dsDNA binding dye. Fluorescence images were captured with a Leica DMRA microscope (Leica Camera, Wetzlar, Germany) and JVC KY F-75 digital camera (JVC, Yokohama, Japan) using Diskus Viewer software (Hilgers Technisches Buero e.K., Koenigswinter, Germany). The results were analyzed according to the recommendations of the European Neuroblastoma Quality Assessment group[68–70]. FISH analysis was performed in cooperation with the neuroblastoma reference laboratory by J. Theissen and W. Lorenz (University Hospital Cologne, Cologne, Germany).

2.5.22 Immunofluorescence staining and microscopy

In preparation for the immunofluorescence supported microscopy, glass cover slips (circle 22 mm, VWR International, Randor, PA, USA) were sterilized in 70% EtOH/ddH_2O shortly and washed with sterile ddH_2O (Thermo Fischer Scientific). Afterwards, one glass cover slip was placed in one well of a clear 6-well flat bottom plate (CELLSTAR®) and covered with poly-L-lysine solution, 0.01% (Sigma-Aldrich). Poly-L-lysine was incubated at sterile conditions at 37°C for 15min. Subsequently, the poly-L-lysine was aspirated and the cover slip was rinsed two times with 1x PBS. The cover slips then were stored in 1x PBS at RT for a maximum duration of 6h. Recipes for buffers and solutions used in the following protocol are found in the supplement section 10.5.8. For seeding of cells, PBS was discarded and the neuroblastoma cell lines NGP, NGP ASPM-FPN-sgRNA87 #1 and #7 and CHP-134 were seeded (see 2.5.1) and treated with siRNA (see 2.5.7) in prepared glass cover slip 6-well plates. Incubation was performed for 4 or 10 days at 37°C and 5% CO_2. Afterwards, the media was aspirated very carefully and cells were washed very carefully two times with 1x PBS. In the following, the cells were fixed with 4% PFA/PBS for 10min. The PFA/PBS was discarded and cells were washed once with 1x PBS. For long-term storage, cells were covered with 30% sucrose/PBS and frozen at -80°C for a maximum duration of 6 weeks. For subsequent preparations, plates were thaw slowly from -80°C at RT, the sucrose/PBS solution was aspirated and cells were washed twice with 1x PBS. Specimen were administered immunofluorescence blocking buffer (5% FCS was added freshly) and incubated at RT for 90min. Recipes for the buffers and solutions used are described in section 10.5.3. Afterwards, the blocking solution was discarded and primary antibody (unconjugated) or fluorochrome pre-conjugated primary antibody (see Table 36 in appendix) was diluted in 1x PBS (100µl total volume per cover slip) and the solution was dropped slowly on the cover slips. After an incubation at 4°C in a dark environment overnight, the slides were rinsed two times with 1x PBS. For further processing, either a secondary fluorochrome conjugated antibody was applied to the cover slips or the slips were mounted directly,

in case of the pre-conjugated rhodamine phalloidin (Cell Signaling Technology). If a secondary antibody was used (diluted in 1x PBS; 100µl total volume per cover slip), the antibody was incubated at RT in a dark environment for 90min. Afterwards, the cover slip was rinsed two times with 1x PBS and mounted on an adhesion SuperFrost cover slide (R. Langenbrinck GmbH, Emmendingen, Germany) using a drop of Vectashield® Antifade Mounting Medium including nuclei counterstaining DAPI (Vector Laboratories Inc., Burlingame, CA, USA). The cover slips were sealed to cover slide using clear nail polish (dm-Drogerie Markt GmbH + Co. KG, Karlsruhe, Germany) and harden at 4°C overnight. Fluorescent images were taken with a light microscope BX43, supported by cellSens dimension software (both Olympus Life Science, Tokyo, Japan). Photography of immunofluorescence specimen was performed with manual lighting in 1376 x 1038 pixels resolution. For analysis of neuronal cell differentiation, F-ACTIN, MAP2, TUBB3 and DCX were stained with Alexa Fluor™ dyes (see Table 36 in appendix). Phalloidin (anti-F-actin) Alexa Fluor™ 555 was stimulated in TRITC (tetramethylrhodamine channel)/red spectrum (absorption 555nm/emission 565nm) for 1s laser exposure time and DAPI was stimulated in DAPI/blue spectrum (absorption 360nm/emission 460nm) for 42ms laser exposure time. ß3-Tubulin, DCX and MAP2 labeled with Alexa Fluor™ 488 were stimulated in FITC/green spectrum (absorption 495nm/emission 519nm) with 1s laser exposure time and DAPI was stimulated in DAPI/blue spectrum (absorption 360nm/emission 460nm) with 100ms laser exposure time, using a shutter of 50%. For analysis of ASPM-FLAG protein expression, Alexa Fluor™ 488 was stimulated in FITC/green spectrum (absorption 495nm/emission 519nm) with 2s laser exposure time and DAPI was stimulated in DAPI/blue spectrum (absorption 360nm / emission 460nm) with 40ms laser exposure time, using a shutter of 50%. Combined and single color channel pictures were saved as .tif and .jpg data files. Image processing with Adobe® Photoshop® and composition with Adobe® Illustrator was performed according to section 2.10.7. Evaluation of ASPM-FLAG Alexa Fluor™ 488 signals was carried out according to section 2.10.8.

2.6 Molecular biology methods

2.6.1 Isolation of genomic DNA from cell line material

DNA was isolated from previously harvested cell line material (2.4.3). Isolation was performed using the NucleoSpin® Tissue kit (Macherey-Nagel GmbH & Co. KG, Düren, Germany) according to the manufacturer's instructions. Isolated DNA was stored at -20°C and several freeze-thaw cycles were avoided. DNA concentration (ng/µl) of isolated cell line DNA has been measured using a NanoDrop 2000 spectrophotometer (Thermo Fischer Scientific), see explained in detail in 2.2.3.

2.6.2 Primer design for PCR assays flanking a *MYCN* or *ATRX* breakpoint

Unique *MYCN* and *ATRX* breakpoint sequences from neuroblastoma tumors or cell lines served as a template for PCR primer design (see 2.9.3). Primer, which are short nucleic acids, function as starter

sequence for a PCR. The primer hybridizes with the template and provides double-stranded DNA which is recognizable by DNA-polymerases, adding free nucleotides to the 3' end of the template complimentary strand[550]. Primer pairs which are flanking the breakpoint were composed of a forward primer (5'), located upstream of the breakpoint aligning to the sense strand (+), and of a reverse strand complementary primer (3'), located downstream of the breakpoint aligning to the anti-sense strand (-). The primer were designed to align at least 5bp upstream and 5bp downstream of the exact breakpoint sequence, and were positioned as not to cover the exact breakpoint due to the possibility of occurring microhomologies[551]. In very rare cases, the primer was designed to span the actual breakpoint, as the upstream/downstream sequences flanking the breakpoint were repetitive sequences or if the targeted sequencing assay had provideded no information about both flanking regions. Primer design was performed using the web applications NCBI Primer-BLAST[552] and Primer3Plus[553], and additional usage of the Reverse Complement JavaScript program[554,555]. The underlying concept of primer design and applied settings to web tools is explained in detail: DNA oligonucleotide primer were created with a length of 18-24 nucleotide bases, focusing on specificity in order to minimize mismatches, but also on the ability to amplify a product in the theoretical optimum[556]. The proportion of the nucleobases G (guanine) and C (cytosine) within a primer sequence is playing an important role regarding the primer melting temperature (T_m). The melting temperature of a primer by definition is the temperature at which one half of the DNA duplex will dissociate to become a single strand and indicates the duplex stability[557,558]. For calculation of the melting temperature, the DNA nearest-neighbor (NN) thermodynamics parameters and specification of the salt correction formula was applied according to SantaLucia et al.[559]. Because C and G base structures pairing with 3 hydrogen bonds and the structures of A (adenine) and T (thymine) bases with 2 hydrogen bonds, the C/G structure requires more energy to melt[560]. Like the length of a primer, specificity is lost with a low T_m, having a greater chance of mispriming. However, if the temperature is too high, the primer may not function properly and will produce insufficient primer-template hybridization, resulting in low PCR product yield[557]. For the designed primers, the T_m was similar in the forward and the reverse primer. Further, most of the primer contained up to 3 G/C bases in the 3' end which promote specific and stronger binding (GC-clamp)[557]. An ideal primer sequence contained a C/G content between 30-60%[556,557]. Both primers, forward and reverse, needed to have a similar content of C and G bases[561]. Sequence repeats (ATATATATAT) were avoided (maximum of 4 bases), in addition to inverse repeats (AATCGGC...GCCGATT) and runs (AGCGGGGGATGGGGG, maximum of 4 bases). Primer sequences with a high affinity for creating secondary structures, like hairpins, self-dimers, and cross-dimers were excluded[557,562]. The primer specificity was verified using the Basic Local Alignment Search Tool (BLAST) of the NCBI[552]. Primers were manufactured by Eurofins Genomics GmbH (Ebersberg, Germany), as custom DNA oligo with salt-free purification and lyophilized. The primer stock solutions (100pmol/µl, lyophilisate solved in ddH_2O; Thermo Fischer Scientific) were aliquoted 1:10 with ddH_2O for further use. Primer designed for this project are listed in the appendix Table 15, Table 17 and Table 20.

2.6.3 Primer design for an allele-specific PCR assay detecting *ALK* c.3824G>A

For detection of *ALK* SNV c.3824G>A (R1275Q), an allele-specific PCR assay was designed which enables the specific detection of an affected sequence in the presence of a wild-type allele. Based on the TaqMAMA technique (allele-specific PCR-based and mismatch amplification mutation assay)[563], the improved ASQ-PCR (allele-specific quantitative PCR) method by Barz (…, Szymansky, ...) et al[564,565] was used for primer design. In the ASQ-PCR, similar to the TaqMAMA method, the 3' end of the designed mutation primer is placed on the SNV. The previous base it is not changed and the third base from the 3' end is designed with a mismatch. The GRCh37 (hg19) publicly available reference sequence was used to design an allele-specific *ALK* SNV c.3824G>A (R1275Q) PCR assay. According to Barz et al[564,565], primer were designed using the Primer3 program[566,567], based on the concept of primer design (2.6.2). The allele-specific primer was built manually in forward and reverse design with a length of 23 nucleotides. The corresponding primer was composed by Primer3 using the default settings. The additional mismatch was caused at the third base closest to the 3' end by a change of the reference nucleotide (C) into one of the three other possible nucleotides (A, T, G) respectively, to increase the specificity of the allele-specific primer[565]. By this method, three different allele-specific primers for *ALK* SNV c.3824G>A (R1275Q) together with a universal reverse primer were obtained (see Table 21).

2.6.4 Conventional PCR (neuroblastoma *MYCN*/*ATRX*/*ALK* PCR)

The PCR is the standard method for *in vitro* amplification of selected DNA sequences up to a maximum size of 5kb[568]. A PCR assay is divided into three individual steps (denaturation, annealing and elongation), which are repeated cyclically. For neuroblastoma *MYCN*/*ATRX* breakpoint and allele-specific *ALK* MRD, DNA of neuroblastoma cell lines, tumor or bone marrow-derived samples were tested in two technical replicates within PCR assays for breakpoint detection. Controls were included for background and false-positive detection using DNA from a *MYCN*-amplified neuroblastoma cell line (Kelly, CHP-134, SK-N-BE or LAN-5), DNA from a non-neuroblastoma cancer cell line (HeLa) and DNA obtained from mononuclear cells (Buffy coat, 2.1.1). Go*Taq*® Hot Start polymerase (Promega Corporation) was used in a standard PCR reaction[569,570] per sample: 7.125µl ddH_2O, 2.5µl 5x Go*Taq*® Flexi buffer (Promega Corporation), 0.5µl $MgCl_2$ 25mM (Promega Corporation), 0.25µl d-NTPs (deoxy-nucleoside triphosphates) 10mM (Bio-Budget Technologies GmbH, Krefeld, Germany), 0.5µl forward primer 10pmol/µl, 0.5µl reverse primer 10pmol/µl, 0.063µl Go*Taq*® polymerase (*Thermus aquaticus)* 5 U/µl (Promega Corporation) using 11µl PCR mixture and 1µl DNA sample 100 ng/µl per reaction. PCR was processed using the calculated mode and applying 95°C for 5min, 95°C for 15s, 50-70°C (depending on primer annealing temperature) for 15s, 72°C for 30s, repeating step 2-4 for 30 times, 72°C for 5min, cool-down to 4°C using a C1000 Touch™ Thermal Cycler (Bio-Rad Laboratories, Inc.). After the PCR was done, the results were analyzed utilizing agarose gel electrophoresis (2.6.6) or automatic capillary electrophoresis (2.6.8).

2.6.5 Conventional PCR (breakpoint PCR product subcloning for sequence validation)

Amplification of breakpoint PCR product was performed using KAPA high-fidelity HotStart polymerase (Hoffmann-La Roche, Basel) or high-fidelity Q5® polymerase (New England Biolabs Inc. (NEB), Ipswich, MA, USA). MRD PCR primers were applied (Table 15, Table 17, Table 20 and Table 21) which produce amplified PCR products with (conventional cloning, see 2.6.11) or without (TOPO™ TA Cloning™, see 2.6.14) restriction sites for the enzymes SalI and XbaI. KAPA HotStart DNA polymerase was used in a standard PCR reaction[569,570] per sample: 7.5µl 2x KAPA HotStart Ready Mix (Hoffmann-La Roche), 0.5µl forward primer 50pmol/µl, 0.5µl reverse primer 50pmol/µl, and 1µl DNA depending on concentration, with a final volume of 15µl per PCR reaction (adjusted with nuclease-free water). PCR was processed using the calculated mode and applying 95°C for 5min, 95°C denaturation for 10s, 50-70°C (depending on primer annealing temperature) for 1s, 72°C elongation for 15s, repeating step 2-4 for 39 times, 72°C for 5min, cool-down to 4°C using a C1000 Touch Thermal Cycler. For high-fidelity Q5® PCR, the reaction mixture was per sample: 5µl 5x Q5® Buffer (NEB), 0.25µl d-NTPs 20mM (Bio-Budget Technologies GmbH) 0.25µl forward primer 50pmol/µl, 0.25µl reverse primer 50pmol/µl, 0.25µl Q5® polymerase (2U/µl; NEB) and 1µl DNA depending on concentration, with a final volume of 25µl per PCR reaction (adjusted with nuclease-free water). PCR was processed using the calculated mode and applying 98°C for 30s, 98°C denaturation for 10s, 50-70°C (depending on primer annealing temperature) for 30s, 72°C elongation for 30s, repeating step 2-4 for 35 times, 72°C for 10min, cool-down to 4°C using a C1000 Touch Thermal Cycler.

2.6.6 Agarose gel electrophoresis

The lengths of the PCR products (2.6.4) were analyzed using agarose gel electrophoresis[571,572]. PCR sample (5µl) was mixed with 2µl gel loading dye with Orange G (10x; Carl Roth GmbH + Co. KG) and loaded onto a 2% agarose gel[571] (w/v) (Biozym Scientific GmbH) containing 0.2% DNA-intercalating EtBr (ethidium bromide; diluted from solution 0.5% i. d. Tincture, Carl Roth GmbH + Co. KG). Gel electrophoresis was performed using a Horizontal Mini Gel System chamber (VWR International) and PowerPac™ Basic Electrophoresis Power Supply (Bio-Rad Laboratories, Inc.) filled with 1x TAE running buffer. Samples were processed together with a molecular mass standard GeneRuler 1kb or 100bp DNA Ladder (Thermo Fischer Scientific; 5µl, 6% dilution in ddH_2O). Information about buffer recipes is listed in section 10.5.1. For size separation, 90V was applied for 90min and results were analyzed by exposing the gel to ultraviolet (UV) light employing a transilluminator (UV table ECX-F20.C V1, Vilber Lourmat, Collégien, France). Pictures were taken with a Charge-coupled device Camera (DOC-Print VX5 and TV Zoom Lens, Vilber Lourmat). Photos were captured using the software DOC-PRINT VX, applying Live, Freeze and Save mode. The pictures were saved with the program in .tif format. DNA fragments or plasmids for further analysis were collected applying the agarose gel extraction method (2.6.7).

2.6.7 Agarose gel extraction

To obtain DNA fragments or plasmids previously separated by gel electrophoresis (2.6.6), the DNA band of interest was excised from the agarose gel with a clean, sharp scalpel (Swann Morton Ltd, Sheffield, UK) and put into a 2ml reaction tube. In the following, gel extraction was performed with the QIAquick® Gel Extraction Kit (QIAGEN) according to the manufacturer's instructions. The DNA concentration was determined by a NanoDrop spectrophotometer (2.2.3).

2.6.8 Automatic capillary electrophoresis

The lengths of the PCR products (2.6.4) were assessed within the neuroblastoma breakpoint MRD project using a QIAxcel® advanced automatic capillary electrophoresis device supported by QIAxcel® ScreenGel software (QIAGEN)[573,574]. A DNA high-resolution gel cartridge was utilized for analysis together with the QIAxcel® DNA High Resolution Kit (1200). In brief, the cartridge type was set to DNA high resolution with a default high resolution v2.0 process profile, including run, analysis and report steps. The high resolution method 0M500 with the parameters sample injection voltage 5kV, injection time 10s, separation voltage 5kV, separation time 500s and runs/repats of 1 loop was applied. Further, row deselection and marker definition was allowed. Analysis properties were set as default: Smoothing filter 15pts, baseline filter 40s and minimum distance 0.25s. For size estimation of the PCR product, a DNA alignment marker QX 15 bp/3 kb (1.5ml) and a DNA size marker QX pUC18/HaeIII (50µl, both QIAGEN) was applied. The gel was run adjusting the size marker as reference marker, which was refreshed and calibrated for every new cartridge. The data was exported in PDF format including report, gel image overview, electropherogram overview, single electropherograms, and a size result table. After electrophoresis, the remaining PCR products were purified (2.6.9).

2.6.9 PCR product purification

PCR products of conventional PCR were cleaned from PCR reaction (2.6.4) and/or automatic capillary electrophoresis reagents (2.6.8) using QIAquick® PCR Purification Kit (QIAGEN) according to the manufacturer's instructions. After cleaning, PCR products were eluated from the spin column using 30µl elution buffer. The purified PCR products were used for Sanger sequencing directly (2.8.2) or subcloning (2.6.10).

2.6.10 Breakpoint PCR product subcloning for sequence validation: Digestion of PCR product and pUC18 vector

For conventional cloning, the amplified PCR product from conventional PCR for breakpoint detection (2.6.4) was purified (2.6.9), subsequently digested with 20 U (1-2µl) of the enzymes SalI and XbaI (both NEB) in 5µl 1x CutSmart® Buffer (10x Stock diluted 1:10; NEB) and adjusted with ddH_2O to 50µl.

The mixture was incubated overnight at 37°C. In parallel, 5µg of the pUC18 plasmid (Agilent Technologies, Inc., see Table 26) were digested with 20 U of the same enzymes, to generate matching DNA overhangs. The next day, digests were mixed with 10x gel loading dye, run on a 1% agarose gel for 90min at 90V (2.6.6) and extracted from the gel (2.6.7) for ligations.

2.6.11 Breakpoint PCR product subcloning for sequence validation: Vector dephosphorylation and ligation of PCR product into pUC18 vector

The next day, the vector was additionally dephosphorylated by adding 6µl 10x alkaline phosphatase buffer and 4 µl rAPid alkaline phosphatase (both Hoffmann-La Roche) and incubated for 30min at 37°C, followed by a heat-inactivation at 72°C for 10min. This should prevent re-circularization of the vector during ligation. Following dephosphorylation, the digested vector was mixed with a 10x gel loading dye, run on a 1% agarose gel for 90min at 90V (2.6.6), and the vector backbone was cut out of the gel. DNA was extracted using the QIAquick® gel extraction kit (2.6.7) and used for ligation with the PCR products. For ligation, a vector-to-insert molar ratio of 1:3 and 1:5 was used. Thereby, the necessary amount of vector and insert were calculated using the formula (see as well Table 2):

$$vector\ [ng] \times \left(\frac{bp\ insert}{bp\ vector}\right) \times ratio = insert\ [ng]$$

Ligations were set up in a 20µl reaction, containing 2µl 10x T4 DNA Ligase Reaction Buffer, 1µl T4 DNA Ligase (both NEB), required amounts of vector and insert and water, and were incubated overnight at 16°C in a ThermoMixer® C (Eppendorf AG). In order to obtain ligated plasmid DNA for subsequent Sanger sequencing (2.8.2), ligations were transformed into chemically competent *Escherichia coli* (*E.coli)* cells (see 0).

Table 2: Mixing ratios for PCR product ligation approach.

	vector-to-insert molar ratio of 1:3	vector-to-insert molar ratio of 1:5	insert only control	vector only control
vector	50ng	50ng	-	50ng
insert	$50 \times \left(\frac{bp\ insert}{bp\ vector}\right) \times 3$	$50 \times \left(\frac{bp\ insert}{bp\ vector}\right) \times 5$	(as much as in the 1:5 preparation)	-
10x T4 buffer	2µl	2µl	2µl	2µl
T4 ligase	1µl	1µl	1µl	1µl
water	add to 20µl	add to 20µl	add to 20µl	add to 20µl

2.6.12 Breakpoint PCR product subcloning for sequence validation: Preparation of chemically competent *E.coli* cells

In order to obtain enough plasmid DNA for subsequent experiments, the plasmid DNA was amplified in chemical competent *E.coli* cells. To generate chemically competent *E.coli* cells, 50ml Lysogeny Broth (LB)-medium were supplemented with 10mM $MgCl_2$ (Carl Roth GmbH + Co. KG) and 37µg/ml chloramphenicol (CAM; Biomol GmbH, Hamburg, Germany) and inoculated with a sample of *E. coli* strain XL10-Gold® Ultracompetent Cells (Agilent Technologies, Inc.) taken from a glycerol stock with a sterile toothpick. The culture was incubated overnight in a shaker (IKA KS 4000 i control; IKA-Werke, Staufen im Breisgau, Germany) at 37°C with an agitation speed of 200rpm. The next day 0.5ml of the overnight culture was added to 300ml LB medium supplemented with 10mM $MgCl_2$ and 37µg/ml CAM, followed by an incubation at 37°C and 200rpm agitation for 3 to 4h until the bacteria culture reached an optical density between 0.4 and 0.6 at 600nm (detected using BioPhotometer®; Eppendorf AG). The culture was aliquoted into six precooled 50ml falcon tubes and incubated for 15min on ice. After that, the cells were centrifuged for 15min at 867×g at 4°C in a precooled centrifuge. The supernatant was discarded, each pellet was dissolved in 1.5ml transformation buffer and when not used immediately, bacteria were stored at -80°C. Buffer and solution recipes are listed in section 10.5.2. Chemically competent *E.coli* cells are used for transformation with the desired insert and plasmid by heat-shock method (2.6.13).

2.6.13 Breakpoint PCR product subcloning for sequence validation: Transformation of chemically competent *E.coli* cells by heat-shock

Chemically competent *E.coli* cells (2.6.12) were incubated on ice for 30min. Aliquots of 200µl chemical competent bacteria were used per transformation and thereby added directly to the 1.5ml reaction tubes containing the ligation reactions (2.6.11) prepared the day before or the TOPO™ TA Cloning™-reactions (2.6.14). After another incubation for 30min on ice, the bacteria were transferred into a 42°C water bath for 90s. This sudden increase in temperature ("heat-shock" method) creates pores in the bacteria cell membranes and allows an uptake of plasmid DNA. Following an incubation on ice for 2min and 800µl super optimal broth (SOC) medium was added to the cells. For recovery of cells from transformation stress, cells were incubated for 1h, shaking at 37°C in a ThermoMixer® C (Eppendorf AG) at 550rpm speed. For plating, bacteria were pelleted by centrifugation for 2min at 3,466×*g* (5,000 rpm) and the supernatant was discarded, the small amount left inside the tube was used to resuspend the pellets. All cells were plated onto LB-agar plates containing 100µg/ml ampicillin (Carl Roth GmbH + Co. KG) using glass beads (Sigma-Aldrich) for equal spreading to obtain single colonies. The plates were incubated overnight at 37°C and were screened for positive clones containing the insert by subsequent DNA isolation (minipreparation, 2.6.15), test-digests (2.6.10) and Sanger sequencing (2.8.2) of the positive clones. Buffer and solution recipes are listed in section 10.5.2.

2.6.14 Breakpoint PCR product subcloning for sequence validation: TOPO TA Cloning

Another approach to subcloning the PCR products is to use TOPO™ TA Cloning™. Hereby PCR products were generated using the KAPA HotStart DNA polymerase approach (2.6.5), which adds A-overhangs to its products. These products can be easily fused to commercially available linearized plasmids containing T-overhangs, by the topoisomerase. The TOPO™ TA Cloning™ Kit for Sequencing was used in this study, wherein the pCR™4-TOPO™ TA vector (obtained with TOPO™ TA Cloning™ Kit; Thermo Fischer Scientific; see Table 26) was already bound to the topoisomerase. For an RT incubation step, for 1h, 1µl PCR product (directly out of PCR, see 2.6.5 or gel purified, see 2.6.7) was mixed with 1µl pCR™4-TOPO™ TA PCR product subcloning vector and 1µl salt-solution in water (6µl reaction in total). Followed by the transformation in chemically competent *E. coli* cells (2.6.13).

2.6.15 Breakpoint PCR product subcloning for sequence validation: Mini-preparation scale of plasmid isolation and sequence validation

Plasmid preparations are methods to extract and purify plasmid DNA from transformed bacteria. For this purpose, a bacterial culture transformed with the plasmid of interest was grown, harvested and the cells were lysed. For DNA Isolation in a small scale ("miniprep"), 5-10 single colonies per construct were picked from the transformation plates (2.6.13) with a sterile toothpick and added to a 13ml plastic tube (Sarstedt AG & Co. KG, Nümbrecht, Germany) containing 4ml LB medium supplemented with 100µg/ml ampicillin. A negative control consisting of only ampicillin containing LB medium was also prepared. The samples and the negative control were incubated overnight at 37°C, shaking at 200rpm. For the plasmid preparation, 1.5ml of each sample were transferred to 1.5ml reaction tubes and centrifuged for 2min at 2,823×*g* (5,000rpm) at RT. The supernatant was discarded and plasmid isolation was performed. Each pellet was resuspended in 200µl buffer P1. Subsequently, 200µl of buffer P2 was added and the tubes were inverted three times. The same was done with buffer P3 (all buffers from QIAGEN), then the samples were centrifuged for 10min at maximum speed (18,213×g, 12,7000rpm). During the centrifugation 800µl 2-propanol (Carl Roth GmbH + Co. KG) was added to a fresh 1.5ml reaction tube per sample. Once the centrifugation was completed, the supernatant of each sample, approximately 600µl, was transferred into one of the isopropanol-containing tubes and mixed shortly by inverting the tubes 8 times. The samples were centrifuged for 30min at maximum speed and 4°C to precipitate the plasmid DNA. The supernatant was discarded by flipping the tube and pellets were washed by adding 500µl 70% EtOH (Carl Roth GmbH + Co. KG). After another centrifugation step at maximum speed for 15min at 4°C, the supernatant was discarded, all remaining supernatant was removed with a pipette and the pellet was air-dried. The dried pellet was resuspended in 50µl 0.1x TE (Tris-EDTA) buffer and stored at -20°C. To identify positive clones, a test-digest with 5 units EcoRI (NEB) was performed with each Mini-DNA (5µl) at 37°C overnight in EcoRI NEBuffer™ Set (NEB).

Buffer and solution recipes are listed in section 10.5.2. For subsequent gel electrophoresis of a 2% agarose gel (2.6.6), positive clones were identified by appearance of a second band matching the size of the desired PCR product. Positive plasmids were analyzed by Sanger sequencing (2.8.2).

2.6.16 Determination of the performance of genomic breakpoint-specific PCR

For each breakpoint sequence given, at least one primer pair was tested and stated to amplify the exact breakpoint sequence with the best possible performance. Primer sequences for breakpoint specific PCR amplification were previously examined computationally by using Primer-Blast for template specificity and useful primer parameters (length, secondary structures and melting temperature)[552,575]. After PCR experiments (see described above), a primer pair for the amplification of a breakpoint sequence was considered successful if, 1) the pair amplifies the exact sequence only (one PCR amplicon, correct base pair size of product, no unspecific products, no amplification was seen within control DNA), 2) the specific PCR product was seen in at least one target cell line or patient sample and in at least one of two technical replicates, 3) with the highest sensitivity (among all tested primer pairs for respective breakpoint), 4) for the primers with the best PCR performance (endpoint-PCR) and e) for the primers with the lowest intra- and inter-assay variance. The breakpoint-specific PCRs were verified using agarose gel electrophoresis (2.6.6) or automatic capillary electrophoresis (2.6.8) and Sanger sequencing of the PCR products (2.8.2) or of the subcloned PCR product (2.6.10).

2.6.17 Real-time quantitative PCR

The RQ-PCR technique was previously described for MRD detection in patients with acute lymphoblastic leukemia[161,576,577]. DNA was isolated from tumors, mononuclear cells or neuroblastoma cell lines (2.2.2). For each cell line / patient, at least one *MYCN* (or *ATRX*) associated breakpoint with best performance (2.6.16) was selected for RQ-PCR analysis. A hydrolyzation probe was applied with the two breakpoint flanking primers together in one reaction. A 20 to 25-mer hydrolyzation oligonucleotide combined with a FAM reporter dye (TaqMan™ system, 6-carboxyfluorescein amidite) located at the 5’ end and combined with a BHQ1 quencher dye (Black Hole Quencher®-1) located at the 3’ end was designed (Figure 23A). Annealing location of the probe was chosen preferred >5 bases upstream of the breakpoint, or, due to repetitive sequences, downstream of the breakpoint. The probe was positioned as not to cover the breakpoint and to anneal at least 5 bp away from any primer. In very rare cases, the probe was designed to match a breakpoint-spanning sequence, if upstream and downstream sequences neighboring the breakpoint were both repetitive sequences. FAM-BHQ1 probes were manufactured by Eurofins Genomics GmbH. Primer and probes designed for this project are listed in the appendix Table 13, Table 15, Table 17 and Table 20. Probe stock solutions (100pmol/µl) were aliquoted 1:10 with ddH_2O for further use. PCR amplified sequences were detected via the FAM tag in real-time.

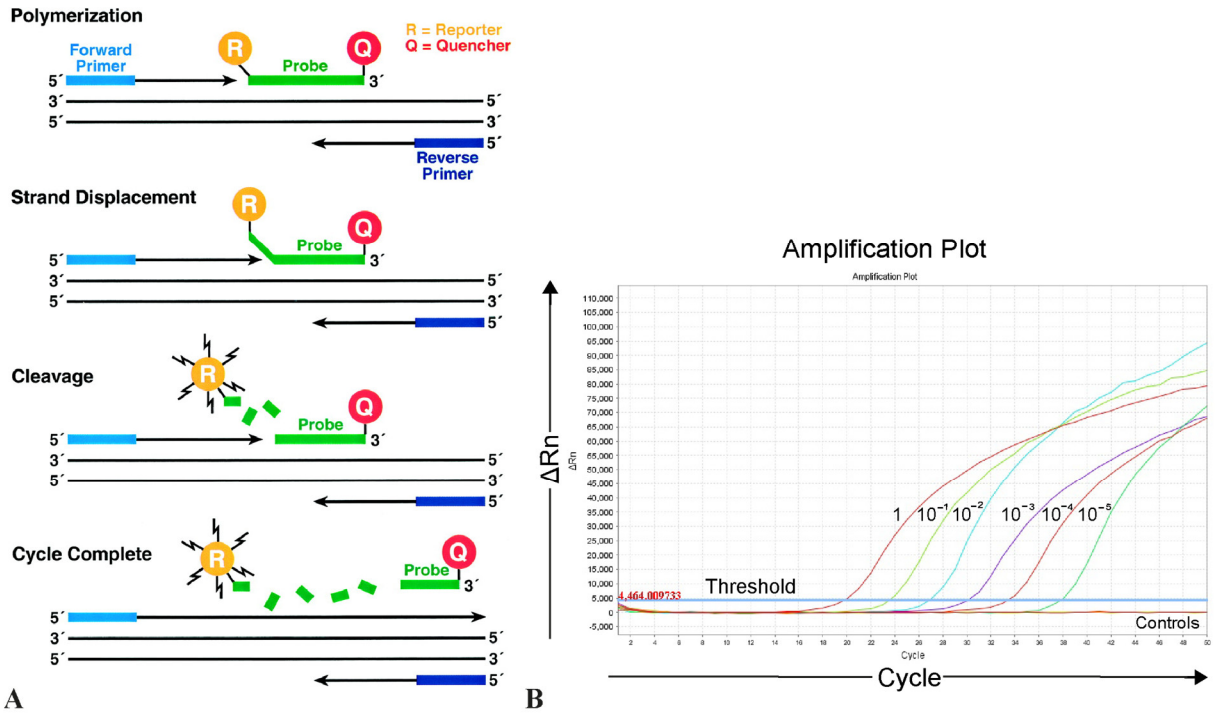

Figure 23: Principle of RQ-PCR detection using a TaqMan™ hydrolysis probe.
(A) Due to the *5´–3´* exonuclease activity of the *Taq* DNA enzyme, TaqMan probes that are designed to hybridize within the target sequence, will be cleaved by *Taq* during polymerization and release the reporter dye emission[578]. Therefore, an increase in the product targeted by the probe at each PCR cycle causes a proportional increase in fluorescence dye. (Figure taken from Yuan et al.[579]) **(B)** The measurable point of fluorescence increase is the threshold cycle (C_T). By creating a dilution series of known DNA, a calibration curve can be generated of $\log_{10}$ concentration against the C_T. The amount of PCR amplicons in an unknown sample can then be calculated from the measured C_T value of this sample[580]. (ΔRn = normalization of the fluorescence emission intensity of the reporter dye obtained by subtracting the baseline (ΔRn = Rn - baseline); the RQ-PCR plot shows the amplification of a part of the *ß-globin* gene, see as well Table 13). For further explanation see as well qPCR section 2.6.35.

Using a RQ-PCR mixture (3.1µl ddH_2O, 3µl $MgCl_2$ 50mM (ThermoFischer Scientific), 2µl 10x Buffer (ThermoFischer Scientific), 2µl d-NTPs 2mM (Bio-Budget Technologies GmbH), 1µl forward primer 10pmol/µl, 1µl reverse primer 10pmol/µl, 0.5µl bovine serum albumin (BSA) 0.20µM sterile filtered (Carl Roth GmbH + Co. KG), 0.5µl FAM-BHQ1 probe 10pmol/µl, 0.2µl Platinum™ *Taq* DNA polymerase 5U/µl (Thermo Fischer Scientific)) and the StepOnePlus™ Real-Time PCR System supported by StepOnePlus™ software (Thermo Fischer Scientific), RQ-PCR was performed at 94°C for 5min, 94°C for 8s, 60-65°C (depending on primer annealing temperature) for 23s, repeating step 2-3 for 50 times, cool-down to 4°C. The choice of detection channel was FAM-NFQMGB (non-fluorescent quencher minor groove binder channel). Due to different conditions of each unique breakpoint RQ-PCR and quality differences of input DNA, it is mandatory to adjust the protocols of every breakpoint assay to reach the highest output[581]. Cell line or patient samples were tested in an oligonucleotide (primer and probe) *specificity assay* at first. By using a minimal amount of each sample (10ng), the general performance of the PCR for breakpoint sequence amplification was evaluated and a specific amplification compared to controls was detected. For patients, different samples from the first sampling time point were tested (DNA of different tumor areas or snap-frozen versus FFPE derived and bone

marrow-derived DNA) within the sensitivity assay. This assay revealed the sample with best PCR performance for a subsequent dilution series for breakpoint quantification for each patient. The next step was a *sensitivity test* of the dilution series sample, related to the assay specificity (see above). An MRD spike-in dilution series of 100% cancer DNA into DNA from healthy volunteers (Buffy coat DNA[161], see 2.1.1) up to a dilution step of 10^{-6} was used to determine assay sensitivity. The total DNA input in one PCR reaction was 600 - 670ng, which corresponds to about 100,000 cells (the amount of DNA in one cell corresponds to 6.0 - 6.7pg[161,582,583]). The cancer DNA used for the dilution series was cell line DNA (in case of cell lines) or the diagnosis sample with high tumor load for patients (tumor sample choice evaluated in specificity test). The sensitivity test revealed the amplification efficacy of the target gene in a dilution series and the ideal annealing temperature (T_a; from 60°C to 65°C). Afterwards, detection of an invariant endogenous control took place. The analysis of a *reference gene* is an important step in RQ-PCR to normalize target gene results. Intra- and inter-kinetic RQ-PCR variations (sample to sample or run-to-run variations) needed to be compensated by normalization of target gene levels. In order to analyze, the target gene value was divided by the value from the control, resulting in a normalized ratio, which then could be compared to other samples[584]. For all quantified patient samples, the control gene represented a part of the *ß-globin* (hemoglobin subunit beta[585]) gene locus (see Table 13 and Figure 23B). Reference gene assays were conducted using technical duplicates. As a fourth and most important step, the *MYCN* (or *ATRX*) breakpoint sequence appearance was *quantified*. Quantification assays were conducted using technical triplicates. A sample was quantified for MRD detection of neuroblastoma cells by calculation of the standard curve applying tumor DNA and the mean C_T of the technical triplicates of a bone marrow-derived DNA sample. For RQ-PCR raw data analysis, the StepOnePlus™ software (Thermo Fischer Scientific) was used (see 2.10.6). The experimental setup for MRD detection and analysis of the RQ-PCR assays was performed regarding the EuroMRD Consortium guidelines[161,586,587]. For neuroblastoma MRD assessment, the "sensitivity" and "quantitative Range" MRD calculation method of van der Velden[161,582] was applied in accordance (see 2.10.6).

2.6.18 Allele-specific quantitative real-time PCR

On the basis of the RQ-PCR[161,576,577] and the TaqMAMA technique[563], MRD detection of ALK SNV c.3824G>A was performed using the ASQ-PCR method[564,565]. DNA was isolated from tumors, mononuclear cells or neuroblastoma cell lines (2.2.2). Similar to the RQ-PCR method (2.6.17), a hydrolyzation probe was applied with the two breakpoint flanking primers together in one reaction. A 20-mer hydrolyzation oligonucleotide combined with a FAM reporter dye or a HEX reporter dye (TaqMan™ system, 6-hexachloro-fluorescein) located at the 5' end and combined with a BHQ1 quencher dye located at the 3' end was designed (Figure 23A). FAM/HEX-BHQ1 probes were manufactured by Eurofins Genomics GmbH. Primer design is explained in 2.6.3, sequences and conditions of primer and probes are listed in Table 21. Probe stock solutions (100pmol/µl) were aliquoted 1:10 with ddH_2O for further use. PCR amplified sequences were detected via the FAM or the

HEX tag in real-time. The ASQ-PCR assay was performed identically to the RQ-PCR assay (2.6.17). The experimental setup for MRD detection and analysis of the ASQ-PCR assays was performed regarding the EuroMRD Consortium guidelines[161,586,587] and Barz et al[564,565]. For neuroblastoma MRD assessment, the "sensitivity" and "quantitative" range MRD calculation method of van der Velden[161,582] was applied in accordance. For quantification of SNVs mutations, the ratio of mutation positive cells to wild-type cells in a sample is calculated using standard curve equations (see 2.10.6).

2.6.19 Breakpoint-specific digital droplet PCR

The ddPCR[188,588] technique was performed using RQ-PCR or ASQ-PCR primer/probe sets (2.6.17 or 2.6.18) on previously DNA isolated (2.2.2). Primer and probes designed for this project are listed in Table 13, Table 15, Table 17 and Table 21. After denaturation for dissociation of DNA double strands (95°C for 10min, chill on ice) 600-670ng tumor DNA sample was diluted within spike-in series (as described for RQ-PCR, 2.6.17). The diluted DNA and controls were then applied within ddPCR mixture (2.1µl ddH_2O, 12µl ddPCR Supermix for Probes (no dUTP, Bio-Rad Laboratories, Inc.)), 1.7µl forward primer 10pmol/µl, 1.7µl reverse primer 10pmol/µl, 0.5µl FAM/HEX-BHQ1 probe 10pmol/µl. The PCR reaction was partitioned into droplets in 70µl Droplet Generation Oil using the QX200™ Droplet Generator (both Bio-Rad Laboratories, Inc.), and 40µl manually transferred to 1 well in a 96-well plate (twin.tec® PCR Plate 96, Eppendorf AG) for PCR in a T100™ Bio-Rad Thermal Cycler: 95°C for 10min followed by 40 cycles of 94°C for 30s and 60-70°C (optimized primer annealing temperature) for 1min, then ramped up to 98°C (2°C/s) for 10min before cool-down to 4°C. After the classical PCR, the droplets were counted using QX200™ Droplet Reader (Bio-Rad Laboratories, Inc.), adjusting for the detection of channel-1: FAM-HEX and absolute quantification. For ASQ-ddPCR, a ddPCR multiplex approach was employed as well. A specific *MYCN* breakpoint was measured via a FAM-BHQ1 probe (channel 1), whereas the *ALK* SNV was detected on another channel HEX-BHQ1 (channel 2). PCR amplification of the ß-globin gene for normalization[585] was likewise RQ-PCR applied (2.6.17). Reference gene assays were conducted using technical duplicates. For analysis, the QuantaSoft™ Software (Bio-Rad Laboratories, Inc., version 1.7) was used with MRD level assessment as previously published for acute lymphoblastic leukemia[203] and in agreement with current ddPCR recommendations of the EuroMRD Consortium (unpublished)[587,587,589] (see 2.10.6).

2.6.20 SiRNA mediated knockdown of *ASPM*: siRNA design

Basic criteria for siRNA design concerning the DNA target site was the exclusion of SNPs (single nucleotide polymorphism) and avoidance of 5'UTR or 3'UTR gene sequences. The target sequence was located in a region about 50-100 nucleotides downstream of the start codon in open reading frame and the GC-content of this region was between 30-50%. The length of a siRNA was around 20-24 nucleotides. Repeats, palindromes, hairpins, internal secondary structures and more than three AAA/UUU (RNA polymerase II tends to end transcription; U = uracil) were avoided. In case of the

nucleotide composition, attention was paid to place GC at the first position, A/U at position 10, >3 A/Us at position 13–19 and A/U at position 19 of the siRNA[590]. For development of siRNA against target sequences, web-based tools were used that assist in the design and quality control of siRNAs for RNA interference. SiRNA tools utilized in this thesis are: GenScript siRNA Target Finder[591] (http://www.genscript.com/tools/sirna-target-finder), IDT Custom Dicer-Substrate siRNA (DsiRNA)[592] (http://eu.idtdna.com/site/order/designtool/index/DSIRNA_CUSTOM) and siSPOTR siRNA/shRNA[593] Design Tool (http://sispotr.icts.uiowa.edu/ sispotr/tools/sispotr/design.html) applying standard settings. *ASPM* target sequence (62,568bp) was extracted from the human reference genome version GRCh38.p12 and either its entire sequence or partial sequences (head/tail), preferably exons, were used for siRNA design. For promising candidates, off-target binding was checked with NCBI Nucleotide BLAST using the human genomic and transcript sequences as reference (GRCh38.p12)[594]. Candidate siRNAs with less than 78% query coverage with other genes or with more than 14 contiguous nucleotides of sequence identity with other known mRNA transcripts were discarded[595]. The siRNA sequence did not carry any known miRNA seed sequence. siRNA sequences were tolerated which match ≥ 15 nucleotides out of total with respective siRNA[590]. All self-designed siRNAs were ordered at Eurofins Genomics GmbH as *siMax siRNA*, sequence-duplex with 5' dTdT overhangs on both strands, purification desalted and lyophilized. Furthermore, a ready-to-use siRNA from QIAGEN was obtained (FlexiTube siRNA; Hs_ASPM_1). As control, pre-designed, randomized, non-specific sequences were carried throughout all experiments (siMAX siRNA controls from Eurofins Genomics GmbH; non-Specific Control Scramble 1 and Scramble 2 in addition). SiRNAs applied in this thesis are listed in Table 24). Five siRNAs against *ASPM* transcripts were designed in total and tested for knockdown efficacy using qPCR analysis (2.6.35) of *ASPM* expression. Three siRNAs showing best knockdown performances were selected for further use in functional assays (Figure 24).

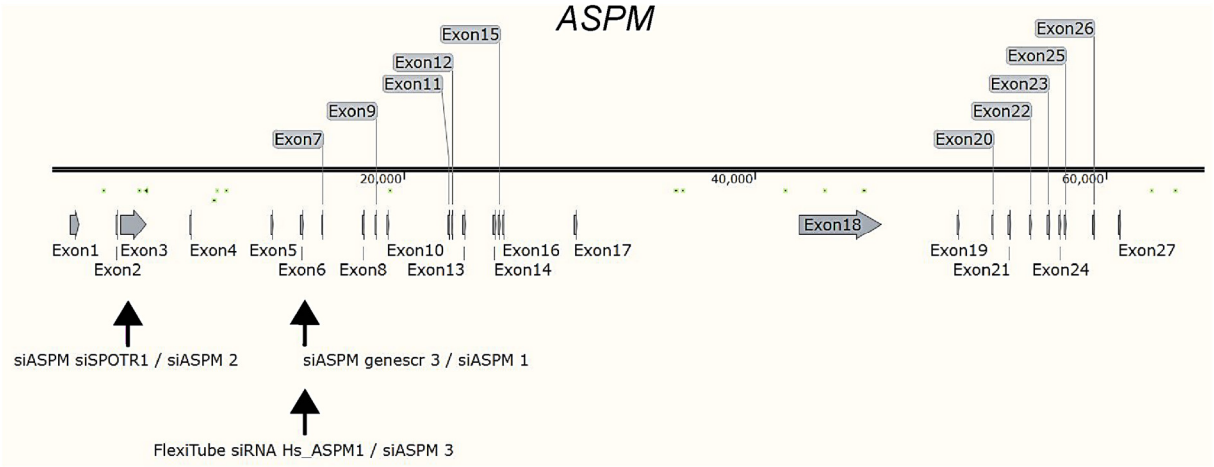

Figure 24: Sequence map of genomic *ASPM* with target sites of siRNA mediated knockdown.
Scheme of complete, genomic *ASPM* sequence, exons are highlighted by grey arrows. SiRNAs (illustrated by purple bars) are attacking different exon sites in transcripts of *ASPM* and lead to *ASPM* expression silencing. SiASPM sequences are listed in Table 24).

2.6.21 ShRNA mediated knockdown of *ASPM:* Origin of vectors

Short hairpin RNA (shRNA) is used to silence the expression of target genes via the RNA interference pathway[519]. A shRNA sequence insert for a vector was constructed in different parts: The 5' end and the 3' end contained a G/C nucleotide. The shRNA contained the target sense sequence (siRNA sequence, design process see 2.6.20) and the siRNA target antisense sequence, connected by a hairpin loop sequence (e.g. TTCAAGAGA[596]). A RNA Pol III terminator sequence (a 5-6 nucleotide poly (T) tract) was added to the 3' end, and closed with the G/C nucleotides[597]. ShRNA target sequences for lentiviral mediated knockdown of *ASPM* were kindly provided by A.M. Kaindl (Charité)[543,544,598]. ShRNA constructs are listed in Table 25 and locations of siRNA target sequences against *ASPM* are displayed in Figure 25. The virus packaging vector (psPAX2) was kindly provided by K. Ahrens[543,544,598] and F. Buttgereit (Charité; for vector information see Hahne et al.[599]). The virus envelope vector (pMD2.G) was kindly provided by A. G. Henssen[543,544,598] (ECRC of the Charité and MDC; for vector information see Henssen et al.[600]) and A. Kentsis (Molecular Pharmacology Program, Sloan Kettering Institute, Memorial Sloan Kettering Cancer Center, New York, NY, USA). The target vector pLKO.1_shASPM_Puro-T2A-GFP was modified from the Addgene vector #1864 ("scramble shRNA"; Addgene, Cambridge, MA, USA) and vector pLKO.1 by A.Winkler[543,544,598] (Charité). The pLKO.1 puro vector was kindly provided by J.J. Molenaar (Princess Máxima Center for Pediatric Oncology; for information see Molenaar et al.[322]; Vector referring to Stewart et al.[601]). Detailed vector information is shown in the appendix, Table 26. In short, the puromycin (puro) selection cassette of plasmid #1864 was replaced by a puro-T2A-GFP cassette (generated by overlap extension PCR) by BamHI/Acc65I digestion (NEB) and ligation. To allow cloning of any shRNA, the scramble sequence was replaced by a linker sequence consisting of three restriction enzyme cutting sites (AgeI, XbaI, EcoRI; NEB), by having two complementary oligos (encoding AgeI, XbaI and EcoRI) heating to 95°C for 5min subsequent cooling down to room-temperature, and ligation into AgeI/EcoRI digested plasmid #1864.

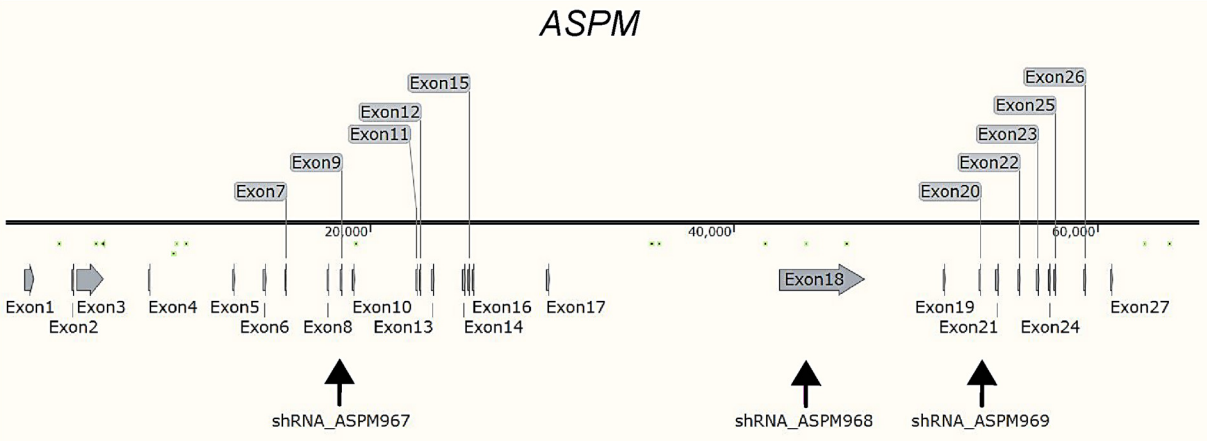

Figure 25: Sequence map of genomic *ASPM* with target sites of shRNA sequences for lentiviral mediated knockdown. ShRNAs processed into siRNAs attacking different exon sites in transcripts of *ASPM* and lead to *ASPM* expression silencing. ShASPM sequences are listed in Table 25.

For all shRNA experiments, the sequence for the shRNA control scramble 1 (scramble P) originates from the Addgene # 1864 vector. The sequence for the shRNA control scramble 2 (scramble W) originates from the vector pTer_shscr. The vector pTer_shscr was kindly provided by F. Westermann (German Cancer Research Center). For vector information see Muth et al.[602]. The generation and preparations of the plasmids for shASPM knockdown was done in in cooperation with A. Winkler (Charité[543,544,598,603]).

2.6.22 ShRNA mediated knockdown of *ASPM*: Cloning of ASPM shRNA oligonucleotides in pLKO.1 vector

ASPM shRNA sequences 967/968/969 (see Table 25) were ordered as custom, single-stranded, unmodified DNA oligonucleotides (two complementary oligonucleotides for each shRNA) from Eurofins Genomics GmbH. For subsequent ligations, oligonucleotides were dissolved to 50µM and 2µl from each primer of the pair was added to 496µl 0.1x TE buffer. The mixture was heated to 95°C for 5min and then left for cooling to RT. Additionally, the pLKO.1_AXE_PTG plasmid (cloning procedure see section 2.6.11, see vector information in appendix Table 26), was digested with 20 units of the AgeI and XbaI (NEB) restriction enzymes each at 37°C overnight (see plasmid digestion in section 2.6.10). The next day, digests were mixed with 10x loading dye, run on an 1% agarose gel for 90min at 90V (see method 2.6.6) and extracted from the gel (see 2.6.7) for ligations. Herein, 1µl of the oligonucleotide annealing is mixed with 1µl gel extracted digested vector and 2µl 10x T4 Ligase buffer (NEB), 1µl T4 DNA Ligase (NEB) and 15µl ddH_2O (20µl reaction volume in total, see method 2.6.11). A sample without oligonucleotide mix is set up as negative control. Ligations were incubated overnight at 16°C and transformed into chemically competent *E.coli* cells the following day (see methods 2.6.12 and 2.6.13). Recipes for the buffers and solutions used are described in section 10.5.2.

2.6.23 ShRNA mediated knockdown of *ASPM*: Mini- and maxi-preparation scale of plasmid isolation and sequence validation

The method of mini-preparation scale of plasmid isolation and sequence validation is explained in section 2.6.15. In arrangement for a plasmid maxi-preparation a validated colony is picked from a replica plate (prepared during miniprep setup) with a sterile toothpick and used to inoculate 200ml LB medium supplemented with 100µg/ml ampicillin. Cultures were grown at 37°C overnight, shaking at 200rpm. Bacteria were harvested, by spinning at 4,000rpm at RT for 20min in the Centrifuge Sorvall® Evolution™ RC Superspeed (Thermo Fisher Scientific). Supernatant was discarded and plasmid isolation was performed using the NucleoBond™ Xtra Midi kit (Macherey-Nagel GmbH & Co. KG) following the manufacturer's instructions. Recipes for the buffers and solutions used are described in section 10.5.2. After performing the isolation, plasmid pellets were resuspended in 500µl 0.1x TE buffer and stored at -20°C until further use. DNA concentration was measured using a Nanodrop spectrometer (see 2.2.3) and plasmids were sent for Sanger sequencing (2.8.2), before target cells were transfected.

2.6.24 CRISPR/Cas9 mediated knockin of 3xFLAG-tag at C-terminal end of *ASPM*

The CRISPR/Cas9 (clustered regularly interspaced short palindromic repeats/Cas9 nuclease) gene editing tool, has become widely used in recent years[604–607]. The discovery of this mechanism led to the proposal that the CRISPR/Cas9 type II system could be used as a genome editing tool outside of its original organisms[608,609]. This was first shown in *E.coli*[610] and later on in eukaryotic cells[611]. To target a gene with CRISPR/Cas9, a single guide RNA (sgRNA[612]) molecule of 20bp size needs to be designed. The only limitation is the required presence of a protospacer adjacent motif (PAM), a short consensus DNA sequence (5'-NGG-3' where N is any nucleobase[613]) The sgRNA can be delivered into a cell encoded on a plasmid together with the cas9 gene. In presence of suitable promotors on the plasmid, Cas9 nuclease and sgRNA get expressed by the cell. Cas9 and sgRNA then form a complex which migrates to the cell nucleus guided by a nucleus localization sequence (NLS) attached to Cas9[611]. Cas9 then scans the genome for PAM sequences and, if successful, unwinds the DNA to pair the sgRNA. Upon successful pairing, Cas9 induces a double-strand break, three base pairs upstream of the PAM. In eukaryotes, the cell has two options to repair the induced damage[614]. If a double-strand break is executed in presence of a template, which is homologous to the targeted region, the cell can make use of homology-directed repair (HDR). Thereby insertion of sequences into the genome can be generated as a knockin, by simply introducing a template with homology arms (HA) matching the targeted region and the desired sequence for insertion. This template can be introduced as single-stranded donor oligonucleotides (ssODN), a PCR product or as a donor plasmid. The versatility of CRISPR/Cas9 makes it an interesting tool for cancer research. CRISPR/Cas9 knockins[615–617] can be used to introduce specific cancer-associated mutations in an isogenic background[618]. In this subproject, *ASPM* was endogenously tagged with a 3x FLAG-tag, mediated by CRISPR/Cas9 (gene "knockin"). The attachment of a FLAG-tag peptide to the ASPM protein would allow the detection with a well-established monoclonal anti-FLAG antibody. The CRISPR/Cas9 knockin, is conducted to target the TAG stop codon in exon 28, thereby attaching the FLAG-tag C-terminally. For this purpose, guide RNAs targeting the *ASPM* locus were designed and cloned into a Cas9 containing vector. For insertion of the FLAG-tag a targeting vector was generated, which serves as a template for HDR after the Cas9 induced double-strand break. The construct was designed as a donor plasmid containing the 3x FLAG sequence, a neomycin resistance gene (NeoR) for selection of cells carrying the knockin and 800bp homology arms flanking the stop codon. Information about the plasmids used is provided in the appendix Table 26. The CRISPR plasmids and the targeting vector were transfected into neuroblastoma cell lines and selected for positive clones. Correct insertion of the tag was then confirmed by PCR, Sanger sequencing and ultimately by Western blotting and Immunofluorescence using an anti-FLAG antibody. The generation of NGP CRISPR/Cas9 *ASPM* 3x FLAG knockin 75/87 cell lines was done in supervision of the biotechnology bachelor student M. Overath and in cooperation with A. Winkler (Charité[543,544,598,603]).

2.6.25 CRISPR/Cas9 mediated *ASPM* 3xFLAG-tag knockin: Selection of single guide RNAs

The knockin was designed targeting the TAG stop codon in exon 28 of *ASPM*, thereby attaching the FLAG-tag C-terminal. For this purpose, guide RNAs targeting the *ASPM* locus were designed and cloned into a Cas9 containing vector. SgRNA sequences targeting the stop codon were designed using the Zhang lab CRISPR Guide design tool[619] (http://crispr.mit.edu; tool exists no longer). Two sgRNAs were selected for cloning into a px459 vector (information is provided in the appendix Table 26; plasmid purchased at Addgene) containing the *CAS9* gene fused to an NLS site and a puromycin selection marker. The two selected sgRNAs presenting with off-target scores 75 and 87 (see for sequence Table 25). Their binding sites at the *ASPM* gene are shown in Figure 26.

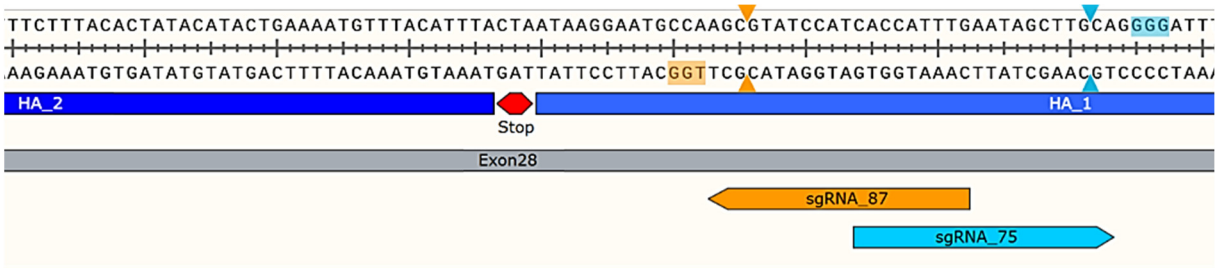

Figure 26: SgRNA binding sites are adjacent to the stop codon of *ASPM*.
Binding and cleavage sites of the two selected sgRNAs in exon 28 of *ASPM* with their respective off-target scores (75 and 87). The PAM sequence (NGG) is highlighted and the theoretical site of the cleavage three base pairs downstream of the PAM sequence is indicated by arrows. The *ASPM* gene is located on the antisense strand on chr.1q31.3 (reference genome version GrCh38). (Scheme was kindly designed by M. Overath (Charité)[544,598,603]).

2.6.26 CRISPR/Cas9 mediated *ASPM* 3xFLAG-tag knockin: Cloning of single guide RNAs into px459

SgRNAs TAG stop 75 and 87 were ordered as DNA oligonucleotides (at Eurofins genomics GmbH; see for sequence Table 25) and upon arrival, were dissolved to 50µM in 0.1 x TE-Buffer. A volume of 2µl of each corresponding oligo pair were mixed with 496µl 0.1x TE buffer, then the mix was heated at 95°C for 5min, followed by 30min incubation time at RT for annealing. Recipes for the buffers and solutions used are described in section 10.5.2.

2.6.27 CRISPR/Cas9 mediated *ASPM* 3xFLAG-tag knockin: Digestion of single guide RNAs and px459 CRISPR vector

In parallel, 5µg of the px459 plasmid was digested with 15 units BbsI (NEB) overnight and was subsequently loaded onto a 1% agarose gel (2.6.6). The corresponding linear DNA band was cut and isolated from the gel using the QIAGEN QIAquick® Gel extraction kit (2.6.7). The annealed oligos were ligated into the digested px459 plasmids at 16°C overnight, using T4 DNA Ligase (NEB; ligation method see 2.6.11) and were then ready for transformation (see 2.6.13) into *E.coli* cells (XL10-Gold Ultracompetent Cells, Agilent Technologies; preparation of chemical competent *E.coli* cells see 2.6.13).

Plasmid isolation was done using mini-preparation and maxi-preparation QIAGEN plasmid kits, for procedure see section 2.6.15 and 2.6.23. Recipes for the buffers and solutions used are described in section 10.5.2. Information about the plasmids used is provided in the appendix Table 26.

2.6.28 CRISPR/Cas9 mediated *ASPM* 3xFLAG-tag knockin: Design of 3xFLAG templates with homology arms and cloning into pBluescript vector

For insertion of the FLAG-tag, a construct was generated, which should serve as a template for HDR after the Cas9 induced double-strand break. The donor plasmid contained the 3x FLAG sequence, a NeoR gene for knockin selection and 800bp long HA oligos flanking the stop codon. Ideally, the stop codon region is cleaved by CRISPR/Cas9 and the resulting double-strand break is repaired by HDR using the HA. FLAG sequence and NeoR are fused through a 2A self-cleaving peptide (P2A), which separates the FLAG-tag and the NeoR after translation. NeoR is cleaved off the ASPM-FLAG protein post-translationally, mediated by the P2A peptide. The FLAG-P2A-Neo cassette was amplified from pFETCh_Donor vector (EMM0021; see detailed information in Table 26; Addgene), using the Q5® High-Fidelity DNA polymerase (NEB).

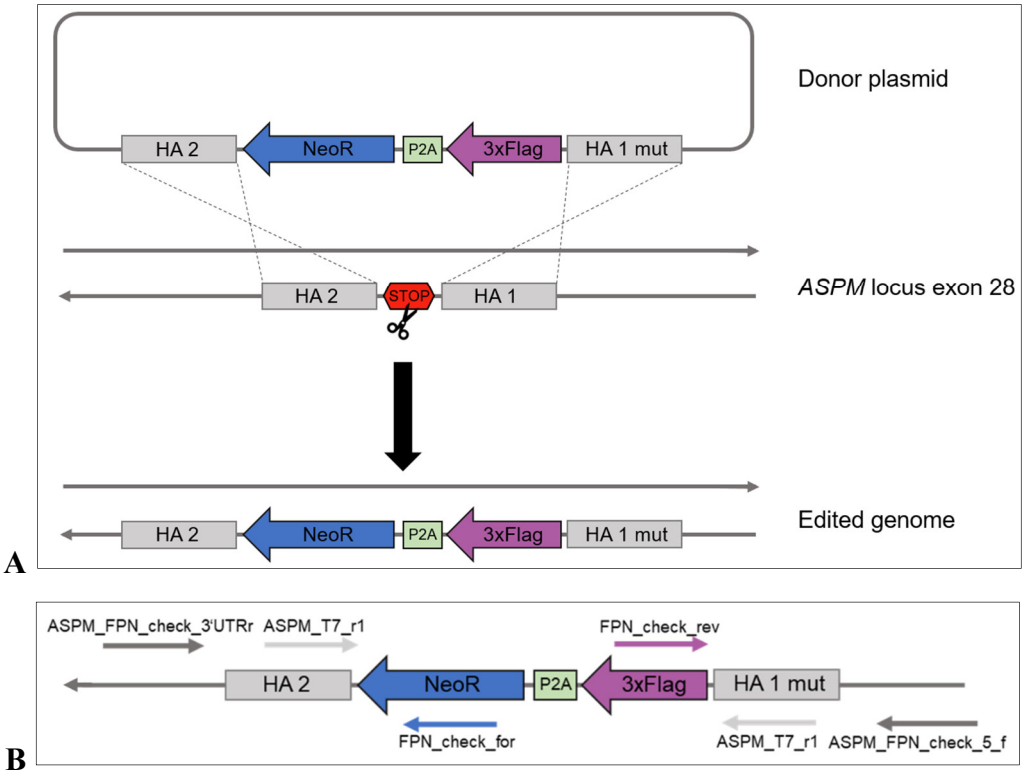

Figure 27: Cloning strategy for stop codon *FLAG* knockin at C-terminal end of *ASPM* guided by a donor plasmid. The *ASPM* gene is located on the antisense strand on chr.1q31.3 (reference genome GrCh38). **(A)** Showing exon 28 of *ASPM* and the donor plasmid with 3x FLAG sequence fused to a NeoR gene by a P2A sequence and two 800bp HA. The HA 1 site is mutated to avoid cleavage by CRISPR/Cas9. A double-strand break is induced adjacent to the TAG stop codon. **(B)** PCR analysis of designed construct: PCR no. 1 with one primer binding in the NeoR sequence and one outside of HA 2. PCR no. 2 with one primer binding in the 3x FLAG sequence and one outside HA 1 (schemes were adapted from M. Overath; Charité)[544,598,603].

As a first step, this part was cloned into pBluescript II KS (+) by EcoRI/BamHI digestion/ligation (NEB). The vector was kindly provided by J.H. Schulte (Charité; sequence author is Stratagene, San Diego, CA, USA). For the insertion of the 800bp homology arms the WI2-3482I04 fosmid (BACPAC Resources Center, Oakland, CA, USA) was used as a PCR template, because it contains parts of the genomic *ASPM* sequence. The 800bp HA were amplified using the Q5® High-Fidelity DNA polymerase. Of note, HA 1 is silently mutated in the donor plasmid, avoiding a cleavage by CRISPR/Cas9, without disturbing the original amino acid composition. This was accomplished, by adding a 50bp overhang to the reverse primer, containing the desired mutated sequence. All components were further cloned into the pBluescript II KS (+) vector (methods see section 2.6.11). The HA 2 site was cloned by EcoRI/XhoI (NEB) digestion/ligation and the HA 1 site was cloned by XbaI/BamHI (NEB), and subsequently transformed in *E.coli* cells (for preparation of chemical competent *E.coli* cells see 2.6.13) for plasmid amplification and isolation (methods see section 2.6.15). Recipes for the buffers and solutions used are described in section 10.5.2. Information about the plasmids used is provided in the appendix Table 26.

2.6.29 CRISPR/Cas9 mediated *ASPM* 3xFLAG-tag knockin: Transfection of NGP neuroblastoma cells with px459 and 3xFLAG donor plasmid

NGP cells were transfected with px459_ASPM_Stop 75/87 Cas9 vector and the pBS_ASPM_FLAG-P2A-Neo_Hom1mutHom2 donor plasmid via electroporation. The px459 empty vector (without sgRNA inserts) was introduced as a transfection control. For electroporation, cells were dissociated with trypsin and centrifuged to obtain a cell pellet (2.4.3), which was washed twice with 1x Dulbecco's Phosphate-Buffered Saline (DPBS). $2x10^6$ NGP cells per approach were dissolved in 500µl Opti-MEM™ (Thermo Fischer Scientific). 10µg of empty px459 vector or sgRNA 75/87 containing px459 vector and 10µg of donor plasmid was mixed with the 500µL of NGP cell suspension in a 4mm electroporation cuvette (Bio-Rad Laboratories, Inc.). The cuvette was then placed into a Bio-RAD Gene Pulser Xcell™ CE module (Bio-Rad Laboratories, Inc.) and the square wave protocol was applied (using the settings: voltage: 200V, pulse length: 20ms, pulse: 1, cuvette: 4mm). Following electroporation, 1ml of RPMI 1640 medium (supplemented with 1% P/S and 10% FCS) was added to electroporated NGP cells and cells were seeded onto a 10cm cell culture dish (Corning, Inc.) immediately. One day after transfection, cells containing the px459 plasmid were checked for a GFP expression signal, by fluorescence microscopy using a Axio Vert.A1. (see 2.4.2). Cells containing px459 vectors were selected for knockin positive cells by addition of 800µg/ml G418 (Geneticin®, Thermo Fischer Scientific), 48h post transfection. Bulk cells were cultured in RPMI 1640 medium (supplemented with 1% P/S and 10% FCS) under constant addition of G418 for selection and cell pellets were harvested (2.4.3) for DNA isolation (2.6.1) in preparation for a T7 assay (2.6.30). Information about the plasmids used is provided in the appendix Table 26.

2.6.30 CRISPR/Cas9 mediated *ASPM* 3xFLAG-tag knockin: T7 DNA Endonuclease I assay

CRISPR/Cas9 evoked mutations were checked by a T7 endonuclease I assay to validate efficacy of the designed guide RNAs[620,621]. In brief, the T7 endonuclease I is an enzyme from the bacteriophage T7 which recognizes and cuts mismatched DNA generated by the hybridization of wild-type and mutated DNA. In preparation for a T7 assay, a PCR with primers flanking the targeted region was performed. The PCRs targeted different bindings sites outside and inside of the knockin sequence, with primer pairs ASPM_FPN_check3'UTR_r + FPN_check_for and FPN_check_rev + ASPM_FPN_check_5f (primer sequences are listed in the appendix Table 23). KAPA2G Fast HotStart DNA polymerase (Hoffmann-La Roche) was used in a standard PCR reaction[569,570] per sample: 7.5µl 2x KAPA2G Fast HotStart ReadyMix, 2.5µl forward primer 10pmol/µl (Eurofins Genomics GmbH), 2.5µl reverse primer 10pmol/µl (Eurofins Genomics GmbH), and DNA depending on concentration with a final volume of 15µl per reaction (adjust with nuclease-free water). PCR was processed using the calculated mode and applying 95°C for 5min, 95°C denaturation for 10s, 60°C annealing for 15s, 72°C elongation for 1min, repeating step 2-4 for 40 times, 72°C for 5min, cool-down to 4°C using a C1000 Touch™ Thermal Cycler (Bio-Rad Laboratories, Inc.). After the PCR was done, the results were analyzed with a 2% agarose gel (2.6.6). The PCR product was processed using the QIAGEN QIAquick® PCR Purification Kit (2.6.7). The product was diluted to 200ng in 9µl ddH_2O and 1µl NEBuffer™ 2.1 (NEB) and hybridized following 95°C for 5min, ramp down to 85°C at -2°C/s, ramp down to 25°C at -0.1°C/s and hold at 4°C. Thereby allowing mutated and wild-type DNA to align and consequently form mismatches. After the PCR run, 0.5µl T7 DNA Endonuclease I (NEB), 4µl ddH_2O and 0.5µl NEBuffer™ 2.1 was added and incubated for 30min at 30°C. The generated fragments were then analyzed on a 2% agarose gel (2.6.6). Recipes for the buffers and solutions used are described in section 10.5.2.

2.6.31 CRISPR/Cas9 mediated *ASPM* 3xFLAG-tag knockin: Generation of single cell clones NGP-ASPM-FLAG and PCR analysis

After confirmation of successful knockins in the bulk of NGP cells, single cell clones were obtained for further analysis (2.5.6). Therefore, transfected NGP cells were seeded with a concentration of 0.5 cells/well onto a 96-well plate to achieve single cell level. Successfully grown NGP single cell populations were checked for positive insertion (see methods 2.6.6, 2.6.7, 2.6.9 and 2.8.2) by performing the same PCRs mentioned in 2.6.30 with KAPA2G Fast HotStart ReadyMix (Hoffmann-La Roche) plus two additional PCRs with binding regions outside the inserted region with primer pairs ASPM-stop_T7_f1 + ASPM-stop_T7_r1 and ASPM_FPN_check3'UTR_r + ASPM_FPN_check_5f (primer sequences are listed in appendix Table 23). Both PCRs used primer pairs binding inside and outside of the inserted region, meaning that only a successful knockin would lead to a PCR product. Furthermore, PCR products from clones with correct inserts were sent to Sanger sequencing for sequence verification (2.8.2; see scheme of 3x FLAG insert at *ASPM* stop codon in Figure 28 and detailed in Figure 139).

Positive NGP-ASPM-FPN (FLAG) clones were grown to 15cm cell culture dish level for harvesting cell pellets (2.4.3) for protein isolation. Protein lysates were used for Western blot analysis (2.7.2).

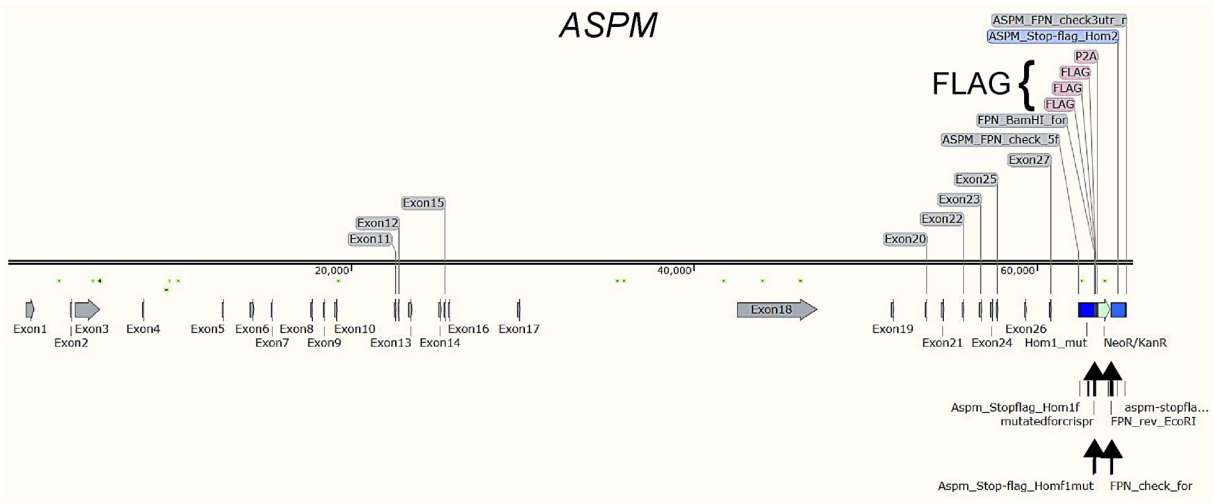

Figure 28: Sequence map of genomic *ASPM* after CRISPR/Cas9 3x FLAG knockin at TAG stop codon site.
The genomic *ASPM* sequence was endogenously tagged with a 3x FLAG-tag, mediated by a CRISPR/Cas9 knockin. The attachment of a FLAG-tag peptide to the ASPM protein would allow a detection with an anti-FLAG antibody. The knockin was conducted targeting the TAG stop codon in exon 28 of *ASPM*, thereby attaching the FLAG-tag C-terminal. The *ASPM* gene is located on the antisense strand on chr. 1q31.3 (reference genome version GrCh38). Detailed sequence displayed in Figure 139.

2.6.32 Isolation of total RNA

RNA was isolated from harvested cell line material (2.4.3) for mRNA expression analysis native or after functional assays (2.5) using the RNeasy® Kits from QIAGEN. For extraction of up to 45µg RNA from small cell samples (e.g. inhibitor treated test series, see 2.5.3, 2.5.4 and 2.5.5), the RNeasy® Micro Kit was used. For extraction of up to 100µg RNA from larger cell samples (e.g. untreated test series), the RNeasy® Mini Kit was used. The isolation of RNA was performed according to the manufacturer's instructions including the optional DNase digestion using the RNase-free DNase set (QIAGEN). The concentration of isolated RNA was measured immediately (2.6.33) and RNA was further processed or stored at -80°C.

2.6.33 Measurement of RNA concentration

RNA concentration (ng/µl) of isolated RNA (2.6.32) have been measured using a NanoDrop™ 2000 Spectrophotometer (Thermo Fischer Scientific) according to the manufacturer's instructions. RNA (1.0µl volume) was measured applying RNA settings with a nucleic acid absorbance wavelength ratio of 260/280nm. The detected signal is used by the NanoDrop 2000 software to calculate the amount of RNA in a solution. An optical density OD_{260} of 1 corresponds to 40µg/ml RNA. Baseline correction was applied with 340nm. Any Protein contamination was detected at 280nm. The quotient from OD_{260} and OD_{280} is 2.0 for pure RNA preparations. Only pure RNA preparations were used for synthetization of cDNA (2.6.34).

2.6.34 Production of complimentary DNA

Previously isolated, total RNA (2.6.32) was transcribed into complimentary DNA (cDNA) by reverse transcription using the Transcriptor First Strand cDNA Synthesis Kit (Hoffmann-La Roche). The synthesis of cDNA was performed according to the manufacturer's instructions for single reactions and further applying random hexamer primer to the synthesis mixture. In general, 1µg RNA (adjusted with DEPC (diethyl dicarbonate)-treated water to 11µl input volume; SERVA Electrophoresis GmbH, Heidelberg, Germany) was transcribed into cDNA per sample (final cDNA volume 20µl). Synthetized cDNA was used for quantitative polymerase chain reaction (qPCR; 2.6.35) or stored at -20°C.

2.6.35 Quantitative polymerase chain reaction

The method of qPCR[622] based on the principle of conventional PCR is used to analyze the transcription of specific genes. In qPCR, the PCR product is measured at every cycle, unlike in traditional (endpoint) PCR, were quantification of the product is performed at the very end. In real-time qPCR, the quantity of cDNA is measured via a fluorescent dye (SYBR Green I, intercalates with DNA) that yield increasing fluorescent signal in direct proportion to the number of PCR product molecules (amplicons) generated. The data collected within the exponential phase of the reaction is necessary to calculate the initial amount of genetic material by comparison with a known standard ("housekeeping gene")[623]. By plotting the fluorescence (ΔRn = normalization of the fluorescence emission intensity of the reporter dye obtained by subtracting the baseline (ΔRn = Rn - baseline)) against the cycle number, the real-time PCR instrument generates an amplification plot that represents the accumulation of product over the duration of the entire PCR reaction[624]. The measureable point of fluorescence increase is named C_T. The amount of PCR amplicons in an unknown sample can then be calculated from the measured C_T value of this sample[580] (see Figure 23 in NB-MRD section 2.6.17). QPCRs for gene expression analyses were performed on the cDNA samples previously synthesized (2.6.34). When possible, 1.5µL cDNA (approximately 75ng of transcribed RNA) was used as input template for qPCR. The FastStart Universal SYBR® Green Master assay (Hoffmann-La Roche) was applied within clear 96 well FrameStar® PCR Platte ABi FAST PCR (4 Titude Ltd, Surrey, UK). The reaction mix contained 10µl of 2x Fast Start Essential SYBR® Green Master, 6.5µl RNase-free H_2O, 1 µl of respective forward (10pmol/µl; Eurofins Genomics GmbH) and 1µl of reverse primer (10pmol/µl; Eurofins Genomics GmbH), and 1.5 µl cDNA template. The primer sequences are reported in Table 23. The qPCR ran under temperature conditions: 2min at 50°C, 10min at 95°C, followed by 40 cycles of 15s at 95°C and 1min at 60°C on a StepOnePlus™ Real-Time PCR System supported by StepOnePlus™ software version 2.2.2. (Thermo Fischer Scientific). By usage of qPCR, mRNA expression levels of *MYCN* were analyzed to evaluate the effects of rigosertib on gene expression. As internal normalization control, a primer pair was used for amplification of the housekeeping gene *UBC1* for gene expression profiling. The gene proved to maintain stable levels of gene expression in neuroblastoma cells and is therefore well suited for the

internal normalization of target gene expression[625]. QPCR was also performed in order to detect the gene expression of *ASPM* by further usage of the endogenous control *B2M*. Primers for *ASPM* and the housekeeping gene *B2M* were obtained from QIAGEN (Hs_ASPM_va.1_SG QuantiTect Primer Assay catalogue #QT02449181; Hs_B2M_1_SG QuantiTect Primer Assay catalogue #QT00088935). Furthermore, the gene expression of differentiation markers was tested, including *MAP2*, *TUBB3* and *DCX*. After treatment with nocodazole, an NGP ASPM-FPN cell clone was tested for expression of cell cycle G2/M-phase markers, *CCNB1* which encodes for the Cyclin B1 protein (G2/mitotic-specific cyclin-B1) and *CDK1* (Cyclin-dependent kinase 1). The C_T values of expressed genes to be analyzed were compared to the C_T values of *UBC1* or *B2M*. The relative gene expression was calculated using the $2^{-\Delta\Delta CT}$-method to the respective control (2.10.1)[626].

2.7 Biochemical methods

2.7.1 SDS-PAGE and Western blot analysis using conventional SDS-PAGE and semi-dry protein transfer

The expression of proteins were visualized using a Western blot assay, to evaluate the effects of rigosertib on neuroblastoma. *MYCN*-amplified IMR5/75 neuroblastoma cells were seeded onto 6-well plates (2.5.1; CELLSTAR®) and treated with their relative IC50 of rigosertib (33nM) for 96h (2.5.3). The lysis of harvested cells (2.4.3) was performed with 25µl protein lysis buffer I (amount per ¼ of 15cm dish) to solve whole cell proteins in an aqueous solution (see 10.5.6), vortexed vigorously and incubated on ice for 30min on an orbital shaker with agitation speed of 180rpm. After centrifugation of the suspension for 30min at 14,000rpm at 4°C, the supernatant was transferred to a new reaction tube to quantify its protein concentration with a BCA (bicinchoninic acid) Protein Assay Kit (Santa Cruz Biotechnology, Inc., Dallas, TX, USA) following the manufacturer's instructions. For calibration, a BSA (solved in protein lysis buffer I; Sigma-Aldrich) standard curve was adduced from 0µg/ml to 2,000µg/ml. For that, 25µl of each BSA standard and 25µl of protein lysates (or respectively 25µl of 1:10 dilution) was added into wells of a clear 96-well-microplate. The reagent mixture AB was added in 200µl to every well containing a sample. Subsequently, the microplate was incubated at 37ºC for 30min (Incubator Heratherm™ Compact Microbiological, Thermo Fischer Scientific). The plate was removed from incubator and equilibrated to RT for 5min. Afterwards, the absorbance was measured at λ 562nm with an Epoch™ Microplate Spectrophotometer supported by Gen5™ Data Analysis Software version 2.04.11.0 (BioTek Instruments Inc.). Protein concentrations were determined using a four-parameter curve-fitting algorithm. Protocols were saved as Gen5™ Protocol .prt file and measured assays were saved as Gen5™ Experiment .xpt files. Using the sodium dodecyl sulphate polyacrylamide gel electrophoresis (SDS-PAGE) method[627], proteins were separated from the sample according to their chain length, which is proportional to their molecular weight (kDa). SDS-gels were prepared as handcast gels (10% polyacrylamide gel, recipes for separation and stacking gel see 10.5.6), using Mini-PROTEAN® Tetra Cell Casting Modules and Mini-PROTEAN® cassettes (both Bio-Rad Laboratories,

Inc.). Thus, 13.5µg of protein lysate was mixed with 5µl of 4x Laemmli Protein Sample Buffer (Bio-Rad Laboratories, Inc.). The samples were linearized by heating the sample up to 95°C for 10min, whereby secondary and tertiary protein structures broke by the interruption of hydrogen bonds. Afterwards, 20µl of each denatured sample was loaded onto the gel using ExactaCruz® Round Gel Loading Tips (Santa Cruz Biotechnology). For size comparison, the Precision Plus Protein™ Dual Color Standard (Bio-Rad Laboratories, Inc.) was applied. The electrophoresis was performed in the Mini-PROTEAN® Tetra Cell System with the PowerPac™ Basic Electrophoresis (both Bio-Rad Laboratories, Inc.) with SDS-Running Buffer at 70V for 30min following 100V for 60min. The proteins were covered by a constant negative charge of the SDS and became anionic. The proteins migrated within the SDS gel towards the positively charged anode through the acrylamide mesh of the gel. Smaller proteins migrated faster through this mesh, while larger proteins were retained in the electric field, which led to their separation. The protein transfer from the SDS gel to a PVDF membrane (polyvinylidene difluoride; Hoffmann-La Roche) was performed employing the Western blot method[628] as a semi-dry approach. Therefore, the PVDF membrane was activated by incubation in methanol ROTIPURAN® ≥99.9% (Carl Roth GmbH + Co. KG) for 5s, following a wash in dH_2O for 1-2min and an equilibration step in transfer buffer. Blotting papers ROTILABO® (Carl Roth GmbH + Co. KG) were soaked in transfer buffer and assembled with the gel and membrane in a sandwich-like manner. The blotting step was performed in a Trans-Blot® Turbo™ Transfer System (Bio-Rad Laboratories, Inc.) for 30min at 25V and 1.0A. The proteins migrated in the direction of an electrical field applied from the SDS gel to the anode of the membrane on which proteins stuck due to hydrophobic interactions. After blotting, the SDS attached to the proteins was washed out, which caused the proteins to resume their secondary and tertiary structures. In the following, free non-specific binding sites of the proteins were blocked with a solution containing 10% low fat milk powder (Carl Roth GmbH + Co. KG) dissolved in TBS-T (phosphate-buffered saline with tween) at RT under constant rotation for 1.5h. The detection of proteins was done with specific primary antibodies which bind to their antigen (immunoblotting[629]). The incubation with a primary antibody in 5% milk was done under constant overnight rotation. For analysis of the effects of rigosertib on protein expression of MYCN, WEE1 and MST1, primary antibodies recognizing the proteins as antigens were used (see Table 36). Antibodies against the GAPDH and the ß-actin protein were employed as loading controls. The membrane was then washed three times with TBS-T, incubated with a secondary antibody under constant rotation for 1.5h and washed again three times (see antibody list in appendix Table 36). The secondary antibody, which specifically bound the primary antibody, was conjugated to a reporter enzyme (horseradish peroxidase, HRP). The detection of secondary antibodies was done by measuring the chemiluminescent reaction of luminol (Santa Cruz Biotechnology) catalyzed by HRP using the Transilluminator Fusion-FX7-826.WL Superbright (Vilber Lourmat) supported by VisionCapt™ software (ANALIS, Suarlée, Belgium). Photography of chemiluminescence was performed with automatic focus. The prestained marker was detected with white light. To combine both signals, the multispectral modus with marker insertion in

the VisionCapt™ software was used. Based on a kDa standard, the protein size was estimated. Pictures were saved as .tif and .jpg data files. Protein lysates were stored at -80°C and several freeze-thaw cycles were avoided. Recipes for the buffers and solutions used are described in section 10.5.6.

2.7.2 SDS-PAGE and Western blot analysis using a combination of the NuPAGE™ system and wet protein transfer

General procedure of SDS-PAGE and Western blot analysis is described in the section 2.7.1. The protocol for the detection of the ASPM protein using the NuPAGE™ SDS-PAGE system and Western blotting in a wet approach was kindly provided by C. Hagemann (University Hospital of Würzburg, Germany)[487]. This protocol was adapted in the present work as descripted below. Recipes for all buffers used are found in the supplement section 10.5.7. The cells were harvested previously (see 2.4.3) after execution of cellular assays (2.5) and cell pellets were then solubilized in protein lysis buffer II. The lysate was incubated on ice for 30min on an orbital shaker with agitation speed of 180rpm, and subsequently centrifuged at 15,000x*g* and at 4°C for 30min. The supernatant which contained soluble proteins was transferred into a new reaction tube. The protein concentration was measured as described in detail in section 2.7.1. An amount of 20-50µg protein lysate was mixed with NuPAGE™ LDS Buffer (4x) and NuPAGE™ Reducing Agent (10x) (both Thermo Fischer Scientific) and incubated at 70°C for 10min to denature secondary protein structures. Afterwards, protein lysates were applied using ExactaCruz® Round Gel Loading Tips into precast NuPAGE™ 3-8% Tris-Acetate protein gels (Thermo Fisher Scientific). Depending on the experiment questioning, a recombinant Posi-Tag Epitope Protein Mix, which contains FLAG™ tag protein (0.3µl, BioLegend) was applied to the gel used as FLAG positive control. The gel was then run for 60min at 60V and then 45min at 100-130V in a XCell SureLock® Mini-Cell Electrophoresis System (Thermo Fischer Scientific) used together with the PowerPac™ 300 Electrophoresis Power Supply (Bio-Rad Laboratories, Inc.). For size comparison, the HiMark™ Pre-stained Protein Standard (Thermo Fischer Scientific) was utilized. Separated Proteins were blotted onto a 0.45µm nitrocellulose membrane (Bio-Rad Laboratories, Inc.) in a wet approach. Therefore, the membrane was moistened with dH_2O for 1-2min and afterwards incubated in transfer buffer. Blotting papers ROTILABO® (Carl Roth GmbH + Co. KG) were soaked in transfer buffer and assembled with the gel and the membrane in a sandwich-like manner. The blotting step was performed in a Mini Trans-Blot® Electrophoretic Transfer Cell with PowerPac™ Basic Electrophoresis (Both Bio-Rad Laboratories, Inc.). Wet blotting was done at 4°C for 90min and at 90V under constant stirring. Afterwards, incubation of antibodies and detection of proteins was carried out as described in detail in section 2.7.1. For analysis of the protein expression of ASPM and (ASPM)-FLAG, primary antibodies recognizing the proteins as antigens were used (see Table 33). Antibodies against the GAPDH protein were employed as loading control.

2.8 DNA Sequencing

2.8.1 Hybrid capture-based panel sequencing (*NB targeted NGS assay*)

Previously sheared cell line or tumor DNA (2.2.2) was subjected in 100-200ng to the custom *NB targeted NGS assay* (NEO New Oncology GmbH). This NGS panel was designed to detect point mutations, small insertions and deletions, copy number alterations and rearrangement/gene fusions and to map the *MYCN* amplicon in a single assay. A detailed list of all targets included in *NB targeted NGS assay* can be found in Table 12 in the appendix section. Regions of interest were used to design target specific hybrid-capture biotinylated probes using NEO New Oncology's proprietary design procedure including application of custom SureSelect^{XT} designs (Agilent Technologies, Inc). Adapters were ligated to sheared sample DNA, and individual genomic regions of interest were enriched using complementary bait sequences (hybrid capture procedure)[630]. Selected baits ensured optimal coverage of all relevant genomic regions. After enrichment, targeted fragments were isolated and amplified (clonal amplification) to create the sequencing library. In the following, the fragments were sequenced in parallel with an average mean sequencing depth of 1,000-2,500x (unfiltered reads)[631]. The *NB targeted NGS assay* was performed by NEO New Oncology GmbH or Institute of Hematopathology Hamburg.

2.8.2 Sanger sequencing for PCR product and vector sequence validation

Purified PCR product (30µl aliquoted into 2x 15µl; see 2.6.9) or vector with PCR product insert (5µl; see 2.6.15) was mixed with either the respective forward or reverse primer (2µl with a concentration of 10pmol/µl). The primer used were equivalent to the previously performed PCR or the vector primer M13-24 reverse in case of PCR product subcloning (for pUC18 and pCR™4-TOPO™ TA vector; M13 reverse (-24mer)[632], LGC Genomics GmbH (Berlin, Germany) standard primer, see sequence in Table 23). Sanger sequencing was performed by TubeSeq Service of Eurofins Genomics GmbH or by Ready2 Run Service of LGC Genomics GmbH. A correct sequence match was confirmed using the Standard Nucleotide BLAST web tool applying the *align two sequences nucleotide* blastn megablast method[594].

2.9 Analyses of WGS, targeted NGS and Microarray Data

2.9.1 Re-analysis of WGS tumor data: *MYCN* breakpoint detection

Publicly available WGS data[43,44,76] were reanalyzed for structural variants in proximity of *MYCN* (genomic location of *MYCN* chr2:16,080,683-16,087,129 in GRCh37 (hg19); size: 6,447 bases; orientation: sense strand[66]) and to define the boundaries of the *MYCN* amplicon in each patient, using the *novoBreak* software (v1.1) with default parameter settings[633]. Variant calls were stringently filtered to include only breakpoints which had strong support in the tumor samples and were absent from the matching control samples. In detail, breakpoints were required to have a quality score greater than 50, at least three high-quality spanning reads (Figure 29) in the tumor (and <1 such reads in the matching

control), and at least 10 high-quality discordant reads pairs in the tumor (and <3 in the control). Analysis of WGS data for *MYCN* breakpoint detection was kindly performed by J. Toedling (Charité)[634,635].

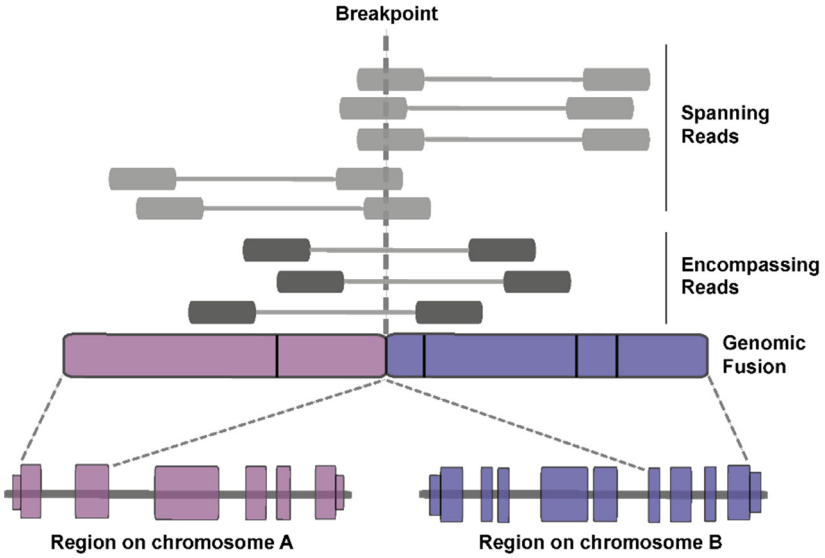

Figure 29: Schematic of spanning and encompassing sequencing reads supporting a genomic breakpoint.
When paired-end sequencing is accomplished, two different arrangements of discordant reads can provide evidence for a fusion gene or genomic rearrangements. Spanning reads directly match the junction site. Read pairs where each mate map on either side of the breakpoint are described encompassing reads. (Figure modified from Arsenijevic and Davis-Dusenbery[636]).

2.9.2 Analysis of *NB targeted NGS assay* sequencing tumor data: *MYCN* breakpoint detection

Computational detection of relevant genomic alterations in a quantitative manner (minor allele frequencies ≥5%) was done by NEO New Oncology GmbH, applying a custom-made proprietary computational biology analysis pipeline. The steps of the pipeline are outlined in Figure 30.

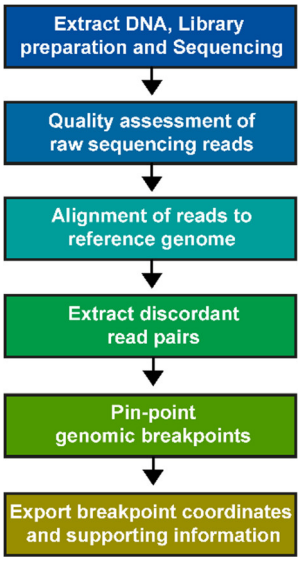

Figure 30: Flow diagram of the analysis of *NB targeted NGS assay* sequencing raw data.
Workflow of breakpoint detection from paired-end genome sequencing data obtained with the *NB targeted NGS assay*.

Briefly, the quality of the raw sequencing reads was assessed and the reads were aligned to the human reference genome assembly GRCh37 (hg19). Discordantly aligned read pairs were subsequently extracted, and the structural variants and their breakpoints were localized. The breakpoint position and the supporting data evidence (spanning and encompassing sequencing reads) were recorded for all detected alterations (Figure 29). Information about structural rearrangements was either provided by NEO New Oncology GmbH directly or located in binary alignment map (BAM) data analysis (see 2.9.3). For the detection of the *ATRX* breakpoint (chrX:76,935,121) in the CHLA-90 non-*MYCN*-amplified cell line the same procedure was followed as for the detection of the *MYCN* breakpoints. The neuroblastoma-focused *NB targeted NGS assay* is described in detail in section 3.1.1 (manuscript in preparation[635]).

2.9.3 Detecting *MYCN* breakpoints in *NB targeted NGS assay* sequencing BAM data and reconstruction of the rearrangement sequences

The information about structural rearrangements supplied by the assay provider (NEO New Oncology GmbH) was validated and further substantiated by analyzing the aligned reads of each sample. The exact breakpoint sequences were either provided by NEO New Oncology GmbH directly or in BAM format. BAM data was generated from *NB targeted NGS assay* sequencing (see 2.9.2). For further MRD detection of *MYCN* related breakpoints within neuroblastoma tumor, bone marrow or cell line DNA samples, the breakpoint sequence was re-constructed from *NB targeted NGS assay* sequencing data. Information about breakpoint regions was either provided by NEO New Oncology GmbH directly or obtained by analyzing the alignment files. If no breakpoint sequence was provided from (1) NEO New Oncology GmbH, the (2) enspan.txt file, a summary of the proceeded enspan.bam file which contained possible gene rearrangements in the sample, was reviewed manually. Genomic rearrangements were taken into consideration if they occur within a two-Mb window centered at *MYCN* (explained in more detail in 2.9.1), and if they show at least a support of two spanning reads (see Figure 29 and Table 18), covering the breakpoint sequence. Using information about the genomic location of breakpoints present in the enspan.txt file (2), rearrangements were searched manually within the .bam data of a sample (3). Additionally, the area of *MYCN* was examined for breakpoints manually by eye within the .bam data (3) (Figure 31). For the manual search of breakpoints, genomic .bam datasets were visualized by the usage of Integrative Genomics Viewer (IGV) (Broad Institute, Cambridge, MA, USA)[637,638]. The sequencing .bam data was loaded into IGV together with a matching index file for one respective sample. As reference, the genome version GRCh37 (hg19) was loaded into IGV and used as described before (see 2.9.2). Alignment settings were used in deviation from the default parameters: filter *duplicate reads*, filter *vendor failed reads*, filter *unmapped pairs* and show *soft-clipped bases*.

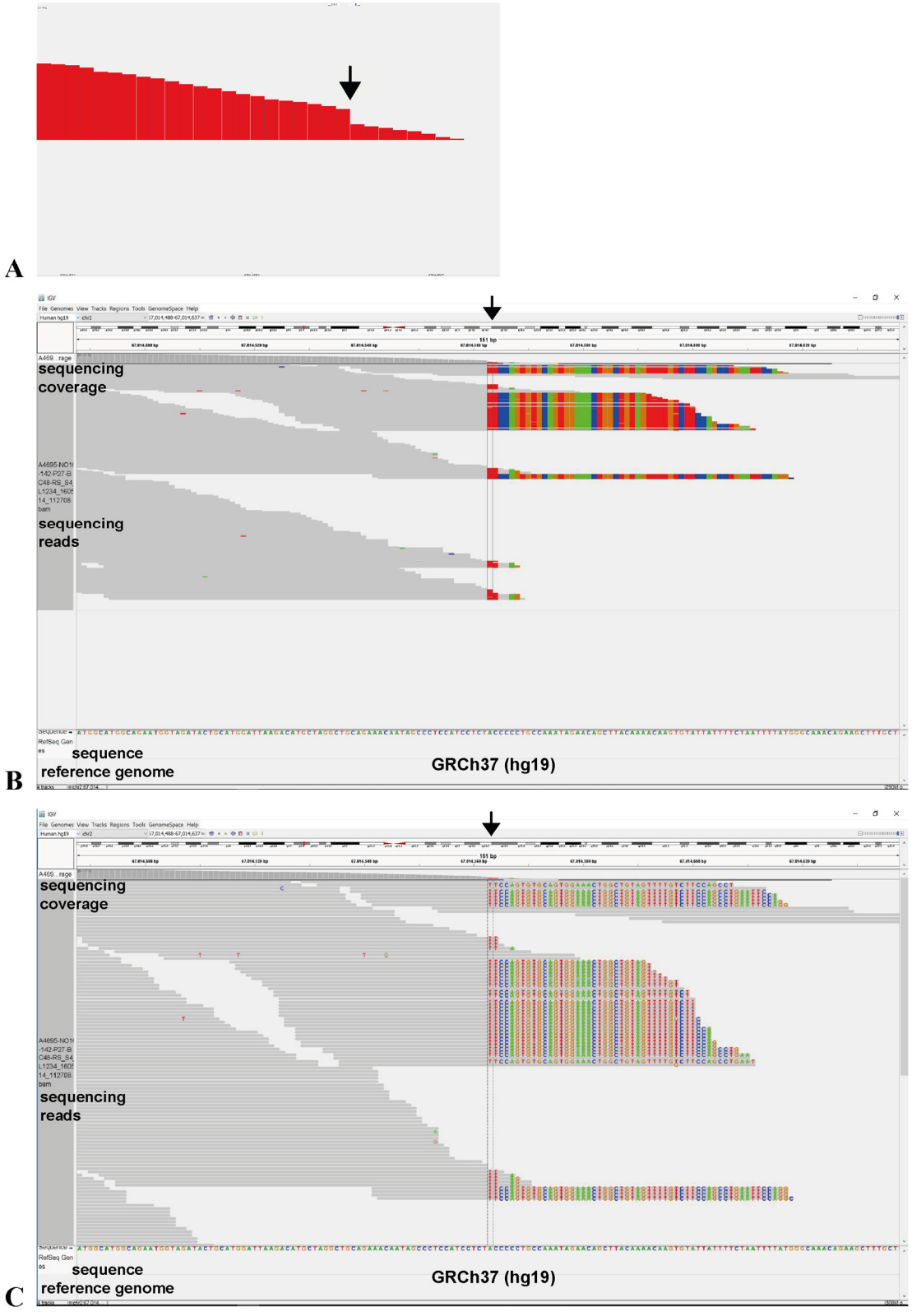

Figure 31: IGV based detection of a *MYCN* amplicon breakpoint.
IGV[637,638] images displaying sequencing-data evidence for the presence of a specific breakpoint of *MYCN* in the IMR-5 neuroblastoma cell line. Display of breakpoint rearrangement intergenic chr2:67,014,561 to *MYCN* chr2:16,083,742. The breakpoint was located on the basis of a sequencing read depth drop **(A)** marked by an arrow. Overview of the genomic region as **(B)** *squished* and **(C)** *expanded feature track* showing multicolored parts of sequence reads, that are in a complete mismatch compared to the grey read parts which align with the reference sequence GRCh37 (hg19). In detail, a part of a *MYCN* intronic chr2:16,083,742 (multicolor) sequence was fused to an intergenic sequence chr2:67,014,561 (grey). The exact breakpoint position is marked by an arrow.

A specific breakpoint related to *MYCN* was found present if a) a typical read depth drop was observed at the exact location of a breakpoint pinpointing to a previous breakage (Figure 31A) and b) if the sequence after the read depth drop does not match entirely comparing to the reference sequence (Figure 31B+C). For every breakpoint detected with method number (2) or (3), a spanning read covering the exact rearrangement was extracted. Afterwards, two encompassing reads neighboring the breakpoint spanning read in upstream and downstream direction were extracted as well. Finally, the breakpoint sequence was compiled from those three reads into one sequence. For breakpoint sequences obtained with every method (1, 2 and 3), gaps between reads, too short sequences (<80bp) or flanking upstream/downstream areas were filled with human reference sequence from GRCh37 (hg19), if necessary for *NB breakpoint MRD assay* design. For the detection of the *ATRX* breakpoint (chrX:76,935,121) in the CHLA-90 non-*MYCN*-amplified cell line the same procedure was followed as for the detection of the *MYCN* breakpoints.

2.9.4 Microarray gene expression data analysis

Preprocessed gene expression data from 25 data sets (n = 3,984 samples in total) comprising three categories (adult tumors, pediatric tumors and normal tissue) were downloaded from the R2 Genomics Platform[496,497] (for sources and details see appendix Table 27). Gene expression data from pan-cancer and normal tissue was obtained utilizing Affymetrix HG-U133-Plus2 Microarrays and processed using the MAS5.0 method[639]. MCPH gene expression across data sets was ordered by hierarchical clustering and heatmap was generated using the R software (CRAN)[640,641] (for MCPH related genes see appendix Table 28). Processed data from the SEQC dataset[42], which comprises data of 498 primary neuroblastomas profiled by RNA-Sequencing, were downloaded from the NCBI GEO database[498,499], analyzed using hierarchical clustering and visualized in form of a heatmap. On the same dataset, all genes whose expression was highly correlated (spearman rank correlation coefficient greater 0.7) with *ASPM* were subjected to a gene set enrichment analysis, using the Gene Ontology (GO) biological process gene sets and the R/*bioconductor*[642–644] package *topGO*[645]. Hierarchical clustering visualized in heatmaps, correlation arrays and GO analyzed were performed in cooperation with J. Toedling[543,544,598] (Charité). Box-plot diagram of gene expression data from 25 Microarray data sets (as described above) was prepared using the R2 Genomics platform[496,497]. For visualization, the settings across datasets, *MegaSampler* (view a gene in more than 1 dataset, *ASPM* NM_018136), type of data microarray from human samples hs/u133p2/MAS5.0, no preset and displaying in graphtype boxplot were applied. Analysis of *ASPM* expression in neuroblastoma (subgroups) was performed employing the SEQC study[42] Microarray SEQC-498-RPM-seqcnb1 data set by usage of the R2 Genomics platform[496,497]. For analysis, the settings *single data set* (SEQC study), *view a gene* (*ASPM* NM_018136), sample filter *parameter group separation* (*MYCN* amplification, low and high risk, INSS stage and death from disease annotated with *mycn_status*, *high_risk*, *inss_stage* and *death_from_disease*) and displaying in *graphtype boxplot* were applied. Kaplan Meier by gene expression survival analysis of neuroblastoma

patients using the SEQC study data was performed with the analysis parameters *Kaplan scan a single gene*, *ASPM* gene, *cutoff_modus median*, type of survival *eventfree* or *overall* and for subgroups *sample filter subset high_risk/high_risk-1* or *mycn_status-1/mycn_status-0*.

2.10 Data processing and analysis

2.10.1 QPCR raw data processing and calculation of $2^{-\Delta\Delta CT}$-method

The amplification of a target DNA sequence was detected using a fluorescent dye applying the qPCR technique (2.6.35). Raw data qPCR results were pre-analyzed using the StepOne Software v2.2.2., adjusting for a *ΔRn vs cycle* amplification plot in linear scale. The threshold was set to a value above the background signals (*baseline*), which ideally included the signals of the controls (gDNA or RNA specimen and the no template control (NTC) sample). Moreover, the threshold was positioned below the plateau of the target amplification within the early exponential phase of the sigmoidal amplification curve (Figure 23B). The number of cycles used to calculate the baseline was reduced if the expression level of a target gene was too high[646]. Adjustments of the threshold and of the baseline were set individually for each target gene for every assay run. However, the same settings were used for all samples measured for the expression of the same gene on one plate. Based on the results, conclusions were drawn about the expression level of a gene. The qPCR results of this work were analyzed using the $2^{-\Delta\Delta CT}$ method[626] in a relative quantitative manner. This method determined changes in the target gene expression in relation to an additionally measured endogenous reference gene, whose expression levels remained relatively stable in response to the applied treatment. As a reference gene, *UBC1* was used in the rigosertib project and *B2M* was used within the ASPM project[625] (see 2.6.35 as well). The calculation of the gene expression was carried out using the obtained threshold cycle (C_T) values. With respect to the $\Delta\Delta$ C_T of the $2^{-\Delta\Delta CT}$ method, ΔC_T is the difference in the C_T between the target and reference genes[647]:

$$\Delta C_T = C_T\,(target\ gene) - C_T\,(reference\ gene)$$

$$\Delta\Delta C_T = \Delta C_T\,(treated) - \Delta C_T\,(untreated)$$

$$2^{-\Delta\Delta C_T} = fold\ difference\ in\ target\ gene\ relative\ to\ untreated$$

2.10.2 Dose-response analyses of monotherapies using GraphPad Prism

Neuroblastoma cells were treated with BET or kinase inhibitors and incubated for three days (2.5.3). Afterwards, the cell viability was measured (2.5.13). The cell viability raw data was saved as .csv and .xml files and processed for dose-response analyses using Excel. The background luminescence signal of the cell culture media, which was measured by a pure media control, was subtracted as the mean of the background from all measurements (*background filtering*). Subsequently, the average of a cell only

control (0nM/without inhibitor) was generated, which also was subtracted from all values with treatment (*relative measurements to control*). The viability signal of the untreated cells should therefore be subtracted from the measured values of the treated cells. If the inhibitor used could only be dissolved in DMSO, the values of cells treated with DMSO only (control without inhibitor) were also taken into account. Subsequently, the median was calculated from all measured technical replicates of the treated cells (*combining technical replicates*). The median biological replicate values of an inhibitor concentration were then imported into GraphPad Prism®. The data is imported into a XY table, whereas the x values are the log-transformed concentrations of the inhibitor (log_{10}) and y values are the number of median replicates within the group. The data of x was then transformed using X=Log(X). Using the transformed data, the *dose-response – inhibition*, in detail *log(Inhibitor) vs. response – variable Slope (four parameters)*, *nonlinear Regression with least squares (ordinary) fit analysis* is applied. Dose response curves, absolute IC50 values (*IC50*, 50%, half maximal inhibitory concentration), relative IC50 values (*EC50*, 50%, half maximal effective concentration) and Emax (*span,* maximal effect) values of the inhibitor monotherapy were interpolated by GraphPad Prism® (*best-fit values*). If the Emax was specified by GraphPad Prism® as above 100%, this value was manually set to 100%. Additionally, the E1000 was calculated manually (defined as inhibition by the drug at a concentration of 1000nM in %). The drug potency cut-off was chosen for E = 1000nM because this pharmacodynamic threshold decisively characterizes the effectiveness (<1000nM) or non-effectiveness (>1000nM) of a drug (according to Drug Target Commons)[648,649]. The dose-response curves are drawn showing the drug concentrations of the inhibitor (10xnM) on the x-axis and the relative luminescence signal (relative light units, RLU) scaled to control in percent, on the y axis.

2.10.3 Dose-response analyses of combinatorial treatments using the R package *SynergyFinder*

The basic concept of synergism analyses of combinatorial therapies is the comparison of the observed drug combination response with the expected effect assuming non-interaction (null hypothesis)[650]. To assess the effect of a combinatorial treatment of the BET inhibitor OTX015 and the kinase inhibitor volasertib, neuroblastoma cells were treated and incubated for three days (2.5.4). Afterwards, the response of the cell viability to the treatment was measured using the CellTiter-Glo® Assay (2.5.13). The cell viability raw data was processed for dose-response analyses using Excel as described above (2.10.2). Furthermore, the treatment effect was calculated as fraction affected/inhibition (Fa = (1 - cell viability measurement)) and the values were transformed into percentages for singular concentrations and in combination[651]. If the cell viability was ≥ 100% the value was set to an effect of 1.0E-6, if the cell viability was ≤ 0% the value was set to an effect of 1.0. In addition, in-depth calculations of a possible synergism of OTX015 and volasertib were carried out using R studio (CRAN) statistical computing[640,641]. For this, the R-package *SynergyFinder*[511] was applied and the data was processed based on the Bliss Independence Model[652,653]. The hypothesis of the Bliss Independence Model is the mutual

non-exclusivity of the combined drugs, which was the underlying assumption for the cellular target structures of the inhibitors OTX015 and volasertib[652,653]. To perform the analyses, the R package *bioconductor* was installed previously in order to execute the script[642–644]. *SynergyFinder* calculations are visualized as dose-response matrices, plots of phenotypic responses for single drugs and 3D synergy heat maps.

2.10.4 Comparison and graphical presentation of drug responses using the R package *nplr*

Neuroblastoma cells were treated with BET or kinase inhibitors and incubated for three days (2.5.3). Afterwards, the cell viability was measured (2.5.13). Dose-response analyses were conducted according to 2.10.2. The absolute IC50, the relative IC50 (EC50), the Emax and the E1000 drug response values were exported from GraphPad Prism® to Excel. The data for the different cell lines and inhibitors was then compared using R studio (CRAN) statistical computing[640,641]. The R package *nplr*[654], which was used for fitting the optimal dose-response was installed in order to execute the script, as well as other required packages: *xlsx*[655], *RcolorBrewer*[656], *extrafont*[657] and *ggplot2*[658]. Drug response data was then imported from Excel using *read.xlsx2*. Aesthetic dot plots were generated as *geom_point* via *ggplot2*, including the following parameters: absolute IC50 values, relative IC50 values (EC50), *MYCN* status (amplified/non-amplified) and percentage of viability reduction at 1000nM drug concentration (in steps: 0%, 25%, 50%, 75% reduction after BET inhibition and 50%, 60%, 70% 80%, 90% and 100% after kinase inhibition).

2.10.5 Data presentation of conventional PCR results and Sanger sequencing

The lengths of the PCR products of the conventional PCR for breakpoint analysis and *NB breakpoint MRD assay* establishment (2.6.4) were verified in a semi-quantitative approach using the QIAxcel® advanced automatic capillary electrophoresis device (QIAGEN; see 2.6.8)[573,574]. For visualization, information about the lengths (in bp) of the alignment and size markers, as well as the length of the PCR product, were displayed utilizing the QIAxcel® ScreenGel software version 1.4.0. The graphical representation of the PCR assays with breakpoint amplicon (target sequence, primer and probe sequence binding to this target sequence), was illustrated using the SnapGene software version 5.0.1. (GSL Biotech LLC, Chicago, IL, USA). Furthermore, electropherograms of the Sanger sequencing results received in .ab1 file format (DNA electropherogram file) were displayed with SnapGene.

2.10.6 MRD calculation and graphical presentation

Raw data of *RQ-PCR MRD assay* was pre-processed using the StepOne Software version 2.2.2., adjusting for a *ΔRn vs cycle* amplification plot on a linear scale. The threshold was set manually using the StepOne Software to a value above the background signals (*baseline*), which included the signals of

the controls (ddH_2O, buffy coat DNA, DNA of other neuroblastoma cell lines and DNA of non-neuroblastoma cell lines, as performed in 2.6.4). Moreover, the threshold was positioned below the plateau of the target amplification within the early exponential phase of the sigmoidal amplification curve (Figure 23B). The number of cycles used to calculate the baseline was reduced if the expression level of a target gene was too high[646]. Adjustments of the threshold and of the baseline were made individually for each target gene for every assay run. However, the same settings were used for all samples measured for the expression of the same gene on one plate. Pre-analyzed data was visualized directly as *ΔRn vs cycle* amplification plot on a linear scale or raw data vector information was loaded into Excel and plotted as a point plot (for example as in Figure 51) with interpolated lines on a linear scale. The MRD level was calculated from pre-processed RQ-PCR data imported into Excel. The calculation followed the MRD analysis guidelines in adaptation to van der Velden[161,582], which is already being implemented for clinical relevant MRD diagnostics (EuroMRD Consortium guidelines[161,586,587]; see Figure 32). The principle of MRD calculation is based on a theoretical content of 6.0 - 6.7pg DNA per cell[161,582]. Since a MRD PCR requires a total of 600-670ng DNA per reaction, this amount corresponds to a total of about 100,000 cells. The threshold of a signal was set on the background fluorescence (as explained above). If a fluorescence signal exceeded the threshold, this corresponded to the C_T (threshold cycle). The C_T value was directly proportional to the amount of the target sequence present. An increase in the fluorescence was indicated as ΔRn (see Figure 32A). Within the RQ-PCR experiments, two standard curves were generated, one was based on the control DNA (buffy coat) within the reference assay and another was based on the target DNA within the quantification assay. Samples with unknown cell content were plotted in the standard curve depending on their C_T value, from which the cell count was calculated based on the fluorescence signal of the target, corresponding to a DNA concentration (see Figure 32B).

$$C_T = slope\ x\ log_{10}\ concentration + axis\ intercept$$

$$log_{10}\ concentration = \frac{(C_T - axis\ intercept)}{slope}$$

$$number\ of\ neuroblastoma\ cells = \frac{100.000\ input\ cells}{10^{target\ concentration}\ x\ 10^{reference\ concentration}}$$

To include a C_T value in the calculation of MRD, the lowest dilution had to show a specific amplification above the determined threshold, as supported by the (sigmoid) shape of the amplification curve. The lowest dilution of the standard curve showed at least two positive technical replicates and the ΔC_T values of all technical replicates were diverging around 1.5 C_T to each other, showing reproducible measurements. Amplifications of the background and controls were in mostly all cases excluded by setting the threshold manually to absolute negative amplifications for all controls (see above). In very rare cases, a control showed a very low amplification and a manually higher adjusted threshold could not assign the control as background. Therefore, an inclusion of the lowest target sample for MRD

calculation was performed only for target C_T values which were ≥3.0 C_T lower than the lowest C_T value of the background signal. Further, the lowest target dilution had to meet the criteria of <20 C_T value range from the undiluted sample or, if this undiluted sample was not included in the standard curve, from the intercept of the standard curve (representing 1). The resulting standard curve spanned a minimum range of three magnitudes and had a correlation coefficient R^2 of ≥0.98 between the variables. A sample was considered to be *MRD positive*, if: the C_T value of at least one (sensitivity range) or two (quantitative range) of the three technical replicates of a sample is ≥1.0 C_T lower than the lowest C_T of the background and is within 4.0 C_T from the highest C_T value of the standard curve. Positive detections calculated above 10^{-0} were set to 1 (100%), if the follow-up sample showed a higher MRD load than the diagnosis sample used to prepare the standard dilution series. Consequently, a sample is considered *MRD negative*, if no amplification is observed at all, if the lowest C_T value of the target is within 1 C_T from the lowest C_T of the background, or if all C_T values are more than 4.0 C_T separated from the highest C_T value of the standard curve.

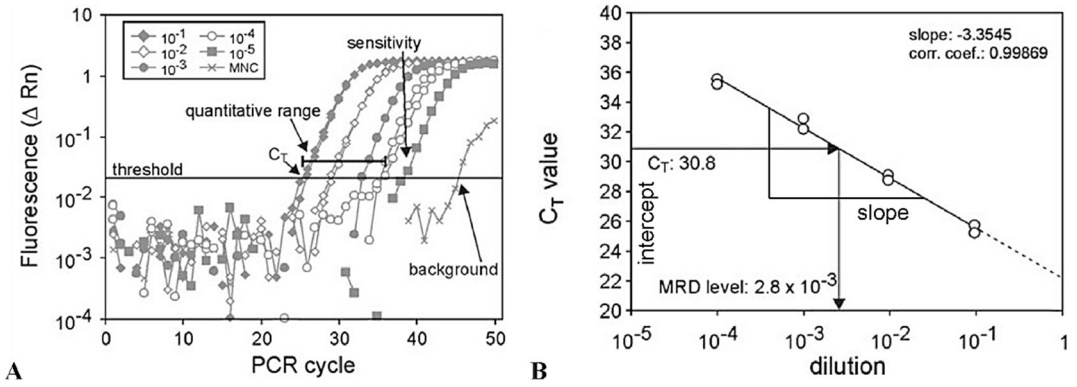

Figure 32: Definitions for analysis of RQ-PCR MRD data.
(A) Amplification plot of RQ-PCR data visualized in $\log_{10}$, showing ideal positions of the C_T, the threshold, the quantitative range, the sensitivity range and the background. In contrast to this example from leukemia MRD, there were no strong signals of background amplification found in the NB MRD RQ-PCR assay. **(B)** Calculation of the standard curve constructed from RQ-PCR data. Based on the mean C_T value of technical triplicates, the cancer cell load of the follow-up sample relative to the (tumor) diagnostic sample can be determined. (Figure modified from van der Velden et al.[161]).

Negative results were set to 10^{-7} (*MRD negative*) and did not contain any detectable neuroblastoma cells. Moreover, the MRD level was corrected according to the DNA quality/quantity of the diagnostic sample and the follow-up sample as determined by RQ-PCR of the control gene. For positive MRD samples, that could not be quantified (if only one technical replicate was found positive or if only one positive technical replicate's C_T value was ≥3.0 lower than the lowest C_T value of the background or if the ΔC_T of the replicates was >1.5), the data is presented as *positive, but not quantifiable* (p.b.n.q.). Concerning the analysis of the *ddPCR MRD assay*, standardized methods have not been published previous to this thesis. Therefore, the MRD analysis of ddPCR data was carried out in agreement with the current ddPCR recommendations of the EuroMRD Consortium (unpublished)[587,587,589,659], which were kindly provided by C. Eckert (Charité)[634].

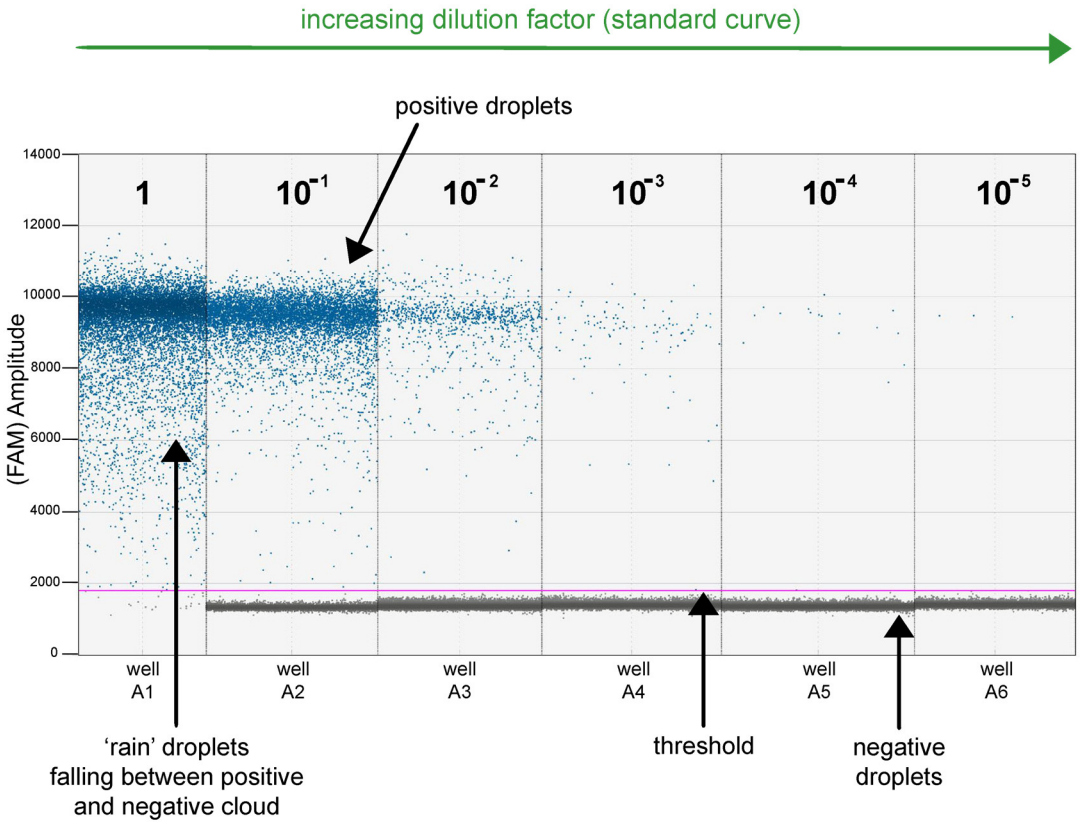

Figure 33: Definition of positive, negative and intermediate ("rain") droplets in ddPCR analysis.
DdPCR 1D plot showing positive, negative and intermediate clusters of the ß-globin reference gene detection. Droplets with intermediate fluorescence values appearing as "rain", but display a positive passed PCR reaction for the specific target[660]. (Figure modified from J. Hurst[661]).

Quantification using ddPCR assay were conducted using technical triplicates. For MRD calculation, a total droplet number between ≥10,000 and ≤20,000 per well were accepted, to estimate a general performance of the PCR assay and the assay run. To exclude false-positive droplets, the threshold of an assay was manually set to absolute negative droplets for all controls (ddH_2O, buffy coat DNA, DNA of other neuroblastoma cell lines and DNA of non-neuroblastoma cell lines, as performed in 2.6.19). Positive droplets of the target DNA were counted if the amplitude of the FAM fluorescence signal was located above the (control adjusted) threshold, which included positive droplet *clouds* as well as intermediate *rain* droplets[660] (see Figure 33). The origin for the occurrence of intermediate droplets is not clear but several factors are discussed, e.g. (mechanical) damaging[662], irregular droplet size[663], clotting of multiple droplets[664], partial PCR inhibition in individual droplets[665] or non-full-length fragments in individual droplets (PCR not completed)[666]. A value of the target DNA was defined as positive when the value of the target amplitude was at least twice the value from the highest droplet count for the buffy coat control DNA (see as well 2.6.19). A value was considered as *MRD positive* if at least one (sensitivity range) or two (quantitative range) of the technical triplicates show >1 positive droplet. For positive MRD samples, that could not be quantified (if positive droplets or copies/µl were detected in only one technical replicate) the data is presented as *positive, but not quantifiable* (p.b.n.q.).

A sample was defined ass *MRD negative*, if no droplets or copies/µl are observed at all or if the copies/µl value was ≤ the value of the background and controls. Negative results were set to 10^{-7} (*MRD negative*) and did not contain any neuroblastoma cells detectable. Moreover, the MRD level was corrected according to the DNA quality/quantity of the diagnostic sample and the follow-up sample as determined by a ddPCR of the control gene. The detected number of (relative) positive droplets was calculated as a mean of sample replicates after application of the Poisson correction by the QuantaSoft™ Software. To calculate the final tumor load, all samples were quantified with the following ratio[587,589,659]:

$$number\ of\ neuroblastoma\ cells = \frac{mean\ copies\ for\ the\ MYCN\ breakpoint\ target\ per\ 20\mu l\ (600-670ng)}{mean\ copies\ of\ the\ reference\ gene\ per\ 20\mu l\ (300-335ng\ x\ 2)}$$

Calculated MRD sensitivities and proportion of neuroblastoma cells within a sample were illustrated using GraphPad Prism® version 7.03. In detail, calculated MRD values were imported from Excel into GraphPad Prism® using a column table format. For individual patient MRD courses, data was drawn as a connected scatter plot. Raw data of MRD assay ddPCR results were displayed using QuantaSoft 1.7.4.0917 or QuantaSoft™ Analysis Pro 1.0.596 software in *1D amplitude*, showing *axis x = total droplet event number* or *well number* and *y = fluorescence amplitude*.

2.10.7 Image processing with Adobe Photoshop and composition with Adobe Illustrator

The quality of microscopy images has been enhanced using the *image sharpness filter* of the software Adobe® Photoshop® version CS6 (64 Bit) (Adobe Inc., San José, CA, USA). For processing of the immunofluorescence microscopy images with Photoshop®, each image taken was refined with the exact same values for a marker. This was initially a *color tone correction* in the RGB channel using *color tone spread* (shadow/midtone/lights) applying the following parameters to the images of a marker: phalloidin 0/0.90/229, MAP2 18/1.37/123, ßIII-TUBULIN 23/1.50/200, DCX 25/1.00/200 and FLAG 25/1.49/218. The *range of the color values* was set as default with 0/225. Subsequently, only the contrast of the DAPI/blue channel was increased by 25% evenly for all images in order to avoid noise in the blue channel spilling over to the TRITC/red or the FITC/green channel in the overall picture. The TRITC/red or the FITC/green channels were not edited separately. Several images or plots were composed using Adobe® Illustrator® version CS6 (Adobe Inc.). Care was taken to preserve the original data and the original meaning. To be specific, Illustrator® was only used to enlarge font sizes and the axis description of individual plots to make them more visible. In addition, individual images and plots were combined into a large figure using Illustrator® and divided into subfigures with recognizable letters. For custom schemes designed with Illustrator®, the vector graphics used for the picture were downloaded license-free from http://www.freepik.com or were self-designed.

2.10.8 Counting of (ASPM-)FLAG positive nuclei from immunofluorescence microscopy pictures

Genetically engineered NGP ASPM-FPN 87 cell clones no. #1 and #7 were seeded on coverslips and treated with siASPM and/or nocodazole (see section 2.5.6 and 2.5.22). The cells were administered with a total of 6 separated treatments: DMSO only, nocodazole only, scramble siRNA 1, siASPM 1, scramble siRNA 1 with nocodazole and siASPM 1 with nocodazole. After the incubation, the cells were stained using a primary anti-FLAG antibody and a secondary Alexa Fluor™ 488 conjugated antibody, as previously described (2.5.22). The pictures were photographed subsequently. For this purpose, only the DAPI/blue channel was set with a 20x magnification and care was taken to ensure that there were as many, but uniform and separate DAPI signals appearing in the image. A DAPI picture was taken, and subsequently a picture of the FITC/green spectrum from the same position was made. Afterwards, the two pictures were combined using the cellSens dimension software. In total, 10 pictures of the respective treatments were taken. All FLAG positive signals of each image were visually counted and added in a calculation for each treatment. A signal was defined as ASPM-FLAG positive if there were two positive/ fluorescent signals in one cell or within two connected cells which were still in mitosis.

3 Results

MYCN amplifications drive the disease in 40-50% of high-risk neuroblastomas[62]. Despite initial remission in response to treatment, more than half the patients with high-risk neuroblastomas relapse and succumb to their disease[14]. This implies that some neuroblastoma cells survive the treatment as MRD. The central task of this thesis was therefore to improve the diagnosis of *MYCN*-amplified neuroblastoma (part 3.1) and to evaluate small molecule inhibitors as an indirect treatment approach towards *MYCN*-amplified cells (part 3.2).

3.1 Detection of neuroblastoma-specific mutations using hybrid capture-based panel NGS and sensitive monitoring of minimal residual tumor cells

In this section, a hybrid-capture-based NGS method was employed for the detection of neuroblastoma-specific mutations, including breakpoints of the *MYCN* amplicon (part 3.1.1). PCR-based detection of cell line and patient-specific genomic *MYCN* amplicon breakpoints allow for highly sensitive and specific MRD detection. Furthermore, MRD analysis by RQ-PCR and ddPCR increase the detection sensitivity of a tumor cell in a vast pool of normal cells. Lastly, clinical feasibility was investigated by applying the MRD method to material of 6 patients, which enabled to distinguish between MRD persistence and good response to the first treatment course (part 3.1.2).

3.1.1 Evaluation of a neuroblastoma hybrid capture-based NGS panel for risk assessment, treatment stratification and detection of *MYCN* amplicon breakpoints

3.1.1.1 *NB targeted NGS assay*: "One fits all", a customized sequencing assay for neuroblastoma-relevant oncogenic targets

Current neuroblastoma risk assessment and therapy stratification is based on the assessment of a combination of molecular and clinical covariates. The German Neuroblastoma Registry (NB Registry 2016) and the GPOH guidelines 2017[30,135,236,237,495] made use of patient age, INSS staging[128,129], presence of metastases, and FISH cytogenetic analyses for the detection of *MYCN* amplifications and loss at chr. 1p36. Only a few genes are recurrently altered in neuroblastoma (i.e., *MYCN, TERT, ATRX,* and *ALK*). However, recent publications shed light on additional genomic alterations[43,44], which are supposed to play a role in high-risk neuroblastoma development and recurrence. Therefore, a targeted cancer sequencing panel was investigated as an advanced diagnostics approach in comparison to the current routine diagnostics. The *NB targeted NGS assay* was designed to detect neuroblastoma relevant mutations and may be implemented as one single assay into routine diagnostics. Genes of interest were previously identified to be of prognostic relevance in high-risk neuroblastoma and defined by M. Fischer (University Hospital Cologne) and J.H. Schulte (Charité), including recommendations from the international consensus of the 4th Neuroblastoma Research Symposium (London Conferences[667]).

The *NB targeted NGS assay* covers all essential covariates for initial classification, provides the detailed genomic information essential for considering targeted treatment approaches (such as PLK1/PI3K inhibition, see section 3.2.2), and is a basis for subsequent disease monitoring (e.g. based on *MYCN* breakpoints, see section 3.1.2).

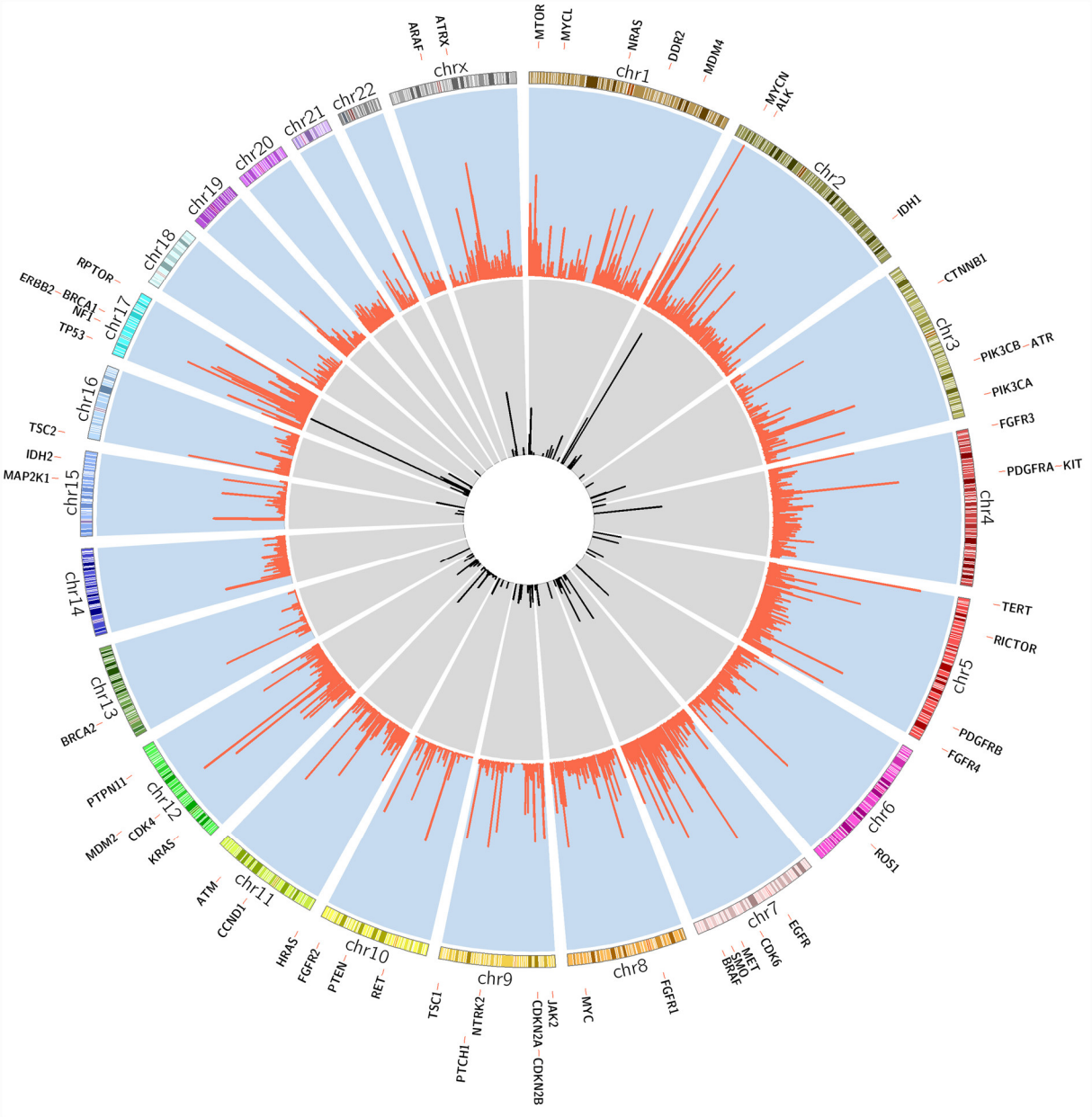

Figure 34: Circos plot of genomic target regions and sequencing coverage of the *NB targeted NGS assay*.
The *NB targeted NGS assay* identifies SNVs and InDels (insertion or deletion of base) in coding regions of 55 selected genes (noted in the outer circle). Furthermore, copy number alterations and structural rearrangements can be detected for selected gene loci and chromosomal regions. Middle circle (orange): genomic coverage of the sequencing assay, the number of aligned reads per Mb of the neuroblastoma cell line TR-14 is displayed (coverage in Mb range and log2 scale). Inner circle (black): hybrid-capture probe coverage of the genes and regions selected for the sequencing panel. (Figure was created in cooperation with J. Tödling (Charité)[634]).

This setup allows for the sensitive identification of SNV, insertions and deletions in coding regions of 55 selected genes. Furthermore, copy number alterations and structural rearrangements (including

translocation breakpoints) can be detected for selected gene loci (*MYCN, ATRX*, *TERT*, *NF1*) and chromosomal regions (chr.1p36, chr.2p24, chr.11q, chr.17q). A detailed list of all targets included in *NB targeted NGS assay* can be found in Table 12 (see section 10 appendix) and an overview of the targets, as well as the genomic coverage is shown in Figure 34. Regions of interest were used to design hybrid-capture oligos using NEO New Oncology's proprietary design procedure[635]. A total of 2486 probes were designed to cover the genomic regions of interest for the Neuroblastoma panel sequencing. Input DNA can be provided from a variety of sources, like snap-frozen tumor biopsies, bone marrow samples FFPE and liquid biopsies. Complimentary probes specifically hybridize to fragmented target DNA. An ultra-high sequencing coverage (1,500 – 2,000x on average) is achieved in subsequent massive parallel sequencing. At the time of submission, 144 complete data sets were available from samples examined with the *NB targeted NGS assay* (Table 3). The DNA for the sequencings was derived from established neuroblastoma cell lines and patient samples. The sample material was sent to NEO New Oncology for analysis as DNA in 42.4% of cases, as peripheral blood in 1.4% of cases or as FFPE in 56.3% of cases, from which DNA was obtained by laser microdissection. In total, 20 neuroblastoma cell lines were analyzed and the DNA was obtained exclusively from cultured cells. Among them, 13 cell lines were *MYCN*-amplified and further 7 cell lines were not amplified for *MYCN*. In addition, 124 patient samples were examined either using DNA or FFPE as input material. The assay was designed to reach a sequencing coverage of on average 1,500 - 2,000x. This sequencing depth was achieved in over a third of the samples (36.1%), 16 samples showed an even better result with a coverage exceeding 2,000x. The sample with the highest coverage was measured with 3,593x and the sample with the lowest coverage was measured with 53x. From 45 samples the information regarding the occurrence of a *MYCN* amplification was provided. Overall, *MYCN* amplifications were detected in about a third of the samples (31.3%). These *MYCN* amplifications were most likely results of genomic rearrangements and therefore harbor unique *MYCN* breakpoints. These breakpoint sequences constitute the basis for the establishment of *MYCN* breakpoint MRD assays (see section 3.1.2). In addition to the deep sequencing of the *MYCN* amplicon, it could be shown that the *NB targeted NGS assay* serves as a robust approach for neuroblastoma diagnostics and staging of the patients. Furthermore, this assay also reports on the treatable molecular targets.

Table 3: Overview of 144 samples processed with the *NB targeted NGS assay*

Sample type	Amount of samples
DNA	61
FFPE	81
Blood	2

Cell line	20
Patient	124

Coverage (in x)	Amount of samples
1-500x	20
501-1,000x	22
1001-1,500x	34
1501-2,000x	52
>2,000x	16

Mutation	Count of detection
MYCN normal	99
MYCN-amplified	45
MYCN CNV mean	60.62
ALK normal	101
ALK rearrangement	1
ALK gain	5
ALK loss	7
ALK SNV	30
TERT normal	137
TERT rearrangement	6
TERT loss	1
ATRX normal	118
ATRX rearrangement	2
ATRX gain	6
ATRX loss	13
ATRX SNV	5

Other mutations found
NF1
JAK2
CDKN2A
RICTOR
CMK4
TP53
MDM4
HRAS/NRAS
FGFR1/FGFR3/FGFR4
PTEN
ATM/ATR
MTOR/RPTOR/RICTOR
NBAS
BRCA1/BRCA2
SMO
PIK3CA
PGFRA
TSC2
CCND1

3.1.1.2 Detecting unique *MYCN* amplicon breakpoints with a targeted sequencing assay

Prior to the panel sequencing, the *MYCN* status in neuroblastoma cell line and tumors was controlled using the FISH technique. FISH supported detection of *MYCN* amplifications is clinical implemented as the "gold standard method" for assessment of the *MYCN* status (example of *MYCN* FISH detection in TR-14 cell line see Figure 35).

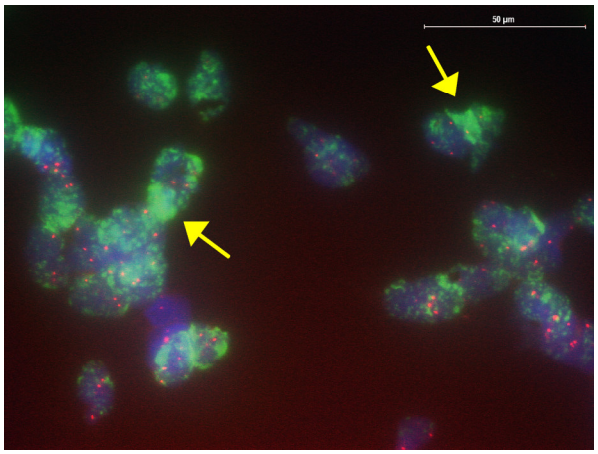

Figure 35: FISH based evidence for *MYCN* amplification found in neuroblastoma cell line TR-14.
MYCN amplifications (green color) were detected in cell nuclei of neuroblastoma cell line TR-14 (DNA probe at chr.2p24). The *MYCN* amplicon is located on DMs[668]. As a reference, a CEP2 probe (red color) which binds a repetitive sequence in the centrosomal area of chromosome 2, was added. Nuclear counterstaining was conducted with DAPI (blue color). (Picture kindly taken by J. Theissen and W. Lorenz (University Hospital Cologne).

The samples of the neuroblastomas (tumor pieces and/or bone marrow spears) included in this study were examined for the *MYCN* status within routine diagnostics of the German neuroblastoma trial (NB2004) and the German Neuroblastoma Registry (NB Registry 2016)[30,236,237,495] at diagnosis time point or in the event of a relapse. FISH analysis was performed in cooperation with the neuroblastoma reference laboratory by J. Theissen and W. Lorenz (University Hospital Cologne). To establish a targeted sequencing assay for detection of tumor-specific breakpoints of the *MYCN* amplicon, first the largest genomic region in which *MYCN* breakpoints frequently occur was defined. Based on previously published data of whole-genome sequencing of 14 primary *MYCN*-amplified neuroblastomas[43,44,76], i.a. focusing on genomic rearrangements that follow telomerase activation, this data was reanalyzed for rearrangements within the genomic neighborhood of *MYCN*. For this, a structural-variant detection using the *novoBreak* software[633] was used, which included stringent filtering of the resulting breakpoints. The analysis of next-generation sequencing data for *MYCN* breakpoint detection was kindly performed by J. Toedling (Charité)[634,635]. Within the 1Mb range of *MYCN*, 376 breakpoints were identified (Figure 36). The majority of breakpoints were located within the *MYCN* gene, upstream to *MYCN* in the intergenic area between *MYCN* and *DDX*, or downstream to *MYCN* in the intergenic region between *MYCN* and *FAM49A*.

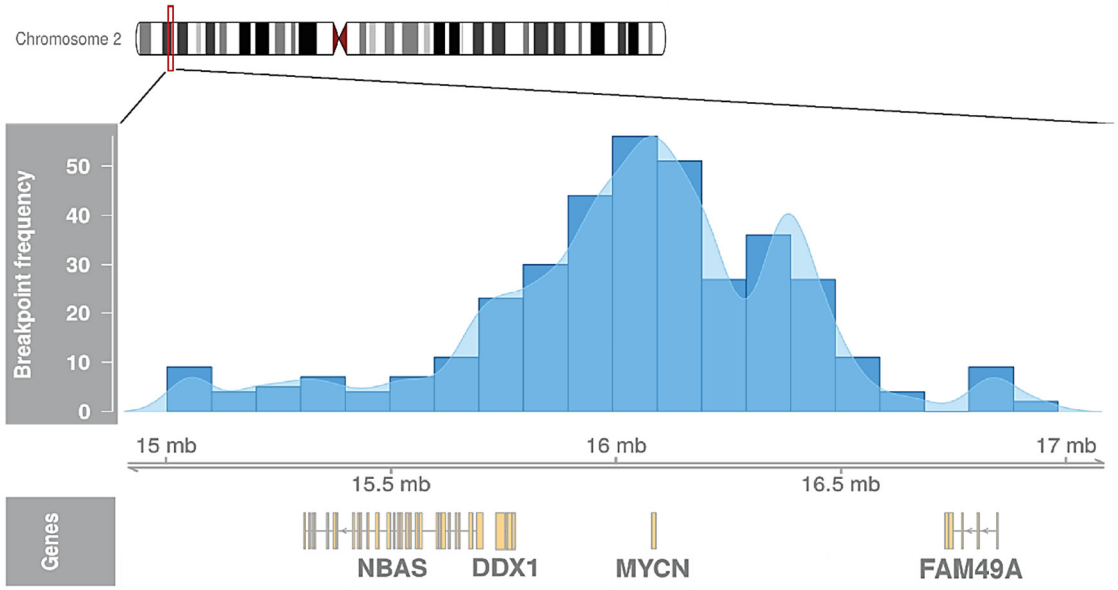

Figure 36: Detection of tumor-specific breakpoints of the *MYCN* amplicon using next-generation sequencing data. GeneRegionTrack plot showing frequency of genomic breakpoints in proximity to *MYCN* on chr.2p24.3. Breakpoints were determined by WGS of 14 primary *MYCN*-amplified neuroblastomas[43,44,76] followed by structural-variant detection using the *novoBreak* software and a stringent filtering of the resulting breakpoints. The distribution of breakpoints is displayed both as a histogram showing the absolute number of breakpoints in an interval and as a smoothed density function. (Figure was created in cooperation with J. Toedling (Charité)[634].)

This 2Mb genomic region was defined as the target region for *MYCN* breakpoint detection and was subsequently included into the design of the *NB targeted NGS assay*. The hybrid capture probes, which were designed to cover the *MYCN* amplicon, were distributed in sequence starting within the *MYCN*

gene as a “hotspot” of genomic rearrangement occurrences and decreasing in probe coverage towards the up- and downstream amplicon outside. The distribution pattern of the *MYCN* breakpoints in the whole-genome sequencing data of the 14 *MYCN*-amplified neuroblastoma tumors (Figure 36) was thus adopted for the probe design for the *NB targeted NGS MYCN* breakpoint detection (Figure 37). In addition to the designed probes in the 2Mb genomic range of the *MYCN* amplicon, additional probes outside the amplicon area were created downstream in the intergenic region between *LINC00276* and *DDX1* and in the area upstream in the intergenic region between *FAM49A* and *RAD51AP2* (see Figure 37 A). These areas were covered by hybrid capture probes, since breakpoints in the next-generation sequencing data can also be found in these regions (breakpoint count ≤ 10) and a possible, clear distinction of the active *MYCN* amplicon rearrangement area should also be investigated. A total of 112 *MYCN* amplicon-related probes, located on chromosome 2 between bases 14,724,671 and 17,527,918, were applied within the *NB targeted NGS assay*.

Figure 37: Genomic regions of sequencing capture probe hybridizations in the *MYCN* amplicon.
Coverage of hybrid capture probes in proximity to the *MYCN* amplicon on chr. 2p24.3-2p24.2. **(A)** Distribution of the hybrid capture probes in the area of the *MYCN* amplicon between the genomic regions upstream in the intergenic region after *LINC00276* at position chr2:14,724,67 and downstream in the intergenic region before *RAD51AP2* at chr2:17,527,918. Starting from *MYCN*, the probes were distributed in a smaller number and density outwardly. **(B)** Detail image of the probe distribution in the *MYCN* gene, which was almost completely covered by hybrid capture probes.

The *MYCN* gene itself was particularly densely covered with hybrid capture probes (Figure 37B). The area of exon 1 was not covered (area not covered: chr2:16,080,560 – chr2:16,080,853), but the intronic area between exon 1 and exon 2 was entirely covered with probes, as was exon 2 itself. In the area of the intronic region between exon 2 and exon 3, almost complete coverage took place (areas not covered: chr2:16,083,439 – chr2:16,083,596, chr2:16,084,800 – chr2:16,085,014 and chr2:16,085,194 – chr2:16,085,421). Exon 3, is again entirely covered by probes, however, coverage of the 3 'UTR area

was almost completely excluded for probe design (area not covered: chr2:16,086,241 – chr2:16,086,662 and chr2:16,086,782 – chr2:16,087,129). In summary, it can be said that 72.8%. of the 6,276 bp of the *MYCN* gene were covered by hybrid capture probes. The *NB targeted NGS assay* was used for targeted sequencing of the amplified *MYCN* locus in 7 cell lines and 13 primary high-risk neuroblastoma samples at an overall coverage of 513x – 2,075x (Table 14 and Table 16 in appendix section).

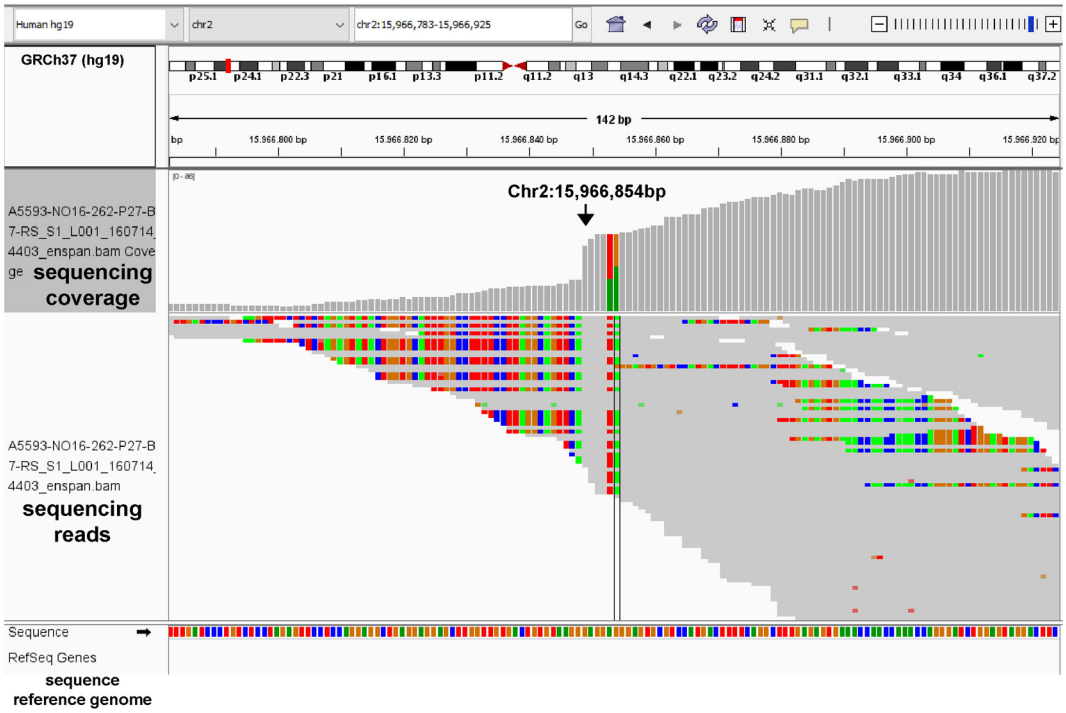

Figure 38: Sequencing read depth drop of *MYCN* amplicon breakpoint in neuroblastoma cell line TR-14.
IGV image displaying sequencing-data evidence for the presence of a specific breakpoint of *MYCN* in TR-14 *MYCN*-amplified neuroblastoma cell line. Display of breakpoint rearrangement intergenic chr2:16,400,242 - intergenic chr2:15,966,854. The breakpoint was located on the basis of a sequencing read depth drop (marked with a black arrow at position chr2:15,966,854; In detail, a part of an intergenic region chr2:16,400,242 (multicolor) sequence was fused to another intergenic sequence chr2:15,966,854 (grey, aligned to GRCh37 (hg19)).

Reads covering the *MYCN* locus in all samples were aligned. The read depth typically showed a steep rise or drop at the exact location of the breakpoint in many cases (example in cell line TR-14 see Figure 38). Discordant read pairs and reads covering a breakpoint were extracted. After the extraction of all breakpoints found within a sample, a quality filtering of the breakpoints followed. For this, the unfiltered breakpoints are catalogued in order of their genomic localization first. The breakpoints are then sorted according to the number and type of supporting sequencing reads. Breakpoints that are supported by many covering sequencing reads (>10 encompassing and spanning reads) were estimated to be of high quality and a presence is assumed to be very likely. These breakpoints were used later on for the neuroblastoma MRD project (see section 3.1.2). Breakpoints supported with a medium number of reads (>2 encompassing and spanning reads) or with a small to no number of reads (≤1 encompassing and spanning read) were deferred for PCR and Sanger sequencing validation. An example based on the cell line TR-14 is displayed in Table 18 (section 10 appendix), which shows all breakpoints found and their

categorization. In summary, 20 breakpoints were detected in 7 cell lines (median: 2.86 per cell line, Table 4) and 35 breakpoints in 13 tumors (median: 2.7 per tumor; Table 5).

Table 4: Breakpoints detected in the genomic *MYCN* amplicon in neuroblastoma cell lines.

Name of cell line	Copy number *MYCN*	*MYCN* associated breakpoints
IMR-5	49.90	2
SK-N-BE	68.06	3
LAN-5	59.50	2
NGP	56.93	3
KELLY	88.00	3
TR-14	57.00	2
SK-N-DZ	43.20	5

Table 5: Breakpoints detected in the genomic *MYCN* amplicon in primary neuroblastoma tumor samples.

Patient number	Copy number of *MYCN*	*MYCN* associated breakpoints
1	61.02	5
2	73.27	4
3	47.90	2
4	54.63	1
5	66.11	1
6	44.50	4
7	14.53	1
8	48.25	1
9	31.15	5
10	28.21	1
11	153.57	3
12	28.75	4
13	112.53	3

The *MYCN* copy number did not correlate strongly with the number of breakpoints per cell line or tumor ($p=0.84$ and $p=0.67$, respectively). The example of the cell line TR-14 shows that the number of breakpoints found has no strong correlation with the detected *MYCN* copy number (detected CNV 57.00, breakpoints 2). Out of 20 samples sequenced, 11 samples show a lower copy number than TR-14 and 8 samples show a higher copy number than TR-14 with a different count of detected breakpoints (see *MYCN* copy number for TR-14 in Figure 39). Of all 55 breakpoints identified, only 4 breakpoints occurred within the *MYCN* gene (Table 14 and Table 16 in appendix section), 2 breakpoints were found in the intron between exons 2 and 3 and the other 2 breakpoints were revealed in exons 2 and 3. Interestingly, 8 of the 51 breakpoints located adjacent to *MYCN* occurred within the *NBAS* gene, while 3 breakpoints occurred in other genes and 40 breakpoints occurred in intergenic regions (Figure 40). All 11 breakpoints within genes other than *MYCN* were detected in intronic and not protein-coding regions.

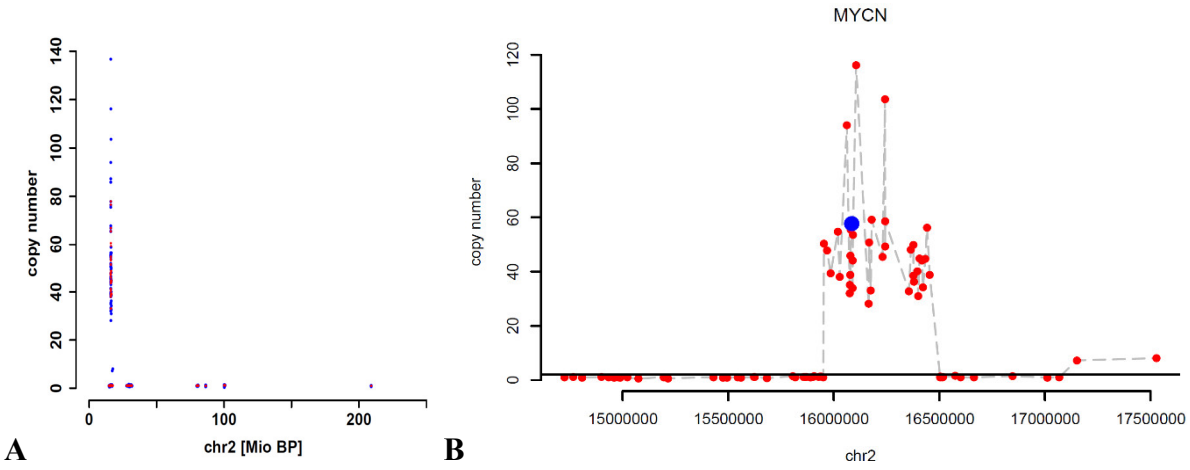

Figure 39: *MYCN* copy number and focality plot of chromosome 2 from neuroblastoma cell line TR-14.
(A) Sequencing evidence for a *MYCN* amplification. Copy number plot displaying a change of the copy number within chromosome arm 2p. **(B)** Focality plot of chromosome 2 shows a copy number change and amplification of the 2p24 region. Red dots display the location of a hybrid capture probe which provides information about the copy number at this position. Blue dot indicates the genomic location of *MYCN* at chr2:16,080,683-16,087,129 in GRCh37 (hg19). The *MYCN* copy number information is taken from this position, displaying a copy number of 57 for TR-14.

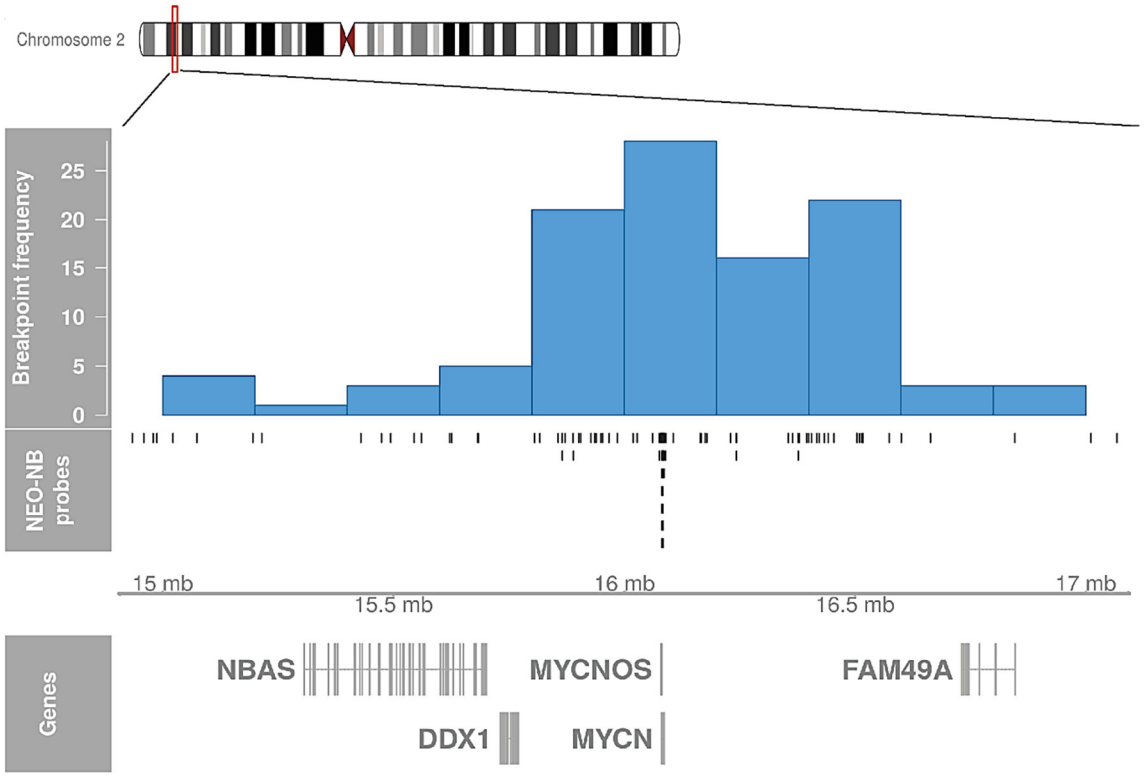

Figure 40: Patient-individual detection of breakpoints of the *MYCN* amplicon using *NB targeted NGS assay*.
GeneRegionTrack plot showing frequency of genomic breakpoints in proximity to *MYCN* on chr.2p24.3. Breakpoints were determined within the 1Mb range of *MYCN* by *NB targeted NGS assay* followed by structural-variant detection using the *novoBreak* software and a stringent filtering of the resulting breakpoints. The *NB targeted NGS assay* detected 35 breakpoints in the amplified *MYCN* locus in 13 primary high-risk neuroblastoma tumor samples. The distribution of breakpoints is displayed both as a histogram showing the absolute number of breakpoints in an interval and as a smoothed density function. (Figure created in cooperation with J. Toedling (Charité)[634].)

All mapped *MYCN* breakpoints were validated orthogonally using Sanger sequencing of PCR amplicons (See section 3.1.2) that included each breakpoint (Table 14 and Table 16 in appendix section). These data show that a robust and effective pipeline to identify patient-specific breakpoints of the *MYCN* amplicon could be established. The results of the *NB targeted NGS assay* could now be used to design a *MYCN* breakpoint patient-specific PCR assay and to expand this PCR setup to an *NB breakpoint MRD assay* that recognizes residual tumor cells in a patient sample.

3.1.1.3 Composition of the genomic sequence of *MYCN* amplicon breakpoints

The results of the NB targeted NGS assay show that unique MYCN breakpoints exist within the *MYCN*-amplified neuroblastoma samples. These breakpoints are most likely the result of a break in the genomic DNA, which is then somehow realigned or repaired afterwards. However, these breakage events do not happen at the exact same genomic site, they occur at different genomic locations. This creates unique breakpoint "scars", which differ to the reference sequence and which can be used in MRD PCR assays for the detection of minimal residual tumor cells (see section 3.1.2).

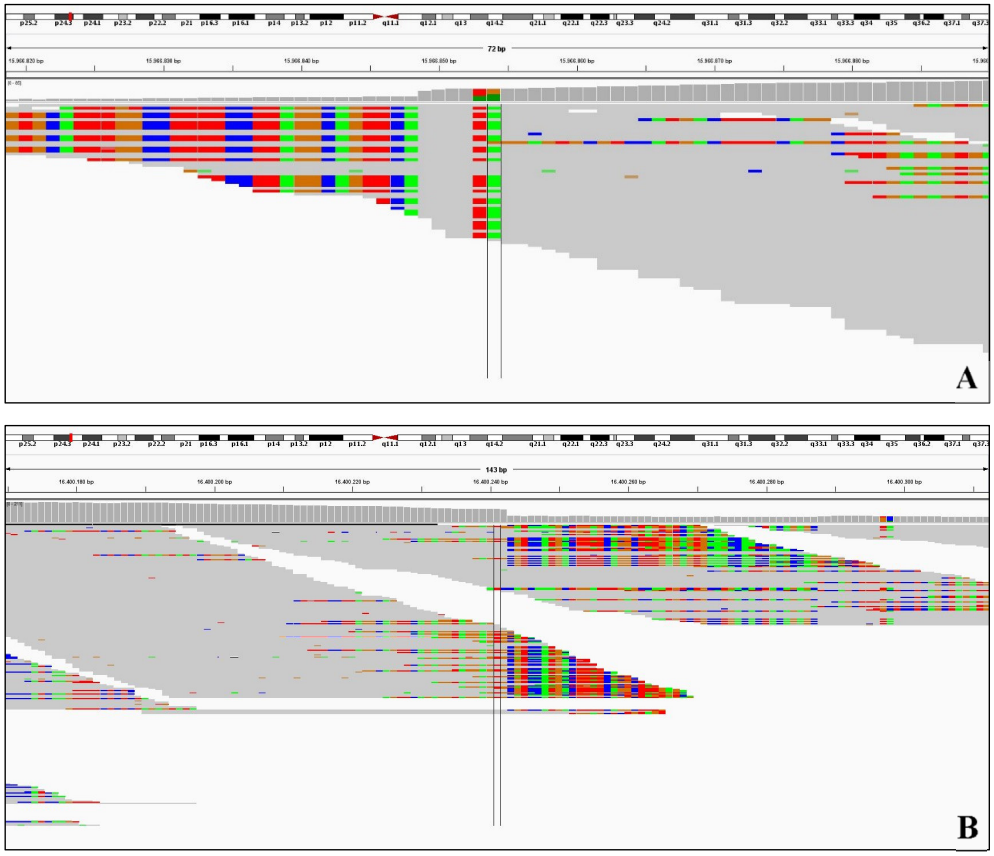

Figure 41: IGV based detection of the TR-14 *MYCN* amplicon breakpoint no.15.
IGV view displaying NGS-data evidence for the presence of a specific breakpoint within the *MYCN* amplicon area in the TR-14 *MYCN*-amplified neuroblastoma cell line. Images in the *squished* feature track display a breakpoint rearrangement at the genomic location intergenic chr2:16,400,242 - intergenic chr2:15,966,854. For each of the fragments showing multicolored parts of sequence reads in complete mismatch compared to grey read parts which align with the reference sequence GRCh37 (hg19). The breakpoint is supported by 14 spanning and 65 encompassing reads. The approximate location of the breakpoint is highlighted with a double line. (**A)** Breakpoint site at intergenic chr2:15,966,854. **(B)** Breakpoint site at intergenic chr2:16,400,242.

Regarding the breakpoint composition in general, there are some recurring patterns that are described in more detail here. The breakpoint sequences for e.g. the *MYCN*-amplified cell line TR-14 and all other specimens were compiled from two genomic rearrangement sites. Breakpoint sequences are displayed using discordant read pairs from the *NB targeted NGS assay*, which can be spanning and encompassing sequencing reads. The consensus sequence of a breakpoint spanning read was extracted without reads which are not discordantly aligned. The breakpoint sequence was either provided by NEO New Oncology GmbH directly (as in case of TR-14 breakpoints; see breakpoint in sequencing data in Figure 41) or extracted from alignment data independently (as explained in 2.9.3). The breakpoint no. 15 of TR-14 is a rearrangement in the closer genomic region of *MYCN*, in the area between 15.97Mb to 16.4Mb, which also includes the amplified *MYCN* gene. The *MYCN* copy number focality plot from TR-14 (Figure 39 B) shows that the genomic locations chr2:15,966,854 and chr2:16,400,242 are involved in the breakpoint composition and could probably display the outer borders of the *MYCN* amplicon. *MYCN* copy number variations and the *MYCN* amplification take place in the region between the genomic locations chr2:15,966,854 and chr2:16,400,242. The sequencing data further indicates a head-to-tail direction of the genomic breakpoint sequence (detailed information in appendix Table 18). Comparing the NGS sequence of the TR-14 breakpoint to the reference genome, a series of events are suggestable that may have led to the final, mutated TR-14 chromosome 2p. First of all, there should have occurred at least two breaks upstream and downstream of *MYCN*. This fragment then was inverted in comparison to the original strand orientation and was re-fused at least twice to the previously broken genomic strand (See Figure 42). It is unclear whether this fragment was broken only at these two locations, or whether there were further breaks within the area between 15.97Mb and 16.4Mb and there were, for example, two small fragments that were broken, inverted and exchanged between the breakpoint sites. In addition to a double-strand break, there may also have been (several) single-strand breaks that were subsequently annealed or repaired.

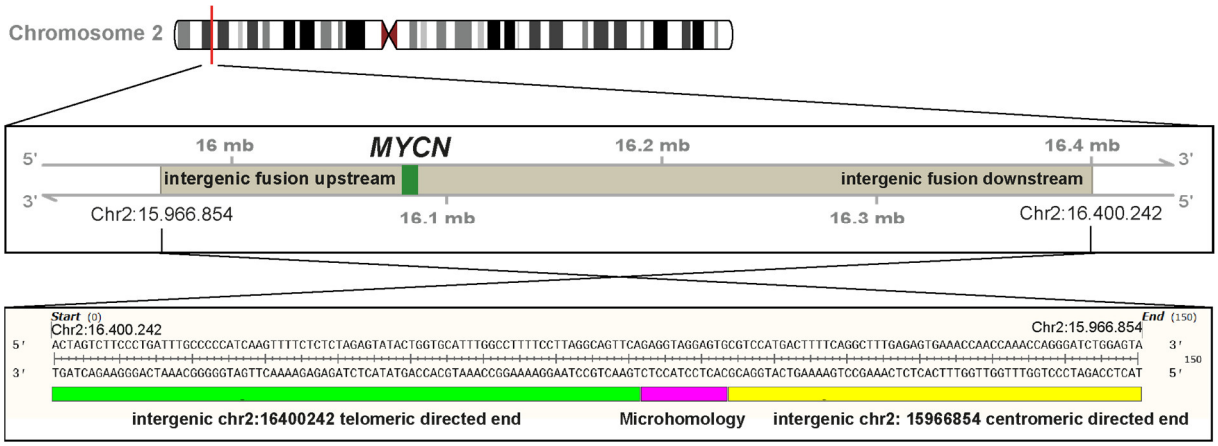

Figure 42: Genomic rearrangement events derive *MYCN* amplicon breakpoint in *MYCN*-amplified TR-14 cell line.
Location of a *MYCN* breakpoint, caused by rearrangement events resulting in an intergenic rearrangement from 15.97Mb to 16.4Mb in neuroblastoma cell line TR-14.

A closer examination of the nucleotide composition shows a GC content of 47%. The sequence also includes 19 open reading frames, 28 potential sites for hairpin formations, 41 potential self-annealing sites, and no 3' complementarity sites. Furthermore, the breakpoint harbors a 12 bp microhomology with the sequence 5'-GAGGTAGGAGTG-3' at the junction site, which pinpoints towards an occurrence of a similar nucleotide sequence in both breakpoint composing strands (Figure 43). Microhomologies are shared or additional nucleotides at the junction side of rearranged fragments[551]. This type of a microhomology, which occurs within the TR-14 *MYCN* breakpoint (breakpoint no. 15), represents a junctional microhomology, which occurs directly at the breakpoint junction of the genomic rearrangement. The microhomology sequence is identical in each of the genomic strands that composes the genomic rearrangement, therefore it is impossible to identify the exact location of the breakpoint[85]. On closer inspection of the microhomology sequence (5'GAGGTAGGAGTG'3), it could be assumed that this sequence displays a chiral or mirror repeat DNA sequence[669]. Excluding the last two 3' end nucleotide bases TG, the sequence GAGGTAGGAG is left and if the 5th or 6th base has been replaced by a transversion mutation (A <-> T), a copy sequence which mirrors between the 5th or 6th base in reverse nucleotide order can be recognized. Equally, the bases GT at the 4th/5th position and bases TG at the 11th/12th position themselves could represent a chiral copy. However, the mechanism behind the breakpoint microhomology occurrence and structural composition cannot be clarified so far. Overall, the existence of the unique *MYCN* rearrangements in different locations of chromosome 2p and the involvement of microhomologies has to be examined in further detail.

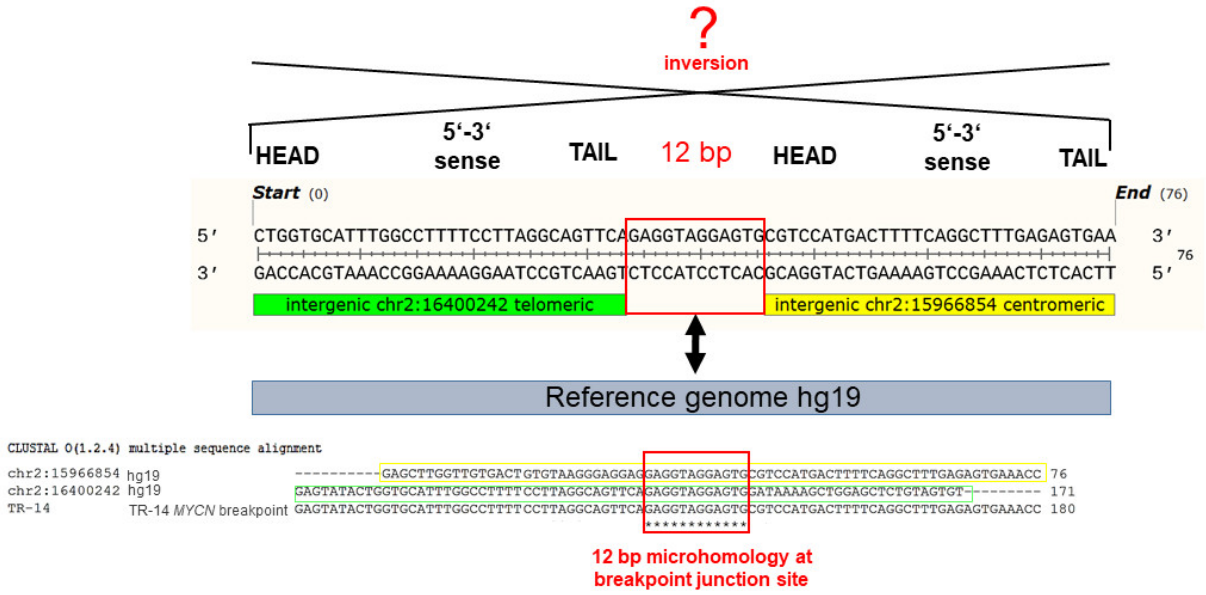

Figure 43: Junctional microhomology in *MYCN* amplicon breakpoint of TR-14 neuroblastoma cell line.
At least two DNA strand breaks upstream and downstream of *MYCN* probably led to this rearrangement in the cell line TR-14. This fragment then was inverted in reverse order to the original strand sequence and then was re-fused at least twice to the previously broken genomic strand. The normal orientation of the DNA strand also remains the same for the fragments which is in head to tail direction. When comparing the reference genome GRCh37 (hg19) of the sequence of the two segments involved in the breakpoint and the actual breakpoint sequence, it is noticeable that the segments share 12bp ("microhomologies") at the breakpoint junction site. These 12bp are identical in sequence in both segments, which is why an affiliation to one of the two segments cannot be determined. This picture shows only a 76bp section.

3.1.1.4 Stability of genomic *MYCN* amplicon breakpoints over the course of the disease

As a prerequisite for using the *MYCN* amplicon breakpoints as MRD markers, it is necessary to assess how stable *MYCN* amplicon breakpoints were over the course of the disease. A first approach to this topic was the sequencing of established neuroblastoma cell lines and their associated sub-clones. The process of sub-cloning and sub-cultivation can lead to possible (genetic) changes in the subclone that were not present in the parental cell line and/or the selection of a specific clone can lead to improved chromosomal stability and a more homogenous population[670]. Therefore, the parental cell line IMR-32 with the sub-clones IMR-5 and IMR-5/75 and the parental cell line SK-N-BE with the sub-clone BE(2)-C were examined in more detail for shared *MYCN* breakpoint sequences.

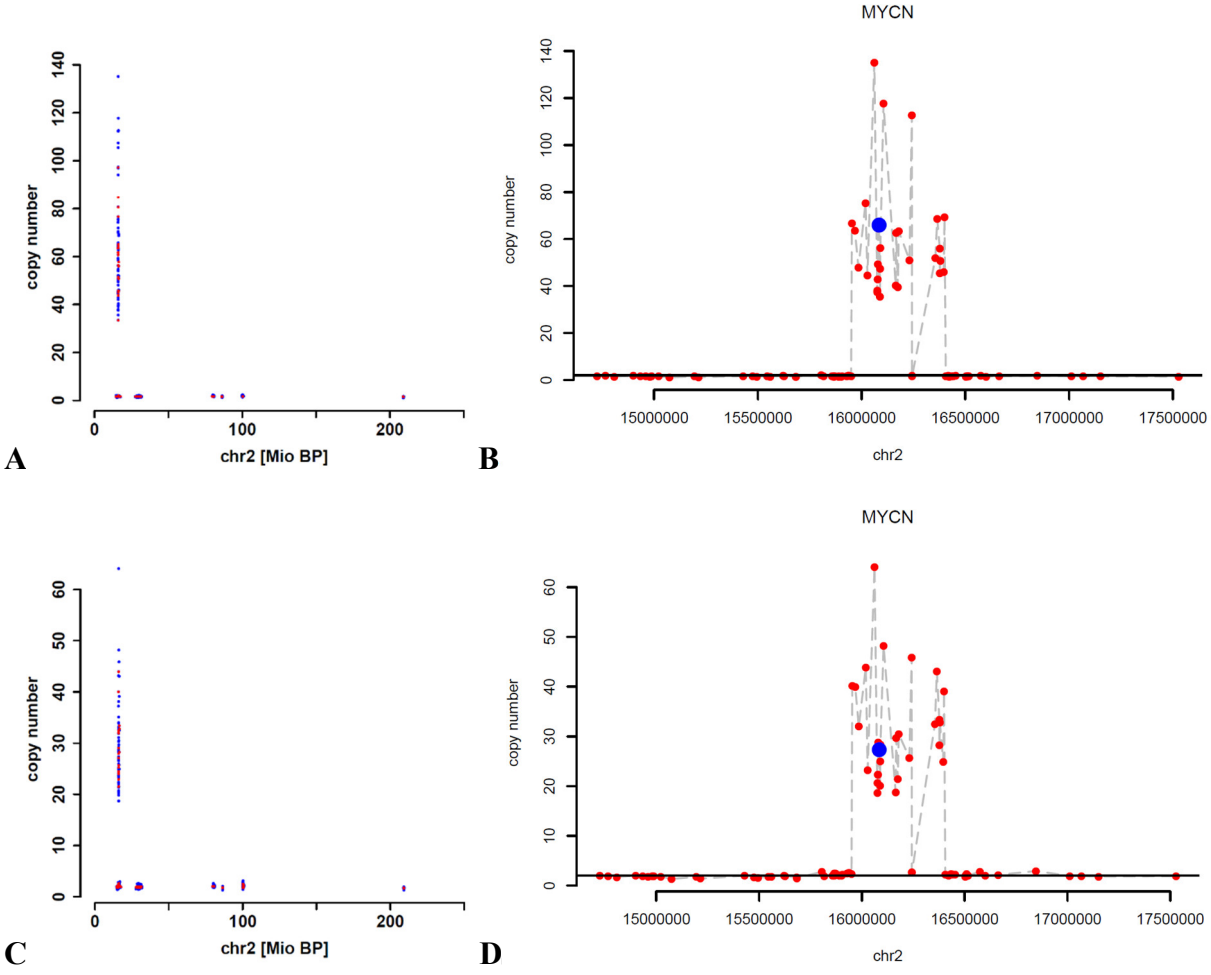

Figure 44: *MYCN* copy number and focality plot of chromosome 2 from matching primary and relapse tumor samples.
(A) Sequencing evidence for a *MYCN* amplification. Copy number plot displaying a change of the copy number within chromosome 2p of the primary tumor sample. **(B)** Focality plot of chromosome 2 shows a copy number change and amplification of the 2p24 region of the primary tumor sample. Red dots display locations of hybrid capture probes. Blue dot indicates the genomic location of *MYCN* at chr2:16,080,683-16,087,129 in GRCh37 (hg19). The *MYCN* copy number information is taken from this position. **(C)** Copy number plot displaying a change of the copy number within chromosome 2p of the relapse tumor sample. **(D)** Focality plot of chromosome 2 shows a copy number change and amplification of the 2p24 region of the relapse tumor sample.

Within a comparison of the breakpoint locations and sequences, it was found that all parental breakpoints were also detectable in the sub-clones (see Table 14 in appendix). In total, one breakpoint from the cell line IMR-32 could be recovered in the sequencing data of the sub-clones IMR-5 and IMR5/75 and three breakpoints from line SK-N-BE could be recovered in the sequencing data of the sub-clone BE(2)C. These results were further validated by breakpoint specific PCRs, Sanger sequencing and MRD PCRs (see section 3.1.2). In a next step, the *NB targeted NGS assay* was used to map the *MYCN* breakpoints in paired tumor biopsies taken at diagnosis and relapse. The examination of the breakpoint stability through the course of the disease in patient material was a prerequisite to further confirm the applicability of MRD detection in patient follow-up samples. The stability of breakpoints was tested in tumor material of the patients no. #2 and #5 (see Table 5). As an example, the *MYCN* amplicon and the *MYCN* breakpoint of patient no. #5 will be described in more detail. The samples from patient no. #5 show a *MYCN* copy number of 66.11 or 27.35 and one major breakpoint, which is supported by > 10 encompassing and spanning reads. Again, the number of breakpoints found displayed no strong correlation with the detected *MYCN* copy number. It should be highlighted that the *MYCN* copy number between primary and relapse tumor sample has been nearly halved, from 66.11 to 27.35. However the focality profile displays only minor changes between both copy number patterns within the *MYCN* amplicon (Figure 44). A qualitatively divergent *NB targeted NGS* is unlikely, since e.g. the coverage for the primary tumor sample (1,554x) and for the relapse tumor sample (1,584x) was detected very high and very similar. Interestingly, the number of breakpoints found does not change due to the changed copy number. The tumor of patient no. #5 shows 5 distinct breakpoints of the *MYCN* amplicon which are supported by many sequencing reads (4 – 498 reads). Moreover, all 5 breakpoints found in the primary tumor sample of the patient can be recovered in the relapse tumor material (see Table 19 in appendix). One breakpoint (intergenic chr2:16,242,896 – intergenic chr2:16,393,725) stands out among the 4 other breakpoints, because this breakpoint has achieved a very high sequencing coverage (477 encompassing and 19 spanning reads in the primary tumor and 70 encompassing and 16 spanning reads in the relapse tumor) and result from a rearrangement in proximity to *MYCN* on chr.2p24.3. In contrast, the other breakpoints are supported with fewer sequencing reads and showed a segment partner that links to a similar location further downstream in the chr.2p22.3 region around chr2:33,141,347. Therefore, the breakpoint at intergenic chr2:16,242,896 had to be classified qualitatively as a *main* breakpoint and all other 4 breakpoints had to be classified as *minor* breakpoints. This main breakpoint was therefore used for further PCR and *NB breakpoint MRD assay* detection (see section 3.1.2). However, if this breakpoint cannot be detected or validated, or if it is necessary to validate more than 1 breakpoint, the other breakpoints represent an alternative option. Overall in this work, 4 and 1 *MYCN* breakpoint(s) were mapped in the primary tumor samples from patients no. #2 and #5 (Table 5 and Table 16). Identical breakpoints were detected in the matched relapsed tumor samples from patients 2 and 5 using the *NB targeted NGS assay*, demonstrating a stability of the breakpoints over the course of the disease. The breakpoint sequences from both time points were aligned to each other to identify even

slight changes, but the aberrant sequences matched exactly. In the matching tumor DNA samples from primary and relapse tumors of patient no. #5 the breakpoint at the location intergenic chr2:16,242,896 could be found at the same genomic position (Figure 45). Furthermore, the sequence for each sample showed the identical same sequence at this position, which is why it can be assumed that it is the exact same breakpoint. This result is supported by the occurrence of a sequencing read depth drop at the precise location of the breakpoint in both samples. Amplification of these breakpoint regions for validation with Sanger sequencing produced the same result, that all breakpoints detected in the primary samples were perfectly preserved in the corresponding relapsed tumor (see Figure 56). The breakpoint (intergenic chr2:16,242,896 – intergenic chr2:16,393,725) of the tumor of patient no. #5 evidences a rearrangement downstream of the genomic region of *MYCN*, in the area between 16.24Mb to 16.39Mb, which does not include the *MYCN* gene directly (Figure 46).

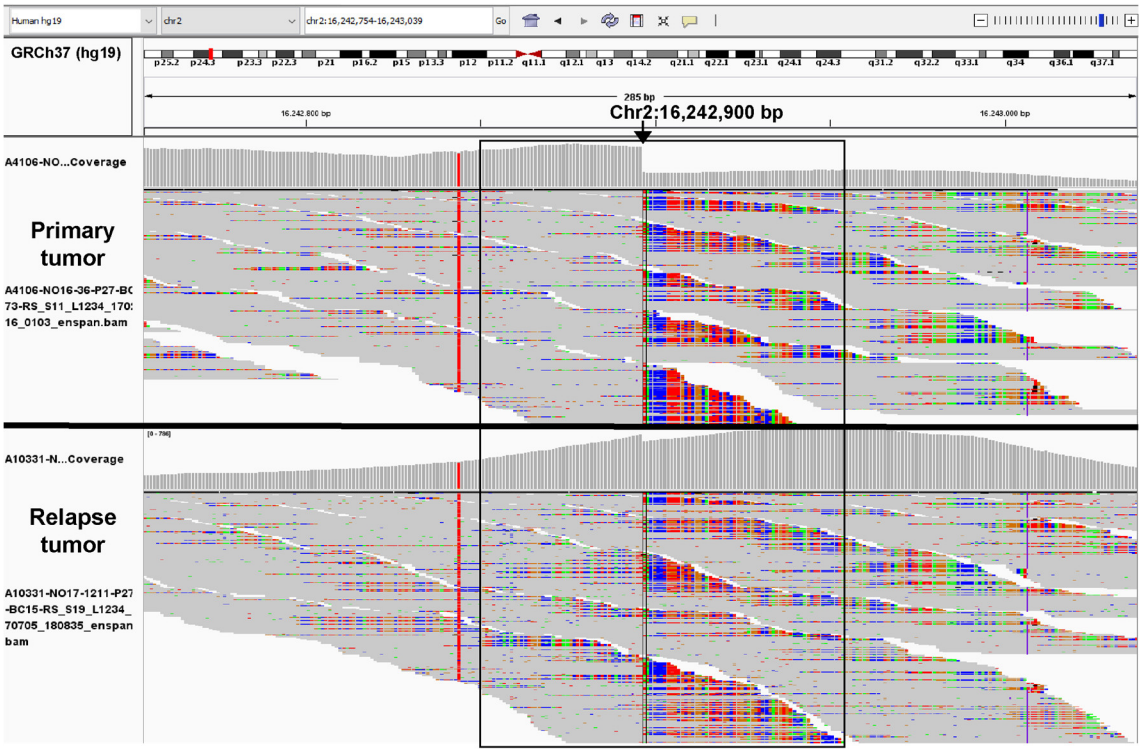

Figure 45: Detection of the same breakpoint of the *MYCN* amplicon in matching primary and relapse tumor samples. IGV image displaying sequencing-data evidence for the presence of a specific genomic breakpoint downstream of *MYCN* at intergenic chr2:16,242,896 in initial tumor material obtained from patient no. #5 (upper panel). In subsequent relapse tumor material obtained, the very same breakpoint was detected (lower panel). The sequencing data for both samples also show a drop in the sequencing coverage which is typical for detected breakpoints. For each of the panels showing multicolored parts of reads in complete mismatch compared to grey read parts which align with the reference sequence GRCh37 (hg19). The black rectangle shows the position of the matching flanking sequence of the breakpoint. The arrow points towards the exact rearrangement site of the breakpoint.

The *MYCN* copy number focality plots from both tumor samples (Figure 44 B+D) show that the rearrangement events, which must have led to the creation of this breakpoint, probably took place at the downstream end of the *MYCN* amplicon. This part of the breakpoint may only represent a small part of a genomic “cassette”, which is located at the end of the *MYCN* amplicon. In addition, there may have occurred other rearrangement events within the *MYCN* amplicon or a spanning rearrangement event

over the whole *MYCN* amplicon. The sequencing data further indicates a tail-to-tail direction of the genomic breakpoint sequence (see Table 19 in appendix). Comparing the NGS sequence of the tumor breakpoint to the sequence of the GRCh37 (hg19) reference genome, a series of events are imaginable that may have led to the final, mutated tumor chromosome 2p sequence. First of all, there should have occured at least two or probably four breaks downstream of *MYCN*. The two segments of this breakpoint were then inverted in comparison to the original strand orientation and were re-fused at least twice to the previously broken genomic strand (see Figure 46). The pattern indicates that there was one break at the front end of the first segment of the breakpoint "cassette" and another break at the end of this first segment. This segment originated from the sense strand and has turned in addition. The second segment at the end of the breakpoint "cassette", which originated from the antisense strand, was also broken from the strand and has turned as well before final refusion. Therefore, both segments of the rearrangement have a telomeric directed end. It is unclear whether this fragment was indeed broken only at these two locations, whether there were further breaks within the area between 16.24Mb and 16.39Mb and wheather there were, for example, two small fragments that were broken, inverted and exchanged between the break sites. As an alternative to a double-strand break, there may also have been (several) single-strand breaks which may have led to the refusion of the sense and antisense strand.

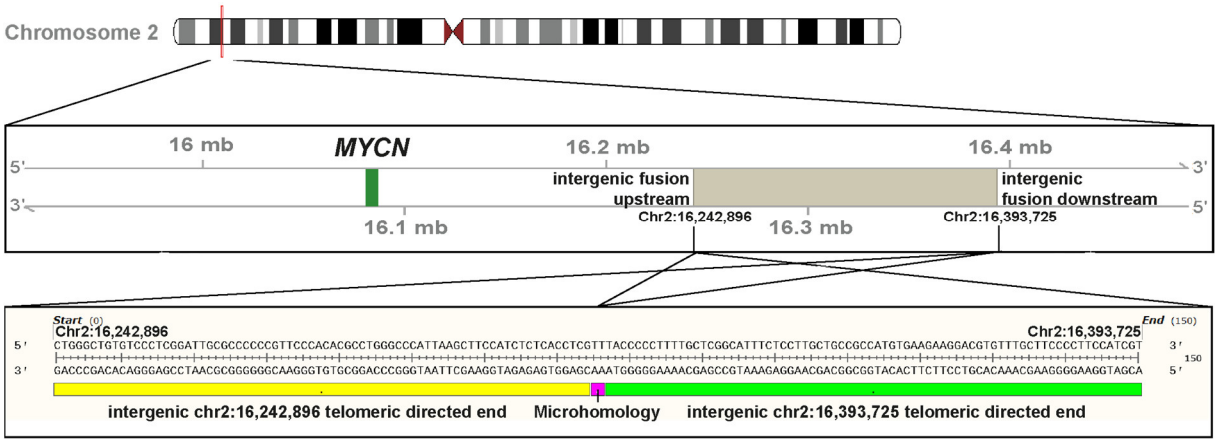

Figure 46: Genomic rearrangement events derive *MYCN* amplicon breakpoint in *MYCN*-amplified tumor of patient no.5. Location of a *MYCN* breakpoint, caused by rearrangement events resulting in an intergenic rearrangement from 16.24Mb to 16.39Mb in the tumor of patient no. #5.

In summary, it could be shown that a unique *MYCN* amplicon breakpoint is present in the paired longitudinal tumor samples from patient no. #5. The data demonstrate that the *MYCN* amplicon breakpoints persist through the course of the disease to relapse, and could serve as MRD markers.

3.1.2 Detection of minimal residual disease based on *MYCN* amplicon breakpoints and other neuroblastoma-relevant mutations

3.1.2.1 Design of sensitive MRD assays based on individual *MYCN* breakpoints

In this part of the work, MRD assays were established based on unique *MYCN* breakpoints, with which residual tumor cells can be detected in the bone marrow. The sequence of these unique *MYCN*-associated

breakpoints was detected using the *NB targeted NGS assay* which made it possible to design cell line or patient-specific PCRs and *NB breakpoint MRD assays*. Exemplary for PCR and MRD assay design, the assay establishment for detection of a *MYCN* breakpoint of the neuroblastoma cell line TR-14 will be discussed in more detail here (no. 15, see Table 14 in appendix). The breakpoint sequences for TR-14 and other specimens were compiled using a consensus sequence of a breakpoint spanning read from the *NB targeted NGS assay* (3.1.2). PCR and MRD assays were designed by composing this (breakpoint-) spanning read, together with one upstream encompassing read and one downstream encompassing read, which were located adjacent to the spanning read. Based on the *MYCN* amplicon breakpoint sequences, the PCR assays were then designed, which are fundamental for further MRD detection. Designed PCR assays were initially established based on the specific *MYCN* breakpoints of neuroblastoma *MYCN*-amplified cell lines. The usage of cell lines has the advantage that, in contrast to the patient material, enough DNA material was available to validate the PCR assays. For each breakpoint for which a PCR assay was designed, at least three different PCR assays, i.e. primer pairs, were designed. The primer pairs were designed at different distances with respect to the specific breakpoint (see Figure 47). Firstly, in a short distance (amplicon length approximately. 60-100bp), secondly in a medium distance (amplicon length approximately 100-200bp) and thirdly in a wide distance (amplicon length approximately 200-400bp).

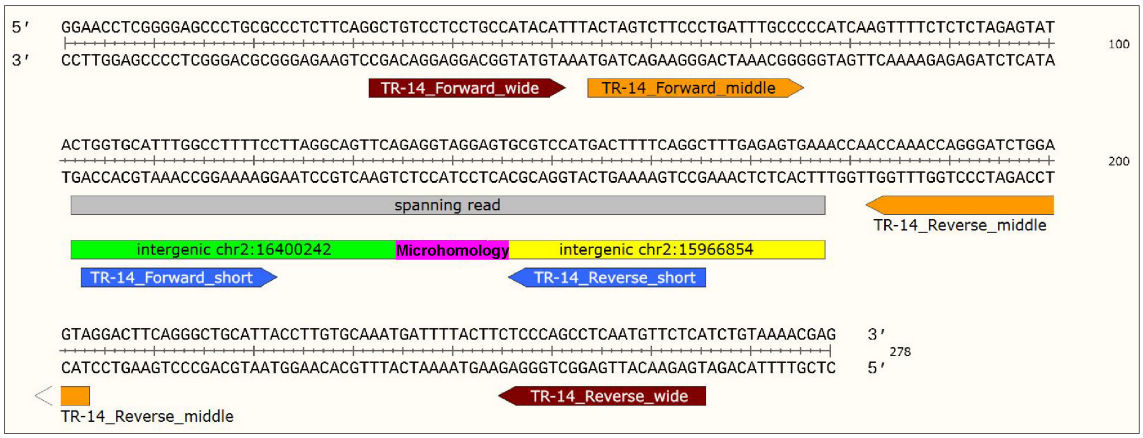

Figure 47: Scheme showing different PCR amplicon length approaches with different distances of the primer to the breakpoint/microhomology.
Primer pair in very short distance to the breakpoint with amplicon length of 63bp (blue color), in medium distance with amplicon length of 150bp (orange color) and in wide distance with amplicon length of 243bp (dark red color). The exact breakpoint sequence and the sequence flanking the breakpoint (rearrangement of two intergenic parts of chromosome 2, shown in yellow and green) are supported by a sequence spanning read (grey). This breakpoint further shows a microhomology (pink). The sequence outside the spanning read matches the GRCh37 (hg19) reference genome. Breakpoint no.15 intergenic chr2:16,400,242 - intergenic chr2:15,966,854 from cell line TR-14 is displayed.

A conventional PCR was then carried out using the primer pairs, and the PCR products were displayed by automated DNA electrophoresis. It turned out that the primer pairs, which were located within or close to the range of the sequence confirmed by a spanning read, represented a rather successful PCR with a single PCR product without or fewer side products. However, a too short PCR amplicon in

approximately 70bp often did not show a clear and single band in the electrophoresis. This was confirmed in case of the PCR breakpoint assay for the cell line TR-14; the primer pair with the medium distance to the breakpoint led to a positive result in DNA electrophoresis. Here, a single PCR product could be detected using the TR-14 DNA sample, which also has the correct bp length displayed by the electropherogram (Figure 48). If the use of a primer pair at a medium or wide distance to the breakpoint was successfully confirmed by electrophoresis, Sanger sequencing was carried out directly from the PCR product for further sequence validation. If exclusive or additionally the primer pair in short distance to the breakpoint showed a successful PCR product, the sequence of the PCR amplicon was too small in bp size to be obtained via Sanger sequencing (up to approximately 100bp).

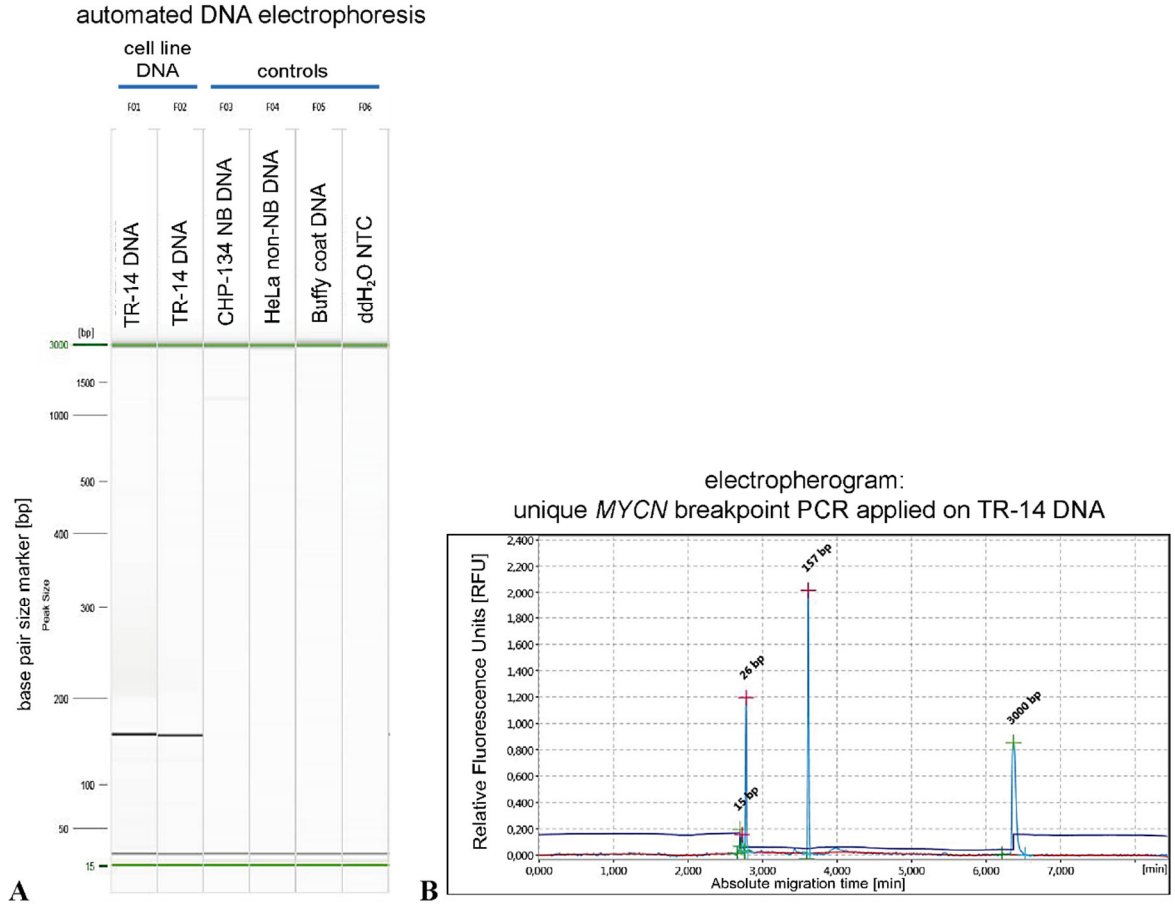

Figure 48: Automated DNA electrophoresis of conventional PCR assay designed to amplify the TR-14 breakpoint no.15 sequence.
(**A**) Validation of TR-14 cell line specific *MYCN* amplicon breakpoint DNA with conventional PCR and automated DNA electrophoresis of PCR products (controls from left to right: NB = CHP-134 cell line DNA, non-NB = HeLa cell line DNA, buffy coat = DNA from ten healthy blood donors, NTC = water). (**B**) Electropherogram of PCR amplicons obtained in TR-14 cell material confirmed the correct PCR amplicon size. The measured size of the actual PCR amplicon (157bp) approximated the length of the predicted amplicon (150bp).

Therefore, the PCR amplicon to be detected or rather the breakpoint sequence had to be determined from the original DNA sample using conventional or Topo™ TA Cloning™ via a Sanger sequencing of the vector. The PCR assay to detect the TR-14 breakpoint was long enough (breakpoint no.15; 150bp) to perform a direct Sanger sequencing from the resulting PCR product. The breakpoint sequence for TR-

14 detected with the *NB targeted NGS assay* could be confirmed in complete agreement using Sanger sequencing of the PCR product.

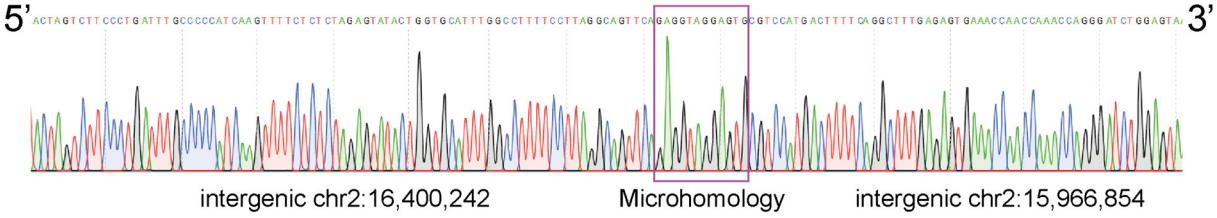

Figure 49: Electropherogram of Sanger sequencing of the PCR amplicon of TR-14 confirmed the exact *MYCN* breakpoint sequence.
Sanger sequencing confirmed the exact *MYCN* amplicon breakpoint sequence and length of the predicted amplicon (150bp).

PCR assays were designed and validated with DNA automated electrophoresis and Sanger sequencing for 20 breakpoints found in 7 cell lines (see Figure 128 and Table 15 in appendix). Applying the short, medium and wide distance primer approach, at least 60 different primer pairs were designed and tested. After the feasibility of establishing PCR assays at *MYCN* breakpoints of neuroblastoma cell lines could be demonstrated, *MYCN* breakpoints in primary and additional tumor samples from patients with neuroblastoma were also validated. Importantly, 35 breakpoints in 13 primary tumor samples could be detected with this technique as well (see Figure 129, Figure 130 and Table 17 in appendix). In addition to the available primary tumor samples, all other available samples were also tested with the same PCR assay for the respective patient. Those include DNA derived from second-look biopsies or whole section surgeries within the treatment course, from biopsies of metastases, from bone marrow samples gained from different locations of the iliac crest and from peripheral blood. Once a PCR assay was established and the sequence from a PCR product or cloning vector was validated using Sanger sequencing, the quantitative MRD assay for the sensitive detection of minimal residual cells was established subsequently. RQ-PCR assays as clinical use gold standard and ddPCR assays were developed according to MRD guidelines followed by the EuroMRD Consortium for leukemia MRD[161,587,671]. *NB breakpoint MRD assay* design for the detection of the *MYCN* breakpoint was also performed for the cell line TR-14 (see PCR assay in Figure 50). Primers flanking each breakpoint were combined with specific dual-labeled fluorescent probes to enable breakpoint detection via fluorescence detection of the unquenched FAM tag either during RQ-PCR in real-time PCR or at the endpoint of digitalized and single droplet reactions in ddPCR. The hydrolyzation probe, a 20 to 25-mer hydrolyzation oligonucleotide with FAM reporter dye at 5' end and BHQ1 quencher dye at 3' end was designed with preference >5 bases upstream of the breakpoint, or, due to repetitive sequences, downstream of the breakpoint. The probe was positioned as not to cover the breakpoint and be at least 5 bp away from any primer, otherwise, the results of the RQ-PCR displayed a poor fluorescence signal with less PCR efficacy. In very rare cases, the probe was designed to match a breakpoint-spanning sequence, if upstream and downstream sequences neighboring the breakpoint were both repetitive sequences. The exact breakpoint site was avoided for MRD assay design in mostly all cases, due to the slight possibility

that rearranged fragments are not directly attached and contain shared or additional nucleotides at the junction side (microhomologies[551]). The length of the amplicon PCR can also be a problem when designing a probe. There had to be enough space between the two primers to place a probe at a suitable location. In particular, if the PCR amplicon was a short amplicon (Figure 47), there were only a few possibilities for positioning a probe. The three oligonucleotides, forward primer, probe, and reverse primer, with an average length of 20 nucleotides in total, already require 60 nucleotides of the amplicon length. Therefore, with a small amplicon of 70bp there was only 10 bp space available between the individual nucleotides. Consequently, either another breakpoint of the same sample that could be detected by a larger PCR amplicon was used for the design of the MRD assays, or a PCR from a combination of a *short distance amplicon PCR primer* and a *medium/wide distance amplicon PCR primer* was used. If neither of the two options mentioned were feasible, a MRD assay was designed as a *short amplicon MRD PCR*. Care was taken, to ensure, that the spacer nucleotides between the oligonucleotides were relatively evenly distributed, e.g. with an amplicon length of about 70bp. The following assay design was used: forward primer (20 nucleotides) - 4bp empty space - probe (22 nucleotides) - 4bp empty space (exact breakpoint within this location) - reverse primer (20 nucleotides).

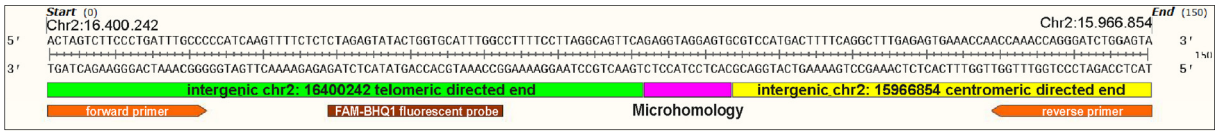

Figure 50: Design of MRD assay on specific *MYCN* breakpoint in *MYCN*-amplified TR-14 cell line.
MYCN amplicon breakpoint (No.15) in neuroblastoma cell line TR-14. Detailed picture shows the design of the PCR assay, using forward and reverse primer and a fluorescent FAM-BHQ1 probe needed for RQ-PCR and ddPCR supported MRD detection.

After designing a suitable MRD assay employing a hydrolysis FAM-BHQ1 probe, the probe was tested together with the PCR assay primers in an RQ-PCR approach and conditions were then optimized for breakpoint detection. The sample DNA was spiked-in normal DNA from purified mononuclear blood cells pooled from 10 healthy donors in a serial dilution series.

Table 6: Sensitivity of RQ-PCR and ddPCR assays for detection of *MYCN* associated breakpoints in neuroblastoma cell lines.

Number of sample analyzed with RQ-PCR/ddPCR	Name of cell line	Breakpoint number	Result RQ-PCR assay sensitivity	Result ddPCR assay sensitivity
1	IMR-5	2	10^{-4}	10^{-4}
2	SK-N-BE	3	10^{-5}	10^{-6}
3	LAN-5	7	10^{-6}	10^{-6}
4	NGP	10	10^{-6}	10^{-6}
5	KELLY	12	10^{-4}	10^{-5}
6	KELLY	13	10^{-4}	10^{-6}
7	TR-14	16	10^{-6}	10^{-6}
8	SK-N-DZ	17	10^{-4}	10^{-6}

With this standard series, a dilution of the tumor cells within the normal healthy cells of the body could be simulated. The standard series for a cell line or patient tumor sample functioned also as a tool to adjust the annealing temperature of the MRD assay (in 1°C steps from 60-70°C), which is crucial to figure out the highest detection sensitivity. *NB breakpoint MRD assay* sensitivity detection limits were first assessed for selected *MYCN* breakpoints identified in neuroblastoma cell lines using *NB targeted NGS assay*. From 20 validated *MYCN* breakpoints found in cell lines (see Table 14 in appendix), eight breakpoints (numbered 1-8 for clarity; see Table 6) in seven cell lines underwent further MRD analysis by RQ-PCR and ddPCR, with amplicons detectable in single tumor cells among up to 10^6 total cells. An optimized RQ-PCR and ddPCR assay for breakpoint number 15 robustly detected TR-14 neuroblastoma cells among up to 10^6 total cells (Figure 51).

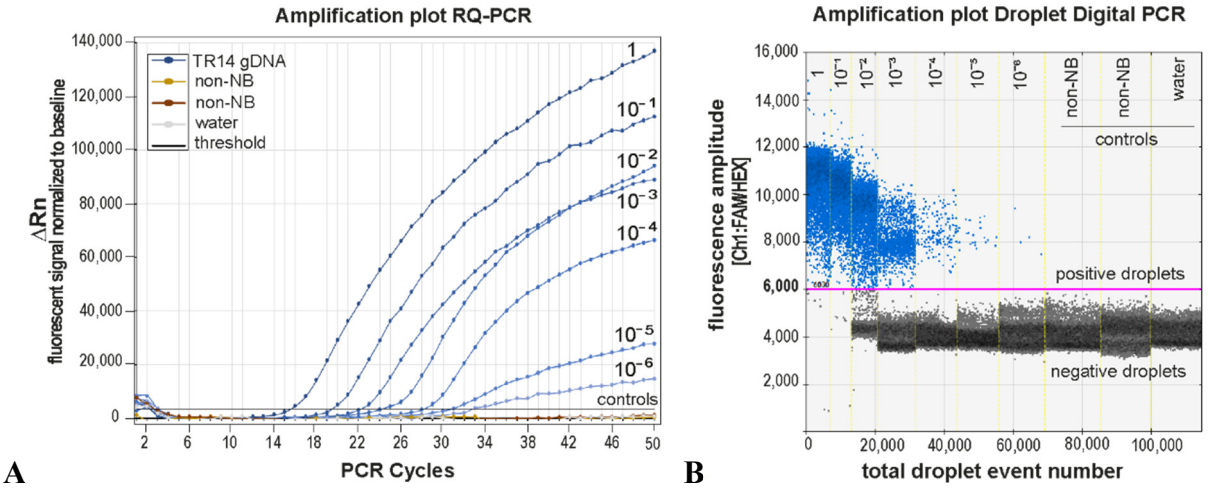

Figure 51: Results of MRD assay on a specific *MYCN* associated breakpoint in the *MYCN*-amplified TR-14 cell line. **(A)** Amplification plot of RQ-PCR analysis, highlighting a detection sensitivity of the TR-14 specific breakpoint of 10^{-6} within a spike-in dilution series experiment (controls: neuroblastoma cell line DNA, non-neuroblastoma cell line DNA, DNA from 10 healthy blood donors, water). **(B)** Amplification plot of ddPCR, displaying a detection sensitivity of the TR-14 specific breakpoint of 10^{-6} within a spike-in dilution series experiment (controls: non-neuroblastoma cell line DNA, DNA from 10 healthy blood donors, water).

Based on all 8 MRD *MYCN* breakpoint assays in cell lines (Table 6), RQ-PCR sensitivity detection ranged from 10^{-4} to 10^{-6}. For comparison of RQ-PCR and ddPCR techniques, the same MRD assays with primer/probe pairs and PCR conditions were used to analyze breakpoints no. 1-8 in ddPCR assays on DNA from the cell lines with the serially diluted spike-in pool of mononuclear reference cells from 10 healthy donors. Even without individually optimizing ddPCR assay conditions, benchmarking using the 8 selected *MYCN* amplicon breakpoints confirmed a higher sensitivity across all breakpoints for ddPCR (Figure 52A and Table 6). Breakpoints 2-4 and 6-8 were detected at a sensitivity of 10^{-6}, and breakpoint 5 was detectable with a sensitivity of 10^{-6}. Subsequently, *NB breakpoint MRD assays* were developed for 14 of 35 *MYCN* amplicon breakpoints identified in 13 primary neuroblastoma samples (see Table 7). Sensitivity was also tested in these assays using the serially diluted spike-in pool of mononuclear reference cells, and assays were conducted using both RQ-PCR and ddPCR.

Table 7: Sensitivity of RQ-PCR and ddPCR assays for the detection of *MYCN* associated breakpoints in neuroblastoma tumors.

Number of samples analyzed with RQ-PCR/ddPCR	Patient number	Breakpoint number	Result RQ-PCR assay sensitivity	Result ddPCR assay sensitivity
1	1	4	10^{-5}	10^{-5}
2	2	7	10^{-6}	10^{-6}
3	2	8	10^{-3}	10^{-6}
4	3	10	10^{-6}	10^{-6}
5	4	12	10^{-6}	10^{-6}
6	5	13	10^{-6}	10^{-6}
7	6	14	10^{-5}	10^{-5}
8	7	18	10^{-4}	10^{-6}
9	8	19	10^{-6}	10^{-6}
10	9	24	10^{-5}	10^{-5}
11	10	25	10^{-4}	10^{-4}
12	11	27	10^{-5}	10^{-6}
13	12	29	10^{-5}	10^{-6}
14	13	33	10^{-4}	10^{-4}

For these 14 breakpoint assays, sensitivity ranged from 10^{-4} to 10^{-6} using ddPCR and 10^{-3} to 10^{-6} using RQ-PCR (Figure 52B and Table 7). Altogether, ddPCR detected *MYCN* amplicon breakpoints more sensitively in both cell lines and tumor samples. These benchmarking results define a framework for establishing sensitive MRD assays using either RQ-PCR or ddPCR and based on patient-individual *MYCN* amplicon breakpoints.

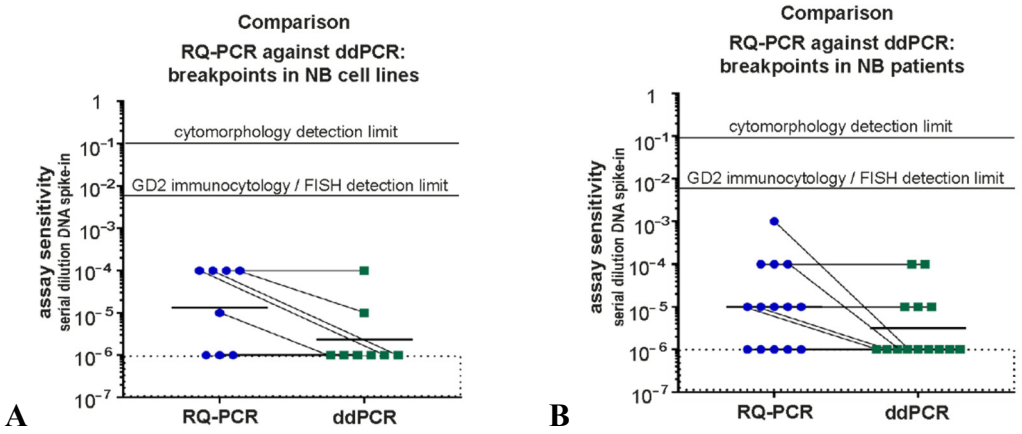

Figure 52: Comparison of detection sensitivity from RQ-PCR and ddPCR *NB breakpoint MRD assays*.
A higher sensitivity of *MYCN* breakpoint detection could be confirmed for ddPCR over RQ-PCR technique. **(A)** MRD assays designed for detection of 8 *MYCN* breakpoints in 7 neuroblastoma cell lines (**B)** MRD assays designed for detection of 14 *MYCN* breakpoints in 13 neuroblastoma tumor samples.

3.1.2.2 Stable *MYCN* breakpoints can be detected with designed PCR and MRD assays over the course of the disease

As a prerequisite for using the breakpoints as MRD markers, initially the clonal and sequence stability of the *MYCN* amplicon breakpoints was assessed using *NB targeted NGS assay*.

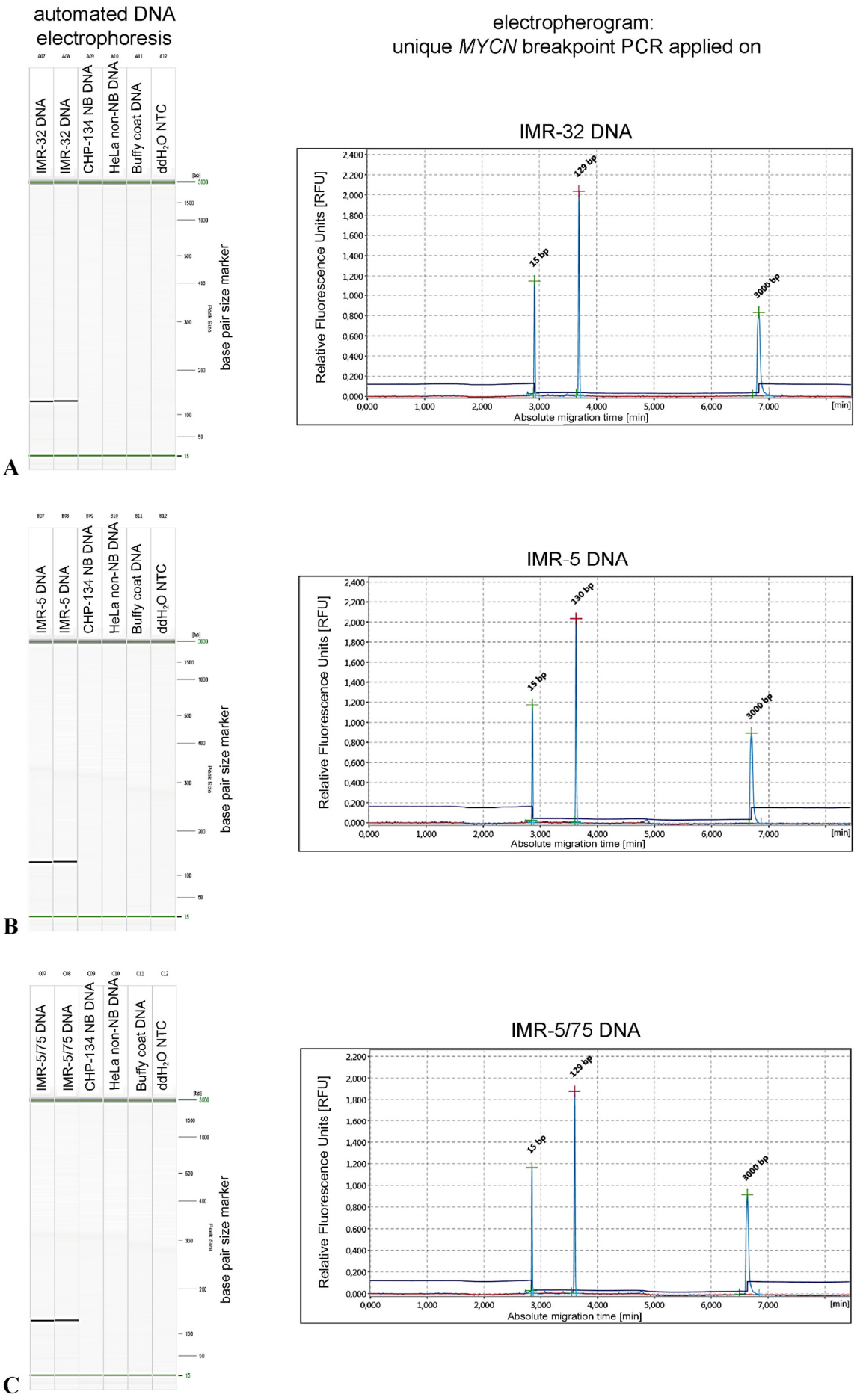
automated DNA electrophoresis
electropherogram: unique *MYCN* breakpoint PCR applied on
IMR-32 DNA
IMR-32 DNA
CHP-134 NB DNA
HeLa non-NB DNA
Buffy coat DNA
ddH2O NTC
base pair size marker
Relative Fluorescence Units [RFU]
Absolute migration time [min]
15 bp
129 bp
3000 bp
A
IMR-5 DNA
IMR-5 DNA
130 bp
B
IMR-5/75 DNA
IMR-5/75 DNA
C

A first approach to this topic was the NGS panel examination of neuroblastoma cell lines and their associated sub-clones (3.1.1). Therefore, the parental cell line IMR-32 with the subclones IMR-5 and IMR-5/75 and the parental cell line SK-N-BE with the subclone BE(2)-C were examined in more detail for shared *MYCN* breakpoint sequences. With reference to the *NB targeted NGS assay* results (Table 14 in appendix and 3.1.1.4), it can be assumed that all parental breakpoints of IMR-32 and SK-N-BE can be recovered applying a PCR assay to the subclone DNA. As an example for these groups, the PCR detection of the recurrent *MYCN* chr2:16,083,742 – intergenic chr2:67,014,561 breakpoint found with the *NB targeted NGS assay* (no. 1 in Table 14 in appendix section) will be shown below on the IMR-32 group. An exact same PCR assay was designed and applied to detect the *MYCN* breakpoint in the DNA of the cell lines IMR-32, IMR-5 and IMR5/75. The PCR products were then resolved using automated DNA electrophoresis and the size of the PCR product was displayed in addition using an electropherogram plot (see Figure 53). Within the DNA electrophoresis, the parental cell line IMR-32 and the subclones IMR-5 and IMR5/75 showed the same PCR product in run height and almost identical bp size. It should also be emphasized that the size of the product in the electropherogram only deviates by 1bp (+1bp for IMR-5). These results strongly suggest that the displayed product is the same PCR amplicon with an identical *MYCN* breakpoint. To further validate the breakpoint and to check sequence similarities, Sanger sequencing of the PCR products was carried out (see Figure 54).

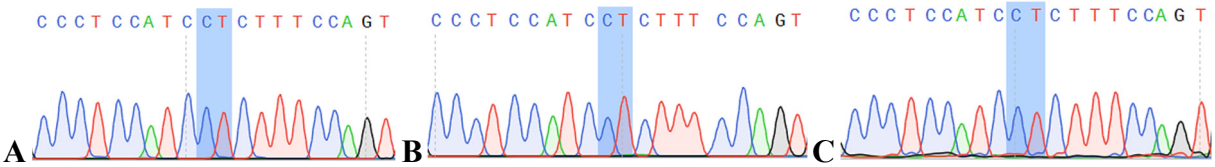

Figure 54: Validation of the *MYCN* breakpoint sequence within parental cell line IMR-32 and sub-clones IMR-5 and IMR5/75 using Sanger sequencing.
Sanger sequencing electropherograms of PCR amplicons obtained in IMR-32 cell line DNA (**A**), IMR-5 cell line DNA (**B**) and IMR5/75 cell line DNA (**C**), confirmed the exact breakpoint sequence. The explicit location of the chr2:16,083,742 – intergenic chr2:67,014,561 breakpoint is highlighted in blue shade.

The results of the Sanger sequencing and the alignment of the detected breakpoint sequences showed an exact sequence homology in all three PCR product samples. The *MYCN* breakpoint located at position *MYCN* chr2:16,083,742 – intergenic chr2:67,014,561 consists of the same sequence in the parent cell line IMR-32 and in the two associated sub-clones, IMR-32 and IMR5/75.

< Figure 53: Validation of a *MYCN* breakpoint within parental cell line IMR-32 and sub-clones IMR-5 and IMR5/75 with conventional PCR.
Automated DNA electrophoresis and associated electropherogram from conventional PCR (**A**) PCR based *MYCN* breakpoint detection in the cell line IMR-32. (**B**) PCR assay shows a similar product with almost identical size in cell line IMR-5 as seen in IMR-32. (**C**) PCR assay shows as well a similar product at the same size in cell line IMR5/75 as seen in IMR-32. The measured size of the actual PCR amplicon (129/130bp) approximated the length of the predicted amplicon (124bp; see Table 15 in appendix section, chr2:16,083,742 – intergenic chr2:67,014,561). (Controls from left to right: neuroblastoma cell line DNA = CHP-134, non-neuroblastoma cell line DNA = HeLa , non-neuroblastoma cell line DNA = DNA from ten healthy blood donors, NTC = water).

Likewise, all three *MYCN* breakpoints of the parental SK-N-BE cell line detected with the *NB targeted NGS assay* were validated using conventional PCR and Sanger sequencing and could also be verified in the sub-clone BE(2)-C (data not shown). Therefore, the possibility of the detection of a stable, conserved *MYCN* breakpoint in two different tumor samples from the same patient is given. For paired tumor biopsies at primary diagnosis and relapse time points of patient no. #2 and no. #5 (Table 16 in appendix section) it could be shown (3.1.1) that the two paired samples contain the same *MYCN* breakpoints with the very same sequence. Therefore, a PCR assay was designed based on the *MYCN* breakpoint sequences from the primary disease tumor material. As an example for these two patients, the PCR and MRD detection of the *MYCN* breakpoint no. 13 will be shown below on patient no. #5. The PCR assay was designed utilizing an alignment of a (breakpoint-) spanning read, one upstream encompassing read and one downstream encompassing read, which were located adjacent to the spanning read (see Figure 55).

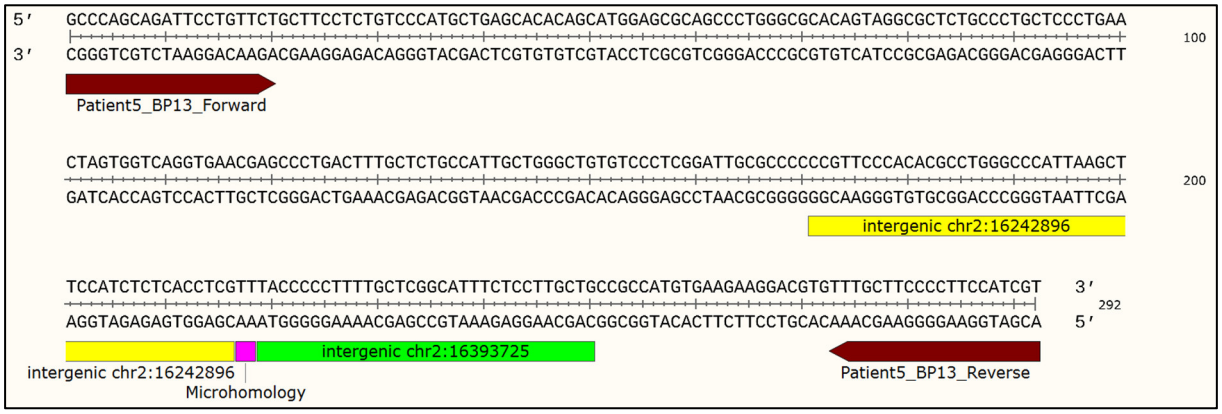

Figure 55: Scheme showing *MYCN* breakpoint PCR assay design and predicted PCR amplicon for neuroblastoma patient number 5.
PCR primer pair (dark red color) was arranged at a wide distance to each other with a predicted PCR amplicon length of 292bp. The breakpoint consists of a rearrangement of two intergenic parts of chromosome 2 (intergenic chr2:16,242,896 – intergenic chr2:16,393,725), shown in yellow and green. This breakpoint further shows a microhomology (5'-TT-3'; pink color). The sequence outside the spanning read matches the GRCh37 (hg19) reference genome. Breakpoint no.13 is displayed (see Table 17 in appendix section).

Amplification of these breakpoint regions with a PCR assay and validation with Sanger sequencing resulted in the exact same sequence, which means that all breakpoints detected in the primary tumor samples were perfectly preserved in the corresponding relapsed tumor. The data shows from both points in time the confirmatory PCR and the alignment from Sanger product sequencing exemplarily for the breakpoint no. 13 present in the paired longitudinal tumor samples from patient no. #5 (Figure 56). After validation of the PCR assay, it was possible to use the primers from this assay for the design of an MRD assay, or rather to extend the PCR assay to an *NB breakpoint MRD assay*. For this purpose, a FAM-BHQ1 probe was designed and added, which binds in front of the breakpoint to be detected in the upstream area of the intergenic chr2:16,242,896 breakpoint fragment site (see for probe sequence Table 17 in appendix). The DNA of both tumor samples, from primary and relapse material, was then spiked-in buffy coat DNA for each sample individually. The samples were then measured using the custom-designed MRD assay applying the RQ-PCR and ddPCR technique (Figure 57).

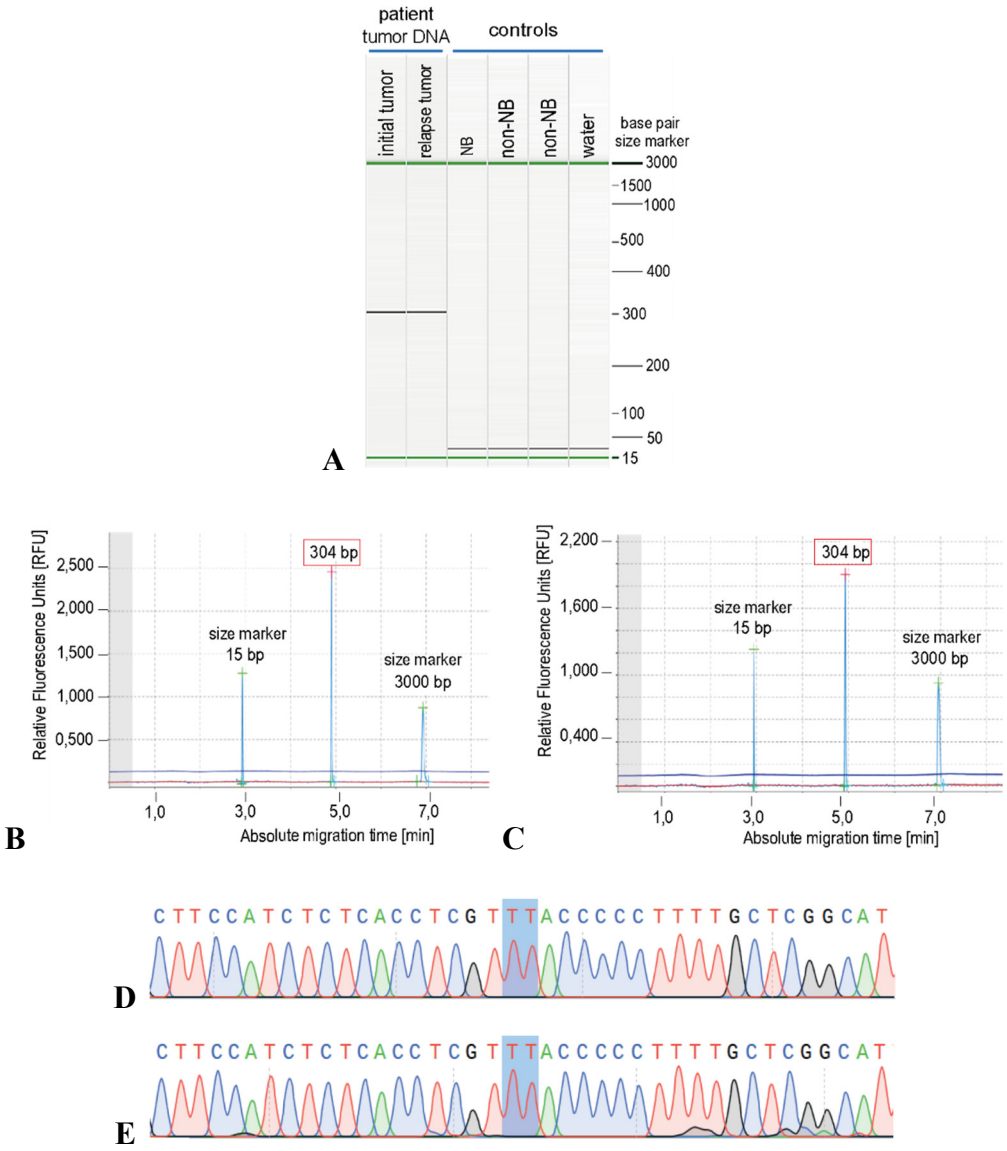

Figure 56: Validation of the patient-specific *MYCN* associated breakpoint in the initial and relapse tumor DNA of patient no. 5 with conventional PCR and Sanger sequencing.
(**A)** Automated DNA electrophoresis shows a PCR product band at the same level in both the primary and relapse tumor material (controls from left to right: neuroblastoma cell line DNA = KELLY, non-neuroblastoma cell line DNA = HeLa, non-neuroblastoma DNA = Buffy coat from ten healthy blood donors, NTC = water). DNA gel electropherograms of PCR amplicons obtained in initial tumor material (**B)** and relapse tumor material (**C)** confirmed the very same amplicon bp size. The measured size of actual PCR amplicon (304bp) approximated the length of the predicted amplicon (292bp). Sanger sequencing electropherograms of PCR amplicons obtained in initial tumor material (**D)** and relapse tumor material (**E)** confirmed the exact breakpoint sequence. The explicit location of the breakpoint is highlighted in blue shade (intergenic chr2:16,242,896 – intergenic chr2:16,393,725).

Afterwards, amplification signals, MRD PCR performance and the archived sensitivity of the results were evaluated. The unique *MYCN* breakpoint could be detected with the MRD assay as done before with the PCR assay without the probe and sequence validation using Sanger sequencing. Overall, the same sensitivity depth of 10^6 could be achieved when using primary and relapse DNA material and applying both methods, RQ-PCR and ddPCR.

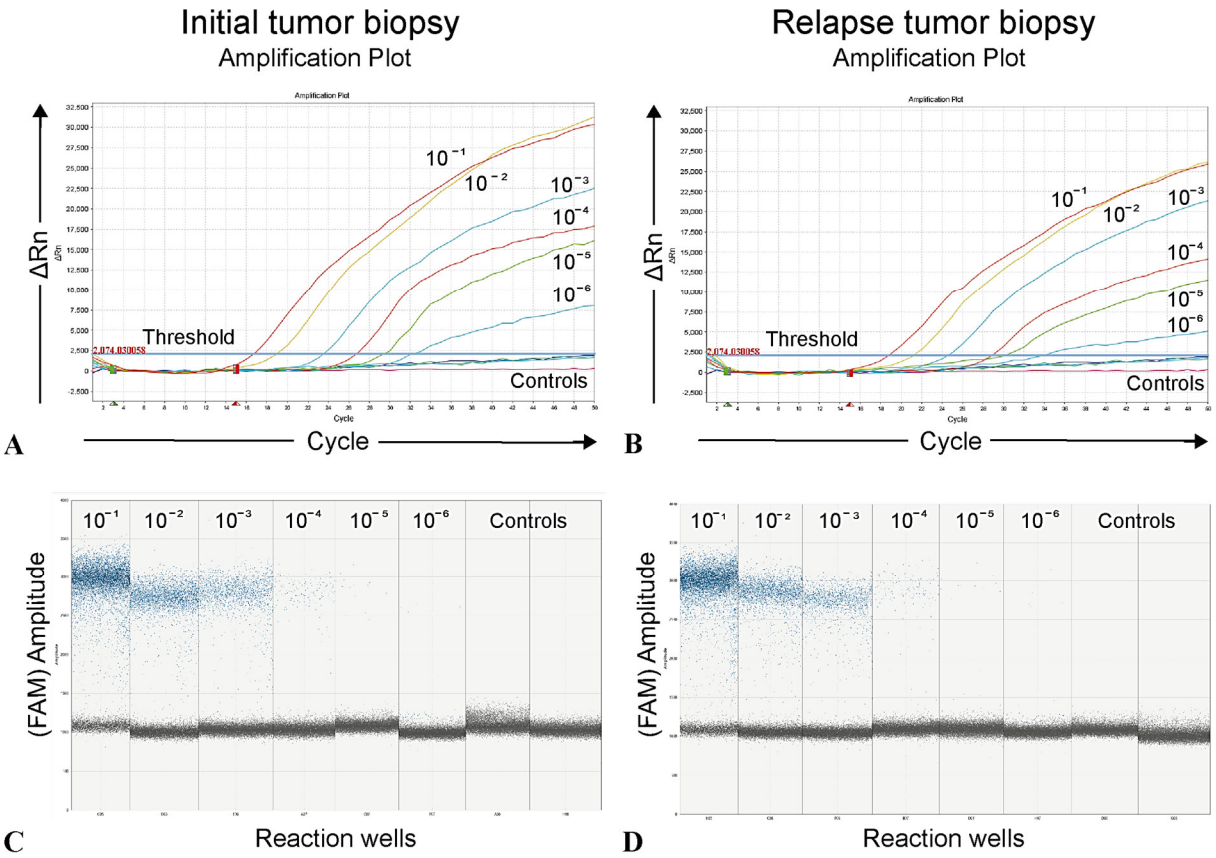

Figure 57: Results of *MYCN* associated breakpoint MRD detection in patient primary and relapse neuroblastoma tumor material.
Amplification plot of RQ-PCR analysis of primary (**A)** and relapse (**B)** tumor DNA samples, showing PCR amplification fluorescence signals of the exact breakpoint (controls: DNA from 10 healthy blood donors, water). Amplification plot of ddPCR, displaying analysis of primary (**C)** and relapse (**D)** tumor DNA samples, showing PCR amplification fluorescence signals of the exact breakpoint (controls: DNA from 10 healthy blood donors, water). Furthermore, this *NB breakpoint MRD assay* shows a sensitivity of 10^6 within a spike-in dilution series using both techniques, RQ-PCR and ddPCR.

These data demonstrate that the *MYCN* amplicon breakpoints persist through the course of the disease up to a relapse. The results point towards the possibility, that an exclusive breakpoint sequence could not only be found in a biopsy of a primary and associated relapse tumor, but could also be detected in tumor cells that were distributed in the body. This makes the unique *MYCN* breakpoint sequences applicable, biological MRD markers, which are patient-specific and consistent in their sequence through the disease.

3.1.2.3 *NB MYCN breakpoint MRD assays* reveal dynamic changes in a pilot patient cohort

The development and application of unique *NB MYCN breakpoint MRD assays* on neuroblastoma cell line and patient DNA has already been achieved. It could also be shown that the *MYCN* breakpoint is stable over the course of the disease. In preparation for clinical use, patient-specific *MYCN* MRD assays were used for the detection of residual cells in bone marrow samples. The framework for the *MYCN* breakpoint MRD assay development was applied to a pilot cohort of 6 patients with *MYCN*-amplified high-risk neuroblastoma (patients #8-13 in Table 16 in appendix section). Patients were treated

according to the German neuroblastoma trial (NB2004) or the German Neuroblastoma Registry (NB Registry 2016)[30,236,237,495]. Diagnostic biopsies were prospectively collected from the primary and relapsed neuroblastomas in addition to bone marrow aspirates collected at initial diagnosis, early during treatment or at relapse and at subsequent time points during therapy to support MRD monitoring over the course of disease. At least one specific *MYCN* breakpoint was selected for each patient, for which a personalized *NB breakpoint MRD assay* using the MRD pipeline was developed and validated. More detailed information on the individual MRD assays can be found in Table 17 in the appendix section. MRD levels were assessed in DNA isolated from purified mononuclear cells from the bone marrow aspirates using the patient's personalized assay. Neuroblastoma was classified as high-risk in all 6 patients based on the presence of the *MYCN* amplification in the primary tumor detected with FISH and the *NB targeted NGS assay*. In addition, nuclear medical images of the sympathetic nervous system using ^{123}I-mIBG scintigraphy combined with SPECT/low-dose-CT were collected throughout a patient's disease. The images were preferably compiled from the same time point as the bone marrow puncture was carried out. (These two examinations are often carried out under the same anesthesia). MRD detection from bone marrow samples added precise quantification of tumor cell burden, revealed persistence of MRD in samples in which no neuroblastoma cells were detectable by cytology and GD2 immunohistochemistry, mirrored the patient's response to therapy, and showed different patterns among the patients (Figure 58 to Figure 63). Considering the clinical and MRD courses of the cohort overall, two different groups can be identified, which show a different response to the cancer therapies and thus also a different MRD level. In patients #8, #10 and #13, initially high MRD levels were observed that dropped early (patients #8 and #10) or late (patient #13) in therapy, mirroring the good response to therapy observed in routine bone marrow analysis as well as clinical assessment (Figure 58, Figure 60 and Figure 63). Patient no. #8 (Figure 58) showed no detectable neuroblastoma cells within initial and subsequent bone marrow smears in routine diagnostics applying cytology. However, the patient-individual MRD assay, a significant level of neuroblastoma cells within the sample at the time point of diagnosis was detected. The MRD level subsequently decreases to a negative MRD in the follow-up samples. In line with these data, patient #8 is in long-term remission at the time of writing (Figure 58). In patient no. #10 (Figure 60), cytology and GD2 immunohistochemistry revealed the presence of neuroblastoma cells in the initial bone marrow smears. However, a second bone marrow smear after chemotherapy revealed no neuroblastoma cell infiltration, based on cytology and GD2 immunohistochemistry, indicating treatment response. In line with cytology and GD2 immunohistochemistry, we could detect a very high level of neuroblastoma cells within the initial bone marrow aspirate using the patient-individual MRD assay. Although this MRD level decreased significantly in the subsequent bone marrow sample, MRD was still detectable at a level of 10^{-3}, demonstrating only partial response in contrast to cytology and GD2 immunohistochemistry. No subsequent samples could be obtained, as the patient unfortunately died of veno-occlusive disease. Patient no. #13 (Figure 63) had fluctuating diagnostic results for conventional and breakpoint MRD

diagnostics at presentation. First, the bone marrow was massive infiltrated, detected by cytology, GD2 immunohistochemistry and breakpoint MRD. During therapy, the infiltration went down. Cytomorphology was not detecting neuroblastoma cells after 24 days, whereas GD2 immunohistochemistry and *MYCN* breakpoint MRD were positive for tumor cells still. No subsequent samples could be obtained, as the patient unfortunately died due to therapy toxicity, veno-occlusive disease and pulmonary hemorrhage. The remaining three patients presented a more varied response to treatment. Patient no. #9 (Figure 59) showed no detectable neuroblastoma cells within therapy and subsequent bone marrow smears in routine diagnostics applying cytology, but nests of GD2-positive cells in the third bone marrow smear occurred. The MRD assay, however, revealed positive MRD levels at time of relapse, and MRD persisted during subsequent salvage therapy. This was in line with clinical presentation and imaging, which showed an increase of the tumor burden and local expansion within the abdomen after initial response to the treatment. This patient finally succumbed to the disease. Two other patients showed increased MRD levels after initial diagnosis in patient #11 (Figure 61) or increased following an initial eradication in patient #12 (Figure 62). For patient no. #11 (Figure 61) cytology and GD2 immunohistochemistry showed a low infiltration of neuroblastoma cells in bone marrow samples within initiation of chemotherapy. In line with the standard diagnostics, MRD assessment revealed a presence of tumor cells within the bone marrow of the patient, but with a higher proportion. Almost a year later, the patient bone marrow samples present a vast infiltration with *MYCN* amplification positive tumor cells. Although the treatment was prolonged using radiation therapy, the patient died from high tumor burden. Patient no. #12 (Figure 62) showed a very low tumor cell infiltration of bone marrow using cytology and GD2 immunohistochemistry techniques, which disappeared after 47 days of treatment. Until the last sampling, the patient showed no neuroblastoma cells detectable with conventional methods. However, neuroblastoma MRD based on *MYCN* breakpoint detection reveals a small number of tumor cells, which start to rise again after 159 days, but subsequently dropped after 305 days. The patient is still in remission at time of writing after an experimental therapy comprised of HSCT and continuing treatment with an ALK inhibitor.

The diagnostic pipeline for personalized MRD monitoring based on *MYCN* amplicon breakpoints was feasible within the clinical treatment schedule and reliably represented the disease course in our pilot patient cohort. Taken together, these data show that *MYCN* amplicon breakpoints can serve as highly sensitive and stable surrogates for neuroblastoma cells to monitor MRD.

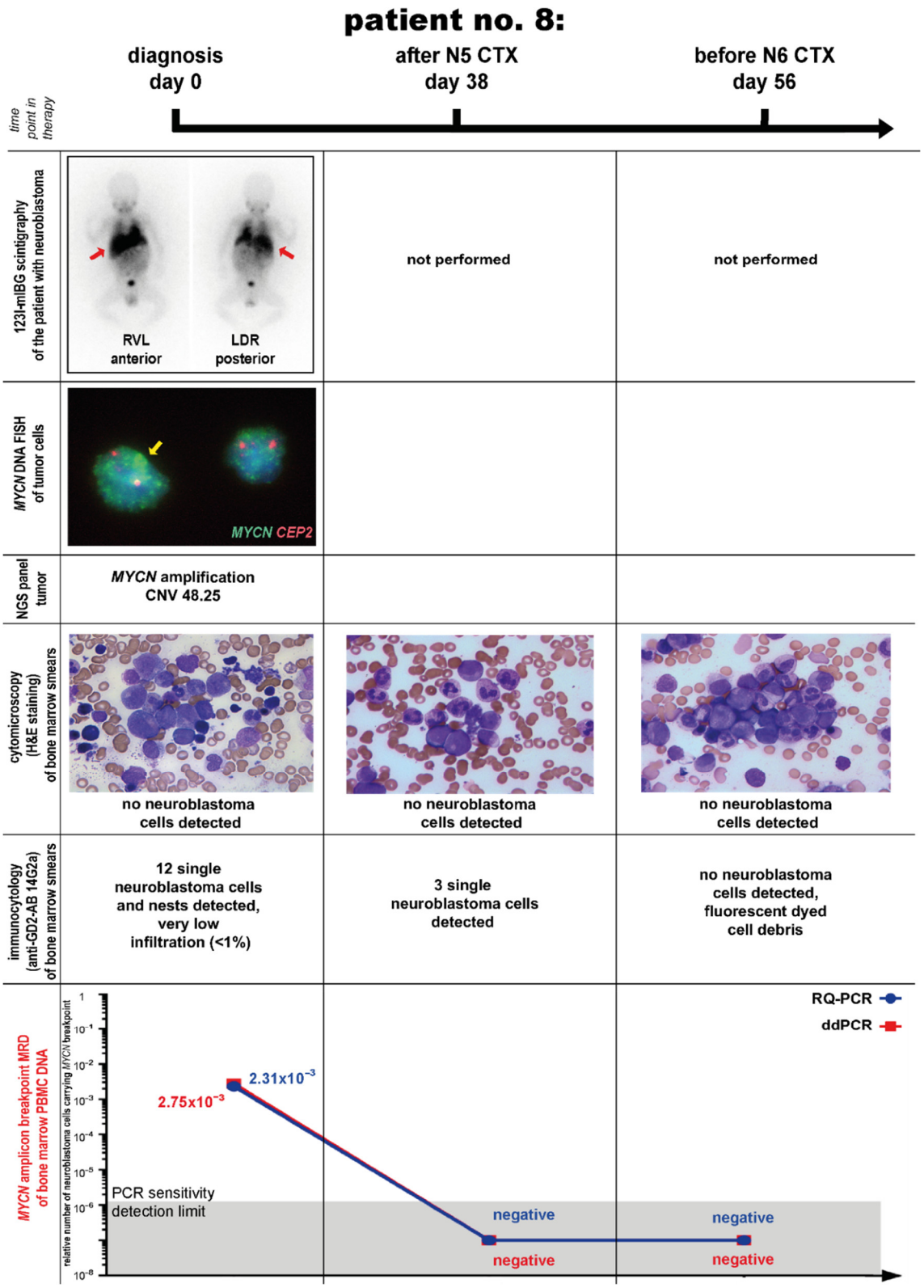

Figure 58: *MYCN* amplicon breakpoint MRD detection in comparison to established diagnostics for patient no. 8. ^{123}I-mIBG scintigraphy taken at diagnosis showed only localized tumors at right adrenal gland with right kidney infiltration. FISH detection of tumor cells showed positive *MYCN* amplification (green color). *MYCN* amplification with CNV of 48.25 was confirmed by *NB targeted NGS assay*. Neuroblastoma cells were not detected in bone marrow smears at diagnosis, after N5 CTX block (day 38) or before N6 CTX block (day 56) by conventional cytology or GD2 immunohistochemistry. The *NB MYCN breakpoint assay* revealed residual neuroblastoma cells in bone marrow at diagnosis using RQ-PCR and ddPCR, and a negative MRD level during follow-up. Today, the patient is in long-term remission. (R=right, V=ventral, L=left, D=dorsal).

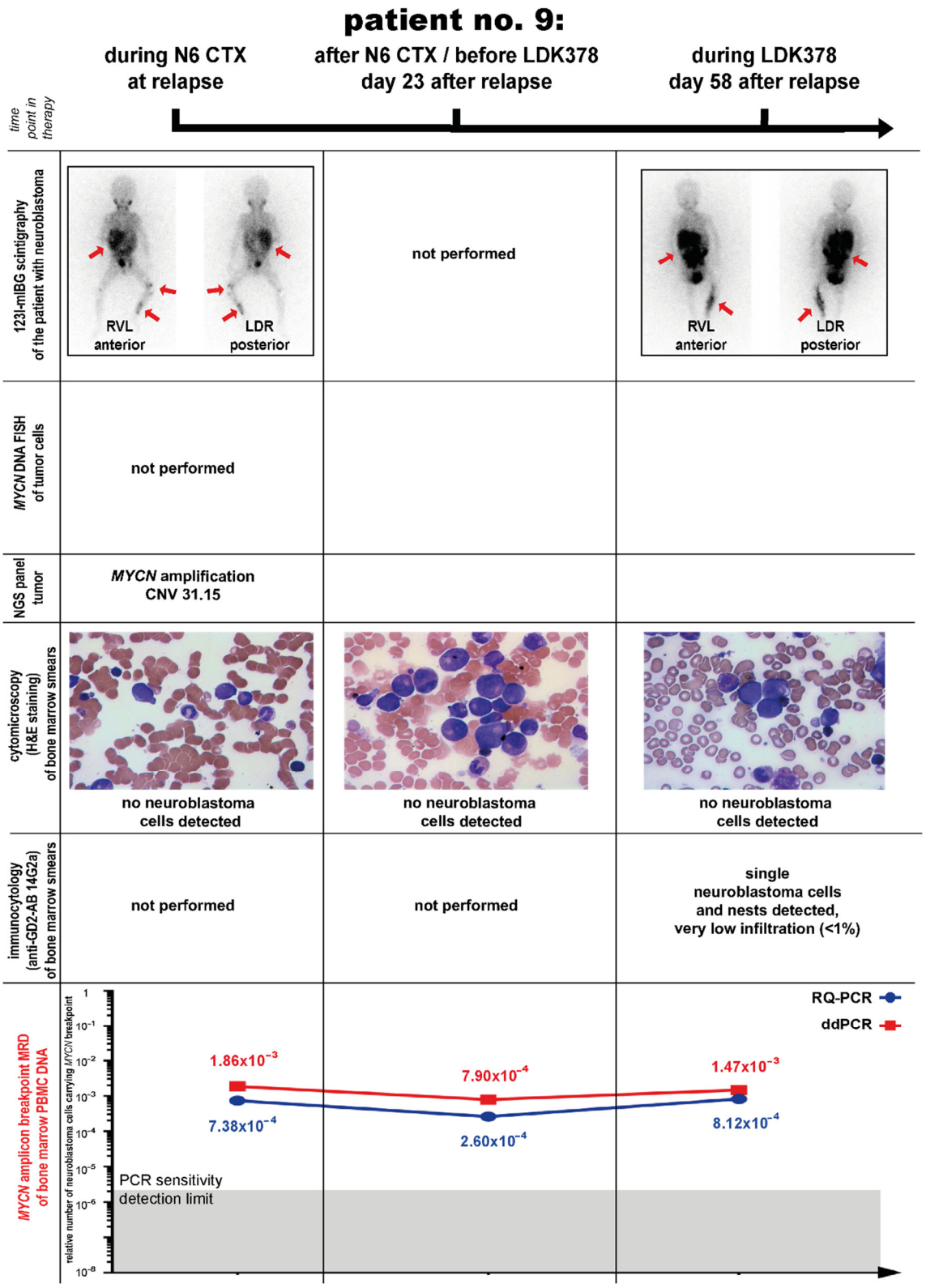

Figure 59: *MYCN* amplicon breakpoint MRD detection in comparison to established diagnostics for patient no. 9. Pictures of ^{123}I-mIBG scintigraphy showed abdominal tumor and extensive, metabolically active metastases. Later, progressive tumor development in the lateral abdominal wall and at metastatic sites. *MYCN* DNA FISH detection could not be performed due to lack of material; however, *MYCN* amplification with CNV of 31.15 was confirmed by *NB targeted NGS assay.* Neuroblastoma cells are not detected in bone marrow smears from any time point, and GD2 immunohistochemistry could only be performed within the last sample, showing a positive signal for neuroblastoma cells. MRD analysis revealed a constantly moderate level of the detected *MYCN* breakpoint. Unfortunately, this patient finally succumbed to the disease. (R=right, V=ventral, L=left, D=dorsal).

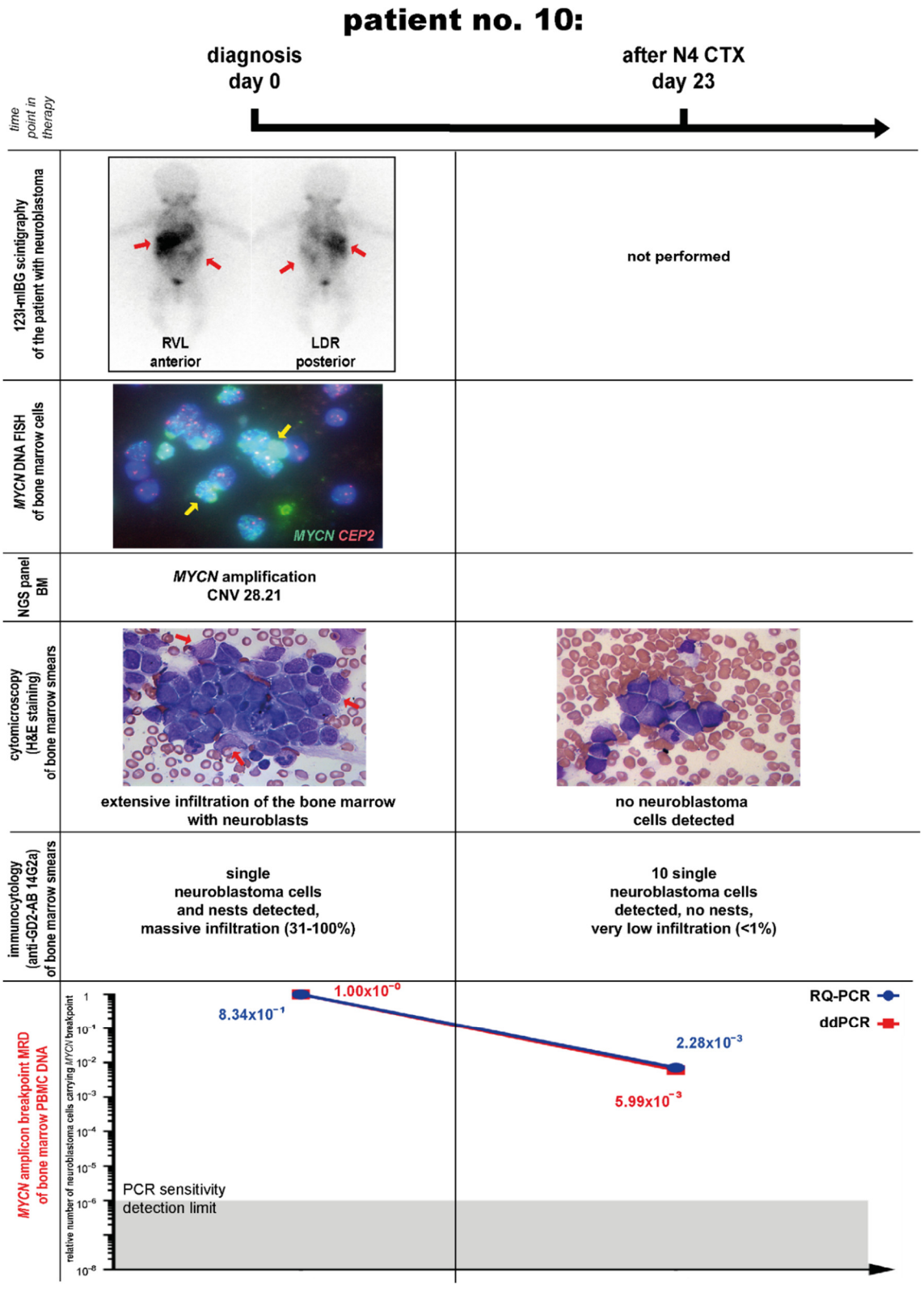

Figure 60: *MYCN* amplicon breakpoint MRD detection in comparison to established diagnostics for patient no. 10. The patient showed a tumor in both adrenal glands and metastasis in ^{123}I-mIBG scintigraphy. FISH detection of tumor cells showed positive *MYCN* amplification (green color). *MYCN* amplification with CNV of 28.21 was confirmed by *NB targeted NGS assay.* Neuroblastoma cells were seen in bone marrow smears at diagnosis by conventional cytology and GD2 immunohistochemistry, but were absent in a follow-up smear after the N4 CTX time point at day 23. The *NB MYCN breakpoint assay* revealed residual neuroblastoma cells and a high MRD level in bone marrow after N4 CTX. Follow-up samples could not be obtained as unfortunately the patient died of veno-occlusive disease. (R=right, V=ventral, L=left, D=dorsal).

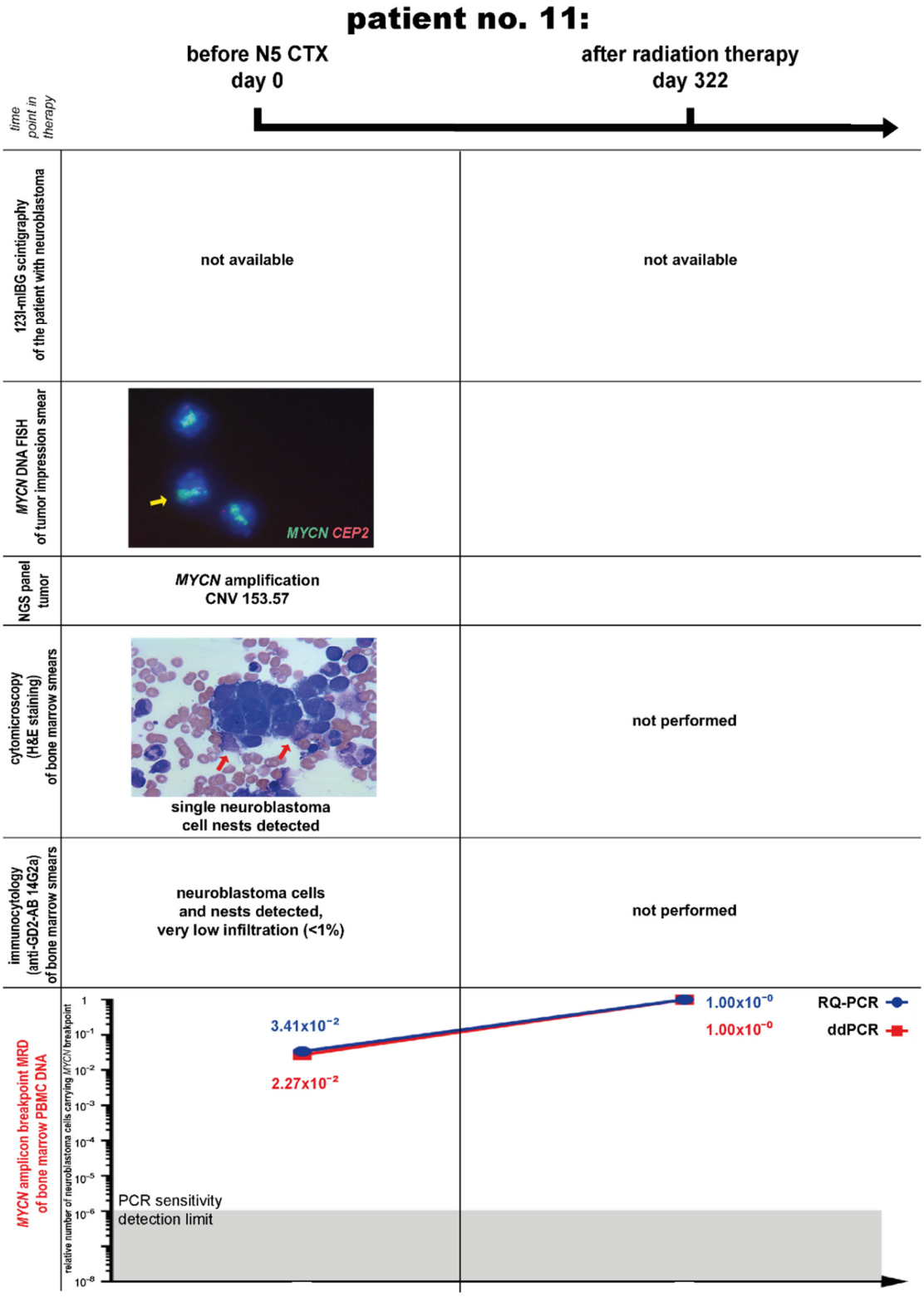

Figure 61: *MYCN* amplicon breakpoint MRD detection in comparison to established diagnostics for patient no. 11. Radiological findings displayed tumor appearance in the left adrenal gland and metastasis of the lymph nodes (pictures not available). FISH detection of tumor cells showed positive *MYCN* amplification (green color). A high *MYCN* amplification within the tumor of CNV of 153.57 was confirmed by *NB targeted NGS assay.* Conventional cytology and GD2 immunohistochemistry showed a low infiltration of neuroblastoma cells in bone marrow within initiation of chemotherapy at Charité. *NB breakpoint MRD assay* reveals residual cells during the therapy, as seen by cytology. Later, the cells outgrow to a very high MRD level. Follow-up samples could not be obtained as the patient responded only moderately to therapy and later succumbed to the disease. (R=right, V=ventral, L=left, D=dorsal).

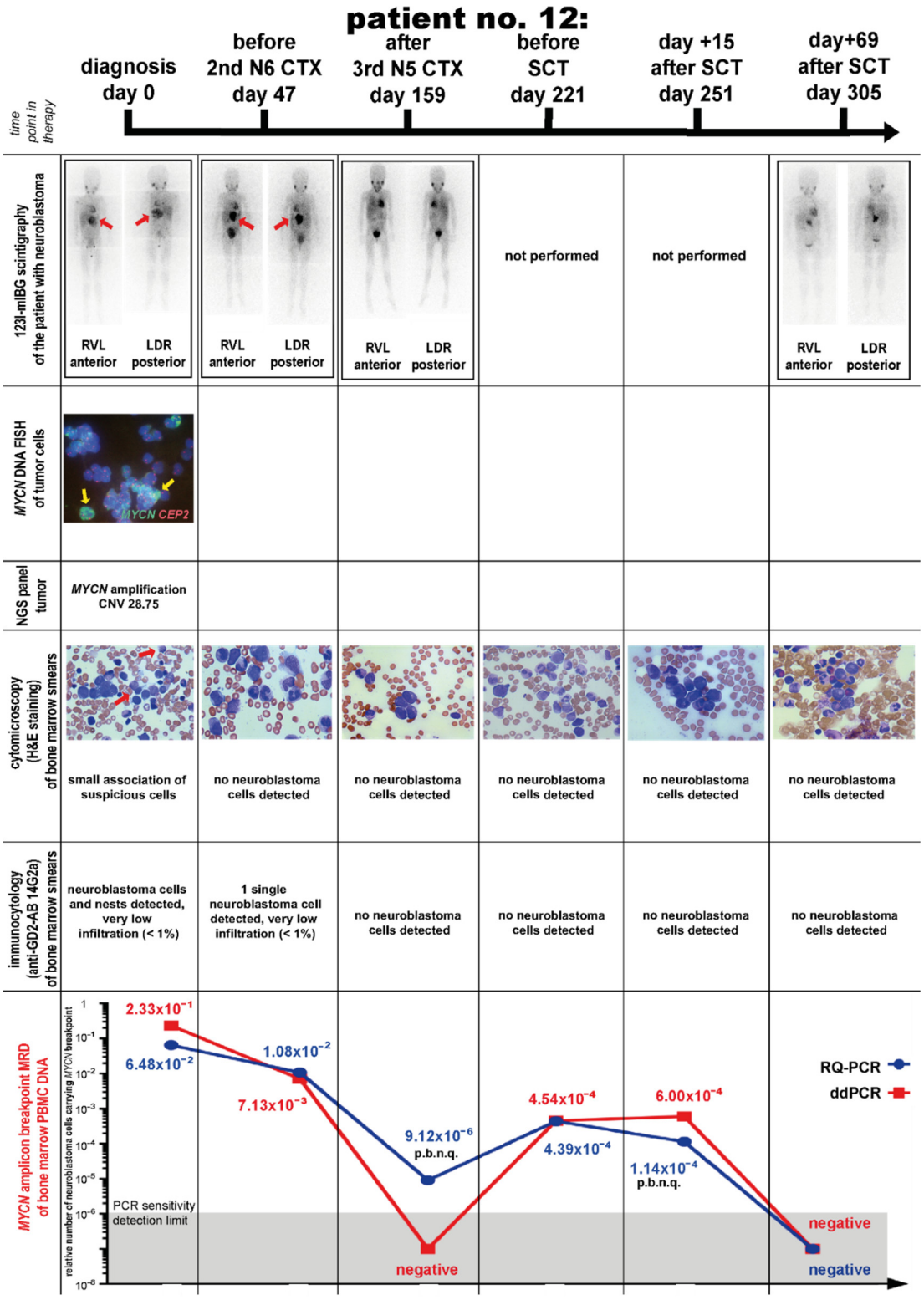

Figure 62: *MYCN* amplicon breakpoint MRD detection in comparison to established diagnostics for patient no. 12. ^{123}I-mIBG scintigraphy taken at diagnosis showed a mass in the abdomen and suspected bone marrow involvement. Later, no evidence of a lesion could be seen. FISH detection of tumor cells showed positive *MYCN* amplification (green color). *MYCN* amplification of the tumor with CNV of 28.75 was confirmed by *NB targeted NGS assay*. Patient showed a very low tumor cell infiltration of bone marrow using cytology and GD2 immunohistochemistry techniques, which disappeared after 47 days of treatment. *NB breakpoint MRD assay* reveals a small number of tumor cells, which start to rise again after 159 days. The patient still is in remission after HSCT and continuing treatment with an ALK inhibitor. (R=right, V=ventral, L=left, D=dorsal, p.b.n.q.=positive but not quantifiable).

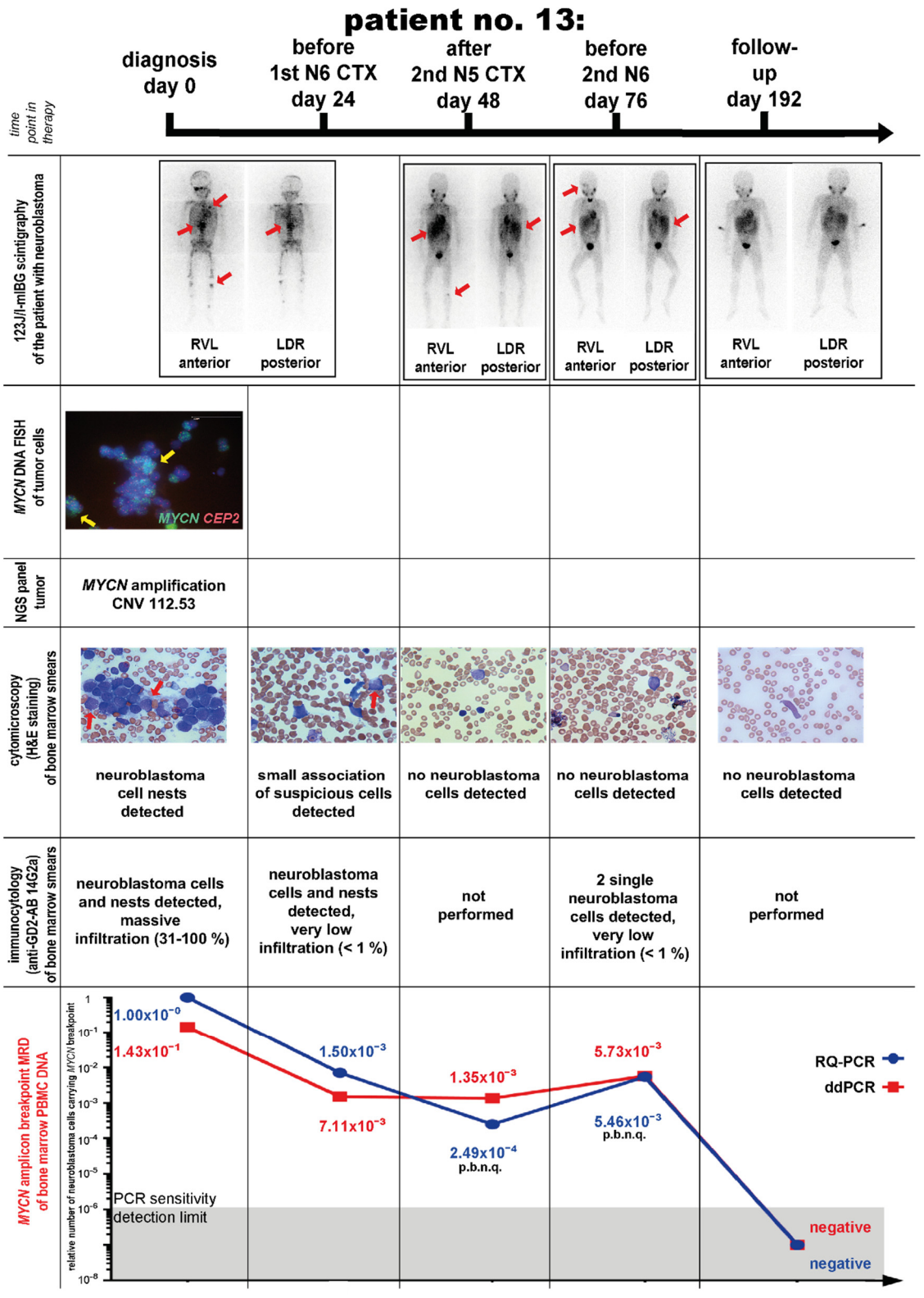

Figure 63: *MYCN* amplicon breakpoint MRD detection in comparison to established diagnostics for patient no. 13. ^{123}I-mIBG scintigraphy showed a positive mass in the abdomen, with disseminated bone metastases. In the course, the tumor burden is decreasing. FISH detection of tumor cells showed positive *MYCN* amplification (green color). *MYCN* amplification of the tumor with CNV of 112.53 was confirmed by *NB targeted NGS assay*. Patient presenting with fluctuate diagnostic results for conventional and breakpoint MRD diagnostics. First, the bone marrow was massively infiltrated, detected by cytology, GD2 immunohistochemistry and breakpoint MRD. During therapy, the infiltration went down. Unfortunately, the patient finally died due to complications of therapy. (R=right, V=ventral, L=left, D=dorsal, p.b.n.q.=positive but not quantifiable).

3.1.2.4 Practical, clinical implementation of *NB breakpoint MRD* detection

The *NB breakpoint MRD assay* could successfully be established and has already demonstrated the detection of stable *MYCN* breakpoints within the cell line and patient samples. The practical application of the assay to bone marrow aspirate samples was confirmed in a small, clinical retrospective cohort. The complete protocol was outlined, starting from the primary tumor biopsy going to MRD detection in follow-up samples using the latest, most sensitive RQ-PCR and ddPCR technology. For a practical application of the *NB breakpoint MRD assay* in a clinical environment, both the infrastructures in the clinical area and in the laboratory have to be taken into consideration. First of all, a piece of the neuroblastoma tumor must be taken at best directly from a tumor biopsy or section from a very early stage of the disease. The tumor should be collected as a snap-frozen sample (i.e. if it was cooled to −196 ° C in liquid nitrogen immediately or shortly after it was removed). This piece is then slowly thawed again on ice for DNA preparation or frozen sections are made. However, often there is no snap-frozen sample available, e.g. because the tumor biopsy or operation was performed long time ago, or there was no possibility in the clinic to store and transport a snap-frozen piece, or because it was simply used up for other diagnostic analyses. In this case, tumor pieces in FFPE or FFPE cuts are also suitable for tumor DNA isolation. Not only recent tumor sections can be examined, but also primary tumors in the case of a recurrent disease, or for example, if the relapse tumor is difficult to reach operatively to take a fresh biopsy. The DNA preparation from a piece of tumor only takes about 3h (taken into account the DNA isolation kit and possibly laser microdissection). The *NB targeted NGS assay* then is performed to analyze the tumor DNA for neuroblastoma specific mutations and rearrangements. If the patient is in outpatient medical treatment and was examined in the same quarter of the year, the costs for the sequencing can be covered by the German statutory health insurance companies. For this purpose, an "outpatient treatment referral form" is filled in, in which the diagnosis, the findings and the order for *NB targeted NGS assay* are noted. The tumor DNA is then send to NEO New Oncology GmbH or Institute of Hematopathology Hamburg together with the referral form, the submission document for molecular pathological examinations and, if necessary, a patient consent (if the patient is not included in a study trial including a consent for molecular genetically examinations). The DNA is processed for the *NB targeted NGS assay* within 5-7 days and a short report and the raw data of the sequencing (see 2.9.3) is provided by the company. Afterwards, the sequencing data can be examined for the presence of the patient-specific *MYCN* breakpoints and a summary list of the breakpoints can be generated (ranking of breakpoints is based on the number of reads supported), which takes around half a day to a day. The PCR assays are then designed based on the 2-4 most promising breakpoints and the primer for the PCR assays are ordered. The PCR assay design takes about half a day and the synthesis and delivery of the primer takes about two days. The PCR assays are then tested for each breakpoint, which is at least three PCR experiments for each breakpoint (see Figure 47). The PCR assays are validated using conventional PCR and visualized through an automated electrophoresis. The PCR was successful, i.e. there was a

clear band at the correct base pair size (height), without by-products or bands in the controls. The PCR products are then send for Sanger sequencing. The performance of PCRs and electrophoresis takes about 1-2 days. If the PCRs were unsuccessful, other PCR assays have to be established again for the same breakpoints. The subsequent Sanger sequencing takes half a day to a whole day. If only a short PCR assay is successful with a small base pair distance between the primers (amplicon length approximately 60-100bp, see Figure 47), an additional PCR product subcloning is necessary in advance of the Sanger sequencing. The subcloning of the PCR product takes about a week. If the PCR assay is successfully validated using classical PCR, automated electrophoresis and Sanger sequencing, then this assay is expanded to an MRD assay. For this purpose, a double-fluorescent probe (FAM-BHQ1) is designed within the PCR amplicon and is ordered. The probe design only takes about 1-2h, but the production of this probe takes about 7-10 days.

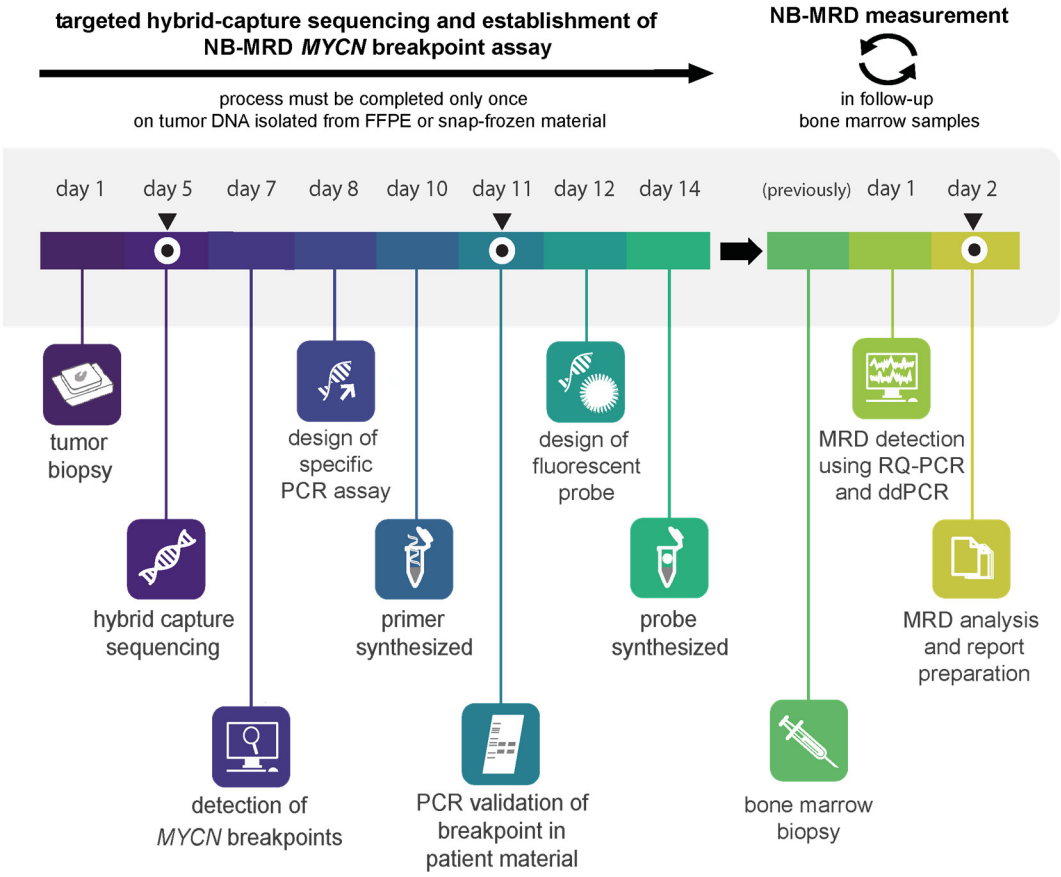

Figure 64: Outline of the clinical implementation of *NB breakpoint MRD assay* detection.
From the tumor biopsy obtained at diagnosis, breakpoints are mapped using the *NB targeted NGS assay*. The entire process to establish the patient-specific MRD assay takes 14 working days. MRD analysis of any additional bone marrow sample takes 2 working days, once the MRD assay has been established.

The MRD assay is then checked by a probe specificity test and a sensitivity test using RQ-PCR. If the RQ-PCRs are successful, i.e. an increasing fluorescence/amplification in low PCR cycles numbers and an overall high fluorescence is visible, the MRD assay is established. In addition, the RQ-PCR product can also be validated using the automated electrophoresis and Sanger sequencing. If there is no successful amplification of the product using RQ-PCR, and there is no improvement even after changing

the PCR parameters (e.g. changing the melting temperature or $MgCl_2$ content), a new probe must be designed and ordered. The DNA isolated from mononuclear cells purified from bone marrow aspirates is then examined with this *NB breakpoint MRD assay.* The mononuclear cells were obtained using the Ficoll technique from the bone marrow aspirates drawn in EDTA vials, which had been taken in the clinic and processed in advance. The MRD sensitivity and quantification analysis is carried out using RQ-PCR and ddPCR and each assay takes approximately one day to process. Since the MRD assays of the *MYCN* breakpoints also can have different melting temperatures than the RQ/ddPCR assay of the internal reference, two different experiments are usually need to be performed for each technique (i.e. a total of four experiments). The raw data is then processed and the MRD level is calculated. This takes about one day and provides an estimation of the remaining tumor cells in the bone marrow of neuroblastoma patients. With this strategy, a patient-specific breakpoint *NB breakpoint MRD assay* can be established at a reasonable cost within 14 working days, including validation and determining sensitivity and specificity (Figure 64). The peculiarity however is, that once the *NB breakpoint MRD assay* is established based on the *NB targeted NGS assay*, this MRD assay can be used to determine residual cells in bone marrow aspirates from the respective patient within only two working days (Figure 64) at the cost of a regular RQ/ddPCR assay. The feasibility of the personalized MRD assay development was shown to be ready for implementation in future (prospective) clinical trials and subsequently clinical routine.

3.1.2.5 The neuroblastoma breakpoint MRD assay is extendable to other neuroblastoma-associated mutations

As already known for leukemia MRD diagnostics, there is usually not only one biomarker for the cancer that can be examined[161,672,673]. The *MYCN NB breakpoint MRD assay* works for breakpoints that are related with the *MYCN* oncogene, yet this procedure could be reached out to other neuroblastoma-pertinent breakpoints, for example, those known to be in (the proximity of) *TERT, ATRX,* chromosome 1p or at 17q, and likewise to SNV in neuroblastoma-important genes, for example, *ALK*.

Alterations in *ATRX* would be suitable for an extension of neuroblastoma MRD detection method. Regarding all neuroblastoma cases, deletions or SNVs in the *ARTX* gene are found in up to 10% of all patients[45]. *ATRX* breakpoints are most likely caused by genomic deletions. Since the *ATRX* deletions are less common in neuroblastoma than *MYCN* amplifications, a possible test cohort includes fewer sample numbers. For the establishment of the assay a neuroblastoma cell line with an *ATRX* deletion, CHLA-90, was used (Figure 65). Similar to the *MYCN* MRD assay, CHLA-90 was examined using the *NB targeted NGS assay* and the exact genomic breakpoint in the X chromosome was processed from the sequencing data. A breakpoint was found between the rearrangement segments chrX:76,935,121 - chrX:76,959,029, which is located directly within the *ATRX* gene (see Table 20 in appendix). The NGS detection of this breakpoint was achieved with a total of 190 spanning and 21 encompassing reads, which indicates a reliable breakpoint sequence.

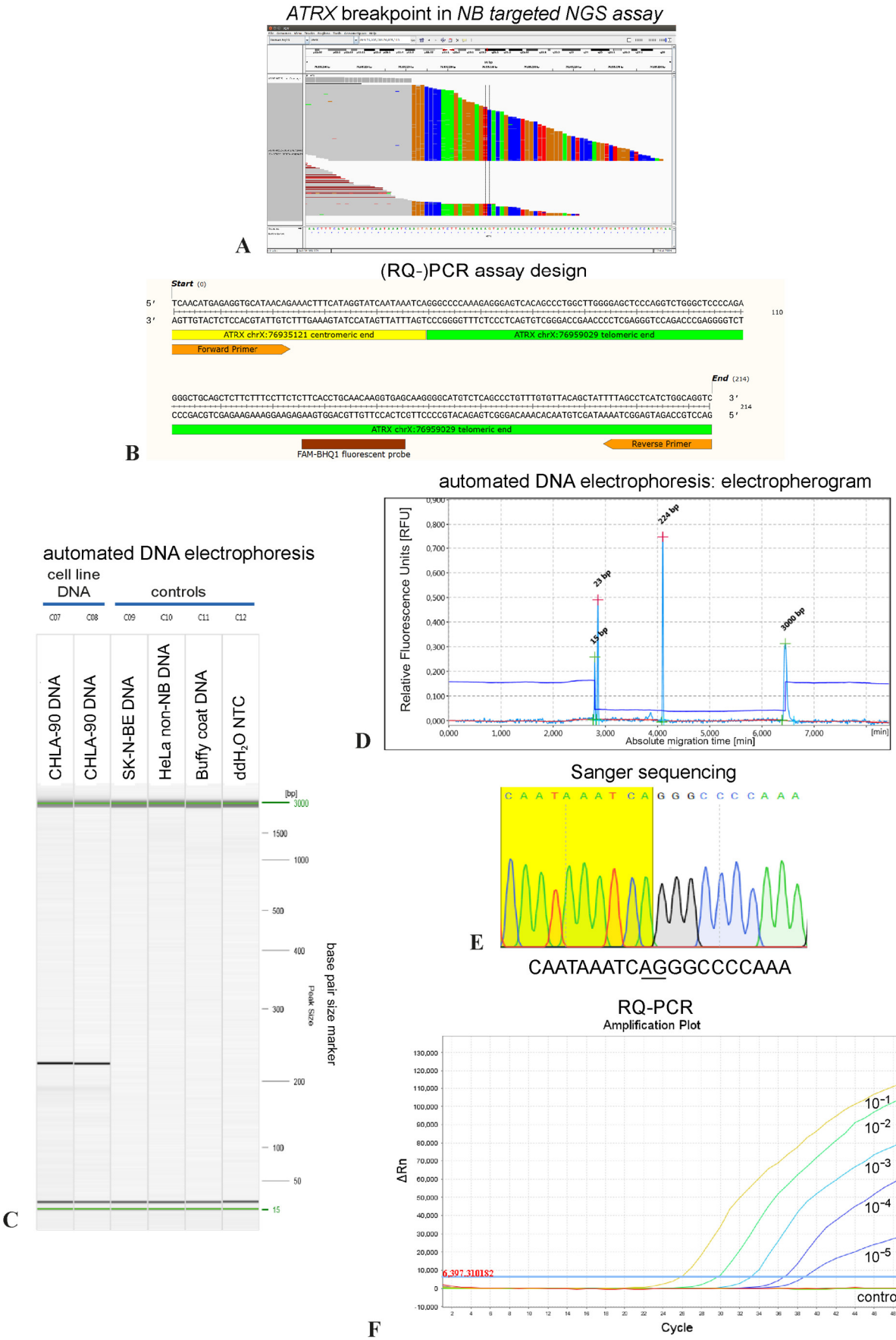
ATRX breakpoint in NB targeted NGS assay
A
(RQ-)PCR assay design
Start (0)
5′ TCAACATGAGAGGTGCATAACAGAAACTTTCATAGGTATCAATAAATCAGGGCCCCAAAGAGGGAGTCACAGCCCTGGCTTGGGGAGCTCCCAGGTCTGGGCTCCCCAGA 110
3′ AGTTGTACTCTCCACGTATTGTCTTTGAAAGTATCCATAGTTATTTAGTCCCGGGGTTTCTCCCTCAGTGTCGGGACCGAACCCCTCGAGGGTCCAGACCCGAGGGGTCT
ATRX chrX:76935121 centromeric end
ATRX chrX:76959029 telomeric end
Forward Primer
End (214)
GGGCTGCAGCTCTTCTTTCCTTCTCTTCACCTGCAACAAGGTGAGCAAGGGGCATGTCTCAGCCCTGTTTGTGTTACAGCTATTTTAGCCTCATCTGGCAGGTC 3′
214
CCCGACGTCGAGAAGAAAGGAAGAAGAAGTGGACGTTGTTCCACTCGTTCCCCGTACAGAGTCGGGACAAACACAATGTCGATAAAATCGGAGTAGACCGTCCAG 5′
ATRX chrX:76959029 telomeric end
FAM-BHQ1 fluorescent probe
Reverse Primer
B
automated DNA electrophoresis: electropherogram
Relative Fluorescence Units [RFU]
Absolute migration time [min]
224 bp
23 bp
15 bp
3000 bp
D
automated DNA electrophoresis
cell line DNA
controls
C07
C08
C09
C10
C11
C12
CHLA-90 DNA
CHLA-90 DNA
SK-N-BE DNA
HeLa non-NB DNA
Buffy coat DNA
ddH2O NTC
[bp]
3000
1500
1000
500
400
300
200
100
50
15
Peak Size
base pair size marker
C
Sanger sequencing
C A A T A A A T C A G G G C C C C A A A
E
CAATAAATCAGGGCCCCAAA
RQ-PCR
Amplification Plot
ΔRn
Cycle
10-1
10-2
10-3
10-4
10-5
6,397.310182
controls
F

The orientation of the two breakpoint flanking segments has not changed, the read direction has maintained "head-to-tail" on the minus strand of chromosome X. The chromosomal alteration led to a deletion of the exons 3-8, in the area of the ADD domain - which is most frequently affected by deletions in neuroblastoma[58,107,674]. The sequence of the *ATRX* deletion in CHLA-90 was used to design a breakpoint specific PCR assay. The results of the PCR experiment and the Sanger sequencing showed a specific amplification of the target, but in not in the control DNA. The measured size of the actual PCR amplicon (224bp) approximated the length of the predicted amplicon (214bp). An RQ-PCR analysis based on this PCR assay using a FAM-BHQ1 TaqMan probe achieved an *ATRX* breakpoint MRD assay sensitivity of 10^{-5}. Thus, a specific *ATRX* breakpoint MRD assay could be established on a neuroblastoma cell line, but a potential application of the method has yet to be evaluated using patient material (tumor or bone marrow aspirates). Further genomic alterations which constitute suitable markers for MRD detection are *ALK* kinase domain SNVs detected in about 9.2% of all neuroblastomas[50,51]. The TaqMAMA technique is already applied for sensitive RQ-PCR detection of biological-relevant point mutations in research approaches in leukemia diagnostics[563,675]. Targeting point mutations is challenging within fundamentally important genes for cancer development with RQ-PCR, because of the specific detection of an affected sequence in the presence of a wild-type allele. An extension of this TaqMAMA technique, the ASQ-PCR method, is published by Barz et al[564,565]. In the ASQ-PCR, similar as in the TaqMAMA method, the 3' end of the designed primer is placed on the SNV. The base before it is not changed (different from TaqMAMA) and the third base from the 3' end is designed with a mismatch. For quantification of SNVs mutations, the ratio of mutation positive cells to wild-type cells in a sample is calculated using standard curve equations. Within this doctoral thesis, a first attempt towards an *NB ALK ASQ-PCR assay* was made. The main focus was set on the *ALK* SNV c.3824G>A (R1275Q), as patient material with this specific mutation was available for this mutation. Other ASQ-PCRs for *ALK* SNVs were also designed (e.g. c.3522C>A/F1174L), but have not been used for the detection of the mutation in patient material so far (data not shown). The GRCh37 (hg19) publicly available reference sequence was used to design an *ALK* SNV c.3824G>A (R1275Q) specific ASQ-PCR assay. Similar to the *MYCN* MRD assay, LAN-5 and tumor material of patient no. #8 was examined using the *NB targeted NGS assay* (Figure 66).

< Figure 65: *ATRX* (deletion) breakpoint neuroblastoma MRD assay in CHLA-90 non-*MYCN*-amplified cell line.
(A) Evidence for an *ATRX* breakpoint (chrX:76,935,121) in *NB targeted NGS assay* data of cell line CHLA-90. (**B)** *ATRX* breakpoint sequence was extracted and conventional PCR assay was designed in breakpoint flanking segments. **(C)** Automated DNA electrophoresis shows PCR amplicons of *ATRX* breakpoint PCR (controls from left to right: NB = SK-N-BE *ATRX* normal cell line DNA, non-NB = HeLa cell line DNA, buffy coat = DNA from ten healthy blood donors, NTC = water). (**D)** Electropherogram of PCR amplicons obtained in CHLA-90 cell material confirmed the correct PCR amplicon size. **(E)** Sequencing chromatogram of the *ATRX* breakpoint region in PCR amplicon. The sequence rearrangement partners are indicated in yellow and white. **(F)** Amplification plot of RQ-PCR analysis, with a detection sensitivity of the breakpoint of 10^{-5} within a spike-in dilution series experiment (controls: neuroblastoma cell line DNA, non-neuroblastoma cell line DNA, DNA from 10 healthy blood donors, water).

The NGS detection of this SNV was achieved with a total coverage of 962 reads and an allelic frequency of 47.8% for LAN-5 and 2026 reads, and an allelic frequency of 38.4% for patient no. #8, which indicates a reliable point mutation detection. For PCR validation of the assay, the LAN-5 neuroblastoma cell line with an *ALK* SNV c.3824G>A was utilized. Moreover, the assay was also tested on tumor and bone marrow material of the patient with neuroblastoma no. #8 (see also Table 16). The ASQ-PCR assay for *ALK* SNV c.3824G>A could show an amplification of the mutated SNV sequence in *ALK* SNV positive DNA of LAN-5, and patient derived samples applying automated DNA electrophoresis. The measured size of the actual PCR amplicon (282bp) approximated the length of the predicted amplicon (277bp). Interestingly, a PCR amplicon for the *ALK* SNV c.3824G>A was revealed as well in DNA of PBMCs derived from the patients' bone marrow, but in a very small proportion only. Presumably, the ASQ-PCR target was not amplified on a large scale because either the proportion of tumor cells in the bone marrow sample was very low, and/or the proportion of *ALK* SNV positive cells was low, and/or the detection method of automated DNA electrophoresis for ASQ-PCR was not sensitive enough. In addition to the ASQ-PCR assay, a HEX-BHQ1 probe for the detection of the *ALK* SNV c.3824G>A was designed, which enables a sensitive fluorophore-based detection of the PCR amplicon. In a ddPCR multiplex approach, a specific *MYCN* breakpoint was measured via a FAM-BHQ1 probe, whereas the *ALK* SNV was detected on another channel HEX-BHQ1. In the first analysis it was detected that in the DNA of PBMCs derived from the patients' bone marrow both single *MYCN* breakpoint and single *ALK* SNV fluorescent signals, as well as signals of both attributes (double-positive) are present in the same cell population. It cannot be concluded that one cell carries both the *MYCN* breakpoint and *ALK* SNV c.3824G>A mutations, however, they are present in the same sample or rather in the same ddPCR droplet. This data showed a first approach for the usage of *ALK* SNVs in neuroblastoma diagnostics as MRD specific markers. In theory, a combination of several pathogenic alterations can be detected in one neuroblastoma tumor (cell)[676]. The various neuroblastoma-relevant mutations (e.g. *TERT, ATRX, ALK*) could therefore also be used for the development of MRD assays. In addition, other recurrent structural chromosomal alterations also occur in neuroblastoma which would be suitable for MRD detection. These are deletions of the chromosomal arms 1p[677], 3p[678], 4p[679] and 11q[680], or gains of 1q[681,682], 2p[683] or 17q[41]. This thesis could demonstrate in a first approach, that *ATRX* and *ALK* mutations are suitable for MRD detection and that they can also be combined with the detection of other mutations (e.g. *MYCN*) in a multiplex assay.

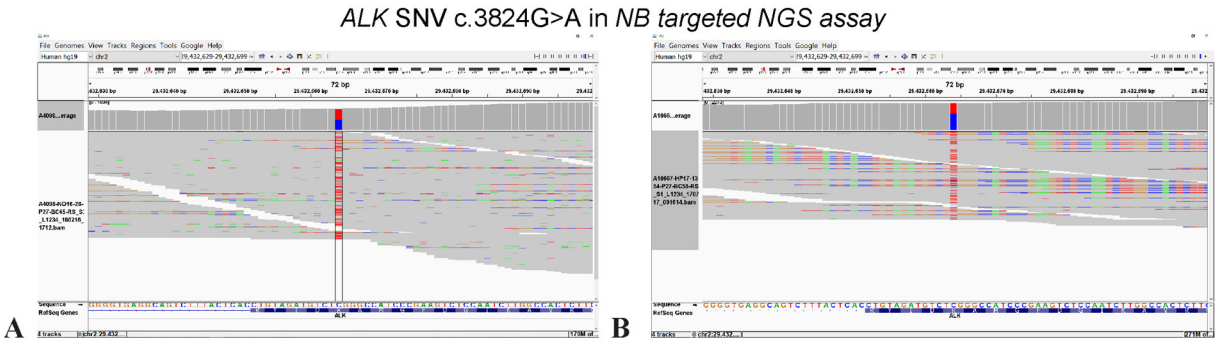
ALK SNV c.3824G>A in NB targeted NGS assay
A
B


ASQ-PCR assay design
Start (0)
Forward primer wildtpye
Forward primer c.3824
ALK SNV c.3824G>A
ALK FAM-HEX Probe
Reverse Primer
End (277)
C

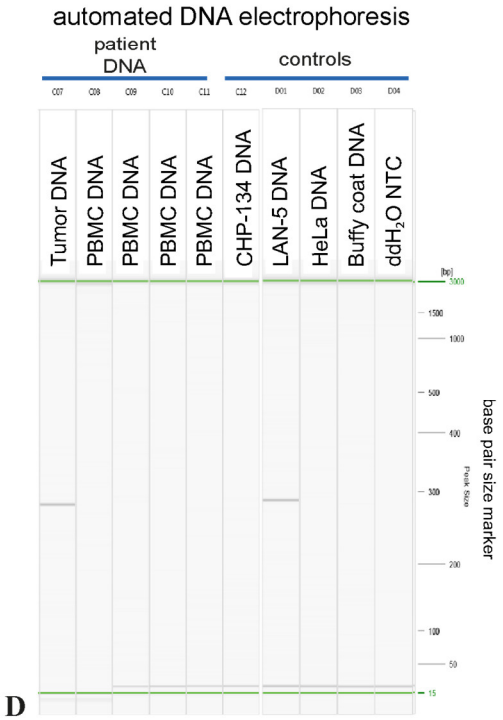
automated DNA electrophoresis
patient DNA
controls
Tumor DNA
PBMC DNA
PBMC DNA
PBMC DNA
PBMC DNA
CHP-134 DNA
LAN-5 DNA
HeLa DNA
Buffy coat DNA
ddH2O NTC
base pair size marker
D

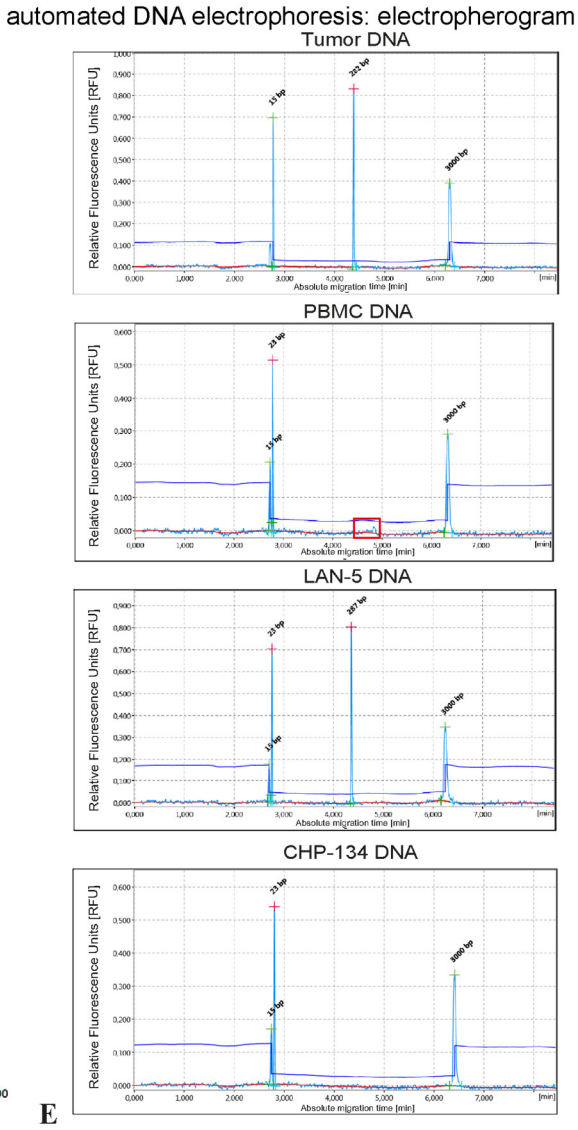
automated DNA electrophoresis: electropherogram
Tumor DNA
PBMC DNA
LAN-5 DNA
CHP-134 DNA
Relative Fluorescence Units [RFU]
Absolute migration time [min]
E

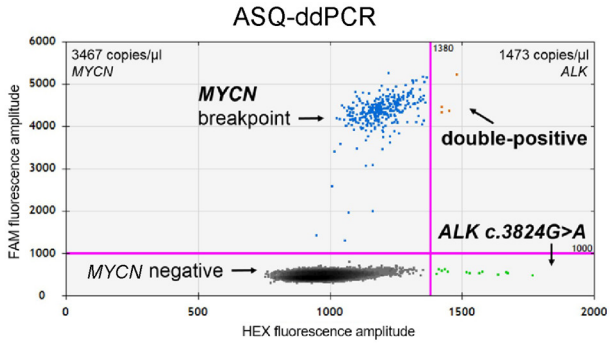
ASQ-ddPCR
3467 copies/µl
MYCN
1473 copies/µl
ALK
MYCN breakpoint
double-positive
ALK c.3824G>A
MYCN negative
FAM fluorescence amplitude
HEX fluorescence amplitude
F

3.2 Influence of the MYCN regulatory network and its targeted therapy

MYCN is the major driver of neuroblastoma development. However, the MYCN protein is not suitable for a targeted drug therapy because it is too small and the surface is inaccessible. Through a therapy of the biological MYCN network, *MYCN*-amplified neuroblastomas can be treated indirectly. In this work, several functional areas of MYCN were investigated for an indirect targeted treatment. Treatment against the transcription of *MYCN* and its activity as transcription factor was investigated using BET inhibitors (part 3.2.1) as well as PLK1/RAS, PI3K and dual-kinase inhibitors (part 3.2.2). In an additional step, a combination therapy of two inhibitors of each of these classes was administered to counteract the resistance formation of individual inhibitors (part 3.2.3). Additionally, the spindle protein ASPM and its functional role in neuroblastoma was evaluated and investigated as a potential small molecule target (part 3.2.4).

3.2.1 Monotherapy with BET inhibitors reduce neuroblastoma cell viability *in vitro*

Previous research already revealed antitumor effects of treatment with BET inhibitors in neuroblastoma[282,285,684,685] and this result was verified in several publications. Individual reports on other pediatric tumor entities[686–689] have also been able to demonstrate the effectiveness of BET inhibitors against tumor cells. However, the efficacy of BET inhibitors was never tested in a larger, cellular *in vitro* screening cohort or in a comparison of several structural similar BET inhibitors. In order to consolidate first clinical pharmaceutical studies with a general biological validity of the BET inhibitors, it was necessary to find out whether the inhibition of BET is applicable for neuroblastoma with different traits and whether there are differences in the effectiveness of the individual compounds, especially in individual cell lines. To assess tumor cell inhibitory effects of BET drugs in neuroblastoma, 12-14 neuroblastoma cell lines were administered with one of the BET inhibitors (+)- JQ1, OTX-015 or TEN-010. In addition, putative effects on cell viability of JQ1, OTX015 and TEN-010 on nonmalignant primary human cells were measured in one or two human fibroblasts after BET treatment. Previously published data[282] shows that BET inhibition is particularly effective against human *MYCN*-driven tumor cells because BRD4 occupies *MYCN* target gene enhancers. For this reason, several *MYCN*-amplified cells (7-9 cell lines) were tested, but also non-*MYCN*-amplified cells (5 cell lines).

< Figure 66: *ALK* SNV c.3824G>A neuroblastoma MRD ASQ-PCR in LAN-5 cell line and samples of patient no. #8. Evidence for *ALK* SNV c.3824G>A in *NB targeted NGS assay* data of **(A)** neuroblastoma cell line LAN-5 and **(B)** in tumor material of patient no. #8. **(C)** Conventional PCR assay was designed as specific ASQ-PCR (*ALK* SNV is located on the anti-sense strand of chromosome 2). **(D)** Automated DNA electrophoresis shows PCR amplicons of *ALK* SNV (controls from left to right: NB = CHP-134 *ALK* normal cell line DNA, non-NB = HeLa cell line DNA, buffy coat = DNA from ten healthy blood donors, NTC = water). (**E)** Electropherogram of PCR amplicons obtained in LAN-5, CHP-134, tumor and bone marrow material. The *ALK* SNV c.3824G>A was detected in *ALK* SNV positive tumor and LAN-5 DNA, but not in *ALK* normal CHP-134 cells. **(F)** Amplification dot plot of multiplex ASQ-ddPCR analysis, highlighting the simultaneous detection of a *MYCN* specific breakpoint (chr2:13,490,249 – chr2:15,815,066) in the FAM channel and the *ALK* SNV c.3824G>A in the HEX channel using DNA of PBMCs derived from the patients' bone marrow.

Since 75% of the neuroblastomas are non-*MYCN*-amplified[60], the question had to be answered if BET inhibition is only specifically attacking *MYCN*-amplified tumors or in general applicable. The BET inhibitors tested were selected according to chemical criteria, putative patient administration and beneficial previous reports[282,305,314,690,691]. Applied concentrations of BET inhibitors ranged from 2.5nM up to 100,000nM, tested in technical triplicates and in two to three biological replicates. The original tool compound JQ1 showed distinct similar shapes of dose-response curves when neuroblastoma cells are inhibited, regardless of whether they are *MYCN*-amplified or non-*MYCN*-amplified (Figure 67A). The fibroblast cell lines showed a less strongly inhibitory dose-response relationship from JQ1 to cell viability. This dose-response curve reached a plateau with remaining cell viability around 34%, and the threshold to overcome a total inhibition has not been reached. The relative IC50 (EC50, effective half inhibitory concentration) concentration is also remarkable similar for *MYCN*-amplified (283nM) and non-*MYCN*-amplified cell lines (224nM). The lowest relative IC50 was measured for *MYCN*-amplified cell lines in the IMR5/75 cell line (107nM) and the highest in the SK-N-BE(2) cell line (748nM). For non-*MYCN*-amplified cells, the lowest relative IC50 was detected in NBL-S (172nM) and the highest value was measured in the GI-ME-N cell line (830nM). The non-malignant fibroblast cell lines display a similar relative IC50 in comparison to each other (VH7 cell line 161nM and PLF cell line 199nM). However, the relative IC50 for the fibroblast cell lines is much lower than for the neuroblastoma cell lines (55nM lower compared to *MYCN*-amplified and 41nM lower compared to non-*MYCN*-amplified neuroblastoma cells in relation to fibroblasts). Furthermore, an almost total inhibition of neuroblastoma cell viability is achieved. Regarding the maximum inhibitory effect (Emax), this was highest in the *MYCN*-amplified cell lines (94.84%). For non-*MYCN*-amplified neuroblastoma cells (75.16%) and fibroblast cells (78.51%) this value was comparatively similar. In a statistical analysis using the non-parametric Mann-Whitney test, a significance of the difference between *MYCN*-amplified and non amplified cells could be demonstrated ($p = 0.06187$; Figure 67B). The lowest maximal inhibitory effect was measured for *MYCN*-amplified cell lines in the SK-N-BE(2) cell line (79.58%) and the highest in the NGP, KELLY, IMR5/75 and LAN-1 cell lines (100%). For non-*MYCN*-amplified cells, the lowest maximal inhibitory effect was detected in SK-N-AS (46.17%) and the highest value was measured in SH-SY5Y cells (96.90%). For fibroblast cell lines, PLF cells displayed a lower maximal inhibitory effect (67.80%) as VH7 cells (88.42%). The BET inhibitor JQ1 has an improved effect on *MYCN*-amplified cell lines because it almost completely inhibited their cell viability (Figure 67C). With regard to the concentrations used, an effective treatment concentration seems to be nearly analogous in all neuroblastoma cell lines (Figure 67C+D). However, JQ1 also inhibited the cell viability of fibroblast cells in lower nanomolar concentrations, although no complete inhibition of the cell viability found even with higher concentrations. In a further screening, the effect of OTX015 was examined on neuroblastoma cells. Cells administered with OTX015 showed similar shapes of dose-response curves when neuroblastoma cells are inhibited, however, *MYCN*-amplified cells displayed a more declining cell viability after OTX015 treatment as compared to other cells (Figure 68A).

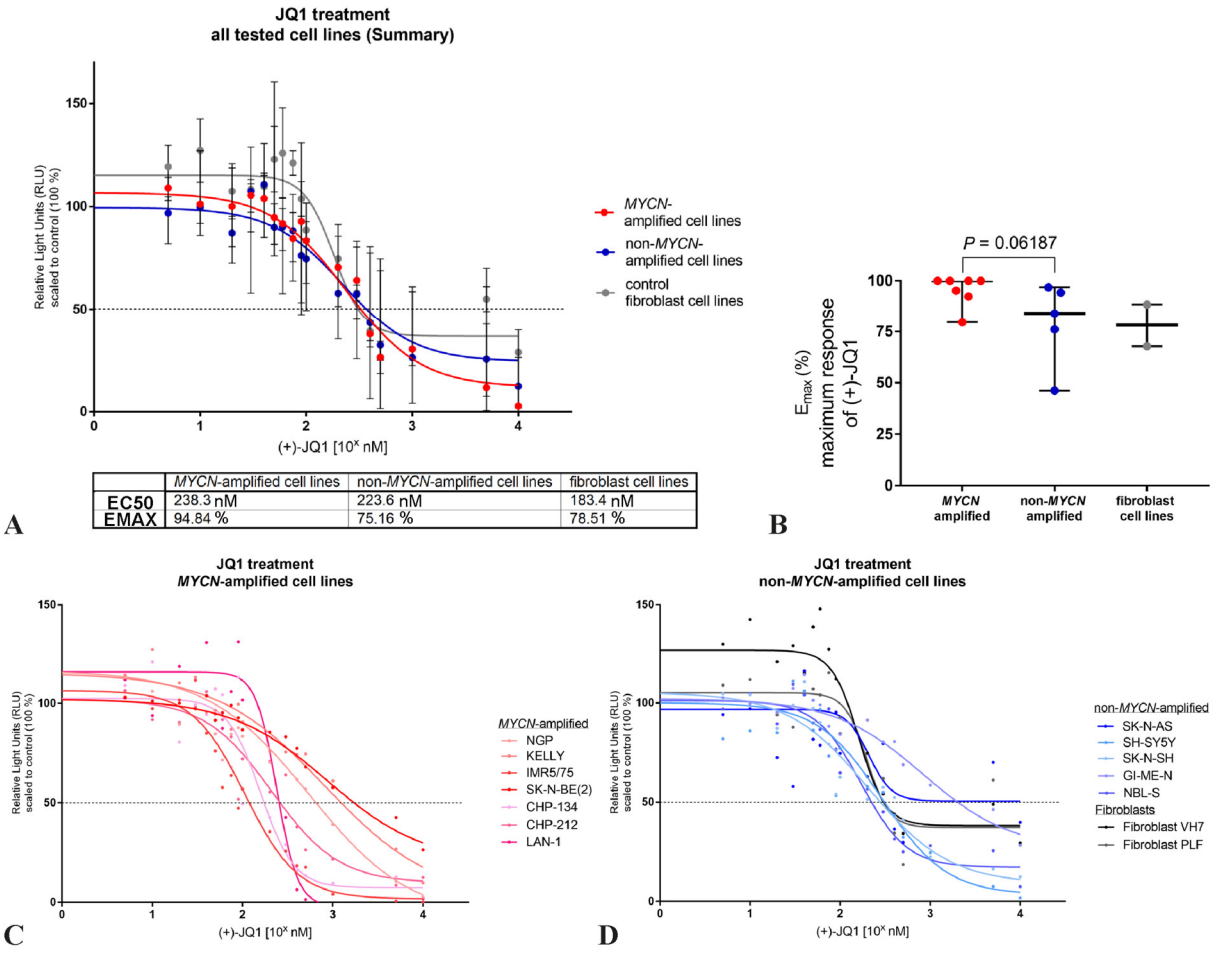

	MYCN-amplified cell lines	non-*MYCN*-amplified cell lines	fibroblast cell lines
EC50	238.3 nM	223.6 nM	183.4 nM
EMAX	94.84 %	75.16 %	78.51 %

Figure 67: (+)-JQ1 dose to cell viability response relationship in neuroblastoma and fibroblast cell lines.
BET inhibitor JQ1 was applied to 14 different cell lines *in vitro* and effect on cell viability was measured three days after treatment. **(A)** Relative IC50 (E50) is displayed. Emax in mean interpolated by GraphPad Prism®. **(B)** Comparison of the Emax of JQ1. The median and range of the Emax value of all respective cell lines is shown. **(C)** 7 *MYCN*-amplified cell lines were tested for their effect of JQ1 on cell viability, the dose-response curve shows median with range for each concentration tested in a cell line. **(D)** Five non-*MYCN*-amplified cell lines and two fibroblast cell lines were administered with JQ1. For each cell line, two to three biological replicates are shown with their respective median and range.

The fibroblast cell lines showed a much weaker inhibitory dose-response relationship from OTX015 to cell viability. This dose-response curve reached a plateau with remaining cell viability around 75% and a total inhibition is not reached. Contrasting the slightly difference of the sigmoid curve shapes between *MYCN*-amplified and non-*MYCN*-amplified neuroblastoma cells, the relative IC50 (E50) concentration was profound similar for *MYCN*-amplified (328nM) and non-*MYCN*-amplified cell lines (300nM). The lowest relative IC50 was measured for *MYCN*-amplified cell lines in the IMR5/75 cell line (129nM) and the highest in the SK-N-BE(2) cell line (1053nM). For non-*MYCN*-amplified cells, the lowest relative IC50 was detected in NBL-S (147nM) and the highest value was measured in the SK-N-AS cell line (~ 500nM). The fibroblast cell lines displayed a similar relative IC50 in comparison to each other (VH7 cell line 216nM and PLF cell line 350nM). These rather low relative IC50 values of the fibroblasts are also notable in comparison with the neuroblastoma cells. The relative IC50 for the fibroblast cell lines hardly differs from the IC50 of the neuroblastoma cells (2nM lower for *MYCN*-amplified and 30nM

lower for non-*MYCN*-amplified neuroblastoma cells compared to fibroblasts). An almost total inhibition of neuroblastoma cell viability was achieved overall for the *MYCN*-amplified cell lines rather than for the non-*MYCN*-amplified cell lines, whereby an almost total inhibition can also be seen in individual cell lines rather than in a group depending on the *MYCN* status.

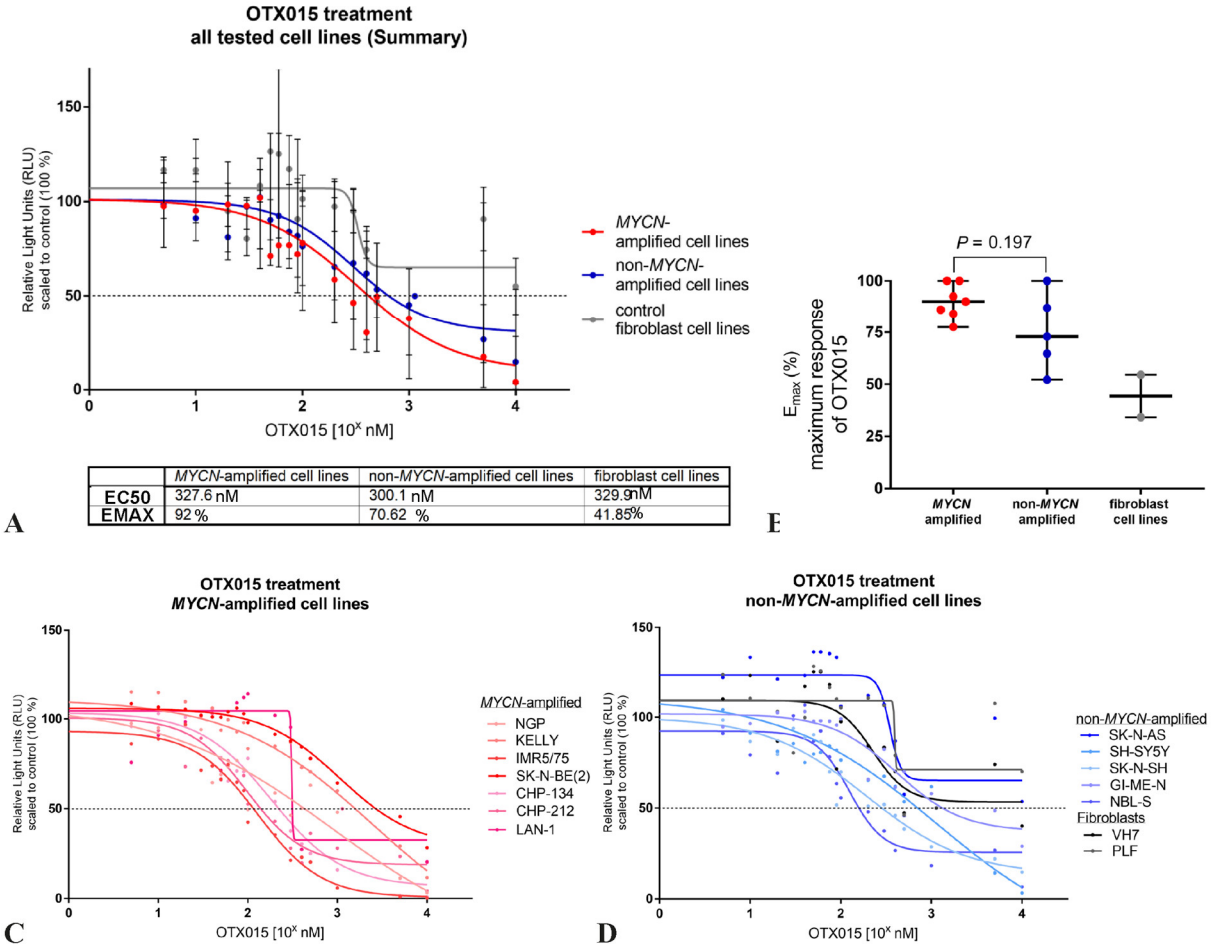

Figure 68: OTX015 dose to cell viability response relationship in neuroblastoma and fibroblast cell lines.
BRD4 inhibitor OTX015 was applied to 14 different cell lines *in vitro* and effect on cell viability was measured three days after treatment. **(A)** Relative IC50 (E50) is displayed. Emax in mean interpolated by GraphPad Prism®. **(B)** Comparison of the Emax of OTX015. The median and range of the Emax value of all respective cell lines is shown. **(C)** 7 *MYCN*-amplified cell lines were tested for their effect of OTX015 on cell viability, the dose-response curve shows median with range. All cell lines displayed a maximum effect with more than 50%. **(D)** Five non-*MYCN*-amplified cell lines and two fibroblast cell lines were administered with OTX015. For each cell line, two to three biological replicates are shown with their respective median and range.

Regarding the maximum inhibitory effect (Emax), this was highest in the *MYCN*-amplified cell lines (92%). The Emax for non-*MYCN*-amplified neuroblastoma cells (70.62%) was less than for *MYCN*-amplified cells, for fibroblast cell lines (41.85%) this value was more than halved. In a statistical analysis using the non-parametric Mann-Whitney test, only a slight significance of the difference between *MYCN*-amplified and non-amplified cells could be demonstrated ($p = 0.197$; Figure 68B). The lowest maximal inhibitory effect was measured for *MYCN*-amplified cell lines in the SK-N-BE(2) cell line (77.57%) and the highest in the NGP and CHP-134 cell lines (100%). For non-*MYCN*-amplified cells, the lowest maximal inhibitory effect was detected in SK-N-AS (52.21%) and the highest value was

measured in SH-SY5Y cells (100%). For fibroblast cell lines, PLF cells displayed a lower maximal inhibitory effect (34.24%) as VH7 cells (54.57%). For the BET inhibitor OTX015 it was possible to show the same inhibition profile that was already published in previous research. The cell viability of *MYCN*-amplified neuroblastoma cells (Figure 68C) is more strongly inhibited by OTX015 than the viability of non-*MYCN*-amplified cells (Figure 68D). This inhibitory potential of OTX015 can also be seen in the maximum inhibitory effect, which is higher for *MYCN*-amplified cells than for non-*MYCN*-amplified cells. Fibroblasts appear to be by far less affected by the inhibitor and although these show a low relative IC50, less than half of the cell viability of the fibroblasts is inhibited displayed in maximum inhibitory effects. The same cell panel that was tested with the inhibitors JQ1 and OTX015 was then tested with the new BET inhibitor TEN-010 from Roche. Two additional *MYCN*-amplified cell lines were added to this panel (BE(2)C and SK-N-DZ) to represent an even wider range of *MYCN*-amplified cell lines. The dose-response curve of inhibition of cell viability to TEN-010 showed a similar curve shape for all cell lines, regardless of whether they are *MYCN*-amplified or not. A slightly stronger response of the *MYCN*-amplified neuroblastoma cell lines can be seen. The results underline that a higher dose of the inhibitor is needed over all cells, but also a higher maximum inhibition was reached (Figure 69A). The fibroblast cell lines showed a similar inhibitory dose-response relationship as neuroblastoma cells from TEN-010 to cell viability. This dose-response curve reached no clear plateau but displayed remaining cell viability around 27.25% at a maximum TEN-010 concentration of 100,000nM and a total inhibition is not reached. Relative IC50 (EC50) concentrations strongly differed between *MYCN*-amplified (1645nM) and non-*MYCN*-amplified (215nM) neuroblastoma cells, however, this difference only seems to occur due to the weaker response of individual *MYCN*-amplified cell lines. The lowest relative IC50 was measured for *MYCN*-amplified cell lines in the IMR5/75 cell line (94nM) and the highest in the SK-N-BE(2) cell line (3737nM). For non-*MYCN*-amplified cells, the lowest relative IC50 was detected in SH-SY5Y (332nM) and the highest value was measured in the GI-ME-N cell line (309nM). The inhibitory response of cell viability of the fibroblasts was also significantly different; While the cell line VH7 showed a low relative IC50 (83nM), cell viability of the cell line PLF was detected with an almost absolute resistance to TEN-010 (20,821nM). A stronger maximal inhibition of neuroblastoma cell viability was achieved overall for the *MYCN*-amplified cell lines rather than for the non-*MYCN*-amplified cell lines, whereby an almost total inhibition was detected for CHP-134 and IMR5/75. Regarding the maximum inhibitory effect, this was highest in the *MYCN*-amplified cell lines (97.08%). The maximum inhibitory effect for non-*MYCN*-amplified neuroblastoma cells (58.12%) was by far less than for *MYCN*-amplified cells, as for fibroblast cell lines (72.15%) this value was only slightly lower. In a statistical analysis using the non-parametric Mann-Whitney test, a slight significance of the difference between *MYCN*-amplified and non-amplified cells could be demonstrated ($p = 0.1469$; Figure 69B). The lowest maximal inhibitory effect was measured for *MYCN*-amplified cell lines in the SK-N-BE(2) cell line (37.03%) and the highest in the NGP cell line (100%). For non-*MYCN*-amplified cells, the lowest maximal inhibitory effect was detected in SK-N-AS (34.24%) and the highest value

was measured in NBL-S cells (88.58%). For fibroblast cell lines, the maximal inhibitory effect was comparable in PLF cells (70%) and in VH7 cells (74.50%). The dose-response profile of TEN-010 administered on various cell lines is very broad. Overall, TEN-010 shows a good inhibition of the cell viability in all neuroblastoma cells, and additionally a very good maximal inhibition effect in the *MYCN*-amplified neuroblastoma cells (Figure 69C+D). However, a dose response is very different for the individual cell lines, either the cells react with a strong response in cell viability inhibition or with a very low to no response.

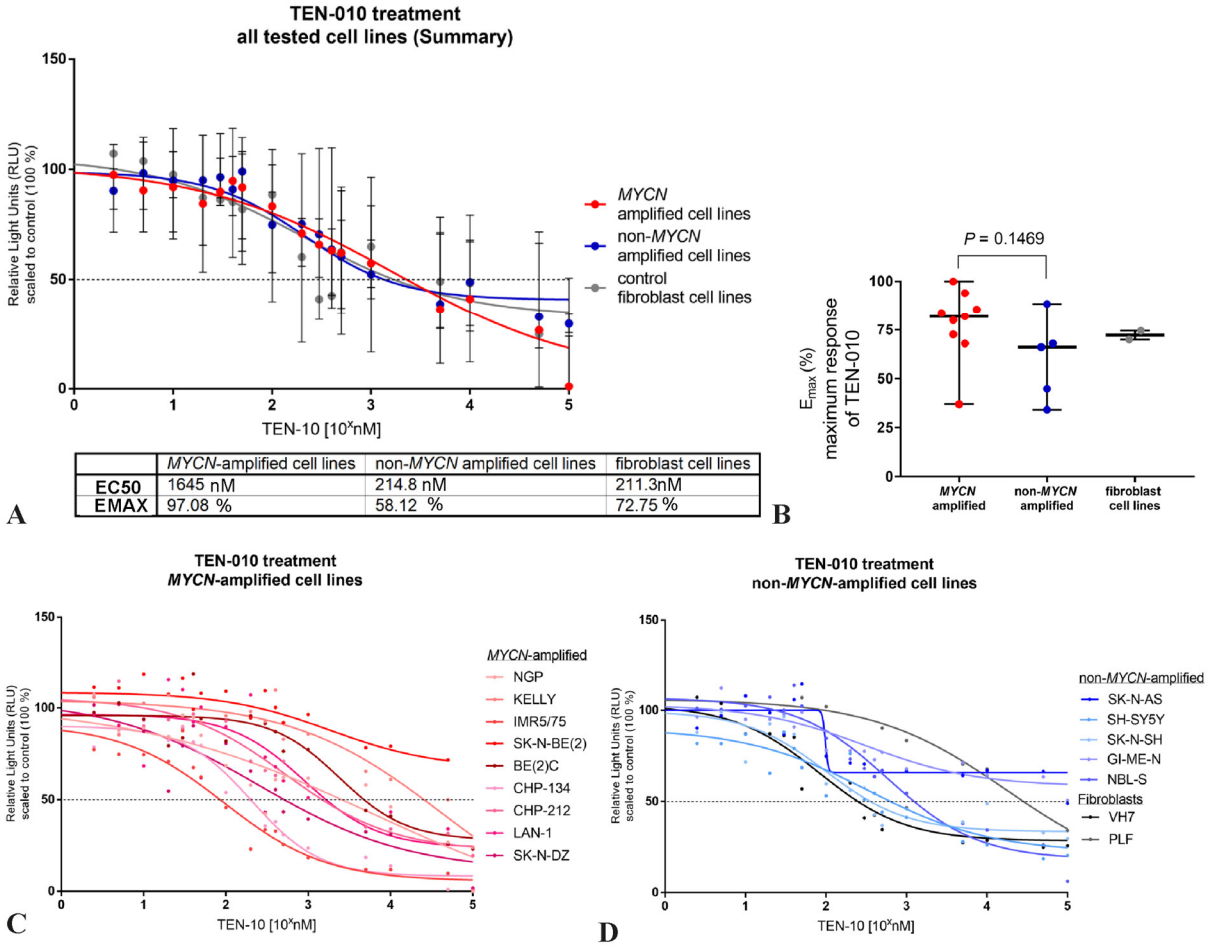

	MYCN-amplified cell lines	non-*MYCN* amplified cell lines	fibroblast cell lines
EC50	1645 nM	214.8 nM	211.3nM
EMAX	97.08 %	58.12 %	72.75 %

Figure 69: TEN-010 dose to cell viability response relationship in neuroblastoma and fibroblast cell lines.
BET inhibitor TEN-010 was applied to 16 different cell lines *in vitro* and effect on cell viability was measured three days after treatment. **(A)** Relative IC50 (E50) is displayed. Emax in mean interpolated by GraphPad Prism®. **(B)** Comparison of the Emax of TEN-010. The median and range of the Emax value of all respective cell lines is shown. **(C)** 9 *MYCN*-amplified cell lines were tested for their effect of TEN-010 on cell viability, dose-response curve shows median with range. All cell lines displayed a maximum effect with more than 50%, except for SK-N-BE(2). **(D)** Five non-*MYCN*-amplified cell lines and two fibroblast cell lines were administered with TEN-010. Only two cell lines, SK-N-AS and GI-ME-N, showed less than 50% maximum effect of TEN-010. For each cell line, two to three biological replicates are shown with their respective median and range.

Following the individual cellular screenings of the BET inhibitors, the three data sets of the dose-response profiles were evaluated and compared with each other. For this purpose, the absolute IC50 values and the relative IC50 (EC50, effective IC50) values were combined with the reduction of cell viability when 1,000nM inhibitor is applied (E1000) or with the maximum inhibition (Emax; see Figure

70). In this comparison, it was found with respect to the absolute IC50 and the E1000 that the inhibitors JQ1 and OTX015 had a similar dose-response profile (Figure 70A). The detected absolute IC50 values were similar for the *MYCN*-amplified neuroblastoma cells. CHP-212 and NGP cells displayed an exception, in which OTX015 showed a lower, absolute IC50. For SK-N-BE(2), JQ1 showed the lowest absolute IC50 value compared to all BET inhibitors. Regarding the non-*MYCN*-amplified cells, JQ1 was able to show an improved effect in the SH-SY5Y cell line. The E1000 inhibition was similar with the JQ1 or OTX015 drugs in all tested cells. Only SK-N-BE(2) showed a 25% stronger inhibition of cell viability using OTX015, this potency was also applicable to SH-SY5Y using JQ1. The compound TEN-010 displayed a different profile compared to JQ1 and OTX015. Some cell lines, regardless of whether they are *MYCN*-amplified or non-amplified, showed a much lower absolute IC50 than with JQ1 or OTX015 (KELLY, SK-N-BE(2), GI-ME-N, SK-N-AS and PLF). Almost all of these cell lines highlighted a lower response in relation to the absolute IC50 values even with inhibition with JQ1 or OTX015. A low response for the fibroblast cells is clearly also desirable for clinical use (PLF EC50 TEN-010 = 20,821nM, JQ1 = 199nM, OTX015 = 350nM). In addition, TEN-010 showed lower absolute IC50 values in *MYCN*-amplified cell lines, e.g. in IMR5/75. A closer look at the relative IC50 values (effective IC50 concentration, EC50) in combination with the E1000 inhibition, revealed two strongly different potency profiles in comparison with all three BET inhibitors (Figure 70B). Cells that were treated with the BET inhibitor JQ1 all showed a low relative IC50 and are at least 50% inhibited when treated with 1,000nM compound. With administration of OTX015, a low relative IC50 was detectable in the majority of the cell lines. However, these relative IC50 values and the cell viability were partly higher with E1000 OTX015 administration than when using JQ1 (e.g. in SH-SY5Y). The screening of TEN-010 showed that this compound has a high activity and reveals low relative IC50 values. This is especially the case in cells which already showed a response to JQ1 and OTX015. However, there were also some cell lines that showed a clearly higher IC50 value (e.g. KELLY or PLF) and/or a low cell viability reduction when using 1,000nM inhibitor (e.g. SK-N-BE(2)). In a comparative analysis of the absolute IC50 values and the maximum reduction in cell viability, all three BET inhibitors showed a different dose-response profile (Figure 70C). The tool compound JQ1 showed very good to medium absolute IC50 values and about 60-100% of cell viability reduction of after maximum inhibition for almost all cell lines. The cell line SK-N-AS stood out, which had a remarkable high, absolute IC50 value and additionally showed a low maximum inhibition of around 40%. When cell viability was inhibited with OTX015, a higher absolute IC50 could be shown in some cell lines compared to JQ1 (e.g. SK-N-BE(2)), but on the other hand also lower absolute IC50 values (e.g. NGP). It is noteworthy that the fibroblast cell lines revealed an extraordinarily high absolute IC50 with a low maximum inhibition of up to 60% after OTX015 treatment. In comparison of all BET inhibitors, a very wide dose-response profile was detected for an application of TEN-010. In general, the neuroblastoma cells showed different absolute IC50 values, but always an increased maximum reduction of 60% and more. Only three cell lines fell out of this pattern, SK-N-BE(2), GI-ME-N and SK-N-AS. These had far higher absolute IC50

values and showed a low viability reduction of below 40% within maximum inhibition. In an analysis of the relative IC50 values (concentration of the effective half maximal inhibition) combined with the maximal inhibition of the three BET inhibitors with each other, the dose-response effects were clearly differentiated (Figure 70D). Using the BET inhibitor JQ1, all cell lines showed low relative IC50 values under 1,000nM. In addition, the maximum reduction in cell viability was increased to 80-100%, only the cell line SK-N-AS was distinctive of the cell panel with a maximum reduction of 40%. However, this good response to JQ1 could also be seen in fibroblasts. Applying OTX015, the relative IC50 values were detected as low as those found under JQ1 treatment, but the relative IC50 was higher for individual cell lines. With regard to the maximum inhibition, the cells under OTX015 showed a cell viability reduction of 40-100%. The fibroblast cell line PLF had clearly less than 40% cell viability with a maximum inhibitor concentration. For cells that were treated with TEN-010, an effect of a wide range of response was observed as well. While the relative IC50 was very low for some cells like IMR5/75, even lower than using JQ1 and OTX015, this level of inhibition for other cell lines like KELLY was greatly increased. A similar pattern was also seen when considering the maximum inhibition, which was above 60% for almost all cell lines. However, for SK-N-BE(2), GI-ME-N and SK-N-AS this cell viability inhibition was below 40%. In summary, the results of the cell viability screening indicate an anti-neuroblastoma activity of all BET inhibitors, JQ1, OTX015, and TEN-010. The inhibitor JQ1 shows a high, potent effect with low IC50 values and a high cell viability reduction. A preference for a stronger inhibition in *MYCN*-amplified cell lines could only be shown with regard to a stronger maximum inhibition. This strong inhibitory effect was not only observed in neuroblastoma cell lines, but also in fibroblast cell lines, which show at least a 50% reduction after application of JQ1. Using OTX015, in particular the *MYCN*-amplified cell lines, responded well. The IC50 values were moderately increased for some neuroblastoma cells. With regard to the inhibition of cell viability of fibroblasts, the maximum value did not raise over 50%, so that the response clearly differs from the neuroblastoma cells. For testing the novel compound TEN-010, the effect profile showed the greatest differences in relation to the utilized cell lines. Some cell lines reacted poorly or very poorly to an application with TEN-010 compared to the other BET inhibitors. However, it also appears that some cell lines, for example *MYCN*-amplified SK-N-BE(2) or non-*MYCN*-amplified SK-N-AS, respond poorly or not at all to BET inhibitors. Other cell lines in turn showed an increased and improved response under TEN-010 treatment. It is also outstanding that the inhibitor TEN-010 could produce almost no effect with respect to IC50 or maximum inhibition in the non-malignant PLF fibroblast cell line. An increased potential is therefore attributed to the BET inhibitor TEN-010, since this inhibitor does not show an unspecific mode of action like JQ1, but only inhibits specific cells in the sense of a targeted therapy.

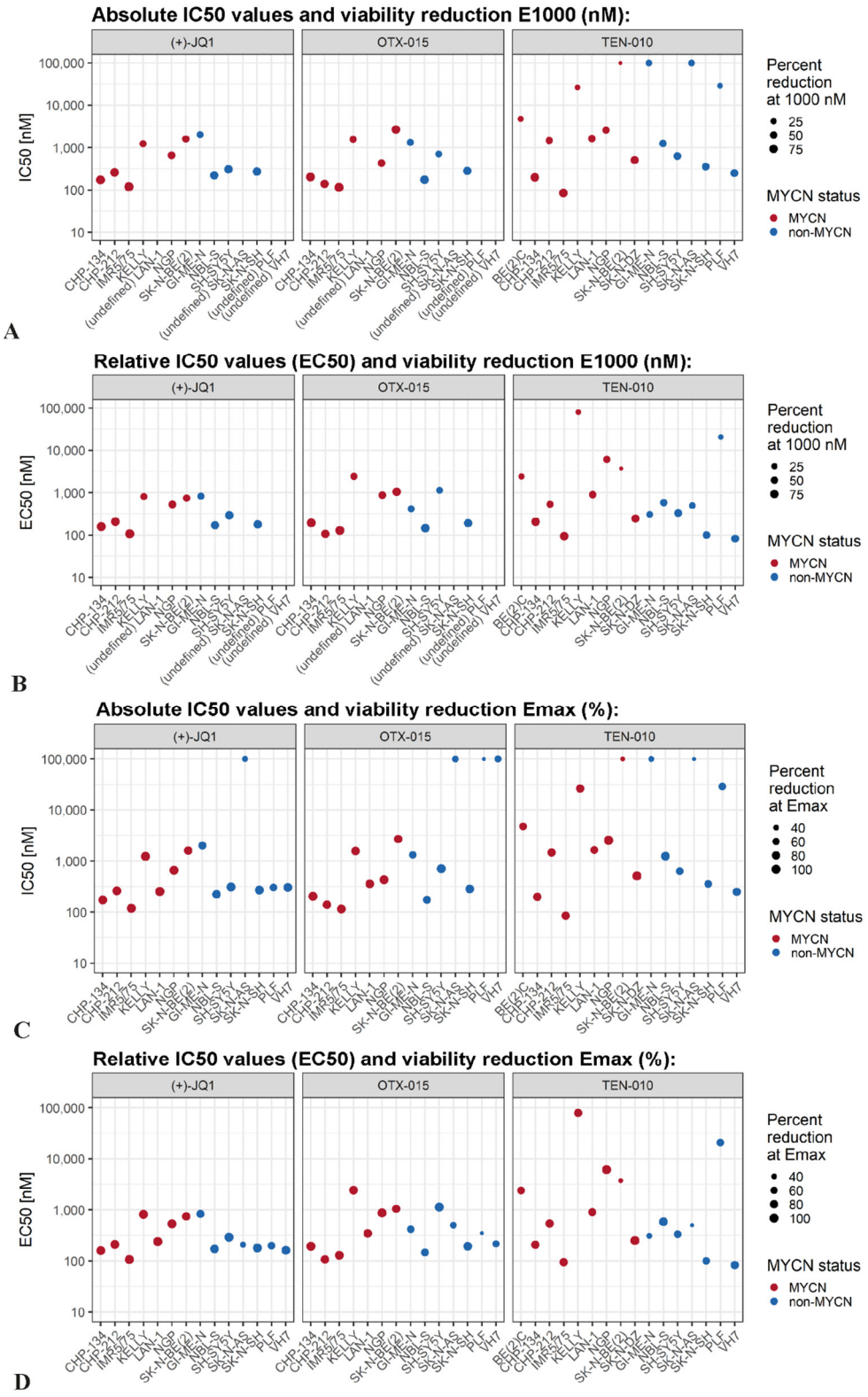

Figure 70: Comparison of inhibitory effects of BET inhibitors (+)-JQ1, OTX-015 and TEN-010 on cell viability. Aesthetic dot plots show variables of BET inhibitor effects mapped to visual properties. BET inhibitors JQ1, OTX-015 and TEN-010 were applied on 12-14 neuroblastoma cell lines and 2 fibroblast cell lines for three days. Combined mapping of the inhibitor effect parameters **(A)** absolute half inhibitory concentration IC50 and effect at 1,000nM inhibitor concentration, **(B)** relative half inhibitory concentration IC50 (EC50) and effect at 1,000nM inhibitor concentration, **(C)** absolute half inhibitory concentration IC50 and Emax and **(D)** relative half inhibitory concentration IC50 (EC50) and Emax. For each cell line, two to three biological replicates are shown with their respective median and range. Due to the lack of 1,000nM concentration values, these could not be mapped for some cell lines.

The experiments indicate that sensitivity to BET inhibition could be partially dependent on the *MYC(N)* status. Cell lines, which are *MYCN*-amplified show stronger effects on cell viability, growth, apoptosis and targets after administration of a BET inhibitor. But also non-*MYCN*-amplified cell lines, demonstrate a response to BET inhibition However, the inhibitor response was much more moderate than the response of the *MYCN*-amplified cell lines. In order to compare the characteristics of the cell lines with a good or bad response to a BET inhibitor, the genetic traits of the cell lines were opposed (see Table 8). First of all, it is noticeable that all cell lines show either a *MYCN* gain, a *MYCN* amplification, a *MYCN*-involving translocation or a *c-MYC* alteration (e.g. translocation). This could indicate a general increased MYCN/c-MYC expression. According to the hypothesis of previous publications, these traits should rather be favorable for an anti-tumor effect of the BET inhibition, but this does not seem to be the case for three cell lines. When comparing other genetic characteristics, namely chromosome 1p loss, 11q loss, *ALK, ATRX, TERT, TP53, CDK4/MDM2* and *CDKN2A*, a common feature of the BET inhibitor resistant cell lines becomes apparent. All of them exhibit a mutation of the *CDKN2A* gene, which encodes for two proteins, the $p14^{ARF}$ and the $p16^{INKa}$ protein[692,693]. Both proteins are tumor suppressors and are involved in the regulation of the cell cycle. $p14^{ARF}$ activates the p53 tumor suppressor, while $p16^{INKa}$ inhibits the cyclin dependent kinases CDK4/6, which leads to a reduction in cellular G1 to the S cell cycle phase transition[693]. The BET inhibitor resistant cells either show a methylation (of the *P14ARF* gene[694,695], GI-ME-N), a heterozygous deletion (SK-N-AS) or a copy number loss with an additional SNV mutation of the *CDKN2A* gene (SK-N-BE(2)), which is located on chromosome 9p[635,696]. Furthermore, two of the three BET inhibitor resistant cell lines show a mutation in the *TP53* gene. Additionally, an enhanced frequency of aberrations in the P53/MDM2/$p14^{ARF}$ pathway was found in neuroblastoma cell lines. On closer examination, it is noticeable that the BET inhibitor sensitive cell line NGP shows the highest possible maximum response (100%), but also an increased relative IC50 value (876nM). In the genetic background of this cell line, the *MDM2* gene is mutated several times (SNV, CNV and a rearrangement), which could indicate a correlation between an increased dose of BET compounds needed for the inhibition and *MDM2* mutations. In addition to these factors, other genetic alterations could also be related to BET inhibitor resistance, such as a rearrangement of the *TERT* gene or an activation of *TERT* expression. The connection between the sensitivity or resistance of neuroblastoma cells to BET inhibition should therefore be investigated more closely in other experimental models and in sequencing data of patient tumors.

Table 8: Summary of cell line features possibly contributing to BET inhibitor sensitivity or resistance.

Cell line name	Median EC50 of BETi (nM)	Median Emax of BETi (%)	designated sensitive / resistant to BETi	*MYCN* *c-MYC* status	Chr. 1p loss CN>1	Chr. 11q loss CN>1	ALK	*ATRX*	*TERT*	*TP53*	*CDK4* / *MDM2*	*CDKN2A* p16 (INK4a) p14 (ARF)
IMR 5/75	106.8	92.55	sensitive	MNA	x	x	rearr	x	high express	x	x	x
NGP	876.2	100	sensitive	MNA	t(1p) chr. 1p36 del	del CN: 0.93	x	CN: 1.17	high express	x	*MDM2* SNV: c.682C>T, rearr, CN: 10.98 *CDK4* CN:14	x
NBL-S	172	84	sensitive	*MYCN* (t(2; 4))	t(1p) del	x	x	x	high express	x	x	x
SH-SY5Y	332.3	96.9	sensitive	*MYCN* gain CN: 3.04 *c-MYC* (t(7; 8))	x	x	SNV: c.3522C<A	CN: 2.80	high express	x	x	x
SK-N-BE(2)	1053	77.57	resistant	MNA	t(1p) chr. 1p36 del	x	x	SNV: c.2265T>G	high express	SNV: c.404G>T CN: 0.89	x	**SNV: c.249C>A CN: 0.75**
GI-ME-N	415.3	64.73	resistant	super en-hancer amp down-stream *c-MYC*	del	x	x	x	*TERT*-r, high express	x	x	**methyl**
SK-N-AS	500	46.17	resistant	*c-MYC* (t(4; 8))	del	x	x	x	high express	mut	x	**HTZ del**

For calculation of the median EC50 (relative IC50) and Emax, the dose-response data of the BET inhibitors JQ1, OTX015 and TEN-010 were combined.
Abbreviations: MNA = MYCN amplification; t = translocation; CN = copy number; del = deletion; TERT-r = rearrangement; SNV = single-nucleotide variant; active = activated; express = expression; mut = mutated; methyl = methylated, HTZ = heterozygous

3.2.2 PLK1 and PI3K dual inhibition shows therapeutic potential in high-risk neuroblastoma models

3.2.2.1 Inhibition of PLK1 and PI3K reduces cell viability of neuroblastoma cells

PLK1 is highly expressed in unfavorable neuroblastomas, stabilizes the MYCN protein and in turn MYCN activates the transcription of PLK1[377,378]. The inhibition of PLK1 has been shown to be a successful treatment against neuroblastoma cells in previous work[379]. Especially the inhibitor volasertib showed significant anti-tumor potential and high selectivity upon single drug application in neuroblastoma and rhabdomyosarcoma models[382,383]. However, problems with PLK1 inhibitors have already been reported in research studies, arguing that PLK1 inhibitors only show their therapeutic effect when the dose is exceeded in the toxic range[697,698]. Another stabilizer of the MYCN protein, PI3K, is an essential node for cellular signal transduction, cell survival and cell metabolism[340]. The small molecule alpelisib showed promising results for the therapy of breast cancer, and could therefore also be a suitable drug against neuroblastoma[344]. PI3K inhibitors applied in neuroblastoma research so far are generally considered to be non-selective, and in the case of the drug wortmannin, the effects of inhibition are even irreversible[343,351]. For this reason, the focus of this work was shifted to PLK1/PI3K combinatorial drugs, which should avoid the disadvantages of single inhibitor application. The small molecule rigosertib is a suitable, dual drug that is worth testing in neuroblastoma cell lines. Rigosertib prevents the activation of RAS, thereby blocking the action of multiple kinases.

PLK1/PI3K inhibitors were tested *in vitro* on several neuroblastoma cell lines. For this purpose, the respective drug was administered to the neuroblastoma cells and after an incubation of three days, the change in cell viability was measured. The dose-response relationship was analyzed in a smaller cohort using the neuroblastoma cell lines IMR5/75, CHP-134, SK-N-AS, GI-ME-N and the non-malignant fibroblast cell line VH7. The PLK1 inhibitor volasertib, the PI3K inhibitor alpelisib, as well as with the dual PLK1 (RAS) and PI3K inhibitor rigosertib were applied to the cells. This series of experiments should reveal whether an inhibition of the cell viability under the dual compound rigosertib is equivalent to the respective individual medication against PLK1 and PI3K (Figure 71). Relative IC50 (E50) was displayed with comparable concentrations for rigosertib and volasertib, whereas the PI3K inhibitor alpelisib shows only a weak inhibitory effect. The relative IC50 values for rigosertib and volasertib either hardly differed at all (0.83nM difference in the cell line SK-N-BE), or only slightly (14.96nM difference in the cell line IMR5/75) or moderately (65.83nM difference in the cell line GI-ME-N) within the same neuroblastoma cell line. Further behind was the PI3K inhibitor alpelisib, which showed high relative IC50 values in neuroblastoma cell lines (e.g. 900nM in CHP-134). This pattern points towards to a slight resistance of the neuroblastoma cell lines to the single PI3K inhibitor, especially because the relative IC50 values were highly increased in single cell lines (104533nM in IMR5/75). Compared to rigosertib, the usage of alpelisib lead to higher relative IC50 values up from 871.62nM (SK-N-AS) or

104501.76nM (IMR5/75). A broad distinct effect on *MYCN*-amplified neuroblastoma cells could not be proven, rather the results show that the PLK1 inhibitors have a specific effect on certain cell lines, e.g. IMR5/75 or SK-N-AS. Fibroblast cell line VH7 displayed a weaker response to all inhibitors as compared to neuroblastoma cells. The maximum inhibitory effect of all three inhibitors always exceeded 50%, but all cells seem to respond less well to alpelisib. All inhibitors also showed a reduced potency in GI-ME-N cells and in the fibroblast cell line VH7.

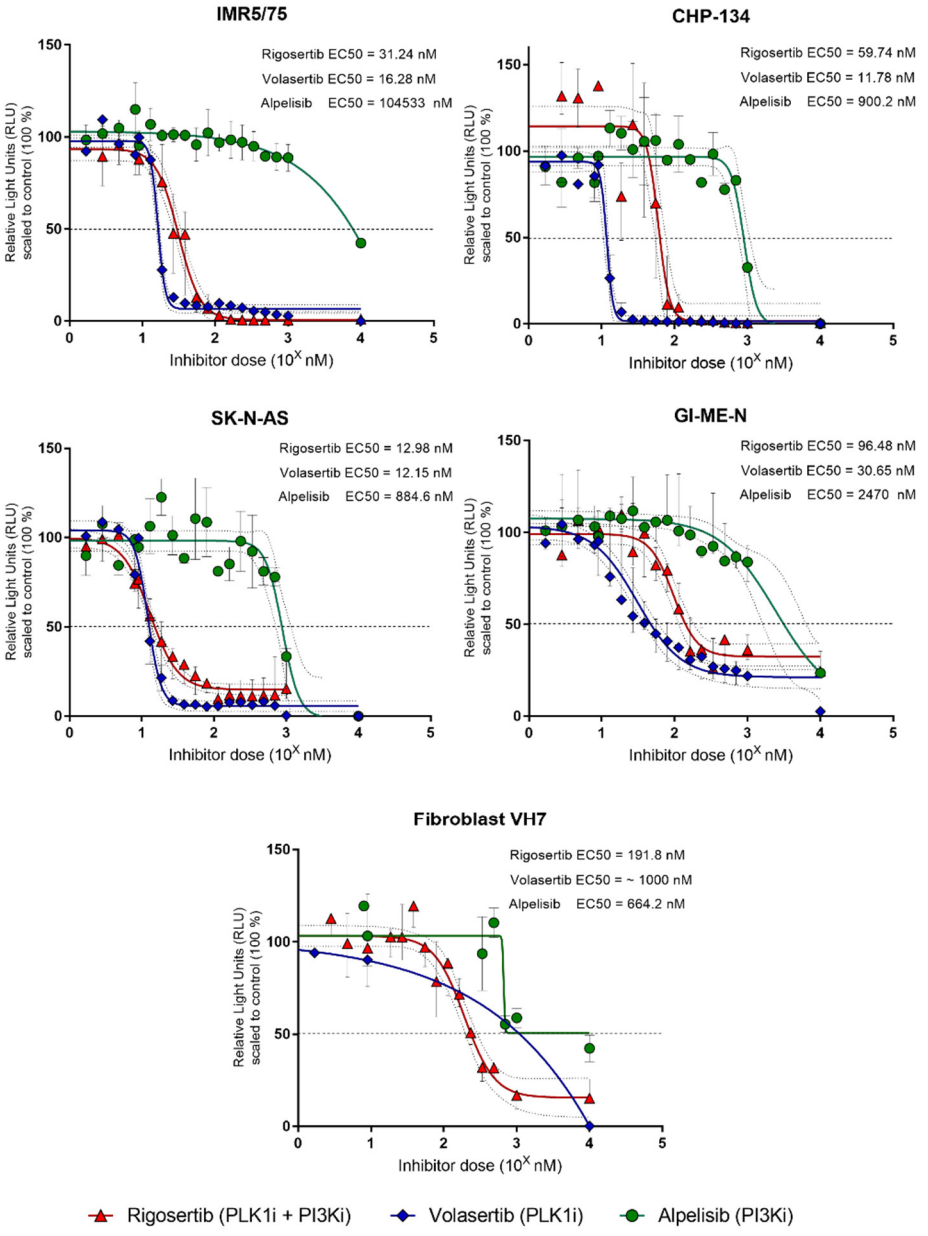

Figure 71: Single treatment inhibitory effects of PLK1 / PI3K inhibitors rigosertib, volasertib and alpelisib on cell viability.
The drugs were applied to 5 different cell lines *in vitro* and effect on cell viability was measured three days after treatment. The EC50 value represents the relative IC50 concentration. For each cell line, two to three biological replicates are shown with their respective median and range.

A closer analysis of the viability reduction when using a inhibitor concentration of 1000nM showed that the dose-response potency results are comparatively similar for volasertib and rigosertib. In contrast, the inhibitory potential of alpelisatib was slightly weaker as compared to volasertib and rigosertib. The inhibitors volasertib and rigosertib reached the highest reduction rate of 50-75% of the cell viability of all cell lines (Figure 72A). After usage of the PI3K inhibitor alpelisib, a cell viability reduction of 50-75% and more only occurred in the cell lines CHP-134, SK-N-AS and VH7. In contrast, the cell lines IMR5/75 and GI-ME-N showed higher relative IC50 values with a low maximum reduction of 25% and less. The maximum inhibitory response in the tested cell lines was found different for all three inhibitors (Figure 72B). A comparison of rigosertib and volasertib showed a high maximum response of 90-100% of the *MYCN*-amplified cell lines IMR5/75 and CHP-134. The cell viability of the non-*MYCN*-amplified cell line GI-ME-N was not completely inhibited by either rigosertib or volasertib. The non-*MYCN*-amplified cell line SK-N-AS only achieved a maximum inhibitory response of 98.4% by utilization of volasertib. The cells CHP-134 and SK-N-AS, which were treated with the PI3K inhibitor alpelisib, showed an almost complete maximum response to the drug inhibition (97.41% in CHP-134 and 99.11% in SK-N-AS). However, the cell lines IMR5/75 and GI-ME-N were not completely affected by alpelisib in terms of maximum dose response (60% for IMR5/75 and 77.50% for GI-ME-N). With regard to the non-malignant fibroblast cell line VH7, the cell viability was least affected by the inhibitor alpelisib. The inhibitory potential of volasertib and rigosertib on the VH7 cell line was roughly equivalent. The relative IC50 was quite low when rigosertib was applied (198nM) compared to volasertib (~ 1000nM), but volasertib showed a completely maximum response (100%) compared to rigosertib (91%). Based on this first comparison of the PI3K, PLK1 and dual inhibitors, the compound rigosertib was assigned an increased inhibitory effect on neuroblastoma cells equivalent to the inhibitor volasertib. Therefore, the dual PLK1 and PI3K inhibitor rigosertib was applied to several *MYCN*-amplified and non-*MYCN*-amplified cell lines as part of a broader *in vitro* screening. Rigosertib was tested on a total of 15 cell lines, including 9 *MYCN*-amplified neuroblastoma cell lines, five non-*MYCN*-amplified cell lines and one fibroblast cell line (Figure 73). Cells administered with rigosertib showed similar shapes of dose-response curves for *MYCN*-amplified cells and non-*MYCN*-amplified cells (Figure 73A). The fibroblast cell line VH7 showed a less strongly inhibitory dose-response relationship from rigosertib to cell viability compared to neuroblastoma cells. This dose-response curve reached a plateau with remaining cell viability around 18% and a total inhibition was not achieved. The relative IC50 (E50) concentration was very similar for *MYCN*-amplified (65nM) and non-*MYCN*-amplified cell lines (53nM). In addition, it is noticable that these IC50 values are very low and that the neuroblastoma cells responded very well to rigosertib. The lowest relative IC50 was measured for *MYCN*-amplified cell lines in the IMR5/75 cell line (33nM) and the highest in the SK-N-BE(2) cell line (238nM). For non-*MYCN*-amplified cells, the lowest relative IC50 was detected in SH-SY5Y (42nM) and the highest value was measured in the GI-ME-N cell line (90nM). The fibroblast cell line VH7 displayed a median IC50 value of 207nM, which is comparable high to neuroblastoma cell lines.

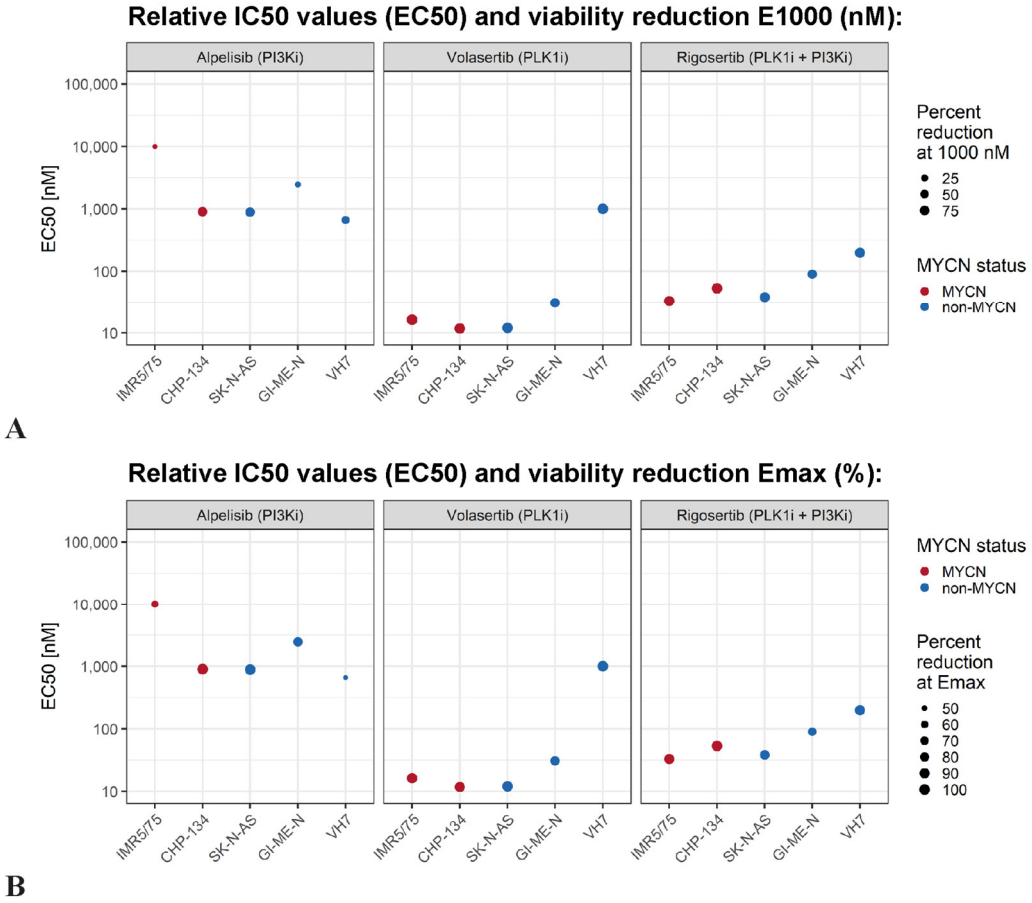

Figure 72: Comparison of inhibitory effects of alpelisib (PI3Ki), volasertib (PLK1i) and rigosertib (PLK1i + PI3Ki) on cell viability.
Aesthetic dot plots shows variables of PI3K and PLK1 inhibitor effects mapped to visual properties. Effects on cell viability after 3 days of treatment are shown. Combined mapping of the inhibitor effect parameters **(A)** relative half inhibitory concentration IC50 (EC50, effective half inhibitory concentration) and effect at 1,000nM inhibitor concentration and **(B)** relative half inhibitory concentration IC50 (EC50) and maximal inhibitory effect Emax. For each cell line, two to three biological replicates are shown with their respective median and range.

The relative IC50 for the fibroblast cell line differs from the IC50 of the neuroblastoma cells (142nM lower relative IC50 for *MYCN*-amplified and 154nM lower for non-*MYCN*-amplified neuroblastoma cells as compared to fibroblasts). An almost total inhibition of neuroblastoma cell viability was achieved overall for the *MYCN*-amplified cell lines rather than for the non-*MYCN*-amplified cell lines. Regarding the maximum inhibitory effect (Emax), this was highest in the *MYCN*-amplified cell lines (98%). The maximum inhibitory effect for non-*MYCN*-amplified neuroblastoma cells (88%) was less than for *MYCN*-amplified cells and comparable to the effect in fibroblast cell lines (91%). In a statistical analysis using the non-parametric Mann-Whitney test, only a slight significance of the difference between *MYCN*-amplified and non-amplified cells could be demonstrated ($p = 0.1469$; Figure 73B). The lowest maximal inhibitory effect was measured for *MYCN*-amplified cell lines in the SK-N-BE(2) cell line (86.69%) and the highest in the CHP-134 cell line (100%). For non-*MYCN*-amplified cells, the lowest maximal inhibitory effect was detected in GI-ME-N (67.61%) and the highest value was measured in NBL-S cells (98.36%). The fibroblast cell line VH7 displayed a maximal inhibitory effect of 91%.

The dual PLK1/PI3K inhibitor rigosertib showed a good response in all cell lines tested and highlights it's potential due to low active relative IC50 values below 100nM. *MYCN*-amplified and non-*MYCN*-amplified neuroblastoma cells responded equally well to the drug, with low relative IC50 values and an almost complete, maximum inhibition (Figure 73C+D). Only a slightly improved effect in *MYCN*-amplified neuroblastoma cells was seen. However, this result is consistent with the biological mode of action of rigosertib, which inhibits kinases and only connect to *MYCN* amplification through the increased proliferation of *MYCN*-mutated neuroblastoma cells. An inhibition of the cell viability of the non-malignant fibroblast cell line VH7 was also detected, but less than in comparison to the neuroblastoma cells.

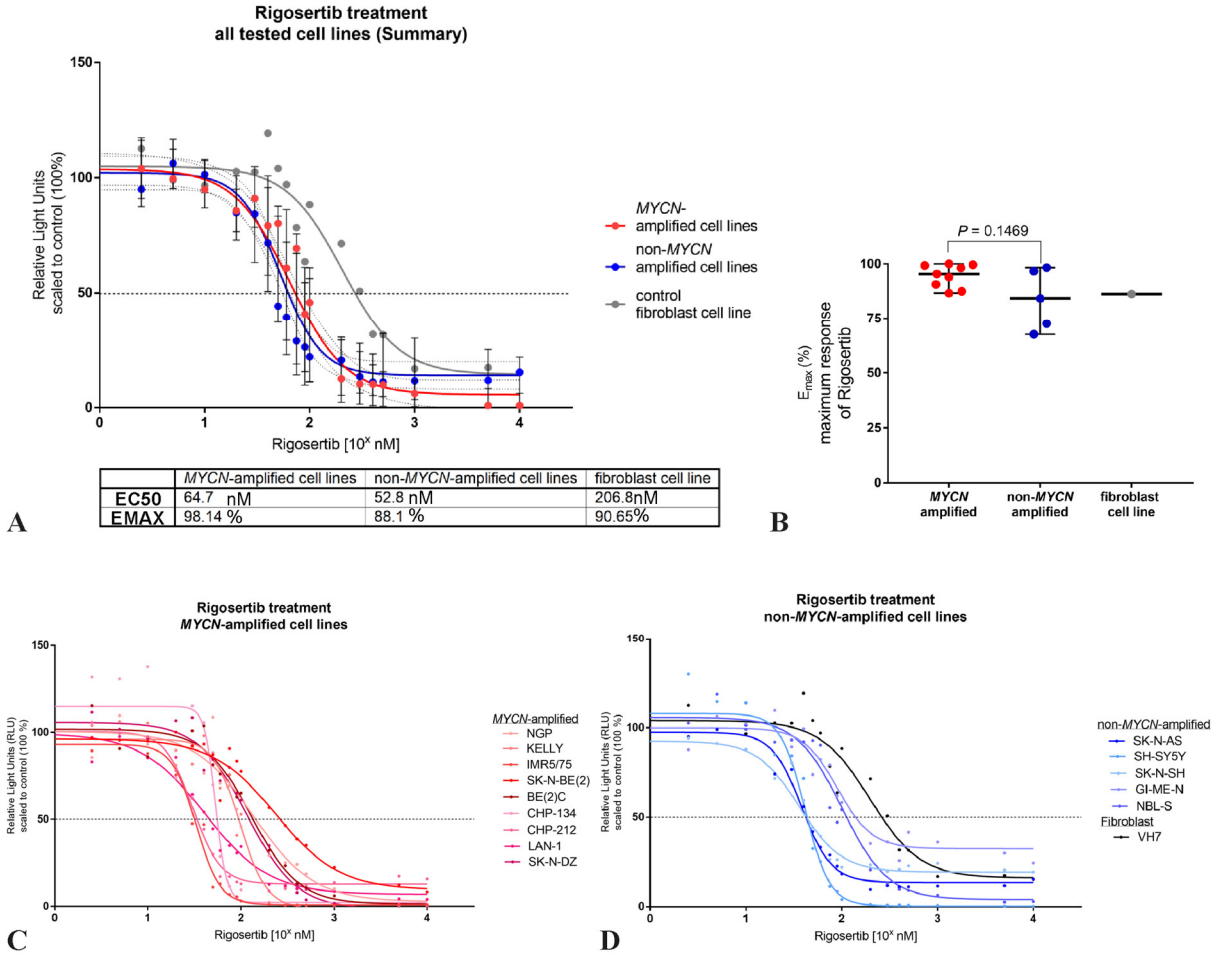

	MYCN-amplified cell lines	non-*MYCN*-amplified cell lines	fibroblast cell line
EC50	64.7 nM	52.8 nM	206.8nM
EMAX	98.14 %	88.1 %	90.65%

Figure 73: Rigosertib dose to cell viability response relationship in neuroblastoma cell lines and VH7 fibroblast cell line.
Dual PLK1 and PI3K inhibitor rigosertib was applied to 15 different cell lines *in vitro* and effect on cell viability was measured three days after treatment. **(A)** Relative IC50 (E50) is displayed. Emax in mean interpolated by GraphPad Prism®. **(B)** A comparision of the Emax of rigosertib, the median and range of the Emax value of all respective cell lines is shown. **(C)** In total, 9 *MYCN*-amplified cell lines were tested, the dose-response curve shows median with range for each concentration tested in a cell line. All cell lines displayed a maximum effect with more than 50%. **(D)** Five non-*MYCN*-amplified cell lines and one fibroblast cell line were treated and showed a maximum effect with more than 50%. The EC50 value represents the relative IC50 concentration. For each cell line, two to three biological replicates are shown with their respective median and range.

The response of individual cell lines to rigosertib was further examined in more detail (Figure 74). A closer investigation of the relative IC50 values of the cell lines showed that a very good response to rigosertib was detected (Figure 74A). Rigosertib relative IC50 (EC50) concentrations range from 22 – 240nM in *MYCN*-amplified neuroblastoma cells, from 21 – 163nM in non-*MYCN*-amplified neuroblastoma cells and from 136 – 258nM in fibroblast cell line VH7. Some cell lines responded equally well to rigosertib and showed similar IC50 values in lower ranges of up to 75nM. Interestingly, this effect was observed across neuroblastoma cells, both *MYCN*-amplified cell lines (CHP-134, CHP-212, IMR5/75 and LAN-1) and non-*MYCN*-amplified cells (SK-N-AS, SH- SY5Y and SK-N-SH) showed a good response. In addition, in some cell lines were less high relative IC50 values measured, e.g. NGP, SK-N-BE(2) or NBL-S. The fibroblast cell line VH7 showed on average high IC50 values. Overall, the cells responded very well to rigosertib treatment, since the cell viability of all lines was far below the cut-off of 1000nM (according to Drug Target Commons[648,649], see for explanation 3.2.1) and thus showed a clear potential for targeted treatments of neuroblastomas.

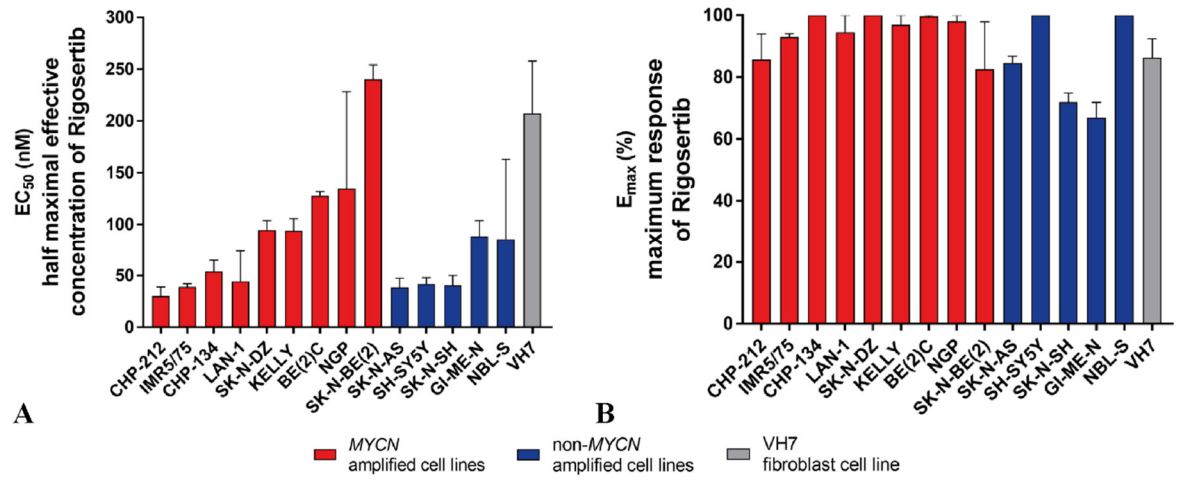

Figure 74: Rigosertib shows inhibitory effectiveness in low concentrations and high maximum response to cell viability .
(A) Rigosertib relative IC50 (EC50) concentrations in neuroblastoma cells and in fibroblast cell line VH7. **(B)** Rigosertib Emax responses in neuroblastoma cells and in fibroblast cell line VH7. The EC50 value represents the relative IC50 concentration. For each cell line, two to three biological replicates are shown with their respective median and range. Red bars indicate *MYCN*-amplified cell lines, and blue bars indicate non-*MYCN*-amplified cell lines.

A comparison of the maximum response (Emax) between all cell lines that received rigosertib also showed a very good response of the cell viability (Figure 74B). The rigosertib Emax responses range from 81 – 100% in *MYCN*-amplified neuroblastoma cells, from 64 – 100% in non-*MYCN*-amplified neuroblastoma cells and from 85 – 92% in fibroblast cell line VH7. There was a slight difference in the maximum response identified between the *MYCN*-amplified cell lines and the non-*MYCN*-amplified cell lines. *MYCN*-amplified cell lines showed an increased maximum response in contrast to the non-*MYCN*-amplified cells. A lower maximum inhibition could only be detected for the cell line SK-N-BE(2). Of the non-*MYCN*-amplified cells, only two cell lines, SH-SY5Y and NBL-S, showed an equally good maximum response as most of the *MYCN*-amplified cell lines. In particular, the cell line GI-ME-N

showed the lowest maximum response to rigosertib in the detection of cell viabilities. Finally, it can be said that the compound rigosertib shows a strong inhibition of neuroblastoma cell viability in the lower nanomolecular range of the drug concentration. The maximum inhibitory response of cell viability was always detected over 50%. *MYCN*-amplified and non-*MYCN*-amplified cells are inhibited almost equally. In summary, the rigosertib dual PLK1/PI3K inhibitor compares with the PLK1 inhibitor volasertib and also showed a superiority over the PI3K inhibitor alpelisib in terms of neuroblastoma cell viability reduction.

3.2.2.2 Simultaneous inhibition of PLK1 and PI3K reduces clonogenicity, suppresses migration and induces apoptosis in neuroblastoma cells

Based on previous reports and own research (3.2.2), the dual inhibition of PLK1 and PI3K with rigosertib was suspected to have an antitumor effect on tumor cells[398,405,699,700]. Therefore, the following functional experiments were carried out in order to investigate the altered cellular processes in neuroblastoma cells after rigosertib inhibition. An effect of rigosertib on neuroblastoma cells was initially be determined visually (Figure 75). After rigosertib was applied to the cell media, the neuroblastoma cells grew less and the cells detached from the ground. The treated cells all had a much more rounded morphology and overall a smaller cell body than in comparison to the cells treated with ddH_2O. One day after the treatment with rigosertib, *MYCN*-amplified neuroblastoma cells IMR5/75 showed a rounded appearance starting from a concentration of 100nM (Figure 75A). With higher doses of rigosertib (as seen with 500nM and especially 1000nM rigosertib), fewer cells were visible on the surface of the dish compared to the control. In addition, the cells showed an even more distinct, rounded appearance. After a total of 48h, the cells that were treated with the vehicle were already widely spread in cell density and in the area offered to them. Upon visual assessment, approximately 90% of the dish surface was covered with cells. When treated with 100nM rigosertib, which corresponds to a relative IC75 of the IMR5/75 cells, the neuroblastoma cells detached from the ground and had a very rounded appearance. It is suspected that these cells may have been apoptotic. Even with a treatment using 500nM rigosertib, the morphology of the neuroblastoma cells was changed. They showed a strongly rounded and less space-consuming cell body. From a concentration of 1000nM rigosertib onwards, only a few neuroblastoma cells were visually recognizable in relation to the control (approximately 30%). GI-ME-N non-*MYCN*-amplified neuroblastoma cells reacted less to rigosertib treatment, which in comparison to IMR5/75 was more attributable to drug resistance (Figure 75A). While the GI-ME-N cells with the control treatment showed no influence in spread or confluence one day after experiment start, the greatest visual difference to the control was only seen from a dose of 1000nM rigosertib. Although a concentration of 500nM meant an inhibition rate of about the relative IC80-90 for the GI-ME-N cells, they visually displayed a similar shape as compared to the control. From a dose of 1000nM, which was far above the relative IC90, significantly fewer cells and a lower cell density was visible on the dish surface. After 48 h, the control was already strongly confluent (approximately 90%), while the treated

GI-ME-N cells showed a less confluence population. In addition, the cell population was less numerous grown on the plate. In terms of morphology, GI-ME-N cells were less branched with increasing concentration and showed fewer neurite-like sprouts. On visual observation, the cells were also less connected to each other by these outgrowths. The higher the concentration of rigosertib and the longer the incubation time, the less branched and elongated was the morphology of the GI-ME-N cells. It could be confirmed that the cell confluence decreases after the application of rigosertib, neuroblastoma cells also showed a more rounded morphology and detached from their growth surface.

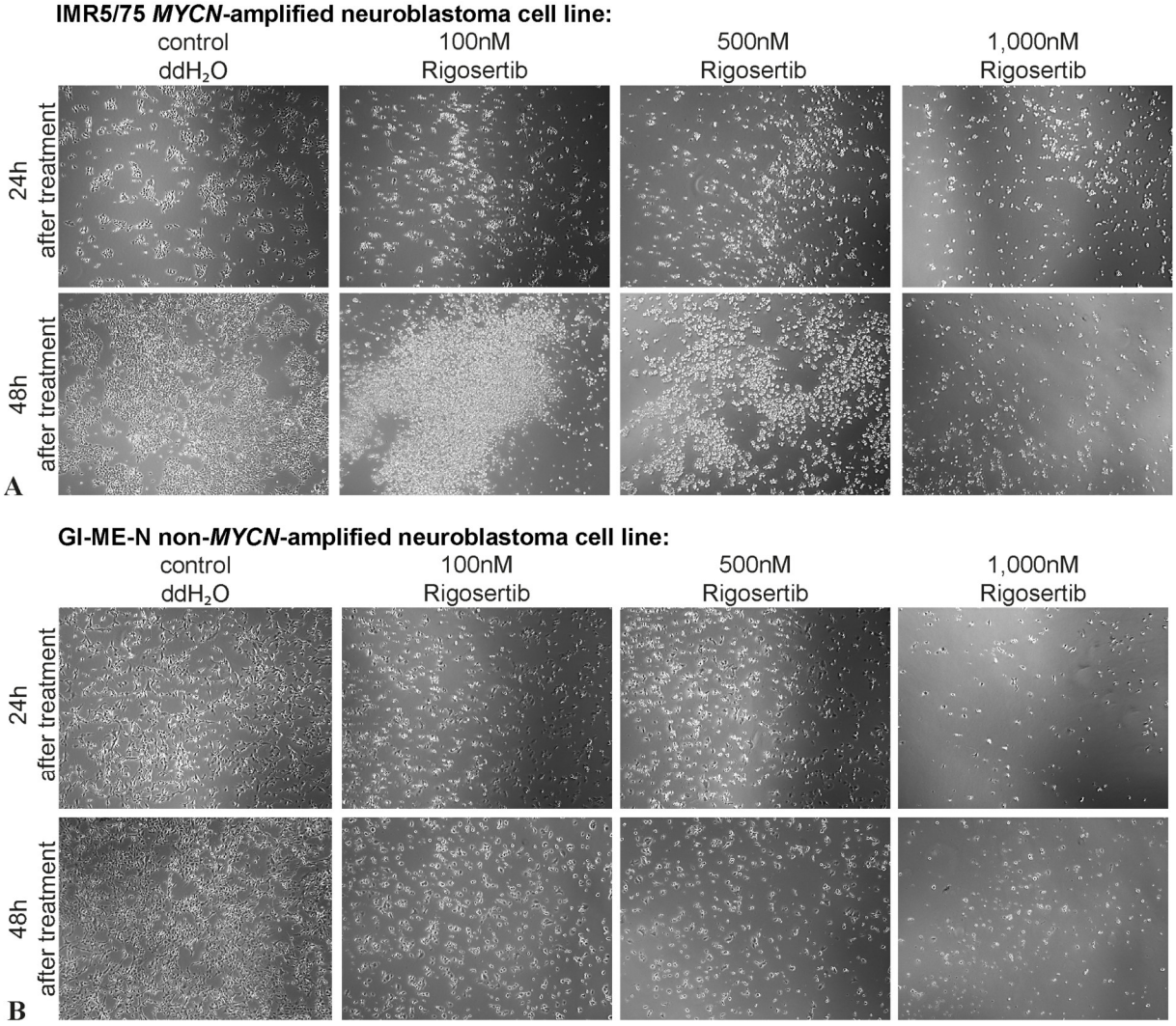

Figure 75: Treatment with rigosertib inhibits cell growth and diminishes the cell population 24 and 48h after application.
After treatment with rigosertib, smaller cell populations were observed as compared to the control treatment. The cells were treated either with rigosertib or with ddH_2O as a control. Comparison of the *MYCN*-amplified **(A)** IMR5/75 cell line with the non-*MYCN*-amplified **(B)** GI-ME-N cell line.

With the help of a clonogenic 2D assay, the visual observations of the reduction in cell confluence after rigosertib treatment should be examined in more detail. Four neuroblastoma cell lines, IMR5/75, CHP-134, SK-N-AS and GI-ME-N were treated with rigosertib and their cell colonies were stained with 1% crystal violet 7 days after the treatment (Figure 76). In comparison, the cell lines showed a different potential of reproductive survival. After treatment with its relative IC50 (EC50) of 4nM, the cell line

IMR5/75 already showed fewer cell colonies and a less expanded growth area. Upon treatment with the relative IC50 (22nM), IMR5/75 colonies were hardly recognizable, they became very narrow and few. After treatment with their relative IC50 (33nM), almost no colonies were visible. In comparison, the CHP-134 cell line reacted even more strongly to rigosertib than the IMR5/75 line. Subsequently of rigosertib application with their relative IC30 of 23nM, only a few cell colonies of CHP-134 were visible. In addition, a change in the shape of the colonies was seen starting from the relative IC20 of 13nM.

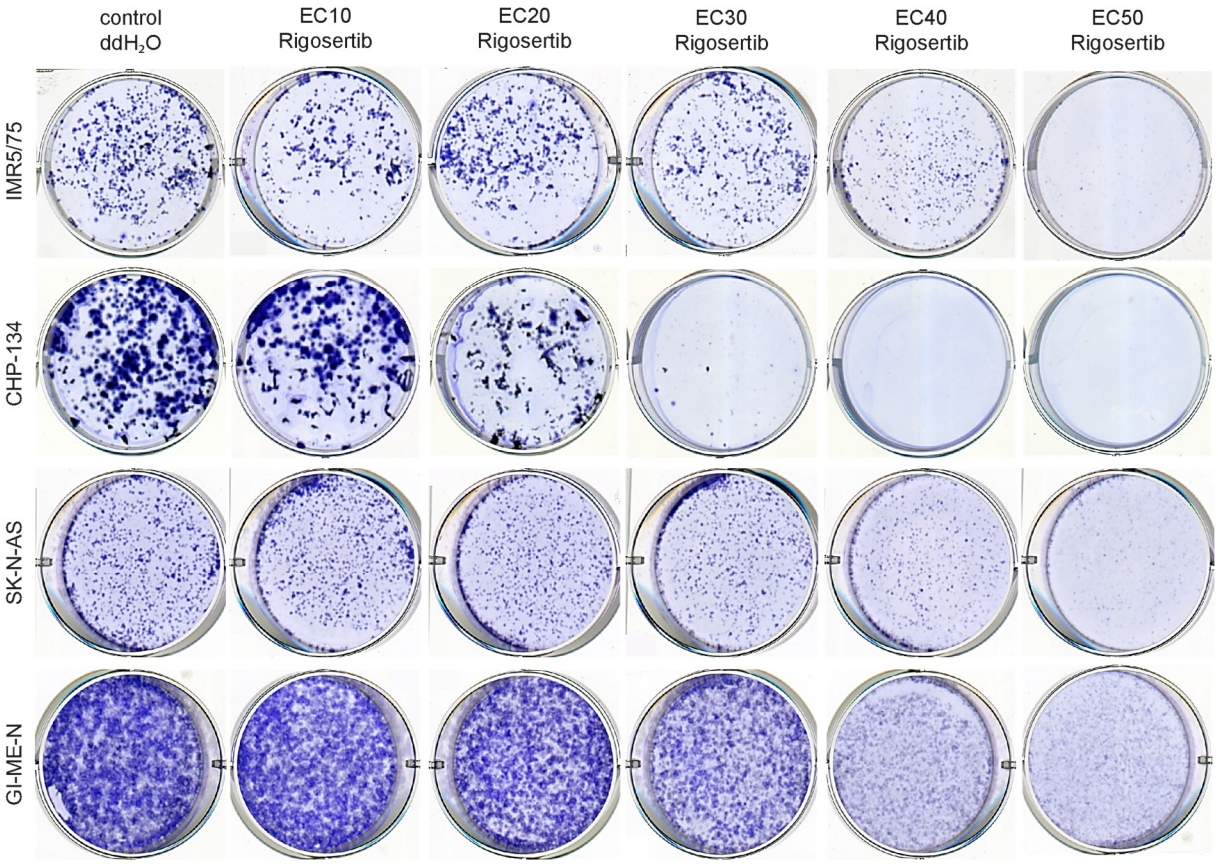

Figure 76: Neuroblastoma cells display reduced reproductive survival and decreased ability to form colonies after rigosertib treatment.
Clonongenic 2D assay shows neuroblastoma cell colonies stained with 1% crystal violet after 7 days of rigosertib treatment. The neuroblastoma cells were treated with their relative IC10 to IC50 (effective EC10-50) concentration of rigosertib. Only a fraction of seeded cells, which did not die due to the treatment, retained the capability to produce colonies.

These CHP-134 colonies were no longer spread out over a large area with a flat appearance, they became narrow and less numerous. The neuroblastoma cell lines IMR5/75 and CHP-134 could thus be assigned as “responders” to rigosertib treatment. The SK-N-AS cell line still shows the ability to form colonies, despite treatment with its relative IC50 from rigosertib (38nM). However, with increasing inhibitor concentration the colonies appeared very narrow and fewer numbers were visible. Overall, the density of colonies decreases with increasing rigosertib concentration for the SK-N-AS cell line. It can therefore be concluded that the SK-N-AS cell line displayed a moderate response to rigosertib. The GI-ME-N cell line shows high cell confluence despite treatment with rigosertib. Even if their relative IC50

corresponding to 90nM rigosertib is added, small and narrow colonies are still visible on the surface of the well. It is therefore assumed that this cell line is a low or non-responder to PLK1/PI3K inhibition by rigosertib. In summary, it was observed that neuroblastoma cells respond differently in their colony formation to the inhibitor rigosertib. While some cells stopped growing and the formation of colonies after rigosertib treatment (e.g. CHP-134), other cells in turn retained their capability of their reproductive survival (GI-ME-N). Nevertheless, there is a clear reduction visible in colony density after rigosertib treatment as compared to control. After it could be shown that the cell confluence and the ability to form colonies decreased upon treatment with rigosertib, further evidences for an influence of the drug on the neuroblastoma cell biology were carried out. Using Ibidi cell culture chambers a gap was created between two populations of IMR5/75 cells and changes in cell motility after treatment with rigosertib was analyzed (Figure 77).

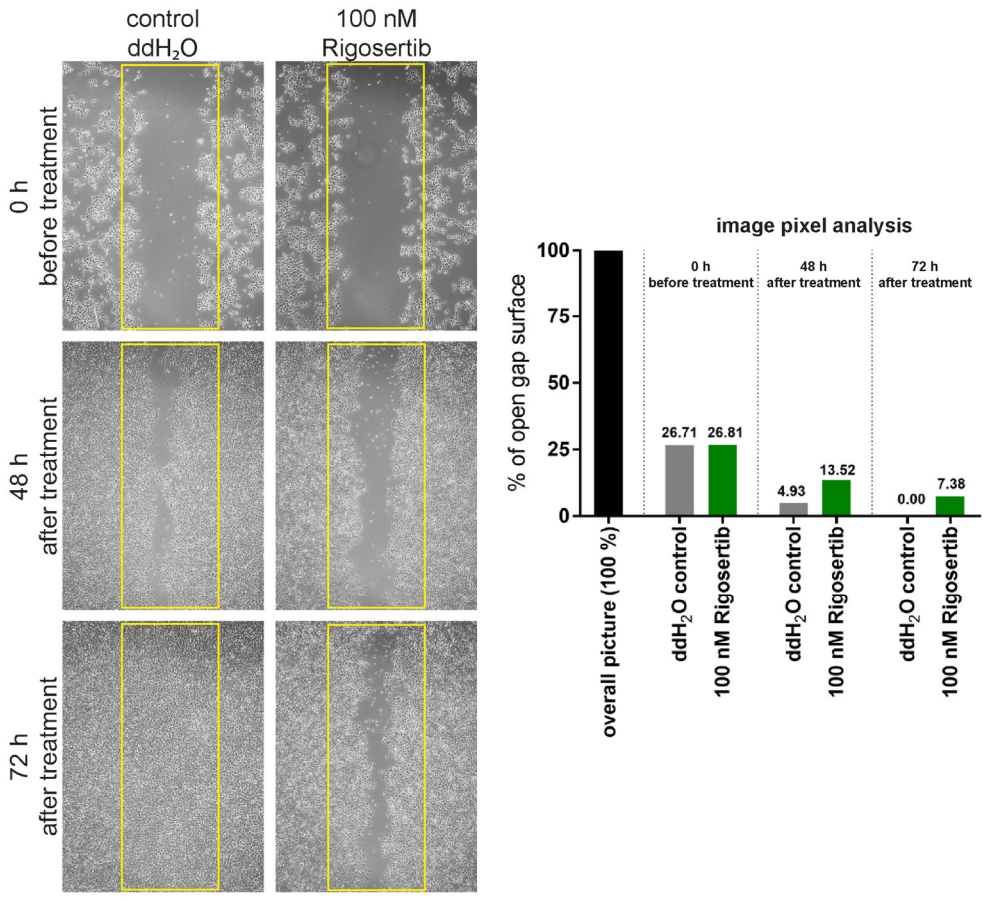

Figure 77: IMR5/75 neuroblastoma cell migration and wound healing is disrupted after administration of rigosertib. Neuroblastoma cells were seeded in Ibidi chambers to create a gap between two cell populations. After treatment with 100nM rigosertib, fewer IMR5/75 cells migrated into the gap compared to the ddH_2O control. Futher, a delayed wound closure or gap closure could be seen after application of rigosertib.

At the beginning, the gap area between the two cell populations was around 26% in relation to the total photo (100%) which was detected utilizing transmitted light microscopy. Two days after the treatment with rigosertib, it was clearly visible that the wound between the two cell fronts closed less well than compared to the ddH_2O control. Furthermore, the borders of the two cell population come into contact within the control well which could not be detected in the rigosertib sample. The wound size of the

rigosertib treated cells still accounted for 14% of the total image, whereas the ddH_2O control displayed gap size with about 5%. After 72h, the wound in the control well was already completely closed. The IMR5/75 cells had all migrated into the gap between the two population fronts and had closed the wound. The cells treated with rigosertib showed a progressive wound closure compared to the previous day (gap size of around 7% compared to the total picture after 72h), but the gap could not be completely closed. Thus, the migratory potential of rigosertib administered IMR5/75 neuroblastoma cells was reduced compared to untreated cells. Because cell migration is a key ability when it comes to tissue formation or cancer progression, rigosertib shows the potential to disrupt cell migration. In the broadest sense, it could therefore be possible to prevent migration of neuroblastoma cells into other non-infiltrated areas using rigosertib. In the microscopic examination of the cells, in the clonogenic assay and in the wound healing assay, an increased detachment of the cells from the ground and a probable induced cell death could be observed after treatment with rigosertib. In order to test this hypothesis whether neuroblastoma cells die after administration with the dual PLK1/PI3K inhibitor, IMR5/75 cells were stained 24 h and 72h after treatment with rigosertib using Annexin V-FITC/PI and were measured applying flow cytometry (Figure 78). After the neuroblastoma cells were short-treated with rigosertib for 24 h, there was no difference in the proportion in apoptotic cells between the cells treated with the relative IC50 (EC50, 33nM) and the control cells treated with ddH_2O. However, if a higher dose of rigosertib was administered (EC80, 132nM), the effects of the inhibition became visible even after 24 h. A proportion of 8.8% of the cells treated with the relative IC80 showed a positive Annexin V signal, which is representative for early apoptosis, compared to 4.24% of the population measured in the control. With regard to the detection of late apoptotic/necrotic cells, the difference between the control and the treated sample was even greater. A positive Annexin-V/PI signal was detected in 10.9% of the rigosertib administered cells, compared to 1.91% in the control. In an analysis of IMR5/75 cells, which were incubated for 72h with the relative IC80 from rigosertib, the proportion of late apoptotic/necrotic cells increased further. This fraction was 30.3% in the treated sample and only 0.3% in the control sample. Is was an increase of 19.4% in the population as compared to the 24h treatment. In contrast, the proportion of early apoptotic cells in the 72h relative IC80 treatment (0.78%) decreased compared to the 24h treatment (8.8%). This could indicate that the Annexin V positive cells could probably additionally become PI positive over the duration of the treatment, which means that not only the inner membrane phospholipids were exposed to the outside, but also the DNA was stained. The reason for this could have been a shift in the population from early apoptosis to late apoptosis or necrosis. Nevertheless, about 10.9% of the late apoptosis/necrosis population was found in addition in the 72h IC80 treated sample compared to the 24h sample. The effect of cell apoptosis is thus even stronger after a longer treatment than a short-term treatment. IMR5/75 neuroblastoma cells respond to treatment with rigosertib with an induction of apoptotic/necrotic processes, and this effect is intensified by the duration of the treatment. Furthermore, a shift from early apoptosis to cell death or necrosis was detected after prolonged treatment with rigosertib.

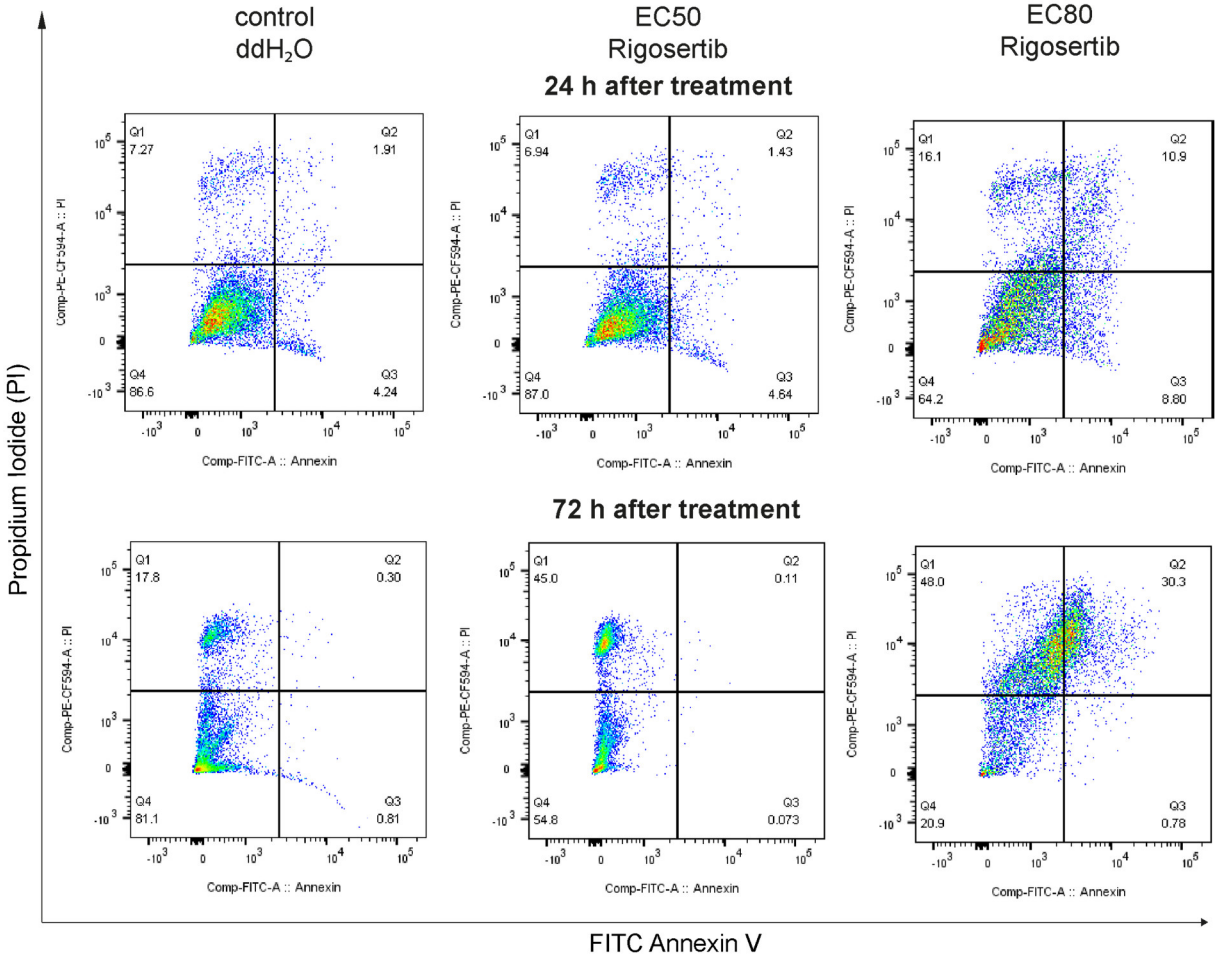

Figure 78: Treatment with the dual PLK1/PI3K inhibitor rigosertib leads to programmed cell death in IMR5/75 cells. Flow cytometry dot-plots of Annexin V-FITC/PI dual staining analysis of neuroblastoma cell apoptosis after administration of rigosertib (relative IC50 (EC50): 33nM and IC80: 132nM) for 24 and 72h. The rate of early apoptosis was higher in relative IC80 treated cells as compared to IC50 treated cells. In addition, late apoptotic or dead cell levels were higher in relative IC80 treated cells as compared to IC50 treated cells. Further, cells harvested after 72 h treatment showed an increased level of late apoptotic or dead cells as compared to cells harvested after 24 h treatment. As control, ddH_2O was applied. One biological replica is shown.

It further was to examined whether the treatment with rigosertib not only inhibits their direct targets PLK1 and PI3K, but whether an application of the drug also leads to a reduction in *MYCN* transcript levels. For this purpose, the RNA transcript levels were checked in a small test experiment using qPCR (Figure 79A). *MYCN*-amplified SK-N-BE(2) cells were treated for 24h with their relative IC50 (EC50, 238nM) concentration of rigosertib and the *MYCN* transcript levels were then measured. After treatment with the inhibitor, the transcript levels of *MYCN* in the SK-N-BE(2) cell line were reduced by 57.73% compared to the cells treated with ddH_2O. This result indicates a decrease of the *MYCN* RNA levels potentially following lower tumorigenicity. In addition, a reduced proliferative behavior of the cells could also have been reduced the *MYCN* levels. To confirm the target activity of rigosertib to kinases in the *in vitro* experiments, the expression of PLK1 and PI3K downstream proteins was assessed applying Western immunoblotting analysis (Figure 79B). *MYCN*-amplified IMR5/75 cells were treated with their relative IC50 (EC50) of 33nM rigosertib for 96h and were subsequently analyzed for their protein expression. Rigosertib treatment led to a significant repression of the MYCN protein. These results are

in line with the observations seen in qPCR analysis. Furthermore, the expression of the PLK1 downstream target WEE1 was reduced, as well as the MST1 protein, which is also found in indirect order downstream in the PI3K signaling pathway. A negative effect of rigosertib on the protein expression of MST1 as well as on the target protein mTOR could also be observed in IMR5/75 cells treated with their relative IC80. In addition, a reduction in the protein expression of WEE1, MST1 and AKT1 was detected after a relative IC50 treatment of SK-N-AS cells (data not shown). The results of these small-scale protein expression experiments are a first indication that a treatment with the dual PLK1/PI3K inhibitor leads to repression of PLK1 and PI3K activity in neuroblastoma cells.

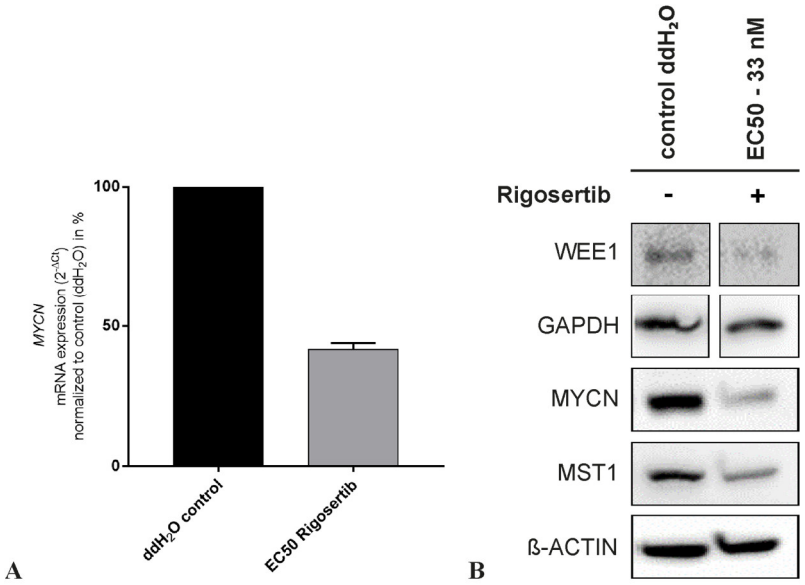

Figure 79: Rigosertib treatment induces reduction of *MYCN* mRNA and protein levels, and leads to repression of PLK1 and PI3K functions in neuroblastoma cell.
(A) After 24h of treatment with rigosertib (relative IC50: 238nM), a reduction of *MYCN* RNA transcript levels was seen in SK-N-BE(2) neuroblastoma cells. As control, ddH_2O was applied. One biological replica is shown with their respective median and range of three technical replicates. **(B)** Western immunoblotting of PLK1 and PI3K downstream targets after incubation of IMR5/75 neuroblastoma cells with rigosertib (relative IC50: 33nM) for 96h. As control, ddH_2O was applied.

Taken together, treatment with the dual PLK1/PI3K inhibitor rigosertib led to a reduction in cell growth, cell spread and to a decreased ability to form cell colonies and migration. Further, the induction of cell apoptosis and necrosis was detectable upon rigosertib treatment. In a preliminary experiment, the inhibitor was able to reduce the *MYCN* RNA transcript levels. In addition, a decline in the protein expression of PLK1 and PI3K downstream targets was observed, this reduction particularly affected the proteins WEE1, MST1 and MYCN in further distance.

3.2.2.3 Rigosertib-mediated dual PLK1 and PI3K inhibition has antitumoral activity against neuroblastoma xenografts

Rigosertib is currently being tested in clinical trials as a single agent, and in combination with azacitidine, in patients with myelodysplastic syndromes[701]. To investigate the efficacy of rigosertib on its anti-tumor potential *in vivo*, a high-risk neuroblastoma PDX was subcutaneously grown in mice.

The mouse experiments were carried out in three independent test series. In the first round, a total of 10 immunodeficient NOG female mice were subcutaneously engrafted with a high-risk *MYCN*-amplified neuroblastoma tumor (Figure 80). The NOG mice with subcutaneously engrafted *MYCN*-amplified neuroblastoma xenografts exhibited significant tumor growth for randomization within the third week after PDX transplantation. The experiment was started at a tumor size of 0.2 – 0.25cm³, mimicking a clinical relapse or therapy-refractory situations at which rigosertib would be administered. The group of 10 mice was then randomized into two groups (n=5), a treatment group and a vehicle group, and the treatment started on day 19 after transplantation. At day 26, a very slightly reduced tumor growth compared to untreated controls was observed. In terms of the tumor volume, the median range was found 0.51cm³ for the vehicle group and 0.461cm³ for the treatment group (Figure 80A).

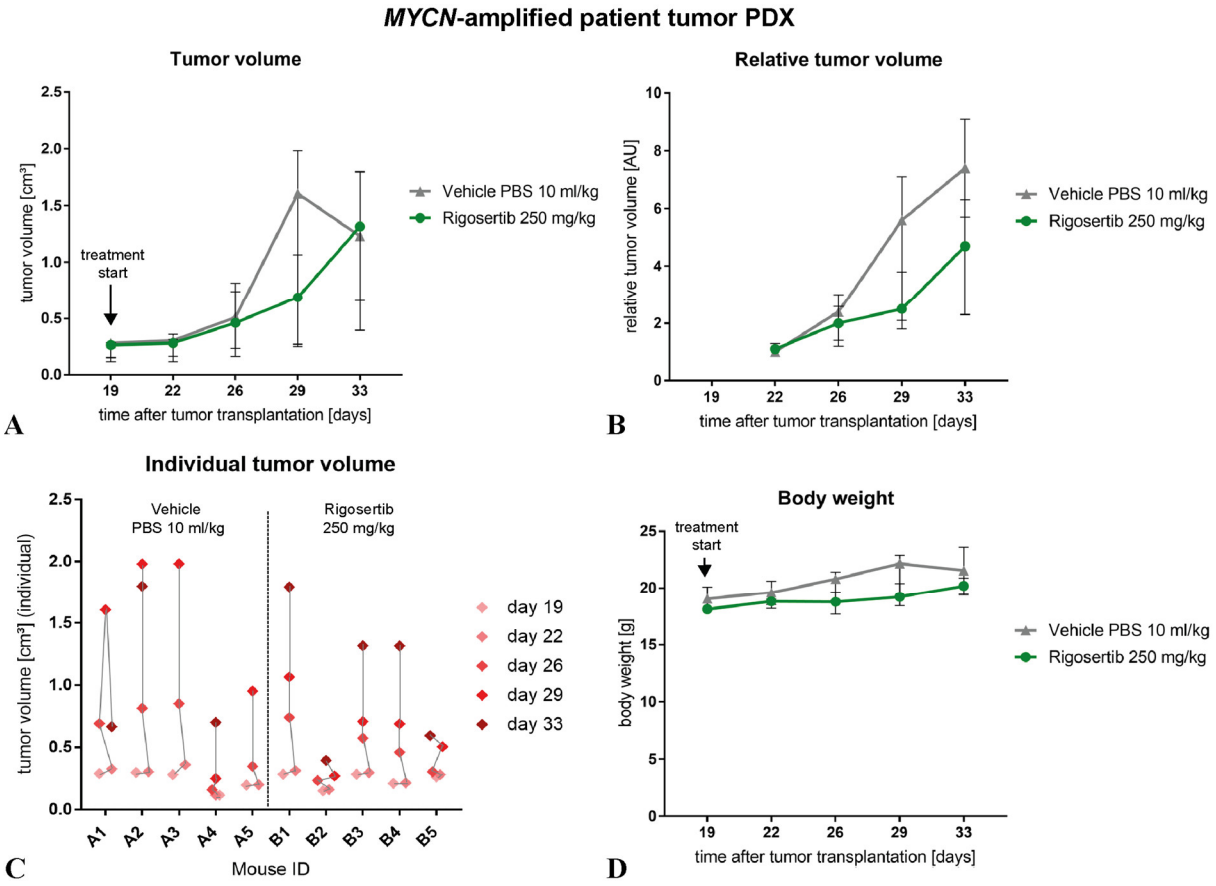

Figure 80: Rigosertib shows antitumor effects against a PDX mice model of a high-risk *MYCN*-amplified neuroblastoma.
After starting the treatment with rigosertib, a slight difference of the **(A)** tumor volume and the **(B)** relative tumor volume between the PBS vehicle and the dual PLK1/PI3K inhibitor group was evident from day 26. By day 29, the difference between the tumor volume of the treatment group was significantly increased. In a last measurement on day 33, the tumor volume was detected with nearly equally values in both treatment groups, but still a difference between the two groups in relation to the relative tumor volume was visible. **(C)** Results of the individual tumor volume showed a generally slightly increased tumor volume in the vehicle control group compared to the rigosertib treatment group. However, tumor growth was poor in individual animals, regardless of treatment. **(D)** The body weight of the animals was not or only slightly influenced during the treatment, which indicates the absence of side effects of the inhibitor. In plot A, B and D, the median with the range of the measurements of 2-5 individual animals are shown.

However, the relative tumor volume already showed a difference of 2.4cm³ to 2cm³ between PBS and rigosertib treatments on day 26 (Figure 80B). Pronounced difference in tumor volume between rigosertib and vehicle treated mice become evident on day 29 after transplantation with a tumor/vehicle ratio of 48% and a tumor growth inhibition index of 63%. Detailed values of tumor volume and relative tumor volume was detected for the vehicle group with medians of 1.607cm³ and 5.6cm³ in contrast to the treatment group which showed a tumor volume of 0.688cm³ and a relative tumor volume of 2.5cm². In a comparison of the individual tumor volume cm³ of the respective animals the tumors showed a generally slightly increased tumor volume in the vehicle control group compared to the rigosertib treatment group (Figure 80C). However, it could be seen that regardless of an administered placebo or active treatment, tumor growth in individual animals was worse than in comparison to other animals. For example, the tumor of the mouse no. #B1 of the inhibitor treatment group reached a volume of 1.796cm³ and the tumor of mouse no. #B2 had a tumor volume of 0.395cm³ on the last measurement day 33. It is therefore unclear for these animals whether the transplanted neuroblastoma tumor initially grew poorly or whether the tumor volume was very low due to an extremely good response to rigosertib. Individual vehicle animals had to be terminated prior to study end due to maximal tolerable tumor size of 1.5cm³. Body weight values and a good general health condition of all animals indicated absence of compound dependent side effects in this study (Figure 80D). Within a second rigosertib efficacy *in vivo* study, a total of 10 mice were subcutaneously engrafted with a high-risk non-*MYCN*-amplified neuroblastoma tumor (Figure 81). The immundeficient NOG female mice with subcutaneously engrafted neuroblastoma xenografts were randomized in two groups (n=5) on day 25 after PDX fragment transplantation. From day three until the end of the study delayed and less pronounced tumor growth was observed in rigosertib treated animals compared to vehicle controls. Differences in the tumor volume were detected starting from day 28, were the median range was found 0.16cm³ for the vehicle group and 0.134cm³ for the treatment group (Figure 81A). However, the relative tumor volume already showed a difference of 1.7cm³ to 1.1cm³ between PBS and rigosertib treatments (Figure 81B). An optimal ratio of tumor/vehicle (49%) was calculated on day 32 after transplantation with a tumor growth inhibition value of 74%. Detailed values of tumor volume and relative tumor volume was detected for the vehicle group with medians of 0.398cm³ and 3.6cm³ in contrast to the treatment group which showed a tumor volume of 0.193cm³ and a relative tumor volume of 1.5cm². In a comparison of the individual tumor volume of the respective animals the tumors showed an increased tumor volume in the vehicle control group compared to the rigosertib treatment group (Figure 81C). The greatest differences in the measured values of the individual tumor volumes was found in the tumor of mouse no. #A3 in the vehicle group which displayed a final size of 1.036cm³ compared to the tumor of mouse no. #B4 in the rigosertib treatment group with a final size of 0.304cm³. Both study groups (n=5) completed the study. Body weight values and good general health condition was monitored for all animals throughout the study indicating good compound tolerability without adverse side effects (Figure 81D).

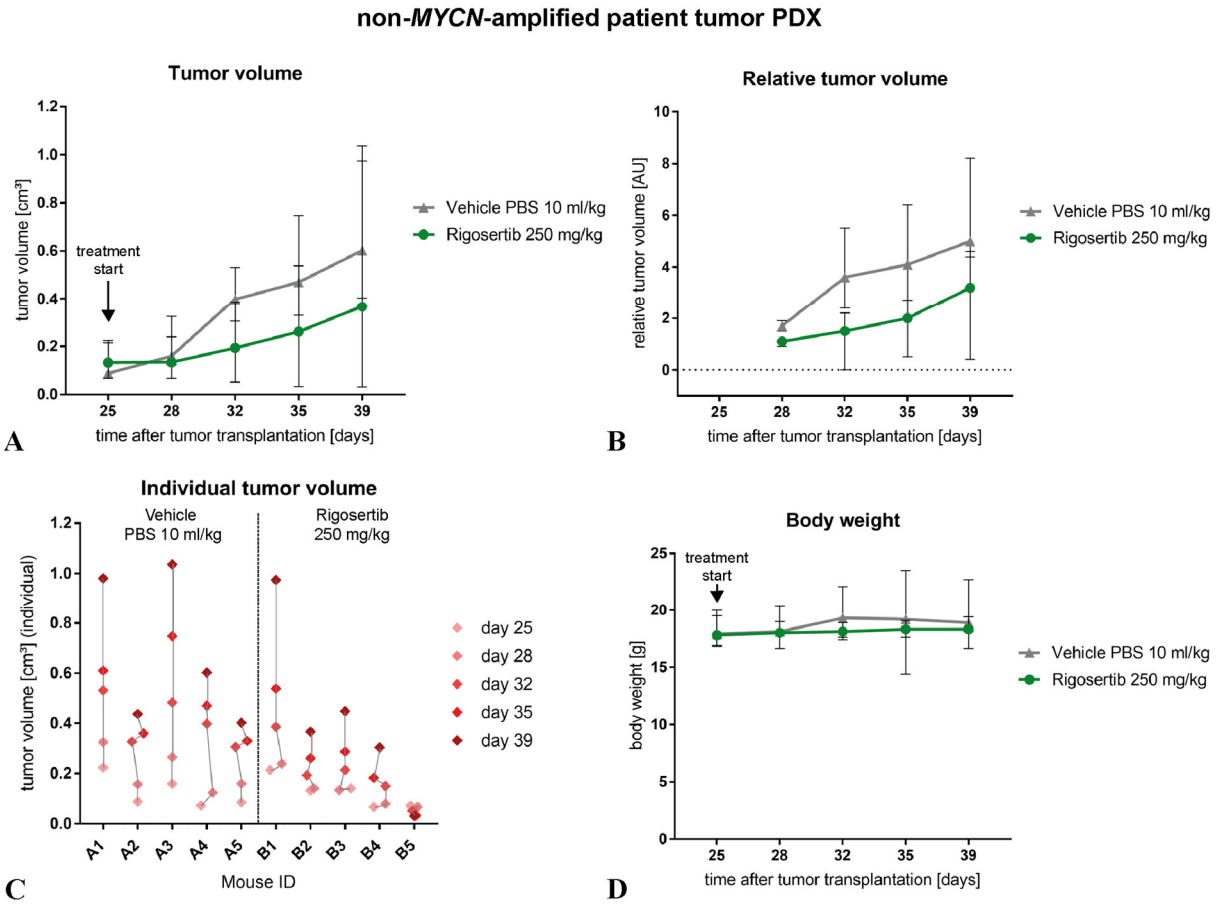

Figure 81: Rigosertib shows antitumor effects against a PDX mice model of a high-risk non-*MYCN*-amplified neuroblastoma.
The effects of treatment with rigosertib or with the PBS vehicle control on the **(A)** tumor volume and the **(B)** relative tumor volume were slightly visible from day 28. By day 32, the difference between the tumor volume of the treatment group was significantly increased. The difference between the measured tumor volumes of the rigosertib treatment group and the vehicle control group increased every day until the last day of the experimental series, day 39. **(C)** Results of the individual tumor volume showed an increased tumor volume in the vehicle control group compared to the rigosertib treatment group. **(D)** The body weight of the animals was not or only slightly influenced during the treatment, which indicates the absence of side effects of the inhibitor. In plot A, B and D, the median with the range of the measurements of 5 individual animals are shown.

Within a third rigosertib efficacy *in vivo* study, a total of 18 mice were subcutaneously engrafted with the *MYCN*-amplified neuroblastoma cell line IMR5/75. Starting from day 2-4 of rigosertib administration, less pronounced tumor growth was observed in rigosertib treated animals compared to vehicle controls. After a treatment of 14 days, the vehicle control showed a median tumor volume of 1.32cm³ whereas the rigosertib treated mice showed a median tumor volume of 0.81cm³. This means that tumor growth was effectively stopped with application of rigosertib (Figure 82A+B). In a comparison of the individual tumor volume of the respective animals the tumors showed an increased tumor volume in the vehicle control group compared to the rigosertib treatment group (Figure 82C). The greatest differences in the measured values of the individual tumor volumes was found in the tumor of mouse no. #A3 in the vehicle group which displayed a final size of 2.128cm³ compared to the tumor of mouse no. #B1 in the rigosertib treatment group with a final size of 0.399cm³. The vehicle control group completed the study (n=8) and in the rigosertib group one animal was treated incorrectly and had to be

excluded (n=7). The body weight of NMRI nude mice is greater than that of NOG mice used in the previous experiments and this is reflected in the body weight measurements. In general, similar body weights were found in the control and treatment groups. The animals were in good physical condition and did not show any adverse side effects after treatment with rigosertib (Figure 82D).

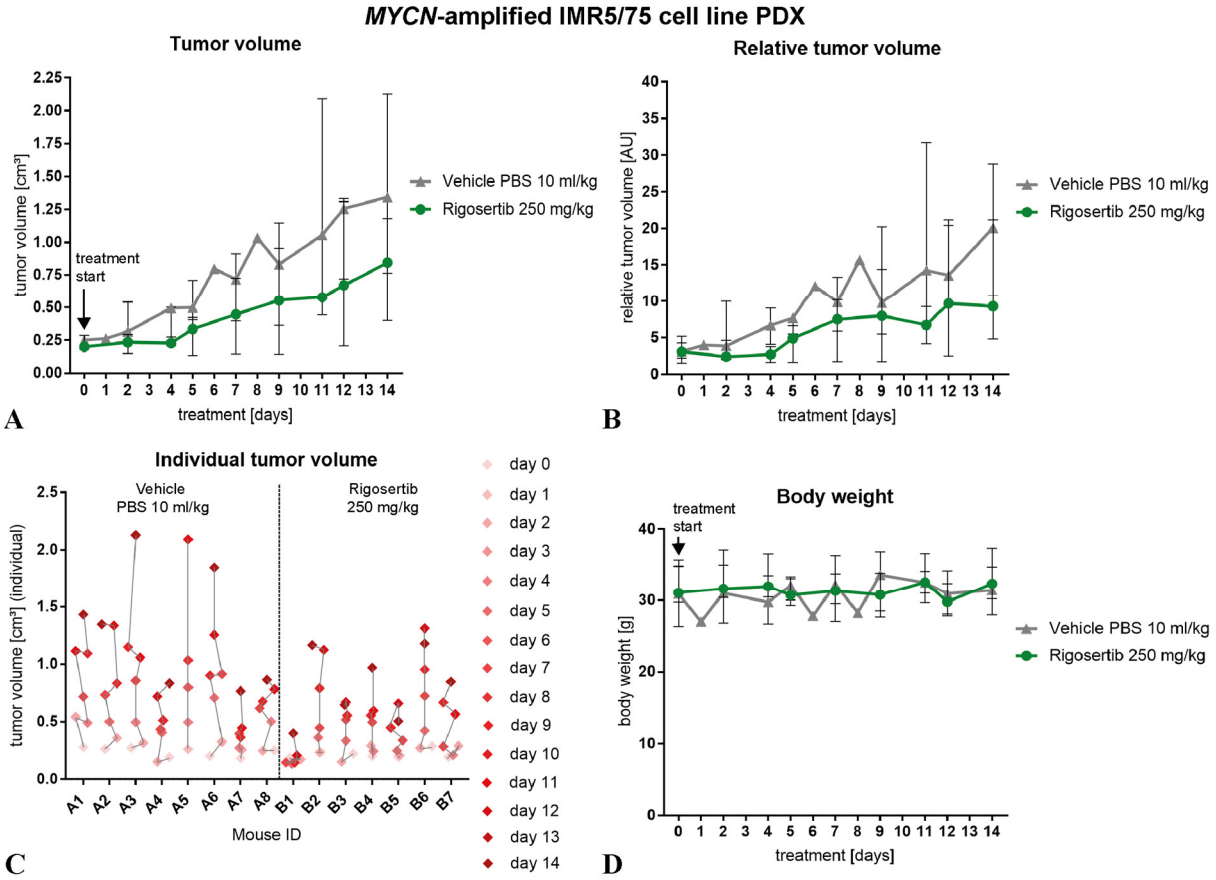

Figure 82: Rigosertib shows antitumor effects against a PDX mice model of the *MYCN*-amplified IMR5/75 cell line. The effects of treatment with rigosertib or with the PBS vehicle control on the **(A)** tumor volume and the **(B)** relative tumor volume were slightly visible after 4 days of application. After 10 days, a greater difference between the durg treatment and the vehicle control could be seen. **(C)** Results of the individual tumor volume showed an increased tumor volume in the vehicle control group compared to the rigosertib treatment group. **(D)** The body weight of the animals was only slightly influenced during the treatment, which indicates the absence of side effects of the inhibitor. In plot A, B and D, the median with the range of the measurements of 7-8 individual animals are shown.

In summary, based on the promising *in vitro* anti-tumor activity of the dual PLK1/PI3K inhibitor rigosertib, it was hypothesized that this drug may show clinically relevant therapeutic activity *in vivo*. The *in vivo* data demonstrated that rigosertib treatment suppresses growth of xenografts derived from neuroblastoma patient tumors with high-risk characteristics. The effect of rigosertib showed no significant difference in tumor volume reduction between *MYCN*-amplified or non-*MYCN*-amplified patient derived xenografts. It remains to be seen whether a reduced growth of the tumor in individual mice is due to the biological characteristics of the unique patient tumor transplanted, the *MYCN* amplification or the rigosertib treatment. Together, treatment with rigosertib significantly repressed

tumor cell growth and cell spread. Inhibitor application leads to induction of cell apoptosis, and to a decline in protein expression of WEE1, MST1 and MYCN. This suggests that dual PLK1/PI3K inhibitors like rigosertib have the potential to show clinically relevant therapeutic activity in patients suffering from high-risk neuroblastomas. *In vivo* rigosertib experiments using PDX mice models was performed in cooperation with Experimental Pharmacology & Oncology Berlin-Buch GmbH (EPO, Berlin, Germany).

3.2.3 Combination of BRD4 and PLK1 inhibition has synergistic anti-tumoral effects in neuroblastoma cell lines

Previous cell viability experiments of this work compared the potential efficacy of the BET inhibitors JQ1, OTX015 and TEN-010. The BET inhibitor OTX015 in particular showed an interesting efficacy profile. After application of OTX015, the cell viability of all neuroblastoma and fibroblast cells was not severely restricted overall, as for example in contrast using the tool compound JQ1. The outstanding effect of OTX015 was reflected in the significant reduction in the cell viability of many different neuroblastoma cells. As BRD4 proteins act as "readers" of the epigenome and control the expression of many signal transduction pathways by initiating the transcription of several factors, a combination therapy is considered. The combination of a BET inhibitor and a PLK1 inhibitor is a possible approach, which allows an intervention on the cellular transcription and on the cell cycle. Previously published data demonstrated that a combination of a BET inhibitor (BI 894999) and a PLK1 inhibitor (volasertib) can prolong the downregulation of *MYC* expression through synergistic effects[702]. Thus, *MYCN*-amplified high-risk neuroblastoma can be treated at different biological targets, including the transcription of *MYCN* and the stabilization of the MYCN protein.

In this part of the work, the BET inhibitor OTX015 and the PLK1 inhibitor volasertib were therefore combined for an anti-tumor treatment against neuroblastoma cells. Both *MYCN*-amplified (IMR5/75 and CHP-134) and non-*MYCN*-amplified cell lines (SK-N-AS and GI-ME-N) were selected to observe the influence of *MYCN* on treatment effects. A fibroblast cell line (VH7) was also used to test for a possible (negative) effect on normal body cells. Initially, the range of action of volasertib on neuroblastoma cells was tested as described in section 3.2.2. The effect of volasertib on cell viability was measured three days after treatment. Reduction of cell viability upon volasertib treatment was found similar in *MYCN*-amplified cell lines IMR5/75, CHP-134 and the non-*MYCN*-amplified cell line SK-N-AS (Figure 83). The non-*MYCN*-amplified cell line GI-ME-N showed a moderate response to volasertib inhibition. The fibroblast cell line VH7 displayed a weaker response to volsertib as compared to neuroblastoma cells. The relative IC50 (E50) values ranged in low nanomolar concentrations from 16nM to 31nM for neuroblastoma cell lines, while the fibroblast cell viability is reduced with a higher concentration (~ 1000nM). All cell lines tested showed an increased maximum effect (98.14% in *MYCN*-amplified, 88.1% in non-*MYCN*-amplified and 90.65% in fibroblast cell lines). All cell lines displayed a maximum effect to volasertib with more than 80%.

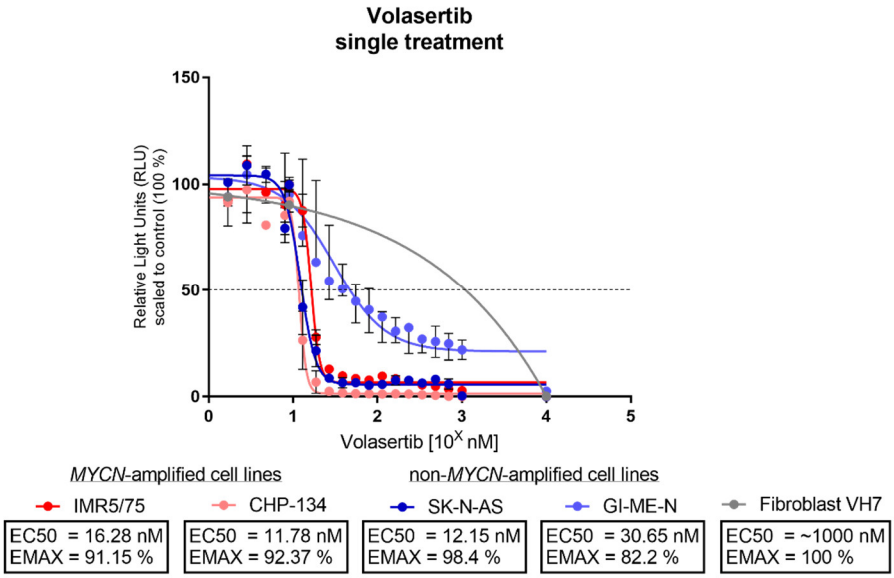

Figure 83: Volasertib dose to cell viability response relationship in neuroblastoma and fibroblast cell lines.
The PLK1 inhibitor volasertib was applied to 5 different cell lines *in vitro* and effect on cell viability was measured three days after treatment. Decrease of cell viability after volasertib treatment was discovered comparative in *MYCN*-amplified cell lines IMR5/75, CHP-134 and the non-*MYCN*-amplified cell line SK-N-AS. The non-*MYCN*-amplified cell lines GI-ME-N and VH7 indicated a moderate to weak reaction after volasertib administration. (Emax in mean interpolated by GraphPad Prism® PRSIM). For each cell line, two to three biological replicates are shown with their respective median and range.

Subsequently, the PLK1 inhibitor volasertib was combined with the BET inhibitor OTX015. The two inhibitors were applied to the neuroblastoma cells in columns and rows and then analyzed with the R package SynergyFinder. A synergistic effect of the combination of OTX015 and volasertib could be demonstrated for all cell lines (Figure 84). The strength of the synergism does not depend largely on the *MYCN* status, but rather on the individual cell lines. The *MYCN*-amplified cell lines IMR5/75 and CHP-134 showed a good response to the combination treatment, with an increased average synergy score of 2,518-4,036. Especially at a higher dose of 100nM OTX015 and 10-15nM volasertib, the results showed that there existed a 97.3-99.6% inhibition of the cell viability (Figure 84A+B). But also the non-*MYCN*-amplified cell line SK-N-AS achieved an average synergy score of 5,681 and a 97.3% inhibition of cell viability using 125nM OXT015 and 15nM volasertib (Figure 84C). Thus, this cell line achieved even a higher synergy score than the *MYCN*-amplified cell lines. The non-*MYCN*-amplified cell line GI-ME-N showed the worst response to the combination treatment (Figure 84D). In this case, even with a high dose of the inhibitors of 6,250nM OTX015 and 50nM volasertib, an average synergy score of 1,934 with an inhibition of 75.8% was only achieved. Overall, 100% inhibition in the single drug dose response was demonstrated using volasertib for all cell lines except GI-ME-N. For GI-ME-N the inhibition was about 70%. The results for a single treatment with OTX015 were slightly poorer, reaching only 40-80% inhibition. The synergistic effect is therefore more likely attributable to the administration of volasertib, which is also reflected in the amount of concentration required for inhibition. The cell line VH7 was tested additionally with the combination treatment.

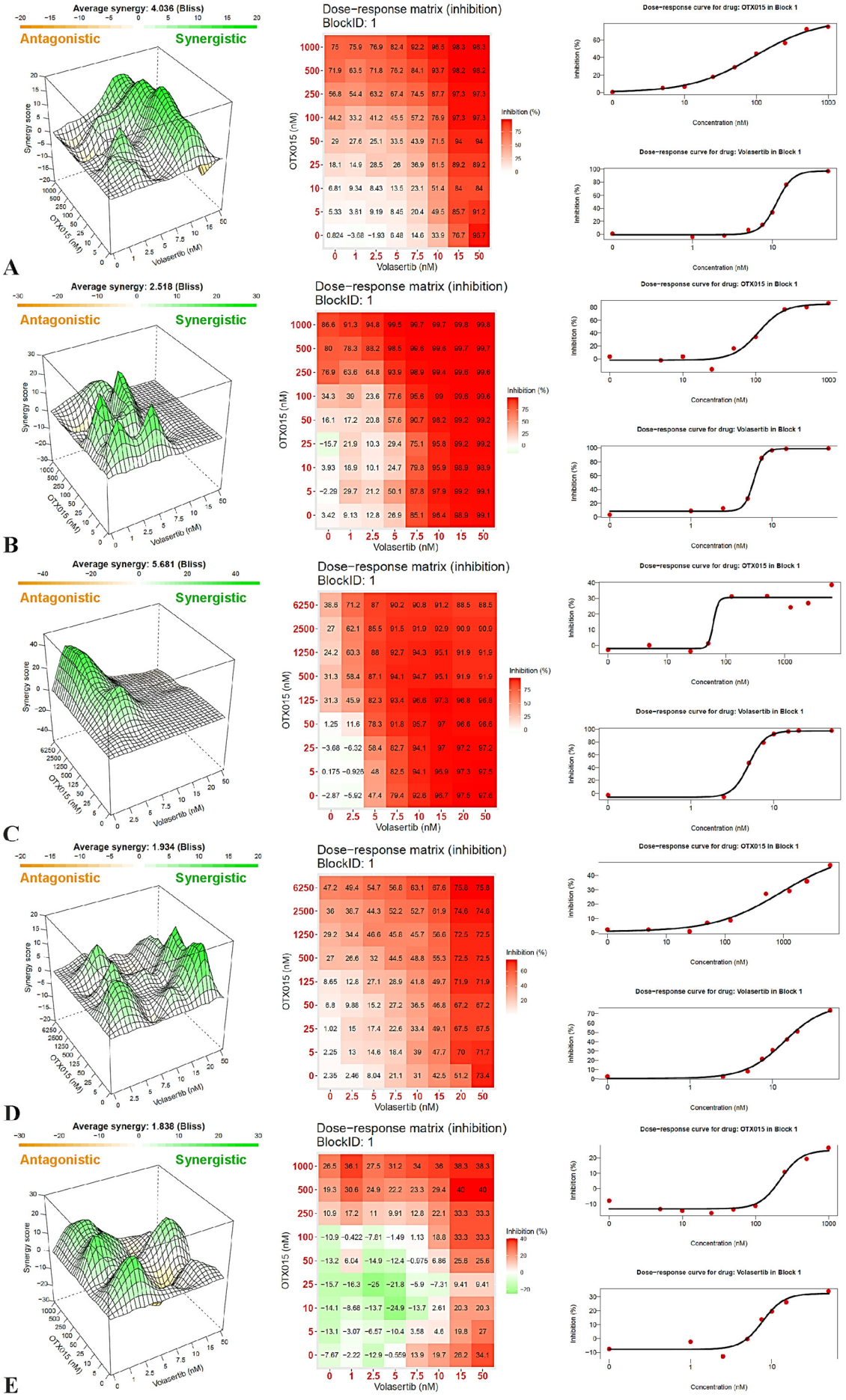
A
Average synergy: 4.036 (Bliss)
Antagonistic
Synergistic
Synergy score
OTX015 (nM)
Volasertib (nM)
Dose−response matrix (inhibition)
BlockID: 1
Inhibition (%)
Dose−response curve for drug: OTX015 in Block 1
Dose−response curve for drug: Volasertib in Block 1
Concentration (nM)
B
Average synergy: 2.518 (Bliss)
C
Average synergy: 5.681 (Bliss)
D
Average synergy: 1.934 (Bliss)
E
Average synergy: 1.838 (Bliss)

Although VH7 also showed a synergistic effect of OTX015 and volasertib (average synergy score 1.838), only a maximum inhibition of 38.3% could be observed when using a high concentration of 1,000nM OTX015 and 50nM volasertib (Figure 84E). This effect is also reflected in the single drug dose response curves, which show a maximum inhibition for OTX015 of about 20% and for volasertib of about 30%. If the combination is administered hypothetically against a neuroblastoma cell line or tumor, a concentration of only 100nM OTX015 and 10nM volasertib is required for almost complete inhibition, which would result in a maximum inhibition against fibroblasts of 18.8%. Compared to a single treatment with OTX015 or volasertib, the combination treatment is an improvement, as smaller amounts of OTX015 or volasertib have to be used (100nM OTX015 in the combination compared to up to 327.6nM in the single treatment and 10nM volasertib in the combination compared to up to 30.65nM in the single treatment). In addition, up to 99.6% inhibition is achieved when using the combination treatment (compared up to 92% for the single treatment with OTX015 and to up to 98.4% for the single treatment with volasertib). The data therefore clearly shows that OTX015 can be combined with volasertib. A synergistic effect of the inhibition using the two drugs could be demonstrated and an improved response of the cell lines was detected with simultaneous reduced inhibitor concentration. This is a first example of indirect *MYCN* inhibition involving different pathways being combined and harmonized.

3.2.4 High expression of *ASPM* is related to an aggressive neuroblastoma

3.2.4.1 MCPH genes are highly expressed in pediatric tumors

While an increased proliferation of neuronal progenitor cells is central in the tumor biology of the embryonal tumors including neuroblastoma, a reduced proliferation of neuronal progenitor cells is a cause of congenital microcephaly[423–425]. The MCPH gene family is known to play important roles in determining the brain size in early development[481,703–705]. To evaluate the expression rate of MCPH genes in normal neuronal tissues, pediatric and adult cancers, 25 publicly available Microarray datasets (see Table 27 in appendix section) were analyzed for gene expression from 3,984 samples. For this purpose, 22 different MCPH genes were selected in advance from biomedical literature, which according to the status in 2019 are supposed to be related to Autosomal recessive primary microcephaly. MCPH genes no. 1-16 represent the group of "classical" MCPH genes, for which several clinical cases have already been identified and (basic) research has been published.

< Figure 84: Analysis of cell viability dose-response after OTX015 and volasertib drug combination in neuroblastoma cells.
In a combination treatment with OTX015 and volasertib, four different neuroblastoma cell lines, including two *MYCN*-amplified and two non-*MYCN*-amplified cell lines were investigated. In addition, the combination therapy was also tested on a non-tumor cell line. Panel **(A)** *MYCN*-amplified IMR5/75 cells, panel **(B)** *MYCN*-amplified CHP-134 cells, panel **(C)** non-*MYCN*-amplified SK-N-AS cells, panel **(D)** non-*MYCN*-amplified GI-ME-N cells and panel **(E)** fibroblast cell line VH7. Displayed from left to right are the respective drug interaction landscape, the drug combination dose-response matrix and the plots for single drug dose-response curves. Synergism analyses were calculated using *SynergyFinder*[511] (CRAN)**.** For each cell line, one biological replica is shown with their respective median and range.

MCPH genes no. 17-23 represent the group of more recently known MCPH mutations, for which there have so far been individual cases reported and rarely basic research published. The expression of the 22 selected genes of the MCPH gene family was examined using hierarchical clustering analysis in adult tumors (12 datasets), and pediatric tumors (9 datasets, including 4 neuroblastoma datasets) and normal healthy tissue (4 datasets, mostly neuronal tissues). While a strong expression of MCPH genes was detected in most tumor entities, the expression of MCPH was higher in pediatric than in adult tumors (Figure 85A). Among pediatric tumors, expression levels of MCPH genes were highest in neuroblastoma. Interestingly, it can be seen that several neural tumor types cluster together with an increased expression of the MCPH genes. As said, these are neuroblastomas, but also glioblastomas, atypical teratoid rhabdoid tumors (ATRT) and medulloblastomas. Tumors of the adulthood and normal tissues cluster together with a lower expression of the MCPH genes at a greater distance from the pediatric neuronal tumors. The MCPH expressions in normal tissue even cluster on a different branch than the group of neuroblastomas and pediatric tumors. Correlation array analysis of all 25 Microarray datasets could also show that the expression of the individual MCPH genes strongly correlated to each other across different cancer types (Figure 85B). In particular, a strong correlation of the gene expression of the microtubule associated proteins ASPM and KIF14 could be demonstrated.

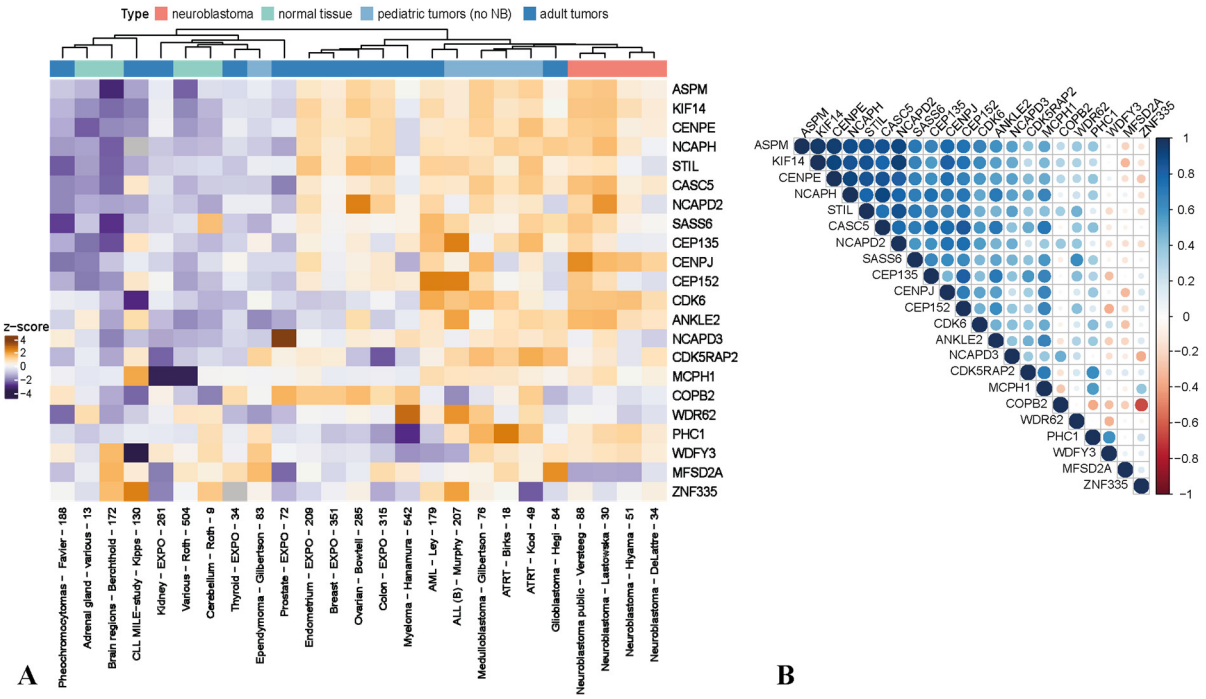

Figure 85: Primary-microcephaly associated MCPH genes are highly expressed in pediatric tumors.
(A) Heatmap of Microarray data showing expression of 22 MCPH genes across datasets from 12 adult tumor data sets, 9 pediatric tumor data sets (including 4 neuroblastoma data sets) and 4 data sets of normal tissue. MCPH genes are highly expressed in pediatric tumors, especially in neuroblastomas. **(B)** Correlation array from 25 Microarray datasets of different origin (adult, pediatric and normal, as stated above) across different MCPH genes. The expression of the *ASPM* gene correlates high with other MCPH genes involved in the Mitosis process, as for example *KIF14*, *CENPE* and *NCAPH*. (Affymetrix HG-U133-Plus2 Microarrays processed using the MAS5.0 method[639]; Figures were kindly prepared by J. Toedling (Charité)[544]).

To further focus on the expression of MCPH genes in neuroblastoma, a dataset was applied comprising mRNA sequencing data obtained from a representative cohort of 498 primary neuroblastomas (SEQC study[42]). Expression levels of the MCPH genes were found to be higher in high-risk neuroblastoma and in particular in *MYCN*-amplified neuroblastoma and neuroblastomas of high INSS stage[128,129] (Figure 86A). This result shows that the high expression of the MCPH genes is clustered together with the clinical characteristics of aggressive neuroblastoma and indicates a correlation of high MCPH gene expression and an adverse outcome. The *ASPM* gene in particular shows the highest expression in connection with high-risk neuroblastomas. Further, the expression of most MCPH genes was found to be highly correlated to each other within the neuroblastoma cohort (Figure 86B). In particular, a strong correlation of the expression of the microtubule and mitotic spindle associated proteins ASPM and CENPE could be displayed. These genes even show a negative correlation compared to the expression of the other MCPH genes involved in cell division and cell cycle processes. Taken together, expression of MCPH genes is high in cancer, with highest expression in pediatric cancers and in particular high-risk neuroblastoma. The microtubule-associated protein ASPM shows the highest expression in high-risk neuroblastomas and its expression is highly correlated with MCPH and other genes involved in cell division and cell cycle processes.

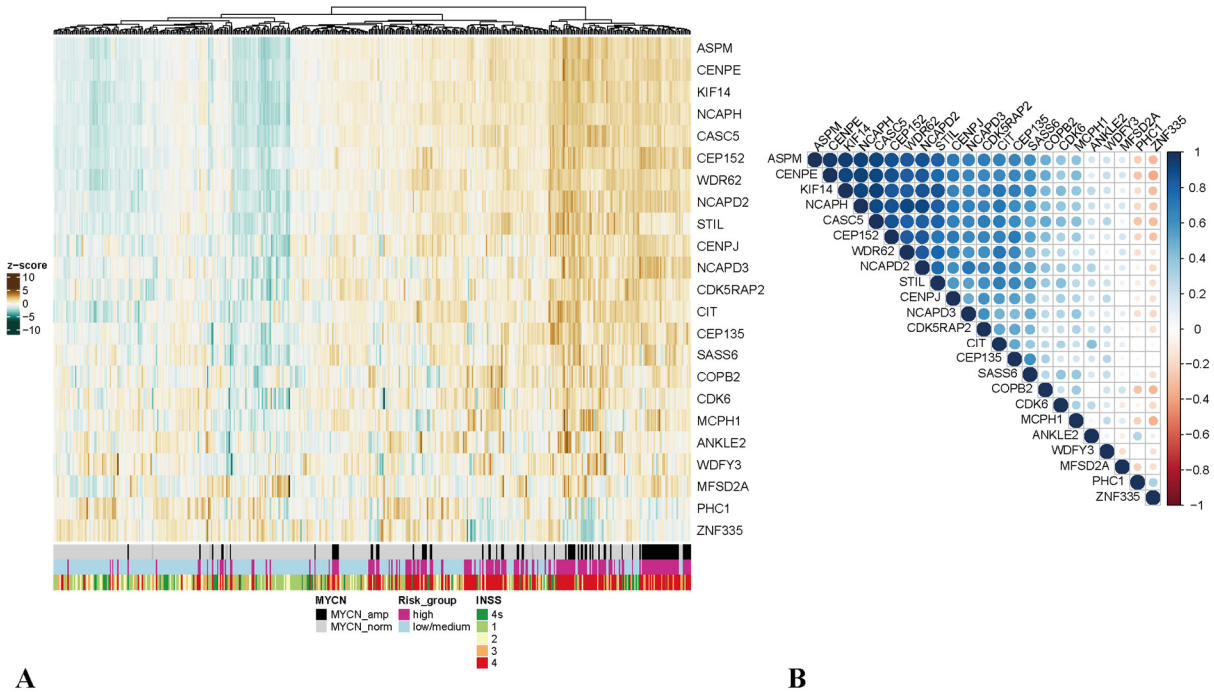

Figure 86: Primary-microcephaly associated MCPH genes are highly expressed in high-risk neuroblastoma.
(A) Heatmap of RNA-Sequencing data (SEQC study[42]) of neuroblastoma patients pinpoint towards a correlation between high expression of MCPH genes and adverse outcome (*MYCN* amplification, high risk group and higher INSS stage[128,129]). Considering the genes which cluster at highest together with clinical characteristics of aggressive neuroblastoma, the MCPH gene *ASPM* is remarkable high. **(B)** Correlation array from RNA-Sequencing data[42] across different MCPH genes expressed in neuroblastoma patient tumors. The expression of the *ASPM* gene correlates high with other MCPH genes involved in the Mitosis process, as for example *CENPE*, *KIF14* and *NCAPH*. (Affymetrix HG-U133-Plus2 Microarrays processed using the MAS5.0 method[639]; Figures were kindly prepared by J. Toedling (Charité)[544]).

3.2.4.2 High *ASPM* expression is associated with aggressiveness and adverse outcome of neuroblastoma

Previously published work could already highlight that the expression of the MCPH gene *ASPM* can be linked to the development of cancer[483,485,706–708]. In combination with this thesis' work (see 3.2.4), observations were made regarding the highly-expressed nature of ASPM in neural-tissue cancers as well as its association with aggressive high-risk neuroblastomas. Therefore, the analyses were further aimed on elucidating the role of ASPM in neuroblastoma. Within a detailed analysis of the *ASPM* gene expression across 25 multiple Microarray datasets (see Table 27 in appendix section) originating form normal tissues, pediatric and adult tumors, high *ASPM* expression could be identified in pediatric tumors (Figure 87).

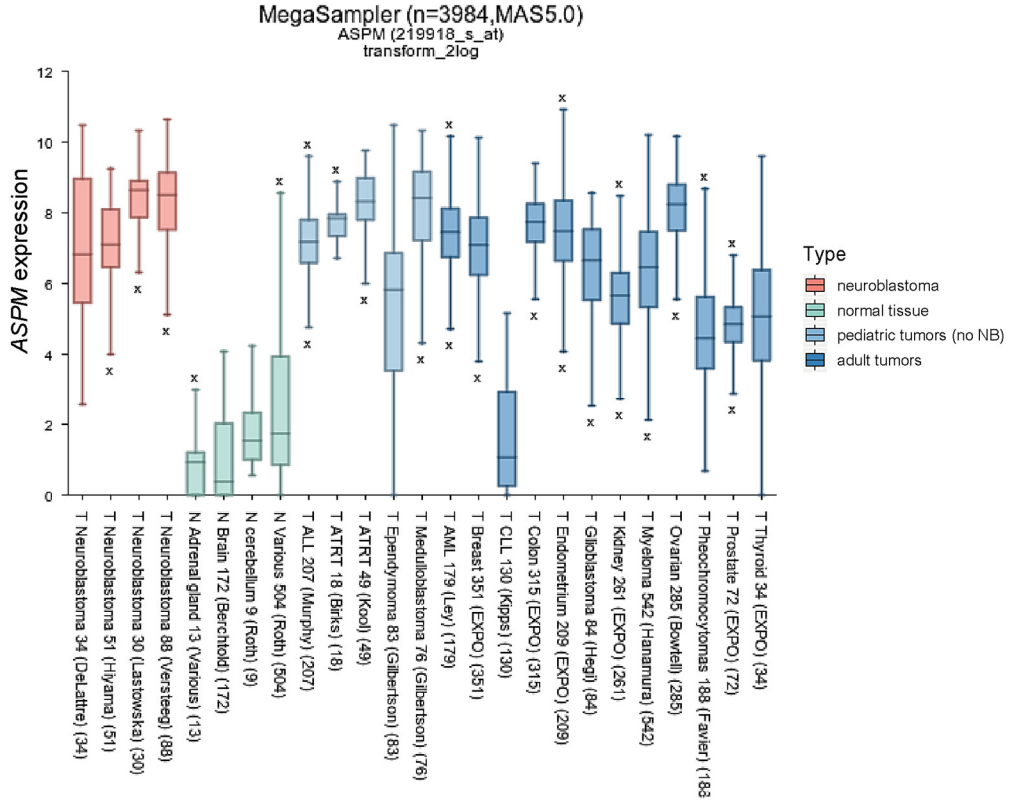

Figure 87: The microtubule-associated protein ASPM is distinct in neuro-pediatric tumors.
Box-plot diagram of Microarray data showing the *ASPM* gene expression profiles in three different sample type groups (adult tumors, pediatric tumors and normal tissue). This reveals that a high RNA expression of *ASPM* accompany together with fast proliferating, neuro-pediatric tumors like neuroblastomas, ATRT tumors or medulloblastomas. **(**Affymetrix HG-U133-Plus2 Microarrays processed using the MAS5.0 method[639]; 25 Microarray datasets of different origin as stated above; figure was created using the R2 Genomics platform[496,497]).

The highest *ASPM* levels were detected in neuroblastoma ($p<3.7\text{x}10^{-114}$), ATRT ($p<4.3\text{x}10^{-105}$) and medulloblastoma ($p<1.6\text{x}10^{-192}$, one-way ANOVA (analysis of variance), each cancer entity compared to normal tissue), all of which are quickly proliferating pediatric tumors of neuronal origin. In contrast, adult tumors displayed a lower level of *ASPM* expression, and even less *ASPM* expression was detected

in normal tissue. Focusing on neuroblastoma, in an analysis of 24 different neuroblastoma cell lines an increased and similar expression of *ASPM* could be demonstrated for all cell lines (see Figure 88).

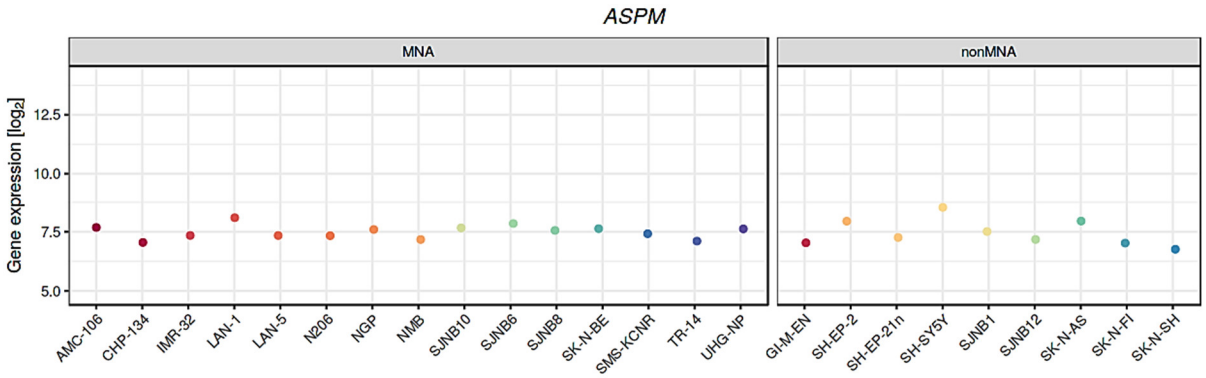

Figure 88: High expression of the microtubule-associated gene *ASPM* in neuroblastoma cell lines.
The expression of the *ASPM* gene is increased in neuroblastoma cell lines (24 cell lines), regardless of whether these are *MYCN*-amplified (15 cell lines, MNA) or non-*MYCN*-amplified (9 cell lines, non-MNA). Expression analyzed from data set: Cellline Neuroblastoma - Versteeg - 24 - MAS5.0 - u133p2 (GEO ID: gse28019). (Figure was created using an R software (CRAN)[640,641] *Shiny* app[709,710] provided by J.Toedling (Charité)).

Focusing on patients with neuroblastoma, the mRNA sequencing data obtained from a representative cohort of 498 primary neuroblastomas (SEQC study[42]) was applied again. In subsequent analyses, the expression level of *ASPM* was examined in connection with clinical and other molecular markers of neuroblastomas (Figure 89). A significant correlation between high *ASPM* expression and *MYCN* oncogene amplification could be detected (Figure 89A, $p<7.67x10^{-21}$, student's t-test). Moreover, a correlation was found between a higher *ASPM* expression in high-risk neuroblastomas compared to a lower *ASPM* expression found in low or intermediate risk neuroblastomas (Figure 89B, $p<7.20x10^{-31}$, student's t-test). Another connection could also be displayed between high *ASPM* expression and an aggressive stage 4 high-risk neuroblastoma (INSS[128,129]) (Figure 89C, $p<9.73x10^{-26}$, student's t-test). Within clinical presentation, patients with high-risk neuroblastomas show primary tumors with dissemination to distant lymph nodes, bone, bone marrow, liver, skin, and / or other organs. Interestingly, the level of *ASPM* expression raises with an increase in the INSS tumor stage. In the special stage 4s neuroblastoma, which shows spontaneous regression without any treatment, a lower *ASPM* expression (compared to the intermediate risk stage 3 or high-risk stage 4) was seen. With regard to the outcome of neuroblastomas, a connection between an increased *ASPM* expression and a death from disease can also be revealed here. Patients with neuroblastomas showing a high *ASPM* expression elevated in the tumor die more frequently from this cancer than patients with neuroblastomas showing a lower *ASPM* expression (Figure 89D, $p<2.74x10^{-20}$, student's t-test). Based on the results that a high *ASPM* expression correlates more strongly with a death from disease event than lower *ASPM* expression, the influence of the *ASPM* expression levels on the survival of the patients with a neuroblastoma was examined (Figure 90).

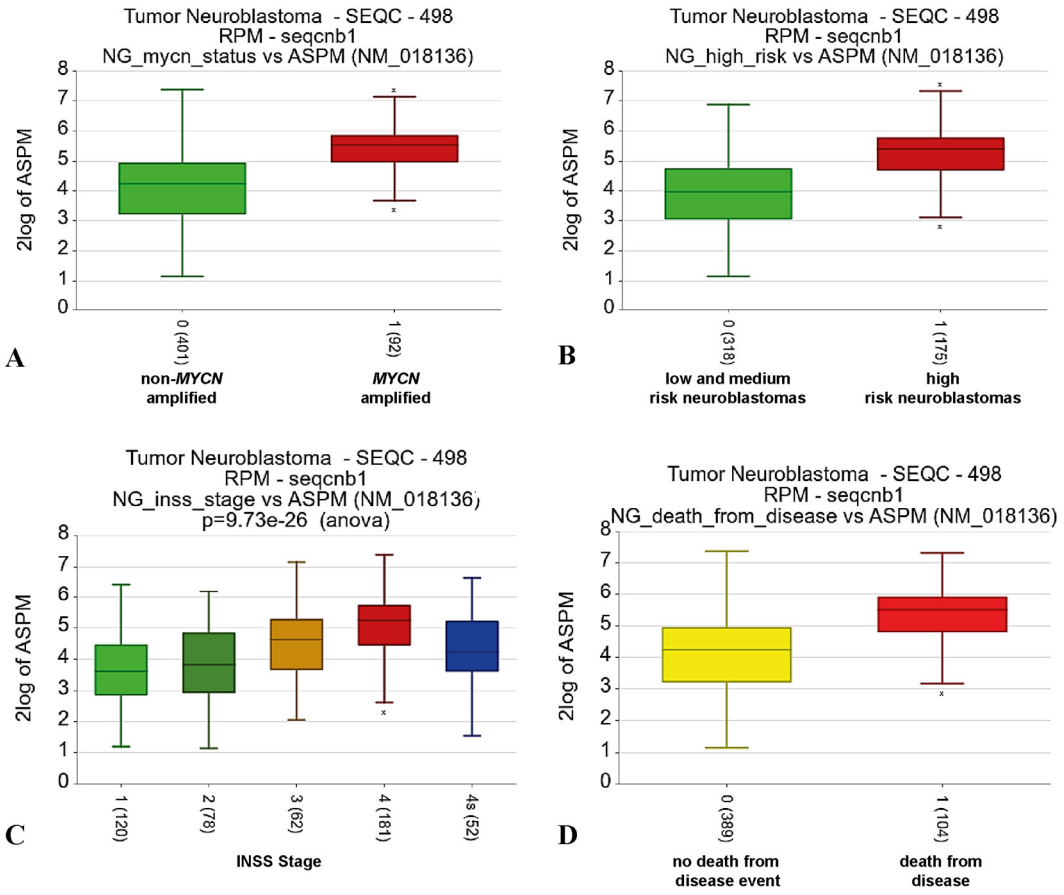

Figure 89: High expression of the microtubule-associated ASPM protein correlates with aggressive neuroblastomas. Box-plot diagrams of RNA-Sequencing data of neuroblastoma tumors (SEQC study[42]) showing **(A)** a correlation between high ASPM expression and *MYCN* oncogene amplification (0=non-*MYCN*-amplified, 1=*MYCN*-amplified), **(B)** a correlation between high *ASPM* expression and high-risk neuroblastoma (0=low/medium risk, 1=high risk), **(C)** a correlation between high *ASPM* expression and advanced tumor stage (high INSS score[128,129], low risk=1 and 4s, medium risk=2 and 3, high-risk=4) and **(D)** a correlation between high *ASPM* expression and death from disease (overall survival, 0=no death event, 1=death from disease). (Microarray SEQC-498-RPM-seqcnb1 data set; figure was created using the R2 Genomics platform[496,497]).

Kaplan-Meier survival analyses revealed a significantly diminished event-free survival ($p<1.0x10^{-13}$, Figure 90A) and overall survival ($p<2.9x10^{-16}$, Figure 90B) of neuroblastoma patients with tumors showing high *ASPM* expression as compared to patients with tumors showing lower *ASPM* expression (*cutoff modus*: median, *cutoff*: 249 neuroblastoma tumors with high expression of *ASPM* from expression cutoff 22.631, see Figure 131 and Figure 132 in appendix section). In event free survival curves, the event of interest is e.g. relapses, because patients may have relapsed but not yet died. In overall survival curves, the event of interest is death from any cause[711]. This shows that patients with neuroblastoma expressing high *ASPM* levels in their tumors have a higher mortality. Even stronger assumptions could be made when comparing the survival probabilities in a subgroup of the total cohort in which only patients harboring a *MYCN*-amplified tumor were selected. Within a comparison of *ASPM* expression levels in an only *MYCN*-amplified tumor subgroup against an only non-*MYCN*-amplified tumor subgroup, it was found that the patients with a *MYCN* amplification and high *ASPM* expression levels showed the worst event-free survival and overall survival probabilities (see Figure 133, Figure

134, Figure 135 and Figure 136 in appendix section). Interestingly, the survival probabilites of the subgroup of non-*MYCN*-amplified patients in combination with a high *ASPM* expression ($p<1.8x10^{-7}$, see Figure 134 and $p<9.7x10^{-8}$, see Figure 136 in appendix) only worsens slightly compared to the results from the total neuroblastoma cohort (Figure 90). In contrast, the subgroup of *MYCN*-amplified neuroblastomas with high *ASPM* expression shows lower survival probabilities ($p<0.061$, see Figure 133 and $p<0.069$, see Figure 135 in appendix) compared to the results from the total neuroblastoma cohort (Figure 90). In a further analysis within a subgroup of high-risk neuroblastomas comparing low versus high *ASPM* expression, greatly reduced event-free survival ($p<0.015$) and overall survival ($p<2.0x10^{-3}$) probabilities were found in high-risk neuroblastomas showing high *ASPM* expression in addition (see Figure 137 and Figure 138 in appendix section).

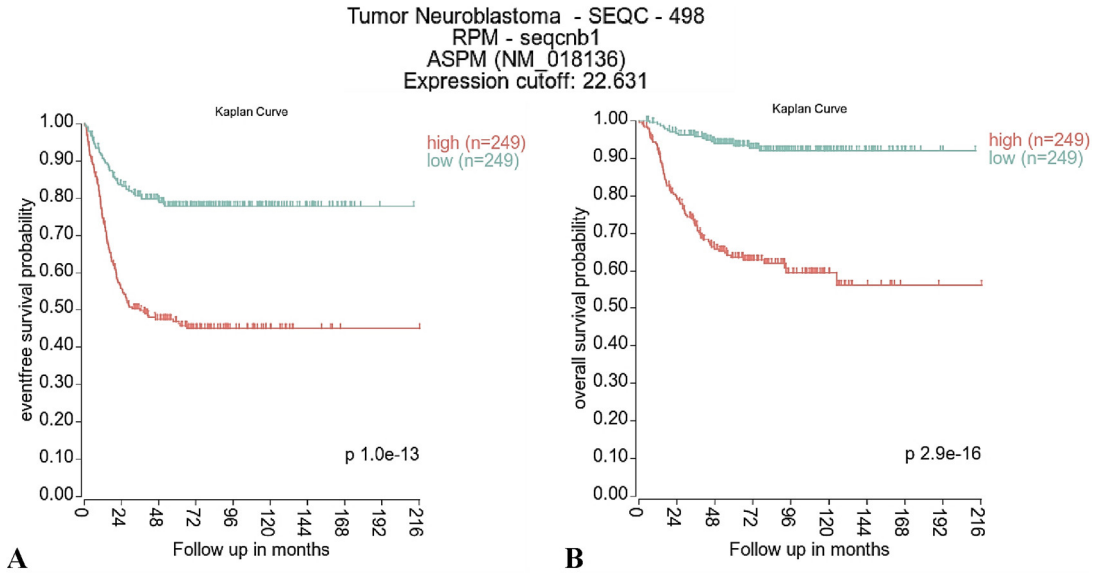

Figure 90: High expression of *ASPM* correlates with adverse outcome and is linked to cell cycle, cell division and DNA replication.
Survival analysis of RNA-Sequencing data of neuroblastoma patients (SEQC study[42]). **(A)** Correlation between event-free survival probability and *ASPM* expression. Low *ASPM* expression follows a high event-free survival probability, whereas a high expression of *ASPM* lead to a lower event-free survival probability. **(B)** Correlation between overall survival probability and *ASPM* expression. Low *ASPM* expression follows a high overall survival probability, whereas a high expression of *ASPM* lead to a lower overall survival probability. **(**Microarray SEQC-498-RPM-seqcnb1 data set; Figure was created using the R2 Genomics platform[496,497]).

To further study the role of *ASPM* in neuroblastoma biology, a list of 324 genes whose expression was highly correlated with *ASPM* was compiled (Spearman correlation coefficient CC≥0.7) from mRNA sequencing data of 498 primary neuroblastomas (SEQC study[42]). The result shows a strong correlation of the expression of *ASPM* together with other MCPH genes displaying a correlation coefficient from *CENPE* to *ASPM* of 0.96, *KIF14* to *ASPM* of 0.95 and *NCAPH* to ASPM of 0.93 (Table 29 in appendix section). In addition to a strong correlation of *ASPM* to other MCPH genes, it was also possible to show a correlation to the expression of genes that have not previously been associated with a primary microcephaly. These genes include a high correlation coefficient of 0.94 within the expression analysis of *ASPM* to *CDCA2* (regulator of chromosome structure), *BUB1* (mitotic checkpoint kinase associated

with the kinetochores) and *NUF2* (kinetochore protein involved in chromosome segregation). In additional investigations, a Gene Ontology term enrichment analysis was performed to identify biological processes linked to ASPM in neuroblastoma. The strongest-enriched GO terms were mostly related to cell cycle, cell division and DNA replication (Figure 91).

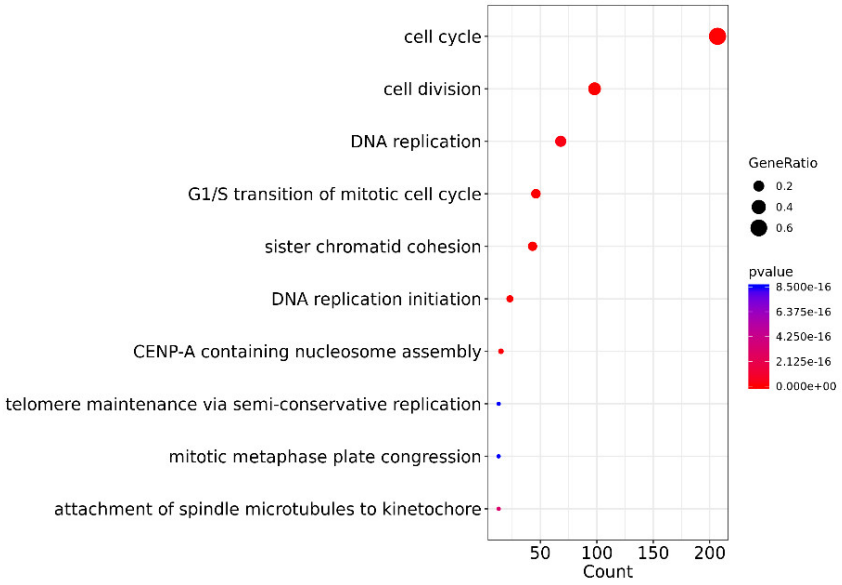

Figure 91: Expression of *ASPM* is linked to cell cycle, cell division and DNA replication.
GO term enrichment analysis of RNA-Sequencing data of neuroblastoma tumors (SEQC study[42]) characterizes *ASPM*s connection to biological process of the cell cycle, cell division and DNA replication. (Microarray SEQC-498-RPM-seqcnb1 data set; figure was kindly prepared by J. Toedling (Charité)).

In line, *ASPM* expression was highly correlated with the expression of the cell cycle regulator *PLK1* (Spearman CC=0.89), the transcriptional activator involved in regulation of the expression of cell cycle genes *FOXM1* (Spearman CC=0.90) and the chromosome collapsing protectant and chromatin organizer *MKI67* (Spearman CC=0.92, Figure 92). In summary, *ASPM* is overexpressed in high-risk neuroblastoma, its expression correlates with adverse outcome of neuroblastoma, and co-expressed proteins of ASPM are fundamentally involved in neuroblastoma cell-cycle and cell-division mechanisms and, consequently, tumor proliferation and aggressiveness.

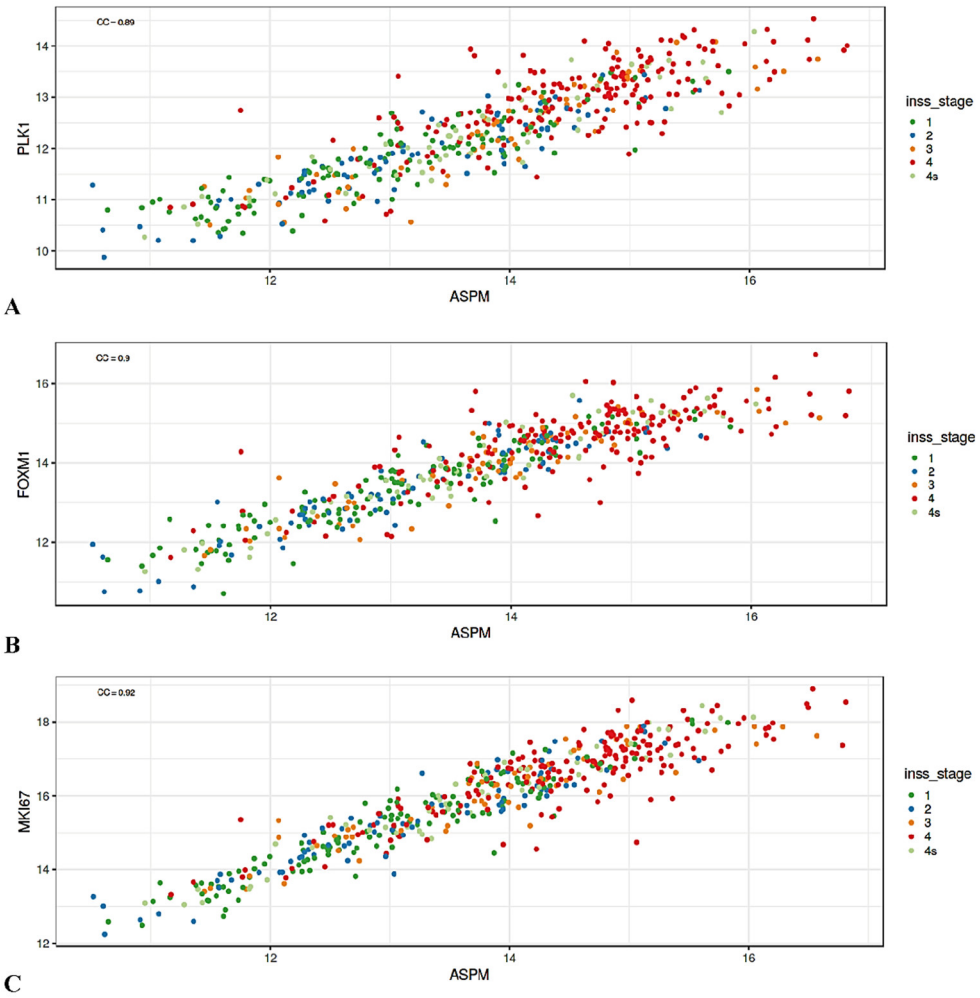

Figure 92: Expression of *ASPM* is highly correlated with the expression of *PLK1*, *FOXM1* and *MKI67*.
The expression of the microtubule-associated protein *ASPM* is highly correlated with the expression of **(A)** *PLK1*, **(B)** *FOXM1* and **(C)** *MKI67*. High-risk neuroblastomas (INSS tumor staging[128,129]) are highlighted with red dots (Microarray SEQC-498-RPM-seqcnb1 data set; figure was created using an R software (CRAN)[640,641] *Shiny* app[709,710] provided by J.Toedling (Charité)).

3.2.4.3 *ASPM* is highly expressed in neuroblastoma cell lines but is no surrogate marker of proliferation

As a prerequisite for subsequent functional studies, the expression levels of *ASPM* were assessed in various neuroblastoma cell lines. *ASPM* RNA levels were first evaluated applying qPCR in 16 neuroblastoma and 7 control cell lines, the latter comprising fibroblasts and cell lines from other tumor entities (Figure 93). A significant difference of *ASPM* expression comparing all three groups within a variance analysis could be shown (Figure 93B, *MYCN*-amplified and non-*MYCN*-amplified neuroblastoma cell lines and control cell lines, FC, *p=0.0007484,* Kruskal-Wallis test). The *ASPM* expression was significantly higher in *MYCN*-amplified neuroblastoma cell lines as compared to non-*MYCN*-amplified neuroblastoma cell lines (FC, *p=0.004,* Kolmogorov-Smirnov test) and in *MYCN*-amplified neuroblastoma cell lines as compared to control cell lines (FC, *p=0.001,* Kolmogorov-Smirnov test, both Figure 93B). In a comparison of non-*MYCN*-amplified neuroblastoma cell lines to

control cell lines, the *ASPM* expression was only slightly different (FC, *p=0.5280,* Kolmogorov-Smirnov test, Figure 93B). Further analyses confirmed high *ASPM* expression in all neuroblastoma cell lines as compared to fibroblast cell lines as well as cell lines from other tumor entities (Figure 93C, FC, *p=0.02004,* Kolmogorov-Smirnov test). Another examination of the data indicates that *MYCN* amplification is associated with high *ASPM* expression. In a comparison of the *MYCN*-amplified neuroblastoma cell lines with all non-*MYCN*-amplified cell lines including control cell lines, *ASPM* expression was found significantly higher in *MYCN*-amplified cell lines (Figure 93D, FC, *p=0.0001312,* Kolmogorov-Smirnov test).

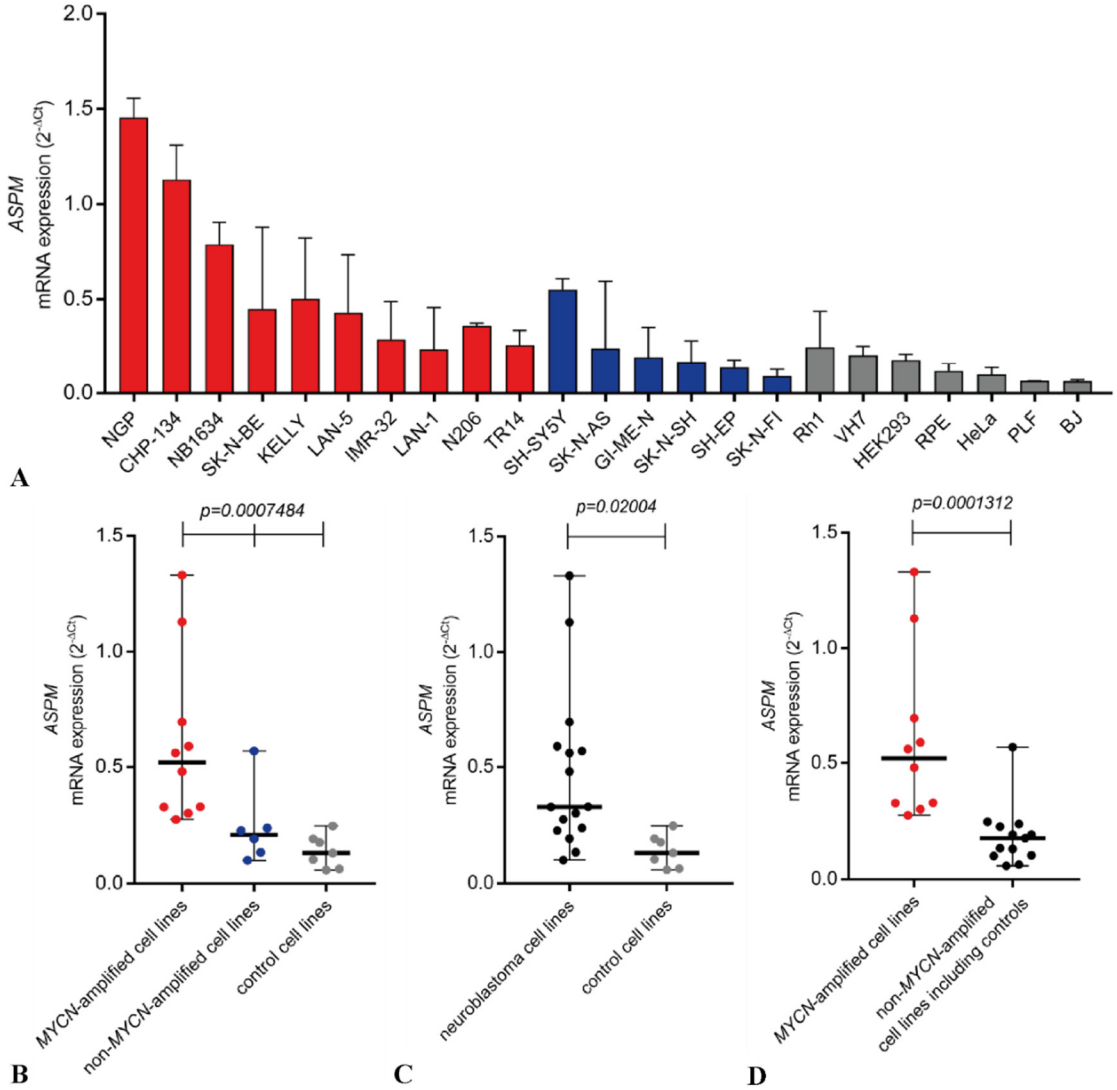

Figure 93: Expression of *ASPM* is raised in neuroblastoma cell lines.
(A) Bar plot diagram showing evaluated *ASPM* RNA levels applying qPCR of different neuroblastoma (red and blue) and other cell lines (grey). A higher gene expression in *MYCN* oncogene amplified neuroblastoma cell lines (red) is found compared to non-*MYCN*-amplified neuroblastoma cell lines (blue). For each cell line, three biological replicates are shown with their respective median and range. **(B)** Scatter dot plot diagram of qPCR data revealing a significant high expression of *ASPM* within a comparison of all three groups. **(C)** Scatter dot plot diagram of qPCR data showing high expression of *ASPM* within a comparison between neuroblastoma cell lines (black) and control cell lines (grey). **(D)** Scatter dot plot diagram of qPCR data showing a significant high expression of *ASPM* within a comparison between *MYCN*-amplified neuroblastoma cell lines (red) and non-*MYCN*-amplified cell lines (neuroblastoma and control cell lines, black).

Although the proliferation rate of the control cell lines was comparable to the proliferation rate of neuroblastoma cell lines (data not shown), there is still the possibility of whether *ASPM* expression in neuroblastoma cells lines was just a surrogate marker of cell proliferation. If this is the case, a reduction of neuroblastoma cell proliferation would simultaneously result in a reduced *ASPM* expression. To address this question, neuroblastoma cells were grown at variable levels of cell density and serum concentration (see cell pictures in Figure 94; 20 or 70 or 100% cell confluence and 10 or 20% serum).

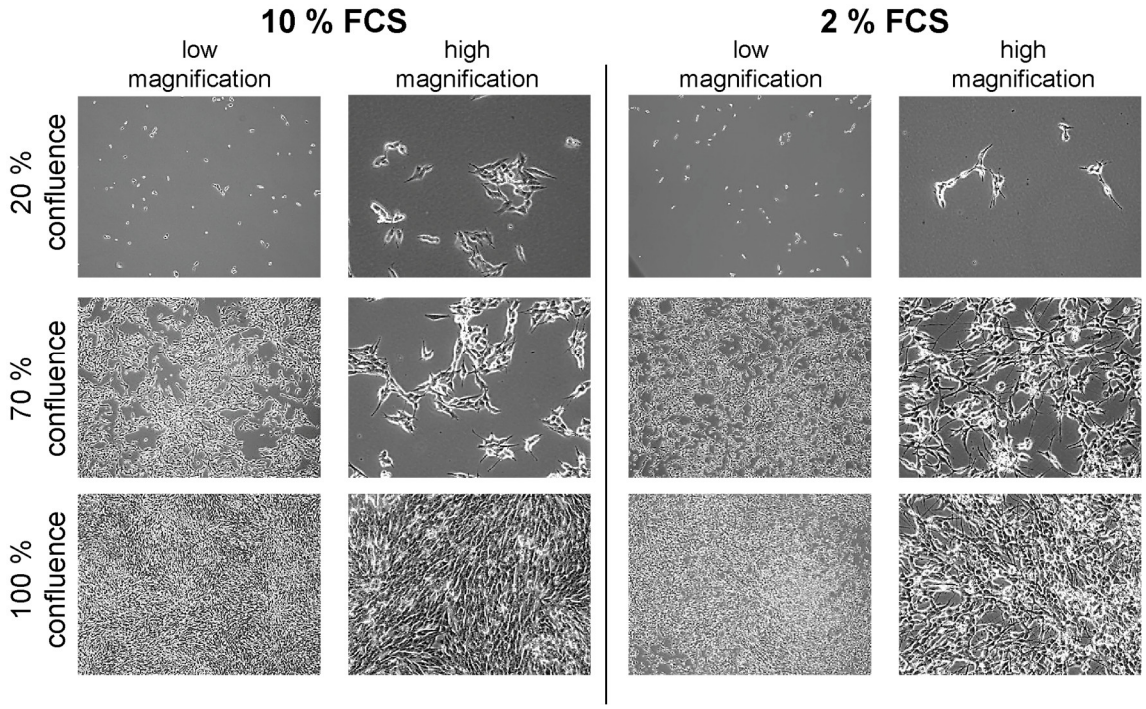

Figure 94: Culturing of NGP neuroblastoma cell line under different serum concentrations and cell densities.
Neuroblastoma NGP cells were grew at variable levels of cell density and serum concentration (20 or 70 or 100% cell confluence and 10 or 20% FCS). These external factors should modulate the cell proliferation and cell cycle. NGP cells were harvested after four days of incubation and analyzed subsequently for changes in *ASPM* expression using qPCR.

These external factors can modulate the cell proliferation and the cell cycle. The cells were subsequently analyzed for changes in cell proliferation and *ASPM* expression. The proliferation rate of NGP neuroblastoma cells were equally dependent on seeded cell numbers and on 2% and 10% FCS in comparison and did not show an excessive proliferation independent of external factors. Thus, the response to different cell densities on neuroblastoma cell proliferation was only minor (not significant, *p=>0.9999-0.3333,* Kolmogorov-Smirnov test), and as expected, cell proliferation of neuroblastoma cells cultured at 2% serum was significantly lower than proliferation of neuroblastoma cells cultured at 10% serum (*p=0.0022,* Kolmogorov-Smirnov test), as revealed by Cell Proliferation ELISA, BrdU (colorimetric) assay (Figure 95A). Even though the neuroblastoma cells were treated with serum starvation media of 2% instead of 10% FCS, inducing cellular stress, and were exposed to different levels of cell confluences, the mRNA expression of *ASPM* do not fluctuate strongly between the different conditions. The examination of the mRNA levels of *ASPM* using qPCR showed that the

expression of *ASPM* was neither significantly affected by cell confluence (FC, not significant, *p=>0.9999-0.3333,* Kolmogorov-Smirnov test) nor by serum concentration levels (FC, not significant, *p=0.9307,* Kolmogorov-Smirnov test; Figure 95B).

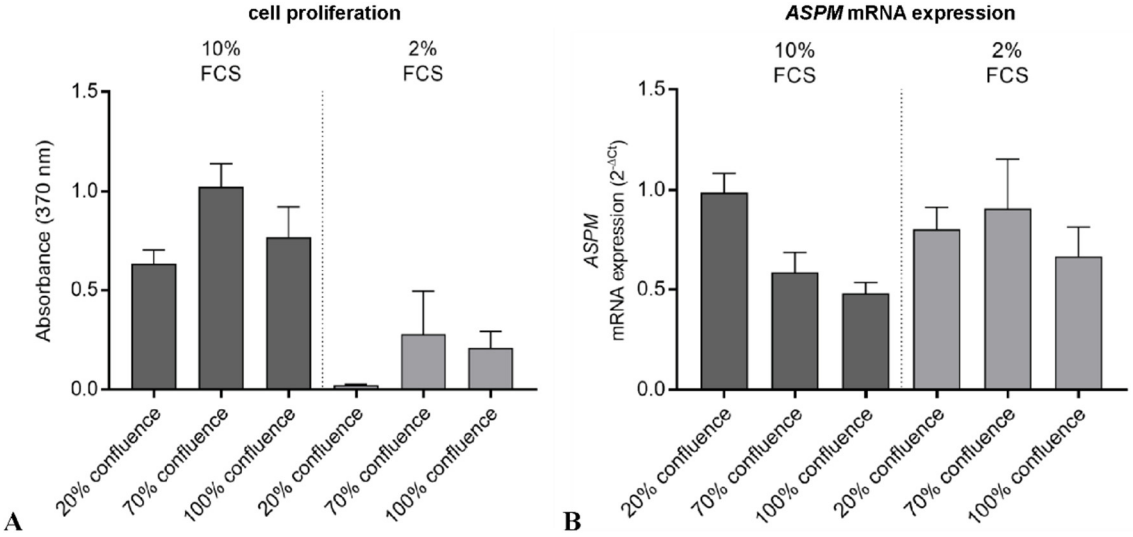

Figure 95: Expression of *ASPM* is largely autonomous of serum and cell density factors in NGP neuroblastoma cell line.
Neuroblastoma NGP cells were exposed to different cell confluence (20-100%) and different serum concentrations (2 and 10%). **(A)** Bar plot diagram of Cell Proliferation ELISA, BrdU (colorimetric) assay. For confluency and FCS content data points, two biological replicates are shown with their respective median and range. **(B)** Bar plot diagram of *ASPM* qPCR data. Two biological replicates are shown with their respective median and range.

In an additional analysis of the effects of confluence and serum differences on NGP cells, the cells were checked in a flow cytometric analysis for changes in the cell cycle (Figure 96). The neuroblastoma cells were growing at variable levels of cell density and serum concentration (20 or 70 or 100% cell confluence and 10 or 20% FCS). These external factors should modulate the cell proliferation and cell cycle. NGP cells were harvested after two days of incubation. The results also show that there was no major change or shift in the cell cycle phases of NGP after exposure to different densities or serum.

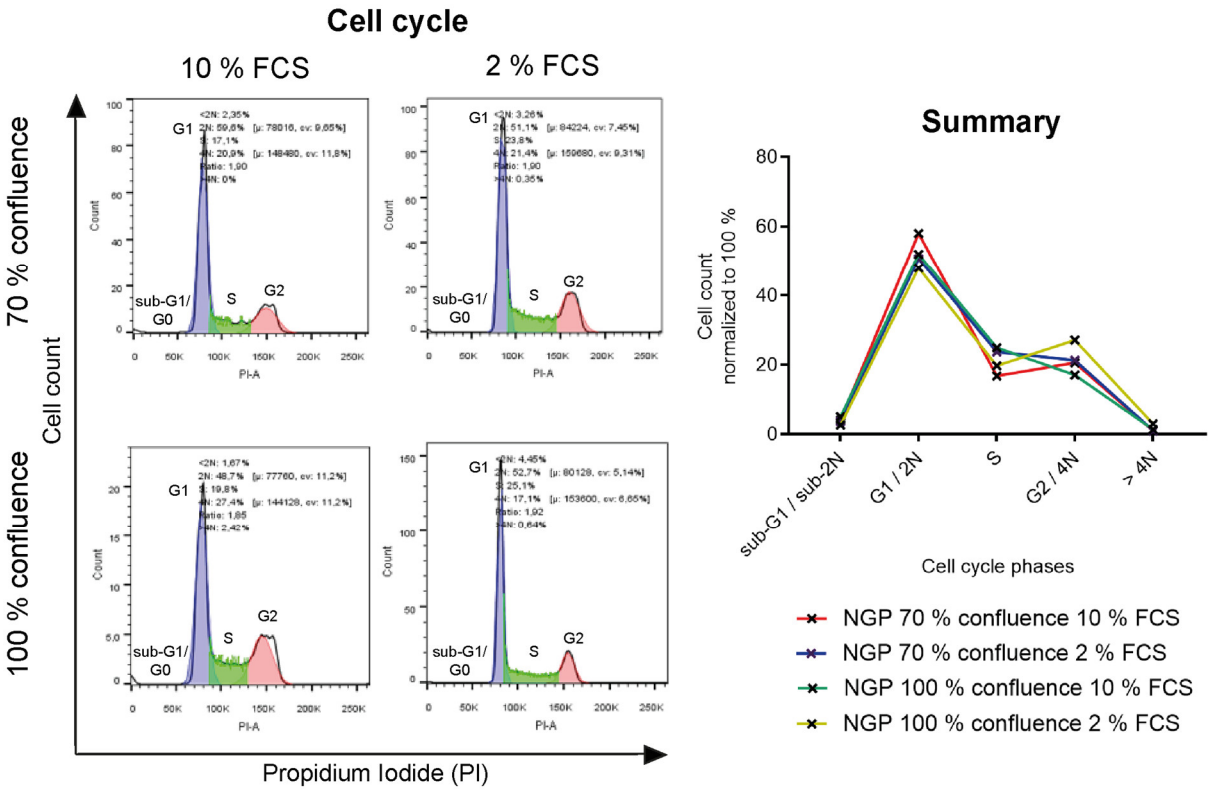

Figure 96: Different serum concentrations and cell densities have no influence on the cell cycle of NGP neuroblastoma cells.
Flow cytometric histograms displaying cell cycle analysis of neuroblastoma NGP cells. Cells were growing at variable levels of cell density and serum concentration (20 or 70 or 100% cell confluence and 10 or 20% FCS). For cell cycle assessment, the cell count was plotted over the area of the PI dye. Unstained cells served as negative control. One biological replica is shown.

These findings could also be demonstrated in smaller experiments in other neuroblastoma cell lines (Figure 97), using LAN-5 (*MYCN*-amplified) and GI-ME-N (non-*MYCN*-amplified) cells. The proliferation rate of GI-ME-N neuroblastoma cells were equally dependent on seeded cell numbers and on 2% and 10% FCS in comparison and did not show an excessive proliferation independent of external factors (Figure 97A). LAN-5 neuroblastoma cells were exposed to different levels on cell density and serum concentrations (Figure 97B). Even though the neuroblastoma cells were treated with serum starvation media of 2% instead of 10% FCS, inducing cellular stress, and were exposed to different levels of cell confluences, the mRNA expression of *ASPM* do not fluctuate strongly between the different conditions. These results are equally to the findings using NGP cells. Taken together, *ASPM* is significantly overexpressed in (*MYCN*-amplified) neuroblastoma cell lines, and reduction of neuroblastoma cell proliferation by altered culture conditions does not strongly affect *ASPM* expression levels.

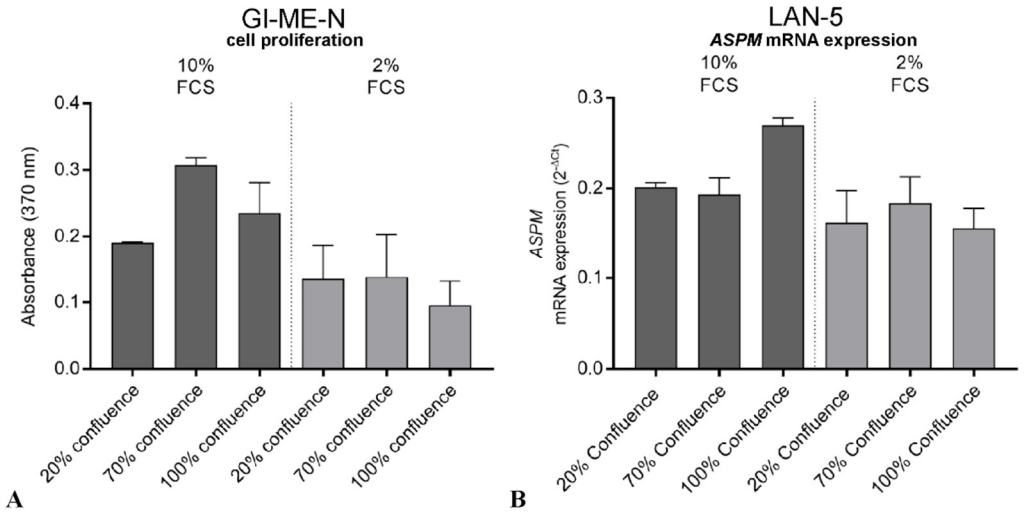

Figure 97: Cell proliferation and expression of *ASPM* is largely autonomous of serum and cell density factors in GI-ME-N and LAN-5 neuroblastoma cell lines.
Neuroblastoma cells were exposed to different cell confluence (20-100%) and different serum concentrations (2 and 10% FCS). **(A)** Bar plot diagram of Cell Proliferation ELISA, BrdU (colorimetric) assay. For confluency and FCS content data points, two biological replicates are shown with their respective median and range. **(B)** Bar plot diagram of *ASPM* qPCR data. Three technical replicates of one biological experiment are shown with their respective median and range.

3.2.4.4 Downregulation of *ASPM* suppresses neuroblastoma cell viability and induces differentiation

To analyze the biological function of *ASPM* in neuroblastoma cells, *ASPM* mRNA was downregulated in neuroblastoma cells using siASPM and subsequently investigated regarding changes on cell viability, proliferation, cell death and neuronal differentiation. Two different siRNAs were used for the knockdown of ASPM, one siRNA attacks exon 3 (siASPM 2) and another siRNA attacks exon 6 (siASPM 1). In all experiments, 1-2 scrambled control siRNAs were carried along in addition (siScramble 1). The NGP *MYCN*-amplified cell line was chosen as neuroblastoma model for the siRNA knockdown experiments, since it had exhibited the highest expression of *ASPM* in the qPCR screening experiments (Figure 93B) shown above. Knockdown of *ASPM* mRNA expression was verified using qPCR after four days, which revealed a downregulation of 64.3% for siASPM 1 and 63.3% for siRNA 2, as compared to scrambled siRNA control (Figure 98A). Assessment of cell viability after treatment with siASPM revealed a strong decrease, showing a lower cell viability of 94.5% for siASPM 1 and 62.7% for siASPM 2, normalized to scrambled siRNA control (Figure 98B). Furthermore, the cell proliferation rate decreased as well after applying siASPM with 95.3% for siASPM 1 and 76.1% for siASPM 2, normalized to scrambled siRNA control (Figure 98C). In contrast, the rate of cell death was strongly enhanced in 122.6% for siASPM 1 and 52% for siASPM 2, as compared to the control (Figure 98D).

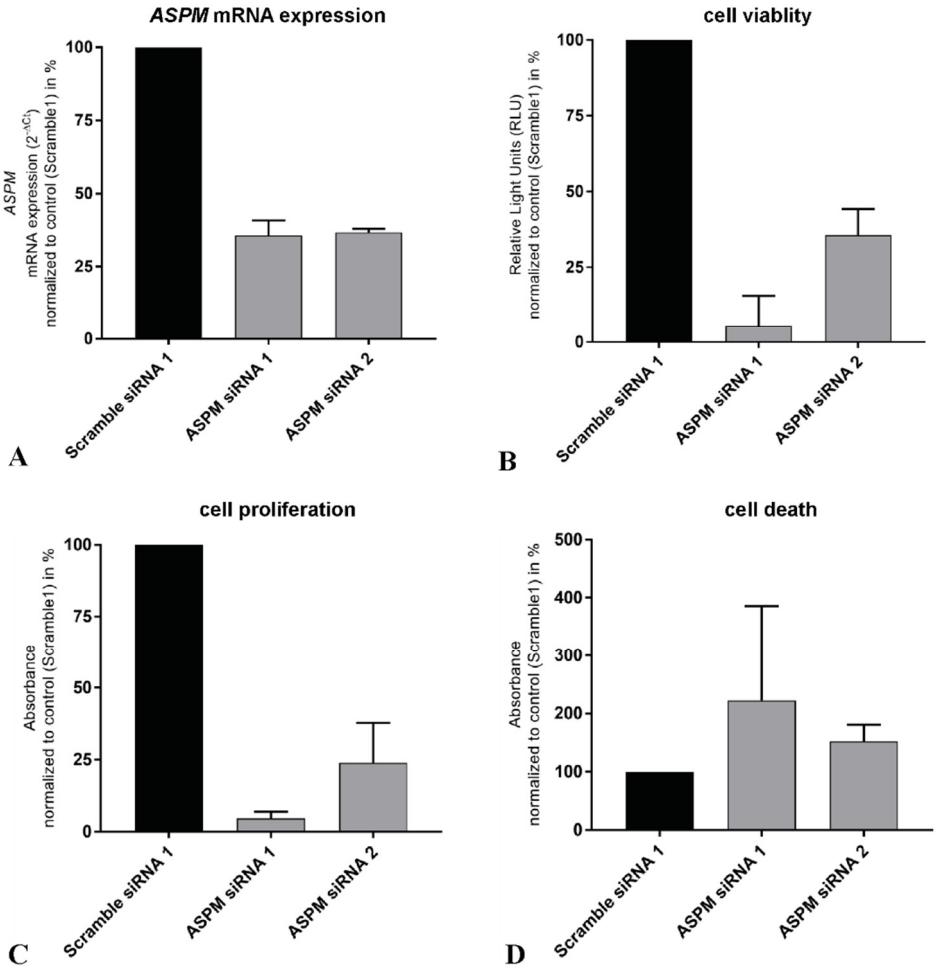

Figure 98: SiRNA knockdown of *ASPM* in NGP neuroblastoma cell line results in decrease of cell viability and proliferation and increase in cell death four days after treatment.
(A) Bar plot diagram of qPCR data of *ASPM* expression levels of NGP cells after knockdown via siRNA. **(B)** Bar plot diagram of Cell Titer Glo cell viability assay, showing a lower cell viability after siASPM treatment. **(C)** Bar plot diagram of Cell Proliferation ELISA, BrdU assay, displaying a lower cell proliferation rate after knockdown of ASPM. **(D)** Bar plot diagram of Cell Death ELISA^{plus} assay, showing a higher rate of cell death after treatment with siASPM. Detection four days after treatment with siRNA against ASPM. All values were normalized to control (scramble siRNA 1) and transformed into percentages. Three biological replicates are shown with their respective median and range.

These experiments were also carried out after a longer treatment with siASPM (read-out after 10 days of siRNA treatment, see Figure 99). The results also showed a reduced expression of *ASPM* in relation to the control when analyzing the cells with qPCR (Figure 99A). In line with the shorter treatment time with siASPM of four days, the knockdown rate for application of siASPM 1 was similar (64%) and for siASPM 2 the decreased expression of *ASPM* was even more pronounced (90.7%). Measurement of cell viability after prolonged treatment with siASPM showed an almost complete diminished cell viablity in relation to the control (Figure 99B). Compared to the shorter treatment time, cell viability was reduced even more and almost came to a standstill (siASPM 1: 99.6% and siASPM 2: 97.2%). It can be assumed that there is no more turnover of ATP in the cell metabolism. Similarly, a comparable to lower cell proliferation of the NGP cells can be measured after siASPM treatment (Figure 99C), this also comes to a complete standstill. In particular, the cell lines which showed remaining proliferative potential after

short-term treatment with siASPM 2 displayed diminished cell proliferation after long-term treatment. Concerning cell death detection after prolonged siASPM treatment, the results shows increased cell death rates for the respective siASPMs applied (Figure 99D). Compared to the shorter siASPM treatment, cells treated with the siASPM 1 no longer show any detectable cell death (-72.2% lower rate of cell death as compared to control); the cell death products may no longer be detectable in a population that has been dead for a long time. Cells treated with siASPM 2 showed a stronger cell death effect than in the shorter treatment (134.8%); this cell death enhancement probably only occurs after a longer treatment with the siASPM 2.

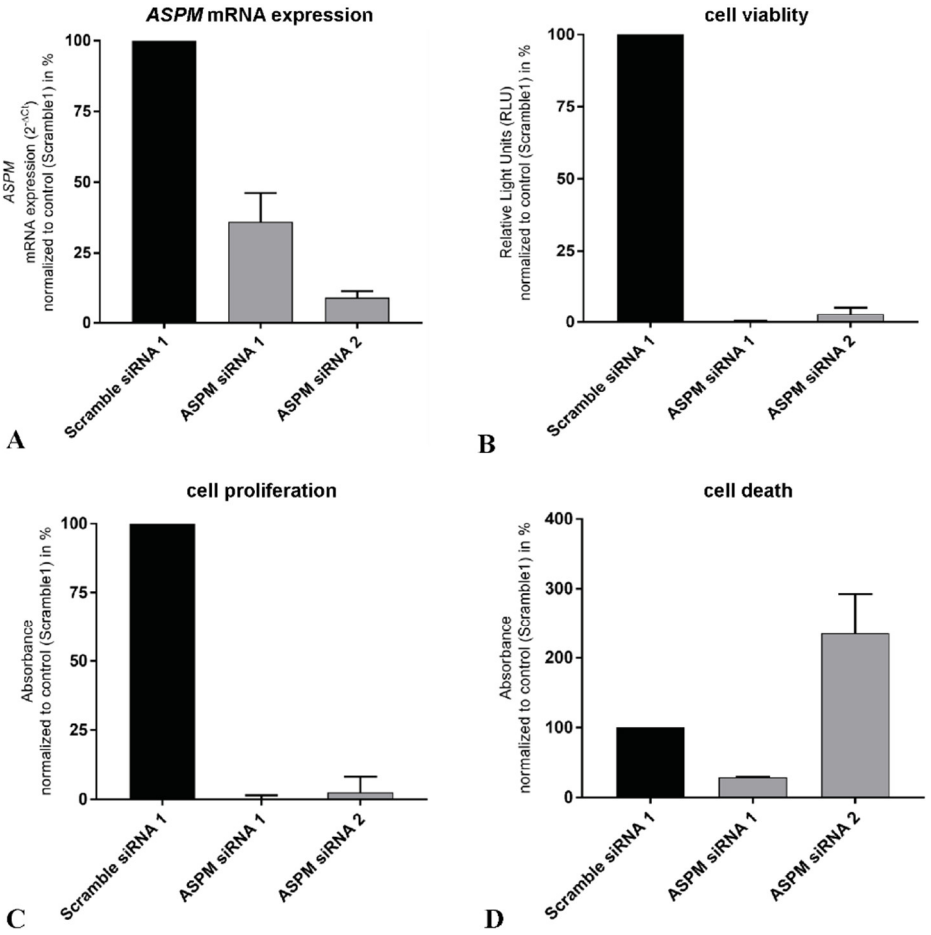

Figure 99: SiRNA knockdown of *ASPM* in NGP cells results in decrease of cell viability and proliferation and increase in cell death after 10 days of treatment.
(A) Bar plot diagram of qPCR data of decreased *ASPM* expression levels in NGP cells after knockdown via siRNA. **(B)** Bar plot diagram of the cell viability assay, showing diminished cell viability after siASPM treatment. **(C)** Bar plot diagram of Cell Proliferation ELISA, BrdU assay, displaying very low cell proliferation rate after knockdown of ASPM. **(D)** Bar plot diagram of Cell Death ELISA^{plus} assay, showing a higher rate of cell death after treatment with siASPM. Detection 10 days after treatment with siRNA against *ASPM*. All values were normalized to control (scramble siRNA 1) and transformed into percentages. Three biological replicates are shown with their respective median and range.

To evaluate the long-term effects and the dynamics of *ASPM* siRNA treatment on neuroblastoma cell proliferation, the NGP cells were observed in live cell imaging. Therefore, the cells were seeded in siRNA containing media only at the beginning of the experiment. The results show a distinctly reduced

cell proliferation of the siASPM treated cells compared to the siScramble treated cells over time (see Figure 100). The cell confluence was lower (see Figure 100A+C) and the number of cells was also reduced after siASPM treatment (see Figure 100B). The siASPM 1 showed a long-term effect, as the cells were permanently impaired in their proliferation. In contrast, the cells treated with siASPM 2 displayed an upturn in proliferation after approximately 125h, which was nevertheless about 20-40% lower than the cells treated with the siScramble control. To maintain the *ASPM* knockdown effect, the cells would therefore have to be treated a second time with the siASPM after 125h at the latest.

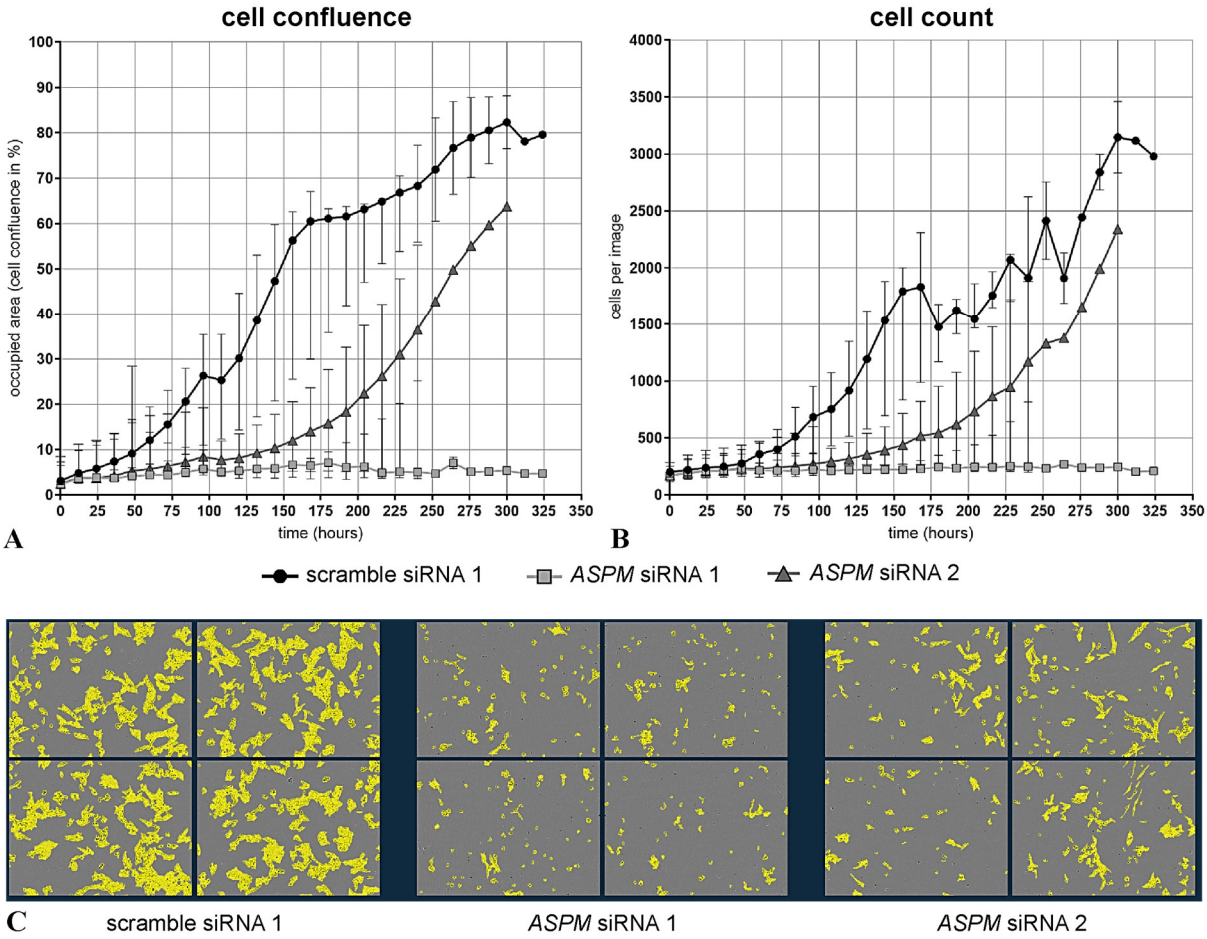

Figure 100: SiRNA knockdown of *ASPM* in NGP cells leads to a reduction of proliferation represented by a lower cell confluence and fewer cell numbers.
Neuroblastoma NGP cells were seeded in medium containing scramble siRNA or siASPM, and occupied area (cell confluence in%) and cell counts (per image) was detected through an IncuCyte® Live-Cell Analysis System. **(A)** Point graph shows NGP cell confluence over time (in h). **(B)** Point graph shows NGP cell count over time (in h). For 0-96h, 7 biological replicates and for 108-324h 1-5 biological replicates are displayed with their respective median and range. **(C)** Cell confluency mask of the IncuCyte® live cell imaging basic analyzer of photos taken 96h after treatment. Each central square covers 1x96-well, in which four images were acquired.

However, it was questionable whether only the neuroblastoma cell line NGP shows a reduced cell viability after ASPM siRNA driven knockdown or whether this effect can also be seen in other cell lines. To test the hypothesis, four further neuroblastoma cell lines were selected, two other *MYCN*-amplified cell lines such as the NGP cell line and two non-*MYCN*-amplified cell lines. As a control, the

non-*MYCN*-amplified fibroblast cell line BJ was carried out in the experiments. A decrease in cell viability was observed for all neuroblastoma cell lines over all experiments (Figure 101).

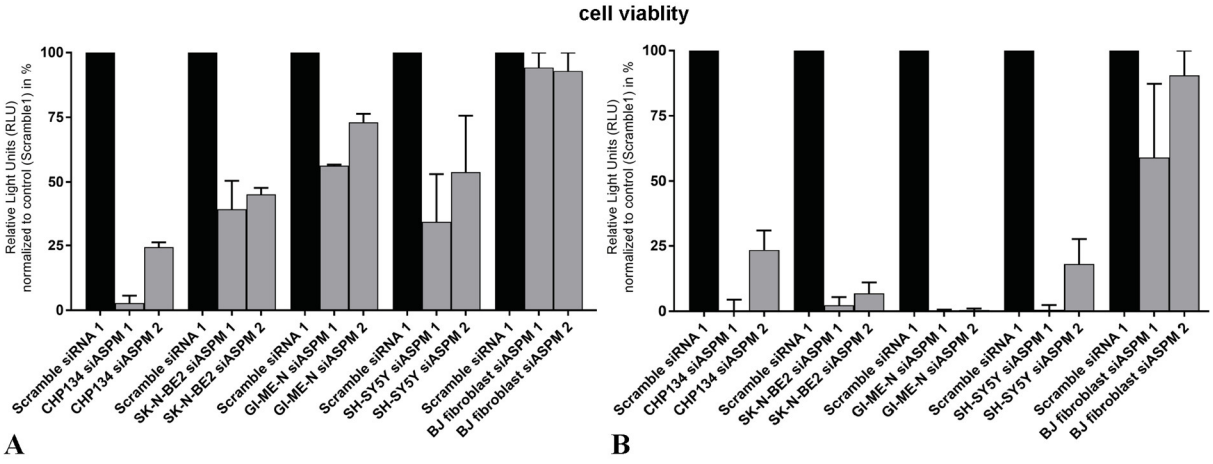

Figure 101: SiRNA knockdown of *ASPM* in neuroblastoma cells results in a decrease of cell viability after four and 10 days of treatment, in contrast only a slight decrease was seen in a fibroblast cell line.
Bar plot diagram of the cell viability assay, showing diminished cell viability **(A)** four days and **(B)** 10 days after siASPM treatment. Detection four or 10 days after treatment with siRNA against *ASPM*. All values were normalized to control (scramble siRNA 1) and transformed into percentages. Three biological replicates are shown with their respective median and range.

Four days after *ASPM* knockdown, the cell viability was found 63% (siASPM 1) and 53.7% (siASPM 2) lower than in comparison to the scrambled siRNA control. In the fibroblast cell line, the reduction in cell viability was only 5.7% (siASPM 1) and 7.2% (siASPM 2), see Figure 101A. After siRNA treatment of the cells over a period of 10 days, the cell viability was again significantly reduced, here the reduction was 99.4% for siASPM 1 and 91.1% for siASPM 2 treated cells. A longer application of the siASPM also had a slight impact on the cell viability of the fibroblast cells, but here the reduction in cell viability was only 41% for siRNA 1 and 9.5% for siRNA 2 treated cells (Figure 101B). Interestingly, when comparing the cell viability values of the *MYCN*-amplified cell lines (NGP, CHP134 and SK-N-BE2) in contrast to the non-*MYCN*-amplified cell lines (GI-ME-N, SH-SY5Y and BJ fibroblasts), it becomes apparent that the groups respond differently to treatment with siASPM. After a short-term treatment, the knockdown rate for *MYCN*-amplified cell lines is 94.2% for siASPM 1 and 62.7% for siASPM 2. For non-*MYCN*-amplified cell lines, however, the knockdown rate is only 43.7% for siASPM 1 and 24.37 for siASPM 2 administered cells (51.9% for siRNA 1 and 31.5% for siRNA 2 without BJ cells). If the cells are subjected to a longer treatment, the evaluation of the cell viability assays results in a knockdown rate of 99.5% using siASPM 1 and 94.7% using siASPM 2 for *MYCN*-amplified cell lines. For non-*MYCN*-amplified cell lines, the knockdown rate is 99.3% applying siASPM 1 and 81.9% applying siASPM 2 (99.5% for siRNA 1 and 91.1% for siRNA 1 without BJ cells). In summary, *MYCN*-amplified cell lines administered with a short-term treatment of siASPM show a greater reduction in cell viability and thus a higher knockdown rate than the non-*MYCN*-amplified cell lines, regardless of an inclusion of BJ fibroblast cells. Applying siASPM long-term treatment, there is no detectable difference between *MYCN*-amplified and non-*MYCN*-amplified cell lines, these cells all have a greatly reduced cell

viability. These experiments also highlight the reproducibility of the down-regulation of *ASPM* by siRNA in different neuroblastoma cell lines showing effects on cell viability. In smaller additional analyses, the SH-SY5Y neuroblastoma cell line also displayed a knockdown effect on *ASPM* mRNA expression and cell proliferation after four days of short-term siRNA treatment (see Figure 102).

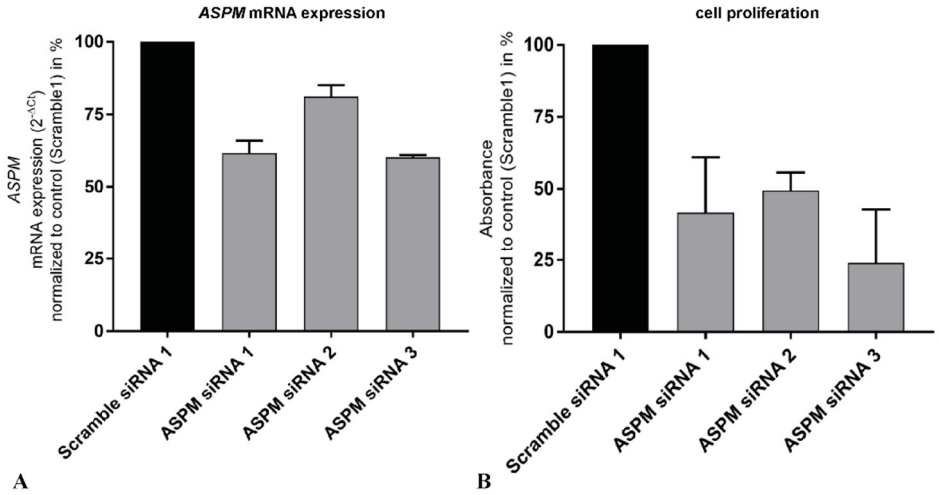

Figure 102: SiRNA knockdown of *ASPM* in SH-SY5Y cells results in decrease of cell proliferation after four days of treatment.
(A) Bar plot diagram of qPCR data of *ASPM* expression levels of SH-SY5Y cells after knockdown via siRNA. **(B)** Bar plot diagram of Cell Proliferation ELISA, BrdU assay, displaying low cell proliferation rate after knockdown of *ASPM*. Detection four days after treatment with siRNA against *ASPM*. All values were normalized to control (scramble siRNA 1) and transformed into percentages. Two to three technical replicates of one biological experiment are shown with their respective median and range.

In further examinations, *ASPM* siRNA treated NGP cells were analyzed via flow cytometry for effects of the downregulation that affect the cell cycle. The Click-iT™ Plus Assay revealed a strong reduction of EdU positive neuroblastoma cells after treatment with siASPM (Figure 103A+C). From the detected cells, 37.1% (siASPM 1, median 3.2% EdU positive cells) and 35.5% (siASPM 2, median 4.8% EdU positive cells) were fewer detected as EdU positive, accounting for fewer proliferating cells after the knockdown, than in the comparison to the scramble siRNA (median 40.3% EdU positive cells). In the reverse observation, the EdU negative flow cytometric detection displayed that the scramble siRNA treated cells only showed a 59.7% EdU negative fractions, accounting for non-proliferating cells. The siASPM 1 treated cells showed a 96.8% EdU negative fraction and siASPM 2 treated cells showed 95.3% EdU negative cells. Taking a closer look at the cell cycle differences (Figure 103B+D), the flow cytometry results highlighted a decline of siASPM administered cells which are in the S-phase. In detail, G1/S transient cells were decreased 9.7% for siASPM 1 (median 0.4%) and 9.5% for siASPM 2 (median 0.7%) treated cells as compared to the control (median 10.1%). Similar results are seen for S/G2 transient cells which were reduced by 21.3% for siASPM 1 (median 2.5%) and 19.9% for siASPM 2 (Median 3.9%) treated cells as compared to the control (median 23.8%). Further, an increase of 38.2% G2/M transient cell populations could be detected for siASPM 1 (median 51.7%) and 35.1% for siASPM 2 (Median 48.6%) treated cells as compared to the control (median 13.4%). No strong difference was

observed in the fraction of cells in G1-phase, where cells were reduced by 9.5% for siASPM 1 (median 35.3%) and 13.4% for siASPM 2 (median 31.4%) treated cells as compared to the control (median 44.8%).

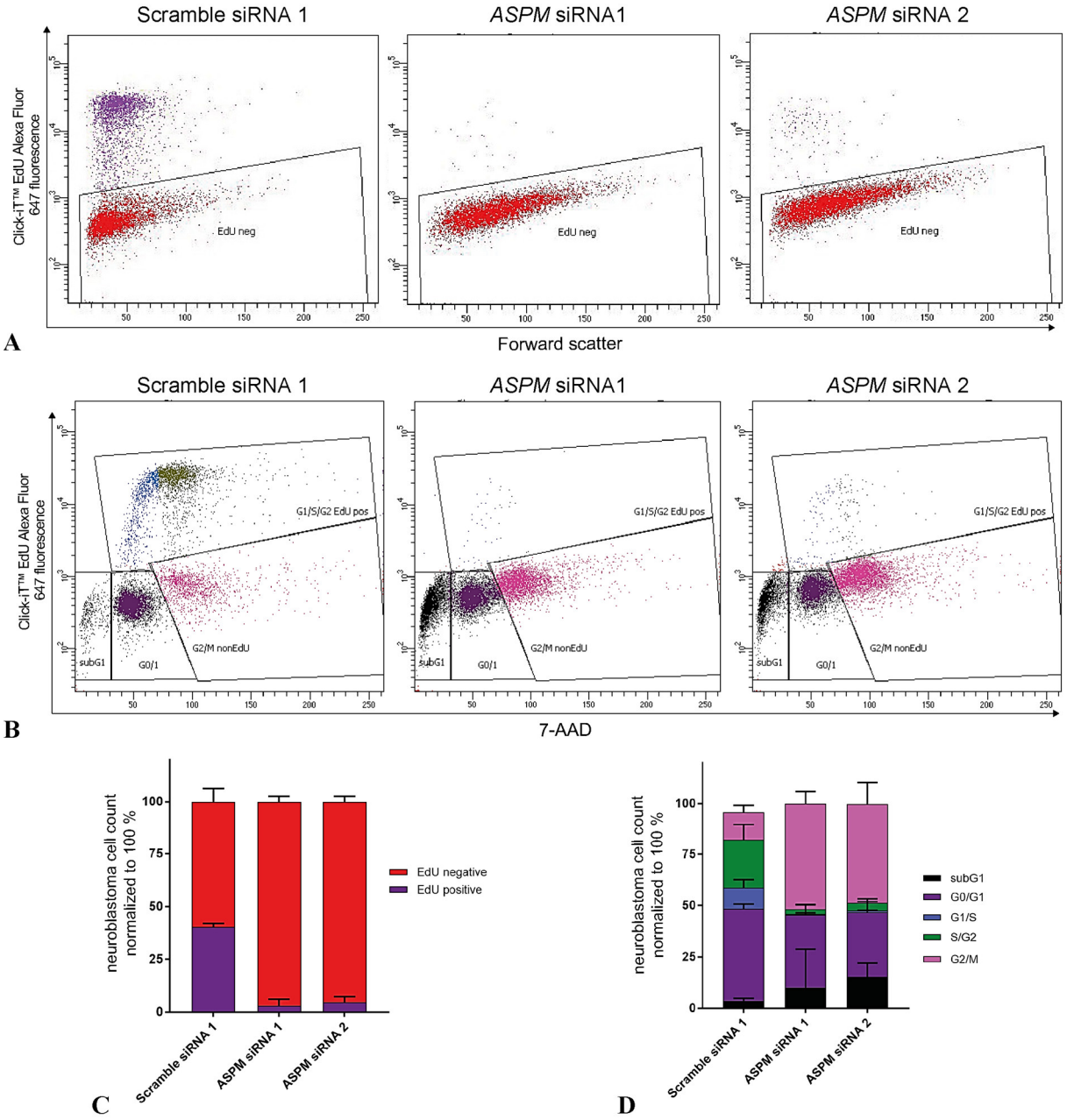

Figure 103: Click-iT™ Plus Assay after siRNA mediated knockdown of *ASPM* in NGP neuroblastoma cell line shows reduction of S-phase, increase in G2/M-phase and increased sub-G1 apoptotic cell fractions.
(A) Flow cytometric dot plot of NGP cells displays loss of EdU positive cells after siASPM treatment. **(B)** Flow cytometric dot-plot of NGP cells after treatment with siASPM show significant increase in the sub-G1 fraction of apoptotic cells with further decreasing S phase in siASPM treated cells. **(C)** Bar-plot of flow cytometric data highlight a loss of EdU positive cells. **(D)** Bar-plot data shows an increase of G2/M phase positive cells after siASPM treatment. For assessment of EdU positive cells and 7-AAD positive cells, EdU (APC channel) was plotted over the area of 7-AAD (PerCP-Cy5-5 channel). Non-siRNA transfected and unstained cells served as negative controls. For (A) and (B), one biological replica is shown; For (C) and (D) three biological replicates are shown with their respective median and range.

Of note, flow cytometry revealed an increase in the sub-G1 fraction of apoptotic cells in siASPM treated cells (6.5% for siASPM 1 (median 10.2%) and 11.7% for siASPM 2 (median 15.3%) treated cells as compared to the control (median 3.7%)), which was in line with the results obtained with Cell Death ELISA (Figure 98D). In summary, it can be shown that the amount of siASPM-treated cells decreases in the cell cycle phases G1 to S and S to G2 and further accumulates higher in the G2 to M phase transition and/or are also found in the sub-G1 apoptotic population. During the siASPM knockdown experiments, it was noticeable that the neuroblastoma cells changed their morphological appearance, especially during a long treatment. To analyze the effect of *ASPM* knockdown on neuronal differentiation, siASPM-treated and scrambled siRNA control NGP neuroblastoma cells were inspected four and 10 days after treatment using transmitted light microscopy, which revealed a more differentiated appearance of siASPM cells, in particular the outgrowth of neurite-like structures was displayed (four days see Figure 104, 10 days see Figure 105). Staining with Alexa Fluor™ 555 labelled phalloidin, which binds actin filaments, revealed a stronger fluorescence signal in siASPM treated cells and confirmed the more differentiated shape with outgrowth of neurite-like structures in comparison to control cells. In addition, immunofluorescence supported microscopy revealed a strong induction of the neuronal differentiation markers MAP2, ßII-TUBULIN and DCX.

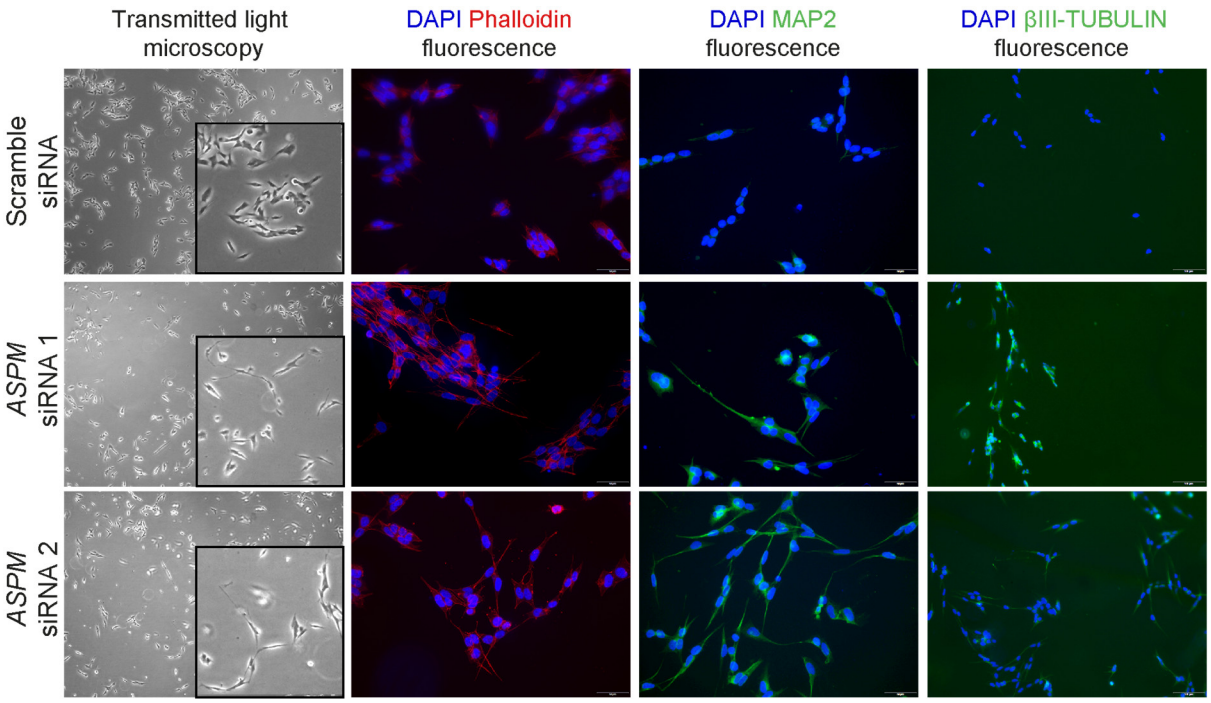

Figure 104: Neuroblastoma NGP cells present with neurite-like shapes and express markers of neuronal differentiation four days after siASPM treatment.
Morphological examination of NGP neuroblastoma cells treated with siASPM for four days. With help of transmitted light microscopy, a reduction in cell population and an appearance of a neurite-like shape of the treated cells became visible. Immunofluorescence supported microscopy confirmed the morphological transition using phalloidin Alexa Fluor™ 555 staining and further revealed positive fluorescence signals of the neuronal differentiation markers MAP2 and ßIII-TUBULIN using Alexa Fluor™ 488. (ßIII-TUBULIN displayed in lower resolution).

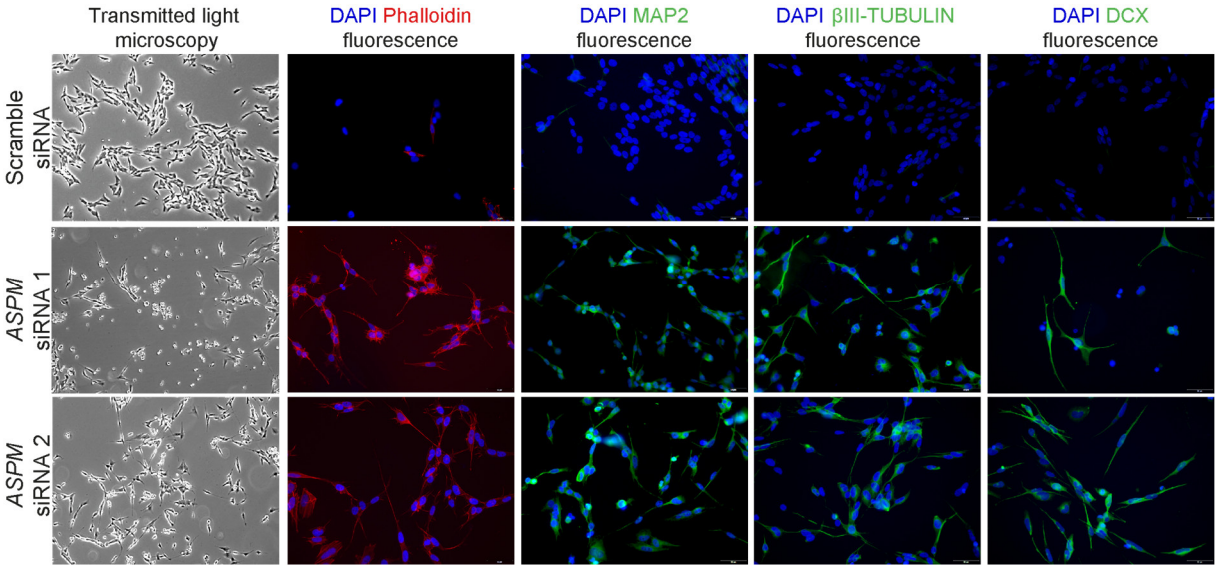

Figure 105: Neuroblastoma NGP cells present with neurite-like shapes and express markers of neuronal differentiation 10 days after siASPM treatment.
Morphological examination of NGP neuroblastoma cells treated for 10 days with siASPM. With help of transmitted light microscopy, a reduction in cell population and an appearance of a neurite-like shape of the treated cells became visible. Immunofluorescence supported microscopy confirmed the morphological transition using phalloidin Alexa Fluor™ 555 staining and further revealed stronger, positive fluorescence signals of the neuronal differentiation markers MAP2, ßIII-TUBULIN and DCX using Alexa Fluor™ 488.

In order to more precisely observe the changes in neuroblastoma cell morphology after treatment with siASPM, the NGP cells were observed in live cell imaging. Therefore, the cells were seeded in siRNA containing media at the beginning of the experiment and pictures were taken automatically every 12h for a total of 12 days. The results show a distinctly reduced cell proliferation of the siASPM treated cells compared to the siScramble treated cells over time (see Figure 107). The siASPM treated cells also achieved a much lower confluence than the cells treated with the siRNA control. These cells did not grow completely to their full area extent and the proliferation was permanently disrupted. The remaining cells, which did not have died, developed long, neurite-like extensions. These neurites became visible after about one week of siASPM treatment and with increasing duration the neurites became longer. The reaction was not reversed within 12 days, the neurite extensions remained intact and did not regress.

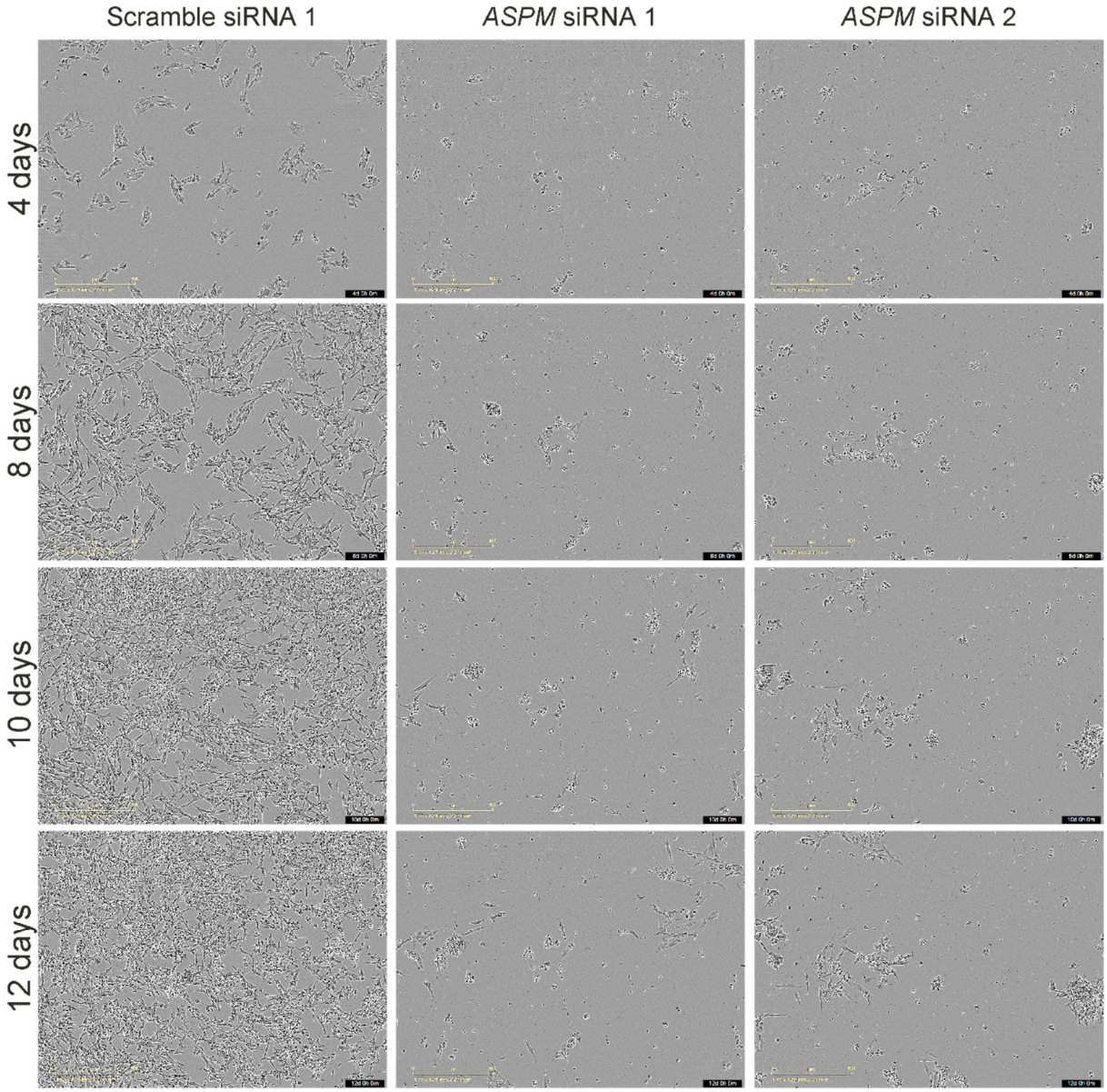

11.5 days in higher magnification:

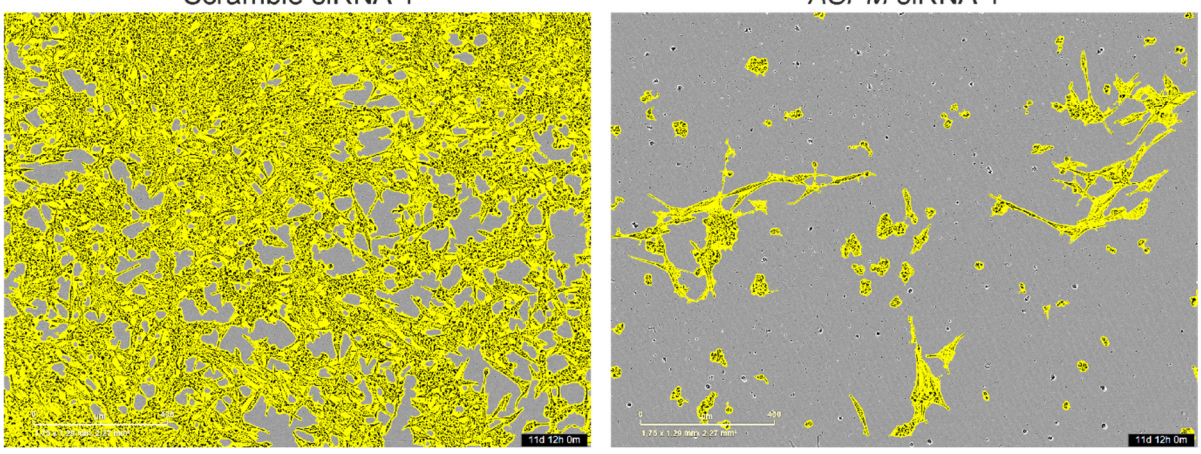

A transition of the undifferentiated neuroblastoma cells towards to a more neurite-like shape including expression of neuronal markers could also be reproduced in other neuroblastoma cells treated with siASPM for ten days (Figure 107).

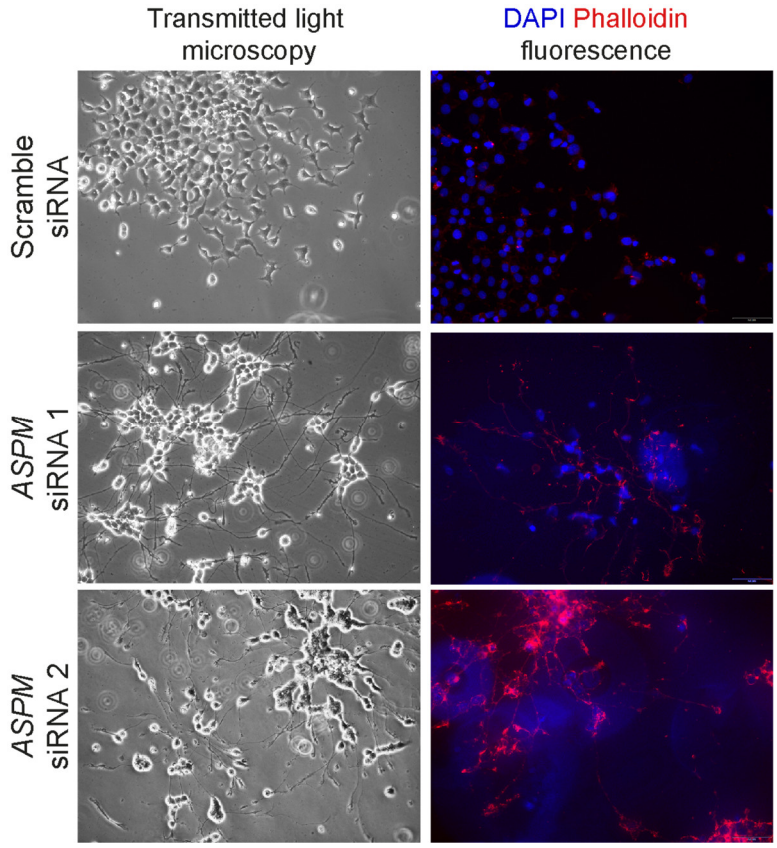

Figure 107: Neuroblastoma CHP-134 cells present with neurite-like shapes and express markers of neuronal differentiation 10 days after siASPM treatment.
Morphological examination of CHP-134 neuroblastoma cells treated with siASPM for 10 days. With help of transmitted light microscopy, a reduction in cell population and an appearance of a neurite-like shape of the transient cells became visible. Immunofluorescence supported microscopy confirmed the morphological transition using phalloidin Alexa Fluor™ 555 staining.

This process of differentiation into neuron-like cells is already known from neuroblastoma cells upon ATRA treatment, which was also used in the past as a possible form of treatment for neuroblastoma tumors[712]. To check the ability of the utilized established neuroblastoma cells to differentiate into neuron-like cells, the neuroblastoma cell line NGP was treated in a control experiment with 1 or 2µM ATRA (DMSO was administered as vehicle; Figure 108). The results showed that the NGP cell line changed its morphology into a neurite-like shape after ATRA treatment of four days, similar to a treatment with siASPM, and also expressed the neuronal markers MAP2 and ßIII-TUBULIN.

< Figure 106: Prolonged siRNA knockdown of *ASPM* in NGP cells leads to a visible reduction of proliferation and a higher cell body eccentricity.
Neuroblastoma NGP cells were seeded in medium containing scramble siRNA or siASPM, and cell growth was tracked with an IncuCyte® Live-Cell Analysis System. A reduction in the cell population and an appearance of a neurite-like shape of the treated cells became apparent, especially through the visualization with the basic analyzer cell confluency mask (enlarged pictures, 11.5h time point). Each image is one of four images taken per treated 1x96-well. The images show the approximate same recording position of a well.

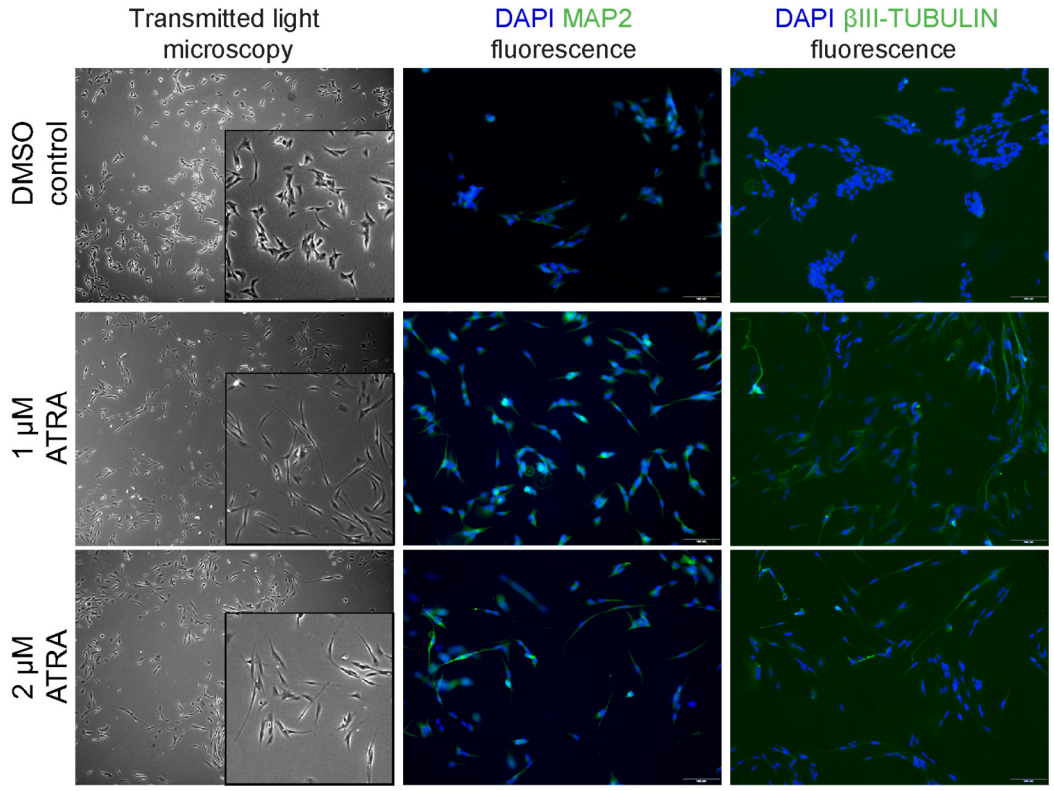

Figure 108: Neuroblastoma NGP cells present with neurite-like shapes and express markers of neuronal differentiation four days after ATRA treatment.
Morphological examination of NGP neuroblastoma cells treated with 1 or 2µM ATRA (DMSO was administered as control) for four days. With help of transmitted light microscopy, an appearance of a neurite-like shape of the transient cells became visible. Immunofluorescence supported microscopy further revealed positive fluorescence signals of the neuronal differentiation markers MAP2 and ßIII-TUBULIN using Alexa Fluor™ 488.

Consistent with the microscopy studies, qPCR assays confirmed a significantly higher expression of neuronal differentiation markers *MAP2*, *TUBB3* and *DCX* in siASPM-treated NGP neuroblastoma cells as compared to controls (Figure 109). The expression of the markers for neuronal differentiation was measured after a four day short-term siASPM treatment (Figure 109A, B and C). For the siASPM application of four days, only a slight effect on the expression of the markers *MAP2*, *TUBB3* and *DCX* could be shown. For the early positive markers *MAP2* and *TUBB3*, an increase in the expression was detected after 10 days of treatment (Figure 109D and E). In detail, expression of *MAP2* was increased by 379.9% using siASPM 1 and 139.7% using siASPM 2 compared to scrambled siRNA (Figure 109D). For *TUBB3*, the expression was increased by 85.5% using siASPM 1 and 25.1% using siASPM 2 compared to scrambled siRNA (Figure 109E). For the late positive marker *DCX*, an increase of 72.6% for siASPM 1 and a decrease of 7.8% for siASPM 2 compared to scrambled siRNA was measured after 10 days (Figure 109F). The strong increase in the expression of the markers compared to the scramble siRNA control displayed after a long term treatment could not be demonstrated for the short term treatment.

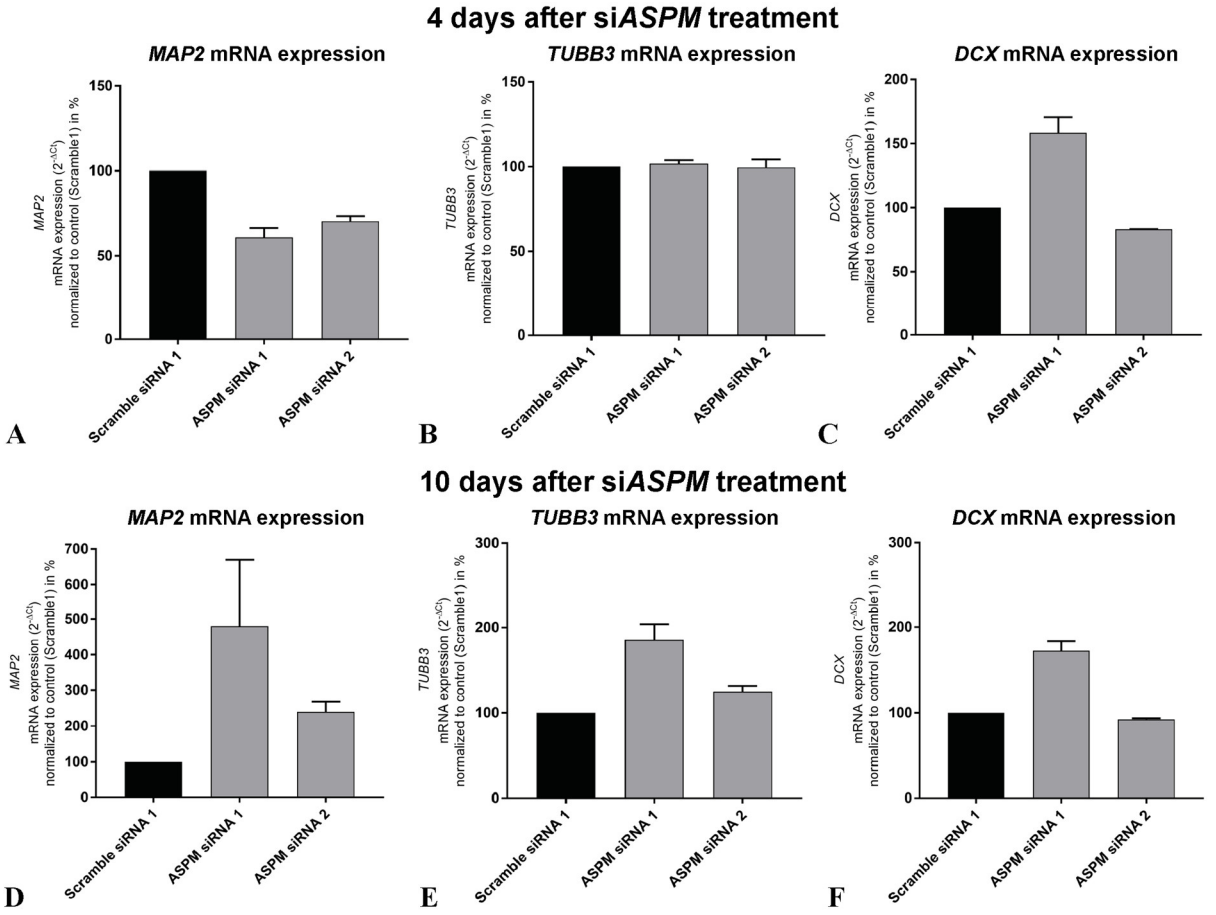

Figure 109: Neuroblastoma NGP cells show low expression of early and late positive markers for neuronal differentiation four and 10 days after siASPM treatment.
Bar plot diagrams of qPCR data of neuronal marker expression of NGP cells after knockdown via siRNA. **(A)** *MAP2* expression, **(B)** *TUBB3* expression and **(C)** *DCX* expression, detection four days after treatment with siRNA against *ASPM*. **(D)** *MAP2* expression, **(E)** *TUBB3* expression and **(F)** *DCX* expression, detection 10 days after treatment with siRNA against *ASPM*. All values were normalized to control (scramble siRNA 1) and transformed into percentages. Three technical replicates are shown with their respective median and range.

Further, a change in expression of a neuronal differentiation marker was detected in other neuroblastoma cell lines after treatment with siASPM for 10 days (Figure 110). The non-*MYCN*-amplified cell lines SH-SY5Y and GI-ME-N showed as well an increase of the late positive marker *DCX*, but not as strong as the *MYCN*-amplified neuroblastoma cell line NGP. Rise of the *DCX* expression of 23.8% using siASPM 1 and 28.6% using siASPM 2 compared to scramble siRNA was detected for the cell line SH-SY5Y (Figure 110A). An increase in *DCX* was found with 38.1% using siASPM 1 and 12.2% using siASPM 2 compared to scramble siRNA for the cell line GI-ME-N (Figure 110B).

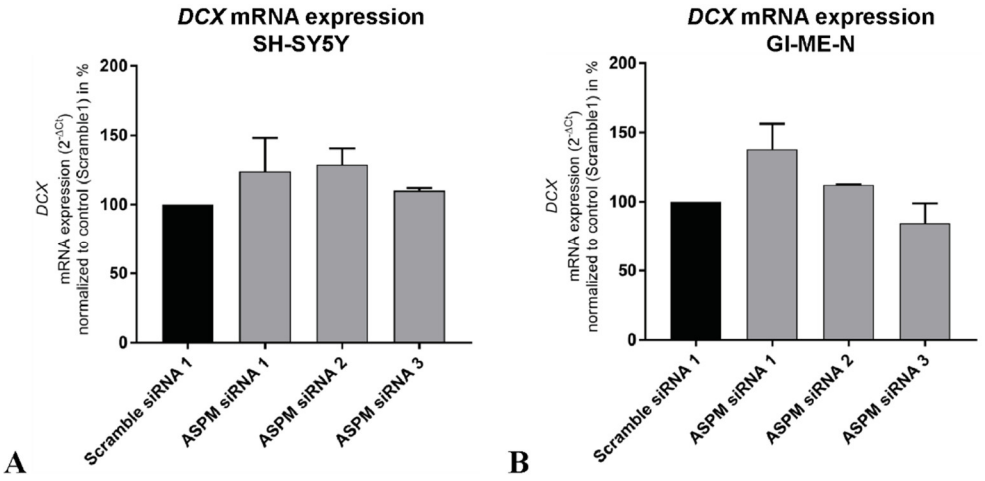

Figure 110: Neuroblastoma SH-SY5Y and GI-ME-N cells show increased expression of late positive marker DCX for neuronal differentiation 10 days after siASPM treatment.
Bar plot diagrams of qPCR data of neuronal marker expression of NGP cells after knockdown via siRNA. **(A)** *DCX* expression in SH-SY5Y cells and **(B)** in GI-ME-N cells. Detection 10 days after treatment with siRNA against *ASPM*. All values were normalized to control (scramble siRNA 1) and transformed into percentages. Two technical replicates are shown with their respective median and range.

The expression was increased by 254.6% compared to the DMSO control for treatment with 1µM ATRA and by 203.7% for treatment with 2µM ATRA. In conclusion, it could be shown that NGP and other neuroblastoma cells undergo a transition towards neuronal differentiation under treatment with siASPM and the effects are similar to a treatment with ATRA. A change in the morphology towards a neurite-like shape and the enhanced expression of differentiation markers seems to increase with additional siASPM treatment days.

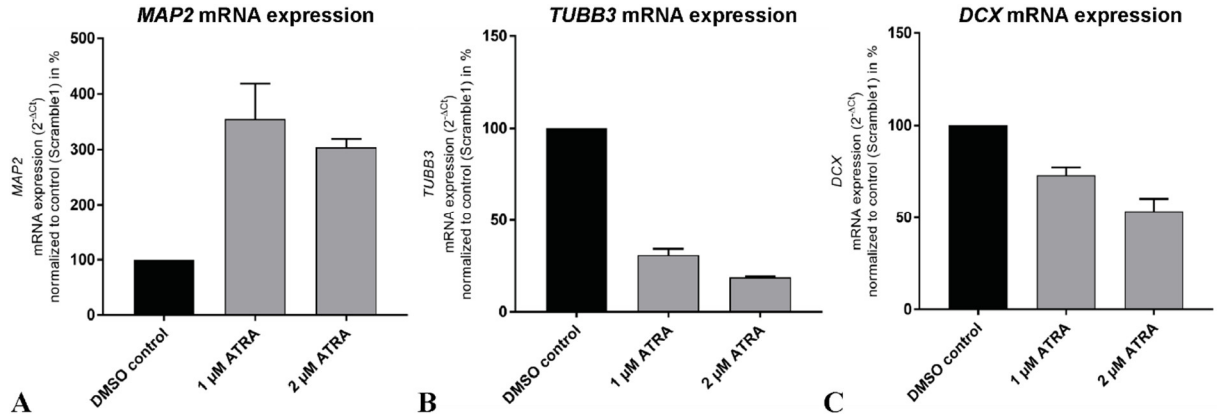

Figure 111: Neuroblastoma NGP cells show variable expression of early and late positive markers for neuronal differentiation 10 days after ATRA treatment.
Bar plot diagrams of qPCR data of neuronal marker expression of NGP cells after treatment with 1 or 2µM ATRA (DMSO was administered as control) for 10 days. **(A)** *MAP2* expression, **(B)** *TUBB3* expression and **(C)** *DCX* expression. All values were normalized to control (DMSO) and transformed into percentages. Three technical replicates are shown with their respective median and range.

To analyze the long term duration of the effects observed in siASPM-treated cells, lentiviral shRNAs (shASPM) were established to stable knockdown *ASPM* (Figure 112A). As with the administration of siASPM, a decrease in cell proliferation was recorded after the cells were treated with shASPM lentiviral

particles (Figure 112B). Furthermore, a stable reduction in cell viability of shASPM-transfected NGP cells was observed at time points 2 days, 4 days, 6 days and 8 days (Figure 112C).

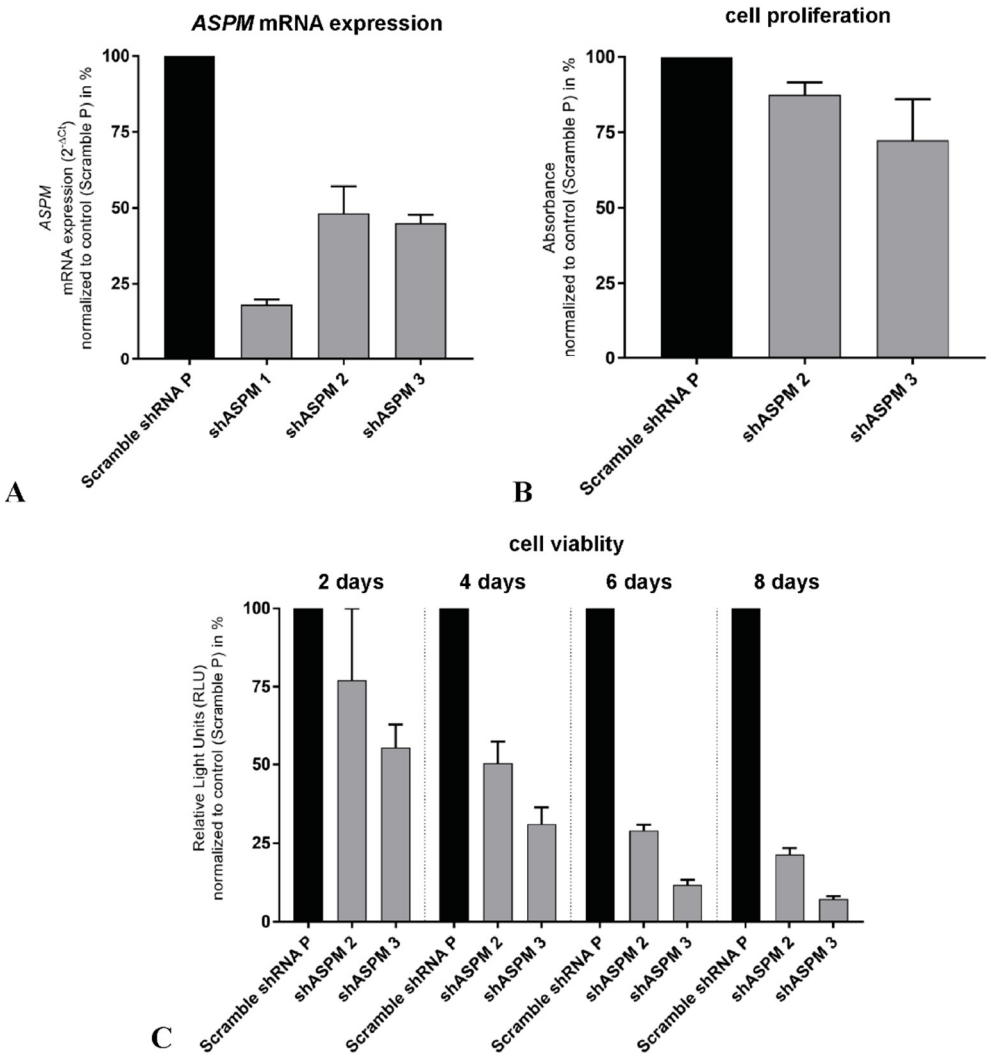

Figure 112: ShRNA lentiviral knockdown of *ASPM* in NGP cells results in decrease of cell viability and proliferation. **(A)** Bar plot diagram of qPCR data of decreasing *ASPM* expression levels in NGP cells four days after knockdown using shRNA. **(B)** Bar plot diagram of Cell Proliferation ELISA, BrdU assay, displaying a lower cell proliferation rate after lentiviral knockdown of *ASPM*. **(C)** Bar plot diagram of cell viability assay, showing diminished cell viability after shASPM treatment. Detection was carried out 2, 4, 6 and 8 days after treatment with shASPM. Each measurement day represents its own biological replica. All values were normalized to control (scramble shRNA P) and transformed into percentages. Three technical replicates are shown with their respective median and range.

When the shASPM-transfected NGP cells were cultivated for a longer period of 10 days, they developed neurite-like outgrows and transformed their morphology from small, compact cells to longer, differentiated-type cells (Figure 113).

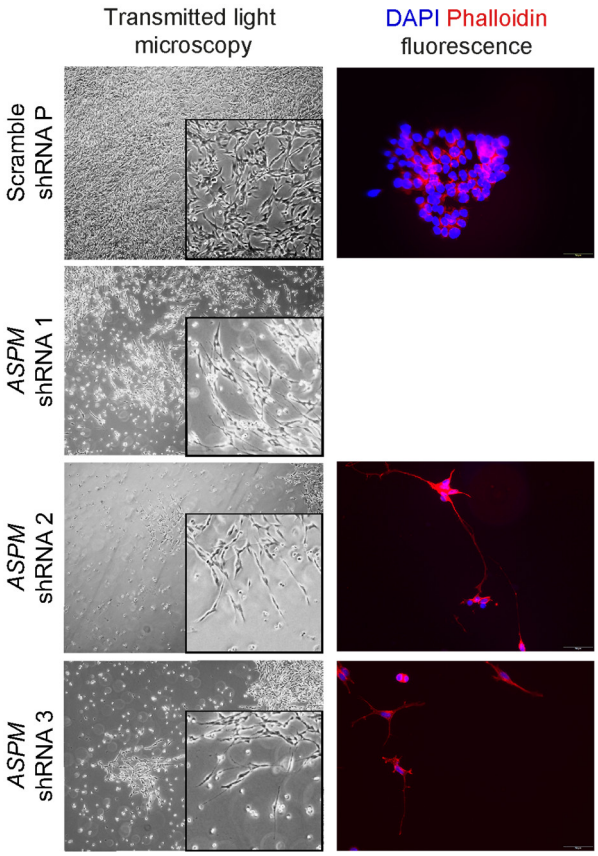

Figure 113: Neuroblastoma NGP cells present with neurite-like shapes and display neuronal differentiation 10 days after shASPM treatment.
Morphological examination of NGP neuroblastoma cells 10 days after treatment with lentiviral shASPM. With help of transmitted light microscopy, a reduction in cell population and an appearance of a neurite-like shape of the transient cells became visible. Immunofluorescence supported microscopy confirmed the morphological transition using phalloidin Alexa Fluor™ 555 staining.

In addition, an increase in the mRNA level of the early neuronal differentiation markers *MAP2* and *TUBB3* were found also in cells administered with shASPM 10 days before (see Figure 114).

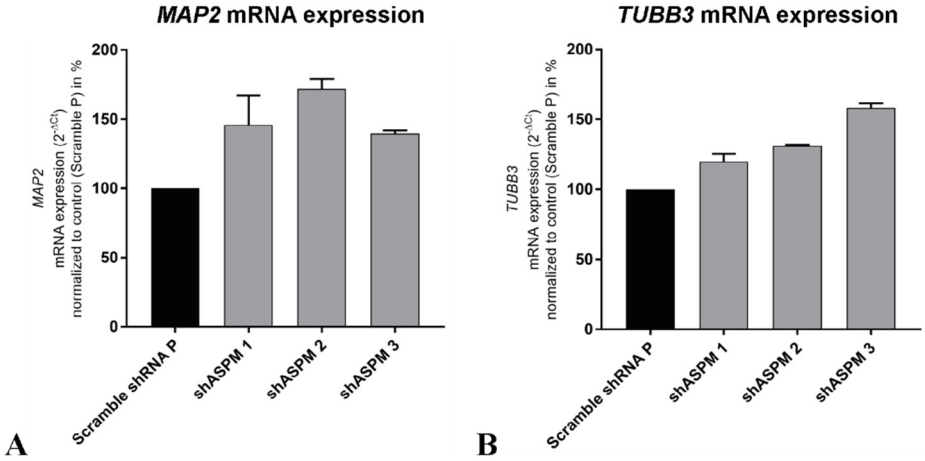

Figure 114: Neuroblastoma NGP cells show increased expression of early positive markers for neuronal differentiation 10 days after shASPM treatment.
Scatter dot plot diagrams of qPCR data of neuronal marker expression of NGP cells 10 days after treatment with lentiviral shASPM. **(A)** Scatter dot plot diagram of *MAP2* expression and **(B)** Scatter dot plot diagram of *TUBB3* expression. All values were normalized to control (scramble shRNA P) and transformed into percentages. Two technical replicates are shown with their respective median and range.

In overall conclusion, downregulation of *ASPM* in neuroblastoma cells with siRNA or shRNA resulted in reduced cell viability and cell proliferation, induction of cell death, G2/M arrest and neuronal differentiation.

3.2.4.5 CRISPR/Cas9 mediated knockin of 3xFLAG to *ASPM* supports validation of siASPM knockdown via detection of ASPM-FPN protein

Effects and altered biological processes after siASPM or shASPM knockdown is conventionally displayed not only with detection of reduced *ASPM* expression in the mRNA level, but also with detection of ASPM protein levels. Determination of a protein lack in the cell is an evidence which demonstrates a direct impact on cellular processes. Detection of ASPM protein levels using the Western blot method was not successful, as various commercial antibodies against ASPM were not found to be functional despite repeated investigations. One possible explanation for this might be that the ASPM protein has a calculated high molecular mass of 410kD and, due to its size, the ASPM protein can only be detected using a gradient Tris-Acetate protein gel. Therefore, *ASPM* was endogenously labeled with a 3x FLAG-tag, mediated by CRISPR/Cas9 (knockin). The attachment of a 3xFLAG-tag peptides to the ASPM protein would allow the detection with a well-established monoclonal anti-FLAG antibody.
The generation of NGP CRISPR/Cas9 *ASPM* 3x FLAG knockin 75/87 cell lines was done in supervision of the biotechnology bachelor student M. Overath and in cooperation with A. Winkler (Charité[543,544,598,603]). The CRISPR/Cas9 knockin was conducted to target the TAG stop codon in exon 28, thereby attaching the FLAG-tag C-terminally. Two sgRNAs with off-target scores 75 and 87 were selected and cloned into the px459 CRISPR/Cas9 vector (see genomic location of sgRNAs in Figure 26). NGP cells transfected with sgRNA 75 or sgRNA 87 displayed the expected fragments generated by the T7 endonuclease upon mismatch between mutated and wildtype. Within a PCR analysis of the successful insertion of the 3xFLAG-tag and NeoR gene into the *ASPM* stop codon site within NGP cells, all px459 sgRNA 75/87 transfected cells showed the expected PCR product. The sgRNA 87 has achieved the best results, especially considering that the sgRNA presenting with a lower off-target score of 87 in the design. Therefore, only NGP ASPM-FPN-sgRNA 87 cells were used for further experiments. The bulk population of NGP ASPM-FPN-sgRNA 87 cells was used to generate single cell clones. Several NGP single cell clones showed the expected PCR product with the size shift and were confirmed for the correct insertion of the ASPM-FLAG-P2A-NeoR (ASPM-FPN-sgRNA87) sequence and the presence of the 3xFLAG sequence. In detail, 6 out of 12 tested NGP ASPM-FPN-sgRNA87 clones were tested positive for ASPM-FLAG-P2A-NeoR insertion, numbered with NGP ASPM-FPN #1, #4, #5, #7, #9 and #11. The clones #1 and #7 in particular showed strong and stand-alone PCR product signals without by-products of the correct insert in gel electrophoresis and are therefore found to be outstanding compared to the other clones. Furthermore, correct insertion of the ASPM-PFN cassette was then confirmed by Sanger sequencing (see final ASPM-FLAG-P2A-NeoR construct in Figure 139 in appendix section). The results of the creation of the NGP ASPM-FPN-sgRNA87 clones

are described in detail elsewhere (manuscript in preparation[544] and Overath 2019[603]). Subsequently, positive NGP ASPM-FPN-sgRNA87 clones were analyzed for FLAG protein expression applying an established monoclonal FLAG antibody within Western blotting protein immunodetection. FLAG protein was detectable in the protein lysates of the NGP ASPM-FPN clones between a molecular mass of 268 and 460kDa (ASPM-FLAG = 413kDa), whereas the NGP wildtype shows no product (Figure 115). To test the specificity of the applied FLAG antibody, a recombinant posi epitope tag was blotted alongside as a control. Detection with the anti-FLAG antibody showed a product at the expected molecular mass of 45kDa.

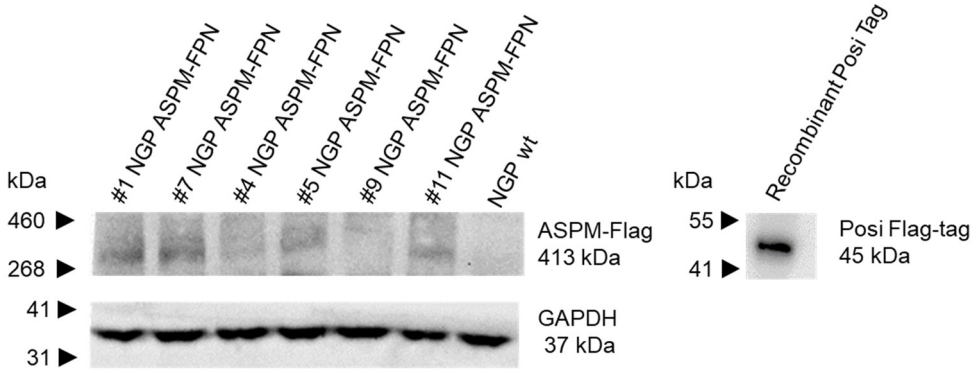

Figure 115: NGP ASPM-FPN single cell clones showed positive detection for FLAG protein at expected weight for ASPM-FPN.
NGP ASPM-FPN clones show a weak protein band between 268 and 460kDa after incubation with an anti-FLAG antibody, while the lysate of NGP wildtype (wt) cells shows no FLAG signal. The anti-GAPDH endogenous control antibody detected a signal at the expected molecular mass of 37kDa and reveals a similar signal intensity for all cells. The recombinant posi epitope tag used as positive control for anti-FLAG antibody detection shows a signal at the expected molecular mass of 45kDa. Figure was kindly prepared by M. Overath (Charité)[543,544].

To amplify the signal of the ASPM-FLAG protein, neuroblastoma NGP cells and related NGP ASPM-FPN clone #1 or #7 were treated with nocodazole and induced a cell cycle arrest and cell synchronization. Treatment with nocodazole further leaded to an accumulation of the ASPM protein, which localizes at the spindle poles during mitotic cell division. Compared to Western blot protein detection without previous nocodazole treatment (Figure 115), the Western blot with nocodazole administration on NGP cells for 20h showed stronger signals and clear bands of the ASPM-FLAG immunodetection (Figure 116). The FLAG protein could be detected in the Recombinant Posi Tag which was applied as positive control, whereas the examined cell lysates of the NGP ASPM-FPN clone #7 without nocodazole treatment showed only a slight signal and the NGP wildtype cells showed no band. It can also be seen that treatment with a small amount of 20ng/ml nocodazole produces a relatively weak protein immunodetection signal, which indicates a low expression of the ASPM-FLAG protein. In contrast, treatment with 30-50ng/ml nocodazole seems to be sufficient to cause an increased accumulation of the ASPM-FLAG protein. QPCR data also provided evidence for increased expression of the *ASPM* mRNA after treatment with nocodazole (Figure 117A). Similar to the Western immunoblot detection (Figure 116), no significant increase in *ASPM* mRNA expression could be detected after a treatment with a small amount of 20ng/ml nocodazole (10.0% higher expression).

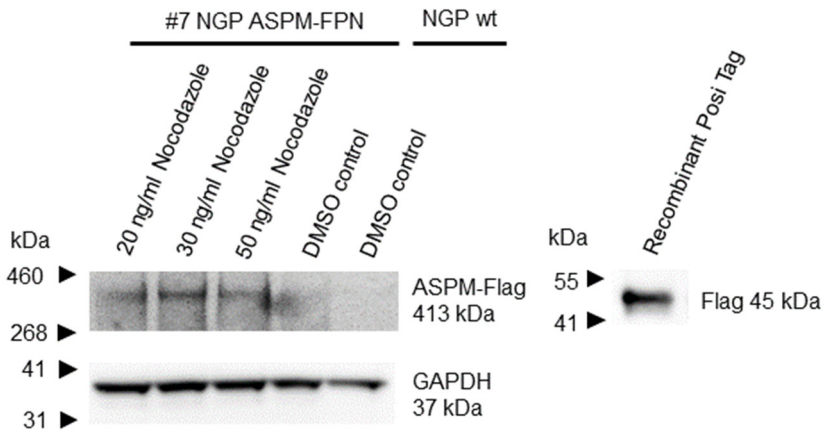

Figure 116: Detection of ASPM-FLAG protein signal increases upon application of nocodazole which blocks polymerization of microtubules.
NGP ASPM-FPN clone #7, which was treated with different concentrations of the antineoplastic agent nocodazole, shows a stronger signal for the ASPM-FLAG protein in Western immunoblotting than comparatively without nocodazole treatment (see Figure 115). The protein lysate of NGP wildtype cells shows no FLAG signal. The anti-GAPDH endogenous control antibody detected a signal at the expected molecular mass of 37kDa and reveals a similar signal intensity for all samples. The Recombinant Posi Epitope Tag used as positive control for anti-FLAG antibody detection shows a signal at the expected molecular mass of 45kDa.

However, if NGP ASPM-FPN cells are treated with 30ng/ml nocodazole or 50ng/ml nocodazole compared to a control treatment with DMSO, an increase of 139.1% (30ng/ml) and 71.5% (50ng/ml) of the *ASPM* mRNA concentration could be measured. In another qPCR analysis it was also checked whether the NGP ASPM-FPN cells were accumulated within the G2/M-phase of the cell cycle after treatment with nocodazole (Figure 117B+C). Indeed, nocodazole treated cells showed higher mRNA expression for *CCNB1* (Figure 117B), which encodes for the Cyclin B1 protein. Cyclin B1 is a controlling molecule at the S/G2 checkpoint whose expression begins to increase during the G2 phase, is most present in mitosis, and is rapidly degraded before completion of the cell cycle.

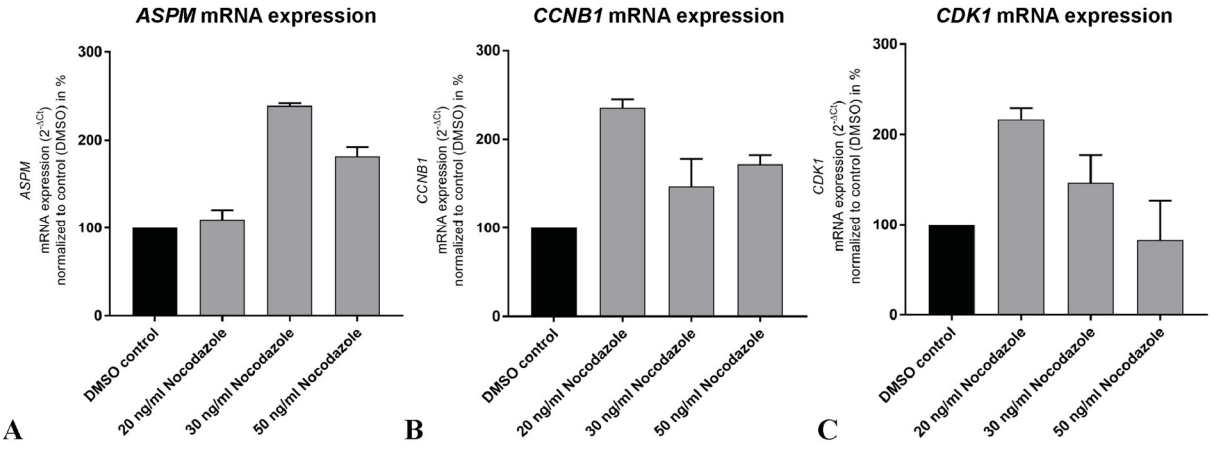

Figure 117: After treatment with nocodazole, NGP ASPM-FPN cell line expresses higher levels of *ASPM* and cell cycle G2/M-phase markers.
Bar plot diagrams show qPCR data of expression levels of *ASPM* and cell cycle G2/M-phase markers in NGP ASPM-FPN clone #7 cells after treatment with nocodazole for 20 h. **(A)** *ASPM* expression, **(B)** *CCNB1* expression and **(C)** *CDK1* expression, detection 20 h after treatment with nocodazole or DMSO. All values were normalized to control (DMSO) and transformed into percentages. Three technical replicates are shown with their respective median and range.

In a detailed examination, it could be shown that the *CCNB1* expression is 135.9% (20ng/ml), 47.3% (30ng/ml) and 63.8% (50ng/ml) higher after administration of nocodazole than without treatment with nocodazole. Cyclin B1 interacts with CDK1 to form a complex known as the M-phase promoting factor, which is essential for G2/M phase cell cycle transitions. In a qPCR analysis of the *CDK1* level within NGP ASPM-FPN cells, it was found that the mRNA expression level of *CDK1* are also increased after nocodazole treatment (Figure 117C). Raised mRNA expression of *CDK1* is identified with 116.7% (20ng/ml) and 47.1% (30ng/ml) higher levels after administration of nocodazole than compared to DMSO application. However, *CDK1* mRNA levels of 50ng/ml nocodazole treatment are found do be similar as compared to the DMSO control. It could now be assumed that treatment of the NGP ASPM-FPN cells with nocodazole increased the mRNA and protein levels of ASPM(-FLAG) and thus enabled detection of the tagged ASPM protein. In order to determine whether the siASPM knockdown can be detected not only via mRNA expression analysis (Figure 98) but also at the protein level, NGP ASPM-FPN cells were treated with siRNAs against *ASPM* and nocodazole simultaneously. During the treatment of the cells and prior to the cell harvest, it was already possible to determine that siASPM administered cells changed their morphology and reduced the number of cells using transmitted light microscopy (Figure 119). In contrast, the cells administered with nocodazole and/or control treatments (DMSO, nocodazole and scramble siRNA) showed no changes in morphology or number of cells. Four days after the treatment of the NGP ASPM-FPN cells with siASPM and optional treatment with 30ng/ml nocodazole for 20h, the cells were fixed and immuno-stained for detection of the FLAG protein.

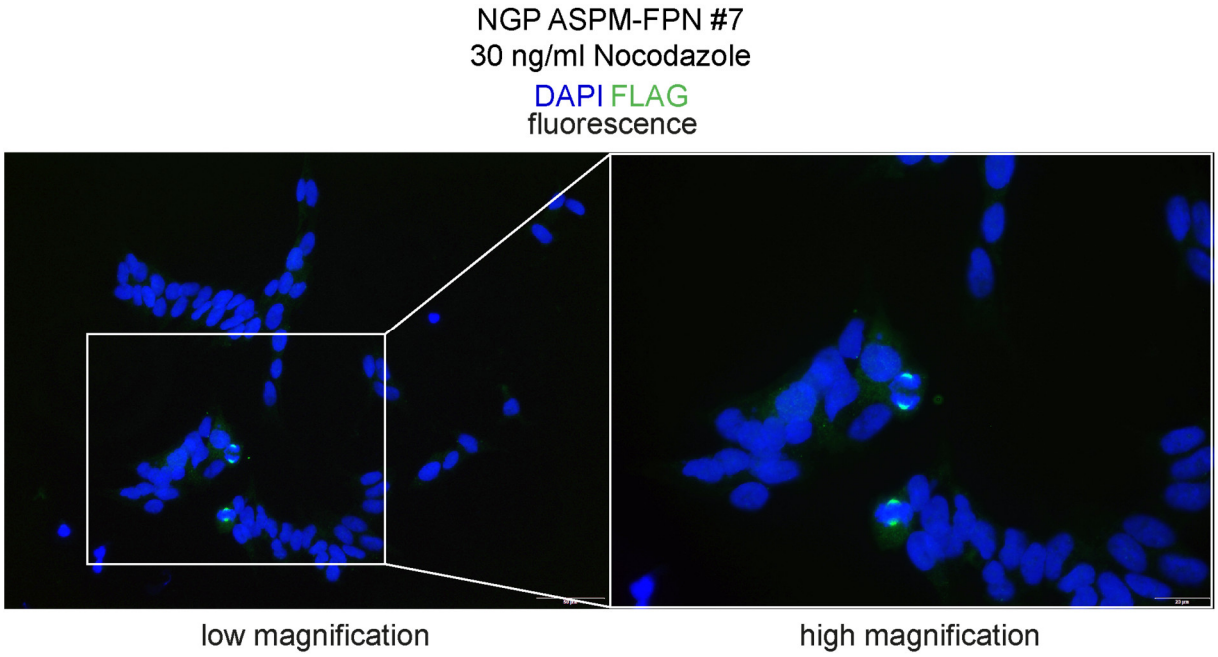

Figure 118: NGP ASPM-FPN cells treated with nocodazole show increased ASPM-FLAG positive signals.
Immunofluorescence microscopy pictures show NGP ASPM-FPN clone #7 cells after 30ng/ml nocodazole treatment for 20h. Immunofluorescence supported microscopy highlights increased Alexa Fluor™ 488 mediated FLAG signals for ASPM-FLAG within cell nuclei of cells which were treated with nocodazole.

ASPM-FLAG positive signals were seen at the approximate spindle pole in the cell nuclei within the DAPI positive area of condensed DNA or very close to the edge of the DAPI positive area (see Figure 118). These ASPM-FLAG signals were part of two spindle apparatuses that were very close to each other in one cell, introducing mitosis, or gradually in up to two almost separate cells, each with one spindle apparatus. From these immunofluorescent images it was evident that cells without nocodazole treatment showed less positive Alexa Fluor™ 488 mediated FLAG signals than cells with nocodazole treatment. In addition, it was shown that under application of siASPM fewer cells displayed a positive signal for ASPM-FLAG than in control treatments with DMSO or scramble siRNA 1 (Figure 119).

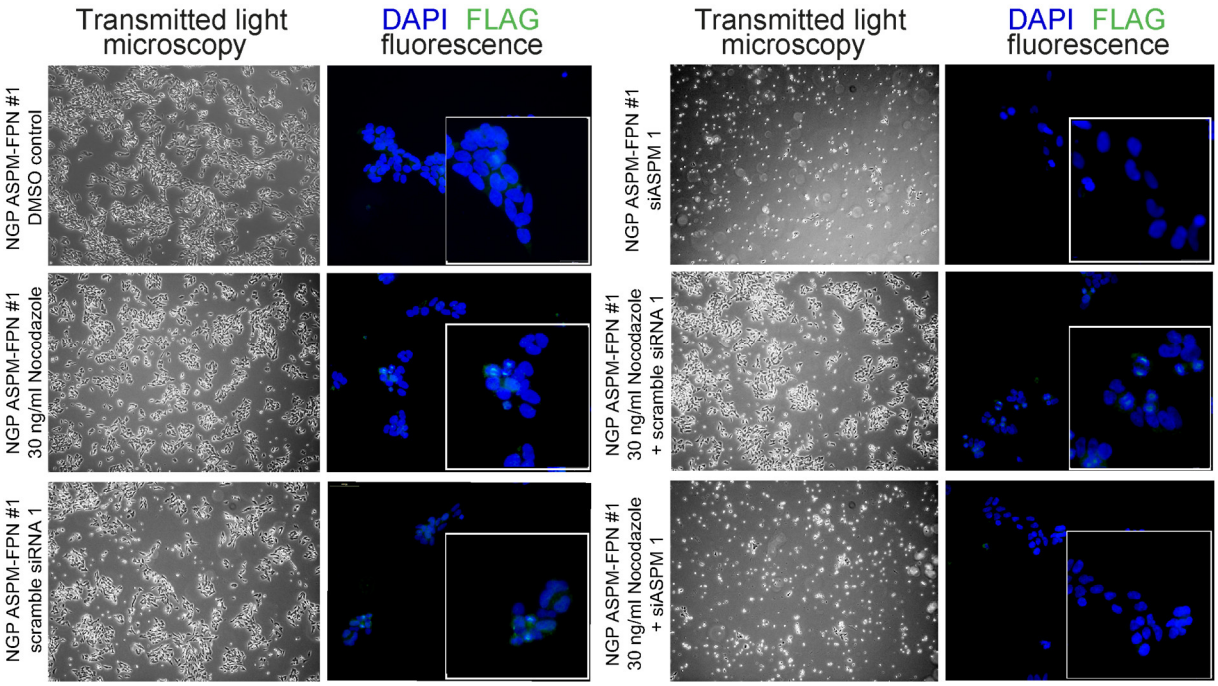

Figure 119: NGP ASPM-FPN cells treated with siASPM and nocodazole exhibit less ASPM-FLAG positive signals as compared to nocodazole treatment alone.
Transmitted light microscopy and immunofluorescence microscopy pictures show NGP ASPM-FPN clone #1 cells after four days of siScramble 1/siASPM 1 treatment and/or 20h of nocodazole treatment. DMSO was applied as a control in comparison to nocodazole. Immunofluorescence supported microscopy highlights increased Alexa Fluor™ 488 mediated FLAG signals for the ASPM-FLAG tagged protein within cell nuclei for nocodazole treated cells.

A reduction of the amount of the positive ASPM-FLAG signals after administration of siASPM to NGP ASPM-FPN cells was further clarified by numerical quantification of the positive signals in immunofluorescent photographs. Using a visually counting method, all positive ASPM-FLAG signals from 10 randomly DAPI/blue channel picked immunofluorescent images with the same resolution from all six different treatments were analyzed. The results could confirm a reduction in the FLAG signal after siASPM treatment (Figure 120A). On application of DMSO or scramble siRNA 1, only 5 and 4 ASPM-FLAG positive signals could be counted, respectively. If the cells were treated with 30ng/ml nocodazole only or in combination with scramble siRNA 1, the signal counts raised to 26 for nocodazole treated cells only and 22 for nocodazole and scramble siRNA 1. However, if siASPM was administered to the NGP ASPM-FPN cells, ASPM-FLAG signal counts were rarely detectable with only 1 positive

signal and was poorly extended to 10 signals upon additional administration of nocodazole. Comparable observations were made in the investigation of the ASPM-FLAG protein using nocodazole and siASPM by Western blotting (Figure 120B). Following a similar procedure as for the immunnofluorescence experiments, the cells were treated with siScramble 1 or siASPM and nocodazole. Cells treated with nocodazole and mock (Opti-MEM™) or scramble siRNA 1 showed a distinct band at the level of the ASPM-FLAG protein at 413kDa, whereas cells without nocodazole showed a much weaker signal. After application of siASPM 1 or siASPM 2, the 413kDa signal of the ASPM-FLAG protein disappeared, independent of nocodazole treatment. In summary, a CRISPR/Cas9 mediated knockin of a FLAG-tag represents an elaborate, but nevertheless great method to allow the detection of a protein with a high molecular mass or a difficult to detect protein. After introduction of an ASPM-FLAG-tag modification in NGP cells, ASPM could be co-detected with the help of FLAG antibodies finally. Thus determining the ASPM protein level in NGP neuroblastoma cells was made possible and functional effects of treatments, eg. siRNAs knockdowns, could be analyzed in more detail.

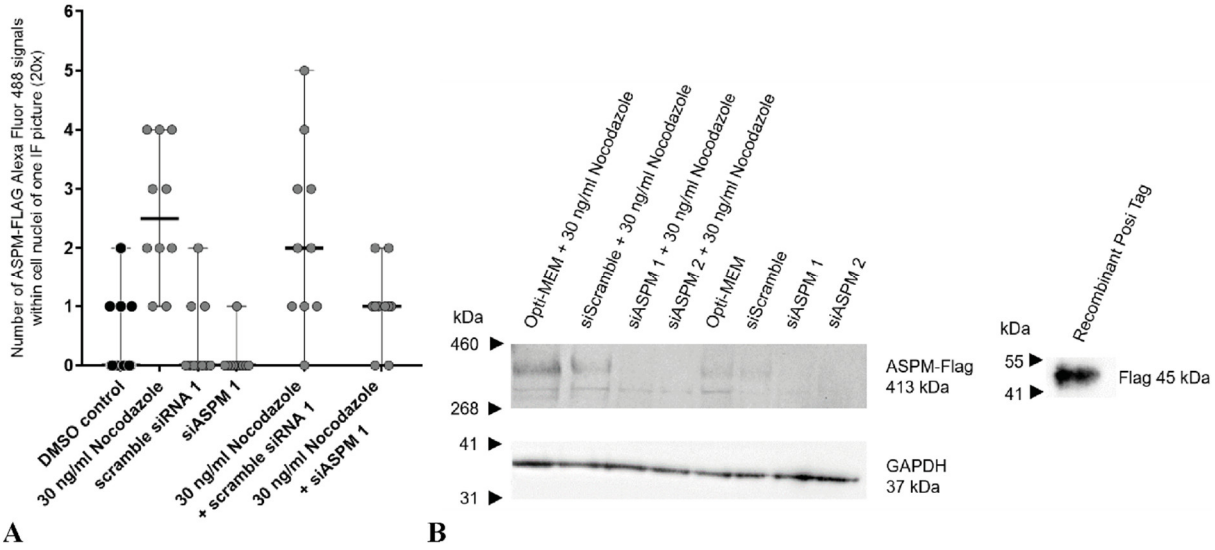

Figure 120: NGP ASPM-FPN cells treated with siASPM and nocodazole exhibit a lower ASPM-FLAG signal as compared to treatment without siASPM.
(A) Scatter dot plot diagrams show summarized count of positive ASPM-FLAG Alexa Fluor™ 488 signals within cell nuclei of one immunofluorescence picture (20x magnification). A total of 10 immunofluorescence supported microscopy images were evaluated for each treatment form applied to the NGP ASPM-FPN clone #1 cells and were checked for one or more positive ASPM-FLAG signals. The results of ten analyzed microscopy pictures are shown with their respective median and range. **(B)** The NGP ASPM-FPN clone #1 was treated with siRNA and with or without nocodazole. The results show a stronger signal for the ASPM-FLAG protein in Western immunoblotting than comparatively without nocodazole treatment, but the signal disappeared if siASPM was applied to the cells in addition. The anti-GAPDH endogenous control antibody detected a signal at the expected molecular mass of 37kDa and reveals a similar signal intensity for all samples. The Recombinant Posi Epitope Tag used as positive control for anti-FLAG antibody detection shows a signal at the expected molecular mass of 45kDa.

4 Discussion

Understanding the patient-specific cancer biology is important in order to make predictions about the tumor behavior and to provide patients with the most effective treatment. An amplification of the *MYCN* gene is the most common mutation in neuroblastoma and a direct treatment of MYCN has not been available to date due to the inaccessible protein structure. With the *NB targeted NGS assay* presented in this thesis a detailed mutation profile of neuroblastomas can be obtained, from which a more accurate risk stratification is possible (see section 4.1). Base-exact sequences of *MYCN* amplicon breakpoints serve as a template for a sensitive *NB breakpoint MRD assay*, which allows the observation of the cancer process during treatment (see section 4.1). In addition, the therapy may be adjusted individually to the patient's neuroblastoma biology. Thus, the small molecule inhibitors described in this work can be selected to treat the aberrant cell physiological MYCN network in addition to conventional chemotherapeutics (see section 4.2).

4.1 Detection of neuroblastoma relevant mutations using a customized hybrid capture-based NGS panel and sensitive monitoring of minimal residual tumor cells

Diagnosis of a neuroblastoma is often challenging, as the clinical presentation in each child is highly distinctive, ranging from spontaneous regression of the disease to patients with an aggressive UHR tumor and particularly poor outcome. The neuroblastoma-specific hybrid-capture-based *NB targeted NGS assay* was found to constitute a clinically applicable technique for the detection of relevant diagnostically and targetable genomic alterations employing a high sequencing depth (see sections 4.1.1, 4.1.3, 4.1.4 and 4.1.6). The base-pair exact resolution of the *NB targeted NGS assay* provided the sequences of specific mutations, e.g. of breakpoints in the *MYCN* amplicon. These unique gene patterns could then be recovered by neuroblastoma MRD PCR in bone marrow derived patient samples. Thus, accumulated minimal residual cells in the bone marrow, which can favor a recurrence, were detected and the molecular response of the neuroblastoma to the treatment was visualized (see sections 4.1.2, 4.1.3, 4.1.5 and 4.1.6).

4.1.1 Mapping of the complex *MYCN* amplicon structure and its unique breakpoints using a neuroblastoma hybrid capture-based NGS panel

The *NB targeted NGS assay* was applied to measure 144 samples in total, including a large number of samples in which a *MYCN* amplification could be detected. A detailed assessment of the *MYCN* amplicon sequence was archived by a distribution of 112 sequencing probes ranging from chr2:14,724,671-17,527,918. The *MYCN* gene itself was entirely covered with probes, but also many parts of the *MYCNOS* gene. Beyond the *MYCN* gen the probes were located upstream starting near

LINC00276 and downstream to the *RAD51AP2* gen. Within the set probes, the *MYCN* amplicon could be detected with base precision, and thus the *MYCN* CNV and genomic breakpoints could be successfully determined. Thus, the *NB targeted NGS assay* is comparable to the classical procedures of routine diagnostics such as *MYCN* FISH analysis, since a *MYCN* amplification and the level of the CNV can be reliably determined. In contrast to FISH diagnostics, not only an approximate range of CNV can be detected, but also a specific value can be assessed. In addition, the *NB targeted NGS assay* provides information about rearrangements and breakpoints, which traditional diagnostic methods applied for neuroblastoma diagnostics are not capable of. In addition, the *NB targeted NGS assay* provided several interesting results with respect to the detected number of *MYCN* copies, the number of *MYCN* breakpoints and first preliminary results on the genomic rearrangement events within the *MYCN* amplicon. This makes the *NB targeted NGS assay* not only a robust and reliable tool to stratify a patient with a neuroblastoma, but also provides information that can be used for MRD diagnostics. Additionally, the results of the assay can support neuroblastoma research and contribute to a better understanding of the disease. However, the NGS panel should always be updated and further refined based on new findings from research studies and clinical practice. Therefore, the following section discusses the improvements that could be implemented in a new version of the *NB targeted NGS assay.*

4.1.1.1 The *MYCN* amplicon possibly extends over large regions of chromosome 2p

By analyzing the total extent of the *MYCN* amplicon and the distribution of related breakpoints on chromosome 2 by WGS and panel NGS, it is noticeable that the *MYCN* amplicon was partially insufficiently covered in the current *NB targeted NGS assay*. The design of the probes mainly focused on the genomic region of the normal (reference) *MYCN* gene and the density of the coverage rapidly decreased upstream and downstream of *MYCN* in the number of probes. From previous reports it can be concluded that the extension of the amplified *MYCN* gene over chromosome 2 can be very extensive. A maximum number of additional *MYCN* copies of up to 700 times higher than in normal tissue has been observed and thus the *MYCN* amplicon can be expected to be very large scaled[64]. In addition, it was published that the size of the *MYCN* amplicon can be variable starting from 350kb up to 8Mb[90,91,713]. Previous findings highlighted as well the existence of a 130kb core region of the *MYCN* amplicon, as well as a possible co-amplification of the upstream located *DDX1* gene (in about 50%) and the *NBAS* gene (in about 54.2%)[92–98,106–108]. In line with those preliminary observations, the results of the *NB targeted NGS assay* could reveal cases of a *MYCN* amplification with an additional co-amplification of *NBAS*. However, the *DDX1* gene was not covered by sequencing probes and therefore an expansion of the *MYCN* amplicon or the occurrence of additional breakpoints could not be detected using the *NB targeted NGS assay*. WGS and panel NGS data also showed that the *MYCN* amplicon extended the defined (probe) detection range from around 15Mb to 17Mb of chromosome 2, and reveals that additional *MYCN* breakpoints maybe have been missed as well in the outer range by the *NB targeted NGS assay* (see Figure 36). Combined with the findings reported earlier, which suggests a large *MYCN*

amplicon in selected neuroblastoma samples, the conclusion is that *MYCN* should be more widely and densely covered with hybrid-capture probes in a new *NB targeted NGS assay* (see Figure 121). Previous descriptions of the *MYCN* amplicon related genomic neighborhood hypothesized an even larger *MYCN* amplicon which exceeds *NBAS*, starting in proximity to the *FAM84A* gene upstream of *MYCN* and ending behind the *KCNS3* gene downstream of *MYCN*[714,715]. In comparison with the results of the *NB targeted NGS assay*, a *MYCN* amplicon related co-amplification up to the *MYCN* upstream located *FAM84A* gene could also be demonstrated. However, this region was covered insufficiently and the detection of involved genes and breakpoints is probably missing. In other studies, it was confirmed that around 33.3% of all *MYCN* amplicons detected also included the downstream located *FAM49A* gene[106]. A further theory mentioned that complex genomic rearrangements such as the *MYCN* amplicon are flanked by common fragile sites that are involved in the formation of extensive rearrangements, either by DNA breakage or by additional DNA replication[106,716]. Studies report that fragile sites are AT-nucleotide-rich, giving the DNA a greater flexibility[717–720]. During DNA replication, stable DNA secondary structures are formed at these sites[717,721,722]. This may impair perturbation of DNA replication and/or progression of the replication fork, which in turn may lead to increased chromosomal breakage[719,723]. Therefore, the *MYCN* amplicon can perhaps be defined much larger than assumed using *FRA2C* common fragile sites located at great distances upstream and downstream of *MYCN* (747 kb *FRA2Ctel* and 746 kb *FRA2Ccen* at chr.2p24.3 and chr.2p24.2, respectively; see Figure 121)[106,716,724–726]. In addition to the oncogene *MYCN*, the sequences of other, possibly neuroblastoma-relevant genes are also located within the *FRA2C* sites. Within the fragile sites of chr.2p there are several genes whose deregulation could also be of importance for the development of an aggressive neuroblastoma. The gene products control for example the genome stability[727–733], the secondary structure of RNA[102], the cellular metabolism[734,735], the plasticity of protrusions and movements[736,737], the synaptic plasticity[738,739], differentiation[740,741], retinoic acid signaling[742,743] and the cell death[744,745]. About the further expansion of the *MYCN* amplicon it has even been reported that the neuroblastoma-relevant *ALK* gene, which is located far downstream of the *MYCN* gene (13.2Mb), can be *MYCN* amplicon co-amplified in around 2% of all cases[110,746]. However, this observation has only been confirmed in this thesis referring to the established neuroblastoma cell line Kelly, which shows a *MYCN-ALK* co-amplification. A previous publication states that the *MYCN* gene is the primary target of genomic amplification, since all investigated amplicons containing other genes always contained *MYCN*[101]. It is therefore believed that the growth advantage of the *MYCN*-amplified cells constitutes a clonal selection benefit of chromosome 2p amplifications. In the present work it was also found that all chr.2p amplifications mainly involve the *MYCN* gene or alternatively the *ALK* gene. In summary, if a minimum size of the *MYCN* amplicon is to be defined, this would be at least the *MYCN* oncogene itself (chr2:16,080,683-16,087,129 (GRCh37/hg19)). A partial expansion of the *MYCN* amplicon into the neighborhood of the *MYCN* gene would then additionally include the *DDX1* and the *NBAS* gene (chr2:15,307,032-16,087,129). With an enlarged definition of the *MYCN* amplicon, the range could be expanded from the *FRA2Ctel* region to

the *FRA2Ccen* region (chr2:14,931,569-19,270,431, see Figure 121). Upon an extensively broad definition of the *MYCN* amplicon including the *ALK* gene, a larger portion of the chr.2p arm would be affected by an amplification (chr2:14,931,569-30,144,477). Since little is known about the *MYCN* amplicon composition and the causing events, further work is needed to determine the relevance of changes in chr. 2p24.3-2p24.2 beyond the classical *MYCN* gene amplification. For these reasons it is important to improve the probe coverage in a new *NB targeted NGS assay* with further regional extension upstream and downstream of *MYCN* including an additional increase in the probe density.

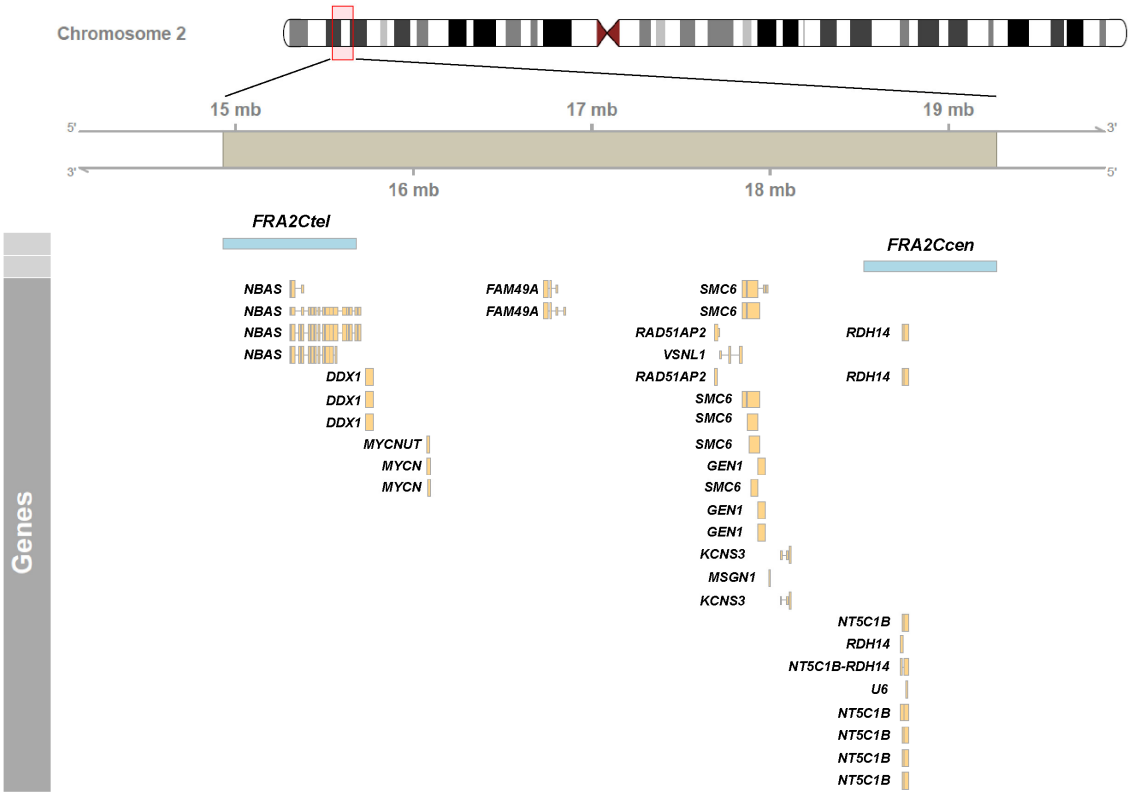

Figure 121: Definition of the *MYCN* amplicon considering *FRA2C* common fragile sites of chromosome 2p as boundaries.
GeneRegionTrack plot showing *FRA2C* sites on chromosome 2p, *MYCN* and surrounding genes. Two *FRA2C* common fragile sites may serve as definition for the *MYCN* amplicon extension. The *FRA2C* sites are located flanking the *MYCN* amplicon (extended *FRA2Ctel* region located on chr2:14,931,569-15,681,340 and *FRA2Ccen* on chr2:18,526,759-19,270,431)[725].

4.1.1.2 The *MYCN* amplicon is stable over the course of the disease

In this thesis it was further found that the *MYCN*-related rearrangements and breakpoints on chromosome 2 are stable across various established cell culture subclones and in patient material over the course of the disease. In line with the present data, the stability of the *MYCN* amplicon was already indicated Oberthuer et al., highlighting the exclusivity and the recurrence of *MYCN* rearrangements in the neuroblastoma cell line IMR-32 and its subclones IMR-5 and IMR-5/75[508]. In an investigation of 32 neuroblastoma tumors by Weber et al., the *MYCN* amplicon structure showed no changes within the course of the disease[60]. The assumption should therefore be excluded that an already detected *MYCN*

related breakpoint is shifted to another, possibly not covered, position in chromosome 2 (interchromosomal rearrangement). A mandatory prerequisite for application in the clinical diagnostic setting is the stability of the marker used to detect MRD. Breakpoint-based MRD detection for neuroblastoma is based on the idea that the stability and clonality of *MYCN* breakpoints make these reliable disease markers, whose sequence and composition remains constant up to relapse. There are reports from previous studies though, showing that the *MYCN* status of neuroblastoma can also be heterogeneous, i.e. a simultaneous occurrence of *MYCN*-amplified and non-*MYCN*-amplified tumor cells. This does not necessarily conflict with the stability of *MYCN* rearrangements and breakpoints over the course of the disease. The *MYCN* amplification of the tumor cells is very likely to remain intact, since a loss of the major cancer driver would be a disadvantage for the tumor cell. Regarding the spatial heterogeneity of neuroblastoma cells, a new publication of the Children's Oncology Group (COG) found that of 5,975 patients examined, only 1% of the patients had a heterogeneous *MYCN* amplification status (only <20% of tumor cells per sample were *MYCN*-amplified). Reports with participation from the SIOPEN biology study group highlight that a *MYCN* amplification was not found in all samples taken from a patient[68,747–749]. The *MYCN* amplifications could be detected in some, but not in all of the sampled biopsies using Affymetrix arrays[747]. These data are supported by the *MYCN*-FISH diagnostics, which also shows a heterogeneous *MYCN* status for these neuroblastoma tumor samples. Either *MYCN* amplifications were reported to be detectable in some sampled tumor pieces but not in all samples of the same tumor, or not in the tumor biopsy but in the bone marrow biopsy, or in primary tumor samples but not in sampled metastasis[68,747]. In a closer examination of all studies, however, only four patients with neuroblastoma were described, whose samples showed a primary heterogeneous *MYCN* status, which was then found to be non-*MYCN*-amplified in further temporal samples[68,748,749]. All other patients described in these studies maintained heterogeneous *MYCN* status during the course of the disease (detected by multiple sampling), or grew into a full *MYCN* amplification from a heterogeneous *MYCN* status, or grew into a full *MYCN* amplification after initial detection of a *MYCN* gain[716,748–750]. It can therefore be assumed that sampling plays a very decisive role in the detection of *MYCN* amplifications and further relevant mutations. A panel NGS examination should therefore be performed with a highly infiltrated tumor sample containing vital cells and, if necessary, multiple samples should be taken if tumor necrosis is suspected. A pooling of isolated tumor DNA from several pieces of the tumor or including different spatial samples could also be performed. In particular, the *NB targeted NGS assay* should include observations from performed *MYCN*-FISH diagnostics on the tumor sample upfront. If a co-existence of *MYCN*-amplified and non-*MYCN*-amplified cells has been detected by *MYCN*-FISH, multisampling for the panel NGS analysis should be considered. It is further very important to adapt the therapy of the heterogeneous *MYCN* patient group. In current treatment protocols, these patients with neuroblastoma were either categorized as having a non-*MYCN* amplification or a *MYCN*-amplified tumor[748]. For safety reasons, the heterogeneous *MYCN*-amplified neuroblastomas are generally upgraded to high-risk diseases after double verification.

4.1.1.3 Rearrangement events of the *MYCN* amplicon and appearance of double minutes

In general, intratumoral heterogeneity in neuroblastoma was described in several publications which was detected in neuroblastoma cell lines[676], PDX[751,752] or patient derived material[38,231,751]. The neuroblastoma is therefore described both genetically and clinically as a heterogeneous disease. However, the development of *MYCN* heterogeneity or the co-existence of *MYCN*-amplified and non-*MYCN*-amplified clones is not completely understood yet. Some reports have hypothesized that *MYCN* amplification, and perhaps *MYCN* heterogeneity, may be the result of a series of events such as chromothripsis and breakage-fusion bridges[78–84].This may result in the formation of additional micronuclei in later stages. In these micronuclei are intermingled with chromothripsis of the damaged, misregulated DNA and leads to a variety of genomic rearrangements and a subsequent re-assembly of a single chromatid[753]. The presence of mitotic segregation errors could be one of the reasons for the appearance of extrachromosomal DMs in neuroblastoma, which are very likely to be involved in the progression of neuroblastoma heterogeneity[72,73]. DMs can also contain several *MYCN* amplicon related genes, such as *DDX1* or parts within the *FRA2Ctel* and *FRA2Ccen* region[105,106]. In previous work it was shown that several clones of an established cell line displayed the exclusive presence of DMs in one subclone and homogenously staining regions in the other subclone[75]. This variation is likely caused by the random and non-binomial distribution of the DMs passed to the daughter cells within mitosis[107,754,755]. Compared to linear chromosomes, DMs have a different mechanism of multiplication and mitotic separation. This circular extrachromosomal DNA does not separate at the anaphase, but later in the G1 phase and its DNA is replicated in the S phase[754,756–759]. Defects in the mitosis processes could support the development of DMs and unequal mitotic distribution of the genetic material. Extrachromosomal circular DNA were recently reported to be a common substrate of high-level oncogene amplification in a variety of solid tumors, including neuroblastoma[74,76]. As such, DMs harbor unique and specific breakpoints at high copy number, that are not present in non-malignant cells. Cell culture experiments have already shown that neuroblastoma cells with *MYCN* DMs have a growth advantage over cells without linear and extrachromosomal *MYCN*[754]. The biology of the DMs makes it difficult to interpret a possible correlation between the *MYCN* CNV and the number of *MYCN*-related breakpoints found, as this could be subject to numerical variations of DMs due to the unequal distribution within a cell population[76,754]. In this work, therefore, a correlation between the *MYCN* CNVs and the number of breakpoints found could not be demonstrated. To determine whether the *MYCN* amplicon is located on chr.2 or on DMs, a *MYCN*-FISH analysis of the cells to be sequenced would first have to be performed. An advanced method for the detection of DMs, which was published recently, is the purification of extrachromosomal circular DNA within the Circle-Seq method[760]. The method includes column purification of circular DNA, exonuclease digestion of linear chromosomal DNA, rolling-circle amplification of extrachromosomal circular DNA, deep sequencing, and mapping[760]. For the TR-14 cell line, FISH-supported analyses could show that the *MYCN* amplicon is located on DMs[668].

Therefore, similar findings may also be observed for other cell lines or neuroblastoma tumors. The *NB targeted NGS assay* performed in this work therefore most likely shows a mixed HSR/DM ratio of *MYCN* amplification and its breakpoints, which is why an additional analysis employing Circle-seq is necessary to prove the existence of DMs in a given sample.

4.1.1.4 Junctional microhomologies were found between both genomic segments of a breakpoint

In addition to the localization of the *MYCN* amplicon on chr.2 or on DMs, a sequence pattern of junctional microhomologies at the *MYCN* breakpoint site was frequently observed when using the *NB targeted NGS assay.* These short DNA sequences are identical in each of the genomic segments involved in the rearrangement, so it is not possible to assign the exact breakpoint location within the junction site or the origin of nucleotides to a segment[85]. The type and length of the microhomology sequences refers to the repair mechanism of the rearrangement that likely have occurred. In this work, in short, around 2-15 bp long microhomologies were found at the junction sites between the segments of the *MYCN* rearrangements. Referring to the work of Kidd et al.[87] and Yang et al.[88], this structural variation indicates the formation of the rearrangement after a double-strand break repair using the alternative end joining mechanism (alt-EJ), also called microhomology-mediated end joining (MMEJ)[85,86]. To perform a MMEJ repair of a double-strand break, individual DNA strands are brought together using microhomology-mediated base-pairing and protruded DNA pieces are cut off[761,762]. This repair mechanism can lead to blunt ends, small sequence insertions and sequence microhomologies at the junction side[85,86,763]. It was further reported, that this repair mechanism is very prone to sequence errors and is associated with the origin of CNVs[85,761,764]. Studies on multiple myeloma and lymphomas have already shown that the MMEJ mechanism is repairing *MYC* rearrangements[765]. These genomic rearrangements also shuffle the *MYC* locus close to super-enhancers, e.g. to super-enhancers of the *FOXO3* gene. For neuroblastoma, too, it has already been highlighted that microhomologies occur at rearrangement junctions with a size of 1-28bp[79]. However, the authors hypothesize that these could be microhomologies created by non-homologous end joining-mediated repair and replicative processes. According to Kidd et al.[87] and Yang et al.[88], a MMEJ mediated repair mechanism is suggested, since the non-homologous end joining-mediated repair does not leave nucleotide insertions or homologies at the junction sites. In a work on *MYCN* rearrangements by Kryh et al.[89], microhomologies at junctions were discovered in all tumors and cell lines examined, ranging from 1-9bp. The authors hypothesize that the microhomology-mediated break-induced replication[85] (MMBIR) is responsible for the repair of the *MYCN* rearrangement junctions. With regard to the publications of Kidd et al.[87] and Yang et al.[88] the characteristic for an MMBIR is defined as a >10 bp insertion at the junction side, which could not be detected in this thesis. Interestingly, in agreement with Kryh et al.[89] an apparently random distribution of the breakpoints without repeating patterns in the same genomic regions could be confirmed in the present work. Moreover, the two papers have described that the majority of *MYCN* rearrangements show a head-to-

tail tandem orientation within the amplicon[79,89]. In the work for this thesis, it was discovered that the *MYCN* rearrangement fragments within the amplicon are not only present in head-to-tail orientation (as for example found in the cell line TR-14), but also in other directions, e.g. tail-to-tail. The rearrangement fragment orientations were rather diverse and there was no evidence of a single orientation type following a specific mechanism. In addition, Kryh et al.[89] discovered that distal *MYCN* breakpoints are located near the *FRA2Ctel* region[105,106]. As this region is not covered by the current *NB targeted NGS assay*, no statement can be made in regard to this present work. Another study describes a similar common fragile site in neuroblastoma, *FRA2H*, which is located on chr. 2q32.1 at a far distance from *MYCN*[766]. The rearrangements in this region show short microhomologies at junction sites, which according to the authors are caused by nonhomologous recombination repair[766]. This observation is in line with the findings made for the *MYCN* amplicon in this thesis. Moreover, a publication by Coquelle et al. indicates that intrachromosomal gene amplification is developed thought the breakage-fusion-bridge cycle mechanism which is initially triggered though the induction of fragile site expression[767,768]. Interestingly, the microhomologies in the rearrangements of the *FRA2H* region also contain LTR (long terminal repeat) and L1 (LINE, long interspersed nuclear elements) retrotransposon elements[766], which were noticed for *FRA2C* regions in proximity to *MYCN* amplicons correspondingly[769]. For other fragile sites (*e.g. FRAXB*, *FRA3B, FRA7G*), several reports highlight that these regions are preferred locations for (oncogenic) viral genome integration[770–773].

However, a comprehensive assessment of the impact of breakage repair mechanisms, fragile sites and especially retroviral elements in the formation of the *MYCN* amplicon and thus a possible connection with the development of high-risk neuroblastomas has not yet been shown. For translation of the biological findings concerning the processes of the development of the *MYCN* amplicon into a clinical environment ("from bench-to-bedside" concept), further studies are required that will also show whether other factors might be of relevance.

4.1.2 Quantitative and highly sensitive detection of neuroblastoma minimal residual disease based on *MYCN* amplicon breakpoints

MRD detection is highly relevant to accurately track the dynamics of the malignancy from primary diagnosis through treatment and follow-up and, in particular, the infiltration of tumor cells in the bone marrow. Within this thesis, a diagnostic assay to assess MRD was presented, specifically tailored to the individual cancer of each patient with high-risk, *MYCN*-amplified neuroblastoma. The patient-specific *MYCN* breakpoints detected by this assay are employed for PCR-based disease follow-up monitoring using RQ-PCR and ddPCR applications. This approach successfully validated and tracked all *MYCN* breakpoints in cell lines and patient samples, and presents itself as a robust neuroblastoma minimal residual disease assay suitable for application in a clinical routine environment.

4.1.2.1 The detection of *MYCN* amplicon breakpoints for neuroblastoma MRD assessment is highly specific and sensitive

The estimation of a bone marrow infiltration is critical for initial disease staging and evaluating the response to treatment in patients with neuroblastoma. In the past, visualization methods have been used primarily to detect neuroblastoma cells in bone marrow samples, such as skeletal scans and bone marrow histocytology[192,193]. With the development of molecular probes, more sophisticated techniques have been introduced to neuroblastoma diagnostics, using the FISH or PCR method (in combination with Southern blotting). In particular, diagnostics focused on the determination of a *MYCN* amplification[229–234]. PCR based assays utilizing SYBR green dyes or TaqMan probes have been developed to detect genomic *MYCN* CNVs or *MYCN* mRNA transcripts in patient-derived material[98,219–222,235,239–242]. However, these applications failed either because the assays were too unwieldy to perform on a large scale, not robust enough to be applied in clinical routine or the expression of markers was altered on treatment at relapse (no stability of markers)[227]. In addition, challenges remain with the stability of RNA, which is not as stable as DNA and does not necessarily reflect the number of gene copies[223–226]. RNA has to be handled with care in diagnostics, when it comes to time delays between collection and detection, temperature fluctuations and isolation methods. Furthermore, the usage of a specialized tube including RNA stabilizing agents for sample collection is recommended[228]. It is therefore beneficial to use stable genetic material and a stable, patient-specific marker for MRD detection. All these limitations can be overcome by a DNA breakpoint-based MRD assay, as has been demonstrated for leukemia before. For long-term observation of patients with leukemia, PCR-based MRD detection is a well-established diagnostics method which has long been applied in clinical environments. Genomic fusion sites have been used as markers before, especially in hematological and mesenchymal malignancies[164,165,167]. The detection of known recurrent distinct genomic alterations, such as *BCR-ABL*[164] fusions, *AML1-ETO*[165] and *ETV6-RUNX1*[168] rearrangements, TCR and Ig VDJ rearrangements[169,774], are standardized approaches for highly sensitive detection of leukemic residual cells. The high medical relevance of bone marrow infiltration and isolated bone marrow relapses of high-risk neuroblastoma cases justifies the use of *MYCN* breakpoints as MRD markers. Referring to the *MYCN* breakpoint MRD assay compiled in this thesis, five previous studies have suggested using genomic breakpoints, e.g. of *MYCN*, to detect neuroblastoma cells in patient samples[60,89,245–247]. In particular, the publication by Ponchel et al. has taken a first step in the development of neuroblastoma MRD assays using genomic rearrangements[246]. Previous experience with TCR rearrangement detection in leukemia samples led to the development of a PCR assay which can measure CNVs, gene rearrangements (T-cell receptor excision circles (TREC) in peripheral blood mononuclear cells) and *MYCN* gene amplifications. Similarly to the results of Ponchel et al., the five previous neuroblastoma MRD studies aimed to present a proof-of-concept assay and not a complete work-flow which can be applied in a clinical setting. The rearrangement sequences of these studies were either assessed using

microarray platforms, which lack the single-base resolution of NGS, or on WGS which remains too cost- and time-intensive to be of practical use for routine diagnostics[60,89,245,247]. Furthermore, the respective downstream PCR assays for the actual MRD detection in patient samples exhibit different strengths in their target specificity. Four of the five published approaches to MRD detection made use of an RQ-PCR system in combination with a SYBR Green dye[60,89,243,247]. In fact, those assays are not suitable for sensitive MRD detection and for precise target amplification due to the application of the unspecific DNA binding dye SYBR-Green I. Only one previously published approach by Van Wenzel et al. employed a more modern StepOnePlus Real-Time PCR device in combination with target-specific TaqMan probes[245]. This approach corresponds to the clinical standards of MRD detection from leukemia diagnostic laboratories[161]. However, they excluded *MYCN* and chromotripsis regions for MRD assessment, because of the complexity of these regions. In contrast, the *NB breakpoint MRD assay* demonstrated in this thesis is very robust and target specific, combining nucleotide-precise detection of *MYCN* breakpoint sequences using hybrid-capture panel NGS and TaqMan reagent-based RQ-PCR detection of MRD cells via the unique *MYCN* breakpoint. Furthermore, future assays in leukemia MRD diagnostics aim to implement the ddPCR technique, which has more recently been introduced for clinical diagnostics[158,188]. Within this thesis, the two techniques were compared for the neuroblastoma breakpoint-based MRD assay and the guidelines were compiled for both applications. The ddPCR technique outperforms the RQ-PCR technique with higher sensitivity across samples and a more straightforward optimization procedure. This observation is line with the comparison of RQ-PCR and ddPCR for leukemia and lymphoma MRD applications[189,775]. For future clinical neuroblastoma MRD diagnostics, the usage of ddPCR is thus highly recommend. The RQ-PCR can reach similarly high sensitivities in some cases, and can also be employed if the hardware or reagents for ddPCR applications are not available within the diagnostic laboratory. In summary, the *MYCN* breakpoint MRD assay reached even higher sensitivities (up to 10^{-6}) than similar methods routinely applied for acute leukemia and lymphoma in the clinical setting (e.g. *BCR-ABL*, sensitivity described up to 10^{-5})[189,776]. Comparing to the sensitivity depths in MRD assessment of VDJ-rearrangements in leukemia, detection is complicated by an elevated background signal from normally occurring rearrangement events in healthy hematopoietic cells. This is why this marker type can lead to a reduced detection sensitivity and/or false positive results. A set of several VDJ-rearrangements is usually employed for MRD detection in leukemia to diminish this problem[161]. In contrast, the patient-specific *MYCN* amplicon breakpoints present a marker whose sequence is completely described and is connected to pathological cell function and particular preliminary cancerous rearrangements events[6]. These characteristics make *MYCN* amplicon breakpoints clear tumor cell markers, which will most likely not occur in healthy cells and makes the use of this single breakpoint sufficient as an MRD marker. As a similar example, single genomic *BCR-ABL1* breakpoints are exclusively used for MRD assessment in pediatric chronic myeloid leukemia[777–781]. Furthermore, the archived sensitivity of the *MYCN* breakpoint MRD assay (up to 10^{-6}) was comparable to the five other neuroblastoma MRD assays in research approaches (sensitivity

described from 10^{-4}-10^{-6})[60,89,245–247]. Of note, the *MYCN* breakpoint neuroblastoma MRD assay reaches the theoretical maximum sensitivity range of up to 10^{-6} for MRD analyses, which is limited by the total amount of assay input DNA in MRD detection (up to 670ng per well/2,010ng in total, referring to up to 6.7pg DNA per single human cell[161,582,782,783]). This result also demonstrates that additional technical optimization of the patient-individual neuroblastoma MRD assay has no potential nor clinical reasonability to increase its sensitivity. In line with the results presented in this thesis, two of the published studies are showing MRD assays based on *MYCN* amplicon rearrangements and reported a high detection sensitivity of up to 10^{-6} [89,247] and in one case even higher at $8x10^{-6}$ [247]. This raises the question whether similar or identical rearrangement sequences occur more often within the *MYCN* amplicon which could be related to the high CNV of *MYCN*. In this study, no correlation could be found between the CNVs and the number of breakpoints detected by the panel NGS. Moreover, the uneven distribution of *MYCN* CNVs per cell can perhaps influence the sensitivity depth, for example through an uneven distribution of DMs[754]. Consequently, any clinical intervention should probably not be considered after a detection of a MRD in the 10^{-6} range within a patient sample.

4.1.2.2 Refinement of the neuroblastoma *MYCN* breakpoint MRD methodology

In order to better analyze the extent of the *MYCN* amplicon, the pattern of breakpoints and the CNV through the amplicon for the translation of the findings into the MRD methodology, it should therefore be considered whether the *MYCN* amplicon requires an investigation applying long-read sequencing, e.g. using the Oxford Nanopore technology. Although this sequencing method would not provide the necessary depth for a reliable detection of the specific *MYCN* breakpoint sequences, but it would aid to reveal identical rearrangements and the general structure of the *MYCN* amplicon[784,785]. Furthermore, already in the pioneering PCR methods for the diagnosis of neuroblastoma, reference genes were used to normalize the *MYCN* amplicon or the *MYCN* mRNA signals. In addition, normal leukocyte DNA samples were carried along as controls[233,242,786], similar to procedures applied for leukemia MRD diagnostics. In the current neuroblastoma *MYCN* breakpoint MRD assay (*MYCN*, chr.2p24.3) the primer/probe used for the detection of a control gene represents a part of the *ß-globin* gene locus[585] (chr.11p15.4), as employed in leukemia MRD diagnostics. Although ß-globin has also been used in neuroblastoma research as an internal control in *MYCN* Southern blot and first PCR analyses before[787–789], a neuroblastoma specific control gene could be introduced as a second reference gene to improve the robustness of the RQ-PCR against the occurrence of large chromosomal aberrations or chromothripsis, which may be present in neuroblastomas. A possible reference gene candidate is *CEP250* (chr.20q11.22)[68], because the sequence is used as a target for *MYCN*-FISH reference probes (Vysis, Abbott Laboratories). Moreover, other neuroblastoma diagnostic research approaches utilize the ß-actin gene (*ACTB*, chr.7p22.1)[239,790] or the RNAseP gene (*RPPH1*, chr.14q11.2)[791]. However, in general, it is recommended to detect a control gene which located on the same chromosome as the target gene. Especially current *MYCN* CNV liquid biopsy attempts make use of the control genes *NAGK*

(chr.2p13.3)[792–794] or *AFF3* (chr.2q11.2)[792]. However, the use of *NAGK* as an endogenous control should be viewed critically, considering this gene is located on the chromosome arm 2p, which can be affected by sequential *MYCN* amplicon gains in neuroblastoma. As well as the inclusion of control genes, the MRD calculation should constantly evaluated and adapted to the latest standards. While the previously published neuroblastoma-specific MRD assays developed their own calculation methods or adapted calculation models used in the qPCR methodology[89,98,245,247], the approach of van der Velden's leukemia MRD calculation model[161,795] was used for the RQ-PCR analysis of the NB *MYCN* breakpoint assay established in this work. With regard to the analysis of the ddPCR results, there are no determined guidelines available yet and various calculation models are under consideration at the moment. For the analysis of the ddPCR results in this work, the official preliminary recommendations of the EuroMRD group for ddPCR analysis were therefore applied[587,589,659]. The main principle of the analysis is the calculation of the ratio between the mean target gene copies against the mean control gene copies which were quantified. Further adjustments of the ddPCR assays is provided in the latest instructions of the EuroMRD group (expected 2020/2021). In the preparation of the ddPCR, different volumes and DNA concentrations shall be used, as well as the single use of consumables being advised, moreover, technical replicates shall be divided into several droplet cartridges and the PCR temperature profile will be different to the current protocol. For the subsequent analysis, a lower number of total droplets is defined as crucial, the threshold should be set based on a positive control and events spilling into other channels should be excluded. The number of copies is further analyzed as mean of copies/µl under additional considering of a housekeeper gene. It is also assumed that one event per well is equivalent to one copy of the target. A sample is confirmed positive if three or more events have been detected in all technical replicates. In addition to these new protocols and analysis methods of the MRD results, the infiltration of the bone marrow sample which is analyzed should be considered additionally. The bone marrow is considered an important diagnostic source of disseminated tumor cells (DTCs), under the assumption that tumor cells from the primary tumor establish a metastatic spread in the bone marrow[153]. As for the NB MRD *MYCN* breakpoint assay presented in this thesis, the number of detectable cells is also limited by the number of cells that can be obtained by bone marrow aspiration. For the accurate detection of a bone marrow infiltration it is recommended to puncture several different localities and each of which is then analyzed for MRD individually[129]. This is also adopted in the new neuroblastoma HR-NBL2/SIOPEN study, in which at least two punctures are recommended, one at the right side of the liliac crest and one at the left side[52]. In comparison, in leukemia studies, such as the IntReALL HR 2010 study, it is recommended to perform even four punctures in right/left and front/back orientation[796]. As early as 1999, Cheung et al. questioned whether GD2 examination of a single bone marrow sample would be sufficient for a reliable diagnosis of a neuroblastoma and proposed a pooling of samples from several punctured sites[797]. In contrast, it has already been shown in leukemia research that spatial heterogeneity is present for anatomically distinct bone marrow samples[798]. Therefore, these samples should not be pooled but individually isolated and analyzed. Beyond the separate collection and isolation

of sample it sould also be considered for prospective MRD studies whether the results from individual bone marrow analyses should be evaluated independently or whether they should be combined (via calculation of the mean). This for, example may, cause an overall positive MRD result whenever each sample alone does not exceed the relevant threshold. In neuroblastoma, no study has been published so far on the sampling and analysis addressing the spatial heterogeneity between different bone marrow punctures, but there are already several research reports available describing spatial heterogeneity between the solid tumor material and bone marrow samples[748,799–802]. In contrast, one study stated that *MYCN*-amplified neuroblastoma DTC clones do not preferentially disseminate from the primary tumor to the bone marrow[748]. This could not be confirmed in the present work, as *MYCN* breakpoint carrying cells were clearly detected in bone marrow specimens, and specifically in selected patient samples in a very high proportion. In this work it was also found that *MYCN*-amplified clones aggressively infiltrate the bone marrow and might be predominant, as they were often found in several distinct bone marrow aspirates taken from the same time point. This observation could be linked to reports stating that high expression levels of the MYCN protein were found to correlate with invasive and metastatic behavior of neuroblastoma[154–156]. In addition, in one case, *MYCN* amplification and *ALK* SNV clones were found exclusive in the separate bone marrow aspirates at one point in time (data not shown due to limited patient samples). The clonality between the different bone marrow samples in neuroblastoma has been poorly studied so far and therefore represents an interesting aspect of the tumor biology of neuroblastoma which should be investigated in further detail.

4.1.3 Detection of other neuroblastoma-associated mutations using the *NB targeted NGS assay* and recovery with the neuroblastoma breakpoint PCR or ASQ-PCR MRD assay

In addition to the in-depth detection of the *MYCN* amplicon, the *NB targeted NGS assay* also allows the detection of other neuroblastoma-related mutations. In addition to large chromosomal aberrations such as a gain of 17q which is present in about 47% of all neuroblastoma cases[41], a loss of 1p[677] and 11q[680] found in 20-30% or gene mutations as in *TERT* (~12.9%)[43,44], *ALK* (~9.2%)[47–52] and *ATRX* (~7.1%)[45] are important for the risk stratification of neuroblastoma. These different mutations were largely recovered by the *NB targeted NGS assay*, making it an appropriate tool for risk stratification of patients with neuroblastoma. However, the following section describes the improvements that can be made with regard to a new version of the *NB targeted NGS assay*. Since the individual gene mutations are of greater importance for the stratification of high-risk neuroblastoma than large chromosomal aberrations, this will be discussed in more detail. Furthermore, the exemplary development and establishment of MRD assays on other neuroblastoma-relevant gene markers beside *MYCN* will be addressed as well. Based on the experience from leukemia studies[161,672,673], consideration could be given for further inclusion of several MRD markers within a patient-tailored, diagnostic MRD panel. This approach would even more improve the reliability of diagnostic MRD reports and regards the possibly of disproportionate distributed DNA fragments and tumor heterogeneity. The *MYCN* breakpoint neuroblastoma MRD assay

can detect the unique *MYCN* oncogene, but this work also provided a first insight that this technique could easily be extended to other genetic mutations, such as those known to be in (the proximity of) *TERT, ATRX,* 1p or at 17q, and most likely also to SNV in neuroblastoma-relevant genes such as *ALK*.

4.1.3.1 Guidance for a neuroblastoma *TERT* breakpoint MRD detection

Similar to the findings for the oncogene *MYCN*, the sequencing coverage of the *TERT* gene is missing decisive probes in the *NB targeted NGS assay* as well. A detailed resolution of the *TERT* region shows that the sequencing coverage before the genomic sequence of *TERT* is decreasing sharp, because only a few probes have been placed outside the actual *TERT* gene on the genomic minus strand (Figure 122). The underlying mutation of *TERT* overexpression is a promotor rearrangement juxtaposing the gene to strong enhancer elements[43,803,804], similar to the *MYCN* amplicon[74], which probably was triggered by double-strand breaks leading to a re-organization of the DNA. The *NB targeted NGS assay* sequence of chromosome 5 of the non-*MYCN*-amplified cell line GI-ME-N reveals that a genomic rearrangement event must have taken place directly in the promotor region or before the *TERT* sequence. Since the region is not covered by the assay, the rearrangement sequence and the region flanking the breakpoint are not sufficiently resolved. This could be due to the fact that the *TERT* target sequence represents a GC rich nucleotide region. Moreover, it was also problematic to identify the matching partner of a *TERT* rearrangement, this was usually not possible to resolve with the *NB targeted NGS assay*. In case of the GI-ME-N cell line, the chromosome 5 *TERT* rearrangement partner could be identified employing WGS. A detailed bioinformatic analysis of the WGS data showed that GI-ME-N contains a translocation of chromosome 5 to chromosome 19, but the sequence around the translocation site was widely repetitive in chromosome 19 (about 1-2kb, unpublished data). These repetitive and GC rich regions are difficult to capture with the *NB targeted NGS assay*, which is based on short-read sequencing, and furthermore it is difficult to map these regions in the subsequent bioinformatic analysis. It is also unclear whether very large fragments (>1kb) can be (hybrid-)captured by the *TERT* probe, which could provide information about the translocation partner. This is why probably only long-read sequencing is suitable at reasonable costs for the detection of *TERT* rearrangements, e.g. through the use of Oxford Nanopore technology[805]. Results from previous studies also show that rearrangements and breakpoints associated with *TERT* occur more often outside of the actual *TERT* sequence (e.g. associated with the *CLPTM1L* gene)[43,44,804,806,807]. These results are also in line with the neuroblastoma causality that a functional *TERT* gene is required for the production of telomerase, which of course is not destroyed by genomic rearrangements[808]. Additionally, it could be shown that *TERT* rearrangements juxtapose the coding sequence to super-enhancer elements[43]. The probe coverage of the *NB targeted NGS assay* should therefore be adapted to these studies. More probes could thus be placed in the upstream region of the *TERT* gene (before chr5:1,253,262 minus strand) and also downstream (from chr5:1,295,184 to 1,345,214 minus strand; GRCh37/hg19). In addition, consideration should be given to the performance of a long-read sequencing if the short-read sequencing resolution of the translocation partners is poor.

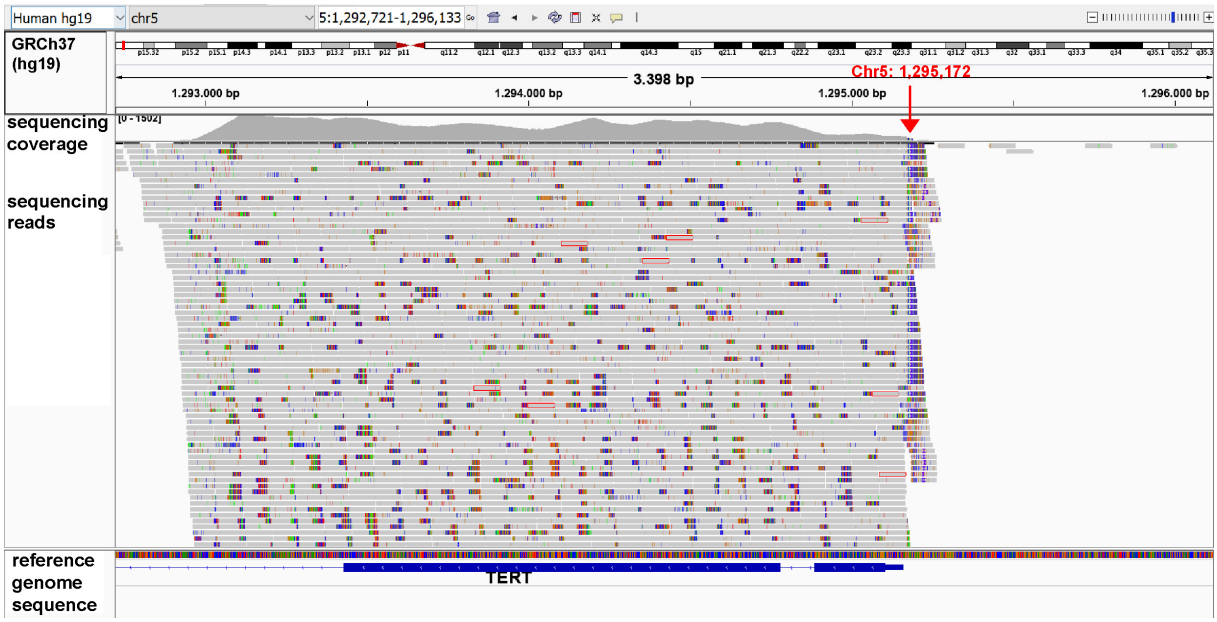

Figure 122: Results of *NB targeted NGS assay* showing sequencing coverage of the 5' end of *TERT* in GI-ME-N.
IGV screenshot displaying the *NB targeted NGS assay* sequencing results for *TERT* (which is located on the minus stand). In detail, the 5' centromeric end region in the non-*MYCN*-amplified cell line GI-ME-N is shown. At *TERT*s furthest 5' end, a breakpoint highlighting an occurred rearrangement (at location chr5:1,295,172) could be detected. However, for a more accurate resolution of the rearrangement a better probe coverage of the targeted NGS assay upstream from *TERT* is missing to fully cover its promotor and rearranged enhancer regions.

Diagnostic MRD analyses of *TERT* have been published extensively for other cancer entities. The detection of MRD is mainly aimed at SNVs within the *TERT* promoter region (chr5:1,295,228 C>T and chr5:1,295,250 C>T). These mutations are associated with increased *TERT* expression and have already been described in basal cell carcinoma[809], glioblastoma multiforme[810], bladder cancer[811], hepatocellular carcinoma[812], cutaneous squamous cell carcinoma[809] and thyroid cancers[813]. For the detection of these SNVs, a variety of PCR analysis methods have been evaluated, including ddPCR[814–820]. With regard to neuroblastoma, an MRD analysis of *TERT* would also be conceivable. However, MRD investigation would focus on the detection of *TERT* rearrangements around the genomic region of this gene (e.g. associated with the *CLPTM1L* gene) rather than the detection of SNVs. In addition to the endogenous control gene *ß-globin* which is already employed in the *MYCN* breakpoint MRD assay, other controls adapted to a *TERT* MRD assay are also indicated. A control for the PCR normalization applying a *TERT* (chr.5p15.33) assay could be in the range of 5q31, similar to the *TERT* FISH approach (ZytoLight SPEC TERT/5q31 dual color probe), which also includes the *EGR1* gene[821]. A *TERT* related breakpoint MRD assay similar to the *MYCN* breakpoint assay is currently being developed in cooperation with the research group of M. Fischer (University Hospital Cologne).

4.1.3.2 A first approach to neuroblastoma *ATRX* breakpoint MRD detection

Identical to the genes *MYCN* and *TERT*, the tumor suppressor gene *ATRX* was also investigated applying the *NB targeted NGS assay*. An *ATRX* mutation in neuroblastomas initiates the alternative lengthening of telomeres, a telomerase-independent pathway to preserve the length of chromosomal telomeres and

to escape senescence and cell death. With regard to the probe coverage of *ATRX* within the *NB targeted NGS assay*, the probes were placed at the important genomic locations. The *ATRX* gene encodes for two functionally relevant domains of the protein: An N-terminal ADD domain (ATRX-DNMT3-DNMT3L) and a C-terminal ATPase/Helicase domain[822,823]. Neuroblastoma-specific mutations in *ATRX* are, besides rare complete losses of *ATRX*[674], long-range deletions of the N-terminal side or SNVs within the C-terminal side (frequently affecting exon 2-11 within a total of 36 exons)[58,107,674]. The *NB targeted NGS assay* covers all exons of the *ATRX* gene. Preferably the probes should be placed more densely and as well in intron areas of the *ATRX* gene to ensure the detection of the whole diversity of *ATRX* deletions. Regarding the C-terminal domain, individual probes of the *NB targeted NGS assay* have been placed within exons and introns. In the same way as for the *TERT* gene, alterations in *ATRX* would be suitable for an extension of neuroblastoma MRD detection method. A need for a sensitive *ATRX* mutation detection was recently found beneficial, since immunohistochemistry guided diagnostics for ATRX can miss *ATRX* mutations[824]. So far there are no published research results on the use of *ATRX* (deletion) rearrangements in MRD detection assays, but indications that a ddPCR approach would be an advantage for neuroblastoma diagnostics[825]. Following the success of the NB *MYCN* breakpoint MRD assay, a first proof-of-concept towards an NB *ATRX* breakpoint assay was made in the framework of this doctoral thesis (breakpoint region in chrX:76,935,121). This data proves the possibility to use breakpoints developed by *ATRX* rearrangements / deletions mechanisms in neuroblastoma diagnostics as MRD specific markers. Detection of *ATRX* deletions in tumor and bone marrow samples of patients with a neuroblastoma could enable the detection of MRD cells, and therefore as well the adaptation of the therapy. As there are no diagnostic PCR based (MRD) assays for the detection of *ATRX* (chr.Xq21.1) deletions existing, there are also no recommendations for a control gene to normalize a PCR at present. However, from X chromosomal gene expression detection (e.g. by qPCR) it is known that this chromosome lacks genes for basic cell functions or more precisely housekeeping genes[826]. One possibility to create a control on the X chromosome is therefore to employ a so-called X inactivation escape gene[827]. For the MRD genomic gene detection, such a control is not as important as for the detection of gene expression, but a control gene might be used variably in different techniques on the samples or with the same laboratory. A possible X inactivation escape gene is the *TXLNG* gene (chr.Xp22.2), which has been described in several datasets as an escape gene[828]. Moreover, *TXLNG* is not in close distance to *ATRX*, therefore a co-deletion can be not assumed. In addition, when evaluating *ATRX* deletion signals and *TXLNG* signals, the human XY/XX diversity (or even more numerical aberrations in the cancer genome) should be taken into account.

4.1.3.3 A first approach to neuroblastoma *ALK* SNV ASQ-PCR MRD detection

A detection of the ALK sequence, which is frequently mutated in neuroblastoma[829], is also included in the *NB targeted NGS assay*. The *NB targeted NGS assay* covers several functionally important SNVs in *ALK* (including c.3824G>A, c.3522C<A, c.2750C>A, c.3733T>G and c.3271G>A in the kinase

domain). However, a recent publication found that low frequency *ALK* SNV mutations in neuroblastoma tumors can only be identified using ultra-deep sequencing (>5,000x). This applies only to a very small proportion of patients (>5,000x, one case with 2.7% ALK I1171 and one case with 8% ALK F1174I allele frequency)[830]. In addition to the occurrence of SNVs and rearrangements of *ALK,* co-amplifications in combination with *MYCN* were detected, but this rare event was only found in this thesis in the cell line KELLY, as reported previously in other studies (found in around 2% of all neuroblastoma cases)[716,831–833]. Therefore, a wide and dense probe coverage of the *ALK* gene is not recommended, but these reports indicate that it is generally advisable to target chromosome 2p more widely and densely with hybrid-capture probes. In summary, for the detection of *ALK* mutations in neuroblastoma the *NB targeted NGS assay* is ideally suited. Mutations in the ALK gene also have relevance in the context of MRD detection. For this purpose, SNVs as well as the rarely found rearrangements can be considered as target sequences. Two different MRD assays for the detection of *ALK* mutations from bone marrow and liquid biopsy material from patients with a neuroblastoma have been published so far. These two analyses included the *ALK* SNV mutations F1174 (c.3520T>C), L1174 (c.3522C>A), R1275Q (c.3824G>A) and the detection of CNV [834] [792,835,836]. The mutations were previously recovered from tumor samples using e.g. Arrax-CGH (CytoScan). In contrast, the *NB targeted NGS assay* provides even more information about additional SNVs in the *ALK* gene encoding for the kinase domain, namely c.2750C>A, c.3733T>G and c.3271G>A. However, it is noticeable, that the mutation c.3520T>C is missing in the *NB targeted NGS assay* and should therefore be included in future versions. The specific *ALK* SNV primers from previous published neuroblastoma MRD projects introduce an exchange of the mutated base at the 3' end of the forward primer[792,834–836]. An improvement of this conventional primer design is known as the TaqMAMA method which ensures that the wild-type allele will not be amplified, since the penultimate 3'-base is changed as well[563]. An extension of this technique is the ASQ-PCR, in which the third base from the 3' end is designed with a mismatch instead of the second base, as highlighted by M.J. Barz,…,A.Szymansky et al. 2020[564,565]. The ASQ-PCR method could achieve an even higher detection specificity and sensitivity than conventional primer designing methods or the TaqMAMA technique. The evaluation and comparison of the three different primer design methods was performed on the *NT5C2* gene, which can harbor a specific SNV p.R39Q (c.116G>A) mutation found in acute lymphoblastic leukemia. The superior performance of the ASQ-PCR assays employing the third base mismatch approach of the SNV primer design could be determined[564,565]. With regard to an *ALK* SNV specific neuroblastoma MRD assay, this thesis presented an ASQ-PCR based *ALK* SNV detection technique, which was exemplary shown for the frequently found c.3824G>A mutation. By using the ASQ-PCR technique with 3’ allele-specific primers with an additional third base mismatch as a highly sensitive and robust tool, the *ALK* SNV c.3824G>A could be sensitively detected in neuroblastoma cells within a pool of other cells as shown previously for the *NT5C2* p.R39Q (c.116G>A) mutation. Interestingly, a PCR amplicon for the *ALK* SNV c.3824G>A was revealed as well in DNA of PBMCs derived from the patient with neuroblastomas’ bone marrow, but in

a very small proportion only. Presumably, the ASQ-PCR target was not amplified on a large scale because either the proportion of tumor cells in the bone marrow sample was very low, and/or the proportion of *ALK* SNV positive cells was low, and/or the automated DNA electrophoresis was not sensitive enough for the detection of the mutation. Therefore, it cannot be said with certainty that in this case PCR amplification of *ALK* SNV has been achieved, but the possibility is given. The ASQ-PCR was further combined in a ddPCR multiplex assay with a *MYCN* rearrangement based breakpoint assay detecting a specific breakpoint at chr2:13,490,249 – chr2:15,815,066. Multiplexing is a recent application within the ddPCR technology and is becoming more popular for diagnostics because it allows the simultaneous measurement of multiple target and reference sequences in one PCR reaction[837,838]. However, these special adaptations of the original *MYCN* MRD assay require further investigation. For example, it is recommended according to the latest findings, that the more difficult or less detectable mutation be identified with a FAM-BHQ1 probe (the *ALK* SNV) while large structural genetic changes are detected with a HEX-BHQ1 probe (the *MYCN* breakpoint)[839,840]. This data proves the possibility to use *ALK* SNVs in neuroblastoma diagnostics as MRD specific markers. Detection of *ALK* SNVs in tumor and bone marrow samples of neuroblastoma patients could not only enable the detection of MRD cells, but also evaluate possible treatment options. *In vitro* and *in vivo* studies could already show that *ALK* SNV mutation driven neuroblastoma tumors respond with reduced growth to the ALK inhibitors repotrectinib[841], ceritinib[842] or alectinib[843,844]. For future *ALK* MRD assay applications, the design of a proper *ALK* SNV control probe should be questioned. For the TaqMAMA, ASQ-PCR and ddPCR approaches, the use of a wild-type primer in contrast to the SNV primer as a mutation control is considered. Moreover, the ß-globin gene was used for PCR normalization within the *NT5C2* p.R39Q (c.116G>A) ASQ-PCR[564,565]. In latest diagnostic studies, a normalization of the *ALK* SNV target signal takes place applying PCR amplification of separate control genes, e.g. *NAGK* or *AFF3*[792,845]. The *AFF3* gene sequence has been used before to position a FISH control probe in an *ALK* amplification/deletion detection assay[846]. However, a classical PCR amplification of a control gene is not expected to mirror the SNV PCR amplification of an ASQ-PCR. Therefore, the inclusion of an (additional) analysis of a common human SNV should be taken into consideration, e.g. in the *NAGK* gene (chr2:71,294,483, C>T [847]), in order to transfer the sequence and assay conditions of the target ASQ-PCR into the control ASQ-PCR in the best possible way.

In theory, a combination of several pathogenic alterations can be detected in one neuroblastoma tumor (cell)[676]. Especially the simultaneous identification of *MYCN* amplification breakpoints and *ALK* SNVs could provide further evidence on prognostic aspects and biological correlations between ALK and MYCN[848]. Nevertheless, *MYCN* amplifications[848], *TERT* rearrangements and *ATRX* mutations have been found mutually exclusive[43,58]. In addition to the detection of mutations in relevant genes, other recurrent structural chromosomal alterations also occur in neuroblastoma. These are deletions of the chromosomal arms 1p[677], 3p[678], 4p[679] and 11q[680], or gains of 1q[681,682], 2p[683] or 17q[41]. Accurate MRD monitoring is especially relevant for patients with UHR neuroblastoma and disseminated disease, displaying a

mutation in at least one of those genetic markers of oncogenic risk. MRD PCR assays with flexible marker combinations and the additional development of multiplex PCRs enable a detailed longitudinal detection of neuroblastoma.

4.1.4 The *NB targeted NGS assay* is preferred to WGS or WES sequencing and applicable for routine diagnostics of neuroblastoma

The *NB targeted NGS assay* is a novelty in neuroblastoma diagnostics with regard to the combination of numerous included chromosome and gene targets. Previous publications have presented cancer, pediatric and even neuroblastoma specific panel NGS assays, but these have never been as comprehensive as the *NB targeted NGS assay*. Either the assays were only specialized for the detection of non-*MYCN*-amplified neuroblastomas[148], or other genes relevant for risk stratification and diagnosis of neuroblastoma such as *TERT* and *ATRX* were not included in the panel[147], or the resolution of the assay was insufficient to detect large chromosomal aberrations, chromosomal rearrangements and breakpoint regions[146,149].

4.1.4.1 A targeted NGS assay is the preferred sequencing method to analyze clinical samples

Since a targeted NGS assay like the *NB assay* is a reduced version of large-scale WGS and WES sequencing, the question of whether the use of a targeted assay has advantages in the detection of pathogenic neuroblastoma genomes compared to available techniques arises. The *NB targeted NGS assay* was designed to detect only specific chromosomal segments and genes that were selected in advance based on their biological relevance. This assay includes the detection of 55 selected genes, chromosomal abbreviation (chr.1p36, chr.2p25, chr.11q, chr.17q), nucleotide changes, structural rearrangements and copy number alterations. The preselection process of relevant sequencing probes also reduced the cost of the targeted assay that would otherwise be incurred by WES or WGS[139,143,145]. A great advantage of the the *NB targeted NGS assay* is that the sequencing costs for patients in Germany are covered by the health insurance companies. In addition, the time of sample processing and pre-analysis is reduced compared to WGS and WES sequencing. The analysis with the *NB targeted NGS assay* was possible within one week. For the selected targets, the *NB targeted NGS assay* achieved a very high sequencing coverage (1,500 – 2,000x on average), revealing even base-exact breakpoint sequences. Preliminary studies also show that, a mean coverage of 300-500x in targeted sequencing is sufficient for an accurate diagnosis and guidance of targeted therapies[142]. A high coverage which is shown with the *NB targeted NGS assay* suggests a high specificity of the probes and good preselection selection of the genes which influence the coverage[139]. Thus an reduction of the genetic background and noise was achieved which is normally found in sample data analyzed with WGS and WES techniques[144,145]. This makes the *NB targeted NGS assay* particularly suitable for the sequencing of clinical samples. In line with the observations made in this thesis, in a comparison of the different sequencing techniques targeted NGS, WES and WGS in clinical questions[139,143,144], the targeted NGS

was also found to be the best application due to these properties. However, the additional application of WGS or WES sequencing should be considered if a genetic diagnosis could not be made using the *NB targeted NGS assay*. Presumably, the mutations for the development of the disease are located outside the genomic regions covered by the *NB targeted NGS assay* or the disease is dependent on multiple, possibly novel, genetic factors[143]. In general, targeted NGS panels are clinically best suited for patients who have already received an initial diagnosis based on other criteria (e.g. the clinical appearance), providing a more in-depth diagnosis and detection of possible drug targets[143]. Since the *NB targeted NGS assay* is a customized panel which is ready for the clinical application, the sequencing results should always be questioned and compared with WGS and WES data available. A comprehensive review of the *NB targeted NGS assay* in comparison with clinical standard diagnostics, WGS and WES is performed in collaboration with F. Hertwig[635] (Figure 123).

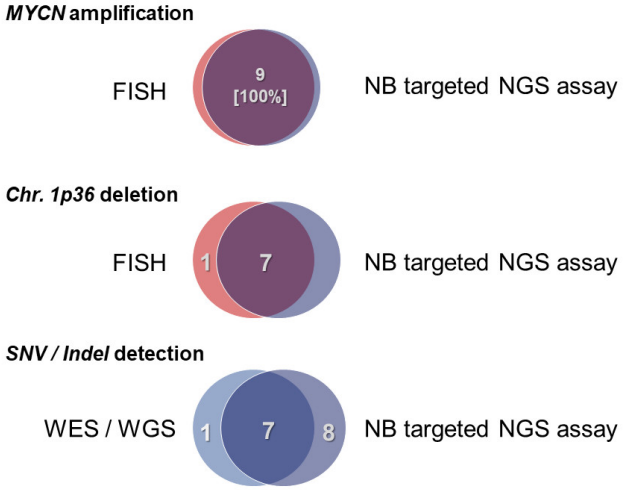

Figure 123: Comparison of matching results in neuroblastoma FISH routine diagnostics, WGS/WES and *NB targeted NGS assay*.
A high concordance for risk markers identified in routine cytogenetic diagnostics and *NB targeted NGS assay* was observed. In detail, panel sequencing detected all 9 *MYCN* amplifications and 7 of the 8 chromosomal changes involving chr.1p36 loss. Additionally, neuroblastoma-relevant SNVs (e.g., mutations in *ALK*, *HRAS*, *NRAS*, in 5 patients) and structural rearrangements involving the *TERT* locus (in 4 patients) were identified with the *NB targeted NGS assay* and was further confirmed by WGS and WES data. (Figure was kindly created by F. Hertwig[635])

4.1.4.2 The *NB targeted NGS assay* covers all mutations relevant for risk stratification of neuroblastoma

In addition, clinically relevant, treatment-critical mutations which were detected using a targeted NGS panel should be double-checked using Sanger sequencing. A study by Ambry Genetics showed that 98.7% of NGS results could be re-found applying Sanger sequencing, whereas 1.3% of the results were detected as false positives, mainly located in complex genomic regions (A/T-rich regions, G/C-rich regions, homopolymer stretches, and pseudogene regions)[849]. A combination of the *NB targeted NGS assay* and the MRD breakpoint analysis as highlighted in this thesis would therefore also provide a

control examination of the diagnostically important targeted NGS results utilizing Sanger sequencing. In turn, due to the high sequencing coverage of the previously determined genomic regions, targeted sequencing is able to determine subclonal mutations and therefore supports MRD monitoring, e.g. by detecting breakpoints[142]. This makes the *NB targeted NGS assay* a useful tool to study the evolution of neuroblastoma, clonal fluctuations and drug resistances. However, a recent report highlights the detection of low frequency *ALK* SNV mutations in neuroblastoma which where only uncovered using ultra-deep sequencing (>5,000x, one case with 2.7% *ALK* I1171 and one case with 8% *ALK* F1174I allele frequency). For the detection of smaller cancer cell populations, targeted sequencing results should therefore be strengthen using additional techniques, such as the *NB breakpoint MRD assay*. In addition, other genes that have only recently been identified as being involved in neuroblastoma development could be included in an updated version of the *NB targeted NGS assay*. These are for instance the genes *ARID1A/B*[850–852], *YAP1*[55,853], *LIN28B*[854,855], *KANK1*[856], *DOCK8*[856], *BARD1*[149], *SHANK2*[857] and *RASSF1A*[52,858]. The ability to dynamically adapt a clinically relevant NGS panel assay to current scientific findings is of particular importance.

4.1.4.3 Inclusion of (virtual) normal controls to differentiate between tumor and germline mutations

The additional sequencing of a matching normal control, e.g. DNA isolated from peripheral blood of the patient, was not performed within the *NB targeted NGS assay* cohort. Thus, the additional blood sampling of the patient, additional time and cost for sequencing and a possible detection of circulating tumor cells at high tumor load was prevented. However, there are also advantages in the sequencing of matching normal controls. During the simultaneous sequencing of a bulk containing tumor and normal cells this process can lead to the detection of germline mutations in the given tissue sample. A comparison of the tumor sample with a normal control and a further comparison with a human reference genome therefore reveals germline mutations present in the patient's DNA. The sequencing costs of double sampling could be reduced by aiming for a lower sequencing coverage of the normal controls. For example, fewer lanes of a flow cell could be used for sequencing. Nevertheless, matching normal controls are not available for every patient in a clinical setting. Especially when retrospective FFPE samples are examined, no control examination is possible. Moreover, special human genetic consultations and ethical considerations are also a prerequisite for the analysis of germline mutations. In this case, two possible methods are applicable to the tumor sequencing results. First, in regions with many variations, the reads could be reassembled (e.g. by HaplotypeCaller[859]) without the existing mapping information and then low-significant calls could be removed[142]. Another method would be to create a dataset of matching normals (e.g. from existing normal samples or non-patient normal samples), which is comparable in characteristics to the study cohort, creating similar normals[860–862]. Furthermore, data from non-neuroblastoma and previous studies can also be used to create a "virtual normal" control[863]. The advantage of the non-patient normal and virtual normal control datasets is that

(cancerous) mutations, which can occur both in germline and somatic samples (e.g. NF1[864]), will separate the tumor exclusive and primary germline mutations. In addition, the use of datasets with anonymized samples would have the advantage of avoiding the ethical dilemma of simultaneous detection of unexpected findings in genes unrelated to the primary treatment questions[143].

4.1.4.4 The *NB targeted NGS assay* would be applicable to liquid biopsy samples

Furthermore, targeted NGS panels such as the *NB targeted NGS assay* could be applied not only to solid tumor samples but also to liquid biopsy samples[825]. The use of liquid biopsies should be considered if, for example, the tumor is not easily accessible by surgery, the tumor samples (especially FFPE) taken contain less than 10% infiltration of vital cells[142] or if conventional tumor sampling cannot be performed due to the patient's state of health or concomitant diseases (e.g. bleeding tendency). First studies have already shown that targeted NGS panel sequencing is also feasible for liquid biopsies[865–868]. In particular, NeoOncology, which also performs the *NB targeted NGS assay* sequencing, has shown that the panel NGS method provides results in concordance between solid tumor material (FFPE) and whole blood samples[866]. However, care should be taken when interpreting the data, as there are indications that not all mutations found in the solid material could be detected in the blood. Therefore, the sensitivity of these NGS-assisted liquid biopsy diagnostics is highly dependent on the tumor burden of the patient[865]. In the worst case, resistant, hiding cell populations could not be detected by a liquid biopsy NGS. In several research projects, sequencing costs and background detection raised due to "oversequencing", as the coverage depth ranged from 10,000x to 37,150x[865,866,869]. A mean coverage similar to the *NB targeted NGS assay* of 1,500 – 2,000x on average seems to be sufficient to also examine liquid biopsies of early-stage and post-treatment patients. Nevertheless, a parallel examination of the solid tumor sample and the blood could be advantageous for the detection of heterogeneous tumor cell populations[870]. A combination of a liquid biopsy targeted NGS and ddPCR detection of mutations is possible as well, but mutations are only detectable at an allele frequency of more than 0.1%[868,871,872]. The detection of liquid biopsies using targeted NGS panels are overall a clinically applicable and a non-invasive method to determine tumor development, tumor heterogeneity and emerging drug resistance.

4.1.5 Utilizing latest MRD techniques to improve the detection of the neuroblastoma cells with the *NB MYCN breakpoint MRD assay*

4.1.5.1 Transferring the *NB MYCN breakpoint MRD assay* to liquid biopsy applications

Initial studies have already shown that whole cells (circulating tumor cells, CTCs) or ctDNA (circulating tumor DNA) in the blood can be identified as neuroblastoma-specific and that blood samples also exhibit a genetic variety compared to bone marrow samples[137,873–876]. The CTCs are tumor cells that have detached from the primary tumor or metastasis, circulate in the blood stream and can cause metastatic growth at their arrest site (e.g. DTCs within the bone marrow)[877,878]. The presence of CTCs in patients with neuroblastoma has been established by culturing peripheral blood *in vitro*, leading to the

establishment of new neuroblastoma cell lines[879,880]. In recent MRD approaches, DTCs are increasingly being detected using immunology and flow cytometry of cell surface markers instead of genetic markers[881]. The occurrence of cfDNA (cell-free DNA) in blood has been known for a long time[882], but only later it was discovered that the cfDNA bulk also consists of tumor-derived cfDNA, which is therefore now called ctDNA[883,884]. The emergence of ctDNA is caused by a combination of active secretion, solid tumor lesions, apoptosis and necrosis[885–888]. It has already been shown that ctDNA in patients with neuroblastoma reflects the tumor disease and is therefore suitable as a compartment for diagnosis and monitoring[806,889]. Especially *MYCN* CNVs could be detected in ctDNA sequences[794,825,836,890–892], but also *ALK* mutations[835,836,890], *ATRX* deletions[825], *LIN28B* amplifications[825], 11q deletions[806,825,876,893] and 17q gains[806,876,894]. Likewise as in the case of ctDNA, in which individual, linear pieces can be detected in liquid body fluids, it might also be possible to detect circular DNA in liquid biopsies. Regarding *MYCN*, it has already been shown that the *MYCN* amplicon can also be found on circular DNA (DMs)[74]. These linear (ctDNA) or circular (DMs) fragments of chromosomes could circulate as free units within a liquid body compartment or inside of extracellular vesicles, the exosomes. Exosomes, which are secreted by tumor cells, are used for intracellular communication[895–897] and can carry DNA fragments[898]. First approaches in neuroblastoma research could already demonstrate that exosomes are used as cargo transporters for the *MYCN* protein and that the genetic *MYCN* amplification also plays a role in exosome presence and adaptation of biological functions[899–901]. Several studies have already shown the relevance of exosomes for cancer diagnosis, monitoring and prognosis[902,903]. The neuroblastoma breakpoint-based *NB breakpoint MRD assay* could therefore further be applied to recover *MYCN* breakpoints in other (non-invasive) sample materials including blood (plasma), liquor or other liquid or solid biopsies. Applying MRD detection on liquid biopsies, the therapy response monitoring and a possible molecular recurrences could be detected early. The extension of the neuroblastoma (*MYCN*) breakpoint MRD detection assay from bone marrow aspirates to additional blood samples could also help to understand the heterogeneity of this cancer[904,905]. In this context, neuroblastoma CTCs in the peripheral blood of patients could represent advanced or more aggressive types of cells displaying a migratory potential. In a leukemia study it is suggested that CTCs must have lost their homing signal and probably developed further traits, such as improved infiltration features for other tissues[906]. Especially liquid biopsies specimens like urine or saliva are non-invasive sampled, but also drainage of peripheral blood is sampled only minimally invasive and easy to obtain in contrast to a bone marrow aspiration[907]. As the new chronic myeloid leukemia guidelines for clinical diagnostics state that the bone marrow MRD monitoring is terminated and that the MRD detection in blood specimen is to be continued, this could be a perspective for other cancer entities[908,909]. In addition, the neuroblastoma (*MYCN*) breakpoint MRD assay may help to detect tumor (cell) contaminations in stem cell harvests from peripheral blood[202,910]. However, a challenge of liquid biopsies is the stability of the target to be measured, which does not necessarily reflect the number of gene copies. CfDNA has to be handled with care in diagnostics, when it comes to time delays between collection and detection, temperature

fluctuations and isolation methods[911–915]. In addition, in many cases a usage of a specialized tube for collection is needed, including stabilizing agents[916]. Likewise, the detection of the various markers and different subsequent analysis methods causing inter-study variability[917]. The PCR assays must also be specially adapted for the detection of small DNA fragments, such as ctDNA. CfDNAs/ctDNAs have a size of only 90-250bp, thus a PCR assay should not exceed this size[898,918–920]. The *NB MYCN breakpoint MRD assay* established in this work has an optimal size of 150bp, exceeding a small ctDNA size of 90bp. It has to be considered to what extent a lower assay performance can be accepted for a shorter PCR amplicon length. A technical minimum of a NB MRD PCR amplicon size of 60bp (20 bp size of forward/reverse primer and probe each) would only allow about 30 additional spacer nucleotides, which would be a tight fit with regard to the structure of the breakpoint harboring additional microhomologies that need to be excluded from the oligonucleotide annealing. Furthermore, the very low level of CTCs and cfDNA concentrations in the blood is a major challenge for successful MRD analysis. These liquid biopsy compartments are usually only present in low concentrations in the blood (CTCs: up to 10 CTCs/ml in whole blood[921]; cfDNA: up to 100ng/ml in healthy humans, ctDNA: up to >1,000ng/ml in cancer patients[922–924]). A large volume of blood is therefore required, which is particularly problematic in case of very young patients. Concentration and purification methods have to be capable of isolating as many tumor-specific CTCs/ctDNAs as possible, and some analyses could not be carried out all at or only in simple technical replicates due to the small amount of material (e.g. multiplex assays). The robustness and reliability of the results must therefore be critically evaluated and questioned. Likewise, the concentration of CTCs/ctDNA in the blood may vary independently of any increase in the tumor burden. CTCs/ctDNAs are also released into the blood of patients that received transplantations[925,926], during surgeries[888], after physiological exercise[927], in inflammation processes and sepsis[928,929]. In addition, it is important to note that MRD levels investigated in liquid biopsies are 10 times lower than MRD levels detected in bone marrow aspirates, which leads to a decrease in the assay sensitivity[161,930]. Although there are technical hurdles in the utilization of liquid biopsies, several research studies successfully report on the sensitive detection of chromosomal rearrangements in CTC/ctDNA sequences derived from cancer patients blood[931–933]. Therefore the application of liquid biopsies for neuroblastoma diagnostics would need to be determined in future research and clinical trials to unfold their value.

4.1.5.2 Latest technological improvements for the *NB MYCN breakpoint MRD assay*

In addition, latest technical possibilities could expand the *NB MYCN breakpoint MRD* assay's practicability and scope within neuroblastoma diagnostics. In diagnostics of hematological malignancies, flow cytometric methods are increasingly used in addition to the PCR based detection of tumor cells. Interestingly, even intracellular fusion proteins can be detected at a single cell level by usage of flow cytometry[934]. Sample preparation and analysis methods become increasingly standardized (EuroFlow[935]). For the diagnosis of neuroblastoma, flow cytometric assessment of tumor markers (e.g. GD2 (+), CD45 (-), CD56 (NCAM; +), CD81 (+) and CD90 (Thy-1)) in bone marrow or blood material

was investigated so far[936–940]. The latest flow cytometric methods in neuroblastoma research make use of the multi-parametric / multi-color or ImageStream techniques[881,941,942]. A detection of MYCN via flow cytometry was performed in research projects only[942,943], and analysis of possible fusion-gene derived proteins has not been considered so far. In addition to flow cytometric MRD methods, there are other systems as well that utilize the cell size, outer surface texture or protein markers to aid in the detection of tumor cells. By means of enrichment and enumeration of CTCs in advance of a downstream molecular genetic assay, efforts are made to further increase the sensitivity of these assays for a specific tumor marker. These new technologies are often based on conventional flow cytometry methods combined with fluorescence activated cell sorting. Frequently, these new cell collectors are coupled with a subsequent analysis of the cells using fluorescence labeling (DEPArray; Menarini - Silicon Biosystems)[944] or nucleotide isolation compartments (VTX-1 Liquid Biopsy System System)[945]. The cell solution to be analyzed is applied to a chip, on which the cells are scanned for cell-specific markers using automated fluorescence microscopy (DEPArray; Menarini - Silicon Biosystems). Some devices attract CTCs within the blood by their specific surface markers (e.g. CD45-, EpCAM+, and cytokeratin 8, 18+, and/or 19+), such as the CELLSEARCH® system (*in vitro*, magnetic enrichment, Janssen Diagnostics)[946] or the GILUPI CellCollector medical wire (*in vivo,* GILUPI GmbH)[947]. Other technologies make use of the physical attributes (size and stiffness) of CTCs, comparable to a mesh or applying centrifugal forces or flow-cycles, e.g. in the CTChip® FR + ClearCell (ClearBridge BioMedics)[948], Parsortix (Angle PLC)[949] or VTX-1 Liquid Biopsy System (Vortex Biosciences). However, the detection and/or enrichment of tumor cells by means of surface markers is difficult for neuroblastoma, because the cells lack a universal and tumor specific marker. Due to their cellular origin, markers known for other tumor entities are expressed in a limited number of neuroblastomas only, such as the neuronal or epithelial cell adhesion molecule (NCAM, EpCAM)[950,951]. An EpCAM based cell enrichment, which is successfully employed e.g. for lung cancer[952], could be transferred to neuroblastoma only in one study[953]. Although there are GD2 molecules located on the surface of neuroblastomas[198,954], GD2 is not a universal marker for a detection or enrichment of neuroblastoma cells. This is because it could already be shown that the GD2 expression is partially or completely absent in some cases (already from diagnosis stage) or GD2-positive clones are lost under chemotherapeutic treatment[258,955,956]. Likewise, bone marrow mesenchymal stromal cells can also express GD2 or even NCAM[957,958]. This makes the detection, enrichment and enumeration of (residual) neuroblastoma cells using surface markers an inaccurate method. Improved PCR systems may therefore represent an important alternative to enhance the detection of minimal residual cells. Centrifugal-microfluidic *LabDisk player* systems have been released more recently, which integrate an automatic DNA extraction with a classical PCR and with a multiplex RQ-PCR[959]. Due to the centrifugal force and usage of temperature changes, dead volumes and bubbles can be avoided which influence the performance of the PCR[960]. The handling is also more extensively automated, which both leads to an increased robustness and sensitivity of the assay. The LabDisk player is currently being tested in a diagnostic MRD study on

acute lymphoblastic leukemia samples[961,962]. Besides the development of new PCR devices, existing PCR technologies are also being improved, e.g. the droplet digital detection (IC3D) PCR system, which combines droplet partitioning, fluorescent multiplex PCR and 3D droplet counting[963]. In terms of the molecular genetic detection of single cells, a PCR assay was developed for single cell multiplex analysis of predefined DNA or RNA sequences in liquid biopsy derived samples[964,965]. Moreover, latest improvements in PCR chemistries may support the detection of residual cells. For example, the mediator probe PCR (MP-PCR) technique is utilizing a classical RQ-PCR detection system with label-free primary probes and standardized secondary fluorogenic reporters[966]. Mediator probes might be interesting to be used instead of hydrolysis probes in order to reduce costs and promote a higher target specificity and sensitivity. The non-fluorescent marked probe binds to the target sequence during the annealing phase of the PCR. Though the exonuclease activity of the *Taq* polymerase a 5' overhang of the mediator probe is cleaved and attaches to a secondary fluorogenic reporter, the universal reporter. The subsequent elongation between the mediator to the quencher releases the fluorophore, which represent a detectable signal (Figure 124).

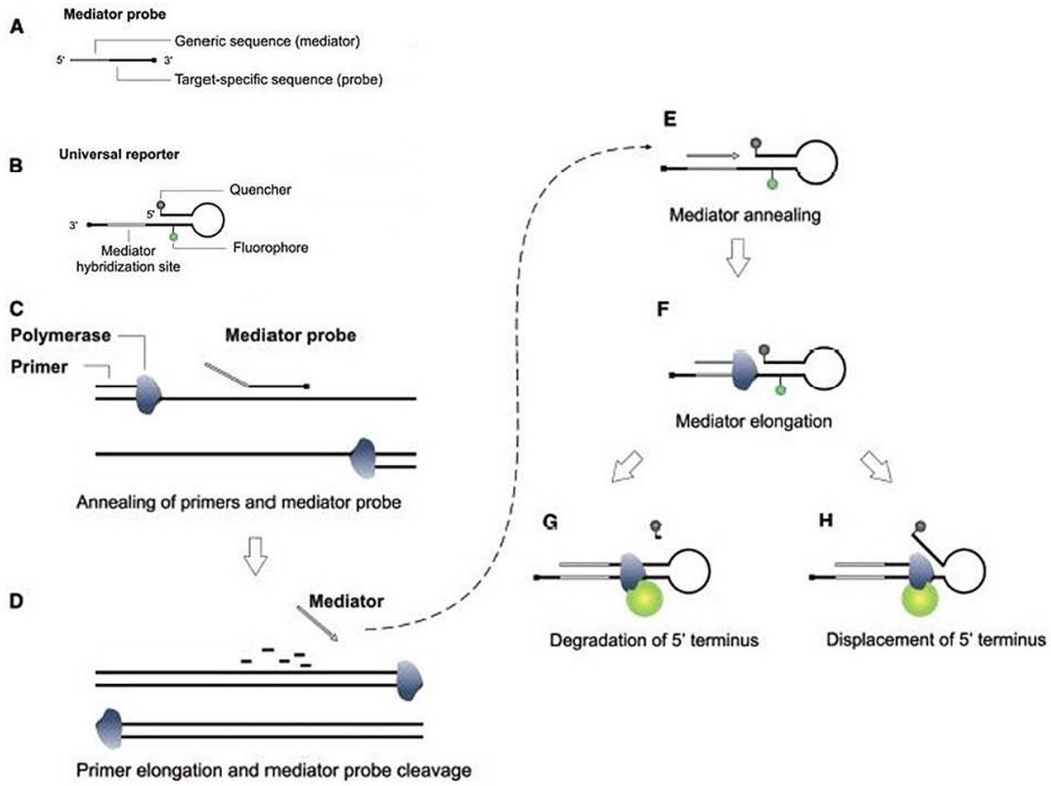

Figure 124: Schematic principle of the Mediator Probe PCR (MP-PCR).
(A) Structure of the oligonucleotide mediator probe, which is used in the MP-PCR assay together with (**B)** the fluorescent universal reporter. (**C)** During the PCR, the mediator probe anneals to the target sequence equally to chosen primer. (**D)** After elongation, the mediator is cleaved from the probe. **(E)** The mediator anneals to the universal reporter. (**F)** The elongation of the mediator releases the fluorophore of the universal reporter via **(G)** sequential degradation of the 5' terminus or (**H)** by displacement of the 5' terminus and unfolding of a hairpin (modified after Faltin et al. 2012[966]).

The greatest advantage is the standardized universal reporter, which is a target-sequence independent oligonucleotide labeled with a fluorophore and can be used to guide the detection of every desired mutation[967,968]. In addition, the amplicon specific mediator probes enable the same target specificity as classical hydrolysis-fluorescent probes but with lower costs due to the missing label (in detail: 3€ for a mediator probe compared to around 100€ for a FAM-BHQ1 probe) The MP-PCR saves costs, reduces intra and inter assay fluorescence deviations and the laboratory handling is simplified. Furthermore, an easier and a more rapid combination of several primers/probes for a multiplex PCR using various fluorophores would be possible. The MP-PCR is currently being developed and tested in a diagnostic study on MRD detection of acute lymphoblastic leukemias[961,969]. Future adjustments to the *NB MYCN breakpoint assay* can therefore include the latest generation of detection devices and may use other sample types, for example CTCs. In summary, patient-tailored MRD detection has the potential to become a valuable and flexible technique in addition to the diagnostic routines used for neuroblastoma so far.

4.1.6 Clinical implementation of the *NB targeted NGS assay* and the *NB MYCN breakpoint assay* into the routine diagnostics of the HR-NBL2/SIOPEN study

4.1.6.1 Translation of the *NB targeted NGS assay* into neuroblastoma study protocols

The *NB targeted NGS assay* is designed to provide the complete molecular diagnostic information required for clinical risk stratification and application of targeted therapies. The success of published hybrid capture based NGS panels that are already in clinical use proves that this approach is feasible for a daily clinical practice[970–972]. Unlike other neuroblastoma risk staging approaches, the *NB targeted NGS assay* is independent of imaging or surgery-based reports. This NGP panel may be implemented into routine diagnostics as a single assay which covers all essential covariates for initial classification. In addition, the assay includes recently for neuroblastoma discovered risk factors (e.g. telomere length measurement, RAS/p53 pathway genes). A turn-around time of about a week quickly provides the molecular information required for considering alternative treatment options (see Figure 64). Another advantage is that the costs for the sequencing can be covered by the German statutory health insurance companies. The promising results of the *NB targeted NGS assay* which were made in connection with this work warrant further evaluation in a prospective study. The SIOPEN MMG/Biology group (liquid biopsy) recently stated a recommendation that an NGS panel with a minimal consensus of 13 genes (e.g. *MYCN*, *ALK*, *TERT, ATRX*, *RASSF1A*) should be utilized in addition to classical techniques to diagnose and characterize neuroblastomas[973]. This guideline will also be adopted within the new HR-NBL2 study protocol[52]. The *NB targeted NGS assay* therefore fulfills the criteria for clinical application in neuroblastoma diagnostics. In addition, the assay provides detailed genomic information for setting up PCR-based monitoring of MRD (e.g. based on *MYCN* breakpoints).

4.1.6.2 Translation of the *NB MYCN breakpoint assay* into neuroblastoma study protocols

As part of the new HR-NBL2/SIOPEN study, MRD research approaches are encouraged to be applied in parallel to the study to investigate the disease and the response to treatment[52]. Bone marrow derived samples will be subjected to immunohistochemical, immunocytological and cytomorphological investigations in order to maintain the gold standard diagnostic. The study committee strongly recommends to obtain bone marrow aspirates in EDTA tubes at 7 fixed time points in the course of the treatment for all patients (i.e. at diagnosis, end of induction and prior to maintenance therapy). The *NB MYCN breakpoint assay* could therefore be ideally implemented in the new neuroblastoma study as an accompanying diagnostic research tool. Within this thesis, a complete protocol was outlined starting from the detection of biomarkers within tumor material up to the MRD assessment in follow-up samples, using the latest routine diagnostic and most sensitive RQ-PCR and ddPCR technology. With this strategy, a *NB breakpoint MRD assay* can be designed at a reasonable cost within 14 working days, including validation and determining sensitivity and specificity (Figure 64). An established assay can be used to determine MRD levels in follow-up bone marrow aspirates from the respective patient within only two working days (Figure 64) at the cost of a regular ddPCR assay. Therefore, the framework for personalized *NB breakpoint MRD assay* development is ready to be implemented in future (prospective) clinical trials and subsequently clinical routine. Once the assay is thoroughly clinically tested, an accurate and specific detection of residual neuroblastoma cells could become a valuable tool for adapting therapy regimen to the MRD level. In patients with acute and myeloid leukemia, the MRD level is used to determine whether allogenic stem cell transplantation should be performed. The *NB MYCN breakpoint assay* could therefore aim to raise the acceptance of autologous stem cells for a transplantation (or promote the alternative use of an allogenic graft) as well as the indication for immunotherapy or to judge the duration of maintenance therapy. In addition, MRD levels could be applied as inclusion criteria or endpoints for future trials testing immunotherapies or the incorporation of targeting agents into current therapy regimens as a precise measure of therapy effectiveness.

4.2 Aiming neuroblastoma at the “untargetable” MYCN oncogenic driver

The MYC family proteins MYCN and c-MYC are major drivers of high-risk neuroblastoma. However, direct targeting of MYC proteins has not yet been implemented for clinical use, as the featureless surface of proteins in particular does not provide a specific target site for small molecules[263]. To circumvent this problem, research is focused on indirect contributors within the cellular network of MYCN. In this thesis, several inhibitor approaches for indirect targeting of MYCN were addressed. This included the inhibition of the transcription of *MYCN* itself as well as the stimulation of the transcription of MYCN targets. Another approach involved the prevention of MYCN protein stabilization and the blockage of subsequent cellular signal transduction. Additionally, limitation of the MYCN-driven cell proliferation was investigated by targeting of a mitotic spindle assembly protein.

4.2.1 Targeting the transcription of *MYCN* using BET inhibitors

The *MYCN* amplicon frequently shows a chimeric structure which enabled reshuffling of ectopic enhancers or formation of neo-enhancers which is in line with the observation that the *MYCN* amplicon contains super-enhancers[74,76,117]. The transcriptional regulation of *MYCN* expression is directly regulated by BET proteins, especially in BRD4[285]. Moreover, the MYCN binds to strong canonical E-box enhancers and a loss of MYCN leads to a global reduction of transcription[116]. These biological conclusions led to the idea of inhibiting the transcription factors binding to *MYCN* (super-) enhancers or the inhibition of their recruitment to avoid an overexpression of the MYCN protein and its target genes. Previous studies have shown that small-molecule inhibitors against BET proteins cause a downregulation of *MYCN* expression *in vitro* and *in vivo*[282,285,684,685]. The treated neuroblastomas showed reduced growth, increased apoptotic signals and downregulation of MYCN protein-regulated transcription[285]. However, these findings are based on the application of first and second generation BET inhibitors with a JQ1 lead structure. A comparison of different BET inhibitors regarding cellular processes has not yet been performed. In this thesis the aim was therefore to find out whether the inhibition of BET is applicable for diverse neuroblastoma cell lines and whether there are effect variations of the individual compounds and in individual cell lines.

4.2.1.1 Neuroblastoma cells treated with a BET inhibitor exhibit a reduction in cell viability

The substances JQ1, OTX015 and TEN-010 were selected for this comparison of the BET inhibitors. JQ1 was as the first tool compound with the potency to downregulate *MYC* gene expression[298], OTX015 was the first BET inhibitor to have shown clinical efficacy[314,974] and TEN-010 is a new substance which is related to JQ1 but has preferable structural chemical and biological properties[305]. In line with previously published data[282,285,684,685], the BET inhibitors showed a good performance in the reduction of cell viability of neuroblastoma cells. Utilizing the BET inhibitor JQ1, the tested cell lines indicated low relative IC50 values under 1,000nM and in addition a maximum reduction in cell viability from 80 to 100%. Applying OTX015, the relative IC50 values were identified as low as those found under JQ1 treatment, however the relative IC50 was higher for singular cell lines. For the maximum inhibition of cell viability, the cells treated with OTX015 indicated a viability decrease of 40-100%. Similar to JQ1 and OTX015, the cells that were administered with TEN-010 showed effects on cell viability ranged from sensitive to inhibition up a to resistance to inhibition. While the relative IC50 was extremely low for certain cells, the IC50 values were significantly expanded for other cell lines. A comparative observation was likewise detected for the maximum inhibitory effect, which was above 60% for nearly all cell lines. In summary, the results of the cell viability screening indicate an anti-neuroblastoma activity of all BET inhibitors, JQ1, OTX015, and TEN-010. The comparison of the cell viability analyses upon treatment with JQ1, OTX015 and TEN-010 revealed the highest efficacy in terms of a combination of the parameters lowest IC50, lowest Emax and lowest effect on fibroblast cells of the inhibitor

OTX015. However, it also appears that some cell lines, for example the *MYCN*-amplified SK-N-BE(2) or the non-*MYCN*-amplified SK-N-AS, respond poorly or not at all to the BET inhibitors applied in this thesis. To investigate the differences of the BET inhibitor response of various neuroblastoma cell lines, preclinical functional assays were performed. For the conduction of these assays the newly developed inhibitor TEN-010 was used, which showed promising effects on the reduction of the neuroblastoma cell viability similar to JQ1 and OTX015. Additionally, TEN-010 stands out from the other inhibitors because the inhibitor caused almost no effect with respect to IC50 or maximum inhibition in the non-malignant PLF fibroblast cell line. An increased potential is therefore attributed to the BET inhibitor TEN-010, since this inhibitor is not reported to show an unspecific mode of action like JQ1, but only inhibits specific cells in the sense of a targeted therapy. In addition, the compound TEN-010 can be administered by subcutaneous injection, which makes the inhibitor attractive for application in pediatric oncology. In order to determine whether the administration of TEN-010 also leads to biological changes in the function of neuroblastoma cells, selected *in vitro* methods were carried out to reveal individual response effects. The experiments of the functional TEN-010 testing on neuroblastoma cell lines were performed by the medical doctoral student K.A. Firle (Charité) in cooperation with and under supervision of A. Krienelke-Szymansky[674,675]. A submission of this work in form of a shared peer-reviewed publication is currently under preparation[975]. The following data represent an excerpt of this joint project.

4.2.1.2 The BET inhibitor TEN-010 shows antitumoral efficacy against neuroblastoma cells

First, the effects of TEN-010 BET inhibition on neuroblastoma cell growth and density were assessed in a visual manner (Figure 125). Treatment with 100, 500 and 1000nM TEN-010 resulted in an altered cell morphology of *MYCN*-amplified IMR5/75 cells compared to the control ddH_2O treated cells (Figure 125A). The TEN-010 treated cells uniformly showed a rounder cell morphology than the untreated cells which kept their long and stretched cell appearance. The cell population of the treated cells was found less densely spread and start to detach from their surface. The change in the morphology and the detachment from the ground could be the signs of diminished cell viability and apoptosis in the broadest sense. In addition, non-*MYCN*-amplified GI-ME-N cells were treated with the same TEN-010 inhibitor concentrations (Figure 125B). The cell density between the TEN-010 and the control ddH_2O treated cells was almost comparable. Only narrower, less spread-out cell bodies and fewer cell-cell contacts of GI-ME-N could be found upon TEN-010 treatment. The microscopic evaluation confirmed that a treatment with TEN-010 greatly limits the growth and cell confluence of *MYCN*-amplified neuroblastoma cells. This effect was hardly visible in non-*MYCN*-amplified neuroblastoma cells, which indicates a connection between the *MYCN* amplification and the sensitivity to BET inhibition. Moreover, these observations on growth inhibition upon BET treatment are in line with other reports of neuroblastoma cells treated with JQ1 or I-BET726[285,976].

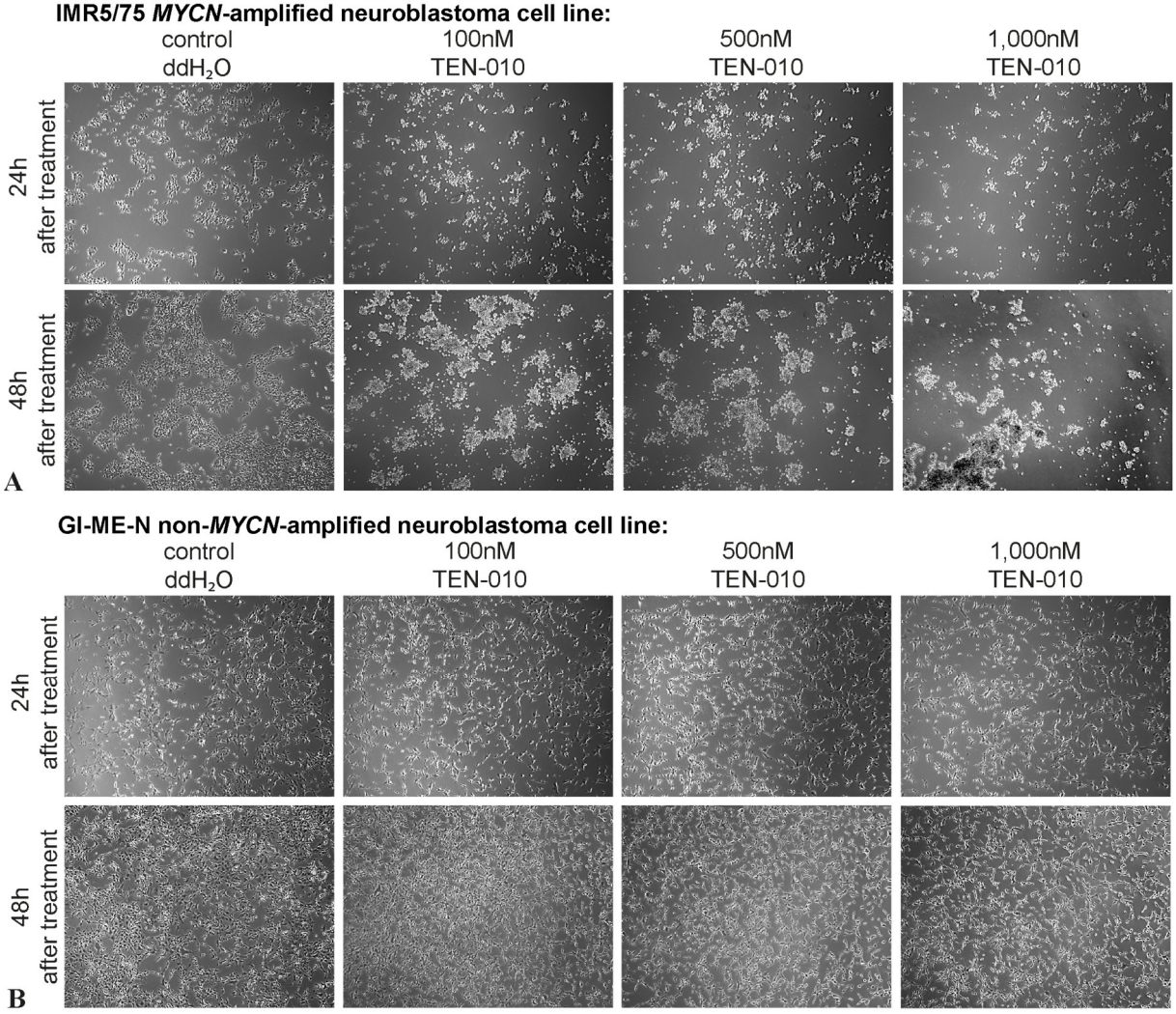

Figure 125: Treatment with TEN-010 inhibits cell growth and reduces the population of *MYCN*-amplified cells 24 and 48h after application.
After treatment of *MYCN*-amplified neuroblastoma cells with TEN-010, smaller cell populations were observed compared to the control treatment. In contrast, the growth and population size of non-*MYCN*-amplified cells is not restricted by administration of TEN-010. **(A)** IMR5/75 *MYCN*-amplified cells and **(B)** GI-ME-N non-*MYCN*-amplified cells. (Picture by A.Krienelke-Szymansky).

In the microscopic examination of TEN-010 treated neuroblastoma cells, a shift to a more rounded cell morphology and an increased detachment of the cells was most likely followed by an induction of cell death. It has already been shown for acute myeloid leukemia cells that a treatment with JQ1 has an effect on the interaction of the BRD4-p53 protein complex, causing cell cycle arrest and programmed cell death[977]. Applying flow cytometry, this hypothesis whether neuroblastoma cells undergo apoptosis after TEN-010 administration was tested. Selected neuroblastoma cell lines were stained 72h after treatment with 500nM TEN-010 using Annexin V-APC/PI dual staining and apoptotic signals were measured (Figure 126, performed in cooperation with K.A. Firle (Charité)[975]). In order to relate the TEN-010 performance to the *MYCN* status, two *MYCN*-amplified cell lines (IMR5/75 and CHP-134) and two non-*MYCN*-amplified cell lines (NBL-S and SK-N-AS) were analyzed. The fibroblast cell line (BJ) was utilized as a non-malignant control. The results of the flow cytometric data presented a higher proportion

in apoptotic signals in TEN-010 treated *MYCN*-amplified cell lines than non-*MYCN*-amplified cell lines (Figure 126, comparison of upper and lower panel). In particular, the Annexin-V/PI positive signals which constituted the late apoptotic/necrotic cell fraction (Q2) is increased in the treated *MYCN*-amplified cell group (1351% increase in *MYCN*-amplified and 236% increase in non-*MYCN*-amplified cells, normalized to ddH_2O treated cells).

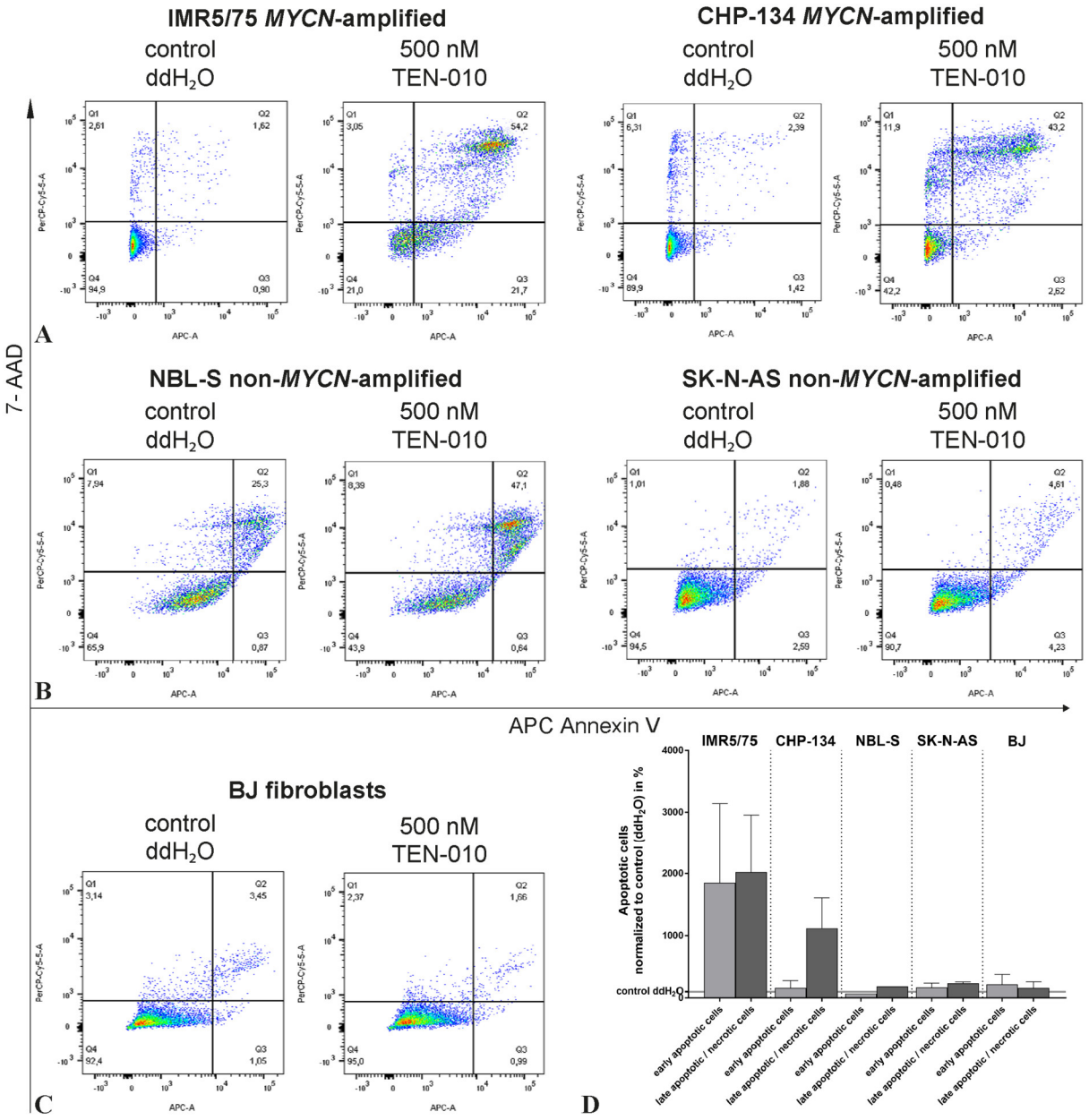

Figure 126: Treatment with the BET inhibitor TEN-010 leads to apoptosis and cell death in neuroblastoma cells. Flow cytrometric Annexin V-APC/PI dual staining analysis of neuroblastoma cell apoptosis after administration of 500nM TEN-010 for 72 h. In a comparison of *MYCN*-amplified and non-*MYCN*-amplified neuroblastoma cells, the increase in apoptotic signals after TEN-010 treatment in *MYCN*-amplified cells was significantly higher than compared to non-*MYCN*-amplified cells. **(A)** *MYCN*-amplified cells IMR5/75 and CHP-134 **(B)** non-*MYCN*-amplified cells NBL-S and SK-N-AS **(C)** BJ fibroblast cells which were utilized as a non-malignant control. **(D)** Summary of the results, normalized to ddH_2O control. One to two biological replicates are shown with their respective median and range. (Picture by A.Krienelke-Szymansky).

In addition, the Annexin-V positive signals for the early apoptotic cell fraction (Q3) are higher in *MYCN*-amplified cells (423% increase in *MYCN*-amplified and 167% increase in non-*MYCN*-amplified cells, normalized to ddH_2O treated cells). A comparison of the individual cell lines in the two groups showed a further difference in the rise of apoptotic signals (Figure 126A). In the group of *MYCN*-amplified cell lines, the IMR5/75 cells showed a greater increase in the late apoptotic cell fraction than the CHP-134 cells (2,021% increase in IMR5/75 and 1123% increase in CHP-134 cells, normalized to ddH_2O treated cells). In addition, the cell line IMR5/75 exhibited a positive signal for the early apoptotic cells after treatment, whereas this cell fraction in CHP-134 was only slightly increased compared to the control (1,855% increase in IMR5/75 and 159% increase in CHP-134 cells, normalized to ddH_2O treated cells). In a detailed analysis of the non-*MYCN*-amplified cells, these cell lines showed a similar proportion in apoptotic cells after treatment (Figure 126B). NBL-S and SK-N-AS neuroblastoma cells displayed only a slight shift of the vital cells towards late apoptosis (186% increase in NBL-S and 236% increase in SK-N-AS cells, normalized to ddH_2O treated cells). Likewise, early apoptosis was not strongly increased in both cell lines and was relatively comparable in this group (74% increase in NBL-S and 167% increase in SK-N-AS cells normalized to ddH2O treated cells). In addition to the neuroblastoma cell lines, the proportion of apoptotic signals was also measured in a TEN-010 treated fibroblast cell line (BJ; Figure 126C). Comparing the untreated and the treated sample, there was hardly any difference detectable in the two apoptotic fractions. The early apoptotic fraction was measured 217% higher than the ddH_2O control and the late apoptotic / necrotic fraction was found 158% higher than the ddH_2O treatment. The treated non-*MYCN*-amplified neuroblastoma cells thus showed similarly weak apoptotic signals after treatment with TEN-010 as the fibroblast cell line BJ. It could therefore indicated that the induction of apoptosis in *MYCN*-amplified neuroblastoma cells using TEN-010 was stronger than compared to non-*MYCN*-amplified neuroblastoma cells. These results are further summarized in a comparison of both apoptotic cell fractions in all cell lines tested (Figure 126D). It further was to be examined whether the treatment with TEN-010 has an impact on the expression of its targets, not only on BRD4 as its direct target, but also if an application of the drug leads to a reduction in *MYCN* transcript levels. For this purpose, *MYCN*-amplified SK-N-BE(2) cells were treated for 24h with 100nM of TEN-010 and *BRD4* and *MYCN* transcript levels were measured using qPCR (Figure 127A). After treatment with the BET inhibitor, the transcript levels of *MYCN* in the SK-N-BE(2) cell line were reduced by 65.41% compared to the cells treated with ddH_2O. Furthermore, a treatment with TEN-010 leads to a negative feedback loop in the transcription, which reduced the *BRD4* transcript levels by 36.73% in SK-N-BE(2). This result indicates a potentially lower tumorigenicity and a reduced proliferation of the cells. These findings should also be confirmed in a large-scale experiment in the future. To confirm the target activity of TEN-010, the expression of proteins involved in the transcription of *MYC(N)* was assessed applying Western immunoblotting analysis (Figure 127B**,** kindly performed by K.A. Firle (Charité)[975]). Two *MYCN*-amplified cell lines (IMR5/75 and CHP-134) and two non-*MYCN*-amplified cell lines (NBL-S and SK-N-AS) were treated with 100nM TEN-010 for 72h and were subsequently analyzed for

their protein expression. The cell lines IMR5/75 and NBL-S show lower BRD4 levels as compared to the ddH_2O treated control samples. It was also evaluated that application of TEN-010 increased the protein level of HEXIM1. These increasing protein levels were found especially in the *MYCN*-amplified cell lines IMR5/75 and CHP-134, but also in the non-*MYCN*-amplified cell line SK-N-AS. In previous reports, upregulation of HEXIM1 has been characterized as a potent and reliable pharmacodynamic marker of BRD4 inhibition[304,978]. HEXIM1 is a BRD4 antagonist which interacts with the protein P-TEFb and inhibits its CDK9 kinase activity, which leads so a further blocking of the RNA polymerase II activation[290,979]. Moreover, it is suggested that HEXIM1 binds to the P53 protein and promotes its phosphorylation and stabilization by blocking the ubiquitination of MDM2[980,981]. The detection of MYC(N) protein levels revealed a downregulation after administration of TEN-010, especially in the *MYCN*-amplified cell line IMR5/75. These results are in line with the observations seen in qPCR analysis (Figure 127A). A decrease in the MYCN protein level was also demonstrated for the non-*MYCN*-amplified cell lines NBL-S and SK-N-AS. However, there was no or only a marginal reduction in the MYC protein levels in SK-N-AS after treatment with TEN-010.

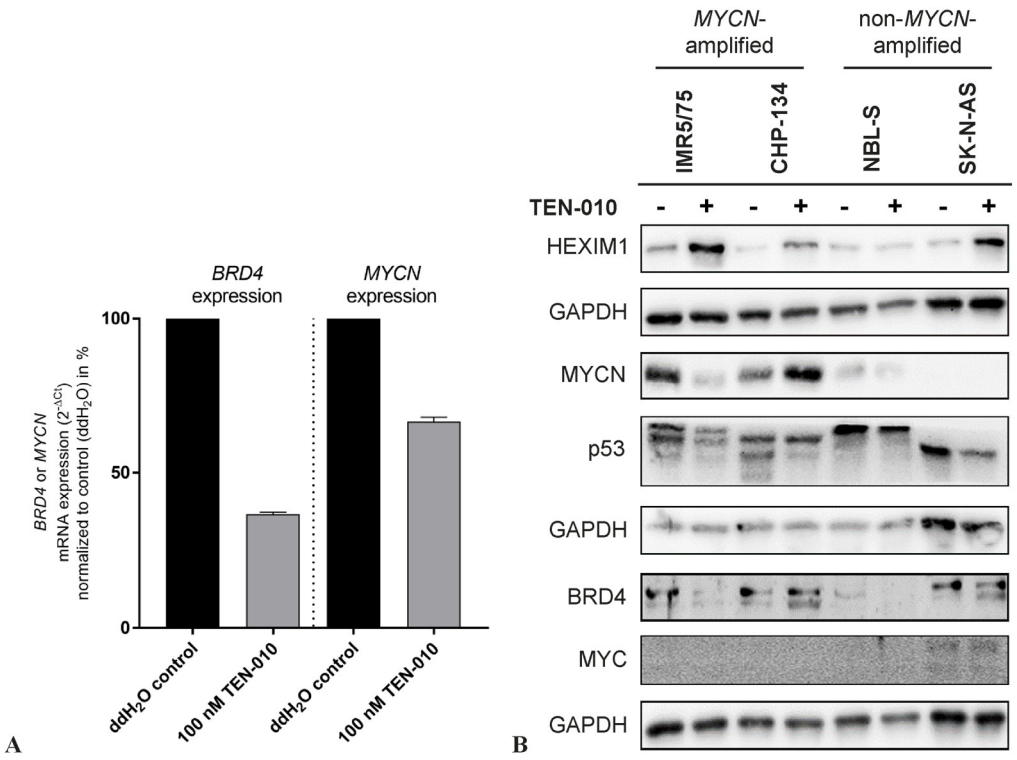

Figure 127: TEN-010 treatment induces reduction of BRD4 and *MYCN* transcript levels, increases protein levels of HEXIM1 and downregulates protein levels of MYCN and p53.
(A) After 24 h of treatment with TEN-010 (100nM), a reduction of *BRD4* and *MYCN* RNA transcript levels was seen in SK-N-BE(2) neuroblastoma cells. As control, ddH_2O was applied. One biological replica is shown with their respective median and range of three technical replicates (Picture by A.Krienelke-Szymansky). **(B)** Protein levels of HEXIM1, MYCN, p53, BRD4 and MYC were determined by western blotting in neuroblastoma cells treated with TEN-010 (100nM) for 72 h. The *MYCN*-amplified cells IMR5/75 and CHP-134 and the non-*MYCN*-amplified cells NBL-S and SK-N-AS were treated with the inhibitor. As control, ddH_2O was applied. Western immunoblotting was kindly performed by K.A. Firle (Charité)[975].

As BRD4 associates with acetylated p53[977], which is further stabilized by HEXIM1, p53 protein levels were investigated after TEN-010 BET inhibition. Protein levels of p53 were found decreased in all examined cell lines. In line with the results, a lower expression of p53 mRNA and protein levels after JQ1 treatment of neuroblastoma cells was also observed in another study[310]. To summarize, a treatment of neuroblastoma cells with the BET inhibitor TEN-010 led to a reduction in cell growth and cell confluence. Further, the induction of cell apoptosis and necrosis was detectable upon TEN-010 treatment. In a preliminary experiment, the inhibitor was able to reduce *BRD4* and *MYCN* RNA transcript levels. In addition, the HEXIM1 protein as pharmacodynamic marker of BRD4 inhibition was upregulated, and TEN-010 treatment diminishes protein levels of BRD4, MYCN and p53. The experiments also indicate that sensitivity to TEN-010 is dependent on the MYC(N) status. Neuroblastoma cell lines, which are *MYCN*-amplified and therefore overexpress the *MYCN* protein, showed strong effects on cell viability, growth, apoptosis and downstream targets after administration of TEN-010. But also non-*MYCN*-amplified cell lines, which have an increased *MYC(N)* expression, demonstrated a response to TEN-010.

4.2.1.3 The resistance to BET inhibition is achieved through genetic mutation advantages

These results reflect the previously published data on the application of BET inhibitors in neuroblastoma[282,285,309]. A direct comparison of the cell viability IC50/Emax results of all BET inhibitors JQ1, OTX015 and TEN-010 and taking into account the results of the functional assay, indicates a different susceptibility of neuroblastoma cells in relation to the *MYCN* status. The *MYCN*-amplified cell lines IMR5/75 and NGP and the non-*MYCN*-amplified cell lines NBL-S and SH-SY5Y react most sensitively to the administration of BET inhibitors. In contrast, the BET compounds showed the least effect on the *MYCN*-amplified cell line SK-N-BE(2), without exception for any BET inhibitor, and on the non-*MYCN*-amplified cell lines SK-N-AS and GI-ME-N. In order to investigate the varying responses of the examined neuroblastoma cells to the employed BET inhibitors, the different characteristics of the cells will be discussed in the following. In a publication by Westermann et al. it was reported that elevated MYC(N) levels may be caused by *MYCN* amplifications on the one hand and by a deregulation of *c-MYC* on the other hand, which are (most likely) important for the development of a high-risk neuroblastoma[982]. A neuroblastoma tumor that lacks *MYCN* amplification can therefore be compensated by *c-MYC* deregulation following increased c-MYC levels, which in turn enhances the MYCN/c-MYC target gene expression. A closer look at the literature reveals that the NBL-S cell line has a chromosome 2p translocation (t(2; 4)) involving *FBXO8* / *HAND2* enhancer hijacking[124]. In line with our observations, the NBL-S cells displayed slight elevated levels of the expressed MYCN protein. The cell line SH-SY5Y shows a translocation of a super-enhancer of the *EXOC4* gene downstream to the *c-MYC* transcriptional start site (t(7; 8))[124]. Similarly, the cell line GI-ME-N shows a super-enhancer amplification downstream of the *c-MYC* coding region, resulting in a low *c-MYC* expression comparable to *c-MYC* aberrant patient tumors[124]. These mechanisms are analogous to an enhancer hijacking event

that activates the c-MYC in the SK-N-AS cell line (t(4; 8))[124], nevertheless, GI-ME-N and SK-N-AS cells showed the high IC50 values and lowest maximum effectiveness in cell viability evaluations after application of JQ1, OTX015 or TEN-010. This suggests that complementary factors may exist in addition to *MYCN* amplification or *MYCN*/*c-MYC* translocation that contribute to the sensitivity or the resistance of neuroblastoma cell lines to BET inhibitors. In a comprehensive summary, cell lines were classified as BET inhibitor resistant if they harbor a mutation in the *CDKN2A* gene, which encodes for two proteins, the $p14^{ARF}$ and the $p16^{INKa}$ protein[692,693]. Both proteins are tumor suppressors and are involved in the regulation of the cell cycle. $p14^{ARF}$ activates the p53 tumor suppressor, while $p16^{INKa}$ inhibits the cyclin dependent kinases CDK4/6, which leads to a reduction in cellular G1 to the S cell cycle phase transition[693]. The BET inhibitor resistant cells either exhibit a methylation (of the *CDKN2A P14ARF* gene[694,695], GI-ME-N), a heterozygous deletion (SK-N-AS) or a copy number loss with an additional SNV mutation of the *CDKN2A* gene (SK-N-BE(2)), which is located on chromosome 9p[635,696]. Deletions of the 9p arm have been repeatedly observed in around 17-36% of neuroblastomas, which highlight this chromosomal region as crucial for tumor development and its progress with regard to regulation of cellular maintenance[714,983–986]. Furthermore, two of the three BET inhibitor resistant cell lines show a mutation in the *TP53* gene, which could support the altered expression of the cell cycle, DNA repair and consequently tumor cell growth[987]. In line with this observation, previous research has shown that low $p14^{ARF}$ expression in neuroblastoma cells is associated with repressed histone mark status, and induction of growth arrest and apoptosis[696]. In addition to the *CDKN2A* mutations occurring in neuroblastoma cell lines[695,696], heterozygous deletions of *CDKN2A* could be found in about 22% of all tumor samples[696], as well as an increased mRNA expression of $p16^{INKa}$ [988]. Additionally, an enhanced frequency of aberrations in the P53/MDM2/$p14^{ARF}$ pathway was found in neuroblastoma cell lines. The MDM2 protein is an E3 ubiquitin protein ligase with the ability to target p53 and therefore promotes its degradation[989,990]. MDM2 thus inhibits P53 mediated gene transactivation[991,992]. Interestingly, the NGP cell line showed a maximum response to BET inhibition, but high concentrations are needed to achieve a full decrease of cell viability. In the genetic background of this cell line, the *MDM2* gene is mutated several times (SNV, CNV and a rearrangement), which could indicate a correlation between an increased dose of BET compounds needed for the inhibition and *MDM2* mutations. In addition, the NGP cell line may bypass the inhibition of CDK4 by $p16^{INKa}$ through an amplification (CNV) in the *CDK4* gene. Since CDK4 together with CDK6 are key actors in cell cycle progression, this could indicate a faster or unrestricted cell cycle progression, especially in the G1 to S phase. In a previous work, the NGP cell line was therefore also attributed to BET inhibitor resistance[310]. However, this could not be confirmed in this thesis, because a 100% maximum effect of BET inhibition could be detected. In any case, it is important to investigate whether a defective P53/MDM2/$p14^{ARF}$ axis contributes to a BET inhibitor resistance[987]. In addition, it was shown that MYCN induces MDM2 and p53 transcription[993]. Apart from that, *TP53* mutations are not highly common acquirements in the disease progress or relapse situation (up to 15%), which is why it was suspected that the neuroblastoma cells require a baseline p53 activity

to resist oncogenic stress[54]. However, an increased MDM2 expression could lower the p53 level, and additionally the MDM2 protein stabilizes the mRNA and the translation of *MYCN*[994]. It can thus be concluded that tumorigenesis promotion through *MYCN* amplification or *c-MYC* translocation, in combination with alterations of the P53/MDM2/p14^{ARF} pathway, is defining a progressive disease which may lead to a relapse[995–997]. In addition to these factors, other genetic alterations could also be related to BET inhibitor resistance. *MYCN* amplification and rearrangements in the *TERT* gene are associated with the activity of telomerase[43]. This means that, firstly, it can be assumed that *MYCN*-amplified cell lines have a higher expression of *TERT* and thus an increased potential for drug resistance development. Secondly, non-*MYCN*-amplified cell lines with a *TERT* rearrangement can also be expected to have an increased drug resistance potential. Within this work, GI-ME-N cell lines were assigned as BET inhibitor resistant. GI-ME-N cells harbor a rearrangement of the *TERT* gene. Therefore, the possibility is given that a presence of long telomeres might promote cellular BET inhibitor resistance. Indications for the BRD4 relationship to *TERT* can be found in previous studies. An increased histone (hyper)-acetylation was be identified on the telomeres, which ensures BRD4 binding to the histone marks which further supports the activity of the telomerase and other proteins[284,998]. In melanoma cancers, *TERT* promoter mutations occur increasingly, which lead to an enrichment of active histone marks[999–1001]. This in turn influences the binding of BRD4 following an increased *TERT* expression. Several studies have shown that application of BET inhibitors or a knockdown of *BRD4* leads to a reduction in *TERT* expression, telomeric shortening and a reduction in cell proliferation[298,1002]. Recent observations have also demonstrated that BET inhibition downregulates *TERT* expression and telomerase activity in *TERT*-rearranged neuroblastoma cell lines[1003]. With regard to the results of this work, a correlation between a BET inhibitor resistance and a *TERT* rearrangement or activation of *TERT* can be considered. Interestingly, records about sporadic aberrations in the *BRD4* gene itself are also documented[310]. Within the pediatric INFORM study (individual therapy for relapsed malignancies in childhood)[1004,1005] a total of three relapsed non-*MYCN*-amplified neuroblastomas were found, which had a mutation in the *BRD4* gene (SNVs, insertions and aberrant gene expression). In addition, ALT was detected in two tumors and a TERT activation in one tumor, which often involves an aberrant p53 pathway[1006]. This indicates that changes in the functional range of the BRD4 protein can promote aggressive behavior and possibly a relapse. In this regard, it is of major importance to include the *BRD4* gene in a genetic screening of relapsed neuroblastomas, such as the *NB targeted NGS assay*[635]. In addition to these genetic traits, other properties can also be included to specify sensitivity or resistance to an inhibitor. One example is the doubling time, which is defined as the average length of cell growth and division as reflected by the cell cycle clock[1007]. Sensitivity and resistance values to a compound are presented in this thesis by IC50 or Emax values, but these parameters are highly sensitive to the number of divisions that take place over the course of an assay[1008]. Previous work suggests that the sensitivity or resistance to BET inhibitors in neuroblastoma cells is also mediated by shorter or longer doubling time[310]. In connection with the assessment of functional data after BET inhibition, it could be assumed that BET sensitivity is mediated

by a shorter or longer doubling time in neuroblastoma cells. This seems to be the most likely for the highly sensitive cell line IMR5/75, which has a low doubling time of 20h, shows a strong reduction in cell viability and high signals of apoptosis after BET application. A rapid cell division therefore also triggers early growth inhibitory effects. For other cell lines, however, this relation can only be shown to a limited extent. NBL-S inhibitor sensitive cells have a doubling time of about 36h and the NGP cell line has a doubling time of 50-70h, which would fit to the assumptions stated above. But in turn, the SK-N-BE(2) cell line has a short doubling time of 30h, although this cell line can be clearly considered to be BET inhibitor resistant as found in this study. At this point, further investigations are necessary to understand the differences in BET protein regulation and the interplay of molecular genetic factors in different neuroblastoma cancers with regard to BET inhibitor resistance. Several reports suggest that resistant cell clones have a particularly high aggressiveness and the ability to expand to a relapse[695,1009]. This indicates that first line therapies should be adapted to existing tumor resistances and that a relapse therapy needs to be selected specifically for acquired mutations.

4.2.1.4 Technical innovations for a new class of BET inhibitors

Moreover, work on improved anti-BET medications should be pursued to overcome resistances and to enable a broad application for as many patients as possible. The small molecules PROteolysis TArgeting Chimeras (PROTAC) have the potential to assist protein degradation in many applications where direct targeting of a specific protein is challenging[1010]. A PROTAC connects an E3 ubiquitin ligase recognition domain via a covalent binding linker to a ligand for a specific target protein[1011]. If a binding to these two ligand molecules occurs, an E3 ligase is then connected to the target protein, e.g. BRD4[1012]. This leads to ubiquitination and degradation of the bound target protein by the proteasome. Already known chemical structures of inhibitors can be converted into the PROTACs[1012], enabling the connection of a classical BET inhibitor via a linker with an E3 ubiquitin ligase recognition domain[1013]. Recent investigations have already been able to design a PROTAC based on the BET inhibitors JQ1[1013–1015], OTX015[1014] or I-BET726[1013]. Due to the different functionality of the PROTACs compared to classical BET inhibitors, depletion of BET proteins by PROTACs probably follows a different mechanism of action[1016,1017]. BET PROTACs show superior antitumoral activity compared to conventional BET inhibitors, lower concentrations are required to achieve a therapeutic effect, and also lead to stronger suppression of target gene expression such as c-MYC[1016–1021]. In preclinical mouse experiments, a favorable effect of the BRD4-PROTACs was observed, even though these drugs showed no increased toxicity[1021–1023]. These findings could qualify PROTAC BET degraders as a new therapy against BET proteins. The PROTAC technology has the disadvantage that specific binding domains or already available ligands of the protein of interest must be available. While this may be the case for BET proteins, it is not the same for MYCN or other interesting candidates. A degron is an advanced approach which functions similarly to PROTACs, but has to be cloned into the genomic vicinity of the protein of interest using the CRISPR/CAS9 knockin technique. These degrons are an attached conditional, portable

degradation sequence which causes a targeted proteolysis of the protein[1024]. In detail, degrons can represent short amino acid sequences, structural motifs or exposed amino acids[1025]. Degrons have the advantage that the protein of interest is only degraded at the protein level, the treatment is doseable, reversible and a direct effect can be immediately demonstrated[1025]. The activation of the degrons is done by an inducer, for example by small molecules. So far, different variants of small-molecule-induced degron systems have been published. The most promising is the SMASh tag (small-molecule-associated shutoff), in which an NS3 (viral nonstructural protein) cleavage site, NS3 protease and a degron derived from the hepatitis C virus (HCV) are fused together to form a polypeptide[1026]. The degron can then be activated with Asunaprevenir, an HCV inhibitor which is already in clinical use. This leads to a stability of the protein carrying the degron tag, followed by the recognition and degradation of the construct through the proteasome machinery. So far, this approach has only been used for the purpose of analysis for cell and developmental biological research. However, there are already reports on the application of light-induced degrons in animal studies, which control the expression of a target protein in the brain[1025,1027]. For clinical translation, there is a considerable lack of (tumor) specific PROTAC or degron constructs and comprehensive preclinical and clinical studies are missing, especially for neuroblastoma. Whether classical BET inhibitors, PROTAC BET degraders or degrons - BET targeting therapies could be a treatment option for neuroblastomas and might possibly be applied within first-line therapy depending on the molecular genetic profile of the tumor.

4.2.1.5 BET inhibition as part of combinatorial therapies for neuroblastoma treatment

In this context, the evaluation of combination therapies is essential, as new drugs are usually introduced into an established study protocol among clinical efficacy proven drugs. A combination therapy of BET inhibitors with other drugs could possibly produce an additional, synergistic effect of the two substances within cancer therapy. In order to enable a possible inclusion of BET inhibitors in a neuroblastoma clinical protocol, a combination with the currently administered cytotoxic drugs would have to be examined. A targeted small-molecule should be applied as early as possible within the therapy protocol to achieve specific anti-cancer effects[1028]. In the current GPOH Guidelines (2017), the recommended induction chemotherapy consists of 6 cycles of alternating N5 (including cisplatin and etoposide) and N6 blocks (including vincristine and doxorubicin)[30]. Therefore, a detailed review of a treatment combination of BET inhibitors with one of these four conventional therapies will be presented. DNA intercalating chemotherapies like cisplatin or doxorubicin bind to DNA and causes its damage. In previous work, the influence of the BET inhibitor JQ1 has already been linked to DNA damage. After treatment with the inhibitor, a significantly higher increase of histone γ-H2AX in cancer cells was found[1029]. As BRD4 associates with acetylated p53[977], BET inhibitors may prevent the BRD4 recruitment to p53 chromatin targets. This results in an altered DNA damage response that would sensitize the neuroblastoma cells to treatment with DNA intercalating or DNA topoisomerase-II poisoning drugs. Thus, BET inhibitors plus cisplatin/doxorubicin/etoposide is a promising

combination[977]. However, p53 negative cells also react to DNA damage caused by cisplatin[1030]. In c-MYC expressing non-small cell lung cancer cell lines, a combinatorial treatment of JQ1 with cisplatin has been found to increase the induction of apoptosis in BET inhibitor sensitive and resistant cell lines. Moreover, a mouse experiment also showed an improved anti-tumor effect[1031]. In breast cancer and ovarian cancer models, the combination of JQ1 and cisplatin have shown a synergistic effect[1032]. JQ1 inhibited cell growth, cell proliferation and induced apoptosis targeting BRD4 and c-MYC[1033]. Furthermore, JQ1 sensitized germ cell tumor cells to cisplatin, which were normally cisplatin-resistant[1034,1035]. Similar observations were made for the use of BET inhibitors in combination with doxorubicin. JQ1 was able to sensitize osteosarcoma cells to the doxorubicin standard therapy[1036]. OTX015 also showed an additive effect within a doxorubicin combination when used in *in vitro* experiments[1037]. For the use of a combination of etoposide and a BET inhibitor there are only few reports so far. One study shows a lower cell viability of small cell lung carcinoma cells treated with etoposide and carboplatin combined with the BET inhibitor MK-8628[1038]. An enhanced apoptotic effect of the combination of etoposide with the BET inhibitor ABT-199 could also be observed in leukemia cells[1039]. Vincristine is another drug of the neuroblastoma treatment regimen and could be part of an interesting chemotherapy combination. Several reports, including studies on leukemia and NUT-midline carcinoma, have shown that the combined administration of vincristine and JQ1 is synergistic and restricts tumor cell viability and tumor growth[1040–1042]. In a comprehensive study of 2500 drugs applied in combination with JQ1 on neuroblastoma cells, Liu et al. were able to demonstrate that vincristine together with JQ1 shows the most potent synergistic anti-cancer effects[1043]. Importantly, the simultaneous administration of vincristine and JQ1 indicated no effect on non-malignant cells. So far the evidence suggests that simultaneous application of vincristine and a BET inhibitor might be the best possible combination within the classical frontline therapy of neuroblastoma. The BET proteins are “readers” of acetylated chromatin and HDACs are responsible for the deacetylation of lysines on histones and non-histone proteins, a process which remodels the compaction of the chromatin[1044]. In various studies, the importance of HDACs for the development of (advanced) neuroblastoma could already been demonstrated[1045–1047]. Furthermore, inhibition of HDACs activates the function of p53 and also reveals a downregulation of *MYCN* expression. In turn, MYCN interacts with HDACs to modulate target gene transcription and induces neuroblastoma cell infiltration[1048,1049]. Thus, an indirect attack on the transcription of *MYCN* would also be conceivable as a combination treatment of an HDAC inhibitor with a BET inhibitor. Suitable agents are pan- or class I HDAC inhibitors that have been published to induce neuroblastoma differentiation[1050]. Regarding a combination treatment of BET and HDAC inhibitors it has already been shown for gallbladder cancer and lymphoma that these inhibitor types’ synergy inhibits the proliferation and cause the death of cancer cells[1051,1052]. These observations were also confirmed in neuroblastoma, where JQ1 and the HDAC inhibitor panobinostat reduced *MYCN* expression and induced anticancer effects[1053]. Furthermore, the latest small molecules are dual BET/HDACs compounds, which in first studies exhibited an even higher antitumor potency[1054,1055].

Similar to the HDAC proteins, the LSD1 protein also modifies histones to regulate gene expression[1056]. In a publication by Amente et al. it was highlighted that LSD1 binds to MYCN and cooperates with MYCN to repress the expression of tumor suppressor genes in neuroblastoma[1057]. In connection, inhibitor studies have shown that LSD1 is a substrate of HDAC1, regulating the functions of LSD1[1058]. For prostate cancer it has been shown that a combination therapy of an LSD1 inhibitor SP-2509 and JQ1 leads to increased effects in terms of inhibition of cancer growth and invastion[1059,1060]. Therefore, a triple combination of HDAC, LSD1 and BET inhibitors for an anti-neuroblastoma treatment would be conceivable. In addition to the BET inhibitors and inhibitors of histone modifiers, there are other small molecules which aim at the transcription level of the MYCN oncoprotein. For example, the THZ1 inhibitor prevents the phosphorylation of CDK7 and the super-enhancer-linked transcription of *MYCN*[1061], which was also found to display a synergy in THZ1 and CDK7 inhibitor combinations[1062]. A synergism between BET inhibition and THZ1 inhibition has also been demonstrated previously[1063]. Another combinatorial option are G-quadruplex (G4) stabilizers such as Quarfloxin, which stabilize guanine-rich tertiary structures in the *MYCN* promoter and thus inhibit its transcription[1064,1065]. Thus, a G-quadruplex stabilizer would be a suitable drug for *MYCN*-amplified and non-*MYCN*-amplified neuroblastomas that present with *ATRX* loss or deletion, as ATRX normally prevent the formation of G-quadruplex structures[58,1066]. A report showed that TERT overexpression in neuroblastoma can be treated using a combination therapy of OTX015 and the proteasome inhibitor carfilzomib which induces cell death and inhibits tumor growth[1003]. Moreover it is possible to utilize the mechanism of DNA breakage by applying a drug combination including BET inhibitors. Studies have found that JQ1 increases the levels of DNA damage[1067]. Poly (ADP-ribose) polymerase (PARP) is a protein that is responsible for DNA repair and cell survival, in particular it also protects against increased DNA damage[1068]. It was found that a *MYCN* amplification or high MYCN expression in neuroblastoma induces replication stress and sensitivity to PARP inhibitors[1069,1070]. Apart from neuroblastoma it has been observed that the simultaneous administration of a BET inhibitor (e.g. JQ1 or I-BET762) and a PARP inhibitor (e.g. olaparib or veliparib) increased the expression of DNA damage markers, decreased the levels DNA repair proteins and led to mitotic catastrophe[1067,1071–1073]. In order to maintain DNA damage levels and to preserve p53 even in the presence of alterations in *TP53* or *MDM2* in neuroblastoma, MDM2 inhibitors could be considered for dual inhibition using BET drugs[1074]. Treatment of neuroblastoma cell lines with the MDM2 inhibitor DS-3032b enhanced *TP53* gene expression and induced G1 cell cycle phase arrest, senescence and cell death[318]. With regard to BET inhibition, two recent studies have shown that after administration of JQ1 or OTX015 to neuroblastoma cells, the protein levels of MDM2 decreased and p53 protein accumulated, leading to apoptosis[1075,1076]. Thus, using a combination of BET and MDM2 inhibitors could possibly have an anti-cancerous effect on neuroblastoma cells that attempt to escape the regulation of the p53/MDM2/p14^{ARF} pathway. A small study on AML (acute myeloid leukemia) cancer has already indicated that only the *TP53* wild type cell lines of model animals responded very well to a dual MDM2 and BET inhibitor therapy[1077]. However, no benefit could be

shown for *TP53* mutant cell lines. A small-molecule therapy which aims to increase p53 activity could also be considered. The small molecule RITA (reactivation of *TP53* and induction of tumor cell apoptosis) achieved anti-medulloblastoma activity independent of the *TP53* status demonstrated in a study[1078]. Another protein which is published for its support of neuroblastoma progression is YAP1 of the Hippo signaling pathway[1079], which enhances the chemosensitivity of cancer cells by induction of *TP53* expression[1080]. *TP53* mutant tumors exhibit an oncogenic activation of YAP1 that supports cell proliferation, tumor growth, migration and chemoresistance[1081]. Moreover, YAP1 is highly expressed in neuronal stem cells and overexpression leads to an increase in the cellular progenitor pool rather than cellular differentiation[1082]. YAP proteins thus shift their function from pro-apoptotic to pro-tumorigenic, and was reported to support cisplatin resistance in neuroblastoma[1083]. It is therefore very convincing that researchers have found that a YAP1 activation is associated with a neuroblastoma relapse[55]. In addition, the *YAP1* associated enhancers include super-enhancer-like capabilities and an occupation of BRD4 at the *YAP1* promoter has already been demonstrated[1084]. Several research studies thus suggest a therapy of YAP1 overexpression via BET inhibition[1085–1087], which could be extended by a YAP1/BET inhibitor combination therapy in the future. It was also demonstrated that a combination of BET and HDAC inhibitors suppress the Hippo/YAP signaling pathway, which again improves this combination as advantageous[1088]. Beyond that, it would also be conceivable to prevent the transcription of *MYCN* and the MYCN-MAX protein binding at the same time[1089]. A report on B-cell lymphomas described the dual application of JQ1 together with a MYCN dimerization blocker (10058-F4) and demonstrated a significant increase in tumor growth inhibition compared to single application[1041]. Presumably, this combination can achieve a long-term reduction of MYCN protein levels. At best, the combinatorial administration of inhibitors is scheduled to suppress the *MYCN* transcriptional expression first and then reduce the residual MYCN protein that has escaped the initial transcriptional inhibition.

4.2.2 Preventing the oncogenic stabilization of the MYCN protein using kinase inhibitors

About one quarter of all neuroblastomas show an amplification of *MYCN* which is accompanied by a pathological overexpression of the MYCN protein[6,28,42]. The targeted attack of the MYCN-MAX interaction is difficult, since the interaction sites of MYCN to MAX do not offer the necessary structures to bind a small molecule inhibitor[263]. Moreover, the MYCN protein is needed for healthy proliferation and cell growth[263]. This suggests that MYCN stabilizing proteins involved in the proliferation and cell cycle processes could be an indirect target. In this thesis inhibitors of the enzymes PI3K, PLK1 and RAS and their effect on neuroblastoma cells were investigated in detail. A dual compound was also evaluated, which simultaneously attacks the proliferation and the cell cycle. In addition, further aspects of combined drug administration to destabilize the MYCN protein are discussed in this section.

4.2.2.1 Targeting the PI3K kinase in neuroblastoma demonstrated a moderate effect on cell viability

The inhibition of the PI3K enzyme, which is part of the PI3K/AKT/mTOR signal pathway, was investigated in this work. In neuroblastoma, unlike in for example glioblastoma, *PIK3CA* mutations are found infrequent (2.9%) and do not occur together with *MYCN* amplification[342]. From the data collected with the *NB targeted NGS assay* it can be concluded that in the cohort of 144 neuroblastoma samples (cell lines and tumor), only one tumor sample was found with a *PIK3CA* gene mutation, encoding for the PI3K protein. However, a publication could show that two isoforms of PI3K (catalytic p110δ and regulatory p85α) are overexpressed in response to RTK stimulation in neuroblastoma cells and primary tumor samples[1090]. Therefore, even in the absence of a *PIK3CA* mutation, a treatment with a PI3K inhibitor should be considered for neuroblastoma. To evaluate the efficacy of PI3K inhibition in neuroblastoma, two *MYCN*-amplified, two *MYCN*-non-amplified neuroblastoma cells and one fibroblast cell line were investigated in this thesis for their response to the PI3K inhibitor alpelisib (BYL719). An improved effect of PI3K inhibition was not related to existing *MYCN* amplification. In contrast, due to the close relationship between the PI3K and the MYCN protein, an improved effect in *MYCN*-amplified neuroblastoma models has been reported[343]. The cell lines CHP-134 and SK-N-AS had a good cell viability response to the inhibitor (<1µM), while the cell lines IMR5/75 and GI-ME-N showed a moderate to poor response (>1µM), which was not connected to the *MYCN* status. However, alpelisib showed a rather moderate anti-tumor effect compared to other kinase inhibitors in terms of cell viability reduction. In relation of the relative IC50 values (EC50), the cell viability reduction E1000 or the Emax of the kinase inhibitors alpelisib (PI3K), volasertib (PLK1) and rigosertib (PLK1 + PI3K), the inhibitor Alpelisib showed the least effect on the neuroblastoma cells but also on the fibroblast cells. Nevertheless, compared with previous investigations of PI3K inhibition in neuroblastoma, alpelisib demonstrated a beneficial viability inhibition. It was published that the PI3K drugs LY294002 inhibited neuroblastoma cells with an approximate IC50 dose of 50µM[343] and PI-103 with an approximate IC50 dose of 10µM and PIW-12 of 0.5µM[347]. In a study combining the PI3K inhibitor PI-103 and doxorubicin, a decrease of cell viability and induction of apoptosis after application was observed[348]. The combination treatment also showed a significant growth inhibition in a xenograft model[348]. In a first approach to the implementation of PI3K inhibitors in a clinical setting, it was found that a sequential dosing of PI3K inhibitors and doxorubicin is needed[341]. A study suggested that high plasma levels of a PI3K inhibitor are necessary before administration of standard chemotherapy to achieve a clinically relevant effect. In addition, targeted treatments are available that represent promising combinations in the PI3K/AKT/mTOR signal pathway. A study could demonstrate that the application of JQ1 leads to cell cycle arrest and induces the apoptosis of glioma cells via the VEGF/PI3K/AKT pathway[1091]. In a drug screening of Burkitt lymphoma, a synergistic effect of drug combinations of PI3K inhibitors was found with molecules targeting BET, AKT, mTOR proteins and doxorubicin[1092]. In a study on

rhabdomyosarcoma, it was shown that the combination treatment of alpelisib and JQ1 induces mitochondrial apoptosis and reduces tumor growth[1093]. Two additional publications made use of a novel dual PI3K/BRD4 inhibitor (SF1126 and SF252) for the treatment of neuroblastoma models and demonstrated reduced cell viability, diminished tumor growth and metastasis in vivo[1094,1095]. A combination treatment of alpelisib and JQ1 could therefore also have an improved anti-tumor effect in neuroblastoma.

4.2.2.2 Targeting the PLK1 kinase in neuroblastoma showed a significant reduction of cell viability

Other kinases besides PI3K also play an important role in the stabilization of the MYCN protein. The PLK1 kinase belongs to the serine/threonine protein kinases and has a central role in the cell cycle and cell division[375]. In this work the effects of inhibition of the PLK1 protein on neuroblastoma cells were investigated in detail. The application of the PLK1 inhibitor volasertib showed a very significant reduction of the cell viability of the tested neuroblastoma cells. The relative IC50 (EC50) values of *MYCN*-amplified and non-*MYCN*-amplified cell lines were found in the low molecular range (11.78nM - 30.65nM). Additionally, a reduced effect on a fibroblast cell line was observed (~1µM). A difference in the effect on *MYCN*-amplified and non-*MYCN*-amplified cell lines could not be detected. In a comparison of the relative IC50 values (EC50), the cell viability reduction E1000 or the Emax of the kinase inhibitors alpelisib, volasertib and rigosertib, volasertib demonstrated the strongest effect on neuroblastoma cells of all three inhibitors. With a simultaneous specificity on tumor cells compared to normal tissue, this PLK1 inhibitor is the primary choice for inhibition of a kinase in neuroblastoma. This data is consistent with the research already published. The PLK1 inhibitor BI 2536 achieved EC50 values of <1µM to 25µM in different neuroblastoma cell lines[377,379,380]. The inhibitor GW-843682X achieved EC50 values of <1µM and >1µM[379] and the inhibitor GSK461364 achieved a GI50 (50% cell growth inhibition) of about 15nM to about 70nM[381]. In a study by Gorlick et al., volasertib was explicitly used to investigate drug treatment of neuroblastoma cells and other childhood cancer cells[382]. volasertib demonstrated cytotoxic activity *in vitro*, with a median EC50 value of 14.1nM, (range 6.0 -135nM). Considering the effect of volasertib in neuroblastoma cells only, the inhibitor exhibited an EC50 between 6.0nM and 34.5nM, depending on the cell line. Thus, the effect of volasertib on cell viability in this thesis is comparable to the effect of volasertib in Gorlick et al. or to the effect of GSK461364 in Pajtler et al[381,382]. Moreover, Pajtler and colleagues highlighted the inhibition of neuroblastoma cell growth regardless of *MYCN* copy number status and presence or absence of *TP53* mutations. Although the efficacy of PLK1 inhibition against neuroblastoma could be shown *in vitro*, initial clinical testing has so far been unable to demonstrate comprehensive clinical applicability[381,382]. However, neuroblastoma and rhabdomyosarcoma xenograft models have demonstrated the efficacy of a combination of PLK1 inhibitors and vinca alkaloids[383,385]. With regard to the combination of targeted inhibitors, a synergistic effect on solid tumor cells could be observed upon simultaneous administration

of a PLK1 inhibitor and a BET inhibitor[386,387]. Previously published data on AML demonstrated that a combination of volasertib and a BET inhibitor (BI 894999) can prolong the downregulation of *MYC* expression through synergistic effects[702]. In addition, the work of Han et al. showed an anti-tumor effect combining volasertib and a BET inhibitor (MK-8628) in *MYC*-amplified medulloblastoma acting on MYC protein stability[387]. These observations were also made in the present thesis. A combination of volasertib with OTX015 showed a synergistic effect in the inhibition of cell viability of neuroblastoma cells. The synergistic effect and the cell viability inhibition was not strictly dependent on the *MYCN* status, but also on the individual cell line. The success of the synergistic treatment therefore also differed in the concentration range of the inhibitors in the respective cell line. Thus, prior to a combination treatment, the cell lines should be tested individually with each inhibitor to define a therapeutic window. Subsequently, the combination treatment can be carried out. It is therefore essential to balance the individual inhibitors (concentrations) to the particular model to be tested. Interestingly, a report stated that several clinically tested kinase inhibitors also inhibit bromodomains with therapeutically relevant potencies and are best classified as dual kinase-bromodomain inhibitors[1096]. This includes the PLK1 inhibitor BI 2536, which has structural similarities to BET inhibitors. Recent knowledge of a similar crystal structure of BET and PLK1 inhibitors has recently been used to design “true” dual BET and PLK1 inhibitors. A publication described a dual kinase BET inhibitor, UMB103, which exhibits tumor specific activity in low nanomolar concentrations against neuroblastoma[1097]. Thus, a simultaneous combination of dual kinase-bromodomain inhibitors with other drugs could also be considered. Besides the transcriptional regulation by the BET inhibitor, the combination with an HDAC inhibitor could likewise offer an effective treatment strategy. It could be demonstrated that the combination of a PLK1 inhibitor (BI 2536 or BI 6727) with an HDAC inhibitor (valproic acid or vorinostat) exerts synergistic anti-tumor effects on prostate cancer cells[388].

4.2.2.3 Targeting the RAS-binding domains of multiple kinases in neuroblastoma demonstrated a high anti-tumoral efficacy

However, single PLK1 inhibitors such as volasertib not only inhibit PLK1 but are also selective against the kinase PLK2 and the PLK3 tumor suppressor, which has fostered the need for specific PLK1 inhibitors[389–391]. Rigosertib attacks the RAS-binding Domain (RBD) of kinases (e.g. PI3K and RAF), leading to the inability for the kinase to bind RAS. The inhibitors rigosertib and volasertib used in this work could therefore possibly be combined, whereas rigosertib blocks the association of RAF and PLK1 and volasertib directly targets the ATP site of PLK1. In an *in vitro* test comparing the single-use of the two inhibitors in this thesis, it was found that both inhibitors are similarly effective in reducing cell viability of neuroblastoma cells. Both inhibitors showed a relative EC50 in the range of low nanomolecular concentration. The effect of volasertib was slightly increased compared to rigosertib, requiring less inhibitor to achieve the same cell viability reduction. The application of volasertib to fibroblast cells was detected to have minor anti-proliferative effects compared to the inhibitor rigosertib.

In contrast, rigosertib showed a lower effect with E1000 and a lower Emax of fibroblast cells compared to volasertib. Based on the already published effects of PLK1 inhibitors against RAS-binding tumor suppressors[391], a reduction of the cell viability of fibroblast cells could have been expected to be more severe. It is possible that the effect of volasertib on other kinases such as PLK3 is not decisive. Moreover, it remains unclear if these observations are connected to the specific mode of action of rigosertib and volasertib. Within the work of Gumireddy et al., little or no effect of rigosertib on lung fibroblast cells was shown and toxic effects were observed only at concentrations above 5µM[406]. These results are similar to the data for volasertib made in this thesis (relative IC50 (EC50) around 1,000nM for fibroblast cells), but rigosertib was found with a lower relative IC50 (EC50) of 192nM for fibroblast cells. However, it was demonstrated that rigosertib did not significantly affect the homeostatis[1098]. rigosertib showed a slight change in the composition of blood cells in young healthy mice, as well as of mesenchymal stromal cells that became significantly stiffer after the treatment. Furthermore, rigosertib treatment was toxic for mesenchymal stromal cells at concentrations of 500nM and above, which is 10 times higher than the relative IC50 (EC50) for neuroblastoma cells (in the range of 50nM) found in this thesis. Further research on the effect of PLK1 inhibitors (volasertib and rigosertib) on non-tumor cells should be done within this context, but these relationships demonstrate the need for a very precise dose adjustment of the inhibitors *in vivo*. In addition to indirect PLK1 inhibition, rigosertib binds directly to the RBD of PI3K. However, previously published biotin pull-down assays have shown that rigosertib does not have a high affinity for the RBD of PI3K (25-100µM, depending on the isoform)[368]. Nevertheless, rigosertib is effective against neuroblastoma tumor cells, as could be shown in this work. These results are consistent with previous observations in other tumor entities. The effect of rigosertib on neuroblastoma cell viability was detected in this thesis with a relative IC50 (EC50) of 65nM in *MYCN*-amplified neuroblastoma cell lines and 53nM in non-*MYCN*-amplified cell lines. These findings are similar to published data for a myelodysplastic syndrome-derived cell line (IC50 = 100nM)[400], for leukemia cell lines (IC50 = 50nM)[401], for head and neck cancer cell lines (IC50 = 80 - 240nM)[402] and for head and neck squamous cell carcinoma cell lines (cell viability 40 - 90% reduced at 1µM)[403]. A closer examination of rigosertib treated neuroblastoma cells under a transmitted light microscope also exhibited a lower cell density and cell population and an inhibition of cell expansion compared to the control treatment. In addition, the cells are more rounded and the cell body is not spread over the given surface. Depending on the neuroblastoma cell line, this effect was visible from 100nM or not until 1µM drug application. These impacts of rigosertib on cell density and cell morphology of cancer cells were also shown by other reports. The density of hepatocellular carcinoma cell lines decreases starting at 2µM rigosertib treatment, causing cells to become round and no longer spread to the surface[398]. Leukemia cell lines treated with 100nM rigosertib grow only 20% of their cell density compared to the control[401]. Myelodysplastic syndrome-derived cells also exhibit a lower cell population density and a rounder shape of the cells treated with rigosertib[400]. In order to enhance the visibility of these findings in this work, neuroblastoma cells were treated with different concentrations (IC10 - IC50, up to 100nM)

in a clonogenic 2D assay and subsequently stained with crystal violet. The treated neuroblastoma cells showed a reduced reproductive survival and decreased ability to form colonies after application of rigosertib. These results are in line with the data obtained on hepatocellular carcinoma cell lines, where in a colony assay hardly any cells were visible after application of 1µM of rigosertib[398]. In an other report, an inhibition of epidermolysis bullosa-associated squamous cell carcinoma could be detected only starting at 1µM in a clonogenic assay using crystal violet[404]. Within this work, first evidence could be obtained that after treatment with rigosertib the migration of neuroblastoma cells and wound healing can be disrupted. Furthermore, this thesis could illustrate the initiation of apoptosis after administration of rigosertib. Neuroblastoma cells treated with the relative IC50 (EC50) showed up to 30% increased signals for programmed cell death compared to the control group. An increase in apoptotic signals was also observed in cells derived from other tumor entities, such as epidermolysis bullosa-associated squamous cell carcinoma lines[404], head and neck cancer cell lines[402], a myelodysplastic syndrome-derived cell line[400] and leukemia cell lines[401]. The impact of rigosertib on the PLK1/PI3K pathway was only fundamentally addressed in this thesis, but a repression of PLK1 and PI3K was found after treatment of the neuroblastoma cells. A study on head and neck cancer cell lines reported that an administration of 1µM rigosertib leads to a 60% reduction in PI3K activity[402]. In addition, the present work has shown that treatment with rigosertib induces the reduction of *MYCN* transcript levels as a consequence. In addition to the *in vitro* experiments, treatment of neuroblastoma PDX mice with rigosertib were performed in the framework of this thesis. Rigosertib reduces the tumor volume and the relative tumor volume while maintaining a stable body weight in comparison to vehicle controls. These results are in line with published reports in which a reduced tumor volume after application of rigosertib in mice models could be observed using epidermolysis bullosa-associated squamous cell carcinoma models[404], diffuse large B-cell lymphoma models[1099] and human liver, breast, and pancreatic cancer mice models[406]. In particular, a head and neck squamous cell carcinoma PDX study reported that the tumor volume was reduced by 60-100% after continuous treatment with rigosertib for 28 days, and the relative tumor growth was found to be up to 60% reduced by the same time[403]. Furthermore, a lower tumor weight of epidermolysis bullosa-associated squamous cell carcinomas[404] and diffuse large B-cell lymphomas[1099] was found in mice experiments. Additionally, fewer KI67 positive cells were found in mice with epidermolysis bullosa-associated squamous cell carcinomas[404]. As in the data of the present thesis it was reported that the body weight of the mice did not differ between treatment and vehicle control, indicating that rigosertib is not toxic for the treated mice[406,1099]. In summary, it can be said that the treatment of neuroblastoma cells or patient tumors (*in vivo*) using rigosertib represses the cancer cell hallmarks, including enhanced cell viability (broadly defined as proliferative signaling), reproductively (replicative immortality), migration (metastasis) and resistance to cell death. These results are consistent with the findings reported in the literature on the use of rigosertib in other tumor entities. Similar to other tumor entities, the treatment of neuroblastoma cells with rigosertib requires only minimal amounts in the nano molarrange (<1µM) of the inhibitor to induce a reduction in cancer cell aggressiveness.

4.2.2.4 Rigosertib as part of combinatorial therapies for neuroblastoma treatment

Since rigoseritib has been frequently used in drug combination studies, this section will discuss possible applications of rigoseritib together with other compounds. A study on rigosertib and gemcitabine combination for metastatic pancreatic adenocarcinoma failed to demonstrate an improvement in survival or response compared to the gemcitabine only group[700]. For a combined application of rigosertib with cisplatin or cisplatin derivatives, there is stronger evidence suggesting a higher efficacy. A study on head and neck cancer cell lines showed improved suppression of cell viability when cisplatin was administered simultaneously with rigosertib[405]. It was also demonstrated in a hepatocellular carcinoma PDX mice model that the tumor volume is significantly decreased when rigosertib and oxaliplatin or doxorubicin are administered concomitantly[406]. Two recent publications further highlight chemically-structurally improved rigosertib derivatives which are related to cisplatin[1100,1101]. In *in vitro* assays, this hybrid drug demonstrated a higher anti-tumor activity than rigosertib or cisplatin alone. For the treatment of *MYCN*-amplified high-risk neuroblastomas, a combination of BET protein inhibitors together with rigosertib could be considered as well. Several publications have already pointed out that the combination of a PI3K inhibitor (e.g. alpelisib) and a BET inhibitor (e.g. JQ1) is synergistic and leads to the modulation of transcription factors including MYC, GLI1, and FOXO3a[1093,1102]. These first reports lead to the initiation of a preliminary testing of the dual application of rigosertib and OTX015 on neuroblastoma cells in *in vitro* assays in this work. For transcriptomic modification of gene expression also a combination together with DNA methyltransferase inhibitors (e.g. azacitidine) could be considered[407,408]. Reports from clinical studies of patients with myelodysplastic syndromes or acute myeloid leukemia who received this combination showed a good tolerability of rigosertib when the DNA methyltransferase inhibitors were administered in advance. An even greater anti-tumor effect could be achieved if rigosertib is combined with an inhibitor of an enzyme of the same pathway, i.e. close to PLK1 or RAS-binding proteins such as PI3K, within the PI3K/AKT/mTOR pathway or the RAS-RAF-MEK-ERK pathway. Inhibitors against ALK, such as ceritinib and lorlatinib, have been proven to be effective against *ALK*-mutated neuroblastomas in pre-clinical experiments and are currently under investigation in trials recruiting pediatric patients[842,1103–1105]. Published studies showed the combined application of PI3K inhibitors (buparlisib or alpelisib) with ALK inhibitors (ceritinib or crizotinib) in the PI3K/AKT/mTOR pathway against ALK-rearranged non-small cell lung cancer (NSCLC)[1106,1107]. Further downstream of the pathway, publications report on a PI3K inhibitor (NVP-BEZ235) applied together with an AKT inhibitor (MK-2206) in bladder cancer[365] and, even more specialized dual PI3K/AKT inhibitors were used in ovarian cancer[1108] and for B-cell-like diffuse large B-cell lymphoma treatment (AZD compounds)[1109]. A publication on pilocytic astrocytoma could confirm a deregulation of the PI3K/AKT pathway after ATRX protein loss[1110], which points towards a possible treatment for *ATRX* deleted neuroblastomas. For the downstream located mTOR protein, many inhibitors are available on the market (e.g. rapamycin, everolimus) and published in terms of their anti-

cancer potential[355,356]. In addition to a combination of separate PI3K (e.g. alpelisib)[358], AKT (e.g. perifosine, A-443654)[359,360] and mTOR inhibitors (e.g. rapamycin)[355,356], dual or triple hybrid compounds have been increasingly used in research on neuroblastoma inhibition[341,361,362]. Particularly interesting are dual PI3K/mTOR inhibitors (e.g. NVP-BEZ235), which demonstrated effective concentrations at low nanomolar range and are produced for an oral formulation[363–365]. Moreover, these dual PI3K/mTOR drugs can be used in combination with MDM2 inhibitors, such as RG7388 which was shown for liposarcomas[1111]. Other combinations are currently being investigated, such as a triple PIM/PI3K/mTOR inhibitor[357]. Targeting the RAS-RAF-MEK-ERK pathway, dual PI3K and RAS inhibitors (BEZ-235 or rigosertib) are reported to aim at this pathway as well[369] and are further described for a dual application with RAF inhibitors (RAF265 or dabrafenib) in thyroid[363] and breast cancer models[370]. Downstream in this pathway, combinations of MEK inhibitors (e.g. trametinib) with PI3K inhibitors (e.g. buparlisib)[372] as well as PLK1 inhibitors (e.g. volasertib)[1112] that exhibit a synergistic anti-tumor activity are already published. In particular, publications on the combined inhibition of MEK and PI3K or PLK1 have highlighted synergistic anti-tumor activity in NRAS mutant melanoma[1113,1114] This suggests a combination of rigosertib and MEK inhibitors (e.g. binimetinib or trametinib) may be an efficient combination therapy for neuroblastoma[1115,1116]. Additionally, publications highlighted the combined PI3K/AKT and RAF/MEK/ERK pathway inhibition in Hodgkin lymphoma[373] and colorectal cancer[374], using PI3K/ERK dual inhibitors (e.g. AEZS-136 or DPS-2). Another possibility of combining rigosertib with another small molecule inhibitor is to interfere with the same molecular function of different proteins. For example, PLK1 is involved in the centrosome maturation[376], as well as the Aurora A kinase[1117]. Aurora A kinase inhibitors were demonstrated to have *in vitro*[1118,1119] and *in vivo*[1120] efficacy in neuroblastoma, and a first clinical phase I study revealed promising results of alisertib (MLN8237) in combination with conventional chemotherapy[1121]. Therefore, a PLK1 inhibitor (rigosertib and/or volasertib) and an Aurora A kinase inhibitor (alisertib) are favorable combinations. In addition, it was shown that a combination treatment of alisertib and the BET inhibitor JQ1 has a synergistic anti-tumor effect on *MYCN*-amplified glioblastoma cells[1122].

In summary, it can be said that the prevention of the MYCN protein stabilization is the small molecule class with the most published work and the widest experience in other cancer entities (also with regard to c-MYC), as well in neuroblastoma. Targeted therapies should therefore be adapted and combined with each other for treatment of neuroblastoma. However, some inhibitors, e.g. such as alpelisib have too little anti-tumor activity[347,1123], and other inhibitors also have undesired bypass activities, e.g. volasertib attacks not only PLK1 but also PLK3[389–391]. This is why a targeted therapy against neuroblastomas is in need for a dual inhibitor like rigosertib, which inhibits PI3K and PLK1 via the RAS binding site[368]. More importantly, rigosertib should be combined e.g. with an mTOR inhibitor (everolimus) in the PI3K/AKT/mTOR pathway or e.g. with a MEK inhibitor (trametinib) in the RAS-RAF-MEK-ERK pathway.

4.2.3 ASPM is a regulator of neuroblastoma cell proliferation and differentiation

The primary-microcephaly associated MCPH gene family are known regulators of the developing brain in neural progenitor cells. In this study, the role of MCPH genes in neuroblastoma was investigated. In general, the MCPH genes, and in particular *ASPM* were found to be higher expressed in neuroblastoma, then in normal tissues and other tumor entities. *ASPM* was found to be highly expressed in neuroblastoma cell lines, and its expression was not affected by tumor cell density or serum starvation. A downregulation of *ASPM* with siRNA or shRNA reduced proliferation and induced cell death, G2/M arrest and induction of neuronal differentiation.

4.2.3.1 ASPM regulates neuronal progenitor mitosis and is highly expressed in pediatric neuronal cancers

Using previously published microarray and RNA-sequencing expression data, the MCPH genes[1124], in particular *ASPM,* were found to be highly-overexpressed in many tumor entities, including gliomas[483,1125], ependymomas,[489] medulloblastomas[485,486,489], melanomas[1126], hepatocellular carcinomas[1127], pancreatic cancers[1128], bladder cancer[708], prostate cancer[1129], breast[1130], ovarian cancers[707] and endometrial cancer[1131,1132], compared to normal tissues. The expression of *ASPM* was identified in this work to be highest in tumors which originate from neuronal precursors such as neuroblastoma, medulloblastoma, ATRT and ependymoma. A connection between the ASPM protein as an essential factor for normal mitotic spindle function, and the embryonic neuroblasts has been known for some time[430]. This thesis has shed further light on ASPM's partners which might be involved in neuronal cell division. The genes whose expression was highly correlated with *ASPM* in neuroblastoma were predominantly involved in in cell cycle regulation and cell division. Among the other MCPH genes, *ASPM* showed the highest correlation in gene expression with *KIF14*, *CENPE*, *NCAPH* and *STIL*. These other MCPH genes with a known function in mitosis[1133–1136] have also been suggested to play role in tumorigenesis[1136–1139] (MCPH genes see Table 28 in appendix). The ASPM protein plays an important role in assembly spindle as well as in chromosome segregation. The preferred localization of ASPM in the cell nucleus and in particular at the spindle poles during mitosis could be confirmed by immunofluorescence detection in this thesis. That raises the question of whether an alteration of the cell division, for example caused by ASPM, could also be involved in a missegregation of the chromosomes in the broadest sense. It has already been shown for other MCPH and mitotic proteins that they are related to chromosomal instability if they are not present or mutated[1140]. In healthy cells, the attachment of microtubules is often released prior to the anaphase in order to resolve incorrect attachments and to avoid missegregation of chromosomes. However, if the adhesion of the microtubules increases, chromosomal instability may occur due to lagging chromosomes[1141]. Increased DNA damage after deletion of *ASPM* was already shown for a medulloblastoma mouse model[485]. In addition, the emergence of lagging chromosomes up to a breakage fusion-bridge caused by excessive microtubule attachment or

a loss of metaphase chromosome alignment may result in the formation of additional micronuclei after the mitosis[83,84]. In these micronuclei, chromothripisis of the damaged, misregulated DNA leads to a variety of genomic rearrangements and a subsequent re-assembly of a single chromatid[753]. Several research groups have already shown that neuroblastoma genomes show traces of chromothripsis as well as ecDNA[76,79–81]. Previous studies have hypothesized that at DMs do not interact with the mitotic spindle in cell division, but may be attached to the chromosomes involved (chromosome tethering)[755,1142]. It has also been shown that DMs in the mitosis are repelled from the spindle poles during their attachment to the chromosome[1142]. Moreover, it is proposed that ecDNA occurring in neuroblastoma were distributed unevenly within mitotic missegregation with subsequent circle integration in tumor suppressor or oncogene loci[76]. It is tempting to speculate that this could occur due to dysregulation of mitosis and its involved proteins, as for example ASPM. Segmental chromosomal gains in neuroblastoma occur frequently in chromosome 2p[1143,1144], but also in chromosome 1q[681,682,1145,1146]. In this regard, it is worth noticing that the *ASPM* gene is located at chr.1q31.3 (GrCh38) and research is already highlighting that the chromosome 1q arm or the close 1q32 region is gained in diverse tumor entities, as for example in neuroblastoma[681,682,1145,1147], melanoma[1148], medulloblastoma[1149], retinoblastoma[1150] and pediatric glioblastoma multiforme[1151]. A report further suggested that the overexpression of genes covarying with copy number alterations (for example 1q gain) have been found to be related to the disregulation of mitotic spindle assembly in neuroblastoma[1145]. In addition, there might be a pathological connection between *ASPM* overexpression and the acquisition of chromosomal aberrations, because spindle defects are also responsible for chromosomal breaks. A defective mitotic spindle (e.g. merotelic attachment) can therefore lead to chromosome rupture at the centromeric region, which in turn can promote double-strand breaks and chromosomal rearrangements with possible chromosomal gains. Especially a 1q chromosomal gain could have risen from a merotelic microtubuli attachment following a pericentromeric break leading to an attachment of the centromere-positive arm[462]. Moreover, chromosomal rearrangements in chromosome 2p lead to an amplification of the *MYCN* gene[1143,1152]. *MYCN*-amplified high-risk neuroblastoma showed the highest *ASPM* expression, compared to moderate *ASPM* expression in non-amplified *MYCN* cells and low *ASPM* expression in other tumor entities and fibroblast cell lines in this work. These results are contrasted by reports from Jung et al.[1153], which states that *ASPM* was overexpressed in glioblastoma cells but not in neuroblastoma. This was proven using the qPCR method, which shows a measurement of the gene expression of *ASPM* in the non-*MYCN*-amplified SK-N-SH cell line. The qPCR data in this study also showed that the *ASPM* gene expression in the SK-N-SH cell line is comparable to the control cell lines or fibroblasts used. However, this does not preclude the assumption that *ASPM* can also be a marker for cellular proliferation. In MCPH microcephaly, neuroepithelial cells with *ASPM* mutations lose the ability to undergo a symmetric division and therefore show an increased frequency of asymmetric division, with a reduction of proliferation[1154]. Opposed to a dysfunctional ASPM protein, *ASPM* overexpression showed an initiation of increasing cellular proliferation in cancer[483,484]. In this thesis it could be shown that a specific ASPM

immunofluorescence signal in the nucleus decreases sharply as soon as *ASPM* was downregulated applying siRNA. This leads to the assumption that the cells involved in the division then are trapped in the in mitosis and discontinue to proliferate, which could also be confirmed by proliferation assays including live cell imaging. In line with the main neuroblastoma dogma, *MYCN*-amplified neuroblastoma cells would have an increased proliferation, which goes hand in hand with a higher mitosis rate, and thus *ASPM* is expected to be higher expressed. In this work, the expression of *ASPM* was not found downregulated upon reduction of neuroblastoma cell proliferation by serum starvation, arguing against the preclusion that *ASPM* gene expression was merely a surrogate marker for cell division. Nevertheless, ASPM was found to be required for neuroblastoma cell proliferation in this work, as reduced cell viability and reduced cell proliferation were observed when *ASPM* was knocked down, which is in line with the results found within fundamental research studies[444] and studies of other cancer types[708,1125,1155,1156]. This especially is shown by Capecchi and Pozner (2015)[1157], highlighting the role of ASPM for regulating the Cyclin E activity which is moreover crucial for the cell fate. In particular, in this thesis the *ASPM* knockdown was found to reduce the number of nucleating microtubules, which are essential for physiological centrosome function, and thus resulted in a G2/M cell-cycle arrest of *MYCN*-amplified neuroblastoma cells. An interplay between the (overexpressed) MYC(N) protein and mitotic factors leading to perturbations is also suggested by a paper from Littler et al[1158]. Moreover, a very recent publication highlights the role of MYCN in the control of the balance between symmetric and asymmetric cell division in neuroblastoma cells[494]. MYC(N) alters various pathways that ultimately affect mitosis, with the PLK1 kinase acting as the main pivot. MYC(N) effects central functions of PLK1, starting with the entry into mitosis or spindle assembly. Thus, overexpressed MYC(N) promotes chromosome instability with an altered spindle morphology, keeping the cells longer in the metaphase to align the chromosomes and entering the anaphase earlier. PLK1 is itself a part of the MTOC, promoting kinetochore to microtubule attachment[460,461]. In this thesis it was found, that *ASPM* mRNA levels strongly correlate with the expression of cell cycle regulators (e.g. *PLK1*, *MKI67*). Interestingly, a report highlights that a *PLK1* and *ASPM* double activation mutant showed a synergistic effect resulting in an increase in the mitotic rate and thus an increased proliferation[444]. It is therefore to be assumed that a knockdown of *ASPM* reduces the mitotic rate. Previously it was shown that the prolonged mitosis of neural progenitors alters the cell fate, leading either to apoptosis or differentiation of neurons. The longer the mitotic duration, the more cells become apoptotic or transform into neurogenic progeny[1159]. It was already reported that a loss of spindle control and the emergence of chromosomal breaks can also lead to the activation of telomerase or disturbed apoptosis signaling[462]. An increased induction of apoptosis was as well detected in this work after siASPM treatment, which is also in agreement with previous observations in breast cancer cells[1160]. Apoptosis upon *ASPM* knockdown has not only been observed *in vitro*, but has also been validated in animal models before[485,1154,1161,1162]. Concordantly, the loss of the ASPM protein in microcephaly also leads to apoptosis of neuronal progenitors[1163,1164]. Thus the cellular localization of ASPM plays a central role in neuronal proliferation and maturation, influencing the

functionality of the neuronal system. The absence of ASPM generates more asymmetric divisions and modified division planes, which can cause premature differentiation over proliferation[434]. Findings in mice experiments[1165–1167] underline the notion that defects in spindle stability can delay mitosis and cause premature differentiation. In this study it could be shown that the ASPM protein has an influence on the maturation of neuroblastoma cells, notably of a differentiating similar cellular phenotype. After a knockdown of *ASPM*, the neuroblastoma cells developed neurite-like outgrowths and showed cytoskeletal changes and increased expression of differentiation markers, such as MAP2, TUBB3 and DCX. Increased differentiation of neuroblasts after *ASPM* knockdown was demonstrated in a medulloblastoma mice model in a previous study[485]. Concordant results in neuroblastoma and in other tumors of neuronal origin suggest a crucial function of ASPM in neuronal-cell differentiation. While ASPM gene/protein loss leads to premature neuronal differentiation in microcephaly and consequently embryonic defects, an overexpression of the gene coincides with increased proliferation of neural progenitor cells and cancer[425,429,1168,1169]. Most likely, this is due to the neuronal origin of these tumors, as well as due to the fact that these embryonal tumors develop from progenitor cells rather than from differentiated cells. The maturation of neurons is coupled with the migration of cells to the respective brain target regions, which is mediated by microtubules[477]. In summary, the assembly of microtubules is critical for a neuron in terms of migration, shape, dendritic transport and plasticity[466]. More importantly, it is therefore possible that the ASPM protein could be involved in six major cellular processes (mitosis, proliferation, differentiation/neuronal growth, information signaling, intracellular transport and migration) and that its overexpression could cause severe changes in these circuits.

4.2.3.2 Implementation of ASPM as biomarker for highly aggressive neuroblastomas

High expression of *ASPM* was found in this work to correlate with aggressive neuroblastoma, which suggests *ASPM* as biomarker for high-risk neuroblastoma. High *ASPM* expression was associated with significantly reduced event-free and overall survival. In addition, high *ASPM* expression turned out to be an additional, significant, adverse prognostic factor, even when established neuroblastoma risk criteria, namely INSS stage and *MYCN* amplification were taken into account. In summary, *ASPM* is suggested a suitable a biomarker for an aggressive neuroblastoma. Similar results have been described for *ASPM* in other cancer entities[1170], and highlight *ASPM* as a possible gastric stem/progenitor cell marker[1171], pancreatic ductal adenocarcinomas[1172] and bladder cancer[1173,1174]. A previous study on gliomas described that *ASPM* expression correlated with malignant progression, higher tumor grade and higher chance of recurrence. *ASPM* was also considered as a biomarker for distinguishing glioma stromal cells from stem-like cells[483,1175]. In addition, in a study including astrocytoma samples it was found that two patients with astrocytoma gained *ASPM* overexpression and progressed to a higher tumor grade[489]. Finally, reduced expression of *ASPM* has been suggested as a response marker for endocrine breast-cancer therapy[1176]. For neuroblastoma, RT-qPCR assays based on the detection of gene

expression are already explored in research settings[203,1177,1178]. Therefore, detection of the *ASPM* expression under MRD detection criteria in patients with neuroblastoma would be conceivable, as already suggested for DCX in neuroblastoma[1179]. It has to be assumed that due to the variability of gene expression (especially under therapy), these test systems only allow a semi-quantitative MRD estimation. Another possibility to consider *ASPM* as a biomarker is connected to the fact that the *ASPM* gene is localized on the chromosome 1q arm, which is a segmental chromosomal gain occurring in neuroblastoma[681,682,1180]. Although a special examination of the chromosome 1q arm is not carried out regularly in neuroblastoma routine diagnostics, there is a clear trend towards a more detailed examination of the genome of neuroblastoma tumors that includes this alteration. Therefore, routine examination of a chromosome 1q gain using FISH, Southern blot or PCR techniques for neuroblastoma diagnostics should be considered, as is already the case for chromosome 1p.

4.2.3.3 Downregulation of *ASPM*: A new approach for neuroblastoma therapy?

Within this work, the highest *ASPM* activity was found in *MYCN*-amplified and metastatic tumors, for which patients with a neuroblastoma are in high medical need for new treatment approaches. Neuroblastoma therapy already aimed to differentiate immature neuroblasts, as for example with 13-cis-retinoic acid[712], but has not been successful thus far[1181]. The observation that neuroblastoma cells require ASPM for proliferation suggests a potential treatment with mitosis and microtubules inhibitors[1182]. The experiments of this work showed that neuroblastoma cells could be effectively treated with nocodazole, an antineoplastic agent which interferes with the polymerization of microtubules and causes cell cycle arrest. The inhibitor vincristine/vindesine has the same mode of action and is already included in current treatment regimens[30]. The drug paclitaxel has a similar function, promoting stabilization of microtubules and delaying mitosis. Presently, nab-paclitaxel it tested in a phase I/II study against recurrent/refractory solid tumors, including neuroblastoma, demonstrating preliminary clinical activity[1183]. Published results on *ASPM* expression in germ cells[1184] and ovarian cancer[707] have proven the indirect mechanic interaction through microtubule disruption between ASPM and nocodazole/paclitaxel. Nocodazole treatment induced the continuous disassembly of microtubules, during which ASPM remained attached until the spindle completely collapses[707,1184]. When paclitaxel is applied, microtubules were excessively polymerized, remaining ASPM attached[707,1184]. Loss of the *ASPM* protein influences double strand break repairs and provoked DNA damage after *ASPM* deletion which could already be shown in tumor cells[485,707]. Therefore platinum compounds would serve as an option for combinatorial treatments. For epithelial ovarian cancer, carboplatin was suggested to treat *ASPM* high expressing tumors with high degree of aneuploidy, inhibiting DNA replication and causing DNA breaks. In contrast, the authors highlight the possibility of chemoresistance to carboplatin of *ASPM* expressing tumor cells[707]. For treatment of glioblastomas, several publications report that knockdown of *ASPM* in tumor cells sensitized cells to DNA damaging agents like cisplatin and radiotherapy[483,1125,1175]. It was even shown that the suppression of ASPM by ionizing radiation alone

could lead to a reduced number of neuronal cells[1185]. A comprehensive description of these relationships has already been made for glioblastoma, which states that ASPM is required for non-homologous end-joining DNA repair and interacts with BRCA1[1186–1188]. The authors further highlight that ASPM determines the sensitivity to a number of chemotherapies[1175]. In contrast to the possibility of effecting the interaction between ASPM and the microtubules or the administration of DNA damaging agents, a direct attack on the ASPM protein is also conceivable. So far, no direct inhibitors of ASPM have been described. However, ASPM was found to contain consensus phosphorylation sites for CDK1 and MAPK which may present targets for small-molecule inhibitors[1189]. Recently published work on neuroblastoma models highlighting that CDK1[1190] and MAPK inhibitors[1115,1191,1192] could serve as an indirect targeted therapy option. An investigation further showed targeted mitosis inhibition via cell division factors[1193]. The *BIRC5* survivin protein is associated with the processing of mitosis as part of the chromosomal passenger complex and co-upregulated with *ASPM* in cholangiocarcinomas[1194]. This protein complex is involved in chromosome condensation, corrects improper binding of microtubules to the kinetochore and initiates the spindle checkpoint[1195]. Survivin is overexpressed in the majority of all tumor entities, which often occurs together with relapses, resistance to chemotherapy and shortened patient survival[1195]. Treatment of neuroblastomas could therefore also be conducted with already available survivin inhibitors[1196–1198], as for example YM155. After administration of riboflavin (vitamin B_2) in high dosages, it was already found that the *ASPM* and *BIRC5* were downregulated upon the treatment and the proliferative potential of human colon epithelial cells was lost[1199]. Likewise, an inhibition is possible of those MCPH proteins whose high expression correlates with the expression of *ASPM* and thus attack cancer mitosis. Targeting the centromere-associated CENP-E protein causes chromosome misalignment, which follows prolonged mitotic arrest and apoptosis of cancer cells[1200,1201]. It was further shown that the MCPH genes *CENPA* and *KIF14* were strongly represented in neuroblastoma cells and depend on HDAC11 which promotes mitotic cell cycle progression and survival[1202]. Suitable agents could therefore be pan-or class I HDAC inhibitors that have already been published to induce neuroblastoma differentiation[1050]. However, there was also an opposite observation found in adenocarcinomas treated with the HDAC inhibitor vorinostat, which stated the enhancement of tumor initiation by expression of *ASPM*, creating a more drug-resistant state in cancer cells[1203]. A promising mitosis aimed option could be the inhibition of known mitotic kinases involved in MTOC and centrosome assembly and maturation, such as Aurora A[1117] or polo-like kinase PLK1[376]. The Aurora A kinase supports the maturation of the centrosome, activates PLK1 in the G2/M-phase transition and stimulates the accumulation of effector molecules such as MAPK[1184,1189,1204–1207]. Previously, Aurora-A kinase inhibitors were demonstrated to have *in vitro*[1118] and *in vivo*[1120] efficacy in neuroblastoma. A first clinical phase I study revealed promising results of alisertib (MLN8237) in combination with conventional chemotherapy[1121]. Although the efficacy of the PLK1 inhibitor GSK461364 against neuroblastoma could be shown[377], initial clinical testing has so far been unable to demonstrate comprehensive clinical applicability[381,382]. Furthermore, studies on neuroblastoma[385] and

rhabdomyosarcoma[383] xenograft models have demonstrated the efficacy of a combination consisting of PLK1 inhibitors and vinca alkaloids. Moreover, a combinatorial treatment of Aurora A kinase and PLK1 inhibitors was shown to induce mitotic breakdown and repressing *ASPM* after 24h of treatment[1193]. Since this work showed a connection between increased *ASPM* expression in aggressive, *MYCN*-amplified neuroblastoma tumors, targeted inhibition of cell proliferation may serve as therapy option. Ongoing studies are investigating increased *ASPM* expression though the EGFR/PI3K/AKT pathway in astrocytoma and oligodendroglioma[1208]. Previously, ASPM was identified as a potential molecular target in glioblastoma[1125], proposing the EGFR inhibitor erlotinib as treatment of choice. Likewise, activation of the PI3K/AKT/mTOR signaling pathway was found to be a poor prognostic indicator of neuroblastoma, which is why *in vitro* and *in vivo* research approaches the applicability of PI3K inhibitors[348,1209]. Moreover, a relationship has been observed between the determination of cell polarization which is regulated by the microtubules and the activation of PI3K[1210]. This makes PI3K an attractive target of overexpressing ASPM neuroblastoma cells using alpelisib. Moreover, the multi-kinase inhibitor rigosertib could be used for the treatment of neuroblastoma tumors showing an increased *ASPM* expression by simultaneously attacking PLK1 (RAS) and PI3K. And indeed, in Bayani et al. it was mentioned that ASPM and PLK1 are functionally connected with relation to a risk signature in breast cancer and the authors stated that a putative targeted therapy could represent volasertib or rigosertib[1211]. In literature, both inhibitors are also classified as MTOC inhibitors[1212]. As already known for these PLK1 (RAS) and PI3K drugs, their administration causes destabilization of microtubules and an abnormal spindle formation in mitosis[1182,1213–1215]. It was further observed that PLK1 depleted cells are unable to activate ASPM at the centrosome. As a result, the microtubules are no longer held in the vicinity of the centrosomes and stable attachment of the microtubules or the spindle to the chromosomes is no longer established[1214–1216]. For the application of rigosertib several research studies have shown that the drug causes a mitotic arrest induced by a mis-chromosome alignment, lack of attachment of microtubules to the chromosomes and the absence of spindle tension between the sister chromosomes[400,407,1217]. It was also discovered that rigosertib binds directly to the microtubules and destabilizes them[1213,1218]. However, it was shown that a ß-tubulin mutant has triggered resistance to rigosertib[1213,1219], which is contradicted by an other statement, which suggested that rigosertib does not bind to ß-tubulin[1220]. The authors claim, that commercially acquired rigosertib is contaminated with about 5% ON01500, an intermediate showing tubulin depolymerizing activity, which is resonsible for the gain of the cellular ß-tubulin resistance within the rigosertib-binding pocket[1220]. Therefore, it remains unclear if small molecules can attack ß-tubulin ends or whether those inhibitors or siRNA (e.g. siASPM) are able to degenerate ASPM. An interesting approach to evaluate a treatment for the ability of microtubules disruption is build on the observersion of lower molecular trafficking of intracellular vesicles from the plasma membrane to early endosomes, which leads to a fragmentation of the Golgi apparatus[1221,1222]. By incubating (inhibitor) treated cells with fluorescent labeled transferrin, it can be determined whether these absorbed vesicles migrate through the cell or remain in the periphery if the

cells are microtubule disruptived. In addition, staining the Golgi apparatus can provide further information about its possible fragmentation. However, these approaches of administering already known inhibitors are only an indirect method of targeting ASPM. As already introduced as a new way for the inhibition of the BET proteins (4.2.1), the design of a PROTAC molecule would allow for protein degradation where direct targeting of a specific protein is challenging[1010]. The PROTAC would connect an E3 ubiquitin ligase recognition domain via a covalent binding linker to a ligand for ASPM[1011]. This mechanism would lead to the ubiquitination and degradation of ASPM by the proteasome. However, since no binding sites for small molecules have been identified nor have specific inhibitors been developed against the ASPM protein, the design of a conditional degron tag for controlling the protein expression of ASPM is another approach to be considered[1025] (see as well 4.2.1). These techniques could therefore be a first step towards the development of an ASPM inhibitor comparable to a PLK1 or FOXM1 inhibitor (thiostrepton), which can be used to treat aggressive neuroblastomas independent of the *MYCN* status of the tumor.

As spindle proteins are crucially for cell division, high expression of such genes might merely be a reflection of increased cell proliferation in tumors. This has already been discussed for mitosis actors *FOXM1* and *PLK1* which are functional linking to *ASPM*[432]. Previous studies argue against this being the case for ASPM. ASPM levels have been found to be crucially decisive for whether neural progenitor cells continue to proliferate as such or undergo differentiation[1223]. Due to this role ASPM has been strongly implicated in the development of medulloblastoma[486]. Neuroblastoma also arises from neural progenitor cells, and our results also suggest some causative function of ASPM in tumor development. Stress-related reduction of cell proliferation did not result in reduced *ASPM* expression, whereas a knockdown of *ASPM* severely impeded neuroblastoma cell proliferation and induced differentiation. In summary, ASPM was found to be highly relevant in high-risk neuroblastoma. Increased *ASPM* expression was associated with poor prognosis and other high-risk neuroblastoma markers. High *ASPM* expression was required for an increased proliferation and an undifferentiated phenotype. The clinical relevance of this finding remains to be seen. Direct inhibition of the protein might not be possible, but indirect targeting via spindle checkpoint inhibitors may warrant further investigations. Last but not least, high *ASPM* levels were found to be a strong, prognostically relevant marker of aggressive high-risk neuroblastoma, and thus ASPM is a prime biomarker candidate.

5 Concluding remarks

This thesis provides clinical implementable means of molecular diagnostics to pinpoint unique *MYCN*-amplified neuroblastoma cells within accessible biopsy material. This concept makes use of a high-coverage, hybrid-capture-based NGS panel to precisely detect relevant neuroblastoma-specific genomic alterations. Unique *MYCN* breakpoints are detected by this assay and are employed for PCR-based disease follow-up in RQ-PCR and ddPCR applications. The approach successfully validated and tracked all *MYCN* breakpoints in cell lines and patient samples, and presents itself as a robust neuroblastoma MRD assay suitable for the application in a clinical routine environment. Furthermore, this thesis touched upon aspects of *MYCN*-amplified high-risk neuroblastoma biology and possible associated vulnerabilities. In addition, this work proposes indirect small molecule-based MYCN therapies and potentially new drug targets for a personalized treatment strategy. Future research is required to investigate in more detail the formation and the structure of the *MYCN* amplicon and its specific breakpoints, the underlying processes of *MYCN* transcription and protein stabilization, and the (combinational) treatment targeting *MYCN*-amplified neuroblastoma cells. Findings of this thesis and other studies suggest that a deregulation of mitotic kinases (e.g. PLK1) and spindle proteins (e.g. ASPM) may lead to genomic instability and a rupture of the chromosome 2. Several cycles of breakage-fusion-bridges during subsequent mitoses could then trigger randomization of the breakages, activation of repair mechanisms and *MYCN* amplification. As a consequence, accompanying effects like enhancer hijacking or focal enhancer amplification may lead to a higher activity of the transcription machinery (e.g. under participation of BRD4) and subsequently to an increase of the *MYCN* oncogene expression and its downstream targets. As discussed in this thesis, RTK-stimulation and signaling pathways (e.g. PI3K/AKT/mTOR or the RAS-RAF-MEK-ERK pathway) may further stabilize the MYCN protein. An ensemble of these pathological processes associated with MYCN finally causes an enhancement of survival, proliferation and cell cycle progression of neuroblastoma cells. Thus, the administration of targeted small molecules should be scheduled to suppress the *MYCN* transcriptional expression first and then reduce the residual MYCN protein that has escaped the initial transcriptional inhibition.

6 Summaries

6.1 Zusammenfassung

Das Neuroblastom, der häufigste extrakranielle solide Krebs im Kindesalter, entsteht aus Vorläuferzellen des sich entwickelnden sympathischen Nervensystems. Eine Amplifikation des *MYCN*-Onkogens ist ein bestimmender Faktor für ein hohes Risiko und tritt bei ~25% der Neuroblastome auf. Trotz intensiver Behandlung erliegt mehr als die Hälfte dieser Patienten ihrer Krankheit, was die Persistenz therapieresistenter, *MYCN*-amplifizierter minimaler Restneuroblastomzellen impliziert. Diese Arbeit stellt ein umfassendes Konzept für den spezifischen, diagnostischen Nachweis des *MYCN*-Amplikons vor und evaluiert neue Behandlungsoptionen für *MYCN*-amplifizierte Neuroblastome. Krankheitsrelevante Nukleotidveränderungen, strukturelle Genrearrangements und Kopienzahlveränderungen wurden im Tumormaterial mit Hilfe eines maßgeschneiderten, zielgerichteten hybrid-capture-basierten Next Generation Sequencing (NGS) Assays nachgewiesen. Einzigartige *MYCN*-Amplikon-Bruchpunkte im rearrangierten Gen stellen eine Zielsequenz für eine personalisierte PCR-Diagnostik der minimalen Resterkrankung (MRD) dar. *MYCN*-Amplikon-Bruchpunkte in Neuroblastom-Zelllinien und Tumoren wurden durch individuelle, semi-quantitative PCR-Assays und Sanger Sequenzierung identifiziert und wiedererkannt. Der Assay wurde für den hochsensitiven, quantitativen Echtzeit- und digitalen Tröpfchen-PCR-Nachweis für ausgewählte *MYCN*-Bruchpunkte in Zelllinien weiterentwickelt. Die MRD Level, die in den während der Therapie gesammelten Knochenmarkaspiraten nachgewiesen wurden, skizzierten die verschiedenen Krankheitsverläufe bei den Patienten, einschließlich der MRD-Persistenz bis zum Rezidiv und des guten Ansprechens auf den ersten Behandlungsabschnitt.

Die Kombination der Multi-Wirkstoff-Chemotherapie in den aktuellen Hochrisikoprotokollen mit indirekten MYCN-Inhibitoren stellt einen möglichen Weg dar, die schlechten Heilungsraten für *MYCN*-amplifizierte Neuroblastome zu verbessern. Verschiedene, hyperaktive biologische Netzwerke in *MYCN*-amplifizierten Neuroblastomen wurden mit niedermolekularen Inhibitoren der Bromdomäne und des extra-terminalen (BET) domänenhaltigen Proteins BRD4, der Phosphoinositid-3-Kinase (PI3K) und der polo-ähnlichen Kinase 1 (PLK1) behandelt. BET (JQ1, OTX015 und TEN-010) und Kinase-Inhibitoren (Alpelisib, Volasertib und Rigosertib) zeigten eine krebshemmende Wirkung, indem sie die Viabilität in zelllinienbasierten Wirkstoff-Screens bei nanomolaren bis niedrigen mikromolaren Konzentrationen verminderten. Die Behandlung mit Rigosertib veränderte die PLK1- und PI3K-Signalübertragung und beeinträchtigte die zelluläre Fähigkeit zur Wundheilung und Koloniebildung stark. In Übereinstimmung mit *In-vitro*-Beobachtungen reduzierte Rigosertib das Tumorwachstum in von Patienten stammenden Neuroblastom-Xenografts bei Mäusen. Die Kombination von OTX015 und Rigosertib erzeugte synergistische antitumorale Aktivität in zwei *MYCN*-amplifizierten Neuroblastom-Zelllinien. Um die MYCN-gesteuerte Proliferation von Tumorzellen zu verhindern, werden weitere

indirekte MYCN-Targets in Betracht gezogen. Ein Beispiel hierfür ist ein Substrat von PLK1, *ASPM*, das in *MYCN*-amplifizierten, primären Neuroblastomen erhöht ist. Das Herunterregulieren von ASPM, einem Mikrotubuli-assoziierten Protein, das an der mitotischen Spindelanordnung beteiligt ist, führte in *MYCN*-amplifizierten Neuroblastom-Zelllinien zu einer verminderten Viabilität und Proliferation, was mit einem neuronalen Differenzierungsphänotyp mit neuritenartigem Auswuchs, zytoskelettalen Veränderungen und erhöhter Expression von Differenzierungsmarkern einherging. Diese Studie stellt eine klinisch umsetzbare, molekulare Diagnostik vor, um einzigartige *MYCN*-amplifizierte Neuroblastomzellen in nicht-invasiv zugänglichem Biopsiematerial zu detektieren, und schlägt indirekte, niedermolekular-basierende MYCN-Therapien und potenziell neue Zielmoleküle für eine personalisierte Krebsbehandlung vor.

6.2 **Abstract**

Neuroblastoma, the most common extracranial solid childhood cancer, arises from precursors of the developing sympathetic nervous system. *MYCN* oncogene amplification is a determinant of high risk and occurs in ~25% of neuroblastomas. Despite intensive treatment, more than half these patients succumb to their disease, implying persistence of therapy-resistant *MYCN*-amplified minimal residual neuroblastoma cells. This thesis proposes a comprehensive concept for the specific diagnostic detection of the *MYCN* amplicon and evaluates new treatment options for *MYCN*-amplified neuroblastoma. Disease-relevant nucleotide changes, structural gene rearrangements and copy number alterations were detected in tumor material by next-generation sequencing of a customized hybrid capture-based targeted panel. Unique *MYCN* amplicon breakpoints in the rearranged gene constitute a target sequence for a personalized minimal residual disease (MRD) PCR diagnostic. *MYCN* amplicon breakpoints in neuroblastoma cell lines and tumors were identified and recovered by individual, semi-quantitative PCR assays and Sanger sequencing. The assay was further developed for highly sensitive, real-time quantitative and droplet digital PCR detection for selected *MYCN* breakpoints in cell lines. MRD level detected in bone marrow aspirates collected during therapy outlined different disease courses in patients, including MRD persistence until relapse and good response to the first treatment course.

Combining multi-agent chemotherapy in current high-risk protocols with indirect MYCN inhibitors provides a potential route to improve poor cure rates for *MYCN*-amplified neuroblastomas. Different hyperactive biological networks in *MYCN*-amplified neuroblastoma were tackled using small molecule inhibitors of the bromodomain and extra-terminal (BET) domain-containing protein BRD4, phosphoinositide 3-kinase (PI3K) and polo-like kinase 1 (PLK1). BET (JQ1, OTX015 and TEN-010) and kinase (alpelisib, volasertib and rigosertib) inhibitors demonstrated anti-cancer activity by diminishing viability in cell line-based drug screens at nanomolar to low micromolar concentrations. Rigosertib treatment altered PLK1 and PI3K signaling and strongly impaired the cellular ability for wound healing and colony formation. In line with *in vitro* observations, rigosertib reduced tumor growth in patient-derived neuroblastoma xenografts in mice. Combining OTX015 and volasertib produced synergistic anti-tumor responses in two *MYCN*-amplified neuroblastoma cell lines. To prevent MYCN-driven proliferation of tumor cells, further indirect MYCN targets are also being considered. This is exemplified by a substrate of PLK1, *ASPM*, which is elevated in *MYCN*-amplified primary neuroblastomas. Knockdown of ASPM, a microtubule-associated protein involved in mitotic spindle assembly, in *MYCN*-amplified neuroblastoma cell lines reduced viability and proliferation, accompanying a neuronal differentiation phenotype with neurite-like outgrowth, cytoskeletal changes and increased expression of differentiation markers. This study presents clinical implementable molecular diagnostics to pinpoint unique *MYCN*-amplified neuroblastoma cells within non-invasively accessible biopsy material, and proposes indirect small molecule-based MYCN therapies and potentially new drug targets for a personalized treatment.

7 List of references

1. Maris JM, Hogarty MD, Bagatell R, Cohn SL. Neuroblastoma. *Lancet*. 2007;369(9579):2106-2120. doi:10.1016/S0140-6736(07)60983-0
2. Maris JM. Recent Advances in Neuroblastoma. *N Engl J Med*. 2010;362:2202-2211. doi:10.1097/MOP.0b013e32832b1240
3. Johnsen JI, Dyberg C, Wickström M. Neuroblastoma—A neural crest derived embryonal malignancy. *Front Mol Neurosci*. 2019;12(9). doi:10.3389/fnmol.2019.00009
4. De Bernardi B, Nicolas B, Boni L, et al. Disseminated neuroblastoma in children older than one year at diagnosis: Comparable results with three consecutive high-dose protocols adopted by the Italian Co-Operatiye Group for Neuroblastoma. *J Clin Oncol*. 2003;21(8):1592-1601. doi:10.1200/JCO.2003.05.191
5. Virchow R. Hyperplasie der Zirbel und der Nebennieren. Die Krankhaften Geschwulste. In: *Vorlesungen Über Pathologie*. Vol 2:1864–186. Verlag von August Hirschwald; 1864:148-150.
6. Huang M, Weiss WA. Neuroblastoma and MYCN. *Cold Spring Harb Perspect Med*. 2013;3(10). doi:10.1101/cshperspect.a014415
7. Wright JH. Neurocytoma or neuroblastoma, a kind of tumor not generally recognized. *J Exp Med*. 1910;12(4):556–561. doi:10.1084/jem.12.4.556
8. Brodeur GM. Neuroblastoma: biological insights into a clinical enigma. *Nat Rev Cancer*. 2003;3(3):203-216. doi:10.1038/nrc1014
9. Kaatsch P, Grabow D, Spix C. *German Childhood Cancer Registry - Annual Report 2018 (1980 - 2017); Insitute of Medical Biostatistics, Epidemiology and Informatics (IMBEI) at the University Medical Center of the Johannes Gutenberg University Mainz*.; 2019. https://www.kinderkrebsregister.de/typo3temp/secure_downloads/22605/0/2df4719687ba2596d4216218a4f4632763b64847/jb2018s.pdf
10. Castleberry RP. Neuroblastoma. *Eur J Cancer Part A*. 1997;33(9):1430-1437. doi:10.1016/S0959-8049(97)00308-0
11. Brodeur GM. Neuroblastoma: Biological insights into a clinical enigma. *Nat Rev Cancer*. 2003;3(3):203-216. doi:10.1038/nrc1014
12. Bosse KR, Maris JM. Advances in the translational genomics of neuroblastoma: From improving risk stratification and revealing novel biology to identifying actionable genomic alterations. *Cancer*. 2016;122(1):20-33. doi:10.1002/cncr.29706
13. Saarinen-Pihkala UM, Jahnukainen K, Wikström S, et al. Ultrahigh-risk group within the high-risk neuroblastoma category. *J Pediatr Hematol Oncol*. 2013;35(6). doi:10.1097/MPH.0b013e318287326b
14. Basta NO, Halliday GC, Makin G, et al. Factors associated with recurrence and survival length following relapse in patients with neuroblastoma. *Br J Cancer*. 2016;115(9):1048-1057. doi:10.1038/bjc.2016.302
15. American Society of Clinical Oncology (ASCO). Neuroblastoma - Childhood - Medical Illustrations. Accessed November 28, 2020. https://www.cancer.net/cancer-types/neuroblastoma-childhood/view-all
16. Bronner ME, Simões-Costa M. The Neural Crest Migrating into the Twenty-First Century. *Curr Top Dev Biol*. 2016;116:115-134. doi:10.1016/bs.ctdb.2015.12.003
17. Janoueix-Lerosey I. Neuroblastoma Pathogenesis. In: Sarnacki S, Pio L, eds. *Neuroblastoma: Clinical and Surgical Management*. 1st ed. Springer International Publishing; 2020:29-56. doi:https://doi.org/10.1007/978-3-030-18396-7
18. Matthay KK, Maris JM, Schleiermacher G, et al. Neuroblastoma. *Nat Rev Dis Prim*. 2016;2(16078). doi:10.1038/nrdp.2016.78
19. Kastriti ME, Kameneva P, Adameyko I. Stem cells, evolutionary aspects and pathology of the adrenal medulla: A new developmental paradigm. *Mol Cell Endocrinol*. 2020;518(110998). doi:10.1016/j.mce.2020.110998
20. Takahashi Y, Sipp D, Enomoto H. Tissue interactions in neural crest cell development and disease. *Science*. 2013;341(6148):860-863. doi:10.1126/science.1230717
21. Furlan A, Dyachuk V, Kastriti ME, et al. Multipotent peripheral glial cells generate neuroendocrine cells

of the adrenal medulla. *Science*. 2017;357(6346):eaal3753. doi:10.1126/science.aal3753

22. Marshall GM, Carter DR, Cheung BB, et al. The prenatal origins of cancer. *Nat Rev Cancer*. 2014;14(4):277-289. doi:10.1038/nrc3679

23. Axelrod J. Neurotransmitters. *Sci Am*. 1974;230(6):59-71. doi:https://doi.org/10.1038/scientificamerican0674-58

24. Nagatsu T, Stjärne L. Catecholamine Synthesis and Release. *Adv Pharmacol*. 1997;42:1-14. doi:https://doi.org/10.1016/S1054-3589(08)60682-1

25. Cheung NK V., Dyer MA. Neuroblastoma: Developmental biology, cancer genomics and immunotherapy. *Nat Rev Cancer*. 2013;13(6):397-411. doi:10.1038/nrc3526

26. Knoepfler PS, Cheng PF, Eisenman RN. N-myc is essential during neurogenesis for the rapid expansion of progenitor cell populations and the inhibition of neuronal differentiation. *Genes Dev*. 2002;16(20):2699-2712. doi:10.1101/gad.1021202.mediate

27. Schulte JH, Lindner S, Bohrer A, et al. MYCN and ALKF1174L are sufficient to drive neuroblastoma development from neural crest progenitor cells. *Oncogene*. 2013;32(8):1059-1065. doi:10.1038/onc.2012.106

28. Boeva V, Louis-Brennetot C, Peltier A, et al. Heterogeneity of neuroblastoma cell identity defined by transcriptional circuitries. *Nat Genet*. 2017;49(9):1408-1413. doi:10.1038/ng.3921

29. Van Groningen T, Koster J, Valentijn LJ, et al. Neuroblastoma is composed of two super-enhancer-associated differentiation states. *Nat Genet*. 2017;49(8):1261-1266. doi:10.1038/ng.3899

30. Simon T, Hero B, Schulte JH, et al. 2017 GPOH Guidelines for Diagnosis and Treatment of Patients with Neuroblastic Tumors. *Klin Padiatr*. 2017;229(3):147-167. doi:10.1055/s-0043-103086

31. Berthold F, Hero B. Neuroblastoma: Current drug therapy recommendations as part of the total treatment approach. *Drugs*. 2000;59(6):1261-1277. doi:10.2165/00003495-200059060-00006

32. Berthold F, Simon T. Clinical Presentation. In: Cheung N-K V, Cohn SL, eds. *Neuroblastoma*. Springer-Verlag Berlin Heidelberg; 2005:63. doi:10.1007/b137762

33. Maris JM, Hogarty MD, Bagatell R, Cohn SL. Neuroblastoma. *Lancet*. 2007;369(9579):2106-2120. doi:10.1016/S0140-6736(07)60983-0

34. Mossé YP, Laudenslager M, Longo L, et al. Identification of ALK as a major familial neuroblastoma predisposition gene. *Nature*. 2008;455(7215):930-935. doi:10.1038/nature07261

35. Janoueix-Lerosey I, Lequin D, Brugières L, et al. Somatic and germline activating mutations of the ALK kinase receptor in neuroblastoma. *Nature*. 2008;455(7215):967-970. doi:10.1038/nature07398

36. Bourdeaut F, Trochet D, Janoueix-Lerosey I, et al. Germline mutations of the paired-like homeobox 2B (PHOX2B) gene in neuroblastoma. *Cancer Lett*. 2005;288(1-2):51-58. doi:10.1016/j.canlet.2005.01.055

37. Hallberg B, Palmer RH. The role of the ALK receptor in cancer biology. *Ann Oncol*. 2016;23(3):iii4-iii15. doi:10.1093/annonc/mdw301

38. Kaneko Y, Knudson AG. Mechanism and relevance of ploidy in neuroblastoma. *Genes Chromosomes Cancer*. 2000;29(2):89-95. doi:10.1002/1098-2264(2000)9999:9999<::aid-gcc1021>3.0.co;2-y

39. Maris JM, Mosse YP, Bradfield JP, et al. Chromosome 6p22 locus associated with clinically aggressive neuroblastoma. *N Engl J Med*. 2008;358(24):2585-2593. doi:10.1056/NEJMoa0708698

40. Vandesompele J, Baudis M, De Preter K, et al. Unequivocal delineation of clinicogenetic subgroups and development of a new model for improved outcome prediction in neuroblastoma. *J Clin Oncol*. 2005;23(10):2280-2299. doi:10.1200/JCO.2005.06.104

41. Theissen J, Oberthuer A, Hombach A, et al. Chromosome 17/17q gain and unaltered profiles in high resolution array-CGH are prognostically informative in neuroblastoma. *Genes Chromosomes Cancer*. 2014;55(8):639-649. doi:10.1002/gcc.22174

42. Zhang W, Yu Y, Hertwig F, et al. Comparison of RNA-seq and microarray-based models for clinical endpoint prediction. *Genome Biol*. 2015;16(1):133. doi:10.1186/s13059-015-0694-1

43. Peifer M, Hertwig F, Roels F, et al. Telomerase activation by genomic rearrangements in high-risk neuroblastoma. *Nature*. 2015;526(7575):700-704. doi:10.1038/nature14980

44. Ackermann S, Cartolano M, Hero B, et al. A mechanistic classification of clinical phenotypes in

neuroblastoma. *Science*. 2018;362(6419):1165-1170. doi:10.1126/science.aat6768

45. Pugh TJ, Morozova O, Attiyeh EF, et al. The genetic landscape of high-risk neuroblastoma. *Nat Genet*. 2013;45(3):279-284. doi:10.1038/ng.2529

46. Nakagawara A, Li Y, Izumi H, Muramori K, Inada H, Nishi M. Neuroblastoma. *Jpn J Clin Oncol*. 2018;48(3):214-241. doi:10.1093/jjco/hyx176

47. De Preter K, Vandesompele J, Heimann P, et al. Human fetal neuroblast and neuroblastoma transcriptome analysis confirms neuroblast origin and highlights neuroblastoma candidate genes. *Genome Biol*. 2006;7(9). doi:10.1186/gb-2006-7-9-r84

48. Osajima-Hakomori Y, Miyake I, Ohira M, Nakagawara A, Nakagawa A, Sakai R. Biological role of anaplastic lymphoma kinase in neuroblastoma. *Am J Pathol*. 2005;167(1):213-222. doi:10.1016/S0002-9440(10)62966-5

49. Passoni L, Longo L, Collini P, et al. Mutation-independent anaplastic lymphoma kinase overexpression in poor prognosis neuroblastoma patients. *Cancer Res*. 2009;69(18):7338-7346. doi:10.1158/0008-5472.CAN-08-4419

50. George RE, Sanda T, Hanna M, et al. Activating mutations in ALK provide a therapeutic target in neuroblastoma. *Nature*. 2008;455(7215):975-978. doi:10.1038/nature07397

51. Bresler SC, Weiser DA, Huwe PJ, et al. ALK Mutations Confer Differential Oncogenic Activation and Sensitivity to ALK Inhibition Therapy in Neuroblastoma. *Cancer Cell*. 2014;26(5):682-694. doi:10.1016/j.ccell.2014.09.019

52. Valteau-Couanet D. High-Risk Neuroblastoma Study 2 of SIOP-Europa-Neuroblastoma (SIOPEN) protocol. *unpublished*. 2019;Version 1.(V1.0_31/01/2019):1-126.

53. Imamura J, Bartram CR, Berthold F, Harms D, Nakamura H, Koeffler HP. Mutation of the p53 Gene in Neuroblastoma and Its Relationship with N-myc Amplification. *Cancer Res*. 1993;53(17):4053-4058.

54. Shohet J, Kim E. Targeted molecular therapy for neuroblastoma: The ARF/MDM2/p53 Axis. *J Natl Cancer Inst*. 2009;101(2):1527-1529. doi:10.1093/jnci/djp376

55. Schramm A, Köster J, Assenov Y, et al. Mutational dynamics between primary and relapse neuroblastomas. *Nat Genet*. 2015;47(8):872-877. doi:10.1038/ng.3349

56. Eleveld TF, Oldridge DA, Bernard V, et al. Relapsed neuroblastomas show frequent RAS-MAPK pathway mutations. *Nat Genet*. 2015;47(8):864-871. doi:10.1038/ng.3333

57. Schleiermacher G, Javanmardi N, Bernard V, et al. Emergence of new ALK mutations at relapse of neuroblastoma. *J Clin Oncol*. 2014;32(25):2727-2734. doi:10.1200/JCO.2013.54.0674

58. Zeineldin M, Federico S, Chen X, et al. MYCN amplification and ATRX mutations are incompatible in neuroblastoma. *Nat Commun*. 2020;11(1):913. doi:10.1038/s41467-020-14682-6

59. Gröbner SN, Worst BC, Weischenfeldt J, et al. The landscape of genomic alterations across childhood cancers. *Nature*. 2018;555(7696):321-327. doi:10.1038/nature25480

60. Weber A, Starke S, Bergmann E, Christiansen H. The coamplification pattern of the MYCN amplicon is an invariable attribute of most MYCN-amplified human neuroblastomas. *Clin Cancer Res*. 2006;12(24):7316-7321. doi:10.1158/1078-0432.CCR-06-0837

61. Irwin MS, Park JR. Neuroblastoma: Paradigm for precision medicine. *Pediatr Clin North Am*. 2015;62(1):225-256. doi:10.1016/j.pcl.2014.09.015

62. Kreissman SG, Seeger RC, Matthay KK, et al. Purged versus non-purged peripheral blood stem-cell transplantation for high-risk neuroblastoma (COG A3973): A randomised phase 3 trial. *Lancet Oncol*. 2013;14(10):999-1008. doi:10.1016/S1470-2045(13)70309-7

63. Schwab M, Alitalo K, Klempnauer KH, et al. Amplified DNA with limited homology to myc cellular oncogene is shared by human neuroblastoma cell lines and a neuroblastoma tumour. *Nature*. 1983;305(5931):345-248. doi:10.1038/305245a0

64. Kohl NE, Kanda N, Schreck RR, et al. Transposition and amplification of oncogene-related sequences in human neuroblastomas. *Cell*. 1983;35(2 Pt 1):359-367. doi:10.1016/0092-8674(83)90169-1

65. Brodeur GM, Seeger RC, Schwab M, Varmus HE, Michael Bishop J. Amplification of N-myc in untreated human neuroblastomas correlates with advanced disease stage. *Science*. 1984;224(4653):1121-1124. doi:10.1126/science.6719137

66. Weizmann Institute of Science. MYCN Gene. Gene Cards: The Human Gene Database. Accessed November 28, 2020. https://www.genecards.org/cgi-bin/carddisp.pl?gene=MYCN

67. EMBL-EBI, part of the European Molecular Biology Laboratory. MYCN Ensembl GRCh37. release 101. Published 2020. Accessed November 28, 2020. http://grch37.ensembl.org/Homo_sapiens/Transcript/Summary?db=core;g=ENSG00000134323;r=2:16080686-16087129;t=ENST00000281043

68. Theissen J, Boensch M, Spitz R, et al. Heterogeneity of the MYCN oncogene in neuroblastoma. *Clin Cancer Res*. 2009;15(6):2085-2090. doi:10.1158/1078-0432.CCR-08-1648

69. Ambros PF, Ambros IM. Pathology and biology guidelines for resectable and unresectable neuroblastic tumors and bone marrow examination guidelines. *Med Pediatr Oncol*. 2001;37(6):492-504. doi:10.1002/mpo.1242

70. Gesellschaft fur Padiatrische Onkologie und Hamatologie - Germany. Observation, Combination Chemotherapy, Radiation Therapy, and/or Autologous Stem Cell Transplant in Treating Young Patients With Neuroblastoma. ClinicalTrials.gov Identifier: NCT00410631. Published 2013. https://clinicaltrials.gov/ct2/show/NCT00410631

71. Seeger RC, Brodeur GM, Sather H, et al. Association of Multiple Copies of the N-myc Oncogene with Rapid Progression of Neuroblastomas. *N Engl J Med*. 1985;313(18):1111-1116. doi:10.1056/NEJM198510313131802

72. Cox D, Yuncken C, Spriggs AI. Minute chromatin bodies in malignant tumours of childhood. *Lancet*. 1965;1(7402):55-58. doi:10.1016/S0140-6736(65)90131-5

73. Vandevanter DR, Piaskowski VD, Casper JT, Douglass EC, Von Hoff DD. Ability of circular extrachromosomal DNA molecules to carry amplified MYCN protooncogenes in human neuroblastomas in vivo. *J Natl Cancer Inst*. 1990;82(23):1815-1821. doi:10.1093/jnci/82.23.1815

74. Helmsauer K, Valieva ME, Ali S, et al. Enhancer hijacking determines extrachromosomal circular MYCN amplicon architecture in neuroblastoma. *Nat Commun*. 2020;11(1):5823. doi:10.1038/s41467-020-19452-y

75. Storlazzi CT, Lonoce A, Guastadisegni MC, et al. Gene amplification as double minutes or homogeneously staining regions in solid tumors: Origin and structure. *Genome Res*. 2010;20(9):1198-1206. doi:10.1101/gr.106252.110

76. Koche RP, Rodriguez-Fos E, Helmsauer K, et al. Extrachromosomal circular DNA drives oncogenic genome remodeling in neuroblastoma. *Nat Genet*. 2020;52(1):29-34. doi:10.1038/s41588-019-0547-z

77. Taub R, Kirsch I, Morton C, et al. Translocation of the c-myc gene into the immunoglobulin heavy chain locus in human Burkitt lymphoma and murine plasmacytoma cells. *Proc Natl Acad Sci USA*. 1982;79(24):7837-7841. doi:10.1073/pnas.79.24.7837

78. Luijten MNH, Lee JXT, Crasta KC. Mutational game changer: Chromothripsis and its emerging relevance to cancer. *Mutat Res - Rev Mutat Res*. 2018;777:29-51. doi:10.1016/j.mrrev.2018.06.004

79. Boeva V, Jouannet S, Daveau R, et al. Breakpoint Features of Genomic Rearrangements in Neuroblastoma with Unbalanced Translocations and Chromothripsis. *PLoS One*. 2013;8(8):e72182. doi:10.1371/journal.pone.0072182

80. Kloosterman WP, Koster J, Molenaar JJ. Prevalence and clinical implications of chromothripsis in cancer genomes. *Curr Opin Oncol*. 2014;26(1):64-72. doi:10.1097/CCO.0000000000000038

81. Molenaar JJ, Koster J, Zwijnenburg D a, et al. Sequencing of neuroblastoma identifies chromothripsis and defects in neuritogenesis genes. *Nature*. 2012;483(7391):589-593. doi:10.1038/nature10910

82. McClintock B. The Stability of Broken Ends of Chromosomes in Zea Mays. *Genetics*. 1941;26(2):234-282.

83. Umbreit NT, Zhang CZ, Lynch LD, et al. Mechanisms generating cancer genome complexity from a single cell division error. *Science*. 2020;368(648):eaba0712. doi:10.1126/science.aba0712

84. Fonseca CL, Malaby HLH, Sepaniac LA, et al. Mitotic chromosome alignment ensures mitotic fidelity by promoting interchromosomal compaction during anaphase. *J Cell Biol*. 2019;218(4):1148-1163. doi:10.1083/jcb.201807228

85. Ottaviani D, Lecain M, Sheer D. The role of microhomology in genomic structural variation. *Trends Genet*. 2014;30(3):85-94. doi:10.1016/j.tig.2014.01.001

86. McVey M, Lee SE. MMEJ repair of double-strand breaks (director's cut): deleted sequences and alternative endings. *Trends Genet*. 2008;24(11):529-538. doi:10.1016/j.tig.2008.08.007

87. Kidd JM, Graves T, Newman TL, et al. Resource A Human Genome Structural Variation Sequencing Resource Reveals Insights into Mutational Mechanisms. *Cell*. 2010;143(5):837-847. doi:10.1016/j.cell.2010.10.027

88. Yang L, Luquette LJ, Gehlenborg N, et al. Diverse mechanisms of somatic structural variations in human cancer genomes. *Cell*. 2013;153(4):919-929. doi:10.1016/j.cell.2013.04.010

89. Kryh H, Abrahamsson J, Jegerås E, et al. MYCN amplicon junctions as tumor-specific targets for minimal residual disease detection in neuroblastoma. *Int J Oncol*. 2011;39(5):1063-1071. doi:10.3892/ijo.2011.1120

90. Hiemstra JL, Schneider SS, Brodeur GM. High-resolution mapping of the N-myc amplicon core domain in neuroblastomas. *Prog Clin Biol Res*. 1994;385:51-57.

91. Beheshti B, Braude I, Marrano P, Thorner P, Zielenska M, Squire JA. Chromosomal localization of DNA amplifications in neuroblastoma tumors using cDNA microarray comparative genomic hybridization. *Neoplasia*. 2003;5(1):53-62. doi:10.1016/s1476-5586(03)80017-9

92. Feiter JL, Brodeur GM. High-resolution mapping of a 130-kb core region of the MYCA/amplicon in neuroblastomas. *Genomics*. 1996;32(1):97-103. doi:10.1006/geno.1996.0081

93. Squire JA, Thorner PS, Weitzman S, et al. Co-amplification of MYCN and a DEAD box gene (DDX1) in primary neuroblastoma. *Oncogene*. 1995;10(7):1417-1422.

94. Manohar CF, Salwen HR, Brodeur GM, Cohn SL. Co-amplification and concomitant high levels of expression of a DEAD box gene with MYCN in human neuroblastoma. *Genes Chromosomes Cancer*. 1995;14(3):196-203. doi:10.1002/gcc.2870140307

95. Weber A, Imisch P, Bergmann E, Christiansen H. Coamplification of DDX1 correlates with an improved survival probability in children with MYCN-amplified human neuroblastoma. *J Clin Oncol*. 2004;22(13):2681-2690. doi:10.1200/JCO.2004.07.192

96. George RE, Kenyon R, McGuckin AG, et al. Analysis of candidate gene co-amplification with MYCN in neuroblastoma. *Eur J Cancer*. 1997;33(12):2037-2042. doi:10.1016/S0959-8049(97)00206-2

97. Storlazzi CT, Lonoce A, Guastadisegni MC, et al. Gene amplification as double minutes or homogeneously staining regions in solid tumors : Origin and structure. *Genome Res*. 2010;20(9):1198-1206. doi:10.1101/gr.106252.110.1198

98. De Preter K, Speleman F, Combaret V, et al. Quantification of MYCN, DDX1, and NAG gene copy number in neuroblastoma using a real-time quantitative PCR assay. *Mod Pathol*. 2002;15(2):159-166. doi:10.1038/modpathol.3880508

99. Kuroda H, White PS, Sulman EP, et al. Physical mapping of the DDX1 gene to 348 kb 5' of MYCN. *Oncogene*. 1996;13(7):1561-1565.

100. Amler LC, Schürmann J, Schwab M. The DDX1 gene maps within 400 kbp 5′ to MYCN and is frequently coamplified in human neuroblastoma. *Genes Chromosomes Cancer*. 1996;15(2):134-137. doi:10.1002/(SICI)1098-2264(199602)15:2<134::AID-GCC9>3.0.CO;2-4.

101. Scott D, Elsden J, Pearson A, Lunec J. Genes co-amplified with MYCN in neuroblastoma: Silent passengers or co-determinants of phenotype? *Cancer Lett*. 2003;197(1-2):81-86. doi:10.1016/S0304-3835(03)00086-7

102. Godbout R, Packer M, Bie W. Overexpression of a DEAD box protein (DDX1) in neuroblastoma and retinoblastoma cell lines. *J Biol Chem*. 1998;273(33):21161-21168. doi:10.1074/jbc.273.33.21161

103. Frühwald MC, Brodeur GM, Plass C, et al. Gene amplification in PNETs/medulloblastomas: Mapping of a novel amplified gene within the MYCN amplicon. *J Med Genet*. 2000;37(7):501-509. doi:10.1136/jmg.37.7.501

104. Akiyama K, Kanda N, Yamada M, et al. Structural organization of MYCN amplicons of neuroblastoma tumors, xenografts, and cell lines characterized by the sequences encompassing the MYCN amplicons in a human neuroblastoma cell line. *Genes Chromosomes Cancer*. 1993;8(1):15-21. doi:10.1002/gcc.2870080104

105. Pandita A, Godbout R, Zielenska M, Thorner P, Bayani J, Squire JA. Relational mapping of MYCN and DDXI in band 2p24 and analysis of amplicon arrays in double minute chromosomes and homogeneously

staining regions by use of free chromatin FISH. *Genes Chromosomes Cancer*. 1997;20(3):243-252. doi:10.1002/(SICI)1098-2264(199711)20:3<243::AID-GCC4>3.0.CO;2-2

106. Blumrich A, Zapatka M, Brueckner LM, Zheglo D, Schwab M, Savelyeva L. The FRA2C common fragile site maps to the borders of MYCN amplicons in neuroblastoma and is associated with gross chromosomal rearrangements in different cancers. *Hum Mol Genet*. 2011;20(8):1488-1501. doi:10.1093/hmg/ddr027

107. Ambros IM, Brunner C, Abbasi R, Frech C, Ambros PF. Ultra-high density snparray in neuroblastoma molecular diagnostics. *Front Oncol*. 2014;4(202). doi:10.3389/fonc.2014.00202

108. Kaneko S, Ohira M, Nakamura Y, Isogai E, Nakagawara A, Kaneko M. Relationship of DDX1 and NAG gene amplification/overexpression to the prognosis of patients with MYCN-amplified neuroblastoma. *J Cancer Res Clin Oncol*. 2007;133(3):185-192. doi:10.1007/s00432-006-0156-y

109. De Brouwer S, De Preter K, Kumps C, et al. Meta-analysis of neuroblastomas reveals a skewed ALK mutation spectrum in tumors with MYCN amplification. *Clin Cancer Res*. 2010;16(17):4353-4362. doi:10.1158/1078-0432.CCR-09-2660

110. Weiser D, Laudenslager M, Rappaport E, et al. Stratification of patients with neuroblastoma for targeted ALK inhibitor therapy. *J Clin Oncol*. 2011;24(1):14. doi:10.1200/jco.2011.29.15_suppl.9514

111. Adhikary S, Eilers M. Transcriptional regulation and transformation by Myc proteins. *Nat Rev Mol Cell Biol*. 2005;6(8):635-645. doi:10.1038/nrm1703

112. Wenzel A, Schwab M. The mycn/max protein complex in neuroblastoma. Short review. *Eur J Cancer*. 1995;31A(4):516-519. doi:10.1016/0959-8049(95)00060-V

113. Blackwood EM, Eisenman RN. Max: A helix-loop-helix zipper protein that forms a sequence-specific DNA-binding complex with Myc. *Science*. 1991;251(4998):1211-1217. doi:10.1126/science.2006410

114. Blackwood EM, Luscher B, Eisenman RN. Myc and Max associate in vivo. *Genes Dev*. 1992;6(1):71-80. doi:10.1101/gad.6.1.71

115. Ayer DE, Eisenman RN. A switch from Myc:Max to Mad:Max heterocomplexes accompanies monocyte/macrophage differentiation. *Genes Dev*. 1993;7(11):2110-2119. doi:10.1101/gad.7.11.2110

116. Zeid R, Lawlor MA, Poon E, et al. Enhancer invasion shapes MYCN-dependent transcriptional amplification in neuroblastoma. *Nat Genet*. 2018;50(4):515-523. doi:10.1038/s41588-018-0044-9

117. Morton AR, Dogan-Artun N, Faber ZJ, et al. Functional Enhancers Shape Extrachromosomal Oncogene Amplifications. *Cell*. 2019;179(6):1330-1341.e13. doi:10.1016/j.cell.2019.10.039

118. Durbin AD, Zimmerman MW, Dharia N V., et al. Selective gene dependencies in MYCN-amplified neuroblastoma include the core transcriptional regulatory circuitry. *Nat Genet*. 2018;50(9):1240-1246. doi:10.1038/s41588-018-0191-z

119. van Groningen T, Akogul N, Westerhout EM, et al. A NOTCH feed-forward loop drives reprogramming from adrenergic to mesenchymal state in neuroblastoma. *Nat Commun*. 2019;10(1):1530. doi:10.1038/s41467-019-09470-w

120. Durbin AD, Zimmerman MW, Dharia N V., et al. Selective gene dependencies in MYCN-amplified neuroblastoma include the core transcriptional regulatory circuitry. *Nat Genet*. 2018;50(9):1240-1246. doi:10.1038/s41588-018-0191-z

121. Matthay KK. MYCN expression in neuroblastoma: A mixed message? *J Clin Oncol*. 2000;18(21):3591-3594. doi:10.1200/JCO.2000.18.21.3591

122. Tang XX, Zhao H, Kung B, et al. The MYCN enigma: Significance of MYCN expression in neuroblastoma. *Cancer Res*. 2006;66(5):2826-2833. doi:10.1158/0008-5472.CAN-05-0854

123. Rickman DS, Schulte JH, Eilers M. The Expanding World of N-MYC – Driven Tumors. *Cancer Discov*. 2018;8(2):150-163. doi:10.1158/2159-8290.CD-17-0273

124. Zimmerman MW, Liu Y, He S, et al. MYC drives a subset of high-risk pediatric neuroblastomas and is activated through mechanisms including enhancer hijacking and focal enhancer amplification. *Cancer Discov*. 2017;8(3):320-335. doi:10.1158/2159-8290.CD-17-0993

125. Wang L, Tan TK, Durbin AD, et al. ASCL1 is a MYCN- and LMO1-dependent member of the adrenergic neuroblastoma core regulatory circuitry. *Nat Commun*. 2019;10(1):1-15. doi:10.1038/s41467-019-13515-5

126. Kohl NE, Kanda N, Schreck RR, et al. Transposition and amplification of oncogene-related sequences in human neuroblastomas. *Cell*. 1983;35(2 Pt 2):359-367. doi:10.1016/0092-8674(83)90169-1

127. Ambros PF, Ambros IM. Pathology and biology guidelines for resectable and unresectable neuroblastic tumors and bone marrow examination guidelines. *Med Pediatr Oncol*. 2001;37(6):492-504. doi:10.1002/mpo.1242

128. Brodeur GM, Seeger RC, Barrett A, et al. International criteria for diagnosis, staging, and response to treatment in patients with neuroblastoma. *J Clin Oncol*. 1988;271:509-524. doi:10.1200/JCO.1988.6.12.1874

129. Brodeur GM, Pritchard J, Berthold F, et al. Revisions of the international criteria for neuroblastoma diagnosis, staging, and response to treatment. *J Clin Oncol*. 1993;385:563-569. doi:10.1200/JCO.1993.11.8.1466

130. Hata Y, Naito H, Sasaki F, et al. Fifteen years' experience of neuroblastoma: A prognostic evaluation according to the Evans and UICC staging systems. *J Pediatr Surg*. 1990;25(3):326-329. doi:10.1016/0022-3468(90)90078-N

131. Cohn SL, Pearson ADJ, London WB, et al. The International Neuroblastoma Risk Group (INRG) classification system: An INRG task force report. *J Clin Oncol*. 2009;27(2):289-297. doi:10.1200/JCO.2008.16.6785

132. Shimada H, Umehara S, Monobe Y, et al. International Neuroblastoma Pathology Classification for prognostic evaluation of patients with peripheral neuroblastic tumors: A report from the Children's Cancer Group. *Cancer*. 1999;92(9):2451-2461. doi:10.1002/1097-0142(20011101)92:9<2451::AID-CNCR1595>3.0.CO;2-S

133. Monclair T, Brodeur GM, Ambros PF, et al. The International Neuroblastoma Risk Group (INRG) staging system: An INRG Task Force report. *J Clin Oncol*. 2009;27(2):298-303. doi:10.1200/JCO.2008.16.6876

134. Gesellschaft für pädiatrische Onkologie und Hämatologie (GPOH); Department of Pediatric Oncology and Hematology University of Cologne. NB2004 Trial Protocol for Risk Adapted Treatment of Children with Neuroblastoma. 2004;1.00(01-Sept-2004):1-264.

135. Simon T, Department of Pediatric Oncology and Hematology University of Cologne. Registry for neonates, infants, children, adolescents, and adults with newly diagnosed and/or relapsed neuroblastic tumors (NB Registry 2016). 2016;Version 2.(from 14.02.2017):1-25. https://webstatic.uk-koeln.de/im/dwn/pboxx-pixelboxx-168208/NB2016-registry-version-200-20170214-versandversion.pdf

136. Morgenstern DA, Bagatell R, Cohn SL, et al. The challenge of defining "ultra-high-risk" neuroblastoma. *Pediatr Blood Cancer*. 2019;66(4):e27556. doi:10.1002/pbc.27556

137. Trigg RM, Shaw JA, Turner SD. Opportunities and challenges of circulating biomarkers in neuroblastoma. *Open Biol*. 2019;9(5):190056. doi:10.1098/rsob.190056

138. Nakagawa H, Fujita M. Whole genome sequencing analysis for cancer genomics and precision medicine. *Cancer Sci*. 2018;109(3):513-522. doi:10.1111/cas.13505

139. Dunn P, Albury CL, Maksemous N, et al. Next generation sequencing methods for diagnosis of epilepsy syndromes. *Front Genet*. 2018;9(20). doi:10.3389/fgene.2018.00020

140. Seleman M, Hoyos-Bachiloglu R, Geha RS, Chou J. Uses of next-generation sequencing technologies for the diagnosis of primary immunodeficiencies. *Front Immunol*. 2017;8(847). doi:10.3389/fimmu.2017.00847

141. Ng SB, Turner EH, Robertson PD, et al. Targeted capture and massively parallel sequencing of 12 human exomes. *Nature*. 2009;461(7261):272-276. doi:10.1038/nature08250

142. Bewicke-Copley F, Arjun Kumar E, Palladino G, Korfi K, Wang J. Applications and analysis of targeted genomic sequencing in cancer studies. *Comput Struct Biotechnol J*. 2019;17:1348-1359. doi:10.1016/j.csbj.2019.10.004

143. Klein CJ, Foroud TM. Neurology Individualized Medicine: When to Use Next-Generation Sequencing Panels. *Mayo Clin Proc*. 2017;92(2):292-305. doi:10.1016/j.mayocp.2016.09.008

144. Pipis M, Rossor AM, Laura M, Reilly MM. Next-generation sequencing in Charcot–Marie–Tooth disease: opportunities and challenges. *Nat Rev Neurol*. 2019;15(11):644-656. doi:10.1038/s41582-019-0254-5

145. Miller EM, Patterson NE, Zechmeister JM, et al. Development and validation of a targeted next generation DNA sequencing panel outperforming whole exome sequencing for the identification of clinically relevant genetic variants. *Oncotarget*. 2017;8(60):102033-102045. doi:10.18632/oncotarget.22116

146. Surrey LF, MacFarland SP, Chang F, et al. Clinical utility of custom-designed NGS panel testing in pediatric tumors. *Genome Med*. 2019;11(1):32. doi:10.1186/s13073-019-0644-8

147. Soukupova J, Zemankova P, Lhotova K, et al. Validation of CZECANCA (CZEch CAncer paNel for Clinical Application) for targeted NGS-based analysis of hereditary cancer syndromes. *PLoS One*. 2018;13(4):e0195761. doi:10.1371/journal.pone.0195761

148. Cao Y, Jin Y, Yu J, et al. Clinical evaluation of integrated panel testing by nextgeneration sequencing for somatic mutations in neuroblastomas with MYCN unamplification. *Oncotarget*. 2017;8(30):49689-49701. doi:10.18632/oncotarget.17917

149. Lasorsa VA, Formicola D, Pignataro P, et al. Exome and deep sequencing of clinically aggressive neuroblastoma reveal somatic mutations that affect key pathways involved in cancer progression. *Oncotarget*. 2016;7(16):21840-218452. doi:10.18632/oncotarget.8187

150. DuBois SG, Kalika Y, Lukens JN, et al. Metastatic sites in stage IV and IVS neuroblastoma correlate with age, tumor biology, and survival. *J Pediatr Hematol Oncol*. 1999;21(3):181-189. doi:10.1097/00043426-199905000-00005

151. Reid MM, Pearson ADJ. Bone-marrow infiltration in neuroblastoma. *Lancet*. 1991;337(8742):681-682. doi:10.1016/0140-6736(91)92506-W

152. De Monte SML, Moore GW, Hutchins GM. Nonrandom distribution of metastases in neuroblastic tumors. *Cancer*. 1983;52(5):915-925. doi:10.1002/1097-0142(19830901)52:5<915::AID-CNCR2820520529>3.0.CO;2-7

153. Pantel K, Alix-Panabières C. Bone marrow as a reservoir for disseminated tumor cells: a special source for liquid biopsy in cancer patients. *Bonekey Rep*. 2014;3(584):1-6. doi:10.1038/bonekey.2014.79

154. Zaizen Y, Taniguchi S, Noguchi S, Suita S. The effect of N-myc amplification and expression on invasiveness of neuroblastoma cells. *J Pediatr Surg*. 1993;28(6):766-769. doi:10.1016/0022-3468(93)90321-B

155. Bénard J. Genetic alterations associated with metastatic dissemination and chemoresistance in neuroblastoma. *Eur J Cancer*. 1995;31A(4):560-564. doi:10.1016/0959-8049(95)00062-N

156. Goodman LA, Liu BCS, Thiele CJ, et al. Modulation of N-myc expression alters the invasiveness of neuroblastoma. *Clin Exp Metastasis*. 1997;15(2):130-139. doi:10.1023/A:1018448710006

157. Foroni L, Harrison CJ, Hoffbrand A V, Potter MN. Investigation of minimal residual disease in childhood and adult acute lymphoblastic leukaemia by molecular analysis. *Br J Haematol*. 1999;105(1):7-24.

158. Starza I Della, Chiaretti S, Propris MS De, et al. Minimal Residual Disease in Acute Lymphoblastic Leukemia : Technical and Clinical Advances. 2019;9(726):1-17. doi:10.3389/fonc.2019.00726

159. Bennett JM, Catovsky D, Daniel M -T, et al. Proposals for the Classification of the Acute Leukaemias French-American-British (FAB) Co-operative Group. *Br J Haematol*. 1976;33(4):451-458. doi:10.1111/j.1365-2141.1976.tb03563.x

160. Szczepański T, Orfão A, Van Der Velden VHJ, San Miguel JF, Van Dongen JJM. Minimal residual disease in leukaemia patients. *Lancet Oncol*. 2001;2(7):409-417. doi:10.1016/S1470-2045(00)00418-6

161. van der Velden VHJ, Cazzaniga G, Schrauder A, et al. Analysis of minimal residual disease by Ig/TCR gene rearrangements: guidelines for interpretation of real-time quantitative PCR data. *Leukemia*. 2007;21(4):604-611. doi:10.1038/sj.leu.2404586

162. Hokland P, Ommen HB. Towards individualized follow-up in adult acute myeloid leukemia in remission. *Blood*. 2011;117(9):2577-2584. doi:10.1182/blood-2010-09-303685

163. Buckley S a, Appelbaum FR, Walter RB. Prognostic and therapeutic implications of minimal residual disease at the time of transplantation in acute leukemia. *Bone Marrow Transplant*. 2013;48(5):630-641. doi:10.1038/bmt.2012.139

164. Cross N, Melo J, Feng L, Goldman J. An optimized multiplex polymerase chain reaction (PCR) for detection of BCR-ABL fusion mRNAs in haematological disorders. *Leukemia*. 1994;8(1):186-189.

165. Xiao Z, Greaves MF, Buffler P, et al. Molecular characterization of genomic AML1-ETO fusions in childhood leukemia. *Leukemia*. 2001;15(12):1906-1913. doi:10.1038/sj.leu.2402318

166. Cayuela JM, Baruchel A, Orange C, et al. TEL-AML1 fusion RNA as a new target to detect minimal residual disease in pediatric B-cell precursor acute lymphoblastic leukemia. *Blood*. 1996;88(1):302-308.

167. Campana D. Progress of minimal residual disease studies in childhood acute leukemia. *Curr Hematol Malig Rep*. 2010;5(3):169-176. doi:10.1007/s11899-010-0056-8

168. Hoffmann J, Krumbholz M, Gutiérrez H, et al. High sensitivity and clonal stability of the genomic fusion as single marker for response monitoring in ETV6-RUNX1 -positive acute lymphoblastic leukemia. 2019;(66):8. doi:10.1002/pbc.27780

169. Salto-Tellez M, Shelat SG, Benoit B, et al. Multiplex RT-PCR for the detection of leukemia-associated translocations: Validation and application to routine molecular diagnostic practice. *J Mol Diagnostics*. 2003;5(4):231-236. doi:10.1016/S1525-1578(10)60479-5

170. Murphy K, Weaver C. *Janeway's Immunobiology*. 9. Edition. Garland Science; 2016. doi:10.1201/9781315533247

171. Bartram CR, Yokota S, Biondi A, Janssen JWG, Hansen-Hagge TE. Detection of Minimal Residual Disease in Acute Lymphoblastic Leukemia Patients by Polymerase Chain Reactions. In: Hiddemann W, Büchner T, Wörmann B, Plunkett W, Keating M, Andreeff M, eds. *Acute Leukemias: Haematology and Blood Transfusion / Hämatologie Und Bluttransfusion*. Volume 34. Springer Berlin Heidelberg; 1992:171-177. doi:10.1007/978-3-642-76591-9_25

172. Eckert C, Biondi A, Seeger K, et al. Prognostic value of minimal residual disease in relapsed childhood acute lymphoblastic leukaemia. *Lancet*. 2001;358(9289):1239-1241. doi:10.1016/S0140-6736(01)06355-3

173. Szczepański T, van der Velden VHJ, Raff T, et al. Comparative analysis of T-cell receptor gene rearrangements at diagnosis and relapse of T-cell acute lymphoblastic leukemia (T-ALL) shows high stability of clonal markers for monitoring of minimal residual disease and reveals the occurence of second T-ALL. *Leukemia*. 2003;17(11):2149-2156. doi:10.1038/sj.leu.2403081

174. Guggemos A, Eckert C, Szczepanski T, et al. Assessment of clonal stability of minimal residual disease targets between 1st and 2nd relapse of childhood precursor B-cell acute lymphoblastic leukemia. *Haematologica*. 2003;88(7):737-746.

175. Pui CH, Robison LL, Look AT. Acute lymphoblastic leukaemia. *Lancet*. 2008;371(9617):1030-1043. doi:10.1016/S0140-6736(08)60457-2

176. Pongers-Willemse MJ, Verhagen OJHM, Tibbe GJM, et al. Real-time quantitative PCR for the detection of minimal residual disease in acute lymphoblastic leukemia using junctional region specific TaqMan probes. *Leukemia*. 1998;12(12):2006-2014. doi:10.1038/sj.leu.2401246

177. Eckert C, Landt O, Taube T, et al. Potential of LightCycler technology for quantification of minimal residual disease in childhood acute lymphoblastic leukemia. *Leukemia*. 2000;14(2):316-323. doi:10.1038/sj.leu.2401655

178. Cave H, van der Werff ten Bosch J, Suciu S, et al. Clinical significance of minimal residual disease in childhood acute lymphoblastic leukemia. European Organization for Research and Treatment of Cancer--Childhood Leukemia Cooperative Group. *N Engl J Med*. 1998;339(9):591-598. doi:10.1056/nejm199808273390904

179. van Dongen JJ, Seriu T, Panzer-Grümayer ER, et al. Prognostic value of minimal residual disease in acute lymphoblastic leukaemia in childhood. *Lancet*. 1998;352(9142):1731-1738. doi:10.1016/S0140-6736(98)04058-6

180. Raetz EA, Borowitz MJ, Devidas M, et al. Reinduction platform for children with first marrow relapse in acute lymphoblastic lymphoma. *J Clin Oncol*. 2008;26(24):3971-3978. doi:10.1200/JCO.2008.16.1414

181. Knechtli CJC, Goulden NJ, Hancock JP, et al. Minimal residual disease status before allogeneic bone marrow transplantation is an important determinant of successful outcome for children and adolescents with acute lymphoblastic leukemia. *Blood*. 1998;92(11):4072-4079. doi:10.1182/blood.v92.11.4072.423k33_4072_4079

182. Van Der Velden VHJ, Joosten SA, Willemse MJ, et al. Real-time quantitative PCR for detection of minimal residual disease before allogeneic stem cell transplantation predicts outcome in children with acute lymphoblastic leukemia. *Leukemia*. 2001;15(9):1485-1487. doi:10.1038/sj.leu.2402198

183. Bader P, Hancock J, Kreyenberg H, et al. Minimal residual disease (MRD) status prior to allogeneic stem cell transplantation is a powerful predictor for post-transplant outcome in children with ALL. *Leukemia*. 2002;16(9):1668-1672. doi:10.1038/sj.leu.2402552

184. Janni W, Rack B, Kasprowicz N, Scholz C, Hepp P. DTCs in breast cancer: Clinical research and practice. *Recent Results Cancer Res*. 2012;195:173-178. doi:10.1007/978-3-642-28160-0_15

185. Cackowski FC, Taichman RS. Minimal residual disease in prostate cancer. In: Julio A. Aguirre-Ghiso, ed. *Biological Mechanisms of Minimal Residual Disease and Systemic Cancer*. Vol 1100. Springer International Publishing; 2018:47-53. doi:10.1007/978-3-319-97746-1_3

186. Herbreteau G, Vallée A, Charpentier S, Normanno N, Hofman P, Denis MG. Circulating free tumor DNA in non-small cell lung cancer (NSCLC): Clinical application and future perspectives. *J Thorac Dis*. 2019;11:S113-S126. doi:10.21037/jtd.2018.12.18

187. Sproll C, Fluegen G, Stoecklein NH. Minimal residual disease in head and neck cancer and esophageal cancer. In: Aguirre-Ghiso JA, ed. *Biological Mechanisms of Minimal Residual Disease and Systemic Cancer*. Vol 1100. Springer International Publishing; 2018:55-82. doi:10.1007/978-3-319-97746-1_4

188. Bio-Rad Laboratories. Droplet Digital™ PCR (ddPCR™) Technology. Biorad. Published 2018. Accessed November 28, 2020. https://www.bio-rad.com/de-de/applications-technologies/droplet-digital-pcr-ddpcr-technology?ID=MDV31M4VY

189. Drandi D, Alcantara M, Benmaad I, et al. Droplet Digital PCR Quantification of Mantle Cell Lymphoma Follow-up Samples From Four Prospective Trials of the European MCL Network. *HemaSphere*. 2020;4(2):e347. doi:10.1097/HS9.0000000000000347

190. Whale AS, Huggett JF, Cowen S, et al. Comparison of microfluidic digital PCR and conventional quantitative PCR for measuring copy number variation. *Nucleic Acids Res*. 2012;40(11). doi:10.1093/nar/gks203

191. Day E, Dear PH, McCaughan F. Digital PCR strategies in the development and analysis of molecular biomarkers for personalized medicine. *Methods*. 2013;59(1):101-107. doi:10.1016/j.ymeth.2012.08.001

192. Kaufman RA, Thrall JH, Keyes JW, Brown ML, Zakem JF. False negative bone scans in neuroblastoma metastatic to the ends of long bones. *Am J Roentgenol*. 1978;130(1):131-135. doi:10.2214/ajr.130.1.131

193. Cozzutto C, de Bernardi B, Comelli A, Guarino M. Bone marrow biopsy in children: A study of 111 patients. *Med Pediatr Oncol*. 1979;6(1):57-64. doi:10.1002/mpo.2950060109

194. Moss TJ, Sanders DG. Detection of neuroblastoma cells in blood. *J Clin Oncol*. 1990;8(4):736-740. doi:10.1200/JCO.1990.8.4.736

195. Moss TJ, Reynolds CP, Sather HN, Romansky SG, Hammond GD, Seeger RC. Prognostic value of immunocytologic detection of bone marrow metastases in neuroblastoma. *NEnglJMed*. 1991;324(4):219-226. doi:10.1056/NEJM199101243240403

196. Tsang KS, Li CK, Tsoi WC, et al. Detection of micrometastasis of neuroblastoma to bone marrow and tumor dissemination to hematopoietic autografts using flow cytometry and reverse transcriptase-polymerase chain reaction. *Cancer*. 2003;97(11):2887-2897. doi:10.1002/cncr.11389

197. Komada Y, Zhang XL, Zhou YW, et al. Flow cytometric analysis of peripheral blood and bone marrow for tumor cells in patients with neuroblastoma. *Cancer*. 1998;82(3):591-599. doi:10.1002/(SICI)1097-0142(19980201)82:3<591::AID-CNCR23>3.0.CO;2-W

198. Schulz G, Cheresh DA, Varki NM, Staffilano LK, Reisfeld RA, Yu A. Detection of Ganglioside GD2 in Tumor Tissues and Sera of Neuroblastoma Patients. *Cancer Res*. 1984;44(12 Pt 1):5914-5920.

199. Cheung NK, Von Hoff DD, Strandjord SE, Coccia PF. Detection of neuroblastoma cells in bone marrow using GD2 specific monoclonal antibodies. *J Clin Oncol*. 1986;4(3):363-369. doi:10.1200/JCO.1986.4.3.363

200. Berthold F, Schneider A, Schumacher R, Bosslet K. Detection of Minimal Disease in Bone Marrow of Neuroblastoma Patients by Immunofluorescence. *Pediatr Hematol Oncol*. 1989;6(2):73-83. doi:10.3109/08880018909034273

201. Moss TJ, Reynolds CP, Sather HN, Romansky SG, Hammond GD, Seeger RC. Prognostic Value of Immunocytologic Detection of Bone Marrow Metastases in Neuroblastoma. *N Engl J Med*. 1991;324(4):219-226. doi:10.1056/NEJM199101243240403

202. van Wezel EM, Stutterheim J, Vree F, et al. Minimal residual disease detection in autologous stem cell

grafts from patients with high risk neuroblastoma. *Pediatr Blood Cancer*. 2015;62(8):1368-1373. doi:10.1002/pbc.25507

203. Cheung NK V., Ostrovnaya I, Kuk D, Cheung IY. Bone marrow minimal residual disease was an early response marker and a consistent independent predictor of survival after anti-GD2 immunotherapy. *J Clin Oncol*. 2015;33(7):755-763. doi:10.1200/JCO.2014.57.6777

204. Stutterheim J, Gerritsen A, Zappeij-Kannegieter L, et al. Detecting minimal residual disease in neuroblastoma: The superiority of a panel of real-time quantitative PCR markers. *Clin Chem*. 2009;55(7):1316-1326. doi:10.1373/clinchem.2008.117945

205. Avigad S, Feinberg-Gorenshtein G, Luria D, et al. Minimal Residual Disease in Peripheral Blood Stem Cell Harvests From High-risk Neuroblastoma Patients. *J Pediatr Hematol Oncol*. 2009;31(1).

206. Cheung IY, Feng Y, Gerald W, Cheung NK V. Exploiting gene expression profiling to identify novel minimal residual disease markers of neuroblastoma. *Clin Cancer Res*. 2008;14(21):7020-7027. doi:10.1158/1078-0432.CCR-08-0541

207. Ootsuka S, Asami S, Sasaki T, et al. Useful markers for detecting minimal residual disease in cases of neuroblastoma. *Biol Pharm Bull*. 2008;31(6):1071-1074. doi:10.1248/bpb.31.1071

208. Pession A, Libri V, Sartini R, et al. Real-time RT-PCR of tyrosine hydroxylase to detect bone marrow involvement in advanced neuroblastoma. *Oncol Rep*. 2003;10(2):357-362. doi:10.3892/or.10.2.357

209. Mhes G, Luegmayr A, Hattinger CM, et al. Outcome prediction by molecular detection of minimal residual disease in bone marrow for advanced neuroblastoma. *Med Pediatr Oncol*. 2001;36(1):203-204. doi:10.1002/1096-911X(20010101)36:1<203::AID-MPO1049>3.0.CO;2-T

210. Viprey VF, Gregory WM, Corrias M V., et al. Neuroblastoma mRNAs predict outcome in children with stage 4 neuroblastoma: A European HR-NBL1/SIOPEN study. *J Clin Oncol*. 2014;32(10):1074-1083. doi:10.1200/JCO.2013.53.3604

211. Beiske K, Burchill SA, Cheung IY, et al. Consensus criteria for sensitive detection of minimal neuroblastoma cells in bone marrow, blood and stem cell preparations by immunocytology and QRT-PCR: Recommendations by the International Neuroblastoma Risk Group Task Force. *Br J Cancer*. 2009;100(10):1627-1637. doi:10.1038/sj.bjc.6605029

212. Fukuda M, Miyajima Y, Miyashita Y, Horibe K. Disease outcome may be predicted by molecular detection of minimal residual disease in bone marrow in advanced neuroblastoma: A pilot study. *Am J Pediatr Hematol Oncol*. 2001;23(1):10-13. doi:10.1097/00043426-200101000-00004

213. Tchirkov A, Greze V, Plantaz D, Rouel N, Vago P, Kanold J. Very long-term molecular follow-up of minimal residual disease in patients with neuroblastoma. *Pediatr Blood Cancer*. 2018;65(12):e27404. doi:10.1002/pbc.27404

214. Chambon F, Tchirkov A, Pereira B, Rochette E, Deméocq F, Kanold J. Molecular assessment of minimal residual disease in PBSC harvests provides prognostic information in neuroblastoma. *Pediatr Blood Cancer*. 2013;60(9):E109-E112. doi:10.1002/pbc.24538

215. Hartomo TB, Kozaki A, Hasegawa D, et al. Minimal residual disease monitoring in neuroblastoma patients based on the expression of a set of real-time RT-PCR markers in tumor-initiating cells. *Oncol Rep*. 2013;29(4):1629-1636. doi:10.3892/or.2013.2286

216. Yáñez Y, Grau E, Oltra S, et al. Minimal disease detection in peripheral blood and bone marrow from patients with non-metastatic neuroblastoma. *J Cancer Res Clin Oncol*. 2011;137(8):1263-1272. doi:10.1007/s00432-011-0997-x

217. Träger C, Vernby Å, Kullman A, Øra I, Kogner P, Kågedal B. mRNAs of tyrosine hydroxylase and dopa decarboxylase but not of GD2 synthase are specific for neuroblastoma minimal disease and predicts outcome for children with high-risk disease when measured at diagnosis. *Int J Cancer*. 2008;123(12):2849-2855. doi:10.1002/ijc.23846

218. Viprey VF, Lastowska MA, Corrias M V., Swerts K, Jackson MS, Burchill SA. Minimal disease monitoring by QRT-PCR: Guidelines for identification and systematic validation of molecular markers prior to evaluation in prospective clinical trials. *J Pathol*. 2008;216(2):245-252. doi:10.1002/path.2406

219. Tanaka S, Tajiri T, Noguchi SI, et al. Clinical Significance of a Highly Sensitive Analysis for Gene Dosage and the Expression Level of MYCN in Neuroblastoma. *J Pediatr Surg*. 2004;39(1):63-68. doi:10.1016/j.jpedsurg.2003.09.015

220. Bordow SB, Norris MD, Haber PS, Marshall GM, Haber M. Prognostic significance of MYCN

oncogene expression in childhood neuroblastoma. *J Clin Oncol*. 1998;16(10):3286-3294. doi:10.1200/JCO.1998.16.10.3286

221. Valent A, Le Roux G, Barrois M, et al. MYCN gene overrepresentation detected in primary neuroblastoma tumour cells without amplification. *J Pathol*. 2002;198(4):495-501. doi:10.1002/path.1244

222. Wagner LM, Burger RA, Guichard SM, et al. Pilot study to evaluate MYCN expression as a neuroblastoma cell marker to detect minimal residual disease by RT-PCR. *J Pediatr Hematol Oncol*. 2006;28(10):635-641. doi:10.1097/01.mph.0000212976.13749.8a

223. Xi X, Li T, Huang Y, et al. RNA biomarkers: Frontier of precision medicine for cancer. *Non-coding RNA*. 2017;3(1):9. doi:10.3390/ncrna3010009

224. Gallego Romero I, Pai AA, Tung J, Gilad Y. RNA-seq: Impact of RNA degradation on transcript quantification. *BMC Biol*. 2014;12:42. doi:10.1186/1741-7007-12-42

225. Die J V., Román B. RNA quality assessment: A view from plant qPCR studies. *J Exp Bot*. 2012;63(17):6069-6077. doi:10.1093/jxb/ers276

226. Graham JR, Hendershott MC, Terragni J, Cooper GM. mRNA Degradation Plays a Significant Role in the Program of Gene Expression Regulated by Phosphatidylinositol 3-Kinase Signaling. *Mol Cell Biol*. 2010;30(22):5295-5305. doi:10.1128/mcb.00303-10

227. Stutterheim J, Zappeij-Kannegieter L, Øra I, et al. Stability of PCR targets for monitoring minimal residual disease in neuroblastoma. *J Mol Diagnostics*. 2012;14(2):168-175. doi:10.1016/j.jmoldx.2011.12.002

228. Thörn I, Olsson-Strömberg U, Ohlsen C, et al. The impact of RNA stabilization on minimal residual disease assessment in chronic myeloid leukemia. *Haematologica*. 2005;90(11):1471-1476. doi:10.1182/blood.v106.11.4490.4490

229. Mathew P, Valentine MB, Bowman LC, et al. Detection of MYCN gene amplification in neuroblastoma by fluorescence in situ hybridization: a pediatric oncology group study. *Neoplasia*. 2001;3(2):105-109. doi:10.1038/sj/neo/7900146

230. Bar-Am I, Mor O, Shiloh Y, Avivi L, Yeger H. Detection of amplified DNA sequences in human tumor cell lines by fluorescence in situ hybridization. *Genes Chromosomes Cancer*. 1992;4(4):314-320. doi:10.1002/gcc.2870040407

231. Squire JA, Thorner P, Marrano P, et al. Identification of MYCN copy number heterogeneity by direct FISH analysis of neuroblastoma preparations. *Mol Diagnosis*. 1996;1(4):281-289. doi:10.1016/S1084-8592(96)70010-3

232. Gilbert J, Norris MD, Haber M, Kavallaris M, Marshall GM, Stewart BW. Determination of N-myc gene amplification in neuroblastoma by differential polymerase chain reaction. *Mol Cell Probes*. 1993;7(3):227-234. doi:https://doi.org/10.1006/mcpr.1993.1033

233. Gallego S, Reventos J, De Toledo JS, Munell F. Differential polymerase chain reaction with serial dilutions for quantification of MYCN gene amplification in neuroblastoma. *Anticancer Res*. 1998;18(2A):1211-1215.

234. Hoebeeck J, Speleman F, Vandesompele J. Real-time quantitative PCR as an alternative to southern blot or fluorescence in situ hybridization for detection of gene copy number changes. *Methods Mol Biol*. 2007;353:205-226. doi:10.1385/1-59745-229-7:205

235. Oude Luttikhuis MEM, Iyer VK, Dyer S, Ramani P, McConville CM. Detection of MYCN amplification in neuroblastoma using competitive PCR quantitation. *Lab Investig*. 2000;80(2):271-273. doi:10.1038/labinvest.3780030

236. Oberthuer A, Juraeva D, Hero B, et al. Revised risk estimation and treatment stratification of low- and intermediate-risk neuroblastoma patients by integrating clinical and molecular prognostic markers. *Clin Cancer Res*. 2015;21(8):1904-1915. doi:10.1158/1078-0432.CCR-14-0817

237. Simon T, Spitz R, Faldum A, Hero B, Berthold F. New definition of low-risk neuroblastoma using stage, age, and 1p and MYCN status. *J Pediatr Hematol Oncol*. 2004;26(12):791-796.

238. Oberthuer A, Hero B, Berthold F, et al. Prognostic impact of gene expression-based classification for neuroblastoma. *J Clin Oncol*. 2010;28(21):3506-3515. doi:10.1200/JCO.2009.27.3367

239. Raggi CC, Bagnoni ML, Tonini GP, et al. Real-time quantitative PCR for the measurement of MYCN

amplification in human neuroblastoma with the TaqMan detection system. *Clin Chem*. 1999;45(11):1918-1924.

240. Boensch M, Oberthuer A, Fischer M, et al. Quantitative real-time PCR for quick simultaneous determination of therapy-stratifying markers MYCN amplification, deletion 1p and 11q. *Diagnostic Mol Pathol*. 2005;14(3):177-182. doi:10.1097/01.pas.0000176767.10800.17

241. Souzaki R, Tajiri T, Higashi M, et al. Clinical implications of a slight increase in the gene dosage of MYCN in neuroblastoma determined using quantitative PCR. *Pediatr Surg Int*. 2008;24(10):1095-1100. doi:10.1007/s00383-008-2228-3

242. Souza ACMF, Souza DRV, Sanabani SS, Giorgi RR, Bendit I. The performance of semi-quantitative differential PCR is similar to that of real-time PCR for the detection of the MYCN gene in neuroblastomas. *Brazilian J Med Biol Res*. 2009;42(9):791-795. doi:10.1590/S0100-879X2009000900004

243. Weber A, Taube S, Starke S, Bergmann E, Christiansen NM, Christiansen H. Technical advance Detection of human tumor cells by amplicon fusion site polymerase chain reaction (AFS-PCR). *J Clin Invest*. 2011;121(2):545-553. doi:10.1172/JCI44415DS1

244. Janoueix-Lerosey I, Schleiermacher G, Michels E, et al. Overall genomic pattern is a predictor of outcome in neuroblastoma. *J Clin Oncol*. 2009;27(7):1026-1033. doi:10.1200/JCO.2008.16.0630

245. Van Wezel EM, Zwijnenburg D, Zappeij-Kannegieter L, et al. Whole-genome sequencing identifies patient-specific DNA minimal residual disease markers in neuroblastoma. *J Mol Diagnostics*. 2015;17(1):43-52. doi:10.1016/j.jmoldx.2014.09.005

246. Ponchel F, Toomes C, Bransfield K, et al. Real-time PCR based on SYBR-Green I fluorescence: An alternative to the TaqMan assay for a relative quantification of gene rearrangements, gene amplifications and micro gene deletions. *BMC Biotechnol*. 2003;3:18. doi:10.1186/1472-6750-3-18

247. Weber A, Taube S, Starke S, Bergmann E, Christiansen NM, Christiansen H. Detection of human tumor cells by amplicon fusion site polymerase chain reaction (AFS-PCR). *J Clin Invest*. 2011;121(2):545-553. doi:10.1172/JCI44415

248. Cheung N-K V., Cohn SL, eds. *Neuroblastoma*. Springer-Verlag Berlin Heidelberg; 2005. doi:https://doi.org/10.1007/b137762

249. Øra I, Eggert A. Progress in treatment and risk stratification of neuroblastoma: Impact on future clinical and basic research. *Semin Cancer Biol*. 2011;21(4):217-228. doi:10.1016/j.semcancer.2011.07.002

250. George RE, Diller L, Bernstein ML. Pharmacotherapy of neuroblastoma. *Expert Opin Pharmacother*. 2010;11(9):1467-1478. doi:10.1517/14656566.2010.482100

251. Ladenstein R, Pötschger U, Pearson ADJ, et al. Busulfan and melphalan versus carboplatin, etoposide, and melphalan as high-dose chemotherapy for high-risk neuroblastoma (HR-NBL1/SIOPEN): an international, randomised, multi-arm, open-label, phase 3 trial. *Lancet Oncol*. 2017;18(4):500-514. doi:10.1016/S1470-2045(17)30070-0

252. Amoroso L, Erminio G, Makin G, et al. Topotecan-vincristine-doxorubicin in stage 4 high-risk neuroblastoma patients failing to achieve a complete metastatic response to rapid COJEC: A SIOPEN study. *Cancer Res Treat*. 2018;50(1):148-155. doi:10.4143/crt.2016.511

253. Malhotra V, Perry MC. Classical chemotherapy: mechanisms, toxicities and the therapeutic window. *Cancer Biol Ther*. 2003;2(4 Suppl 1):2-4. doi:10.4161/cbt.199

254. Sweiss KI, Beri R, Shord SS. Encephalopathy after high-dose ifosfamide: A retrospective cohort study and review of the literature. *Drug Saf*. 2008;31(11):989-996. doi:10.2165/00002018-200831110-00003

255. Laverdiere C, Cheung NK V, Kushner BH, et al. Long term complications from treatment in survivors of high risk neuroblastoma. *J Clin Oncol*. 2004;22(14_suppl):8543. doi:10.1200/jco.2004.22.90140.8543

256. Keyel ME, Reynolds CP. Spotlight on dinutuximab in the treatment of high-risk neuroblastoma: Development and place in therapy. *Biol Targets Ther*. 2019;13:1-12. doi:10.2147/BTT.S114530

257. Schengrund CL, Shochat SJ. Gangliosides in Neuroblastomas. *Neurochem Pathol*. 1988;8(3):189-202. doi:10.1007/BF03160146

258. Schumacher-Kuckelkorn R, Volland R, Gradehandt A, Hero B, Simon T, Berthold F. Lack of immunocytological GD2 expression on neuroblastoma cells in bone marrow at diagnosis, during treatment, and at recurrence. *Pediatr Blood Cancer*. 2017;64(1):46-56. doi:10.1002/pbc.26184

259. U.S. National Library of Medicine. Phase I Study of LDK378 in Pediatric, Malignancies With a Genetic Alteration in Anaplastic Lymphoma Kinase (ALK). ClinicalTrials.gov Identifier: NCT01742286. Published 2020. Accessed November 28, 2020. https://clinicaltrials.gov/ct2/show/NCT01742286

260. U.S. National Library of Medicine. NANT 2015-02: A Phase 1 Study of Lorlatinib (PF-06463922). ClinicalTrials.gov Identifier: NCT03107988. Published 2019. Accessed November 28, 2020. https://clinicaltrials.gov/ct2/show/NCT03107988

261. Sawyers C. Targeted cancer therapy. *Nature*. 2004;432(7015):294-297. doi:10.1038/nature03095

262. Wang LL, Teshiba R, Ikegaki N, et al. Augmented expression of MYC and/or MYCN protein defines highly aggressive MYC-driven neuroblastoma: A Children's Oncology Group study. *Br J Cancer*. 2015;113(1):57-63. doi:10.1038/bjc.2015.188

263. Prochownik E V., Vogt PK. Therapeutic Targeting of Myc. *Genes Cancer*. 2010;1(6):650-659. doi:10.1177/1947601910377494

264. Esposito MR, Aveic S, Seydel A, Tonini GP. Neuroblastoma treatment in the post-genomic era. 2017;24(1):14. doi:10.1186/s12929-017-0319-y

265. Kantarjian H, O'Brien S, Jabbour E, et al. Improved survival in chronic myeloid leukemia since the introduction of imatinib therapy: A single-institution historical experience. *Blood*. 2012;119(9):1981-1987. doi:10.1182/blood-2011-08-358135

266. Speleman F, Park JR, Henderson TO. Neuroblastoma: A Tough Nut to Crack. *Am Soc Clin Oncol - Educ B*. 2016;35:e548-557. doi:10.1200/EDBK_159169

267. Barone G, Anderson J, Pearson ADJ, Petrie K, Chesler L. New strategies in neuroblastoma: Therapeutic targeting of MYCN and ALK. *Clin Cancer Res*. 2013;19(21):5814-5821. doi:10.1158/1078-0432.CCR-13-0680

268. Yardley DA. Drug Resistance and the Role of Combination Chemotherapy in Improving Patient Outcomes. *Int J Breast Cancer*. 2013;2013(13741). doi:10.1155/2013/137414

269. Saputra EC, Huang L, Chen Y, Tucker-Kellogg L. Combination therapy and the evolution of resistance: The theoretical merits of synergism and antagonism in cancer. *Cancer Res*. 2018;78(9):2419-2431. doi:10.1158/0008-5472.CAN-17-1201

270. Serfling E, Lübbe A, Dorsch-Häsler K, Schaffner W. Metal-dependent SV40 viruses containing inducible enhancers from the upstream region of metallothionein genes. *EMBO J*. 1985;4(13B):3851-3859. doi:10.1002/j.1460-2075.1985.tb04157.x

271. Hnisz D, Abraham BJ, Lee TI, et al. Super-enhancers in the control of cell identity and disease. *Cell*. 2013;155(4):934-947. doi:10.1016/j.cell.2013.09.053

272. Saint-André V, Federation AJ, Lin CY, et al. Models of human core transcriptional regulatory circuitries. *Genome Res*. 2016;26(3):385-396. doi:10.1101/gr.197590.115

273. Jia Y, Chng WJ, Zhou J. Super-enhancers: Critical roles and therapeutic targets in hematologic malignancies. *J Hematol Oncol*. 2019;12(1):77. doi:10.1186/s13045-019-0757-y

274. Creyghton MP, Cheng AW, Welstead GG, et al. Histone H3K27ac separates active from poised enhancers and predicts developmental state. *Proc Natl Acad Sci USA*. 2010;107(50):21931-21936. doi:10.1073/pnas.1016071107

275. Upton K, Modi A, Patel K, et al. Epigenomic profiling of neuroblastoma cell lines. *Sci Data*. 2020;7(1):116. doi:10.1038/s41597-020-0458-y

276. Allfrey VG, Mirsky AE. Structural modifications of histones and their possible role in the regulation of RNA synthesis. *Science*. 1964;144(3618):559. doi:10.1126/science.144.3618.559

277. Bannister AJ, Kouzarides T. Regulation of chromatin by histone modifications. *Cell Res*. 2011;21(3):381-395. doi:10.1038/cr.2011.22

278. Marushige K. Activation of chromatin by acetylation of histone side chains. *Proc Natl Acad Sci USA*. 1976;73(11):3937-3941. doi:10.1073/pnas.73.11.3937

279. Shi J, Vakoc CR. The Mechanisms behind the Therapeutic Activity of BET Bromodomain Inhibition. *Mol Cell*. 2014;54(5):728-736. doi:10.1016/j.molcel.2014.05.016

280. Ferri E, Petosa C, McKenna CE. Bromodomains: Structure, function and pharmacology of inhibition. *Biochem Pharmacol*. 2016;106:1-18. doi:10.1016/j.bcp.2015.12.005

281. Jain AK, Barton MC. Bromodomain Histone Readers and Cancer. *J Mol Biol*. 2017;429(13):2003-2010. doi:10.1016/j.jmb.2016.11.020

282. Henssen A, Althoff K, Odersky A, et al. Targeting MYCN-driven transcription by BET-bromodomain inhibition. *Clin Cancer Res*. 2016;22(10):2470-2481. doi:10.1158/1078-0432.CCR-15-1449

283. Pivot-Pajot C, Caron C, Govin J, Vion A, Rousseaux S, Khochbin S. Acetylation-Dependent Chromatin Reorganization by BRDT, a Testis-Specific Bromodomain-Containing Protein. *Mol Cell Biol*. 2003;23(15):5354-5365. doi:10.1128/mcb.23.15.5354-5365.2003

284. Donati B, Lorenzini E, Ciarrocchi A. BRD4 and Cancer: Going beyond transcriptional regulation. *Mol Cancer*. 2018;17(1):164. doi:10.1186/s12943-018-0915-9

285. Puissant A, Frumm SM, Alexe G, et al. Targeting MYCN in neuroblastoma by BET bromodomain inhibition. *Cancer Discov*. 2013;3(3):308-323. doi:10.1158/2159-8290.CD-12-0418

286. Belkina AC, Denis G V. BET domain co-regulators in obesity, inflammation and cancer. *Nat Rev Cancer*. 2012;12(7):465-477. doi:10.1038/nrc3256

287. Morgado-Pascual JL, Rayego-Mateos S, Tejedor L, Suarez-Alvarez B, Ruiz-Ortega M. Bromodomain and extraterminal proteins as novel epigenetic targets for renal diseases. *Front Pharmacol*. 2019;10:1315. doi:10.3389/fphar.2019.01315

288. Devaiah BN, Singer DS. Two faces of BRD4: Mitotic bookmark and transcriptional lynchpin. *Transcription*. 2013;4(1):13-17. doi:10.4161/trns.22542

289. Filippakopoulos P, Picaud S, Mangos M, et al. Histone recognition and large-scale structural analysis of the human bromodomain family. *Cell*. 2012;149(1):214-231. doi:10.1016/j.cell.2012.02.013

290. Moon KJ, Mochizuki K, Zhou M, Jeong HS, Brady JN, Ozato K. The bromodomain protein Brd4 is a positive regulatory component of P-TEFb and stimulates RNA polymerase II-dependent transcription. *Mol Cell*. 2005;19(4):523-534. doi:10.1016/j.molcel.2005.06.027

291. Yang Z, He N, Zhou Q. Brd4 Recruits P-TEFb to Chromosomes at Late Mitosis To Promote G1 Gene Expression and Cell Cycle Progression. *Mol Cell Biol*. 2008;28(3):967-976. doi:10.1128/mcb.01020-07

292. Devaiah BN, Case-Borden C, Gegonne A, et al. BRD4 is a histone acetyltransferase that evicts nucleosomes from chromatin. *Nat Struct Mol Biol*. 2016;23(6):540-548. doi:10.1038/nsmb.3228

293. Devaiah BN, Lewis BA, Cherman N, et al. BRD4 is an atypical kinase that phosphorylates Serine2 of the RNA Polymerase II carboxy-terminal domain. *Proc Natl Acad Sci USA*. 2012;109(18):6927-6932. doi:10.1073/pnas.1120422109

294. Kanno T, Kanno Y, Leroy G, et al. BRD4 assists elongation of both coding and enhancer RNAs by interacting with acetylated histones. *Nat Struct Mol Biol*. 2014;21(12):1047-1057. doi:10.1038/nsmb.2912

295. French CA. Pathogenesis of NUT midline carcinoma. *Annu Rev Pathol Mech Dis*. 2012;7:247-265. doi:10.1146/annurev-pathol-011811-132438

296. Filippakopoulos P, Qi J, Picaud S, et al. Selective inhibition of BET bromodomains. *Nature*. 2010;468(7327):1067-1073. doi:10.1038/nature09504

297. Pasqua AE, Wilding B, Cheeseman MD, Jones K. Targeting Protein Synthesis, Folding, and Degradation Pathways in Cancer. In: Chackalamannil S, Rotella D, Ward SEBT-CMCIII, eds. *Comprehensive Medicinal Chemistry III (Reference Module in Chemistry, Molecular Sciences and Chemical Engineering)*. Elsevier; 2017:202-280. doi:https://doi.org/10.1016/B978-0-12-409547-2.12395-9

298. Delmore JE, Issa GC, Lemieux ME, et al. BET bromodomain inhibition as a therapeutic strategy to target c-Myc. *Cell*. 2011;146(6):904-917. doi:10.1016/j.cell.2011.08.017

299. Stathis A, Bertoni F. BET proteins as targets for anticancer treatment. *Cancer Discov*. 2018;8(1):24-36. doi:10.1158/2159-8290.CD-17-0605

300. Lee S, Rellinger EJ, Kim KW, et al. Bromodomain and extraterminal inhibition blocks tumor progression and promotes differentiation in neuroblastoma. *Surg (United States)*. 2015;158(3):819-826. doi:10.1016/j.surg.2015.04.017

301. Li F, MacKenzie KR, Jain P, Santini C, Young DW, Matzuk MM. Metabolism of JQ1, an inhibitor of bromodomain and extra terminal bromodomain proteins, in human and mouse liver microsomes. *Biol Reprod*. 2020;103(2):427-436. doi:10.1093/biolre/ioaa043

302. Herait P, Dombret H, Thieblemont C, et al. BET-bromodomain (BRD) inhibitor OTX015: Final results of the dose-finding part of a phase I study in hematologic malignancies. *Ann Oncol*. 2015;26(Supplement 2):Page ii10. doi:10.1093/annonc/mdv085.3

303. Noel JK, Iwata K, Ooike S, Sugahara K, Nakamura H, Daibata M. Abstract C244: Development of the BET bromodomain inhibitor OTX015. *Mol Cancer Ther*. 2013;12(11 Supplement):C244 LP-C244. doi:10.1158/1535-7163.TARG-13-C244

304. Lin X, Huang X, Uziel T, et al. HEXIM1 as a robust pharmacodynamic marker for monitoring target engagement of BET family bromodomain inhibitors in tumors and surrogate tissues. *Mol Cancer Ther*. 2017;16(2):388-396. doi:10.1158/1535-7163.MCT-16-0475

305. Shapiro GI, Dowlati A, LoRusso PM, et al. Abstract A49: Clinically efficacy of the BET bromodomain inhibitor TEN-010 in an open-label substudy with patients with documented NUT-midline carcinoma (NMC). *Mol Targets Cancer Ther*. 2015;14(12 Supplement 2):A49. doi:10.1158/1535-7163.targ-15-a49

306. U.S. National Library of Medicine. TEN-010 clinical trials. Published 2020. Accessed November 28, 2020. https://clinicaltrials.gov/ct2/results?cond=&term=TEN-010&cntry=&state=&city=&dist=

307. Liu Z, Wang P, Chen H, et al. Drug Discovery Targeting Bromodomain-Containing Protein 4. *J Med Chem*. 2017;60(11):4533-4558. doi:10.1021/acs.jmedchem.6b01761

308. Felgenhauer J, Tomino L, Selich-Anderson J, Bopp E, Shah N. Dual BRD4 and AURKA Inhibition Is Synergistic against MYCN-Amplified and Nonamplified Neuroblastoma. *Neoplasia*. 2018;20(10):965-974. doi:10.1016/j.neo.2018.08.002

309. Wyce A, Ganji G, Smitheman KN, et al. BET Inhibition Silences Expression of MYCN and BCL2 and Induces Cytotoxicity in Neuroblastoma Tumor Models. *PLoS One*. 2013;8(8):e72967. doi:10.1371/journal.pone.0072967

310. Nortmeyer MC. MYCN dependency of MYCN amplified neuroblastoma cell lines analyzed in relation to their interaction with BET proteins and in a novel orthotopic mouse model. Published online 2019. https://doi.org/10.11588/heidok.00026656

311. Postel-Vinay S, Herbschleb K, Massard C, et al. First-in-human phase I study of the bromodomain and extraterminal motif inhibitor BAY 1238097: emerging pharmacokinetic/pharmacodynamic relationship and early termination due to unexpected toxicity. *Eur J Cancer*. 2019;109:103-110. doi:10.1016/j.ejca.2018.12.020

312. U.S. National Library of Medicine, National Institutes of Health. ClinicalTrials.gov: BET inhibitor studies. Published 2020. Accessed November 28, 2020. https://clinicaltrials.gov/ct2/results?cond=&term=BET+inhibitor&cntry=&state=&city=&dist=

313. Stonestrom AJ, Hsu SC, Werner MT, Blobel GA. Erythropoiesis provides a BRD's eye view of BET protein function. *Drug Discov Today Technol*. 2016;19:23-28. doi:10.1016/j.ddtec.2016.05.004

314. Amorim S, Stathis A, Gleeson M, et al. Bromodomain inhibitor OTX015 in patients with lymphoma or multiple myeloma: A dose-escalation, open-label, pharmacokinetic, phase 1 study. *Lancet Haematol*. 2016;3(4):196-204. doi:10.1016/S2352-3026(16)00021-1

315. Ocana A, Corrales-Sanchez V, Perez Peña J, et al. Anti-proliferative activity of bromodomain inhibitors JQ1 and OTX015 in triple negative breast cancer. *J Clin Oncol*. 2015;33(15_suppl):e12078-e12078. doi:10.1200/jco.2015.33.15_suppl.e12078

316. Rizzitano S, Cavanè A, Piazzoni M, et al. Synergistic Anti-Tumor Efficacy of BET Inhibitors JQ1 and Otx-015 in Combination with Dasatinib in Preclinical Models of T-Cell Lymphomas. *Blood*. 2016;128(22):3967. doi:10.1182/blood.V128.22.3967.3967

317. Gu L, Zhang H, He J, Li J, Huang M, Zhou M. MDM2 regulates MYCN mRNA stabilization and translation in human neuroblastoma cells. *Oncogene*. 2012;31(11):1342-1353. doi:10.1038/onc.2011.343

318. Arnhold V, Schmelz K, Proba J, et al. Reactivating TP53 signaling by the novel MDM2 inhibitor DS-3032b as a therapeutic option for high-risk neuroblastoma. *Oncotarget*. 2018;9(2):2304-2319. doi:10.18632/oncotarget.23409

319. Van Maerken T, Rihani A, Dreidax D, et al. Functional analysis of the p53 pathway in neuroblastoma cells using the small-molecule MDM2 antagonist nutlin-3. *Mol Cancer Ther*. 2011;10(6):983-993. doi:10.1158/1535-7163.MCT-10-1090

320. Toledo F, Wahl GM. Regulating the p53 pathway: In vitro hypotheses, in vivo veritas. *Nat Rev Cancer*. 2006;6(12):909-923. doi:10.1038/nrc2012

321. Powers JT, Tsanov KM, Pearson DS, et al. Multiple mechanisms disrupt the let-7 microRNA family in neuroblastoma. *Nature*. 2016;535(7611):246-251. doi:10.1038/nature18632

322. Molenaar JJ, Domingo-Fernández R, Ebus ME, et al. LIN28B induces neuroblastoma and enhances MYCN levels via let-7 suppression. *Nat Genet*. 2012;44(11):1199-1206. doi:10.1038/ng.2436

323. Wang QZ, Lv YH, Gong YH, et al. Double-stranded Let-7 mimics, potential candidates for cancer gene therapy. *J Physiol Biochem*. 2012;68(1):107-119. doi:10.1007/s13105-011-0124-0

324. Fontana L, Fiori ME, Albini S, et al. Antagomir-17-5p abolishes the growth of therapy-resistant neuroblastoma through p21 and BIM. *PLoS One*. 2008;3(5):e2236. doi:10.1371/journal.pone.0002236

325. Tivnan A, Orr WS, Gubala V, et al. Inhibition of neuroblastoma tumor growth by targeted delivery of microRNA-34a using anti-disialoganglioside GD2 coated nanoparticles. *PLoS One*. 2012;7(5):e38129. doi:10.1371/journal.pone.0038129

326. Maeshima R, Moulding D, Stoker AW, Hart SL. MYCN Silencing by RNA Interference Induces Neurogenesis and Suppresses Proliferation in Models of Neuroblastoma with Resistance to Retinoic Acid. *Nucleic Acid Ther*. 2020;30(4):237-248. doi:10.1089/nat.2019.0831

327. Nara K, Kusafuka T, Yoneda A, Oue T, Sangkhathat S, Fukuzawa M. Silencing of MYCN by RNA interference induces growth inhibition, apoptotic activity and cell differentiation in a neuroblastoma cell line with MYCN amplification. *Int J Oncol*. 2007;30(5):1189-1196. doi:10.3892/ijo.30.5.1189

328. Feng C, Wang T, Tang R, et al. Silencing of the MYCN gene by siRNA delivered by folate receptor-targeted liposomes in LA-N-5 cells. *Pediatr Surg Int*. 2010;26(12):1185-1191. doi:10.1007/s00383-010-2703-5

329. Li Y, Zhuo B, Yin Y, et al. Anti-cancer effect of oncolytic adenovirus-armed shRNA targeting MYCN gene on doxorubicin-resistant neuroblastoma cells. *Biochem Biophys Res Commun*. 2017;491(1):134-139. doi:10.1016/j.bbrc.2017.07.062

330. Adams D, Gonzalez-Duarte A, O'Riordan WD, et al. Patisiran, an RNAi therapeutic, for hereditary transthyretin amyloidosis. *N Engl J Med*. 2018;379(1):11-21. doi:10.1056/NEJMoa1716153

331. Bonneau E, Neveu B, Kostantin E, Tsongalis GJ, De Guire V. How close are miRNAs from clinical practice? A perspective on the diagnostic and therapeutic market. *Electron J Int Fed Clin Chem Lab Med*. 2019;30(2):114-127.

332. Hanna J, Hossain GS, Kocerha J. The potential for microRNA therapeutics and clinical research. *Front Genet*. 2019;10:478. doi:10.3389/fgene.2019.00478

333. Stanton BR, Perkins AS, Tessarollo L, Sassoon DA, Parada LF. Loss of N-myc function results in embryonic lethality and failure of the epithelial component of the embryo to develop. *Genes Dev*. 1992;6(12A):2235-2247. doi:10.1101/gad.6.12a.2235

334. Kramer M, Ribeiro D, Arsenian-Henriksson M, Deller T, Rohrer H. Proliferation and survival of embryonic sympathetic neuroblasts by MYCN and activated ALK signaling. *J Neurosci*. 2016;36(40):10425-10439. doi:10.1523/JNEUROSCI.0183-16.2016

335. Xu F, Na L, Li Y, Chen L. Roles of the PI3K/AKT/mTOR signalling pathways in neurodegenerative diseases and tumours. *Cell Biosci*. 2020;10:54. doi:10.1186/s13578-020-00416-0

336. Berry T, Luther W, Bhatnagar N, et al. The ALKF1174L Mutation Potentiates the Oncogenic Activity of MYCN in Neuroblastoma. *Cancer Cell*. 2012;22(1):117-130. doi:10.1016/j.ccr.2012.06.001

337. Zhu S, Lee JS, Guo F, et al. Activated ALK Collaborates with MYCN in Neuroblastoma Pathogenesis. *Cancer Cell*. 2012;21(3):362-373. doi:10.1016/j.ccr.2012.02.010

338. Umapathy G, Wakil A El, Witek B, et al. The kinase ALK stimulates the kinase ERK5 to promote the expression of the oncogene MYCN in neuroblastoma. *Sci Signal*. 2014;7(349):ra102. doi:10.1126/scisignal.2005470

339. Brana I, Siu LL. Clinical development of phosphatidylinositol 3-kinase inhibitors for cancer treatment. *BMC Med*. 2012;10:161. doi:10.1186/1741-7015-10-161

340. Engelman JA. Targeting PI3K signalling in cancer: Opportunities, challenges and limitations. *Nat Rev Cancer*. 2009;550:62. doi:10.1038/nrc2664

341. Westhoff MA, Faham N, Marx D, et al. Sequential dosing in chemosensitization: Targeting the PI3K/Akt/mTOR pathway in neuroblastoma. *PLoS One*. 2013;8(12):e83128. doi:10.1371/journal.pone.0083128

342. Dam V, Morgan BT, Mazanek P, Hogarty MD. Mutations in PIK3CA are infrequent in neuroblastoma. *BMC Cancer*. 2006;6:177. doi:10.1186/1471-2407-6-177

343. Chesler L, Schlieve C, Goldenberg DD, et al. Inhibition of phosphatidylinositol 3-kinase destabilizes Mycn protein and blocks malignant progression in neuroblastoma. *Cancer Res*. 2006;66(16):8139-8146. doi:10.1158/0008-5472.CAN-05-2769

344. Markham A. Alpelisib: First Global Approval. *Drugs*. 2019;79(11):1249-1253. doi:10.1007/s40265-019-01161-6

345. Zhang M, Jang H, Nussinov R. PI3K inhibitors: review and new strategies. *Chem Sci*. 2020;11(23):5855-5865. doi:10.1039/d0sc01676d

346. Barra F, Ferro Desideri L, Ferrero S. Inhibition of PI3K/AKT/mTOR pathway for the treatment of endometriosis. *Br J Pharmacol*. 2018;175(17):3626-3627. doi:10.1111/bph.14391

347. Cage TA, Chanthery Y, Chesler L, et al. Downregulation of MYCN through PI3K inhibition in mouse models of pediatric neural cancer. *Front Oncol*. 2015;5:111. doi:10.3389/fonc.2015.00111

348. Geng X, Xie L, Xing H. PI3K Inhibitor Combined With Chemotherapy Can Enhance the Apoptosis of Neuroblastoma Cells In Vitro and In Vivo. *Technol Cancer Res Treat*. 2015;15(5):716-722. doi:10.1177/1533034615597366

349. Kang J, Rychahou PG, Ishola TA, Mourot JM, Evers BM, Chung DH. N-myc is a novel regulator of PI3K-mediated VEGF expression in neuroblastoma. *Oncogene*. 2008;27(28):3999-4007. doi:10.1038/onc.2008.15

350. Weiss WA, Aldape K, Mohapatra G, et al. Targeted expression of MYCN causes neuroblastoma in transgenic mice. *EMBO J*. 1997;16(11):2985-2995. doi:10.1093/emboj/16.11.2985

351. Arrowsmith CH, Audia JE, Austin C, et al. The promise and peril of chemical probes. *Nat Chem Biol*. 2015;11(8):536-541. doi:10.1038/nchembio.1867

352. U.S. National Library of Medicine. Clinical Trials Using Alpelisib. Published 2020. Accessed November 28, 2020. https://www.cancer.gov/about-cancer/treatment/clinical-trials/intervention/alpelisib

353. U.S. National Library of Medicine. Study of Safety and Efficacy of Alpelisib With Everolimus or Alpelisib With Everolimus and Exemestane in Advanced Breast Cancer Patients, Renal Cell Cancer and Pancreatic Tumors. ClinicalTrials.gov Identifier: NCT02077933. Published 2020. Accessed November 28, 2020. https://clinicaltrials.gov/ct2/show/NCT02077933

354. Avendaño C, Menéndez JC. Drugs That Inhibit Signalling Pathways for Tumor Cell Growth and Proliferation. In: Avendaño C, Menéndez JC, eds. *Medicinal Chemistry of Anticancer Drugs*. 1st ed. Elsevier; 2008:251-305. doi:10.1016/b978-0-444-52824-7.00009-3

355. Kiessling MK, Curioni-Fontecedro A, Samaras P, et al. Targeting the mTOR complex by everolimus in NRAS mutant neuroblastoma. *PLoS One*. 2016;11(1):e0147682. doi:10.1371/journal.pone.0147682

356. Zhang H, Dou J, Yu Y, et al. MTOR ATP-competitive inhibitor INK128 inhibits neuroblastoma growth via blocking mTORC signaling. *Apoptosis*. 2015;20(1):50-62. doi:10.1007/s10495-014-1066-0

357. Mohlin S, Hansson K, Radke K, et al. Anti-tumor effects of PIM / PI3K/ mTOR triple kinase inhibitor IBL-302 in neuroblastoma. *EMBO Mol Med*. 2019;11(8):e10058. doi:10.15252/emmm.201810058

358. Hart LS, Chen L, Batra V, et al. Abstract 3494: Combined MEK1/2 and PI3K inhibition induces synergistic caspase-dependent apoptosis in neuroblastoma. *Cancer Res*. 2015;75(15 Supplement):pp.3494. doi:doi.org/10.1158/1538-7445.AM2015-3494

359. Kurmasheva RT, Harwood FC, Houghton PJ. Differential regulation of vascular endothelial growth factor by Akt and mammalian target of rapamycin inhibitors in cell lines derived from childhood solid tumors. *Mol Cancer Ther*. 2007;6(5):1620-1628. doi:10.1158/1535-7163.MCT-06-0646

360. Li Z, Tan F, Liewehr DJ, Steinberg SM, Thiele CJ. In vitro and in vivo inhibition of neuroblastoma tumor cell growth by AKT inhibitor perifosine. *J Natl Cancer Inst*. 2010;102(11):758-770. doi:10.1093/jnci/djq125

361. Segerström L, Baryawno N, Sveinbjörnsson B, et al. Effects of small molecule inhibitors of PI3K/Akt/mTOR signaling on neuroblastoma growth in vitro and in vivo. *Int J Cancer*. 2011;129(12):2958-2965. doi:10.1002/ijc.26268

362. Vaughan L, Clarke PA, Barker K, et al. Inhibition of mTOR-kinase destabilizes MYCN and is a potential therapy for MYCN-dependent tumors. *Oncotarget*. 2016;7(36):57525-57544.

doi:10.18632/oncotarget.10544

363. Jin N, Jiang T, Rosen DM, Nelkin BD, Ball DW. Synergistic action of a RAF inhibitor and a dual PI3K/mTOR inhibitor in thyroid cancer. *Clin Cancer Res*. 2011;17(20):6482-6489. doi:10.1158/1078-0432.CCR-11-0933

364. Bhatt AP, Bhende PM, Sin SH, Roy D, Dittmer DP, Damania B. Dual inhibition of PI3K and mTOR inhibits autocrine and paracrine proliferative loops in PI3K/Akt/mTOR-addicted lymphomas. *Blood*. 2010;115(22):4455-4463. doi:10.1182/blood-2009-10-251082

365. Sathe A, Chalaud G, Oppolzer I, et al. Parallel PI3K, AKT and mTOR inhibition is required to control feedback loops that limit tumor therapy. *PLoS One*. 2018;13(1):e0190854. doi:10.1371/journal.pone.0190854

366. Seitz C, Hugle M, Cristofanon S, Tchoghandjian A, Fulda S. The dual PI3K/mTOR inhibitor NVP-BEZ235 and chloroquine synergize to trigger apoptosis via mitochondrial-lysosomal cross-talk. *Int J Cancer*. 2013;132(11):2682-2693. doi:10.1002/ijc.27935

367. Hugle M, Fulda S. Dual phosphatidylinositol 3-kinase/mammalian target of rapamycin inhibitor NVP-BEZ235 synergizes with chloroquine to induce apoptosis in embryonal rhabdomyosarcoma. *Cancer Lett*. 2015;360(1):1-9. doi:10.1016/j.canlet.2014.12.016

368. Athuluri-Divakar SK, Vasquez-Del Carpio R, Dutta K, et al. A Small Molecule RAS-Mimetic Disrupts RAS Association with Effector Proteins to Block Signaling. *Cell*. 2016;165(3):643-655. doi:10.1016/j.cell.2016.03.045

369. Ritt DA, Abreu-Blanco MT, Bindu L, et al. Inhibition of Ras/Raf/MEK/ERK Pathway Signaling by a Stress-Induced Phospho-Regulatory Circuit. *Mol Cell*. 2016;64(5):875-887. doi:10.1016/j.molcel.2016.10.029

370. Urasaki Y, Fiscus RR, Le TT. Detection of the Cell Cycle-Regulated Negative Feedback Phosphorylation of Mitogen-Activated Protein Kinases in Breast Carcinoma using Nanofluidic Proteomics. *Sci Rep*. 2018;8(1):9991. doi:10.1038/s41598-018-28335-8

371. Schafer JM, Lehmann BD, Gonzalez-Ericsson PI, et al. Targeting MYCN-expressing triple-negative breast cancer with BET and MEK inhibitors. *Sci Transl Med*. 2020;12(534):eaaw8275. doi:10.1126/scitranslmed.aaw8275

372. McNeill RS, Canoutas DA, Stuhlmiller TJ, et al. Combination therapy with potent PI3K and MAPK inhibitors overcomes adaptive kinome resistance to single agents in preclinical models of glioblastoma. *Neuro Oncol*. 2017;19(11):1469-1480. doi:10.1093/neuonc/nox044

373. Locatelli SL, Careddu G, Stirparo GG, Castagna L, Santoro A, Carlo-Stella C. Dual PI3K/ERK inhibition induces necroptotic cell death of Hodgkin Lymphoma cells through IER3 downregulation. *Sci Rep*. 2016;6:35745. doi:10.1038/srep35745

374. Goulielmaki M, Assimomytis N, Rozanc J, et al. DPS-2: A Novel Dual MEK/ERK and PI3K/AKT Pathway Inhibitor with Powerful Ex Vivo and In Vivo Anticancer Properties. *Transl Oncol*. 2019;12(7):932-950. doi:10.1016/j.tranon.2019.04.005

375. Van De Weerdt BCM, Medema RH. Polo-like kinases: A team in control of the division. *Cell Cycle*. 2006;5(8):853-864. doi:10.4161/cc.5.8.2692

376. Petronczki M, Lénárt P, Peters JM. Polo on the Rise-from Mitotic Entry to Cytokinesis with Plk1. *Dev Cell*. 2008;14(5):646-659. doi:10.1016/j.devcel.2008.04.014

377. Ackermann S, Goeser F, Schulte JH, et al. Polo-like kinase 1 is a therapeutic target in high-risk neuroblastoma. *Clin Cancer Res*. 2011;17(4):731-741. doi:10.1158/1078-0432.CCR-10-1129

378. Xiao D, Yue M, Su H, et al. Polo-like Kinase-1 Regulates Myc Stabilization and Activates a Feedforward Circuit Promoting Tumor Cell Survival. *Mol Cell*. 2016;64(3):493-506. doi:10.1016/j.molcel.2016.09.016

379. Grinshtein N, Datti A, Fujitani M, et al. Small molecule kinase inhibitor screen identifies polo-like kinase 1 as a target for neuroblastoma tumor-initiating cells. *Cancer Res*. 2011;71(4):1385-1395. doi:10.1158/0008-5472.CAN-10-2484

380. Li Z, Yang C, Li X, et al. The dual role of BI 2536, a small-molecule inhibitor that targets PLK1, in induction of apoptosis and attenuation of autophagy in neuroblastoma cells. *J Cancer*. 2020;11(11):3274-3287. doi:10.7150/jca.33110

381. Pajtler KW, Sadowski N, Ackermann S, et al. The GSK461364 PLK1 inhibitor exhibits strong antitumoral activity in preclinical neuroblastoma models. 2017;8(4):6730-6741. doi:10.18632/oncotarget.14268

382. Gorlick R, Kolb EA, Keir ST, et al. Initial testing (stage 1) of the polo-like kinase inhibitor volasertib (BI 6727), by the pediatric preclinical testing program. *Pediatr Blood Cancer*. 2014;61(1):158-164. doi:10.1002/pbc.24616

383. Abbou S, Lanvers-Kaminsky C, Daudigeos-Dubus E, et al. Polo-like Kinase Inhibitor Volasertib Exhibits Antitumor Activity and Synergy with Vincristine in Pediatric Malignancies. *Anticancer Res*. 2016;36(2):599-609.

384. Rudolph D, Steegmaier M, Hoffmann M, et al. BI 6727, a polo-like kinase inhibitor with improved pharmacokinetic profile and broad antitumor activity. *Clin Cancer Res*. 2009;15(9):3094-3102. doi:10.1158/1078-0432.CCR-08-2445

385. Czaplinski S, Hugle M, Stiehl V, Fulda S. Polo-like kinase 1 inhibition sensitizes neuroblastoma cells for vinca alkaloid-induced apoptosis. *Oncotarget*. 2016;7(8):8700-8711. doi:10.18632/oncotarget.3901

386. Ember SW, Lambert QT, Berndt N, et al. Potent dual BET bromodomain-kinase inhibitors as value-added multitargeted chemical probes & cancer therapeutics. *Mol Cancer Ther*. 2017;16(6):1054-1067. doi:10.1158/1535-7163.MCT-16-0568-T

387. Han Y, Lindner S, Bei Y, et al. Synergistic activity of BET inhibitor MK-8628 and PLK inhibitor Volasertib in preclinical models of medulloblastoma. *Cancer Lett*. 2018;445:24-33. doi:10.1016/j.canlet.2018.12.012

388. Wissing MD, Mendonca J, Kortenhorst MSQ, et al. Targeting prostate cancer cell lines with polo-like kinase 1 inhibitors as a single agent and in combination with histone deacetylase inhibitors. *FASEB J*. 2013;27(10):4279-4293. doi:10.1096/fj.12-222893

389. Strebhardt K, Becker S, Matthess Y. Thoughts on the current assessment of Polo-like kinase inhibitor drug discovery. *Expert Opin Drug Discov*. 2015;10(1):1-8. doi:10.1517/17460441.2015.962510

390. Janning M, Fiedler W. Volasertib for the treatment of acute myeloid leukemia: A review of preclinical and clinical development. *Futur Oncol*. 2014;10(7):1157-1165. doi:10.2217/fon.14.53

391. Baxter M, Chapagai D, Craig S, et al. Peptidomimetic Polo-Box-Targeted Inhibitors that Engage PLK1 in Tumor Cells and Are Selective against the PLK3 Tumor Suppressor. *ChemMedChem*. 2020;15(12):1058-1066. doi:10.1002/cmdc.202000137

392. Helmke C, Becker S, Strebhardt K. The role of Plk3 in oncogenesis. *Oncogene*. 2016;35(2):135-147. doi:10.1038/onc.2015.105

393. Gjertsen BT, Schöffski P. Discovery and development of the Polo-like kinase inhibitor volasertib in cancer therapy. *Leukemia*. 2015;29(11):11-19. doi:10.1038/leu.2014.222

394. Selleck chemicals. Rigosertib (ON-01910) Catalog No.S1362. Published 2013. Accessed November 28, 2020. https://www.selleckchem.com/products/ON-01910.html

395. Mundt KE, Golsteyn RM, Lane HA, Nigg EA. On the regulation and function of human polo-like kinase 1 (PLK1): Effects of overexpression on cell cycle progression. *Biochem Biophys Res Commun*. 1997;239(2):377-385. doi:10.1006/bbrc.1997.7378

396. Yuan TL, Wulf G, Burga L, Cantley LC. Cell-to-cell variability in PI3K protein level regulates PI3K-AKT pathway activity in cell populations. *Curr Biol*. 2011;21(3):173-183. doi:10.1016/j.cub.2010.12.047

397. Ackermann S, Goeser F, Schulte JH, et al. Cancer Therapy : Preclinical Polo-Like Kinase 1 is a Therapeutic Target in High-Risk Neuroblastoma. 2010;(10):731-742. doi:10.1158/1078-0432.CCR-10-1129

398. Dietrich P, Freese K, Mahli A, Thasler WE, Hellerbrand C, Bosserhoff AK. Combined effects of PLK1 and RAS in hepatocellular carcinoma reveal rigosertib as promising novel therapeutic “dual-hit” option. *Oncotarget*. 2018;9(3):3605-3618. doi:10.18632/oncotarget.23188

399. Mielgo A, Seguin L, Huang M, et al. A MEK-independent role for CRAF in mitosis and tumor progression. *Nat Med*. 2011;17(12):1641-1645. doi:10.1038/nm.2464

400. Hyoda T, Tsujioka T, Nakahara T, et al. Rigosertib induces cell death of a myelodysplastic syndrome-derived cell line by DNA damage-induced G2/M arrest. *Cancer Sci*. 2015;106(3):287-293.

doi:10.1111/cas.12605

401. Okabe S, Tauchi T, Tanaka Y, Sakuta J, Ohyashiki K. Efficacy of the polo-like kinase inhibitor rigosertib, alone or in combination with abelson tyrosine kinase inhibitors, against break point cluster region-c-abelson-positive leukemia cells. *Oncotarget*. 2015;6(24):20231-20240. doi:10.18632/oncotarget.4047

402. Prasad A, Khudaynazar N, Tantravahi R V., Gillum AM, Hoffman BS. ON 01910.Na (rigosertib) inhibits PI3K/Akt pathway and activates oxidative stress signals in head and neck cancer cell lines. *Oncotarget*. 2016;7(48):79388-79400. doi:10.18632/oncotarget.12692

403. Anderson RT, Keysar SB, Bowles DW, et al. The dual pathway inhibitor rigosertib is effective in direct patient tumor xenografts of head and neck squamous cell carcinomas. *Mol Cancer Ther*. 2013;12(10):1994-2005. doi:10.1158/1535-7163.MCT-13-0206

404. Atanasova VS, Pourreyron C, Farshchian M, et al. Identification of rigosertib for the treatment of recessive dystrophic epidermolysis bullosa–associated squamous cell carcinoma. *Clin Cancer Res*. 2019;25(11):3384-3391. doi:10.1158/1078-0432.CCR-18-2661

405. Prasad A, Khudaynazar N, Tantravahi R V, Gillum AM. ON 01910.Na (rigosertib) inhibits PI3K/Akt pathway and activates oxidative stress signals in head and neck cancer cell lines. *Oncotarget*. 2016;7(48):79388-79400. doi:10.18632/oncotarget.12692

406. Gumireddy K, Reddy MVR, Cosenza SC, et al. ON01910, a non-ATP-competitive small molecule inhibitor of Plk1, is a potent anticancer agent. *Cancer Cell*. 2005;7(3):275-286. doi:10.1016/j.ccr.2005.02.009

407. Silverman LR, Greenberg P, Raza A, et al. Clinical activity and safety of the dual pathway inhibitor rigosertib for higher risk myelodysplastic syndromes following DNA methyltransferase inhibitor therapy. *Hematol Oncol*. 2015;33(2):57-66. doi:10.1002/hon.2137

408. Navada SC, Garcia-Manero G, OdchimarReissig R, et al. Rigosertib in combination with azacitidine in patients with myelodysplastic syndromes or acute myeloid leukemia: Results of a phase 1 study. *Leuk Res*. 2020;94:106369. doi:10.1016/j.leukres.2020.106369

409. Müller I, Larsson K, Frenzel A, et al. Targeting of the MYCN protein with small molecule c-MYC inhibitors. *PLoS One*. 2014;9(5). doi:10.1371/journal.pone.0097285

410. Mo H, Vita M, Crespin M, Henriksson M. Myc overexpression enhances apoptosis induced by small molecules. *Cell Cycle*. 2006;5(19):2191-2194. doi:10.4161/cc.5.19.3320

411. Zirath H, Frenzel A, Oliynyk G, et al. MYC inhibition induces metabolic changes leading to accumulation of lipid droplets in tumor cells. *Proc Natl Acad Sci*. 2013;110(25):10258-10263. doi:10.1073/pnas.1222404110

412. Clausen DM, Guo J, Parise RA, et al. In vitro cytotoxicity and in vivo efficacy, pharmacokinetics, and metabolism of 10074-G5, a novel small-molecule inhibitor of c-Myc/Max dimerization. *J Pharmacol Exp Ther*. 2010;335(3):715-727. doi:10.1124/jpet.110.170555

413. Guo J, Parise RA, Joseph E, et al. Efficacy, pharmacokinetics, tisssue distribution, and metabolism of the Myc-Max disruptor, 10058-F4 [Z,E]-5-[4-ethylbenzylidine]-2-thioxothiazolidin-4- one, in mice. *Cancer Chemother Pharmacol*. 2009;63(4):615-625. doi:10.1007/s00280-008-0774-y

414. Struntz NB, Chen A, Deutzmann A, et al. Stabilization of the Max Homodimer with a Small Molecule Attenuates Myc-Driven Transcription. *Cell Chem Biol*. 2019;26(5):711-723.e14. doi:10.1016/j.chembiol.2019.02.009

415. Castell A, Yan Q, Fawkner K, et al. A selective high affinity MYC-binding compound inhibits MYC:MAX interaction and MYC-dependent tumor cell proliferation. *Sci Rep*. 2018;8(1):10064. doi:10.1038/s41598-018-28107-4

416. Soucek L, Helmer-Citterich M, Sacco A, Jucker R, Cesareni G, Nasi S. Design and properties of a Myc derivative that efficiently homodimerizes. *Oncogene*. 1998;17(19):2463-2472. doi:10.1038/sj.onc.1202199

417. Soucek L, Nasi S, Evan GI. Omomyc expression in skin prevents Myc-induced papillomatosis. *Cell Death Differ*. 2004;11(9):1038-1045. doi:10.1038/sj.cdd.4401443

418. Jung LA, Gebhardt A, Koelmel W, et al. OmoMYC blunts promoter invasion by oncogenic MYC to inhibit gene expression characteristic of MYC-dependent tumors. *Oncogene*. 2017;36(14):1911-1924. doi:10.1038/onc.2016.354

419. Savino M, Annibali D, Carucci N, et al. The action mechanism of the Myc inhibitor termed Omomyc may give clues on how to target Myc for cancer therapy. *PLoS One*. 2011;6(7):e22284. doi:10.1371/journal.pone.0022284

420. Soucek L, Whitfield J, Martins CP, et al. Modelling Myc inhibition as a cancer therapy. *Nature*. 2008;455(7213):679-683. doi:10.1038/nature07260

421. Beaulieu ME, Soucek L. Finding MYCure. *Mol Cell Oncol*. 2019;6(5):e1618178. doi:10.1080/23723556.2019.1618178

422. Beaulieu ME, Jauset T, Massó-Vallés D, et al. Intrinsic cell-penetrating activity propels omomyc from proof of concept to viable anti-myc therapy. *Sci Transl Med*. 2019;11(484):eaar5012. doi:10.1126/scitranslmed.aar5012

423. Gogolin S, Batra R, Harder N, et al. MYCN-mediated overexpression of mitotic spindle regulatory genes and loss of p53-p21 function jointly support the survival of tetraploid neuroblastoma cells. *Cancer Lett*. 2013;331(1):35-45. doi:10.1016/j.canlet.2012.11.028

424. Cahill DP, Lengauer C, Yu J, et al. Mutations of mitotic checkpoint genes in human cancers. *Nature*. 1998;392(6673):300-303. doi:10.1038/32688

425. Kaindl AM. Autosomal recessive primary microcephalies (MCPH). *Eur J Paediatr Neurol*. 2014;18(4):547-548. doi:10.1016/j.ejpn.2014.03.010

426. Kaindl AM, Passemard S, Kumar P, et al. Many roads lead to primary autosomal recessive microcephaly. *Prog Neurobiol*. 2010;90(3):363-383. doi:10.1016/j.pneurobio.2009.11.002

427. Woods CG, Bond J, Enard W. Autosomal recessive primary microcephaly (MCPH): A review of clinical, molecular, and evolutionary findings. *Am J Hum Genet*. 2005;76(5):717-728. doi:10.1086/429930

428. Naveed M, Kazmi SK, Amin M, et al. Comprehensive review on the molecular genetics of autosomal recessive primary microcephaly (MCPH). *Genet Res (Camb)*. 2018;100:e7. doi:10.1017/S0016672318000046

429. Zaqout S, Morris-Rosendahl D, Kaindl AM. Autosomal Recessive Primary Microcephaly (MCPH): An Update. *Neuropediatrics*. 2017;48(03):135-142. doi:10.1055/s-0037-1601448

430. Gonzalez C, Saunders RDC, Casal J, et al. Mutations at the asp locus of Drosophila lead to multiple free centrosomes in syncytial embryos, but restrict centrosome duplication in larval neuroblasts. *J Cell Sci*. 1990;4:605-616.

431. Fish JL, Kosodo Y, Enard W, Pääbo S, Huttner WB. Aspm specifically maintains symmetric proliferative divisions of neuroepithelial cells. *Proc Natl Acad Sci USA*. 2006;103(27):10438-10443. doi:10.1073/pnas.0604066103

432. Zeng WJ, Cheng Q, Wen ZP, et al. Aberrant ASPM expression mediated by transcriptional regulation of FoxM1 promotes the progression of gliomas. *J Cell Mol Med*. 2020;24(17):9613-9626. doi:10.1111/jcmm.15435

433. Li R, Sun L, Fang A, Li P, Wu Q, Wang X. Recapitulating cortical development with organoid culture in vitro and modeling abnormal spindle-like (ASPM related primary) microcephaly disease. *Protein Cell*. 2017;8(11):823-833. doi:10.1007/s13238-017-0479-2

434. Lang PY, Gershon TR. A New Way to Treat Brain Tumors: Targeting Proteins Coded by Microcephaly Genes?: Brain tumors and microcephaly arise from opposing derangements regulating progenitor growth. Drivers of microcephaly could be attractive brain tumor targets. *BioEssays*. 2018;40(5):1-14. doi:10.1002/bies.201700243

435. Pattison L, Crow YJ, Deeble VJ, et al. A Fifth Locus for Primary Autosomal Recessive Microcephaly Maps to Chromosome 1q31. *Am J Hum Genet*. 2000;67(6):1578-1580. doi:10.1086/316910

436. Jamieson CR, Fryns J-P, Jacobs J, Matthijs G, Abramowicz MJ. Primary Autosomal Recessive Microcephaly: MCPH5 Maps to 1q25-q32. *Am J Hum Genet*. 2000;67(6):1575-1577. doi:10.1086/316909

437. van der Voet M, Berends CWH, Perreault A, et al. NuMA-related LIN-5, ASPM-1, calmodulin and dynein promote meiotic spindle rotation independently of cortical LIN-5/GPR/Gα. *Nat Cell Biol*. 2009;11(3):269-277. doi:10.1038/ncb1834

438. Zhang J. Evolution of the Human ASPM Gene , a Major Determinant of Brain Size. *Genetics*.

2003;165(4):2063-2070. doi:10.1093/genetics/165.4.2063

439. Kouprina N, Pavlicek A, Mochida GH, et al. Accelerated evolution of the ASPM gene controlling brain size begins prior to human brain expansion. *PLoS Biol*. 2004;2(5):653-663. doi:10.1371/journal.pbio.0020126

440. Wong PCM, Wong PCM, Wong PCM, et al. ASPM-lexical tone association in speakers of a tone language: Direct evidence for the genetic-biasing hypothesis of language evolution. *Sci Adv*. 2020;6(22):eaba5090. doi:10.1126/sciadv.aba5090

441. Kouprina N, Pavlicek A, Collins NK, et al. The microcephaly ASPM gene is expressed in proliferating tissues and encodes for a mitotic spindle protein. *Hum Mol Genet*. 2005;14(15):2155-2165. doi:10.1093/hmg/ddi220

442. Tungadi EA, Ito A, Kiyomitsu T, Goshima G. Human microcephaly ASPM protein is a spindle pole-focusing factor that functions redundantly with CDK5RAP2. *J Cell Sci*. 2017;130(21):3676-3684. doi:10.1242/jcs.203703

443. Jiang K, Rezabkova L, Hua S, et al. Microtubule minus-end regulation at spindle poles by an ASPM-katanin complex. *Nat Cell Biol*. 2017;19(5):480-492. doi:10.1038/ncb3511

444. Gonzalez C, Sunkel CE, Glover DM. Interactions between mgr, asp, and polo: asp function modulated by polo and needed to maintain the poles of monopolar and bipolar spindles. *Chromosoma*. 1998;107(6-7):452-460. doi:10.1007/s004120050329

445. Sanchez AD, Feldman JL. Microtubule-organizing centers: from the centrosome to non-centrosomal sites. *Curr Opin Cell Biol*. 2017;44:93-101. doi:10.1016/j.ceb.2016.09.003

446. Avides MDC, Glover DM. Abnormal spindle protein, Asp, and the integrity of mitotic centrosomal microtubule organizing centers. *Science*. 1999;283(5408):1733-1735. doi:10.1126/science.283.5408.1733

447. Job D, Valiron O, Oakley B. Microtubule nucleation. *Curr Opin Cell Biol*. 2003;15(1):111-117. doi:10.1016/S0955-0674(02)00003-0

448. Brinkley BR. Microtubule organizing centers. *Annu Rev Cell Biol*. 1985;1:145-172. doi:10.1146/annurev.cb.01.110185.001045

449. Xu D, Dai W. The function of mammalian Polo-like kinase 1 in microtubule nucleation. *Proc Natl Acad Sci USA*. 2011;108(28):11301-11302. doi:10.1073/pnas.1107723108

450. Bornens M. The centrosome in cells and organisms. *Science*. 2012;335(6067):422-426. doi:10.1126/science.1209037

451. Conduit PT, Wainman A, Raff JW. Centrosome function and assembly in animal cells. *Nat Rev Mol Cell Biol*. 2015;16(10):611-624. doi:10.1038/nrm4062

452. Chabin-Brion K, Marceiller J, Perez F, et al. The Golgi complex is a microtubule-organizing organelle. *Mol Biol Cell*. 2001;12(7):2047-2060. doi:10.1091/mbc.12.7.2047

453. Rodionov V, Nadezhdina E, Borisy G. Centrosomal control of microtubule dynamics. *Proc Natl Acad Sci USA*. 1999;96(1):115-120. doi:10.1073/pnas.96.1.115

454. Wu J, Akhmanova A. Microtubule-Organizing Centers. *Annu Rev Cell Dev Biol*. 2017;33:51-75. doi:10.1146/annurev-cellbio-100616-060615

455. Gai M, Bianchi FT, Vagnoni C, et al. ASPM and CITK regulate spindle orientation by affecting the dynamics of astral microtubules. *EMBO Rep*. 2016;34(3):e201541823. doi:10.15252/embr.201541823

456. Rivas RJ, Hatten ME. Motility and cytoskeletal organization of migrating cerebellar granule neurons. *J Neurosci*. 1995;15(2):981-989. doi:10.1523/jneurosci.15-02-00981.1995

457. Kapitein LC, Hoogenraad CC. Building the Neuronal Microtubule Cytoskeleton. *Neuron*. 2015;87(3):492-506. doi:10.1016/j.neuron.2015.05.046

458. Hoogenraad CC, Bradke F. Control of neuronal polarity and plasticity - a renaissance for microtubules? *Trends Cell Biol*. 2009;19(12):669-676. doi:10.1016/j.tcb.2009.08.006

459. Falnikar A, Tole S, Baas PW. Kinesin-5, a mitotic microtubule-associated motor protein, modulates neuronal migration. *Mol Biol Cell*. 2011;22(9):1561-1574. doi:10.1091/mbc.E10-11-0905

460. Liu XS, Song B, Tang J, Liu W, Kuang S, Liu X. Plk1 Phosphorylates Sgt1 at the Kinetochores To Promote Timely Kinetochore-Microtubule Attachment. *Mol Cell Biol*. 2012;32(19):4053-4067.

doi:10.1128/mcb.00516-12

461. Lera RF, Norman RX, Dumont M, et al. Plk1 protects kinetochore–centromere architecture against microtubule pulling forces. *EMBO Rep*. 2019;20(10):e48711. doi:10.15252/embr.201948711

462. Martínez-A C, Van Wely KHM. Are aneuploidy and chromosome breakage caused by a CINgle mechanism? *Cell Cycle*. 2010;9(12):2275-2280. doi:10.4161/cc.9.12.11865

463. MacKerell AD, Lee GU. Structure, force, and energy of a double-stranded DNA oligonucleotide under tensile loads. *Eur Biophys J*. 1999;28(5):415-426. doi:10.1007/s002490050224

464. Higgins J, Midgley C, Bergh AM, et al. Human ASPM participates in spindle organisation, spindle orientation and cytokinesis. *BMC Cell Biol*. 2010;11(85). doi:10.1186/1471-2121-11-85

465. Jiang K, Rezabkova L, Hua S, et al. Microtubule minus-end regulation at spindle poles by an ASPM-katanin complex. *Nat Cell Biol*. 2017;19(5):480-492. doi:10.1038/ncb3511

466. Baas PW, Rao AN, Matamoros AJ, Leo L. Stability properties of neuronal microtubules. *Cytoskeleton*. 2016;73(9):442-260. doi:10.1002/cm.21286

467. Flynn KC, Hellal F, Neukirchen D, et al. ADF/Cofilin-Mediated Actin Retrograde Flow Directs Neurite Formation in the Developing Brain. *Neuron*. 2012;76(6):1091-1107. doi:10.1016/j.neuron.2012.09.038

468. Wang H, Brust-Mascher I, Civelekoglu-Scholey G, Scholey JM. Patronin mediates a switch from kinesin-13-dependent poleward flux to anaphase b spindle elongation. *J Cell Biol*. 2013;203(1):35-46. doi:10.1083/jcb.201306001

469. Rogers GC, Rogers SL, Schwimmer TA, et al. Two mitotic kinesins cooperate to drive sister chromatid separation during anaphase. *Nature*. 2004;427(6972):364-370. doi:10.1038/nature02256

470. Hirokawa N, Takemura R. Molecular motors and mechanisms of directional transport in neurons. *Nat Rev Neurosci*. 2005;6(3):201-214. doi:10.1038/nrn1624

471. Conde C, Cáceres A. Microtubule assembly, organization and dynamics in axons and dendrites. *Nat Rev Neurosci*. 2009;10(5):319-332. doi:10.1038/nrn2631

472. Cooper GM, Hausman RE. *The Cell: A Molecular Approach*. 4th ed. Sinauer Associates, Inc.; 2006.

473. Yu W, Baas PW. Changes in microtubule number and length during axon differentiation. *J Neurosci*. 1994;14(5 Pt 1):2818-2829. doi:10.1523/jneurosci.14-05-02818.1994

474. Fridoon FJ, Baas PW. Microtubules released from the neuronal centrosome are transported into the axon. *J Cell Sci*. 1995;108(Pt 8):2761-2769.

475. Baas PW, Ahmad FJ. The transport properties of axonal microtubules establish their polarity orientation. *J Cell Biol*. 1993;120(6):1427-1437. doi:10.1083/jcb.120.6.1427

476. Yu W, Centonze VE, Ahmad FJ, Baas PW. Microtubule nucleation and release from the neuronal centrosome. *J Cell Biol*. 1993;122(2):349-359. doi:10.1083/jcb.122.2.349

477. Marín O, Valiente M, Ge X, Tsai LH. Guiding neuronal cell migrations. *Cold Spring Harb Perspect Biol*. 2010;2(2):a001834. doi:10.1101/cshperspect.a001834

478. Xie Z, Sanada K, Samuels BA, Shih H, Tsai LH. Serine 732 phosphorylation of FAK by Cdk5 is important for microtubule organization, nuclear movement, and neuronal migration. *Cell*. 2003;114(4):469-482. doi:10.1016/S0092-8674(03)00605-6

479. Bond J, Roberts E, Mochida GH, et al. ASPM is a major determinant of cerebral cortical size. *Nat Genet*. 2002;32(2):316-320. doi:10.1038/ng995

480. Jeff Hardin, Wayne M. Becker, Lewis J. Kleinsmith JH. *Becker's World of the Cell*. 8. Edition. Pearson; 2011.

481. Montgomery SH, Capellini I, Venditti C, Barton RA, Mundy NI. Adaptive evolution of four microcephaly genes and the evolution of brain size in anthropoid primates. *Mol Biol Evol*. 2011;28(1):625-638. doi:10.1093/molbev/msq237

482. Otani T, Marchetto MC, Gage FH, Simons BD, Livesey FJ. 2D and 3D Stem Cell Models of Primate Cortical Development Identify Species-Specific Differences in Progenitor Behavior Contributing to Brain Size. *Cell Stem Cell*. 2016;18(4):467-480. doi:10.1016/j.stem.2016.03.003

483. Bikeye SNN, Colin C, Marie Y, et al. ASPM-associated stem cell proliferation is involved in malignant progression of gliomas and constitutes an attractive therapeutic target. *Cancer Cell Int*. 2010;10(1).

doi:10.1186/1475-2867-10-1

484. Pai VC, Hsu C, Chan T, et al. ASPM promotes prostate cancer stemness and progression by augmenting Wnt − Dvl-3 − β -catenin signaling. *Oncogene*. 2018;38(8):1340-1353. doi:10.1038/s41388-018-0497-4

485. Williams SE, Garcia I, Crowther AJ, et al. Aspm sustains postnatal cerebellar neurogenesis and medulloblastoma growth in mice. *Dev*. 2015;142(22):3921-3932. doi:10.1242/dev.124271

486. Vulcani-Freitas TM, Saba-Silva N, Cappellano A, et al. ASPM gene expression in medulloblastoma. *Child's Nerv Syst*. 2011;27(1):71-74. doi:10.1007/s00381-010-1252-5

487. Hagemann C, Anacker J, Gerngras S, et al. Expression analysis of the autosomal recessive primary microcephaly genes MCPH1 (microcephalin) and MCPH5 (ASPM, abnormal spindle-like, microcephaly associated) in human malignant gliomas. *Oncol Rep*. 2008;20(2):301-308. doi:10.3892/or_00000007

488. Horvath S, Zhang B, Carlson M, et al. Analysis of oncogenic signaling networks in glioblastoma identifies ASPM as a molecular target. *Proc Natl Acad Sci USA*. 2006;103(46):17402-17407. doi:10.1073/pnas.0608396103

489. Cabral de Carvalho Corrêa D, Dias Oliveira I, Mascaro Cordeiro B, et al. Abnormal spindle-like microcephaly-associated (ASPM) gene expression in posterior fossa brain tumors of childhood and adolescence. *Child's Nerv Syst*. 2020;37(1):137-145. doi:10.1007/s00381-020-04740-1

490. Lin S-Y, Pan H-W, Liu S-H, et al. ASPM is a novel marker for vascular invasion, early recurrence, and poor prognosis of hepatocellular carcinoma. *Clin Cancer Res*. 2008;14(15):4814-4820. doi:10.1158/1078-0432.CCR-07-5262

491. Xie J-J, Zhuo Y-J, Zheng Y, et al. High expression of ASPM correlates with tumor progression and predicts poor outcome in patients with prostate cancer. *Int Urol Nephrol*. 2017;49(5):817-823. doi:10.1007/s11255-017-1545-7

492. Brüning-Richardson A, Bond J, Alsiary R, et al. ASPM and microcephalin expression in epithelial ovarian cancer correlates with tumour grade and survival. *Br J Cancer*. 2011;104(10):1602-1610. doi:10.1038/bjc.2011.117

493. Xu Z, Zhang Q, Luh F, et al. Overexpression of the ASPM gene is associated with aggressiveness and poor outcome in bladder cancer. *Oncol Lett*. 2018;17(2):1865-1876. doi:10.3892/ol.2018.9762

494. Izumi H, Kaneko Y, Nakagawara A. The Role of MYCN in Symmetric vs. Asymmetric Cell Division of Human Neuroblastoma Cells. *Front Oncol*. 2020;10(570815). doi:10.3389/fonc.2020.570815

495. Oberthuer A, Theissen J, Westermann F, Hero B, Fischer M. Molecular characterization and classification of neuroblastoma. *Future Oncol*. 2009;5(5):625-639. doi:10.2217/fon.09.41

496. Koster J, Volckmann R, Zwijnenburg D, Molenaar P, Versteeg R. Abstract 2490: R2: Genomics analysis and visualization platform. In: *AACR Annual Meeting 2019*. Vol 79. American Association for Cancer Research; 2019:2490 LP - 2490. doi:10.1158/1538-7445.SABCS18-2490

497. Koster J. R2: Genomics Analysis and Visualization Platform. Accessed November 28, 2020. http://r2.amc.nl

498. Edgar R. Gene Expression Omnibus: NCBI gene expression and hybridization array data repository. *Nucleic Acids Res*. 2002;30(1):207-210. doi:10.1093/nar/30.1.207

499. Barrett T, Wilhite SE, Ledoux P, et al. NCBI GEO: Archive for functional genomics data sets - Update. *Nucleic Acids Res*. 2013;41((Database issue):D991-5). doi:10.1093/nar/gks1193

500. Smith MA, Morton CL, Phelps D, Girtman K, Neale G, Houghton PJ. SK-NEP-1 and Rh1 are Ewing family tumor lines. *Pediatr Blood Cancer*. 2008;50(3):703-706. doi:10.1002/pbc.21099

501. DuBridge RB, Tang P, Hsia HC, Leong PM, Miller JH, Calos MP. Analysis of mutation in human cells by using an Epstein-Barr virus shuttle system. *Mol Cell Biol*. 1987;7(1):379-387. doi:10.1128/mcb.7.1.379

502. Wiebusch L, Hagemeier C. P53-and p21-dependent premature APC/C-Cdh1 activation in G2 is part of the long-term response to genotoxic stress. *Oncogene*. 2010;29(24):3477-3489. doi:10.1038/onc.2010.99

503. Yeo C, Saunders N, Locca D, et al. Ficoll-paque™ versus lymphoprep™: A comparative study of two density gradient media for therapeutic bone marrow mononuclear cell preparations. *Regen Med*. 2009;4(5):689-696. doi:10.2217/rme.09.44

504. Bøyum A. Isolation of Lymphocytes, Granulocytes and Macrophages. *Scand J Immunol*. 1976;5:9-15.

doi:10.1111/j.1365-3083.1976.tb03851.x

505. Krentz S, Hof J, Mendioroz A, et al. Prognostic value of genetic alterations in children with first bone marrow relapse of childhood B-cell precursor acute lymphoblastic leukemia. *Leukemia*. 2013;27(2):295-304. doi:10.1038/leu.2012.155

506. Nuthalapati S, Zhou Q, Guo P, et al. Preclinical pharmacokinetic and pharmacodynamic evaluation of novel anticancer agents, ON01910.Na (Rigosertib, Estybon™) and ON013105, for brain tumor chemotherapy. *Pharm Res*. 2012;29(9):2499-2511. doi:10.1007/s11095-012-0780-y

507. Chun AW, Cosenza SC, Taft DR, Maniar M. Preclinical pharmacokinetics and in vitro activity of on 01910.Na, a novel anti-cancer agent. *Cancer Chemother Pharmacol*. 2009;65(1):177-186. doi:10.1007/s00280-009-1022-9

508. Oberthuer A, Skowron M, Spitz R, et al. Characterization of a complex genomic alteration on chromosome 2p that leads to four alternatively spliced fusion transcripts in the neuroblastoma cell lines IMR-5, IMR-5/75 and IMR-32. *Gene*. 2005;363:41-50. doi:10.1016/j.gene.2005.07.038

509. Parekh A, Das D, Das S, et al. Bioimpedimetric analysis in conjunction with growth dynamics to differentiate aggressiveness of cancer cells. *Sci Rep*. 2018;8(1):783. doi:10.1038/s41598-017-18965-9

510. Brú A, Albertos S, Subiza JL, García-Asenjo JL, Brú I. The Universal Dynamics of Tumor Growth. *Biophys J*. 2003;85(5):2948-2961. doi:10.1016/S0006-3495(03)74715-8

511. He L, Kulesskiy E, Saarela J, et al. Methods for high-throughput drug combination screening and synergy scoring. *Methods Mol Biol*. 2018;1711:351-398. doi:10.1007/978-1-4939-7493-1_17

512. Sidell N, Altman A, Haussler MR, Seeger RC. Effects of retinoic acid (RA) on the growth and phenotypic expression of several human neuroblastoma cell lines. *Exp Cell Res*. 1983;148(1):21-30. doi:10.1016/0014-4827(83)90184-2

513. Hoebeke J, Van Nijen G, De Brabander M. Interaction of oncodazole (R 17934), a new anti-tumoral drug, with rat brain tubulin. *Biochem Biophys Res Commun*. 1976;69(2):319-324. doi:10.1016/0006-291X(76)90524-6

514. Kuhn M. The microtubule depolymerizing drugs nocodazole and colchicine inhibit the uptake of Listeria monocytogenes by P388D1 macrophages. *FEMS Microbiol Lett*. 1998;160(1):87-90. doi:10.1016/S0378-1097(98)00017-2

515. Wendell KL, Wilson L, Jordan MA. Mitotic block in HeLa cells by vinblastine: Ultrastructural changes in kinetochore-mcirotubule attachment and in centrosomes. *J Cell Sci*. 1993;104(Pt 2):261-174.

516. Zieve GW, Turnbull D, Mullins JM, McIntosh JR. Production of large numbers of mitotic mammalian cells by use of the reversible microtubule inhibitor Nocodazole. Nocodazole accumulated mitotic cells. *Exp Cell Res*. 1980;126(2):397-405. doi:10.1016/0014-4827(80)90279-7

517. Matzke MA, Birchler JA. RNAi-mediated pathways in the nucleus. *Nat Rev Genet*. 2005;6(1):24-35. doi:10.1038/nrg1500

518. Thermo Fisher Scientific. Transient Transfection. Transfection Methods. Accessed November 28, 2020. https://www.thermofisher.com/de/de/home/references/gibco-cell-culture-basics/transfection-basics/transfection-methods/transient-transfection.html

519. Paddison PJ, Caudy AA, Bernstein E, Hannon GJ, Conklin DS. Short hairpin RNAs (shRNAs) induce sequence-specific silencing in mammalian cells. *Genes Dev*. 2002;16(8):948-958. doi:10.1101/gad.981002

520. Manjunath N, Wu H, Subramanya S, Shankar P. Lentiviral delivery of short hairpin RNAs. *Adv Drug Deliv Rev*. 2009;61(9):732-745. doi:10.1016/j.addr.2009.03.004

521. Ghosh C, Song W, Lahiri DK. Efficient DNA transfection in neuronal and astrocytic cell lines. *Mol Biol Rep*. 2000;27(2):113-121. doi:10.1023/A:1007173906990

522. Kingston RE, Chen CA, Okayama H. Calcium Phosphate Transfection. *Curr Protoc Immunol*. 2001;Chapter 10(Unit 10.13). doi:10.1002/0471142735.im1013s31

523. Kwon M, Firestein BL. DNA Transfection: Calcium Phosphate Method. *Methods Mol Biol*. 2013;1018:107-110. doi:10.1007/978-1-62703-444-9_10

524. Merck KGaA. Antibiotic Kill Curve. Published 2020. Accessed November 28, 2020. https://www.sigmaaldrich.com/technical-documents/articles/biology/antibiotic-kill-curve.html

525. Higashikawa F, Chang LJ. Kinetic analyses of stability of simple and complex retroviral vectors. *Virology*. 2001;280(1):124-131. doi:10.1006/viro.2000.0743

526. Materials AB. The Lentivirus - An Introduction. Applied Biological Materials Inc. Accessed November 28, 2020. https://www.abmgood.com/marketing/knowledge_base/The_Lentivirus_System.php#moi

527. Davis HE, Rosinski M, Morgan JR, Yarmush ML. Charged Polymers Modulate Retrovirus Transduction via Membrane Charge Neutralization and Virus Aggregation. *Biophys J*. 2004;86(2):1234-1242. doi:10.1016/S0006-3495(04)74197-1

528. Puck TT, Marcus PI. Action of x-rays on mammalian cells. *J Exp Med*. 1956;103(5):653-666. doi:10.1084/jem.103.5.653

529. Franken NAP, Rodermond HM, Stap J, Haveman J, van Bree C. Clonogenic assay of cells in vitro. *Nat Protoc*. 2006;1(5):2315-2319. doi:10.1038/nprot.2006.339

530. Rodriguez LG, Wu X, Guan JL. Wound-healing assay. *Methods Mol Biol*. 2005;294:23-29. doi:10.1385/1-59259-860-9:023

531. Riss T, Promega Corporation. Selecting cell-based assays for drug discovery screening. *Cell notes*. 2005;(13). https://beta-static.fishersci.com/content/dam/fishersci/en_US/documents/programs/scientific/brochures-and-catalogs/publications/promega-selecting-cell-based-assays-drug-screening-publication.pdf

532. Crouch SPM, Kozlowski R, Slater KJ, Fletcher J. The use of ATP bioluminescence as a measure of cell proliferation and cytotoxicity. *J Immunol Methods*. 1993;160(1):81-88. doi:10.1016/0022-1759(93)90011-U

533. Shaner NC, Steinbach PA, Tsien RY. A guide to choosing fluorescent proteins. *Nat Methods*. 2005;2(12):905-909. doi:10.1038/nmeth819

534. Zhang J, Campbell RE, Ting AY, Tsien RY. Creating new fluorescent probes for cell biology. *Nat Rev Mol Cell Biol*. 2002;3(12):906-918. doi:10.1038/nrm976

535. Chalfie M, Tu Y, Euskirchen G, Ward WW, Prasher DC. Green fluorescent protein as a marker for gene expression. *Science*. 1994;263(5148):802-805. doi:10.1126/science.8303295

536. Cormack BP, Valdivia RH, Falkow S. FACS-optimized mutants of the green fluorescent protein (GFP). *Gene*. 1996;173((1 Spec No)):33-38. doi:10.1016/0378-1119(95)00685-0

537. Picot J, Guerin CL, Le Van Kim C, Boulanger CM. Flow cytometry: Retrospective, fundamentals and recent instrumentation. *Cytotechnology*. 2012;64(2):109-130. doi:10.1007/s10616-011-9415-0

538. Givan AL. Flow cytometry: an introduction. *Methods Mol Biol*. 2004;263:1-32. doi:10.1385/1-59259-773-4:001

539. Riley R, Idowu M. *Principles and Applications of Flow Cytometry*. Medical College of Virginia/VCU Health Systems Virginia Commonwealth University http://www.flowlab-childrens-harvard.com/yahoo_site_admin/assets/docs/principlesandapplications.29464931.pdf

540. Abcam Plc. Introduction to flow cytometry. Accessed November 28, 2020. https://www.abcam.com/protocols/introduction-to-flow-cytometry#measurement of scsattered light and fluorescence

541. Pozarowski P, Darzynkiewicz Z. Analysis of cell cycle by flow cytometry. *Methods Mol Biol*. 2004;281:301-311. doi:10.1385/1-59259-811-0:301

542. Cobb L. Cell Based Assays: the Cell Cycle, Cell Proliferation and Cell Death. *Mater Methods*. 2013;3(172). doi:10.13070/mm.en.3.172 ; https://www.labome.com/method/The-Cell-Cycle-Analysis.html

543. Szymansky A, Becker L-L, Overath M, et al. ASPM is a novel risk factor of aggressive neuroblastoma. In: *Advances in Neuroblastoma Research Conference*. Advances in Neuroblastoma Research Association; 2018. https://www.anrmeeting.org/anr2018-abstracts/meetings-2018_abstracts.php

544. Szymansky A, Becker L-L, Overath MD, et al. ASPM is a regulator of neuroblastoma cell proliferation and differentiation. *Manuscript in preparation*. 2020;28th(November).

545. Watson J V., Chambers SH, Smith PJ. A pragmatic approach to the analysis of DNA histograms with a definable G1 peak. *Cytometry*. 1987;8(1):1-8. doi:10.1002/cyto.990080101

546. Dean PN, Jett JH. Mathematical analysis of dna distributions derived from flow microfluorometry. *J Cell*

Biol. 1974;60(2):523-527. doi:10.1083/jcb.60.2.523

547. Invitrogen, Scientific TF. *Click-IT™ Plus EdU Flow Cytometry Assay Kits*.; 2019. https://assets.thermofisher.com/TFS-Assets/LSG/manuals/Click_iT_Plus_EdU_FC_Assay_50_UG.pdf

548. BioLegend. APC Annexin V Apoptosis Detection Kit with 7-AAD Manual. *Manual*. 2014;1. https://www.biolegend.com/fr-fr/global-elements/pdf-popup/apc-annexin-v-apoptosis-detection-kit-with-7-aad-9754?filename=APC Annexin V Apoptosis Detection Kit with 7-AAD.pdf&pdfgen=true

549. Poon IKH, Hulett MD, Parish CR. Molecular mechanisms of late apoptotic/necrotic cell clearance. *Cell Death Differ*. 2010;17(3):381-397. doi:10.1038/cdd.2009.195

550. Cox MM, Doudna JA, O'Donnell M. *Molecular Biology : Principles and Practice*. 1st ed. W.H. Freeman and Company; 2015.

551. Ottaviani D, LeCain M, Sheer D. The role of microhomology in genomic structural variation. *Trends Genet*. 2014;30(3):85-94. doi:10.1016/j.tig.2014.01.001

552. Ye J, Coulouris G, Zaretskaya I, Cutcutache I, Rozen S, Madden TL. Primer-BLAST: a tool to design target-specific primers for polymerase chain reaction. *BMC Bioinformatics*. 2012;13:134. doi:10.1186/1471-2105-13-134

553. Untergasser A, Nijveen H, Rao X, Bisseling T, Geurts R, Leunissen JAM. Primer3Plus, an enhanced web interface to Primer3. *Nucleic Acids Res*. 2007;35(SUPPL.2). doi:10.1093/nar/gkm306

554. Paul Stothard. Reverse Complement web tool. Agricultural Life and Environmental Sciences. Published 2000. Accessed November 28, 2020. https://www.bioinformatics.org/sms/rev_comp.html

555. Stothard P. The sequence manipulation suite: JavaScript programs for analyzing and formatting protein and DNA sequences. *Biotechniques*. 2000;28(6):1002. doi:10.2144/00286ir01

556. Dieffenbach CW, Lowe TMJ, Dveksler GS. General concepts for PCR primer design. *Genome Res*. 1993;3(3):S30-37. doi:10.1101/gr.3.3.S30

557. Apte A, Daniel S. PCR primer design. *Cold Spring Harb Protoc*. 2009;2009(3):pdb.ip65. doi:10.1101/pdb.ip65

558. Singh VK, Kumar A. PCR primer design. *Mol Biol Today*. 2001;2(2):27-32. https://www.caister.com/backlist/mbt/v/v2/06.pdf

559. SantaLucia J. A unified view of polymer, dumbbell, and oligonucleotide DNA nearest-neighbor thermodynamics. *Proc Natl Acad Sci USA*. 1998;95(4):1460-1465. doi:10.1073/pnas.95.4.1460

560. Lindell Bromham. *Reading the Story in DNA: A Beginner's Guide to Molecular Evolution*. Oxford University Press; 2008. doi:0199290911

561. M. J. McPherson, P. Quirke GRT. *Pcr: A Practical Approach*. Oxford University Press; 1991.

562. Nybo K. Primer design. *Biotechniques*. 2013;54(5):249-250. doi:10.2144/000114025

563. Li B, Kadura I, Fu DJ, Watson DE. Genotyping with TaqMAMA. *Genomics*. 2004;83(2):311-320. doi:10.1016/j.ygeno.2003.08.005

564. Barz MJ, Hof J, Groeneveld-Krentz S, et al. Subclonal NT5C2 mutations are associated with poor outcomes after relapse of pediatric acute lymphoblastic leukemia. *Blood*. 2020;135(12):921-933. doi:10.1182/blood.2019002499

565. Liu J, Huang SM, Sun MY, et al. An improved allele-specific PCR primer design method for SNP marker analysis and its application. *Plant Methods*. 2012;8(1):34. doi:Artn 34\r10.1186/1746-4811-8-34

566. Rozen S, Untergasser A, Remm M, Koressaar T, Skaletsky H. Primer3 Input. input.htm v 4.1.0. Accessed November 28, 2020. https://primer3.ut.ee/

567. Untergasser A, Cutcutache I, Koressaar T, et al. Primer3-new capabilities and interfaces. *Nucleic Acids Res*. 2012;40(15):1-12/e115. doi:10.1093/nar/gks596

568. Saiki RK, Scharf S, Faloona F, et al. Enzymatic amplification of β-globin genomic sequences and restriction site analysis for diagnosis of sickle cell anemia. *Science*. 1985;230(4732):1350-1354. doi:10.1126/science.2999980

569. Saiki RK, Gelfand DH, Stoffel S, et al. Primer-directed enzymatic amplification of DNA with a thermostable DNA polymerase. *Science*. 1988;239(4839):487-491. doi:10.1126/science.2448875

570. Mullis K, Faloona F, Scharf S, Saiki R, Horn G, Erlich H. Specific enzymatic amplification of DNA in

vitro: the polymerase chain reaction. 1986. *Biotechnology*. 1992;24:17-27. doi:10.1101/sqb.1986.051.01.032

571. Aaij C, Borst P. The gel electrophoresis of DNA. *BBA Sect Nucleic Acids Protein Synth*. 1972;269(2):192-200. doi:10.1016/0005-2787(72)90426-1

572. Green MR, Sambrook J. Agarose gel electrophoresis. *Cold Spring Harb Protoc*. 2019;2019(1). doi:10.1101/pdb.prot100404

573. Nikolayevskyy V, Trovato A, Broda A, Borroni E, Cirillo D, Drobniewski F. MIRU-VNTR genotyping of mycobacterium tuberculosis strains using qiaxcel technology: A multicentre evaluation study. *PLoS One*. 2016;11(3). doi:10.1371/journal.pone.0149435

574. Sint D, Raso L, Kaufmann R, Traugott M. Optimizing methods for PCR-based analysis of predation. *Mol Ecol Resour*. 2011;11(5):795-801. doi:10.1111/j.1755-0998.2011.03018.x

575. NCBI. Design PCR primers and check them for specificity. National Center for Biotechnology Information. Published 2017. Accessed November 28, 2020. https://www.ncbi.nlm.nih.gov/guide/howto/design-pcr-primers/

576. Heid CA, Stevens J, Livak KJ, Williams PM. Real time quantitative PCR. *Genome Res*. 1996;6(10):986-994.

577. Eckert C, Landt O. Real-time PCR to detect minimal residual disease in childhood ALL. *Methods Mol Med*. 2003;91:172-182. doi:10.1385/1-59259-433-6:175

578. Holland PM, Abramson RD, Watson R, Gelfand DH. Detection of specific polymerase chain reaction product by utilizing the 5′ → 3′ exonuclease activity of Thermus aquaticus DNA polymerase. *Proc Natl Acad Sci USA*. 1991;88(16):7276-7280. doi:10.1073/pnas.88.16.7276

579. Yuan CC, Peterson RJ, Wang CD, Goodsaid F, Waters DJ. 5' Nuclease assays for the loci CCR5-+/Δ32, CCR2-V64I, and SDF1-G801A related to pathogenesis of AIDS. *Clin Chem*. 2000;46(1):24-30.

580. Raeymaekers L. Basic principles of quantitative PCR. *Mol Biotechnol*. 2000;15(2):115-122. doi:10.1385/MB:15:2:115

581. Raso A, Mascelli S, Nozza P, et al. Troubleshooting fine-tuning procedures for qPCR system design. *J Clin Lab Anal*. 2011;25(6):389-394. doi:10.1002/jcla.20489

582. van der Velden VHJ, Hochhaus A, Cazzaniga G, Szczepanski T, Gabert J, van Dongen JJM. Detection of minimal residual disease in hematologic malignancies by real-time quantitative PCR: principles, approaches, and laboratory aspects. *Leukemia*. 2003;17(6):1013-1034. doi:10.1038/sj.leu.2402922

583. Morton NE. Parameters of the human genome. *Proc Natl Acad Sci USA*. 1991;88(17):7474-7476. doi:10.1073/pnas.88.17.7474

584. Pfaffl MW. A new mathematical model for relative quantification in real-time RT-PCR. *Nucleic Acids Res*. 2001;29(9):e45. doi:10.1093/nar/29.9.e45

585. Eckert C, Landt O. Real-time PCR to detect minimal residual disease in childhood ALL. N. Goulden and C. Steward E, ed. *Methods Mol Med*. 2004;91:175-182. doi:10.1385/1-59259-433-6:175

586. Bruggemann M. Standardized mrd monitoring in european all trials. *Ann Hematol*. 2013;92(February 2013):1–60. doi:http://dx.doi.org/10.1007/s00277-012-1669-x

587. Prof. Dr. Jacques J.M. van Dongen. EuroMRD Board (EuroMRD Consortium). EuroMRD-ESLHO. Published 2011. Accessed November 24, 2019. http://www.euromrd.org/usr/pub/pub.php

588. Bio-Rad Laboratories Inc. QX100™ Droplet Digital™ PCR System. *Bulletin*. 2013;6311 Rev C(15-0846 0615 Slg 1214):1-16. https://www.bio-rad.com/webroot/web/pdf/lsr/literature/Bulletin_6311.pdf

589. EuroMRD Board. *Instructions for DdPCR Task.*; 2019. https://www.euromrd.org/usr/pub/pub.php

590. Fakhr E, Zare F, Teimoori-Toolabi L. Precise and efficient siRNA design: A key point in competent gene silencing. *Cancer Gene Ther*. 2016;23(4):73-82. doi:10.1038/cgt.2016.4

591. Wang L, Mu FY. A web-based design center for vector-based siRNA and siRNA cassette. *Bioinformatics*. 2004;20(11):1818-1820. doi:10.1093/bioinformatics/bth164

592. Integrated DNA Technologies Inc. (IDT). Custom Dicer-Substrate siRNA (DsiRNA). Accessed November 28, 2020. https://eu.idtdna.com/site/order/designtool/index/DSIRNA_CUSTOM

593. Boudreau RL, Spengler RM, Hylock RH, et al. SiSPOTR: A tool for designing highly specific and

potent siRNAs for human and mouse. *Nucleic Acids Res*. 2013;41(1):e9. doi:10.1093/nar/gks797

594. Altschul SF, Gish W, Miller W, Myers EW, Lipman DJ. Basic local alignment search tool. *J Mol Biol*. 1990;215(3):403-410. doi:10.1016/S0022-2836(05)80360-2

595. Jackson AL, Burchard J, Schelter J, et al. Widespread siRNA "off-target" transcript silencing mediated by seed region sequence complementarity. *RNA*. 2006;12(7):1179-1187. doi:10.1261/rna.25706

596. Mello CC, Conte D. Revealing the world of RNA interference. *Nature*. 2004;431(7006):338-342. doi:10.1038/nature02872

597. Song H, Yang P-C. Construction of shRNA lentiviral vector. *N Am J Med Sci*. 2010;2(12):598-601. doi:10.4297/najms.2010.2598

598. Overath MD, Szymansky A, Witthauer MJ, et al. ASPM is a novel risk factor of aggressive neuroblastoma. *Klin Padiatr*. 2017;229(03):A26. doi:10.1055/s-0037-1602208

599. Hahne M. Analyse zum Einfluss der Hypoxie induzierbaren Faktoren HIF-1 und HIF-2 auf die Angiogenese von Endothelzellen. Published online 2013. doi:10.14279/depositonce-3529

600. Henssen AG, Koche R, Zhuang J, et al. PGBD5 promotes site-specific oncogenic mutations in human tumors. *Nat Genet*. 2017;49(7):1005-1014. doi:10.1038/ng.3866

601. Stewart SA, Dykxhoorn DM, Palliser D, et al. Lentivirus-delivered stable gene silencing by RNAi in primary cells. *RNA*. 2003;9(4):493-501. doi:10.1261/rna.2192803

602. Muth D, Ghazaryan S, Eckerle I, et al. Transcriptional repression of SKP2 is impaired in MYCN-amplified neuroblastoma. *Cancer Res*. 2010;70(9):3791-3802. doi:10.1158/0008-5472.CAN-09-1245

603. Overath MD. The functional relevance of the centrosomal mitotic-spindle protein ASPM as a novel risk factor in neuroblastoma. Published online 2019. https://www.tu.berlin/ub/suchen-ausleihen/nichts-gefunden/abschlussarbeiten/

604. Wang HX, Li M, Lee CM, et al. CRISPR/Cas9-Based Genome Editing for Disease Modeling and Therapy: Challenges and Opportunities for Nonviral Delivery. *Chem Rev*. 2017;117(15):9874-9906. doi:10.1021/acs.chemrev.6b00799

605. Suo L. CRISPR-Based Gene Editing. *Reprod Biomed Online*. 2019;38(1):E10. doi:10.1016/j.rbmo.2019.03.019

606. Gruzdev A, Scott GJ, Hagler TB, Ray MK. CRISPR/Cas9-assisted genome editing in murine embryonic stem cells. *Methods Mol Biol*. 2019;1960:1-21. doi:10.1007/978-1-4939-9167-9_1

607. Nishiyama J. Genome editing in the mammalian brain using the CRISPR–Cas system. *Neurosci Res*. 2019;141:4-12. doi:10.1016/j.neures.2018.07.003

608. Ishino Y, Shinagawa H, Makino K, Amemura M, Nakatura A. Nucleotide sequence of the iap gene, responsible for alkaline phosphatase isoenzyme conversion in Escherichia coli, and identification of the gene product. *J Bacteriol*. 1987;169(12):5429-5433. doi:10.1128/jb.169.12.5429-5433.1987

609. Haft DH, Selengut J, Mongodin EF, Nelson KE. A guild of 45 CRISPR-associated (Cas) protein families and multiple CRISPR/cas subtypes exist in prokaryotic genomes. *PLoS Comput Biol*. 2005;1(6):e60. doi:10.1371 /journal.pcbi.0010060

610. Brouns SJJ, Jore MM, Lundgren M, et al. Small CRISPR RNAs guide antiviral defense in prokaryotes. *Science*. 2008;321(5891):960-964. doi:10.1126/science.1159689

611. Cong L, Ran FA, Cox D, et al. Multiplex genome engineering using CRISPR/Cas systems. *Science*. 2013;339(6121):819-823. doi:10.1126/science.1231143

612. Jinek M, Chylinski K, Fonfara I, Hauer M, Doudna JA, Charpentier E. A programmable dual-RNA-guided DNA endonuclease in adaptive bacterial immunity. *Science*. 2012;337(6096):816-821. doi:10.1126/science.1225829

613. Shah SA, Erdmann S, Mojica FJM, Garrett RA. Protospacer recognition motifs. *RNA Biol*. 2013;10(5):891-899. doi:10.4161/rna.23764

614. Pardo B, Gómez-González B, Aguilera A. DNA repair in mammalian cells: DNA double-strand break repair: how to fix a broken relationship. *Cell Mol Life Sci*. 2009;66(6):1039-1056. doi:10.1007/s00018-009-8740-3

615. Lyu Q, Dhagia V, Han Y, et al. CRISPR-Cas9-mediated epitope tagging provides accurate and versatile assessment of myocardin-brief report. *Arterioscler Thromb Vasc Biol*. 2018;38(9):2184-2190.

doi:10.1161/ATVBAHA.118.311171

616. Moen MJ, Adams HHH, Brandsma JH, et al. An interaction network of mental disorder proteins in neural stem cells. *Transl Psychiatry*. 2017;7(4):e1082. doi:10.1038/tp.2017.52

617. Banan M. Recent advances in CRISPR/Cas9-mediated knock-ins in mammalian cells. *J Biotechnol*. 2019;308:1-9. doi:10.1016/J.JBIOTEC.2019.11.010

618. Fellmann C, Gowen BG, Lin PC, Doudna JA, Corn JE. Cornerstones of CRISPR-Cas in drug discovery and therapy. *Nat Rev Drug Discov*. 2017;16(2):89-100. doi:10.1038/nrd.2016.238

619. Zhang F. CRISPR/Cas9 guide design tool. Accessed November 28, 2020. http://crispr.mit.edu

620. Vouillot L, Thélie A, Pollet N. Comparison of T7E1 and surveyor mismatch cleavage assays to detect mutations triggered by engineered nucleases. *G3 Genes, Genomes, Genet*. 2015;5(3):407-415. doi:10.1534/g3.114.015834

621. Guschin DY, Waite AJ, Katibah GE, Miller JC, Holmes MC, Rebar EJ. A rapid and general assay for monitoring endogenous gene modification. J. M, D. S, eds. *Methods Mol Biol*. 2010;649:247-256. doi:10.1007/978-1-60761-753-2_15

622. Bustin SA, Benes V, Garson JA, et al. The MIQE guidelines: Minimum information for publication of quantitative real-time PCR experiments. *Clin Chem*. 2009;55(4):611-622. doi:10.1373/clinchem.2008.112797

623. Arya M, Shergill IS, Williamson M, Gommersall L, Arya N, Patel HRH. Basic principles of real-time quantitative PCR. *Mol Biotechnol*. 2005;5(2):209-219. doi:10.1586/14737159.5.2.209

624. Applied Biosystems Life Technologies. Life Technologies: Real-time PCR handbook. *B Chapter*. Published online 2012:1-70. https://www.thermofisher.com/content/dam/LifeTech/global/Forms/PDF/real-time-pcr-handbook.pdf

625. Vandesompele J, De Preter K, Pattyn F, et al. Accurate normalization of real-time quantitative RT-PCR data by geometric averaging of multiple internal control genes. *Genome Biol*. 2002;3(7):RESEARCH0034. doi:10.1186/gb-2002-3-7-research0034

626. Livak KJ, Schmittgen TD. Analysis of relative gene expression data using real-time quantitative PCR and the 2^(-ΔΔCT) method. *Methods*. 2001;25(4):402-408. doi:10.1006/meth.2001.1262

627. Schägger H, von Jagow G. Tricine-sodium dodecyl sulfate-polyacrylamide gel electrophoresis for the separation of proteins in the range from 1 to 100 kDa. *Anal Biochem*. 1987;166(2):368-379. doi:10.1016/0003-2697(87)90587-2

628. Burnette WN. "Western Blotting": Electrophoretic transfer of proteins from sodium dodecyl sulfate-polyacrylamide gels to unmodified nitrocellulose and radiographic detection with antibody and radioiodinated protein A. *Anal Biochem*. 1981;112(2):195-203. doi:10.1016/0003-2697(81)90281-5

629. Ni D, Xu P, Gallagher S. Immunoblotting and immunodetection. *Curr Protoc Protein Sci*. 2017;88(10):10.10.1-10.10.37. doi:10.1002/cpps.32

630. Plenker D, Bertrand M, de Langen AJ, et al. Structural alterations of MET trigger response to MET kinase inhibition in lung adenocarcinoma patients. *Clin Cancer Res*. 2018;24(6):1337-1343. doi:10.1158/1078-0432.CCR-17-3001

631. Müller JN, Falk M, Talwar J, et al. Concordance between Comprehensive Cancer Genome Profiling in Plasma and Tumor Specimens. *J Thorac Oncol*. 2017;12(10):1503-1511. doi:10.1016/j.jtho.2017.07.014

632. Messing J. New M13 Vectors for Cloning. *Methods Enzymol*. 1983;101:20-78. doi:10.1016/0076-6879(83)01005-8

633. Chong Z, Ruan J, Gao M, et al. novoBreak: local assembly for breakpoint detection in cancer genomes. *Nat Methods*. 2017;14(1):6-11. doi:10.1038/nmeth.4084

634. Szymansky A, Hertwig F, Winkler A, et al. Quantitative and highly sensitive detection of neuroblastoma minimal residual disease based on MYCN amplicon breakpoints. *Manuscript in submission*. 2020;.

635. Hertwig F, Menon R, Ackermann S, et al. Neuroblastoma Risk Assessment and Treatment Stratification with Hybrid Capture-based Panel Sequencing. *Manuscript in preparation*. 2020;.

636. Arsenijevic V, Davis-Dusenbery BN. Reproducible, Scalable Fusion Gene Detection from RNA-Seq. Grützmann R, Pilarsky C, eds. *Cancer Gene Profiling Methods Protoc*. 2016;1381:223–237. doi:0.1007/978-1-4939-3204-7_13

637. Thorvaldsdóttir H, Robinson JT, Mesirov JP. Integrative Genomics Viewer (IGV): High-performance genomics data visualization and exploration. *Brief Bioinform*. 2013;14(2):178-192. doi:10.1093/bib/bbs017

638. Robinson JT, Thorvaldsdóttir H, Winckler W, et al. Integrative genomics viewer. *Nat Biotechnol*. 2011;29(1):24-26. doi:10.1038/nbt.1754

639. Pepper SD, Saunders EK, Edwards LE, Wilson CL, Miller CJ. The utility of MAS5 expression summary and detection call algorithms. *BMC Bioinformatics*. 2007;8(273). doi:10.1186/1471-2105-8-273

640. R Development Core Team. *R: A Language and Environment for Statistical Computing.* R Foundation for Statistical Computing; 2018. http://www.r-project.org/

641. Rstudio Team. RStudio: Integrated development for R. RStudio, Inc., Boston MA. *RStudio*. Published online 2016.

642. Gentleman R, Carey V. Visualization and Annotation of Genomic Experiments. In: Irizarry RA, Zeger SL, eds. *The Analysis of Gene Expression Data*. Springer; 2003:46-72. doi:10.1007/0-387-21679-0_2

643. Rédei GP. Bioconductor. In: *Encyclopedia of Genetics, Genomics, Proteomics and Informatics*. 3rd Ed. Springer; 2008:1- 2231. doi:doi:10.1007/978-1-4020-6754-9_1773

644. Gentleman RC, Carey VJ, Bates DM, et al. Bioconductor: open software development for computational biology and bioinformatics. *Genome Biol*. 2004;5(10):R80. doi:10.1186/gb-2004-5-10-r80

645. Alexa A, Rahnenführer J, Lengauer T. Improved scoring of functional groups from gene expression data by decorrelating GO graph structure. *Bioinformatics*. 2006;22(13):1600-1607. doi:10.1093/bioinformatics/btl140

646. Qiagen. *Critical Factors for Successful Real-Time PCR.*; 2010. https://www.qiagen.com/gb/resources/download.aspx?id=f7efb4f4-fbcf-4b25-9315-c4702414e8d6&lang=en

647. Rao X, Huang X, Zhou Z, Lin X. An improvement of the 2ˆ(-delta delta CT) method for quantitative real-time polymerase chain reaction data analysis. *Biostat Bioinforma Biomath*. 2013;3(3):71-85.

648. Tanoli ZR, Alam Z, Vähä-Koskela M, et al. Drug Target Commons 2.0: A community platform for systematic analysis of drug-target interaction profiles. *Database*. 2018;2018:1-13. doi:10.1093/database/bay083

649. Edwards PD, Wolanin DJ, Andisik DW, Davis MW. Peptidyl alpha-ketoheterocyclic inhibitors of human neutrophil elastase. 2. Effect of varying the heterocyclic ring on in vitro potency. *J Med Chem*. 1995;38(1):76-85. doi:10.1021/jm00001a013

650. Berenbaum MC. What is synergy? *Pharmacol Rev*. 1989;41(2):93-141.

651. Chou TC. Drug combination studies and their synergy quantification using the Chou-Talalay method. *Cancer Res*. 2010;70(2):440-446. doi:10.1158/0008-5472.CAN-09-1947

652. Bliss CI. The calculation of microbial assays. *Bacteriol Rev*. 1956;20(4):243-258. doi:10.1128/br.20.4.243-258.1956

653. Fitzgerald JB, Schoeberl B, Nielsen UB, Sorger PK. Systems biology and combination therapy in the quest for clinical efficacy. *Nat Chem Biol*. 2006;2(9):458-466. doi:10.1038/nchembio817

654. Commo F, Bot BM. R package nplr n-parameter logistic regressions. *vignettes*. Published online 2016:1-11. https://cran.r-project.org/web/packages/nplr/vignettes/nplr.pdf

655. Dragulescu AA. *Package ' Xlsx . '*; 2012. https://cran.r-project.org/web/packages/xlsx/xlsx.pdf

656. Neuwirth E. RColorBrewer: ColorBrewer palettes. *R Packag version 11-2*. Published online 2014. https://rdrr.io/cran/RColorBrewer/man/ColorBrewer.html

657. Chang W. Package 'extrafont.' *Tools for using fonts*. Published online 2014. Accessed November 28, 2020. https://github.com/wch/extrafont

658. Wickham H. *Ggplot2 Elegant Graphics for Data Analysis*. 2nd ed. Springer; 2016. doi:10.1007/978-3-319-24277-4

659. Eckert C. ddPCR MRD calculation. Published online 2016:pers. comm.

660. Witte AK, Mester P, Fister S, Witte M, Schoder D, Rossmanith P. A Systematic Investigation of Parameters Influencing Droplet Rain in the Listeria monocytogenes prfA Assay - Reduction of

Ambiguous Results in ddPCR. *PLoS One*. 2016;11(12):e0168179. doi:10.1371/journal.pone.0168179

661. Hurst J. definetherain. MIT - Massachusetts Institute of Technology. Published 2014. Accessed November 28, 2020. http://definetherain.org.uk/

662. Jones M, Williams J, Gärtner K, Phillips R, Hurst J, Frater J. Low copy target detection by Droplet Digital PCR through application of a novel open access bioinformatic pipeline, "definetherain." *J Virol Methods*. 2014;202(100):46-53. doi:10.1016/j.jviromet.2014.02.020

663. Strain MC, Lada SM, Luong T, et al. Highly Precise Measurement of HIV DNA by Droplet Digital PCR. *PLoS One*. 2013;8(4):e55943. doi:10.1371/journal.pone.0055943

664. Trypsteen W, Vynck M, De Neve J, et al. ddpcRquant: threshold determination for single channel droplet digital PCR experiments. *Anal Bioanal Chem*. 2015;407(19):5827-5834. doi:10.1007/s00216-015-8773-4

665. Dingle TC, Sedlak RH, Cook L, Jerome KR. Tolerance of droplet-digital PCR vs real-time quantitative PCR to inhibitory substances. *Clin Chem*. 2013;59(11):1670-1672. doi:10.1373/clinchem.2013.211045

666. BioRad. Droplet Digital™ PCR: Rare Mutation Detection Best Practices Guidelines. *Bulletin*. Bulletin 6:14-1824 0215 Sig 1214. https://www.bio-rad.com/webroot/web/pdf/lsr/literature/Bulletin_6628.pdf

667. Neuroblastoma UK. 4th Neuroblastoma Research Symposium. Published 2015. Accessed November 28, 2020. https://www.neuroblastoma.org.uk/neuroblastoma-events/2015/11/26/4th-neuroblastoma-research-symposium

668. Schleiermacher G, Janoueix-Lerosey I, Combaret V, et al. Combined 24-color karyotyping and comparative genomic hybridization analysis indicates predominant rearrangements of early replicating chromosome regions in neuroblastoma. *Cancer Genet Cytogenet*. 2003;141(1):32-42. doi:10.1016/S0165-4608(02)00644-1

669. Deveson IW, Madala BS, Blackburn J, et al. Chiral DNA sequences as commutable controls for clinical genomics. *Nat Commun*. 2019;10(1):1342. doi:10.1038/s41467-019-09272-0

670. Vcelar S, Melcher M, Auer N, et al. Changes in Chromosome Counts and Patterns in CHO Cell Lines upon Generation of Recombinant Cell Lines and Subcloning. *Biotechnol J*. 2018;13(3):e1700495. doi:10.1002/biot.201700495

671. Brüggemann M, Schrauder A, Raff T, et al. Standardized MRD quantification in European ALL trials: proceedings of the Second International Symposium on MRD assessment in Kiel, Germany, 18-20 September 2008. In: *Leukemia*. Vol 24. ; 2010:521-535. doi:10.1038/leu.2009.268

672. Stanulla M, Dagdan E, Zaliova M, et al. IKZF1 plus defines a new minimal residual disease-dependent very-poor prognostic profile in pediatric b-cell precursor acute lymphoblastic leukemia. *J Clin Oncol*. 2018;36(12):1240-1249. doi:10.1200/JCO.2017.74.3617

673. Pott C, Brüggemann M, Ritgen M, Van Der Velden VHJ, Van Dongen JJM, Kneba M. MRD Detection in B-Cell Non-Hodgkin Lymphomas Using Ig Gene Rearrangements and Chromosomal Translocations as Targets for Real-Time Quantitative PCR. *Methods Mol Biol*. 2013;1956:199-228. doi:10.1007/978-1-62703-269-8_10

674. Cheung N-K V, Zhang J, Lu C, et al. Association of age at diagnosis and genetic mutations in patients with neuroblastoma. *JAMA*. 2012;307(10):1062-1071. doi:10.1001/jama.2012.228

675. Archambeault S, Flores NJ, Yoshimi A, et al. Development of an allele-specific minimal residual disease assay for patients with juvenile myelomonocytic leukemia. *Blood*. 2008;111(3):1124-1127. doi:10.1182/blood-2007-06-093302

676. Cariati F, Borrillo F, Shankar V, Nunziato M, D'argenio V, Tomaiuolo R. Dissecting intra-tumor heterogeneity by the analysis of copy number variations in single cells: The neuroblastoma case study. *Int J Mol Sci*. 2019;20(4):893. doi:10.3390/ijms20040893

677. Maris JM, White PS, Beltinger CP, et al. Significance of Chromosome 1p Loss of Heterozygosity in Neuroblastoma. *Cancer Res*. 1995;55(20):4664-4669.

678. Hallstensson K, Thulin S, Aburatani H, Hippo Y, Martinsson T. Representational difference analysis and loss of heterozygosity studies detect 3p deletions in neuroblastoma. *Eur J Cancer*. 1997;33(12):1966-1970. doi:10.1016/S0959-8049(97)00228-1

679. Caron H, Van Sluis P, Buschman R, et al. Allelic loss of the short arm of chromosome 4 in neuroblastoma suggests a novel tumour suppressor gene locus. *Hum Genet*. 1996;97(6):834-837.

doi:10.1007/BF02346199

680. Carén H, Kryh H, Nethander M, et al. High-risk neuroblastoma tumors with 11q-deletion display a poor prognostic, chromosome instability phenotype with later onset. *Proc Natl Acad Sci USA*. 2010;107(9):4323-4328. doi:10.1073/pnas.0910684107

681. Pezzolo A, Rossi E, Gimelli S, et al. Presence of 1q gain and absence of 7p gain are new predictors of local or metastatic relapse in localized resectable neuroblastoma. *Neuro Oncol*. 2009;11(2):192-200. doi:10.1215/15228517-2008-086

682. Oldridge DA, Truong B, Russ D, et al. Differences in Genomic Profiles and Outcomes Between Thoracic and Adrenal Neuroblastoma. *J Natl Cancer Inst*. 2019;111(11):1192-1201. doi:10.1093/jnci/djz027

683. Szewczyk K, Wieczorek A, Młynarski W, et al. Unfavorable Outcome of Neuroblastoma in Patients With 2p Gain. *Front Oncol*. 2019;9(1018):eCollection 2019. doi:10.3389/fonc.2019.01018

684. Schnepp RW, Maris JM. Targeting MYCN: A Good BET for improving neuroblastoma therapy? *Cancer Discov*. 2013;3(3):255-257. doi:10.1158/2159-8290.CD-13-0018

685. Veneziani I, Fruci D, Compagnone M, Pistoia V, Rossi P. The BET-bromodomain inhibitor JQ1 renders neuroblastoma cells more resistant to NK cell-mediated recognition and killing by downregulating ligands for NKG2D and DNAM-1 receptors. 2019;10(22):2151-2160.

686. Di Micco R, Fontanals-Cirera B, Low V, et al. Control of embryonic stem cell identity by brd4-dependent transcriptional elongation of super-enhancer-associated pluripotency genes. *Cell Rep*. 2014;9(1):234-247. doi:10.1016/j.celrep.2014.08.055

687. Tang Y, Gholamin S, Schubert S, et al. Epigenetic targeting of Hedgehog pathway transcriptional output through BET bromodomain inhibition. *Nat Med*. 2014;20(7):732-740. doi:10.1038/nm.3613

688. Bandopadhayay P, Bergthold G, Nguyen B, et al. BET bromodomain inhibition of MYC-amplified medulloblastoma. *Clin Cancer Res*. 2014;20(4):912-925. doi:10.1158/1078-0432.CCR-13-2281

689. Henssen A, Thor T, Odersky A, et al. BET bromodomain protein inhibition is a therapeutic option for medulloblastoma. *Oncotarget*. 2013;4(11):2080-2095. doi:10.18632/oncotarget.1534

690. Alqahtani A, Choucair K, Ashraf M, et al. Bromodomain and extra-terminal motif inhibitors: A review of preclinical and clinical advances in cancer therapy. *Futur Sci OA*. 2019;5(3):FSO372. doi:10.4155/fsoa-2018-0115

691. Berthon C, Raffoux E, Thomas X, et al. Bromodomain inhibitor OTX015 in patients with acute leukaemia: A dose-escalation, phase 1 study. *Lancet Haematol*. 2016;3(4):e186-95. doi:10.1016/S2352-3026(15)00247-1

692. Foulkes WD, Flanders TY, Pollock PM, Hayward NK. The CDKN2A (p16) gene and human cancer. *Mol Med*. 1997;3(1):5-20. doi:10.1007/bf03401664

693. Sharpless NE. INK4a/ARF: A multifunctional tumor suppressor locus. *Mutat Res - Fundam Mol Mech Mutagen*. 2005;576(1-2):22-38. doi:10.1016/j.mrfmmm.2004.08.021

694. Esteller M, Tortola S, Toyota M, et al. Hypermethylation-associated inactivation of p14(ARF) is independent of p16(INK4a) methylation and p53 mutational status. *Cancer Res*. 2000;60(1):129-133.

695. Carr J, Bell E, Pearson ADJ, et al. Increased frequency of aberrations in the p53/MDM2/p14ARF pathway in neuroblastoma cell lines established at relapse. *Cancer Res*. 2006;66(4):2138-2145. doi:10.1158/0008-5472.CAN-05-2623

696. Dreidax D, Gogolin S, Schroeder C, et al. Low p14ARF expression in neuroblastoma cells is associated with repressed histone mark status, and enforced expression induces growth arrest and apoptosis. *Hum Mol Genet*. 2013;22(9):1735-1745. doi:10.1093/hmg/ddt020

697. Lee KS, Burke TR, Park JE, Bang JK, Lee E. Recent Advances and New Strategies in Targeting Plk1 for Anticancer Therapy. *Trends Pharmacol Sci*. 2015;36(12):858-877. doi:10.1016/j.tips.2015.08.013

698. Gutteridge REA, Ndiaye MA, Liu X, Ahmad N. Plk1 inhibitors in cancer therapy: From laboratory to clinics. *Mol Cancer Ther*. 2016;15(7):1427-1435. doi:10.1158/1535-7163.MCT-15-0897

699. Bowles DW, Diamond JR, Lam ET, et al. Phase i study of oral rigosertib (ON 01910.NA), a dual inhibitor of the PI3K and PLK1 pathways, in adult patients with advanced solid malignancies. *Clin Cancer Res*. 2014;20(6):1656-1665. doi:10.1158/1078-0432.CCR-13-2506

700. O'Neil BH, Scott AJ, Ma WW, et al. A phase II/III randomized study to compare the efficacy and safety of rigosertib plus gemcitabine versus gemcitabine alone in patients with previously untreated metastatic pancreatic cancer. *Ann Oncol*. 2015;26(9):1923-1929. doi:10.1093/annonc/mdv264

701. Garcia-Manero G, Fenaux P, Al-Kali A, et al. Rigosertib versus best supportive care for patients with high-risk myelodysplastic syndromes after failure of hypomethylating drugs (ONTIME): a randomised, controlled, phase 3 trial. *Lancet Oncol*. 2016;17(4):496-508. doi:10.1016/S1470-2045(16)00009-7

702. Tontsch-Grunt U, Rudolph D, Waizenegger I, et al. Synergistic activity of BET inhibitor BI 894999 with PLK inhibitor volasertib in AML in vitro and in vivo. *Cancer Lett*. 2018;421:112-120. doi:10.1016/j.canlet.2018.02.018

703. Shi L, Lin Q, Su B. Human-specific hypomethylation of CENPJ, a key brain size regulator. *Mol Biol Evol*. 2014;31(3):594-604. doi:10.1093/molbev/mst231

704. Evans PD, Gilbert SL, Mekel-Bobrov N, et al. Microcephalin, a gene regulating brain size, continues to evolve adaptively in humans. *Science*. 2005;309(5741):1717-1720. doi:10.1126/science.1113722

705. Cox J, Jackson AP, Bond J, Woods CG. What primary microcephaly can tell us about brain growth. *Trends Mol Med*. 2006;12(8):358-366. doi:10.1016/j.molmed.2006.06.006

706. Timaner M, Shaked Y. Elucidating the roles of ASPM isoforms reveals a novel prognostic marker for pancreatic cancer. *J Pathol*. 2020;250(2):123-125. doi:10.1002/path.5355

707. Brüning-Richardson A, Bond J, Alsiary R, et al. ASPM and microcephalin expression in epithelial ovarian cancer correlates with tumour grade and survival. *Br J Cancer*. 2011;104(10):1602-1610. doi:10.1038/bjc.2011.117

708. Xu Z, Zhang QI, Luh F, Jin B, Liu X. Overexpression of the ASPM gene is associated with aggressiveness and poor outcome in bladder cancer. *Oncol Lett*. 2019;17(2):1865-1876. doi:10.3892/ol.2018.9762

709. Ishimaru S, Weppner J, Poxrucker A, Kunze K, Lukowicz P, Kise K. Shiny: an activity logging platform for Google Glass. In: *Proceedings of the 2014 ACM International Joint Conference on Pervasive and Ubiquitous Computing*. Vol UbiComp '1. ; 2014:283–286. doi:10.1145/2638728.2638798

710. RStudio Inc. Shiny: Easy web applications in R. *http://shiny.rstudio.com/*. Published online 2014.

711. Rich JT, Neely JG, Paniello RC, Voelker CCJ, Nussenbaum B, Wang EW. A practical guide to understanding Kaplan-Meier curves. *Otolaryngol - Head Neck Surg*. 2010;143(3):331-336. doi:10.1016/j.otohns.2010.05.007

712. Matthay KK, Reynolds CP, Seeger RC, et al. Long-term results for children with high-risk neuroblastoma treated on a randomized trial of myeloablative therapy followed by 13-cis-retinoic acid: A children's oncology group study. *J Clin Oncol*. 2009;27(7):1007-1013. doi:10.1200/JCO.2007.13.8925

713. Akiyama K, Kanda N, Yamada M, Tadokoro K, Matsunaga T, Nishi Y. Megabase-scale analysis of the origin of N-myc amplicons in human neuroblastomas. *Nucleic Acids Res*. 1994;22(2):187-193. doi:10.1093/nar/22.2.187

714. Carén H, Erichsen J, Olsson L, et al. High-resolution array copy number analyses for detection of deletion, gain, amplification and copy-neutral LOH in primary neuroblastoma tumors: Four cases of homozygous deletions of the CDKN2A gene. *BMC Genomics*. 2008;9(353). doi:10.1186/1471-2164-9-353

715. Michels E, Vandesompele J, Hoebeeck J, et al. Genome wide measurement of DNA copy number changes in neuroblastoma: Dissecting amplicons and mapping losses, gains and breakpoints. *Cytogenet Genome Res*. 2006;115(3-4):273-282. doi:10.1159/000095924

716. Villamón E, Berbegall AP, Piqueras M, et al. Genetic Instability and Intratumoral Heterogeneity in Neuroblastoma with MYCN Amplification Plus 11q Deletion. *PLoS One*. 2013;8(1):e53740. doi:10.1371/journal.pone.0053740

717. Vinogradov AE, Anatskaya O V. DNA helix: the importance of being AT-rich. *Mamm Genome*. 2017;28(9-10):455-464. doi:10.1007/s00335-017-9713-8

718. Dekker J. GC- and AT-rich chromatin domains differ in conformation and histone modification status and are differentially modulated by Rpd3p. *Genome Biol*. 2007;8(6):R116. doi:10.1186/gb-2007-8-6-r116

719. Irony-Tur Sinai M, Salamon A, Stanleigh N, et al. AT-dinucleotide rich sequences drive fragile site formation. *Nucleic Acids Res*. 2019;47(18):9685-9695. doi:10.1093/nar/gkz689

720. Schwartz M, Zlotorynski E, Kerem B. The molecular basis of common and rare fragile sites. *Cancer Lett*. 2006;232(1):13-26. doi:10.1016/j.canlet.2005.07.039

721. Zlotorynski E, Rahat A, Skaug J, et al. Molecular Basis for Expression of Common and Rare Fragile Sites. *Mol Cell Biol*. 2003;23(20):7143-7151. doi:10.1128/mcb.23.20.7143-7151.2003

722. Burrow AA, Marullo A, Holder LR, Wang YH. Secondary structure formation and DNA instability at fragile site FRA16B. *Nucleic Acids Res*. 2010;38(9):2865-2877. doi:10.1093/nar/gkp1245

723. W. Dillon L, A. Burrow A, Wang Y-H. DNA Instability at Chromosomal Fragile Sites in Cancer. *Curr Genomics*. 2010;11(5):326-337. doi:10.2174/138920210791616699

724. Lipska BS, Koczkowska M, Wierzba J, et al. On the significance of germline cytogenetic rearrangements at MYCN locus in neuroblastoma. *Mol Cytogenet*. 2013;6(1):43. doi:10.1186/1755-8166-6-43

725. Savelyeva L, Brueckner LM. Molecular characterization of common fragile sites as a strategy to discover cancer susceptibility genes. *Cell Mol Life Sci*. 2014;71(23):4561-4575. doi:10.1007/s00018-014-1723-z

726. Glover TW, Berger C, Coyle J, Echo B. DNA polymerase α inhibition by aphidicolin induces gaps and breaks at common fragile sites in human chromosomes. *Hum Genet*. 1984;67(2):136-142. doi:10.1007/BF00272988

727. Schild D, Wiese C. Overexpression of RAD51 suppresses recombination defects: A possible mechanism to reverse genomic instability. *Nucleic Acids Res*. 2010;38(4):1061-1070. doi:10.1093/nar/gkp1063

728. Bindra RS, Schaffer PJ, Meng A, et al. Down-Regulation of Rad51 and Decreased Homologous Recombination in Hypoxic Cancer Cells. *Mol Cell Biol*. 2004;24(19):8504-8518. doi:10.1128/mcb.24.19.8504-8518.2004

729. Roy MA, Dhanaraman T, D'Amours D. The Smc5-Smc6 heterodimer associates with DNA through several independent binding domains. *Sci Rep*. 2015;5(9797). doi:10.1038/srep09797

730. Yong-Gonzales V, Hang LE, Castellucci F, Branzei D, Zhao X. The Smc5-Smc6 Complex Regulates Recombination at Centromeric Regions and Affects Kinetochore Protein Sumoylation during Normal Growth. *PLoS One*. 2012;7(12):e51540. doi:10.1371/journal.pone.0051540

731. Moradi-Fard S, Sarthi J, Tittel-Elmer M, et al. Smc5/6 Is a Telomere-Associated Complex that Regulates Sir4 Binding and TPE. *PLoS Genet*. 2016;12(8):e1006268. doi:10.1371/journal.pgen.1006268

732. Sobhy MA, Bralić A, Raducanu VS, et al. Resolution of the Holliday junction recombination intermediate by human GEN1 at the single-molecule level. *Nucleic Acids Res*. 2019;47(4):1935-1949. doi:10.1093/nar/gky1280

733. Punatar RS, Martin MJ, Wyatt HDM, Chan YW, West SC. Resolution of single and double Holliday junction recombination intermediates by GEN 1. *Proc Natl Acad Sci USA*. 2017;114(3):443-450. doi:10.1073/pnas.1619790114

734. Sala-Newby GB, Newby AC. Cloning of a mouse cytosolic 5′-nucleotidase-I identifies a new gene related to human autoimmune infertility-related protein. *Biochim Biophys Acta - Gene Struct Expr*. 2001;1521(1-3):12-18. doi:10.1016/S0167-4781(01)00278-0

735. Aoki T, Ichimura S, Itoh A, et al. Identification of the neuroblastoma-amplified gene product as a component of the syntaxin 18 complex implicated in Golgi-to-endoplasmic reticulum retrograde transport. *Mol Biol Cell*. 2009;20(11):2639-2649. doi:10.1091/mbc.E08-11-1104

736. Fort L, Batista JM, Thomason PA, et al. Fam49/CYRI interacts with Rac1 and locally suppresses protrusions. *Nat Cell Biol*. 2018;20(10):1159-1171. doi:10.1038/s41556-018-0198-9

737. Whitelaw JA, Lilla S, Paul NR, Fort L, Zanivan S, Machesky LM. CYRI/ Fam49 Proteins Represent a New Class of Rac1 Interactors. *Commun Integr Biol*. 2019;12(1):112-118. doi:10.1080/19420889.2019.1643665

738. Fu J, Zhang J, Jin F, Patchefsky J, Braunewell KH, Klein-Szanto AJ. Promoter regulation of the visinin-like subfamily of neuronal calcium sensor proteins by nuclear respiratory factor-1. *J Biol Chem*. 2009;284(40):27577-27587. doi:10.1074/jbc.M109.049361

739. Lin CW, Chang LC, Tseng GC, Kirkwood CM, Sibille EL, Sweet RA. VSNL1 co-expression networks

in aging include calcium signaling, synaptic plasticity, and Alzheimer's disease pathways. *Front Psychiatry*. 2015;6(30). doi:10.3389/fpsyt.2015.00030

740. Fior R, Maxwell AA, Ma TP, et al. The differentiation and movement of presomitic mesoderm progenitor cells are controlled by mesogenin 1. *Dev*. 2012;139(24):4656-4665. doi:10.1242/dev.078923

741. Liu D, Zhang Q, Zhang H, et al. A comprehensive transcriptomic analysis of differentiating embryonic stem cells in response to the overexpression of Mesogenin 1. *Aging (Albany NY)*. 2016;8(10):2324-2336. doi:10.18632/aging.101049

742. Zhang Y, Zhang X, Wang X, et al. Gen1 Modulates Metanephric Morphology Through Retinoic Acid Signaling. *DNA Cell Biol*. 2019;38(3):263-271. doi:10.1089/dna.2018.4426

743. Belyaeva O V., Korkina O V., Stetsenko A V., Kedishvili NY. Human retinol dehydrogenase 13 (RDH13) is a mitochondrial short-chain dehydrogenase/reductase with a retinaldehyde reductase activity. *FEBS J*. 2008;275(1):138-147. doi:10.1111/j.1742-4658.2007.06184.x

744. Williams TA, Monticone S, Crudo V, Warth R, Veglio F, Mulatero P. Visinin-like 1 is upregulated in aldosterone-producing adenomas with KCNJ5 mutations and protects from calcium-induced apoptosis. *Hypertension*. 2012;59(4):833-839. doi:10.1161/HYPERTENSIONAHA.111.188532

745. Barbagallo D, Condorelli A, Ragusa M, et al. Dysregulated miR-671-5p / CDR1-AS / CDR1 / VSNL1 axis is involved in glioblastoma multiforme. *Oncotarget*. 2016;7(4):4746-4759. doi:10.18632/oncotarget.6621

746. De Brouwer S, De Preter K, Kumps C, et al. Meta-analysis of neuroblastomas reveals a skewed ALK mutation spectrum in tumors with MYCN amplification. *Clin Cancer Res*. 2010;16(17):4353-4362. doi:10.1158/1078-0432.CCR-09-2660

747. Bogen D, Brunner C, Walder D, et al. The genetic tumor background is an important determinant for heterogeneous MYCN-amplified neuroblastoma. *Int J Cancer*. 2016;139(1):153-163. doi:10.1002/ijc.30050

748. Berbegall AP, Bogen D, Pötschger U, et al. Heterogeneous MYCN amplification in neuroblastoma: A SIOP Europe Neuroblastoma Study. *Br J Cancer*. 2018;118(11):1502-1512. doi:10.1038/s41416-018-0098-6

749. Marrano P, Irwin MS, Thorner PS. Heterogeneity of MYCN amplification in neuroblastoma at diagnosis, treatment, relapse, and metastasis. *Genes Chromosomes Cancer*. 2017;56(1):28-41. doi:10.1002/gcc.22398

750. Campbell K, Naranjo A, Hibbitts E, et al. Association of heterogeneous MYCN amplification with clinical features, biological characteristics and outcomes in neuroblastoma: A report from the Children's Oncology Group. *Eur J Cancer*. 2020;133:112-119. doi:10.1016/j.ejca.2020.04.007

751. Thole TM, Toedling J, Sprüssel A, et al. Reflection of neuroblastoma intratumor heterogeneity in the new OHC-NB1 disease model. *Int J Cancer*. 2020;146(4):1031-1041. doi:10.1002/ijc.32572

752. Braekeveldt N, Von Stedingk K, Fransson S, et al. Patient-derived xenograft models reveal intratumor heterogeneity and temporal stability in neuroblastoma. *Cancer Res*. 2018;78(20):5958-5969. doi:10.1158/0008-5472.CAN-18-0527

753. Zhang CZ, Spektor A, Cornils H, et al. Chromothripsis from DNA damage in micronuclei. *Nature*. 2015;522(7555):179-184. doi:10.1038/nature14493

754. Lundberg G, Rosengren AH, Håkanson U, et al. Binomial mitotic segregation of MYCN-carrying double minutes in neuroblastoma illustrates the role of randomness in oncogene Amplification. *PLoS One*. 2008;3(8):e3099. doi:10.1371/journal.pone.0003099

755. Solovei I, Kienle D, Little G, et al. Topology of double minutes (dmins) and homogeneously staining regions (HSRs) in nuclei of human neuroblastoma cell lines. *Genes Chromosomes Cancer*. 2000;29(4):297-308. doi:10.1002/1098-2264(2000)9999:9999<::AID-GCC1046>3.0.CO;2-H

756. Levan G, Mandahl N, Bregula U, Klein G, Levan A. Double minute chromosomes are not centromeric regions of the host chromosomes. *Hereditas*. 1976;83(1):83-90. doi:10.1111/j.1601-5223.1976.tb01573.x

757. Deng X, Zhang L, Zhang Y, et al. Double minute chromosomes in mouse methotrexate-resistant cells studied by atomic force microscopy. *Biochem Biophys Res Commun*. 2006;346(4):1228-1233. doi:10.1016/j.bbrc.2006.06.041

758. Schoenlein P V., Barrett JT, Kulharya A, et al. Radiation therapy depletes extrachromosomally amplified drug resistance genes and oncogenes from tumor cells via micronuclear capture of episomes and double minute chromosomes. *Int J Radiat Oncol Biol Phys*. 2003;55(4):1051-1065. doi:10.1016/S0360-3016(02)04473-5

759. Itoh N, Shimizu N. DNA replication-dependent intranuclear relocation of double minute chromatin. *J Cell Sci*. 1998;11(pt 22):3275-3285.

760. Møller HD, Bojsen R, Tachibana C, Parsons L, Botstein D, Regenberg B. Genome-wide purification of extrachromosomal circular DNA from eukaryotic cells. *J Vis Exp*. 2016;110:e54239. doi:10.3791/54239

761. Seol JH, Shim EY, Lee SE. Microhomology-mediated end joining: Good, bad and ugly. *Mutat Res - Fundam Mol Mech Mutagen*. 2018;809:81-87. doi:10.1016/j.mrfmmm.2017.07.002

762. Wang H, Xu X. Microhomology-mediated end joining: New players join the team. *Cell Biosci*. 2017;7(6). doi:10.1186/s13578-017-0136-8

763. Bennardo N, Cheng A, Huang N, Stark JM. Alternative-NHEJ is a mechanistically distinct pathway of mammalian chromosome break repair. *PLoS Genet*. 2008;4(6):e1000110. doi:10.1371/journal.pgen.1000110

764. Hastings PJ, Ira G, Lupski JR. A microhomology-mediated break-induced replication model for the origin of human copy number variation. *PLoS Genet*. 2009;5(1). doi:10.1371/journal.pgen.1000327

765. Mikulasova A, Ashby C, Tytarenko RG, et al. Microhomology-mediated end joining drives complex rearrangements and over expression of MYC and PVT1 in multiple myeloma. *Haematologica*. 2020;105(4):1055-1066. doi:10.3324/haematol.2019.217927

766. Brueckner LM, Sagulenko E, Hess EM, et al. Genomic rearrangements at the FRA2H common fragile site frequently involve non-homologous recombination events across LTR and L1(LINE) repeats. *Hum Genet*. 2012;131(8):1345-1359. doi:10.1007/s00439-012-1165-3

767. Coquelle A, Pipiras E, Toledo F, Buttin G, Debatisse M. Expression of fragile sites triggers intrachromosomal mammalian gene amplification and sets boundaries to early amplicons. *Cell*. 1997;89(2):215-225. doi:10.1016/S0092-8674(00)80201-9

768. Kuo MT, Vyas RC, Jiang LX, Hittelman WN. Chromosome breakage at a major fragile site associated with P-glycoprotein gene amplification in multidrug-resistant CHO cells. *Mol Cell Biol*. 1994;14(8):5202-5211. doi:10.1128/mcb.14.8.5202

769. Defferrari R, Tonini GP, Conte M, et al. Concomitant DDX1 and MYCN gain in neuroblastoma. *Cancer Lett*. 2007;256(1):56-63. doi:10.1016/j.canlet.2007.05.010

770. Ferber MJ, Thorland EC, Brink AATP, et al. Preferential integration of human papillomavirus type 18 near the c-myc locus in cervical carcinoma. *Oncogene*. 2003;22(46):7233-7242. doi:10.1038/sj.onc.1207006

771. Szafranski P, Kośmider E, Liu Q, et al. LINE- and Alu-containing genomic instability hotspot at 16q24.1 associated with recurrent and nonrecurrent CNV deletions causative for ACDMPV. *Hum Mutat*. 2018;39(12):1916-1925. doi:10.1002/humu.23608

772. Hu Z, Zhu D, Wang W, et al. Genome-wide profiling of HPV integration in cervical cancer identifies clustered genomic hot spots and a potential microhomology-mediated integration mechanism. *Nat Genet*. 2015;47(2):158-163. doi:10.1038/ng.3178

773. Hellman A, Zlotorynski E, Scherer SW, et al. A role for common fragile site induction in amplification of human oncogenes. *Cancer Cell*. 2002;1(1):89-97. doi:10.1016/S1535-6108(02)00017-X

774. Pui C-H, Robison LL, Look AT. Acute lymphoblastic leukaemia. *Lancet*. 2008;371(9617):1030-1043. doi:10.1016/S0140-6736(08)60457-2

775. Franke GN, Maier J, Wildenberger K, et al. Comparison of Real-Time Quantitative PCR and Digital Droplet PCR for BCR-ABL1 Monitoring in Patients with Chronic Myeloid Leukemia. *J Mol Diagnostics*. 2020;22(1):81-89. doi:10.1016/j.jmoldx.2019.08.007

776. Chen X, Wood BL. Monitoring minimal residual disease in acute leukemia: Technical challenges and interpretive complexities. *Blood Rev*. 2017;31(2):63-75. doi:10.1016/j.blre.2016.09.006

777. Krumbholz M, Goerlitz K, Albert C, Lawlor J, Suttorp M, Metzler M. Large amplicon droplet digital PCR for DNA-based monitoring of pediatric chronic myeloid leukaemia. *J Cell Mol Med*. 2019;23(8):4955-4961. doi:10.1111/jcmm.14321

778. Hovorkova L, Zaliova M, Venn NC, et al. Monitoring of childhood ALL using BCR-ABL1 genomic breakpoints identifies a subgroup with CML-like biology. *Blood*. 2017;129(20):2771-2781. doi:10.1182/blood-2016-11-749978

779. Krumbholz M, Karl M, Tauer JT, et al. Genomic BCR - ABL1 Breakpoints in Pediatric Chronic Myeloid Leukemia. *Genes Chromosomes Cancer*. 2012;51(11):1045-1053. doi:10.1002/gcc.21989

780. Moser O, Krumbholz M, Thiede C, et al. Sustained Complete Molecular Remission after Imatinib Discontinuation in Children with Chronic Myeloid Leukemia. *Pediatr Blood aCancerCancer*. 2014;61(11):2080-2082. doi:10.1002/pbc

781. Cumbo C, Impera L, Minervini CF, et al. Genomic BCR-ABL1 breakpoint characterization by a multi-strategy approach for " personalized monitoring " of residual disease in chronic myeloid leukemia patients. 2018;9(13):10978-10986.

782. Butler JMJM. *Forensic DNA Typing: Biology, Technology, and Genetics of STR Markers*. 2. Edition. Academic Press; 2005. doi:10.1007/s13398-014-0173-7.2

783. Bäumer C, Fisch E, Wedler H, Reinecke F, Korfhage C. Exploring DNA quality of single cells for genome analysis with simultaneous whole-genome amplification. *Sci Rep*. 2018;8(1):7476. doi:10.1038/s41598-018-25895-7

784. Stangl C, de Blank S, Renkens I, et al. Partner independent fusion gene detection by multiplexed CRISPR-Cas9 enrichment and long read nanopore sequencing. *Nat Commun*. 2020;11(1):2861. doi:10.1038/s41467-020-16641-7

785. Imaizumi T, Yamamoto-Shimojima K, Yanagishita T, Ondo Y, Yamamoto T. Analyses of breakpoint junctions of complex genomic rearrangements comprising multiple consecutive microdeletions by nanopore sequencing. *J Hum Genet*. 2020;65(9):735-741. doi:10.1038/s10038-020-0762-6

786. Fischer M, Skowron M, Berthold F. Reliable transcript quantification by real-time reverse transcriptase-polymerase chain reaction in primary neuroblastoma using normalization to averaged expression levels of the control genes HPRT1 and SDHA. *J Mol Diagn*. 2005;7(1):89-96. doi:10.1016/S1525-1578(10)60013-X

787. Hiyama E, Hiyama K, Yokoyama T, et al. Rapid detection of MYCN gene amplification and telomerase expression in neuroblastoma. *Clin Cancer Res*. 1999;5(3):601-609.

788. Hiyama E, Hiyama K, Yokoyama T, Ishii T. Immunohistochemical analysis of N-myc protein expression in neuroblastoma: Correlation with prognosis of patients. *J Pediatr Surg*. 1991;26(7):838-843. doi:10.1016/0022-3468(91)90151-I

789. Hiyama E, Yokoyama T, Ichikawa T, Ishii T, Hiyama K. N-myc gene amplification and other prognosis-associated factors in neuroblastoma. *J Pediatr Surg*. 1990;25(10):1095-1099. doi:10.1016/0022-3468(90)90227-Z

790. Lara SJP, Morantes SJ, Gutierrez FAA. Development and validation of a TaqMan multiplex PCR assay for the Gene Dosage Quantification in cancer. *Rev Colomb Ciencias Químico - Farm*. 2012;41(1):81-98. http://www.scielo.org.co/scielo.php?script=sci_arttext&pid=S0034-74182012000100006

791. Somasundaram DB, Aravindan S, Yu Z, et al. Droplet digital PCR as an alternative to FISH for MYCN amplification detection in human neuroblastoma FFPE samples. *BMC Cancer*. 2019;19(1):106. doi:10.1186/s12885-019-5306-0

792. Lodrini M, Sprüssel A, Astrahantseff K, et al. Using droplet digital PCR to analyze MYCN and ALK copy number in plasma from patients with neuroblastoma. 2017;8(49):85234-85251.

793. Ma Y, Lee JW, Park SJ, et al. Detection of MYCN Amplification in Serum DNA Using Conventional Polymerase Chain Reaction. *J Korean Med Sci*. 2016;31(9):1392-1396. https://doi.org/10.3346/jkms.2016.31.9.1392

794. Iehara T, Yagyu S, Gotoh T, et al. A prospective evaluation of liquid biopsy for detecting MYCN amplification in neuroblastoma patients. *Jpn J Clin Oncol*. 2019;49(8):743-748. doi:10.1093/jjco/hyz063

795. Van Dongen JJM, Van Der Velden VHJ, Brüggemann M, Orfao A. Minimal residual disease diagnostics in acute lymphoblastic leukemia: Need for sensitive, fast, and standardized technologies. *Blood*. 2015;125(26):3996-4009. doi:10.1182/blood-2015-03-580027

796. U.S. National Library of Medicine. International Study for Treatment of High Risk Childhood Relapsed ALL 2010. ClinicalTrials.gov Identifier: NCT03590171. Published 2020. Accessed November 28, 2020. https://clinicaltrials.gov/ct2/show/NCT03590171

797. Cheung NK V., Heller G, Kushner BH, Kramer K. Detection of neuroblastoma in bone marrow by immunocytology: Is a single marrow aspirate adequate? *Med Pediatr Oncol*. 1999;32(2):84-87. doi:10.1002/(SICI)1096-911X(199902)32:2<84::AID-MPO2>3.0.CO;2-1

798. Ojamies PN, Kontro M, Edgren H, et al. Case studies investigating genetic heterogeneity between anatomically distinct bone marrow compartments in acute myeloid leukemia. *Leuk Lymphoma*. 2018;59(12):3002-3005. doi:10.1080/10428194.2018.1453067

799. Bogen D, Brunner C, Walder D, et al. The genetic tumor background is an important determinant for heterogeneous MYCN-amplified neuroblastoma. *Int J Cancer*. 2016;139(1):153-163. doi:10.1002/ijc.30050

800. Abbasi MR, Rifatbegovic F, Brunner C, et al. Impact of disseminated neuroblastoma cells on the identification of the relapse-seeding clone. *Clin Cancer Res*. 2017;23(15):4224-4232. doi:10.1158/1078-0432.CCR-16-2082

801. Thole TM, Toedling J, Sprüssel A, et al. Reflection of neuroblastoma intratumor heterogeneity in the new OHC-NB1 disease model. *Int J Cancer*. 2020;146(4):1031-1041. doi:10.1002/ijc.32572

802. Hansford LM, McKee AE, Zhang L, et al. Neuroblastoma cells isolated from bone marrow metastases contain a naturally enriched tumor-initiating cell. *Cancer Res*. 2007;67(23):11234-11243. doi:10.1158/0008-5472.CAN-07-0718

803. Huang M, Zeki J, Sumarsono N, et al. Epigenetic targeting of TERT-associated gene expression signature in human neuroblastoma with TERT overexpression. *Cancer Res*. 2020;80(5):1024-1035. doi:10.1158/0008-5472.CAN-19-2560

804. Valentijn LJ, Koster J, Zwijnenburg DA, et al. TERT rearrangements are frequent in neuroblastoma and identify aggressive tumors. *Nat Genet*. 2015;47(12):1411-1414. doi:10.1038/ng.3438

805. Mikheyev AS, Tin MMY. A first look at the Oxford Nanopore MinION sequencer. *Mol Ecol Resour*. 2014;14(6):1097-1102. doi:10.1111/1755-0998.12324

806. Chicard M, Boyault S, Daage LC, et al. Genomic copy number profiling using circulating free tumor DNA highlights heterogeneity in neuroblastoma. *Clin Cancer Res*. 2016;22(22):5564-5573. doi:10.1158/1078-0432.CCR-16-0500

807. Duan X, Zhao Q. TERT -mediated and ATRX -mediated Telomere Maintenance and Neuroblastoma. *J Pediatr Hematol Oncol*. 2018;40(1):1-6. doi:10.1097/MPH.0000000000000840

808. Webb CJ, Wu Y, Zakian VA. DNA repair at telomeres: Keeping the ends intact. *Cold Spring Harb Perspect Biol*. 2013;5(6):a012666. doi:10.1101/cshperspect.a012666

809. Scott GA, Laughlin TS, Rothberg PG. Mutations of the TERT promoter are common in basal cell carcinoma and squamous cell carcinoma. *Mod Pathol*. 2014;27(4):516-523. doi:10.1038/modpathol.2013.167

810. Killela PJ, Reitman ZJ, Jiao Y, et al. TERT promoter mutations occur frequently in gliomas and a subset of tumors derived from cells with low rates of self-renewal. *Proc Natl Acad Sci USA*. 2013;110(15):6021-6026. doi:10.1073/pnas.1303607110

811. Liu X, Wu G, Shan Y, Hartmann C, Von Deimling A, Xing M. Highly prevalent TERT promoter mutations in bladder cancer and glioblastoma. *Cell Cycle*. 2013;12(10):1637-1638. doi:10.4161/cc.24662

812. Nault JC, Mallet M, Pilati C, et al. High frequency of telomerase reverse-transcriptase promoter somatic mutations in hepatocellular carcinoma and preneoplastic lesions. *Nat Commun*. 2013;4(2218). doi:10.1038/ncomms3218

813. Liu T, Wang N, Cao J, et al. The age-and shorter telomere-dependent tert promoter mutation in follicular thyroid cell-derived carcinomas. *Oncogene*. 2014;33(42):4978-4984. doi:10.1038/onc.2013.446

814. Diplas BH, Liu H, Yang R, et al. Sensitive and rapid detection of TERT promoter and IDH mutations in diffuse gliomas. *Neuro Oncol*. 2019;21(4):440-450. doi:10.1093/neuonc/noy167

815. Akuta N, Suzuki F, Kobayashi M, et al. Detection of TERT promoter mutation in serum cell-free DNA using wild-type blocking PCR combined with Sanger sequencing in hepatocellular carcinoma. *J Med Virol*. 2020;92:3604-3608. doi:10.1002/jmv.25724

816. Martínez-Ricarte F, Mayor R, Martínez-Sáez E, et al. Molecular diagnosis of diffuse gliomas through sequencing of cell-free circulating tumor DNA from cerebrospinal fluid. *Clin Cancer Res*.

2018;24(12):2812-2819. doi:10.1158/1078-0432.CCR-17-3800

817. Corless BC, Chang GA, Cooper S, et al. Development of Novel Mutation-Specific Droplet Digital PCR Assays Detecting TERT Promoter Mutations in Tumor and Plasma Samples. *J Mol Diagnostics*. 2019;21(2):274-285. doi:10.1016/j.jmoldx.2018.09.003

818. Colebatch AJ, Witkowski T, Waring PM, McArthur GA, Wong SQ, Dobrovic A. Optimizing amplification of the GC-Rich TERT promoter region using 7-Deaza-dGTP for droplet digital PCR quantification of TERT promoter mutations. *Clin Chem*. 2018;64(4):745-747. doi:10.1373/clinchem.2017.284257

819. McEvoy AC, Calapre L, Pereira MR, et al. Sensitive droplet digital PCR method for detection of TERT promoter mutations in cell free DNA from patients with metastatic melanoma. *Oncotarget*. 2017;8(45):78890-78900. doi:10.18632/oncotarget.20354

820. Deniel A, Marguet F, Beaussire L, et al. TERTp Mutation Detection in Plasma by Droplet-Digital Polymerase Chain Reaction in Spinal Myxopapillary Ependymoma with Lung Metastases. *World Neurosurg*. 2019;130:405-409. doi:10.1016/j.wneu.2019.07.111

821. Bryce LA, Morrison N, Hoare SF, Muir S, Keith WN. Mapping of the gene for the human telomerase reverse transcriptase, hTERT, to chromosome 5p15.33 by fluorescence in situ hybridization. *Neoplasia*. 2000;2(3):197-201. doi:10.1038/sj.neo.7900092

822. Argentaro A, Yang JC, Chapman L, et al. Structural consequences of disease-causing mutations in the ATRX-DNMT3-DNMT3L (ADD) domain of the chromatin-associated protein ATRX. *Proc Natl Acad Sci USA*. 2007;104(29):11939-11944. doi:10.1073/pnas.0704057104

823. Dhayalan A, Tamas R, Bock I, et al. The ATRX-ADD domain binds to H3 tail peptides and reads the combined methylation state of K4 and K9. *Hum Mol Genet*. 2011;20(11):2195-2203. doi:10.1093/hmg/ddr107

824. Chami R, Marrano P, Teerapakpinyo C, et al. Immunohistochemistry for ATRX Can Miss ATRX Mutations: Lessons from Neuroblastoma. *Am J Surg Pathol*. 2019;43(9):1203-1211. doi:10.1097/PAS.0000000000001322

825. Van Roy N, Van Der Linden M, Menten B, et al. Shallow whole genome sequencing on circulating cell-free DNA allows reliable noninvasive copy-number profiling in neuroblastoma patients. *Clin Cancer Res*. 2017;23(20):6305-6315. doi:10.1158/1078-0432.CCR-17-0675

826. Hurst LD, Ghanbarian AT, Forrest ARR, et al. The Constrained Maximal Expression Level Owing to Haploidy Shapes Gene Content on the Mammalian X Chromosome. *PLoS Biol*. 2015;13(12):e1002315. doi:10.1371/journal.pbio.1002315

827. Berletch JB, Yang F, Xu J, Carrel L, Disteche CM. Genes that escape from X inactivation. *Hum Genet*. 2011;130(2):237-245. doi:10.1007/s00439-011-1011-z

828. Wainer Katsir K, Linial M. Human genes escaping X-inactivation revealed by single cell expression data. *BMC Genomics*. 2019;20(1):201. doi:10.1186/s12864-019-5507-6

829. Trigg RM, Turner SD. ALK in neuroblastoma: Biological and therapeutic implications. *Cancers (Basel)*. 2018;10(4):113. doi:10.3390/cancers10040113

830. Javanmardi N, Fransson S, Djos A, et al. Low Frequency ALK Hotspots Mutations In Neuroblastoma Tumours Detected By Ultra-deep Sequencing: Implications For ALK Inhibitor Treatment. *Sci Rep*. 2019;9(1):3-14. doi:10.1038/s41598-018-37240-z

831. McDermott U, Iafrate AJ, Gray NS, et al. Genomic alterations of anaplastic lymphoma kinase may sensitize tumors to anaplastic lymphoma kinase inhibitors. *Cancer Res*. 2008;68(9):3389-3395. doi:10.1158/0008-5472.CAN-07-6186

832. Fransson S, Hansson M, Ruuth K, et al. Intragenic anaplastic lymphoma kinase (ALK) rearrangements: Translocations as a novel mechanism of ALK activation in neuroblastoma tumors. *Genes Chromosomes Cancer*. 2015;54(2):99-109. doi:10.1002/gcc.22223

833. De Brouwer S, De Preter K, Kumps C, et al. Meta-analysis of neuroblastomas reveals a skewed ALK mutation spectrum in tumors with MYCN amplification. *Clin Cancer Res*. 2010;16(17):4353-4362. doi:10.1158/1078-0432.CCR-09-2660

834. Durand S, Pierre-eugène C, Mirabeau O, Louis- C. ALK mutation dynamics and clonal evolution in a neuroblastoma model exhibiting two ALK mutations. 2019;10(48):4937-4950.

835. Combaret V, Iacono I, Bellini A, et al. Detection of tumor ALK status in neuroblastoma patients using peripheral blood. *Cancer Med*. 2015;4(4):540-550. doi:10.1002/cam4.414

836. Kobayashi K, Mizuta S, Yamane N, et al. Cell-free DNA Oncogene Copy Number as a Surrogate Molecular Biomarker in ALK/MYCN-coamplified Neuroblastoma. *J Pediatr Hematol Oncol*. 2021;43(2):e165-e168.

837. Rowlands V, Rutkowski AJ, Meuser E, Carr TH, Harrington EA, Barrett JC. Optimisation of robust singleplex and multiplex droplet digital PCR assays for high confidence mutation detection in circulating tumour DNA. *Sci Rep*. 2019;9(1):12620. doi:10.1038/s41598-019-49043-x

838. Alcaide M, Cheung M, Bushell K, et al. A Novel Multiplex Droplet Digital PCR Assay to Identify and Quantify KRAS Mutations in Clinical Specimens. *J Mol Diagnostics*. 2019;21(2):214-227. doi:10.1016/j.jmoldx.2018.09.007

839. Karlin-Neumann G, Bizouarn F. Entering the pantheon of 21st century molecular biology tools: A perspective on digital PCR. *Methods Mol Biol*. 2018;1768:3-10. doi:10.1007/978-1-4939-7778-9_1

840. Francisco Bizouarn. Biorad: ddPCR. In: *EMBL Course: Liquid Biopsies*. EMBL; 2018:pers.commun.

841. Cervantes-Madrid D, Szydzik J, Lind DE, et al. Repotrectinib (TPX-0005), effectively reduces growth of ALK driven neuroblastoma cells. *Sci Rep*. 2019;9(1):19353. doi:10.1038/s41598-019-55060-7

842. Guan J, Fransson S, Siaw JT, et al. Clinical response of the novel activating ALK-I1171T mutation in neuroblastoma to the ALK inhibitor ceritinib. *Cold Spring Harb Mol Case Stud*. 2018;4(4):a002550. doi:10.1101/mcs.a002550

843. Alam MW, Borenäs M, Lind DE, et al. Alectinib, an Anaplastic Lymphoma Kinase Inhibitor, Abolishes ALK Activity and Growth in ALK-Positive Neuroblastoma Cells. *Front Oncol*. 2019;9(579). doi:10.3389/fonc.2019.00579

844. Heath JA, Campbell MA, Thomas A, Solomon B. Good clinical response to alectinib, a second generation ALK inhibitor, in refractory neuroblastoma. *Pediatr Blood Cancer*. 2018;65(7):e27055. doi:10.1002/pbc.27055

845. Peitz C, Sprüssel A, Linke RB, et al. Multiplexed Quantification of Four Neuroblastoma DNA Targets in a Single Droplet Digital PCR Reaction. *J Mol Diagnostics*. 2020;22(11):1309-1323. doi:10.1016/j.jmoldx.2020.07.006

846. Carén H, Abel F, Kogner P, Martinsson T. High incidence of DNA mutations and gene amplifications of the ALK gene in advanced sporadic neuroblastoma tumours. *Biochem J*. 2008;416(2):153-159. doi:10.1042/BJ20081834

847. Consortium 1000 Genomes Project, Auton A, Abecasis GR, et al. A global reference for human genetic variation. *Nature*. 2015;526(7571):68-74. doi:10.1038/nature15393

848. Chang HH, Lu MY, Yang YL, et al. The prognostic roles of and correlation between ALK and MYCN protein expression in neuroblastoma. *J Clin Pathol*. 2020;73(3):154-161. doi:10.1136/jclinpath-2019-206063

849. Mu W, Lu HM, Chen J, Li S, Elliott AM. Sanger Confirmation Is Required to Achieve Optimal Sensitivity and Specificity in Next-Generation Sequencing Panel Testing. *J Mol Diagnostics*. 2016;18(6):923-932. doi:10.1016/j.jmoldx.2016.07.006

850. Kothari P, Yang J, Berger MF, Shukla NN, Modak S, Tsui D. Noninvasive molecular profiling of high-risk relapsed neuroblastoma by plasma cell-free DNA analysis. *J Clin Oncol*. 2017;35(15_suppl):10552. doi:10.1200/JCO.2017.35.15_suppl.10552

851. Shi H, Tao T, Abraham BJ, et al. ARID1A loss in neuroblastoma promotes the adrenergic-to-mesenchymal transition by regulating enhancer-mediated gene expression. *Sci Adv*. 2020;6(29):eaaz3440. doi:10.1126/sciadv.aaz3440

852. García-López J, Wallace K, Otero JH, et al. Large 1p36 Deletions Affecting Arid1a Locus Facilitate Mycn-Driven Oncogenesis in Neuroblastoma. *Cell Rep*. 2020;30(2):454-464.e5. doi:10.1016/j.celrep.2019.12.048

853. Schoenbeck K, Witthauer M, Winkler A, et al. The Hippo-YAP1-pathway is activated in relapsed and MYCN-nonamplified neuroblastoma. *Klin Pädiatrie*. 2017;229(03):182-195. doi:10.1055/s-0037-1602205

854. Szymansky A, Winkler A, Witthauer M, et al. Interfering with the LIN28B-let-7-MYCN pathway in

neuroblastoma. *Klin Pädiatrie*. 2017;229(03):182-195. doi:10.1055/s-0037-1602201

855. Molenaar JJ, Domingo-Fernández R, Ebus ME, et al. LIN28B induces neuroblastoma and enhances MYCN levels via let-7 suppression. *Nat Genet*. 2012;44(11):1199-1206. doi:10.1038/ng.2436

856. Monferrer E, Sanegre S, Martin-Vano S, et al. Digital Image Analysis Applied to Tumor Cell Proliferation, Aggressiveness, and Migration-Related Protein Synthesis in Neuroblastoma 3D Models. *Int J Mol Sci*. 2020;17(21):22. doi:10.3390/ijms21228676

857. Brady SW, Liu Y, Ma X, et al. Pan-neuroblastoma analysis reveals age- and signature-associated driver alterations. *Nat Commun*. 2020;11(1):5183. doi:10.1038/s41467-020-18987-4

858. van Zogchel LMJ, van Wezel EM, van Wijk J, et al. Hypermethylated RASSF1A as Circulating Tumor DNA Marker for Disease Monitoring in Neuroblastoma. *JCO Precis Oncol*. 2020;4:PO.19.00261. doi:10.1200/PO.19.00261

859. Poplin R, Ruano-Rubio V, DePristo MA, et al. Scaling accurate genetic variant discovery to tens of thousands of samples. *bioRxiv*. Published online 2017:201178. doi:10.1101/201178

860. Shin HT, Choi Y La, Yun JW, et al. Prevalence and detection of low-allele-fraction variants in clinical cancer samples. *Nat Commun*. 2017;8(1):1377. doi:10.1038/s41467-017-01470-y

861. Pastore A, Jurinovic V, Kridel R, et al. Integration of gene mutations in risk prognostication for patients receiving first-line immunochemotherapy for follicular lymphoma: A retrospective analysis of a prospective clinical trial and validation in a population-based registry. *Lancet Oncol*. 2015;16(9):1111-1122. doi:10.1016/S1470-2045(15)00169-2

862. Teer JK, Zhang Y, Chen L, et al. Evaluating somatic tumor mutation detection without matched normal samples. *Hum Genomics*. 2017;11(1):22. doi:10.1186/s40246-017-0118-2

863. Hiltemann S, Jenster G, Trapman J, Van Der Spek P, Stubbs A. Discriminating somatic and germline mutations in tumor DNA samples without matching normals. *Genome Res*. 2015;25(9):1382-1390. doi:10.1101/gr.183053.114

864. Patil S, Chamberlain RS. Neoplasms Associated with Germline and Somatic NF1 Gene Mutations. *Oncologist*. 2012;17(1):101-116. doi:10.1634/theoncologist.2010-0181

865. Shu Y, Wu X, Tong X, et al. Circulating Tumor DNA Mutation Profiling by Targeted Next Generation Sequencing Provides Guidance for Personalized Treatments in Multiple Cancer Types. *Sci Rep*. 2017;7(1):583. doi:10.1038/s41598-017-00520-1

866. Müller JN, Falk M, Talwar J, et al. Concordance between Comprehensive Cancer Genome Profiling in Plasma and Tumor Specimens. *J Thorac Oncol*. 2017;12(10):1503-1511. doi:10.1016/j.jtho.2017.07.014

867. Chen J, Chen J, He F, et al. Design of a targeted sequencing assay to detect rare mutations in circulating tumor DNA. *Genet Test Mol Biomarkers*. 2019;23(4):264-269. doi:10.1089/gtmb.2018.0173

868. Sato KA, Hachiya T, Iwaya T, et al. Individualized mutation detection in circulating tumor DNA for monitoring colorectal tumor burden using a cancer-associated gene sequencing panel. *PLoS One*. 2016;11(1):e0146275. doi:10.1371/journal.pone.0146275

869. Newman AM, Bratman S V., To J, et al. An ultrasensitive method for quantitating circulating tumor DNA with broad patient coverage. *Nat Med*. 2014;20(5):548-554. doi:10.1038/nm.3519

870. Guo Q, Wang J, Xiao J, et al. Heterogeneous mutation pattern in tumor tissue and circulating tumor DNA warrants parallel NGS panel testing. *Mol Cancer*. 2018;17(1):131. doi:10.1186/s12943-018-0875-0

871. Nishizuka SS, Sato KA, Hachiya T. A pipeline for ctDNA detection following primary tumor profiling using a cancer-related gene sequencing panel. *Methods Mol Biol*. 2019;1908:229-241. doi:10.1007/978-1-4939-9004-7_16

872. Diehl F, Li M, Dressman D, et al. Detection and quantification of mutations in the plasma of patients with colorectal tumors. *Proc Natl Acad Sci USA*. 2005;102(45):16368-16373. doi:10.1073/pnas.0507904102

873. Kuroda T, Morikawa N, Matsuoka K, et al. Prognostic significance of circulating tumor cells and bone marrow micrometastasis in advanced neuroblastoma. *J Pediatr Surg*. 2008;43(12):2182-2185. doi:10.1016/j.jpedsurg.2008.08.046

874. Marachelian A, Villablanca JG, Liu CW, et al. Expression of five neuroblastoma genes in bone marrow or blood of patients with relapsed/refractory neuroblastoma provides a new biomarker for disease and

prognosis. *Clin Cancer Res*. 2017;23(18):5374-5383. doi:10.1158/1078-0432.CCR-16-2647

875. Yamamoto N, Kozaki A, Hartomo TB, et al. Differential expression of minimal residual disease markers in peripheral blood and bone marrow samples from high-risk neuroblastoma patients. *Oncol Lett*. 2015;10(5):3228-3232. doi:10.3892/ol.2015.3710

876. Chicard M, Colmet-Daage L, Clement N, et al. Whole-exome sequencing of cell-free DNA reveals temporo-spatial heterogeneity and identifies treatment-resistant clones in neuroblastoma. *Clin Cancer Res*. 2018;24(4):939-949. doi:10.1158/1078-0432.CCR-17-1586

877. Gupta GP, Massagué J. Cancer Metastasis: Building a Framework. *Cell*. 2006;127(4):679-695. doi:10.1016/j.cell.2006.11.001

878. Follain G, Osmani N, Azevedo AS, et al. Hemodynamic Forces Tune the Arrest, Adhesion, and Extravasation of Circulating Tumor Cells. *Dev Cell*. 2018;45(1):33-52.e12. doi:10.1016/j.devcel.2018.02.015

879. Gerson J, Schlesinger H, Sereni P, Moorhead P, Hummeler K. Isolation and characterization of a neuroblastoma cell line from peripheral blood in a patient with disseminated disease. *Cancer*. 1977;Jun;39(6):

880. Lanino E, Melodia A, Casalaro A, Cornaglia-Ferraris P. Neuroblastoma Cells Circulate in Peripheral Blood. *Pediatr Hematol Oncol*. 1989;6(2):193-195. doi:10.3109/08880018909034286

881. Merugu S, Chen L, Gavens E, et al. Detection of circulating and disseminated neuroblastoma cells using the imageStream flow cytometer for use as predictive and pharmacodynamic biomarkers. *Clin Cancer Res*. 2020;26(1):122-134. doi:10.1158/1078-0432.CCR-19-0656

882. Mandel P, Metais P. Les acides nucléiques du plasma sanguin chez l'homme. *C R Seances Soc Biol Fil*. 1948;142(3-4):241-243.

883. Sorenson GD, Pribish DM, Valone FH, Memoli VA, Bzik DJ, Yao SL. Soluble Normal and Mutated DNA Sequences from Single-Copy Genes in Human Blood. *Cancer Epidemiol Biomarkers Prev*. 1994;3(1):67-71.

884. Vasioukhin V, Anker P, Maurice P, Lyautey J, Lederrey C, Stroun M. Point mutations of the N-ras gene in the blood plasma DNA of patients with myelodysplastic syndrome or acute myelogenous leukaemia. *Br J Haematol*. 1994;86(4):774-779. doi:10.1111/j.1365-2141.1994.tb04828.x

885. Giacona MB, Ruben GC, Iczkowski KA, Roos TB, Porter DM, Sorenson GD. Cell-free DNA in human blood plasma: Length measurements in patients with pancreatic cancer and healthy controls. *Pancreas*. 1998;17(1):89-97. doi:10.1097/00006676-199807000-00012

886. Jahr S, Hentze H, Englisch S, et al. DNA fragments in the blood plasma of cancer patients: Quantitations and evidence for their origin from apoptotic and necrotic cells. *Cancer Res*. 2001;61(4):1659-1665.

887. Jiang P, Chan CWM, Chan KCA, et al. Lengthening and shortening of plasma DNA in hepatocellular carcinoma patients. *Proc Natl Acad Sci USA*. 2015;112(11):E1317-1325. doi:10.1073/pnas.1500076112

888. Mohme M, Riethdorf S, Dreimann M, et al. Circulating Tumour Cell Release after Cement Augmentation of Vertebral Metastases. *Sci Rep*. 2017;7(1):7196. doi:10.1038/s41598-017-07649-z

889. Wang X, Wang L, Su Y, et al. Plasma cell-free DNA quantification is highly correlated to tumor burden in children with neuroblastoma. *Cancer Med*. 2018;7(7):3022-3030. doi:10.1002/cam4.1586

890. Lodrini M, Sprüssel A, Astrahantseff K, et al. Using droplet digital PCR to analyze MYCN and ALK copy number in plasma from patients with neuroblastoma. *Oncotarget*. 2017;8(49):85234-85251. doi:10.18632/oncotarget.19076

891. Gotoh T, Hosoi H, Iehara T, et al. Prediction of MYCN amplification in neuroblastoma using serum DNA and real-time quantitative polymerase chain reaction. *J Clin Oncol*. 2005;23(22):5205-5210. doi:10.1200/JCO.2005.02.014

892. Yagyu S, Iehara T, Tanaka S, et al. Serum-Based quantification of MYCN gene amplification in young patients with neuroblastoma: Potential utility as a surrogate biomarker for neuroblastoma. *PLoS One*. 2016;11(8):e0161039. doi:10.1371/journal.pone.0161039

893. Yagyu S, Iehara T, Gotoh T, et al. Preoperative analysis of 11q loss using circulating tumor-released DNA in serum: A novel diagnostic tool for therapy stratification of neuroblastoma. *Cancer Lett*. 2011;309(2):185-189. doi:10.1016/j.canlet.2011.05.032

894. Combaret V, Bréjon S, Iacono I, et al. Determination of 17q gain in patients with neuroblastoma by

analysis of circulating DNA. *Pediatr Blood Cancer*. 2011;56(5):757-761. doi:10.1002/pbc.22816

895. Yáñez-Mó M, Siljander PRM, Andreu Z, et al. Biological properties of extracellular vesicles and their physiological functions. *J Extracell Vesicles*. 2015;4(27066). doi:10.3402/jev.v4.27066

896. Van Niel G, D'Angelo G, Raposo G. Shedding light on the cell biology of extracellular vesicles. *Nat Rev Mol Cell Biol*. 2018;19(4):213-228. doi:10.1038/nrm.2017.125

897. Colombo M, Raposo G, Théry C. Biogenesis, Secretion, and Intercellular Interactions of Exosomes and Other Extracellular Vesicles. *Annu Rev Cell Dev Biol*. 2014;30:255-289. doi:10.1146/annurev-cellbio-101512-122326

898. Minciacchi VR, Zijlstra A, Rubin MA, Di Vizio D. Extracellular vesicles for liquid biopsy in prostate cancer: Where are we and where are we headed? *Prostate Cancer Prostatic Dis*. 2017;20(3):251-258. doi:10.1038/pcan.2017.7

899. Fonseka P, Liem M, Ozcitti C, Adda CG, Ang CS, Mathivanan S. Exosomes from N-Myc amplified neuroblastoma cells induce migration and confer chemoresistance to non-N-Myc amplified cells: implications of intra-tumour heterogeneity. *J Extracell Vesicles*. 2019;8(1):1597614. doi:10.1080/20013078.2019.1597614

900. Nakata R, Shimada H, Fernandez GE, et al. Contribution of neuroblastoma-derived exosomes to the production of pro-tumorigenic signals by bone marrow mesenchymal stromal cells. *J Extracell Vesicles*. 2017;6(1):1332941. doi:10.1080/20013078.2017.1332941

901. Haug BH, Hald ØH, Utnes P, et al. Exosome-like extracellular vesicles from MYCN-amplified neuroblastoma cells contain oncogenic miRNAs. *Anticancer Res*. 2015;35(5):2521-2530.

902. Li W, Li C, Zhou T, et al. Role of exosomal proteins in cancer diagnosis. *Mol Cancer*. 2017;16(1):145. doi:10.1186/s12943-017-0706-8

903. Hoshino A, Costa-Silva B, Shen TL, et al. Tumour exosome integrins determine organotropic metastasis. *Nature*. 2015;527(7578):329-335. doi:10.1038/nature15756

904. Mazzotti Ć, Buisson L, Maheo S, et al. Myeloma MRD by deep sequencing from circulating tumor DNA does not correlate with results obtained in the bone marrow. *Blood Adv*. 2018;2(21):2811-2813. doi:10.1182/bloodadvances.2018025197

905. Alix-Panabières C, Riethdorf S, Pantel K. Circulating tumor cells and bone marrow micrometastasis. *Clin Cancer Res*. 2008;14(16):5013-5021. doi:10.1158/1078-0432.CCR-07-5125

906. Lv C, Sun L, Guo Z, et al. Circular RNA regulatory network reveals cell-cell crosstalk in acute myeloid leukemia extramedullary infiltration. *J Transl Med*. 2018;16(1):361. doi:10.1186/s12967-018-1726-x

907. Combaret V, Audoynaud C, Iacono I, et al. Circulating MYCN DNA as a tumor-specific marker in neuroblastoma patients. *Cancer Res*. 2002;62(13):3646-3648.

908. Løvvik Juul-Dam K, Guldborg Nyvold C, Vålerhaugen H, et al. Measurable residual disease monitoring using Wilms tumor gene 1 expression in childhood acute myeloid leukemia based on child-specific reference values. *Pediatr Blood Cancer*. 2019;66(6):e27671. doi:10.1002/pbc.27671

909. Rautenberg C, Pechtel S, Hildebrandt B, et al. Wilms' Tumor 1 Gene Expression Using a Standardized European LeukemiaNet-Certified Assay Compared to Other Methods for Detection of Minimal Residual Disease in Myelodysplastic Syndrome and Acute Myelogenous Leukemia after Allogeneic Blood Stem Cell Transp. *Biol Blood Marrow Transplant*. 2018;24(11):2337-2343. doi:10.1016/j.bbmt.2018.05.011

910. Moss TJ, Cairo M, Santana VM, Weinthal J, Hurvitz C, Bostrom B. Clonogenicity of circulating neuroblastoma cells: Implications regarding peripheral blood stem cell transplantation. *Blood*. 1994;83(10):3085-3089. doi:10.1182/blood.v83.10.3085.3085

911. Diaz EH, Yachnin J, Grönberg H, Lindberg J. The in vitro stability of circulating tumour DNA. *PLoS One*. 2016;11(12):e0168153. doi:10.1371/journal.pone.0168153

912. Barrett AN, Thadani HA, Laureano-Asibal C, Ponnusamy S, Choolani M. Stability of cell-free DNA from maternal plasma isolated following a single centrifugation step. *Prenat Diagn*. 2014;34(13):1283-1288. doi:10.1002/pd.4468

913. Szpechcinski A, Chorostowska-Wynimko J, Struniawski R, et al. Cell-free DNA levels in plasma of patients with non-small-cell lung cancer and inflammatory lung disease. *Br J Cancer*. 2015;113(3):476-483. doi:10.1038/bjc.2015.225

914. Parpart-Li S, Bartlett B, Popoli M, Adleff V, Tucker L. The effect of preservative and temperature on the

analysis of circulating tumor DNA. *Clin Cancer Res*. 2016;23(10):2471-2477. doi:10.1158/1078-0432.CCR-16-1691

915. Lu J-L, Liang Z-Y. Circulating free DNA in the era of precision oncology: Pre- and post-analytical concerns. *Chronic Dis Transl Med*. 2016;2(4):223-230. doi:10.1016/j.cdtm.2016.12.001

916. Viprey VF, Corrias M V., Burchill SA. Identification of reference microRNAs and suitability of archived hemopoietic samples for robust microRNA expression profiling. *Anal Biochem*. 2012;421(2):566-572. doi:10.1016/j.ab.2011.10.022

917. Trigg RM, Martinson LJ, Parpart-Li S, Shaw JA. Factors that influence quality and yield of circulating-free DNA: A systematic review of the methodology literature. *Heliyon*. 2018;4(7):e00699. doi:10.1016/j.heliyon.2018.e00699

918. Lapin M, Oltedal S, Tjensvoll K, et al. Fragment size and level of cell-free DNA provide prognostic information in patients with advanced pancreatic cancer. *J Transl Med*. 2018;16(1):300. doi:10.1186/s12967-018-1677-2

919. Mouliere F, Chandrananda D, Piskorz AM, et al. Enhanced detection of circulating tumor DNA by fragment size analysis. *Sci Transl Med*. 2018;10(466):eaat4921. doi:10.1126/scitranslmed.aat4921

920. Underhill HR, Kitzman JO, Hellwig S, et al. Fragment Length of Circulating Tumor DNA. *PLoS Genet*. 2016;12(7):e1006162. doi:10.1371/journal.pgen.1006162

921. Yu M, Stott S, Toner M, Maheswaran S, Haber DA. Circulating tumor cells: Approaches to isolation and characterization. *J Cell Biol*. 2011;192(3):373-382. doi:10.1083/jcb.201010021

922. Mirtavoos-Mahyari H, Ghafouri-Fard S, Khosravi A, et al. Circulating free DNA concentration as a marker of disease recurrence and metastatic potential in lung cancer. *Clin Transl Med*. 2019;8(1):14. doi:10.1186/s40169-019-0229-6

923. Schwarzenbach H, Hoon DSB, Pantel K. Cell-free nucleic acids as biomarkers in cancer patients. *Nat Rev Cancer*. 2011;11(426-437). doi:10.1038/nrc3066

924. Thierry AR, El Messaoudi S, Gahan PB, Anker P, Stroun M. Origins, structures, and functions of circulating DNA in oncology. *Cancer Metastasis Rev*. 2016;35(3):347-376. doi:10.1007/s10555-016-9629-x

925. Sharon E, Shi H, Kharbanda S, et al. Quantification of transplant-derived circulating cell-free DNA in absence of a donor genotype. *PLoS Comput Biol*. 2017;13(8):e1005629. doi:10.1371/journal.pcbi.1005629

926. Burnham P, Khush K, De Vlaminck I. Myriad applications of circulating cell-free DNA in precision organ transplant monitoring. *Ann Am Thorac Soc*. 2017;14(Supplement_3):S237-S241. doi:10.1513/AnnalsATS.201608-634MG

927. Tug S, Helmig S, Deichmann ER, et al. Exercise-induced increases in cell free DNA in human plasma originate predominantly from cells of the haematopoietic lineage. *Exerc Immunol Rev*. 2015;21:164-173.

928. Jackson Chornenki NL, Coke R, Kwong AC, et al. Comparison of the source and prognostic utility of cfDNA in trauma and sepsis. *Intensive Care Med Exp*. 2019;7(1):29. doi:10.1186/s40635-019-0251-4

929. van der Meer AJ, Kroeze A, Hoogendijk AJ, et al. Systemic inflammation induces release of cell-free DNA from hematopoietic and parenchymal cells in mice and humans. *Blood Adv*. 2019;3(5):724-728. doi:10.1182/bloodadvances.2018018895

930. Kruse A, Abdel-Azim N, Kim HN, et al. Minimal Residual Disease Detection in Acute Lymphoblastic Leukemia. *Int J Mol Sci*. 2020;21(3):1054. doi:10.3390/ijms21031054

931. Kim YW, Kim YH, Song Y, et al. Monitoring circulating tumor DNA by analyzing personalized cancer-specific rearrangements to detect recurrence in gastric cancer. *Exp Mol Med*. 2019;51(8):1-10. doi:10.1038/s12276-019-0292-5

932. Olsson E, Winter C, George A, et al. Serial monitoring of circulating tumor DNA in patients with primary breast cancer for detection of occult metastatic disease. *EMBO Mol Med*. 2015;7(8):1034-1047. doi:10.15252/emmm.201404913

933. Carpinetti P, Donnard E, Bettoni F, et al. The use of personalized biomarkers and liquid biopsies to monitor treatment response and disease recurrence in locally advanced rectal cancer after neoadjuvant chemoradiation. *Oncotarget*. 2015;6(35):38360-38371. doi:10.18632/oncotarget.5256

934. Weerkamp F, Dekking E, Ng YY, et al. Flow cytometric immunobead assay for the detection of BCR-

ABL fusion proteins in leukemia patients. *Leukemia*. 2009;23(6):1106-1117. doi:10.1038/leu.2009.93

935. Van Dongen JJM, Orfao A, EuroFlow Consortium. EuroFlow: Resetting leukemia and lymphoma immunophenotyping. Basis for companion diagnostics and personalized medicine. *Leukemia*. 2012;26(9):1899-1907. doi:10.1038/leu.2012.121

936. Swerts K, De Moerloose B, Dhooge C, et al. Detection of residual neuroblastoma cells in bone marrow: Comparison of flow cytometry with immunocytochemistry. *Cytom Part B - Clin Cytom*. 2004;61(1):9-19. doi:10.1002/cyto.b.20019

937. Morandi F, Corrias MV, Pistoia V. Evaluation of bone marrow as a metastatic site of human neuroblastoma. *Ann N Y Acad Sci*. 2015;1335:23-31. doi:10.1111/nyas.12554

938. Warzynski MJ, Graham DM, Axtell RA, Higgins J V., Hammers YA. Flow Cytometric Immunophenotyping Test for Staging/Monitoring Neuroblastoma Patients. *Clin Cytom*. 2002;50(6):298-304. doi:10.1002/cyto.10159

939. Martins SA, Correia PD, Dias RA, Da Cruz E Silva OAB, Vieira SI. CD81 promotes a migratory phenotype in neuronal-like cells. *Microsc Microanal*. 2019;25(1):229-235. doi:10.1017/S1431927618015532

940. Nagai JI, Ishida Y, Koga N, et al. A new sensitive and specific combination of CD81/CD56/CD45 monoclonal antibodies for detecting circulating neuroblastoma cells in peripheral blood using flow cytometry. *Am J Pediatr Hematol Oncol*. 2000;22(1):20-26. doi:10.1097/00043426-200001000-00004

941. Popov A, Druy A, Shorikov E, et al. Prognostic value of initial bone marrow disease detection by multiparameter flow cytometry in children with neuroblastoma. *J Cancer Res Clin Oncol*. 2019;145(2):535-542. doi:10.1007/s00432-018-02831-w

942. Manrique B, López MJ, Cacciavillano W, Rossi J. Multi-parametric Flow Cytometry for Neuroblastoma, a new and possible diagnostic tool: Case report. *Arch Argent Pediatr*. 2016;114(2):e100-103. doi:10.5546/aap.2016.eng.e100

943. Gazitt Y, Ju He Y, Chang L, Koza S, Fisk D, Graham-Pole J. Expression of N-wyc, c-myc, and MDR-1 Proteins in Newly Established Neuroblastoma Cell Lines: A Study by Immunofluorescence Staining and Flow Cytometry. *Cancer Res*. 1992;52(10):2957-2965.

944. Di Trapani M, Manaresi N, Medoro G. DEPArray™ system: An automatic image-based sorter for isolation of pure circulating tumor cells. *Cytom Part A*. 2018;93(12):1260-1266. doi:10.1002/cyto.a.23687

945. Sollier-Christen E, Renier C, Kaplan T, Kfir E, Crouse SC. VTX-1 Liquid Biopsy System for Fully-Automated and Label-Free Isolation of Circulating Tumor Cells with Automated Enumeration by BioView Platform. *Cytom Part A*. 2018;93(12):1240-1245. doi:10.1002/cyto.a.23592

946. Lim S Bin, Di Lee W, Vasudevan J, Lim W-T, Lim CT. Liquid biopsy: one cell at a time. *NPJ Precis Oncol*. 2019;3(23). doi:10.1038/s41698-019-0095-0

947. Dizdar L, Fluegen G, van Dalum G, et al. Detection of circulating tumor cells in colorectal cancer patients using the GILUPI CellCollector: results from a prospective, single-center study. *Mol Oncol*. 2019;13(7):1548-1558. doi:10.1002/1878-0261.12507

948. Lee Y, Guan G, Bhagat AA. ClearCell® FX, a label-free microfluidics technology for enrichment of viable circulating tumor cells. *Cytom Part A*. 2018;93(12):1251-1254. doi:10.1002/cyto.a.23507

949. Miller MC, Robinson PS, Wagner C, O'Shannessy DJ. The Parsortix™ Cell Separation System—A versatile liquid biopsy platform. *Cytom Part A*. 2018;93(12):1234-1239. doi:10.1002/cyto.a.23571

950. Korja M, Jokilammi A, Salmi TT, et al. Absence of polysialylated NCAM is an unfavorable prognostic phenotype for advanced stage neuroblastoma. *BMC Cancer*. 2009;9(57). doi:10.1186/1471-2407-9-57

951. Valentiner U, Mühlenhoff M, Lehmann U, Hildebrandt H, Schumacher U. Expression of the neural cell adhesion molecule and polysialic acid in human neuroblastoma cell lines. *Int J Oncol*. 2011;39(2):417-424. doi:10.3892/ijo.2011.1038

952. De Wit S, Van Dalum G, Lenferink ATM, et al. The detection of EpCAM+ and EpCAM– circulating tumor cells. *Sci Rep*. 2015;5(12270). doi:10.1038/srep12270

953. Liu X, Zhang Z, Zhang B, et al. Circulating tumor cells detection in neuroblastoma patients by EpCAM-independent enrichment and immunostaining-fluorescence in situ hybridization. *EBioMedicine*. 2018;35:244-250. doi:10.1016/j.ebiom.2018.08.005

954. Wu ZL, Schwartz E, Ladisch S, Seeger R. Expression of gd2 ganglioside by untreated primary human neuroblastomas. *Cancer Res*. 1986;46(1):440-443.

955. Kramer K, Gerald WL, Kushner BH, Larson SM, Hameed M, Cheung NK V. Disialoganglioside G(D2) loss following monoclonal antibody therapy is rare in neuroblastoma. *Clin Cancer Res*. 1998;4(9):2135-2139. doi:10.1002/1096-911x(20010101)36:1<194::aid-mpo1046>3.3.co;2-2

956. Schumacher-Kuckelkorn R, Hero B, Ernestus K, Berthold F. Lacking immunocytological GD2 expression in neuroblastoma: Report of three cases. *Pediatr Blood Cancer*. 2005;45(2):195-201. doi:10.1002/pbc.20301

957. Skog MS, Nystedt J, Korhonen M, et al. Expression of neural cell adhesion molecule and polysialic acid in human bone marrow-derived mesenchymal stromal cells. *Stem Cell Res Ther*. 2016;7(1):113. doi:10.1186/s13287-016-0373-5

958. Martinez C, Hofmann TJ, Marino R, Dominici M, Horwitz EM. Human bone marrow mesenchymal stromal cells express the neural ganglioside GD2: A novel surface marker for the identification of MSCs. *Blood*. 2007;109(10):4245-4248. doi:10.1182/blood-2006-08-039347

959. Czilwik G, Messinger T, Strohmeier O, et al. Rapid and fully automated bacterial pathogen detection on a centrifugal-microfluidic LabDisk using highly sensitive nested PCR with integrated sample preparation. *Lab Chip*. 2015;15(18):3749-3759. doi:10.1039/c5lc00591d

960. Hin S, Paust N, Keller M, et al. Temperature change rate actuated bubble mixing for homogeneous rehydration of dry pre-stored reagents in centrifugal microfluidics. *Lab Chip*. 2018;18(2):362-370. doi:10.1039/c7lc01249g

961. Bundesministerium für Bildung und Forschung. IRMA-4-ALL, Förderkennzeichen: 01EK1508A. Accessed November 28, 2020. https://www.gesundheitsforschung-bmbf.de/de/irma-4-all.php

962. Juelg P, Specht M, Kipf E, et al. Automated serial dilutions for high-dynamic-range assays enabled by fill-level-coupled valving in centrifugal microfluidics. *Lab Chip*. 2019;19(13):2205-2219. doi:10.1039/c9lc00092e

963. Ou CY, Vu T, Grunwald JT, et al. An ultrasensitive test for profiling circulating tumor DNA using integrated comprehensive droplet digital detection. *Lab Chip*. 2019;19(6):993-1005. doi:10.1039/c8lc01399c

964. Ståhlberg A, Krzyzanowski PM, Jackson JB, Egyud M, Stein L, Godfrey TE. Simple, multiplexed, PCR-based barcoding of DNA enables sensitive mutation detection in liquid biopsies using sequencing. *Nucleic Acids Res*. 2016;44(11):e105. doi:10.1093/nar/gkw224

965. Ståhlberg A, Kubista M. Technical aspects and recommendations for single-cell qPCR. *Mol Aspects Med*. 2018;59:28-35. doi:10.1016/j.mam.2017.07.004

966. Faltin B, Wadle S, Roth G, Zengerle R, Von Stetten F. Mediator probe PCR: A novel approach for detection of real-time PCR based on label-free primary probes and standardized secondary universal fluorogenic reporters. *Clin Chem*. 2012;58(11):1546-1556. doi:10.1373/clinchem.2012.186734

967. Wadle S, Lehnert M, Schuler F, et al. Simplified development of multiplex real-time PCR through master mix augmented by universal fluorogenic reporters. *Biotechniques*. 2016;61(3):123-128. doi:10.2144/000114443

968. Wadle S, Rubenwolf S, Lehnert M, et al. Mediator probe PCR: Detection of real-time PCR by label-free probes and a universal fluorogenic reporter. *Methods Mol Biol*. 2014;1160:55-73. doi:10.1007/978-1-4939-0733-5_6

969. Institut für Mikrosystemtechnik - IMTEK, Albert-Ludwigs-Universität Freiburg. Mediator Probe PCR. Published 2020. Accessed November 28, 2020. https://www.imtek.de/professuren/anwendungsentwicklung/forschung/lab-on-a-chip/mediatorsonden-technologie/mediatorsonden

970. Cheng DT, Mitchell TN, Zehir A, et al. Memorial sloan kettering-integrated mutation profiling of actionable cancer targets (MSK-IMPACT): A hybridization capture-based next-generation sequencing clinical assay for solid tumor molecular oncology. *J Mol Diagnostics*. 2015;17(3):251-264. doi:10.1016/j.jmoldx.2014.12.006

971. Schrock AB, Pavlick D, Klempner SJ, et al. Hybrid capture–based genomic profiling of circulating tumor DNA from patients with advanced cancers of the gastrointestinal tract or anus. *Clin Cancer Res*. 2018;24(8):1881-1890. doi:10.1158/1078-0432.CCR-17-3103

972. Drilon A, Wang L, Arcila ME, et al. Broad, hybrid capture-based next-generation sequencing identifies actionable genomic alterations in lung adenocarcinomas otherwise negative for such alterations by other genomic testing approaches. *Clin Cancer Res*. 2015;21(16):3631-3639. doi:10.1158/1078-0432.CCR-14-2683

973. Tytgat GAM, Burchill SA, Schleiermacher G. Summary of joint MMG/Biology meeting "liquid biopsy meeting" focus on HR-NBL2. In: *SIOPEN MMG/Biology Meeting Krakow*. ; 2019.

974. Stathis A, Zucca E, Bekradda M, et al. Clinical response of carcinomas harboring the BRD4–NUT oncoprotein to the targeted bromodomain inhibitor OTX015/MK-8628. *Cancer Discov*. 2016;6(5):492-500. doi:10.1158/2159-8290.CD-15-1335

975. Firle KA&, Szymansky A, Witthauer MJ, et al. Preclinical evaluation of BET-bromodomain inhibitor TEN-010 as monotherapy and combination therapy in MYC-driven neuroblastoma. *Manuscript in preparation*. 2020;.

976. Wyce A, Ganji G, Smitheman KN, et al. BET Inhibition Silences Expression of MYCN and BCL2 and Induces Cytotoxicity in Neuroblastoma Tumor Models. *PLoS One*. 2013;8(8):e72967. doi:10.1371/journal.pone.0072967

977. Stewart HJS, Horne GA, Bastow S, Chevassut TJT. BRD4 associates with p53 in DNMT3A-mutated leukemia cells and is implicated in apoptosis by the bromodomain inhibitor JQ1. *Cancer Med*. 2013;2(6):826-835. doi:10.1002/cam4.146

978. Devaraj SGT, Fiskus W, Bhavin S, et al. Mechanistic role of HEXIM1 induction in BRD4-antagonist mediated growth inhibition, differentiation and in vivo lethal activity against human AML blast progenitor cells. *Blood*. 2014;124(21):3534. doi:https://doi.org/10.1182/blood.V124.21.3534.3534

979. Yang Z, Yik JHN, Chen R, et al. Recruitment of P-TEFb for stimulation of transcriptional elongation by the bromodomain protein Brd4. *Mol Cell*. 2005;19(4):535-545. doi:10.1016/j.molcel.2005.06.029

980. Lew QJ, Chia YL, Chu KL, et al. Identification of HEXIM1 as a positive regulator of p53. *J Biol Chem*. 2012;287(43):36443-36454. doi:10.1074/jbc.M112.374157

981. Lew QJ, Chu KL, Chia YL, Cheong N, Chao SH. Hexim1, a new player in the p53 pathway. *Cancers (Basel)*. 2013;5(3):838-856. doi:10.3390/cancers5030838

982. Westermann F, Muth D, Benner A, et al. Distinct transcriptional MYCN/c-MYC activities are associated with spontaneous regression or malignant progression in neuroblastomas. *Genome Biol*. 2008;9(10):R150. doi:10.1186/gb-2008-9-10-r150

983. Marshall B, Isidro G, Martins AG, Boavida MG. Loss of heterozygosity at chromosome 9p21 in primary neuroblastomas: Evidence for two deleted regions. *Cancer Genet Cytogenet*. 1997;96(2):134-139. doi:10.1016/S0165-4608(96)00300-7

984. Takita J, Hayashi Y, Yokota J. Loss of heterozygosity in neuroblastomas - An overview. *Eur J Cancer*. 1997;33(12):1971-1973. doi:10.1016/S0959-8049(97)00292-X

985. Giordani L, Iolascon A, Servedio V, Mazzocco K, Longo L, Tonini GP. Two regions of deletion in 9p22∼p24 in neuroblastoma are frequently observed in favorable tumors. *Cancer Genet Cytogenet*. 2002;135(1):42-47. doi:10.1016/S0165-4608(01)00640-9

986. Takita J, Hayashi Y, Kohno T, et al. Deletion map of chromosome 9 and p16 (CDKN2A) gene alterations in neuroblastoma. *Cancer Res*. 1997;57(5):907-912.

987. Petroni M, Veschi V, Gulino A, Giannini G. Molecular mechanisms of MYCN-dependent apoptosis and the MDM2-p53 pathway: An Achille's heel to be exploited for the therapy of MYCN-amplified neuroblastoma. *Front Oncol*. 2012;2(141). doi:10.3389/fonc.2012.00141

988. Omura-Minamisawa M, Diccianni MB, Chang RC, et al. p16/p14ARF cell cycle regulatory pathways in primary neuroblastoma: p16 expression is associated with advanced stage disease. *Clin Cancer Res*. 2001;7(11):3481-3490.

989. Haupt Y, Maya R, Kazaz A, Oren M. Mdm2 promotes the rapid degradation of p53. *Nature*. 1997;387(6630):296-299. doi:10.1038/387296a0

990. Zhang Y, Xiong Y, Yarbrough WG. ARF promotes MDM2 degradation and stabilizes p53: ARF-INK4a locus deletion impairs both the Rb and p53 tumor suppression pathways. *Cell*. 1998;92(6):725-734. doi:10.1016/S0092-8674(00)81401-4

991. Oliner JD, Pietenpol JA, Thiagalingam S, Gyuris J, Kinzler KW, Vogelstein B. Oncoprotein MDM2

conceals the activation domain of tumour suppressor p53. *Nature*. 1993;362(6423):857-860. doi:10.1038/362857a0

992. Zhang R, Wang H. MDM2 Oncogene as a Novel Target for Human Cancer Therapy. *Curr Pharm Des*. 2005;6(4):393-416. doi:10.2174/1381612003400911

993. Slack A, Chen Z, Tonelli R, et al. The p53 regulatory gene MDM2 is a direct transcriptional target of MYCN in neuroblastoma. *Proc Natl Acad Sci USA*. 2005;102(3):731-736. doi:10.1073/pnas.0405495102

994. He J, Gu L, Zhang H, Zhou M. Crosstalk between MYCN and MDM2-p53 signal pathways regulates tumor cell growth and apoptosis in neuroblastoma. *Cell Cycle*. 2011;10(17):2994-3002. doi:10.4161/cc.10.17.17118

995. Hill RM, Kuijper S, Lindsey JC, et al. Combined MYC and P53 defects emerge at medulloblastoma relapse and define rapidly progressive, therapeutically targetable disease. *Cancer Cell*. 2015;27(1):72-84. doi:10.1016/j.ccell.2014.11.002

996. Tsang HC, Mathew S, Magro CM. An Aggressive Primary Cutaneous Follicle Center Lymphoma With c-MYC Translocation and CDKN2A (9p21) Deletion: A Case Report and Review of the Literature. *Am J Dermatopathol*. 2017;39(3):e44-e49. doi:10.1097/DAD.0000000000000738

997. Durot E, Patey M, Luquet I, Gaillard B, Kolb B, Delmer A. An aggressive B-cell lymphoma with rearrangements of MYC and CCND1 genes: A rare subtype of double-hit lymphoma. *Leuk Lymphoma*. 2013;54(3):649-652. doi:10.3109/10428194.2012.710329

998. Akıncılar SC, Khattar E, Boon PLS, Unal B, Fullwood MJ, Tergaonkar V. Long-range chromatin interactions drive mutant TERT promoter activation. *Cancer Discov*. 2016;6(11):1276-1291. doi:10.1158/2159-8290.CD-16-0177

999. Horn S, Figl A, Rachakonda PS, et al. TERT promoter mutations in familial and sporadic melanoma. *Science*. 2013;339(6122):959-961. doi:10.1126/science.1230062

1000. Huang FW, Hodis E, Xu MJ, Kryukov G V., Chin L, Garraway LA. Highly recurrent TERT promoter mutations in human melanoma. *Science*. 2013;339(6122):957-959. doi:10.1126/science.1229259

1001. Harland M, Petljak M, Robles-Espinoza CD, et al. Germline TERT promoter mutations are rare in familial melanoma. *Fam Cancer*. 2016;15(1):139-144. doi:10.1007/s10689-015-9841-9

1002. Wang S, Pike AM, Lee SS, Strong MA, Connelly CJ, Greider CW. BRD4 inhibitors block telomere elongation. *Nucleic Acids Res*. 2017;45(14):8403-8410. doi:10.1093/nar/gkx561

1003. Chen J, Nelson C, Liu P, et al. Abstract 5209: Efficacious targeting of TERT oncogene rearrangement with BET bromodomain inhibitor and proteasome inhibitor combination therapy. *Cancer Res*. 2019;79((13 Supplement)):5209. doi:10.1158/1538-7445.sabcs18-5209

1004. Deutsches Krebsforschungszentrum / Universitätsklinikum Heidelberg. INFORM-Register Studie INdividualized Therapy FOr Relapsed Malignancies in Childhood. Published 2014. Accessed November 28, 2020. https://www.drks.de/drks_web/navigate.do?navigationId=trial.HTML&TRIAL_ID=DRKS00007623

1005. Worst BC, van Tilburg CM, Balasubramanian GP, et al. Next-generation personalised medicine for high-risk paediatric cancer patients – The INFORM pilot study. *Eur J Cancer*. 2016;65:91-101. doi:10.1016/j.ejca.2016.06.009

1006. Farooqi AS, Dagg RA, Choi LMR, Shay JW, Reynolds CP, Lau LMS. Alternative lengthening of telomeres in neuroblastoma cell lines is associated with a lack of MYCN genomic amplification and with p53 pathway aberrations. *J Neurooncol*. 2014;119(1):17-26. doi:10.1007/s11060-014-1456-8

1007. Bertuzzi A, Gandolfi A, Sinisgalli C, Starace G, Ubezio P. Cell loss and the concept of potential doubling time. *Cytometry*. 1997;29(1):34-40. doi:10.1002/(SICI)1097-0320(19970901)29:1<34::AID-CYTO3>3.0.CO;2-D

1008. Hafner M, Niepel M, Chung M, Sorger PK. Growth rate inhibition metrics correct for confounders in measuring sensitivity to cancer drugs. *Nat Methods*. 2016;13(6):521-527. doi:10.1038/nmeth.3853

1009. Carr-Wilkinson J, O'Toole K, Wood KM, et al. High frequency of p53/MDM2/p14ARF pathway abnormalities in relapsed neuroblastoma. *Clin Cancer Res*. 2010;16(4):1108-1118. doi:10.1158/1078-0432.CCR-09-1865

1010. Toure M, Crews CM. Small-molecule PROTACS: New approaches to protein degradation. *Angew*

Chemie - Int Ed. 2016;55(6):1966-1973. doi:10.1002/anie.201507978

1011. Cermakova K, Courtney Hodges H. Next-generation drugs and probes for chromatin biology: From targeted protein degradation to phase separation. *Molecules*. 2018;23(8):1958. doi:10.3390/molecules23081958

1012. Bondeson DP, Crews CM. Targeted Protein Degradation by Small Molecules. *Annu Rev Pharmacol Toxicol*. 2017;57:107-123. doi:10.1146/annurev-pharmtox-010715-103507

1013. Chan KH, Zengerle M, Testa A, Ciulli A. Impact of Target Warhead and Linkage Vector on Inducing Protein Degradation: Comparison of Bromodomain and Extra-Terminal (BET) Degraders Derived from Triazolodiazepine (JQ1) and Tetrahydroquinoline (I-BET726) BET Inhibitor Scaffolds. *J Med Chem*. 2018;61(2):504-513. doi:10.1021/acs.jmedchem.6b01912

1014. Lu J, Qian Y, Altieri M, et al. Hijacking the E3 Ubiquitin Ligase Cereblon to Efficiently Target BRD4. *Chem Biol*. 2015;22(6):755-763. doi:10.1016/j.chembiol.2015.05.009

1015. Zengerle M, Chan KH, Ciulli A. Selective Small Molecule Induced Degradation of the BET Bromodomain Protein BRD4. *ACS Chem Biol*. 2015;10(8):1770-1777. doi:10.1021/acschembio.5b00216

1016. Saenz DT, Fiskus W, Qian Y, et al. Novel BET protein proteolysis-Targeting chimera exerts superior lethal activity than bromodomain inhibitor (BETi) against post-myeloproliferative neoplasm secondary (s) AML cells. *Leukemia*. 2017;31(9):1951-1961. doi:10.1038/leu.2016.393

1017. Winter GE, Buckley DL, Paulk J, et al. Phthalimide conjugation as a strategy for in vivo target protein degradation. *Science*. 2015;348(241):1376-1381. doi:10.1126/science.aab1433

1018. Raina K, Lu J, Qian Y, et al. PROTAC-induced BET protein degradation as a therapy for castration-resistant prostate cancer. *Proc Natl Acad Sci USA*. 2016;113(26):7124-7129. doi:10.1073/pnas.1521738113

1019. Shi C, Zhang H, Wang P, et al. PROTAC induced-BET protein degradation exhibits potent anti-osteosarcoma activity by triggering apoptosis. *Cell Death Dis*. 2019;10(11):815. doi:10.1038/s41419-019-2022-2

1020. Zhou B, Hu J, Xu F, et al. Discovery of a Small-Molecule Degrader of Bromodomain and Extra-Terminal (BET) Proteins with Picomolar Cellular Potencies and Capable of Achieving Tumor Regression. *J Med Chem*. 2018;61(2):462-481. doi:10.1021/acs.jmedchem.6b01816

1021. Bai L, Zhou B, Yang CY, et al. Targeted degradation of BET proteins in triple-negative breast cancer. *Cancer Res*. 2017;77(9):2476-2487. doi:10.1158/0008-5472.CAN-16-2622

1022. Bolden JE, Tasdemir N, Dow LE, et al. Inducible in vivo silencing of Brd4 identifies potential toxicities of sustained BET protein inhibition. *Cell Rep*. 2014;8(6):1919-1929. doi:10.1016/j.celrep.2014.08.025

1023. Qin C, Hu Y, Zhou B, et al. Discovery of QCA570 as an Exceptionally Potent and Efficacious Proteolysis Targeting Chimera (PROTAC) Degrader of the Bromodomain and Extra-Terminal (BET) Proteins Capable of Inducing Complete and Durable Tumor Regression. *J Med Chem*. 2018;61(15):6685-6704. doi:10.1021/acs.jmedchem.8b00506

1024. Trauth J, Scheffer J, Hasenjäger S, Taxis C. Synthetic Control of Protein Degradation during Cell Proliferation and Developmental Processes. *ACS Omega*. 2019;4(2):2766-2778. doi:10.1021/acsomega.8b03011

1025. Natsume T, Kanemaki MT. Conditional Degrons for Controlling Protein Expression at the Protein Level. *Annu Rev Genet*. 2017;51:83-102. doi:10.1146/annurev-genet-120116-024656

1026. Chung HK, Jacobs CL, Huo Y, et al. Tunable and reversible drug control of protein production via a self-excising degron. *Nat Chem Biol*. 2015;11(9):713-720. doi:10.1038/nchembio.1869

1027. Fenno L, Yizhar O, Deisseroth K. The Development and Application of Optogenetics. *Annu Rev Neurosci*. 2011;34:389-412. doi:10.1146/annurev-neuro-061010-113817

1028. Eggert A. *Early Application of Targeted Therapies within a Therapy Protocol*.; 2019. per. comm.

1029. Floyd SR, Pacold ME, Huang Q, et al. The bromodomain protein Brd4 insulates chromatin from DNA damage signalling. *Nature*. 2013;498(7453):246-250. doi:10.1038/nature12147

1030. Dasari S, Bernard Tchounwou P. Cisplatin in cancer therapy: Molecular mechanisms of action. *Eur J Pharmacol*. 2014;740:364-378. doi:10.1016/j.ejphar.2014.07.025

1031. Klingbeil O, Lesche R, Gelato KA, Haendler B, Lejeune P. Inhibition of bet bromodomain-dependent

XIAP and FLIP expression sensitizes KRAS-mutated NSCLC to pro-apoptotic agents. *Cell Death Dis*. 2016;7(9):e2365. doi:10.1038/cddis.2016.271

1032. Yang L, Zhang Y, Shan W, et al. Repression of BET activity sensitizes homologous recombination-proficient cancers to PARP inhibition. *Sci Transl Med*. 2017;9(400):eaal1645. doi:10.1126/scitranslmed.aal1645

1033. Zanellato I, Colangelo D, Osella D. JQ1, a BET Inhibitor, Synergizes with Cisplatin and Induces Apoptosis in Highly Chemoresistant Malignant Pleural Mesothelioma Cells. *Curr Cancer Drug Targets*. 2017;18(8):816-828. doi:10.2174/1568009617666170623101722

1034. Oing C, Skowron MA, Bokemeyer C, Nettersheim D. Epigenetic treatment combinations to effectively target cisplatin-resistant germ cell tumors: past, present, and future considerations. *Andrology*. 2019;7(4):487-497. doi:10.1111/andr.12611

1035. Jostes S, Nettersheim D, Fellermeyer M, et al. The bromodomain inhibitor JQ1 triggers growth arrest and apoptosis in testicular germ cell tumours in vitro and in vivo. *J Cell Mol Med*. 2017;21(7):1300-1314. doi:10.1111/jcmm.13059

1036. Baker EK, Taylor S, Gupte A, et al. BET inhibitors induce apoptosis through a MYC independent mechanism and synergise with CDK inhibitors to kill osteosarcoma cells. *Sci Rep*. 2015;5(10120). doi:10.1038/srep10120

1037. Boi M, Gaudio E, Bonetti P, et al. The BET bromodomain inhibitor OTX015 affects pathogenetic pathways in preclinical B-cell tumor models and synergizes with targeted drugs. *Clin Cancer Res*. 2015;21(7):1628-1638. doi:10.1158/1078-0432.CCR-14-1561

1038. Teicher BA, Silvers T, Selby M, et al. Small cell lung carcinoma cell line screen of etoposide/carboplatin plus a third agent. *Cancer Med*. 2017;6(8):1952-1964. doi:10.1002/cam4.1131

1039. Grundy M, Seedhouse C, Jones T, et al. Predicting effective pro-apoptotic anti-leukaemic drug combinations using cooperative dynamic BH3 profiling. *PLoS One*. 2018;13(1):e0190682. doi:10.1371/journal.pone.0190682

1040. Beesley AH, Stirnweiss A, Ferrari E, et al. Comparative drug screening in NUT midline carcinoma. *Br J Cancer*. 2014;110(5):1189-1198. doi:10.1038/bjc.2014.54

1041. Cinar M, Rosenfelt F, Rokhsar S, et al. Concurrent inhibition of MYC and BCL2 is a potentially effective treatment strategy for double hit and triple hit B-cell lymphomas. *Leuk Res*. 2015;39(7):730-738. doi:10.1016/j.leukres.2015.04.003

1042. Loosveld M, Castellano R, Gon S, et al. Therapeutic Targeting of c-Myc in T-Cell Acute Lymphoblastic Leukemia (T-ALL). *Oncotarget; Vol 5, No 10*. 2014;5(10):3168-3172. https://www.oncotarget.com/article/1873/

1043. Liu PY, Sokolowski N, Guo ST, et al. The BET bromodomain inhibitor exerts the most potent synergistic anticancer effects with quinone-containing compounds and anti- microtubule drugs. *Oncotarget*. 2016;7(48):79217-79232. doi:10.18632/oncotarget.12640

1044. Olzscha H, Bekheet ME, Sheikh S, La Thangue NB. HDAC Inhibitors. Sarkar S, ed. *Methods Mol Biol*. 2016;1436:281-303. doi:10.1007/978-1-4939-3667-0_19

1045. Witt O, Deubzer H, Lodrini M, Milde T, Oehme I. Targeting Histone Deacetylases in Neuroblastoma. *Curr Pharm Des*. 2009;15(4):436-447. doi:10.2174/138161209787315774

1046. Oehme I, Deubzer HE, Wegener D, et al. Histone deacetylase 8 in neuroblastoma tumorigenesis. *Clin Cancer Res*. 2009;15(1):91-99. doi:10.1158/1078-0432.CCR-08-0684

1047. Sun Y, Liu PY, Scarlett CJ, et al. Histone deacetylase 5 blocks neuroblastoma cell differentiation by interacting with N-Myc. *Oncogene*. 2014;33(23):2987-2994. doi:10.1038/onc.2013.253

1048. Marshall GM, Gherardi S, Xu N, et al. Transcriptional upregulation of histone deacetylase 2 promotes Myc-induced oncogenic effects. *Oncogene*. 2010;29(44):5957-5968. doi:10.1038/onc.2010.332

1049. Liu T, Tee A, Flemming C, Norris MD, Haber M, Marshall GM. MYCN interacts with histone deacetylase to modulate target gene transcription. *Cancer Res*. 2006;66(8):1018 LP - 1018.

1050. Frumm SM, Fan ZP, Ross KN, et al. Selective HDAC1/HDAC2 inhibitors induce neuroblastoma differentiation. *Chem Biol*. 2013;20(5):713-725. doi:10.1016/j.chembiol.2013.03.020

1051. Bhadury J, Nilsson LM, Muralidharan SV, et al. BET and HDAC inhibitors induce similar genes and biological effects and synergize to kill in Myc-induced murine lymphoma. *Proc Natl Acad Sci USA*.

2014;111(26):E2721-2730. doi:10.1073/pnas.1406722111

1052. Liu S, Li F, Pan L, et al. BRD4 inhibitor and histone deacetylase inhibitor synergistically inhibit the proliferation of gallbladder cancer in vitro and in vivo. *Cancer Sci*. 2019;110(8):2493-2506. doi:10.1111/cas.14102

1053. Shahbazi J, Liu PY, Atmadibrata B, et al. The bromodomain inhibitor jq1 and the histone deacetylase inhibitor panobinostat synergistically reduce n-myc expression and induce anticancer effects. *Clin Cancer Res*. 2016;22(10):2534-2544. doi:10.1158/1078-0432.CCR-15-1666

1054. He S, Dong G, Li Y, Wu S, Wang W, Sheng C. Potent Dual BET/HDAC Inhibitors for Efficient Treatment of Pancreatic Cancer. *Angew Chemie - Int Ed*. 2020;59(8):3028-3032. doi:10.1002/anie.201915896

1055. Amemiya S, Yamaguchi T, Hashimoto Y, Noguchi-Yachide T. Synthesis and evaluation of novel dual BRD4/HDAC inhibitors. *Bioorganic Med Chem*. 2017;25(14):367-3684. doi:10.1016/j.bmc.2017.04.043

1056. Shi YJ, Matson C, Lan F, Iwase S, Baba T, Shi Y. Regulation of LSD1 histone demethylase activity by its associated factors. *Mol Cell*. 2005;19(6):857-864. doi:10.1016/j.molcel.2005.08.027

1057. Amente S, Milazzo G, Sorrentino MC, et al. Lysine-specific demethylase (LSD1/KDM1A) and MYCN cooperatively repress tumor suppressor genes in neuroblastoma. *Oncotarget*. 2015;6(16):14572-14583. doi:10.18632/oncotarget.3990

1058. Nalawansha DA, Pflum MKH. LSD1 substrate binding and gene expression are affected by HDAC1-mediated deacetylation. *ACS Chem Biol*. 2017;12(1):254-264. doi:10.1021/acschembio.6b00776

1059. Wang J, Yu Q, Qiu Z, et al. The combined effect of epigenetic inhibitors for LSD1 and BRD4 alters prostate cancer growth and invasion. *Aging (Albany NY)*. 2020;12(1):397-415. doi:10.18632/aging.102630

1060. Huang Y, Vasilatos SN, Boric L, Shaw PG, Davidson NE. Inhibitors of histone demethylation and histone deacetylation cooperate in regulating gene expression and inhibiting growth in human breast cancer cells. *Breast Cancer Res Treat*. 2012;131(3):777-789. doi:10.1007/s10549-011-1480-8

1061. Chipumuro E, Marco E, Christensen CL, et al. CDK7 inhibition suppresses super-enhancer-linked oncogenic transcription in MYCN-driven cancer. *Cell*. 2014;159(5):1126-1139. doi:10.1016/j.cell.2014.10.024

1062. Tee AE, Ciampa OC, Wong M, et al. Combination therapy with the CDK7 inhibitor and the tyrosine kinase inhibitor exerts synergistic anticancer effects against MYCN -amplified neuroblastoma. *Int J Cancer*. 2020;147(7):1928-1938. doi:10.1002/ijc.32936

1063. Liu F, Jiang W, Sui Y, et al. CDK7 inhibition suppresses aberrant hedgehog pathway and overcomes resistance to smoothened antagonists. *Proc Natl Acad Sci USA*. 2019;116(26):12986-12995. doi:10.1073/pnas.1815780116

1064. George SL, Parmar V, Lorenzi F, et al. Novel therapeutic strategies targeting telomere maintenance mechanisms in high-risk neuroblastoma. *J Exp Clin Cancer Res*. 2020;39(1):78. doi:10.1186/s13046-020-01582-2

1065. Bidzinska J, Cimino-Reale G, Zaffaroni N, Folini M. G-quadruplex structures in the human genome as novel therapeutic targets. *Molecules*. 2013;18(10):12368-12395. doi:10.3390/molecules181012368

1066. Wang Y, Yang J, Wild AT, et al. G-quadruplex DNA drives genomic instability and represents a targetable molecular abnormality in ATRX-deficient malignant glioma. *Nat Commun*. 2019;10(1):943. doi:10.1038/s41467-019-08905-8

1067. Mio C, Gerratana L, Bolis M, et al. BET proteins regulate homologous recombination-mediated DNA repair: BRCAness and implications for cancer therapy. *Int J Cancer*. 2019;144(4):755-766. doi:10.1002/ijc.31898

1068. Morales JC, Li L, Fattah FJ, et al. Review of poly (ADP-ribose) polymerase (PARP) mechanisms of action and rationale for targeting in cancer and other diseases. *Crit Rev Eukaryot Gene Expr*. 2014;24(1):15-28. doi:10.1615/CritRevEukaryotGeneExpr.2013006875

1069. King D, Li XD, Almeida GS, et al. MYCN expression induces replication stress and sensitivity to PARP inhibition in neuroblastoma. *Oncotarget*. 2020;11(23):2141-2159. doi:10.18632/oncotarget.27329

1070. Colicchia V, Petroni M, Guarguaglini G, et al. PARP inhibitors enhance replication stress and cause mitotic catastrophe in MYCN-dependent neuroblastoma. *Oncogene*. 2017;36(33):4682-4691.

doi:10.1038/onc.2017.40

1071. Miller AL, Fehling SC, Garcia PL, et al. The BET inhibitor JQ1 attenuates double-strand break repair and sensitizes models of pancreatic ductal adenocarcinoma to PARP inhibitors. *EBioMedicine*. 2019;44:419-430. doi:10.1016/j.ebiom.2019.05.035

1072. Fehling SC, Miller AL, Garcia PL, Vance RB, Yoon KJ. The combination of BET and PARP inhibitors is synergistic in models of cholangiocarcinoma. *Cancer Lett*. 2020;468:48-58. doi:10.1016/j.canlet.2019.10.011

1073. Karakashev S, Zhu H, Yokoyama Y, et al. BET Bromodomain Inhibition Synergizes with PARP Inhibitor in Epithelial Ovarian Cancer. *Cell Rep*. 2017;21(12):3398-3405. doi:10.1016/j.celrep.2017.11.095

1074. Shangary S, Wang S. Small-Molecule Inhibitors of the MDM2-p53 Protein-Protein Interaction to Reactivate p53 Function: A Novel Approach for Cancer Therapy. *Annu Rev Pharmacol Toxicol*. 2009;49:223-241. doi:10.1146/annurev.pharmtox.48.113006.094723

1075. Mazar J, Gordon C, Naga V, Westmoreland TJ. The Killing of Human Neuroblastoma Cells by the Small Molecule JQ1 Occurs in a p53-Dependent Manner. *Anticancer Agents Med Chem*. 2020;20(12):1613-1625. doi:10.2174/1871520620666200424123834

1076. Maser T, Zagorski J, Kelly S, et al. The MDM2 inhibitor CGM097 combined with the BET inhibitor OTX015 induces cell death and inhibits tumor growth in models of neuroblastoma. *Cancer Med*. 2020;9(21):8144-8158. doi:10.1002/cam4.3407

1077. Latif A-L, Cole JJ, Monteiro Campos J, et al. Dual Inhibition of MDM2 and BET Cooperate to Eradicate Acute Myeloid Leukemia. *Blood*. 2015;126(23):674. doi:10.1182/blood.v126.23.674.674

1078. Gottlieb A, Althoff K, Grunewald L, et al. RITA displays anti-tumor activity in medulloblastomas independent of TP53 status. *Oncotarget*. 2017;8(17):27882-27891. doi:10.18632/oncotarget.15840

1079. Schönbeck K, Winkler A, Witthauer MJ, et al. Hippo-YAP pathway activation favors neuroblastoma progression. *Klin Padiatr*. 2018;230(03):30. doi:10.1055/s-0038-1645011

1080. Bai N, Zhang C, Liang N, et al. Yes-associated protein (YAP) increases chemosensitivity of hepatocellular carcinoma cells by modulation of p53. *Cancer Biol Ther*. 2013;14(6):511-520. doi:10.4161/cbt.24345

1081. Di Agostino S, Sorrentino G, Ingallina E, et al. YAP enhances the pro-proliferative transcriptional activity of mutant p53 proteins. *EMBO Rep*. 2016;17(2):188-201. doi:10.15252/embr.201540488

1082. Ding R, Weynans K, Bossing T, Barros CS, Berger C. The Hippo signalling pathway maintains quiescence in Drosophila neural stem cells. *Nat Commun*. 2016;7(10510). doi:10.1038/ncomms10510

1083. Yang C, Tan J, Zhu J, Wang S, Wei G. YAP promotes tumorigenesis and cisplatin resistance in neuroblastoma. *Oncotarget*. 2017;8(23):37154-37163. doi:10.18632/oncotarget.16209

1084. Zanconato F, Battilana G, Forcato M, et al. Transcriptional addiction in cancer cells is mediated by YAP/TAZ through BRD4. *Nat Med*. 2018;24(10):1599-1610. doi:10.1038/s41591-018-0158-8

1085. Zhang HT, Gui T, Sang Y, et al. The BET Bromodomain Inhibitor JQ1 Suppresses Chondrosarcoma Cell Growth via Regulation of YAP/p21/c-Myc Signaling. *J Cell Biochem*. 2017;118(8):2182-2192. doi:10.1002/jcb.25863

1086. Gobbi G, Donati B, Do Valle IF, et al. The Hippo pathway modulates resistance to BET proteins inhibitors in lung cancer cells. *Oncogene*. 2019;38(6801-6817). doi:10.1038/s41388-019-0924-1

1087. Song S, Li Y, Xu Y, et al. Targeting Hippo coactivator YAP1 through BET bromodomain inhibition in esophageal adenocarcinoma. *Mol Oncol*. 2020;14(6):1410-1426. doi:10.1002/1878-0261.12667

1088. Heinemann A, Cullinane C, De Paoli-Iseppi R, et al. Combining BET and HDAC inhibitors synergistically induces apoptosis of melanoma and suppresses AKT and YAP signaling. *Oncotarget*. 2015;6(25):21507-21521. doi:10.18632/oncotarget.4242

1089. Fletcher S, Prochownik E V. Small-molecule inhibitors of the Myc oncoprotein. *Biochim Biophys Acta - Gene Regul Mech*. 2015;1849(5):525-543. doi:10.1016/j.bbagrm.2014.03.005

1090. Boller D, Schramm A, Doepfner KT, et al. Targeting the phosphoinositide 3-kinase isoform p110δ impairs growth and survival in neuroblastoma cells. *Clin Cancer Res*. 2008;14(4):1172-1181. doi:10.1158/1078-0432.CCR-07-0737

1091. Wen N, Guo B, Zheng H, et al. Bromodomain inhibitor jq1 induces cell cycle arrest and apoptosis of glioma stem cells through the VEGF/PI3K/AKT signaling pathway. *Int J Oncol*. 2019;55(4):879-895. doi:10.3892/ijo.2019.4863

1092. Tomska K, Kurilov R, Lee KS, et al. Drug-based perturbation screen uncovers synergistic drug combinations in Burkitt lymphoma. *Sci Rep*. 2018;8(1):12046. doi:10.1038/s41598-018-30509-3

1093. Boedicker C, Hussong M, Grimm C, et al. Co-inhibition of BET proteins and PI3Kα triggers mitochondrial apoptosis in rhabdomyosarcoma cells. *Oncogene*. 2020;39(19):3837-3852. doi:10.1038/s41388-020-1229-0

1094. Erdreich-Epstein A, Singh AR, Joshi S, et al. Association of high microvessel α v β 3 and low PTEN with poor outcome in stage 3 neuroblastoma: rationale for using first in class dual PI3K/BRD4 inhibitor, SF1126. *Oncotarget*. 2017;8(32):52193-52210. doi:10.18632/oncotarget.13386

1095. Andrews FH, Singh AR, Joshi S, et al. Dual-activity PI3K-BRD4 inhibitor for the orthogonal inhibition of MYC to block tumor growth and metastasis. *Proc Natl Acad Sci USA*. 2017;114(7):E1072-E1080. doi:10.1073/pnas.1613091114

1096. Ciceri P, Müller S, O'Mahony A, et al. Dual kinase-bromodomain inhibitors for rationally designed polypharmacology. *Nat Chem Biol*. 2014;10(4):305-312. doi:10.1038/nchembio.1471

1097. Timme N, Han Y, Liu S, et al. Small-Molecule Dual PLK1 and BRD4 Inhibitors are Active Against Preclinical Models of Pediatric Solid Tumors. *Transl Oncol*. 2019;13(2):221-232. doi:10.1016/j.tranon.2019.09.013

1098. Balaian E, Weidner H, Wobus M, et al. Effects of rigosertib on the osteo-hematopoietic niche in myelodysplastic syndromes. *Ann Hematol*. 2019;98(9):2063-2072. doi:10.1007/s00277-019-03756-1

1099. Dai Y, Hung L, Chen R, Lai C, Chang K. ON 01910 . Na inhibits growth of diffuse large B-cell lymphoma by cytoplasmic sequestration of sumoylated C-MYB / TRAF6 complex. *Transl Res*. 2016;175:129-143.e13. doi:10.1016/j.trsl.2016.04.001

1100. Liu Z, Wang M, Wang H, Fang L, Gou S. Targeting RAS-RAF pathway significantly improves antitumor activity of Rigosertib-derived platinum(IV) complexes and overcomes cisplatin resistance. *Eur J Med Chem*. 2020;194(112269). doi:10.1016/j.ejmech.2020.112269

1101. Liu Z, Wang M, Wang H, Fang L, Gou S. Platinum-Based Modification of Styrylbenzylsulfones as Multifunctional Antitumor Agents: Targeting the RAS/RAF Pathway, Enhancing Antitumor Activity, and Overcoming Multidrug Resistance. *J Med Chem*. 2020;63(1):186-204. doi:10.1021/acs.jmedchem.9b01223

1102. Tinsley S, Meja K, Shepherd C, Khwaja A. Synergistic induction of cell death in haematological malignancies by combined phosphoinositide-3-kinase and BET bromodomain inhibition. *Br J Haematol*. 2015;170(2):275-278. doi:10.1111/bjh.13283

1103. Tucker ER, Tall JR, Danielson LS, et al. Immunoassays for the quantification of ALK and phosphorylated ALK support the evaluation of on-target ALK inhibitors in neuroblastoma. *Mol Oncol*. 2017;11(8):996-1006. doi:10.1002/1878-0261.12069

1104. Guan J, Tucker ER, Wan H, et al. The ALK inhibitor PF-06463922 is effective as a single agent in neuroblastoma driven by expression of ALK and MYCN. *DMM Dis Model Mech*. 2016;9(9):941-952. doi:10.1242/dmm.024448

1105. Infarinato NR, Park JH, Krytska K, et al. The ALK/ROS1 inhibitor PF-06463922 overcomes primary resistance to crizotinib in ALK-driven neuroblastoma. *Cancer Discov*. 2016;6(1):96-107. doi:10.1158/2159-8290.CD-15-1056

1106. Yang L, Li G, Zhao L, Pan F, Qiang J, Han S. Blocking the PI3K pathway enhances the efficacy of ALK-targeted therapy in EML4-ALK-positive nonsmall-cell lung cancer. *Tumor Biol*. 2014;35(10):9759-9767. doi:10.1007/s13277-014-2252-y

1107. Di Tomaso E, Linnartz R, Li F, Massacesi C, Hirawat S. Abstract 4698: Combination of ceritinib (LDK378) with PI3K inhibitors (buparlisib [BKM120] and alpelisib [BYL719]) demonstrates synergistic preclinical antitumor activity in ALK-rearranged non-small cell lung cancer (NSCLC). *Cancer Res*. 2015;75(15):4698 LP - 4698. doi:10.1158/1538-7445.AM2015-4698

1108. Wu Y-H, Huang Y-F, Chen C-C, Huang C-Y, Chou C-Y. Comparing PI3K/Akt Inhibitors Used in Ovarian Cancer Treatment. *Front Pharmacol*. 2020;11:206. doi:10.3389/fphar.2020.00206

1109. Erdmann T, Klener P, Lynch JT, et al. Sensitivity to PI3K and AKT inhibitors is mediated by divergent

molecular mechanisms in subtypes of DLBCL. *Blood*. 2017;130(3):310-322. doi:10.1182/blood-2016-12-758599

1110. Olar A, Tran D, Mehta VP, et al. ATRX protein loss and deregulation of PI3K/AKT pathway is frequent in pilocytic astrocytoma with anaplastic features. *Clin Neuropathol*. 2019;38(2):59-73. doi:10.5414/NP301105

1111. Laroche A, Chaire V, Algeo MP, Karanian M, Fourneaux B, Italiano A. MDM2 antagonists synergize with PI3K/mTOR inhibition in well-differentiated/dedifferentiated liposarcomas. *Oncotarget*. 2017;8(33):53968-53977. doi:10.18632/oncotarget.16345

1112. Zhan T, Brüggemann D, Heigwer F, et al. A kinome wide CRISPR/Cas9 screen uncovers novel resistance factors to MEK inhibition in colorectal cancer. *Z Gastroenterol*. 2015;53(KG194). doi:10.1055/s-0035-1559220

1113. Posch C, Moslehi H, Feeney L, et al. Combined targeting of MEK and PI3K/mTOR effector pathways is necessary to effectively inhibit NRAS mutant melanoma in vitro and in vivo. *Proc Natl Acad Sci USA*. 2013;110(10):4015-4020. doi:10.1073/pnas.1216013110

1114. Posch C, Cholewa BD, Vujic I, et al. Combined Inhibition of MEK and Plk1 Has Synergistic Antitumor Activity in NRAS Mutant Melanoma. *J Invest Dermatol*. 2015;135(10):2475-2483. doi:10.1038/jid.2015.198

1115. Tanaka T, Higashi M, Kimura K, et al. MEK inhibitors as a novel therapy for neuroblastoma: Their in vitro effects and predicting their efficacy. *J Pediatr Surg*. 2016;51(12):2074-2079. doi:10.1016/j.jpedsurg.2016.09.043

1116. Woodfield SE, Zhang L, Scorsone KA, Liu Y, Zage PE. Binimetinib inhibits MEK and is effective against neuroblastoma tumor cells with low NF1 expression. *BMC Cancer*. 2016;16(172). doi:10.1186/s12885-016-2199-z

1117. Hannak E, Kirkham M, Hyman AA, Oegema K. Aurora-A kinase is required for centrosome maturation in Caenorhabditis elegans. *J Cell Biol*. 2001;155(7):1109-1116. doi:10.1083/jcb.200108051

1118. Michaelis M, Selt F, Rothweiler F, et al. Aurora kinases as targets in drug-resistant neuroblastoma cells. *PLoS One*. 2014;9(9):e108758. doi:10.1371/journal.pone.0108758

1119. Brockmann M, Poon E, Berry T, et al. Small Molecule Inhibitors of Aurora-A Induce Proteasomal Degradation of N-Myc in Childhood Neuroblastoma. *Cancer Cell*. 2013;24(1):75-89. doi:10.1016/j.ccr.2013.05.005

1120. Faisal A, Vaughan L, Bavetsias V, et al. The aurora kinase inhibitor CCT137690 downregulates MYCN and sensitizes MYCN-amplified neuroblastoma in Vivo. *Mol Cancer Ther*. 2011;10(11):2115-2123. doi:10.1158/1535-7163.MCT-11-0333

1121. DuBois SG, Marachelian A, Fox E, et al. Phase I Study of the Aurora A Kinase Inhibitor Alisertib in Combination With Irinotecan and Temozolomide for Patients With Relapsed or Refractory Neuroblastoma: A NANT (New Approaches to Neuroblastoma Therapy) Trial. *J Clin Oncol*. 2016;34(12):1368-1375. doi:10.1200/JCO.2015.65.4889

1122. Čančer M, Drews LF, Bengtsson J, et al. BET and Aurora Kinase A inhibitors synergize against MYCN-positive human glioblastoma cells. *Cell Death Dis*. 2019;10(12):881. doi:10.1038/s41419-019-2120-1

1123. Krienelke-Szymansky A. The MYCN oncogene as a minimal residual disease marker and therapeutic target in neuroblastoma. *Thesis, Freie Univ Berlin*. 2020;.

1124. Thornton GK, Woods CG. Primary microcephaly: do all roads lead to Rome? *Trends Genet*. 2009;25(11):501-510. doi:10.1016/j.tig.2009.09.011

1125. Horvath S, Zhang B, Carlson M, et al. Analysis of oncogenic signaling networks in glioblastoma identifies ASPM as a molecular target. *Proc Natl Acad Sci USA*. 2006;103(46):17402-17407. doi:10.1073/pnas.0608396103

1126. Kabbarah O, Nogueira C, Feng B, et al. Integrative genome comparison of primary and metastatic melanomas. *PLoS One*. 2010;5(5):e10770. doi:10.1371/journal.pone.0010770

1127. Lin SY, Pan HW, Liu SH, et al. ASPM is a novel marker for vascular invasion, early recurrence, and poor prognosis of hepatocellular carcinoma. *Clin Cancer Res*. 2008;14(15):4814-4820. doi:10.1158/1078-0432.CCR-07-5262

1128. Wang WY, Hsu CC, Wang TY, et al. A gene expression signature of epithelial tubulogenesis and a role

for ASPM in pancreatic tumor progression. *Gastroenterology*. 2013;145(5):1110-1120. doi:10.1053/j.gastro.2013.07.040

1129. Xie JJ, Zhuo YJ, Zheng Y, et al. High expression of ASPM correlates with tumor progression and predicts poor outcome in patients with prostate cancer. *Int Urol Nephrol*. 2017;49(5):817-823. doi:10.1007/s11255-017-1545-7

1130. Tang J, Lu M, Cui Q, et al. Overexpression of ASPM, CDC20, and TTK Confer a Poorer Prognosis in Breast Cancer Identified by Gene Co-expression Network Analysis. *Front Oncol*. 2019;9(310):1-14. doi:10.3389/fonc.2019.00310

1131. Shi S, Tan Q, Feng F, et al. Identification of core genes in the progression of endometrial cancer and cancer cell-derived exosomes by an integrative analysis. *Sci Rep*. 2020;10(1):9862. doi:10.1038/s41598-020-66872-3

1132. Zhou J-W, Wang H, Sun W, Han N-N, Chen L. ASPM is a predictor of overall survival and has therapeutic potential in endometrial cancer. *Am J Transl Res*. 2020;12(5):1942-1953.

1133. Carleton M, Mao M, Biery M, et al. RNA Interference-Mediated Silencing of Mitotic Kinesin KIF14 Disrupts Cell Cycle Progression and Induces Cytokinesis Failure. *Mol Cell Biol*. 2006;26(10):3853-3863. doi:10.1128/mcb.26.10.3853-3863.2006

1134. Ciossani G, Overlack K, Petrovic A, et al. The kinetochore proteins CENP-E and CENP-F directly and specifically interact with distinct BUB mitotic checkpoint Ser/Thr kinases. *J Biol Chem*. 2018;293(26):10084-10101. doi:10.1074/jbc.RA118.003154

1135. Yin L, Jiang LP, Shen QS, et al. NCAPH plays important roles in human colon cancer. *Cell Death Dis*. 2017;8(3):e2680. doi:10.1038/cddis.2017.88

1136. Arquint C, Gabryjonczyk AM, Imseng S, et al. STIL binding to Polo-box 3 of PLK4 regulates centriole duplication. *Elife*. 2015;4:e07888. doi:10.7554/eLife.07888

1137. Huang W, Wang J, Zhang D, et al. Inhibition of KIF14 Suppresses Tumor Cell Growth and Promotes Apoptosis in Human Glioblastoma. *Cell Physiol Biochem*. 2015;37(5):1659-1670. doi:10.1159/000438532

1138. Zhu X, Luo X, Feng G, et al. CENPE expression is associated with its DNA methylation status in esophageal adenocarcinoma and independently predicts unfavorable overall survival. *PLoS One*. 2019;14(2):e0207341. doi:10.1371/journal.pone.0207341

1139. Patwardhan D, Mani S, Passemard S, Gressens P, El Ghouzzi V. STIL balancing primary microcephaly and cancer. *Cell Death Dis*. 2018;9(2):65. doi:10.1038/s41419-017-0101-9

1140. Bianchi FT, Tocco C, Pallavicini G, et al. Citron Kinase Deficiency Leads to Chromosomal Instability and TP53-Sensitive Microcephaly. *Cell Rep*. 2017;18(7):1674-1686. doi:10.1016/j.celrep.2017.01.054

1141. Bakhoum SF, Genovese G, Compton DA. Deviant Kinetochore Microtubule Dynamics Underlie Chromosomal Instability. *Curr Biol*. 2009;19(22):1937-1942. doi:10.1016/j.cub.2009.09.055

1142. Kanda T, Otter M, Wahl GM. Mitotic segregation of viral and cellular acentric extrachromosomal molecules by chromosome tethering. *J Cell Sci*. 2001;114(Pt 1):49-58.

1143. Matthay KK, Maris JM, Schleiermacher G, et al. Neuroblastoma. *Nat Rev Dis Prim*. 2016;2:16078. doi:10.1038/nrdp.2016.78

1144. Uryu K, Nishimura R, Kataoka K, et al. Identification of the genetic and clinical characteristics of neuroblastomas using genome-wide analysis. *Oncotarget*. 2017;8(64):107513-107529. doi:10.18632/oncotarget.22495

1145. Ooi WF, Re A, Sidarovich V, et al. Segmental chromosome aberrations converge on overexpression of mitotic spindle regulatory genes in high-risk neuroblastoma. *Genes Chromosomes Cancer*. 2012;51(6):545-556. doi:10.1002/gcc.21940

1146. Gilbert F, Feder M, Balaban G, et al. Human Neuroblastomas and Abnormalities of Chromosomes 1 and 17. *Cancer Res*. 1984;44(11):5444-5449.

1147. Khan FH, Pandian V, Ramraj S, et al. Acquired genetic alterations in tumor cells dictate the development of high-risk neuroblastoma and clinical outcomes. *BMC Cancer*. 2015;15(514). doi:10.1186/s12885-015-1463-y

1148. Jönsson G, Dahl C, Staaf J, et al. Genomic profiling of malignant melanoma using tiling-resolution arrayCGH. *Oncogene*. 2007;26(32):4738-4748. doi:10.1038/sj.onc.1210252

1149. Lo KC, Ma C, Bundy BN, Pomeroy SL, Eberhart CG, Cowell JK. Gain of 1q is a potential univariate negative prognostic marker for survival in medulloblastoma. *Clin Cancer Res*. 2007;13(23):7022-7028. doi:10.1158/1078-0432.CCR-07-1420

1150. Bowles E, Corson TW, Bayani J, et al. Profiling genomic copy number changes in retinoblastoma beyond loss of RB1. *Genes Chromosomes Cancer*. 2007;46(2):118-129. doi:10.1002/gcc.20383

1151. Giunti L, Pantaleo M, Sardi I, et al. Genome-wide copy number analysis in pediatric glioblastoma multiforme. *Am J Cancer Res*. 2014;4(3):293-303.

1152. Campbell K, Gastier-Foster JM, Mann M, et al. Association of MYCN copy number with clinical features, tumor biology, and outcomes in neuroblastoma: A report from the Children's Oncology Group. *Cancer*. 2017;123(21):4224-4235. doi:10.1002/cncr.30873

1153. Hyun MJ, Choi SJ, Jin KK. Expression profiles of SV40-immortalization-associated genes upregulated in various human cancers. *J Cell Biochem*. 2009;106(4):703-713. doi:10.1002/jcb.22063

1154. Pulvers JN, Bryk J, Fish JL, et al. Mutations in mouse Aspm (abnormal spindle-like microcephaly associated) cause not only microcephaly but also major defects in the germline. *Proc Natl Acad Sci USA*. 2010;107(38):16595-16600. doi:10.1073/pnas.1010494107

1155. Buchman JJ, Durak O, Tsai LH. ASPM regulates Wnt signaling pathway activity in the developing brain. *Genes Dev*. 2011;25(18):1909-1914. doi:10.1101/gad.16830211

1156. Alsiary R, Brüning-Richardson A, Bond J, Morrison EE, Wilkinson N, Bell SM. Deregulation of microcephalin and ASPM expression are correlated with epithelial ovarian cancer progression. *PLoS One*. 2014;9(5):e97059. doi:10.1371/journal.pone.0097059

1157. Capecchi MR, Pozner A. ASPM regulates symmetric stem cell division by tuning Cyclin E ubiquitination. *Nat Commun*. 2015;6(May):8763. doi:10.1038/ncomms9763

1158. Littler S, Sloss O, Geary B, Pierce A, Whetton AD, Taylor SS. Oncogenic MYC amplifies mitotic perturbations. *Open Biol*. 2019;9(8):190136. doi:10.1098/rsob.190136

1159. Pilaz LJ, McMahon JJ, Miller EE, et al. Prolonged Mitosis of Neural Progenitors Alters Cell Fate in the Developing Brain. *Neuron*. 2016;89(1):83-99. doi:10.1016/j.neuron.2015.12.007

1160. Komatsu M, Yoshimaru T, Matsuo T, et al. Molecular features of triple negative breast cancer cells by genome-wide gene expression profiling analysis. *Int J Oncol*. 2013;42(2):478-506. doi:10.3892/ijo.2012.1744

1161. Johnson MB, Sun X, Kodani A, et al. Aspm knockout ferret reveals an evolutionary mechanism governing cerebral cortical size letter. *Nature*. 2018;556(7701):370-375. doi:10.1038/s41586-018-0035-0

1162. Garcia I, Crowther AJ, Gershon TR. MB-51. Aspm, a target of sonic hedgehog, is a key element in cerebellar development and medulloblastoma pathogenesis. *Neuro Oncol*. 2012;14(suppl_1):i82–i105. doi:https://doi.org/10.1093/neuonc/nos093

1163. Poulton CJ, Schot R, Kia SK, et al. Microcephaly with simplified gyration, epilepsy, and infantile diabetes linked to inappropriate apoptosis of neural progenitors. *Am J Hum Genet*. 2011;89(2):265-276. doi:10.1016/j.ajhg.2011.07.006

1164. O'Neill RS, Schoborg TA, Rusan NM. Same but different: Pleiotropy in centrosome-related microcephaly. *Mol Biol Cell*. 2018;29(3):241-246. doi:10.1091/mbc.E17-03-0192

1165. Chen JF, Zhang Y, Wilde J, Hansen KC, Lai F, Niswander L. Microcephaly disease gene Wdr62 regulates mitotic progression of embryonic neural stem cells and brain size. *Nat Commun*. 2014;5(3885). doi:10.1038/ncomms4885

1166. Sgourdou P, Mishra-Gorur K, Saotome I, et al. Disruptions in asymmetric centrosome inheritance and WDR62-Aurora kinase B interactions in primary microcephaly. *Sci Rep*. 2017;7(43708). doi:10.1038/srep43708

1167. Li H, Kroll T, Moll J, et al. Spindle Misorientation of Cerebral and Cerebellar Progenitors Is a Mechanistic Cause of Megalencephaly. *Stem Cell Reports*. 2017;9(4):1071-1080. doi:10.1016/j.stemcr.2017.08.013

1168. Kaindl AM, Passemard S, Kumar P, et al. Many roads lead to primary autosomal recessive microcephaly. *Prog Neurobiol*. 2010;90(3):363-383. doi:10.1016/j.pneurobio.2009.11.002

1169. Fujimori A, Itoh K, Goto S, et al. Disruption of Aspm causes microcephaly with abnormal neuronal

differentiation. *Brain Dev*. 2014;36(8):661-669. doi:10.1016/j.braindev.2013.10.006

1170. Liu H, Li H, Luo K, Sharma A, Sun X. Prognostic Gene Expression Signature Revealed the Involvement of Mutational Pathways in Cancer Genome. *J Cancer*. 2020;11(15):4510-4520. doi:10.7150/jca.40237

1171. Bruland T, Beisvag V, Erlandsen SE, et al. Genome-wide analysis of the oxyntic proliferative isthmus zone reveals ASPM as a possible gastric stem/progenitor cell marker over-expressed in cancer. *J Pathol*. 2015;237(4):447-459. doi:10.1002/path.4591

1172. Hsu CC, Liao WY, Chan TS, et al. The differential distributions of ASPM isoforms and their roles in Wnt signaling, cell cycle progression, and pancreatic cancer prognosis. *J Pathol*. 2019;249(4):498-508. doi:10.1002/path.5341

1173. Chen Q, Hu J, Deng J, Fu B, Guo J. Bioinformatics Analysis Identified Key Molecular Changes in Bladder Cancer Development and Recurrence. Guan X, ed. *Biomed Res Int*. 2019;2019:3917982. doi:10.1155/2019/3917982

1174. Saleh AA, Gohar SF, Hemida AS, Elgharbawy M, Soliman SE. Evaluation of ASPM and TEF Gene Expressions as Potential Biomarkers for Bladder Cancer. *Biochem Genet*. 2020;58(3):490-507. doi:10.1007/s10528-020-09962-1

1175. Kato TA, Okayasu R, Jeggo PA, Fujimori A. ASPM influences DNA double-strand break repair and represents a potential target for radiotherapy. *Int J Radiat Biol*. 2011;87(12):1189-1195. doi:10.3109/09553002.2011.624152

1176. Turnbull AK, Arthur LM, Renshaw L, et al. Accurate Prediction and Validation of Response to Endocrine Therapy in Breast Cancer. *J Clin Oncol*. 2015;33(20):2270-2278. doi:10.1200/JCO.2014.57.8963

1177. Stutterheim J, Gerritsen A, Zappeij-Kannegieter L, et al. Detecting minimal residual disease in neuroblastoma: The superiority of a panel of real-time quantitative PCR markers. *Clin Chem*. 2009;55(7):1316-1326. doi:10.1373/clinchem.2008.117945

1178. Stutterheim J, Gerritsen A, Zappeij-Kannegieter L, et al. PHOX2B is a novel and specific marker for minimal residual disease testing in neuroblastoma. *J Clin Oncol*. 2008;26(33):5443-5449. doi:10.1200/JCO.2007.13.6531

1179. Oltra S, Martinez F, Orellana C, et al. The doublecortin gene, a new molecular marker to detect minimal residual disease in neuroblastoma. *Diagnostic Mol Pathol*. 2005;14(1):53-57. doi:10.1097/01.pas.0000149876.32376.c0

1180. Fiedler S, Ladenstein RL, Poetschger U, et al. Risk prediction based on post induction bone marrow response and genomic profile: A new way to stratify stage M neuroblastoma patients? *J Clin Oncol*. 2018;3(15_suppl):10550-10550. doi:10.1200/jco.2018.36.15_suppl.10550

1181. Kohler JA, Imeson J, Ellershaw C, Lie SO. A randomized trial of 13-Cis retinoic acid in children with advanced neuroblastoma after high-dose therapy. *Br J Cancer*. 2000;83(9):1124-1127. doi:10.1054/bjoc.2000.1425

1182. Patterson JC, Joughin BA, Prota AE, et al. VISAGE Reveals a Targetable Mitotic Spindle Vulnerability in Cancer Cells. *Cell Syst*. 2019;9(1):74-92.e8. doi:10.1016/j.cels.2019.05.009

1183. Moreno L, Casanova M, Chisholm JC, et al. Phase I results of a phase I/II study of weekly nab-paclitaxel in paediatric patients with recurrent/refractory solid tumours: A collaboration with innovative therapies for children with cancer. *Eur J Cancer*. 2018;100:27-34. doi:10.1016/j.ejca.2018.05.002

1184. Xu XL, Ma W, Zhu YB, et al. The Microtubule-Associated Protein ASPM Regulates Spindle Assembly and Meiotic Progression in Mouse Oocytes. *PLoS One*. 2012;7(11):e49303. doi:10.1371/journal.pone.0049303

1185. Fujimori A, Yaoi T, Ogi H, et al. Ionizing radiation downregulates ASPM, a gene responsible for microcephaly in humans. *Biochem Biophys Res Commun*. 2008;369(3):953-957. doi:10.1016/j.bbrc.2008.02.149

1186. Rogakou EP, Pilch DR, Orr AH, Ivanova VS, Bonner WM. DNA double-stranded breaks induce histone H2AX phosphorylation on serine 139. *J Biol Chem*. 1998;273(10):5858-5868. doi:10.1074/jbc.273.10.5858

1187. Bae I, Jeong KR, Hee JK, et al. BRCA1 regulates gene expression for orderly mitotic progression. *Cell Cycle*. 2005;4(11):1641-1666. doi:10.4161/cc.4.11.2152

1188. Zhong X, Liu L, Zhao A, Pfeifer GP, Xu X. The abnormal spindle-like, microcephaly-associated (ASPM) gene encodes a centrosomal protein. *Cell Cycle*. 2005;4(9):1227-1229. doi:10.4161/cc.4.9.2029

1189. Saunders RDC, Do Carmo Avides M, Howard T, Gonzalez C, Glover DM. The Drosophila gene abnormal spindle encodes a novel microtubule- associated protein that associates with the polar regions of the mitotic spindle. *J Cell Biol*. 1997;137(4):881-890. doi:10.1083/jcb.137.4.881

1190. Swadi RR, Sampat K, Herrmann A, Losty PD, See V, Moss DJ. CDK inhibitors reduce cell proliferation and reverse hypoxia-induced metastasis of neuroblastoma tumours in a chick embryo model. *Sci Rep*. 2019;9(1):9136. doi:10.1038/s41598-019-45571-8

1191. Takeuchi Y, Tanaka T, Higashi M, et al. In vivo effects of short- and long-term MAPK pathway inhibition against neuroblastoma. *J Pediatr Surg*. 2018;53(12):2454-2459. doi:10.1016/j.jpedsurg.2018.08.026

1192. Li H, Yu Y, Zhao Y, et al. Small molecule inhibitor agerafenib effectively suppresses neuroblastoma tumor growth in mouse models via inhibiting ERK MAPK signaling. *Cancer Lett*. 2019;457:129-141. doi:10.1016/j.canlet.2019.05.011

1193. Zhang C, Zhang B, Meng D, Ge C. Comprehensive analysis of DNA methylation and gene expression profiles in cholangiocarcinoma. *Cancer Cell Int*. 2019;19(1):352. doi:10.1186/s12935-019-1080-y

1194. Caldas H, Jiang Y, Holloway MP, et al. Survivin splice variants regulate the balance between proliferation and cell death. *Oncogene*. 2005;24(12):1994-2007. doi:10.1038/sj.onc.1208350

1195. Unruhe B, Schröder E, Wünsch D, Knauer SK. An Old Flame Never Dies: Survivin in Cancer and Cellular Senescence. *Gerontology*. 2016;62(2):173-181. doi:10.1159/000432398

1196. Li F, Aljahdali I, Ling X. Cancer therapeutics using survivin BIRC5 as a target: What can we do after over two decades of study? *J Exp Clin Cancer Res*. 2019;38(1):368. doi:10.1186/s13046-019-1362-1

1197. Peery RC, Liu JY, Zhang JT. Targeting survivin for therapeutic discovery: past, present, and future promises. *Drug Discov Today*. 2017;22(10):1466-1477. doi:10.1016/j.drudis.2017.05.009

1198. Radic-Sarikas B, Halasz M, Huber KVM, et al. Lapatinib potentiates cytotoxicity of YM155 in neuroblastoma via inhibition of the ABCB1 efflux transporter. *Sci Rep*. 2017;7(1):3091. doi:10.1038/s41598-017-03129-6

1199. Nakano E, Mushtaq S, Heath PR, et al. Riboflavin depletion impairs cell proliferation in adult human duodenum: Identification of potential effectors. *Dig Dis Sci*. 2011;56(4):1007-1019. doi:10.1007/s10620-010-1374-3

1200. Henderson MC, Shaw YJY, Wang H, et al. UA62784, a novel inhibitor of centromere protein E kinesin-like protein. *Mol Cancer Ther*. 2009;8(1):36-44. doi:10.1158/1535-7163.MCT-08-0789

1201. Ohashi A, Ohori M, Iwai K, et al. A novel time-dependent CENP-E inhibitor with potent antitumor activity. *PLoS One*. 2015;10(12):e0144675. doi:10.1371/journal.pone.0144675

1202. Thole TM, Lodrini M, Fabian J, et al. Neuroblastoma cells depend on HDAC11 for mitotic cell cycle progression and survival. *Cell Death Dis*. 2017;8(3):e2635. doi:10.1038/cddis.2017.49

1203. Kuo WY, Wu CY, Hwu L, et al. Enhancement of tumor initiation and expression of KCNMA1, MORF4L2 and ASPM genes in the adenocarcinoma of lung xenograft after vorinostat treatment. *Oncotarget*. 2015;6(11):8663-8675. doi:10.18632/oncotarget.3536

1204. Liu X, Yan S, Zhou T, Terada Y, Erikson RL. The MAP kinase pathway is required for entry into mitosis and cell survival. *Oncogene*. 2004;23(3):763-776. doi:10.1038/sj.onc.1207188

1205. Hoshi M, Ohta K, Gotoh Y, et al. Mitogen-activated-protein-kinase-catalyzed phosphorylation of microtubule-associated proteins, microtubule-associated protein 2 and microtubule-associated protein 4, induces an alteration in their function. *Eur J Biochem*. 1992;203(1-2):43-52. doi:10.1111/j.1432-1033.1992.tb19825.x

1206. Joukov V, De Nicolo A. Aurora-PLK1 cascades as key signaling modules in the regulation of mitosis. *Sci Signal*. 2018;11(543):eaar4195. doi:10.1126/scisignal.aar4195

1207. Wang H, Qiu Z, Liu B, et al. PLK1 targets CtIP to promote microhomology-mediated end joining. *Nucleic Acids Res*. 2018;46(20):10724-10739. doi:10.1093/nar/gky810

1208. Petritsch CK. Investigating ASPM regulation of asymmetric division for therapeutic opportunities. University of California San Francisco, San Francisco, CA, United States. Published 2016. Accessed November 28, 2020. http://grantome.com/grant/NIH/R21-NS099836-01

1209. Westhoff M-A, Karpel-Massler G, Brühl O, et al. A critical evaluation of PI3K inhibition in Glioblastoma and Neuroblastoma therapy. *Mol Cell Ther*. 2014;2(32). doi:10.1186/2052-8426-2-32

1210. Wang J, Ramirez T, Ji P, Jayapal SR, Lodish HF, Murata-Hori M. Mammalian erythroblast enucleation requires PI3K-dependent cell polarization. *J Cell Sci*. 2012;125(Pt 2):340-349. doi:10.1242/jcs.088286

1211. Bayani J, Yao CQ, Quintayo MA, et al. Molecular stratification of early breast cancer identifies drug targets to drive stratified medicine. *npj Breast Cancer*. 2017;3(3). doi:10.1038/s41523-016-0003-5

1212. Kobayashi I, Ubukawa K, Sugawara K, et al. Erythroblast enucleation is a dynein-dependent process. *Exp Hematol*. 2016;44(4):247-256.e12. doi:10.1016/j.exphem.2015.12.003

1213. Jost M, Chen Y, Gilbert LA, Steinmetz MO, Tanenbaum ME, Weissman JS. Combined CRISPRi / a-Based Chemical Genetic Screens Reveal that Rigosertib Is a Microtubule- Destabilizing Agent Article Combined CRISPRi / a-Based Chemical Genetic Screens Reveal that Rigosertib Is a Microtubule-Destabilizing Agent. *Mol Cell*. 2017;68(1):210-223.e6. doi:10.1016/j.molcel.2017.09.012

1214. Barr FA, Silljé HHW, Nigg EA. Polo-like kinases and the orchestration of cell division. *Nat Rev Mol Cell Biol*. 2004;5(6):429-440. doi:10.1038/nrm1401

1215. Glover DM, Hagan IM, Tavares ÁAM. Polo-like kinases: A team that plays throughout mitosis. *Genes Dev*. 1998;12(24):3777-3787. doi:10.1101/gad.12.24.3777

1216. Sumara I, Giménez-Abián JF, Gerlich D, et al. Roles of polo-like kinase 1 in the assembly of functional mitotic spindles. *Curr Biol*. 2004;14(19):1712-1722. doi:10.1016/j.cub.2004.09.049

1217. Mäki-Jouppila JHE, Laine LJ, Rehnberg J, et al. Centmitor-1, a novel acridinyl-acetohydrazide, possesses similar molecular interaction field and antimitotic cellular phenotype as rigosertib, on 01910.Na. *Mol Cancer Ther*. 2014;13(5):1054-1066. doi:10.1158/1535-7163.MCT-13-0685

1218. Twarog NR, Low JA, Currier DG, Miller G, Chen T, Shelat AA. Robust classification of small-molecule mechanism of action using a minimalist high-content microscopy screen and multidimensional phenotypic trajectory analysis. *PLoS One*. 2016;11(2):e0149439. doi:10.1371/journal.pone.0149439

1219. Gigant B, Wang C, Ravelli RBG, et al. Structural basis for the regulation of tubulin by vinblastine. *Nature*. 2005;435(7041):519-522. doi:10.1038/nature03566

1220. Baker SJ, Cosenza SC, Athuluri-Divakar S, et al. A Contaminant Impurity, Not Rigosertib, Is a Tubulin Binding Agent. *Mol Cell*. 2020;79(1):180-190.e4. doi:10.1016/j.molcel.2020.05.024

1221. Tanabe K, Takei K. Dynamic instability of microtubules requires dynamin 2 and is impaired in a Charcot-Marie-Tooth mutant. *J Cell Biol*. 2009;185(6):939-948. doi:10.1083/jcb.200803153

1222. Tanabe K. Microtubule depolymerization by kinase inhibitors: Unexpected findings of dual inhibitors. *Int J Mol Sci*. 2017;18(12):2508. doi:10.3390/ijms18122508

1223. Kouprina N, Pavlicek A, Collins NK, et al. The microcephaly ASPM gene is expressed in proliferating tissues and encodes for a mitotic spindle protein. *Hum Mol Genet*. 2005;14(15):2155-2165. doi:10.1093/hmg/ddi220

1224. Thiele CJ. Neuroblastoma Cell Lines. In: Masters J, ed. *Human Cell Culture*. Vol 1. Kluwer Academic Publishers; 1998:21-53. https://ccr.cancer.gov/sites/default/files/neuroblastoma_cell_lines_-_molecular_features.pdf

1225. Thiele C.J. Neuroblastoma. In: Masters JRW, Palsson B, eds. *Human Cell Culture*. vol. 1. Springer; 2002:21-53. doi:https://doi.org/10.1007/0-306-46872-7_2

1226. Bairoch A. The cellosaurus, a cell-line knowledge resource. *J Biomol Tech*. 2018;29(2):25-38. doi:10.7171/jbt.18-2902-002

1227. Berns KI, Bond EC, Manning FJ, eds. *Resource Sharing in Biomedical Research*. The National Academies Press; 1996. doi:10.17226/5429

1228. Leibniz Institute. DSMZ-German Collection of Microorganisms and Cell Cultures GmbH. Published 2019. Accessed November 28, 2020. https://www.dsmz.de/collection/catalogue/human-and-animal-cell-lines/catalogue

1229. Corning Incorporated Life Sciences. Surface Areas and Recommended Medium Volumes for Corning®Cell Culture Vessels. Published online 2012:1-4. https://www.corning.com/catalog/cls/documents/application-notes/CLS-AN-209.pdf

1230. Norrander J, Kempe T, Messing J. Construction of improved M13 vectors using oligodeoxynucleotide-

directed mutagenesis. *Gene*. 1983;26(1):101-106. doi:10.1016/0378-1119(83)90040-9

1231. Sarbassov DD, Guertin DA, Ali SM, Sabatini DM. Phosphorylation and regulation of Akt/PKB by the rictor-mTOR complex. *Science*. 2005;307(5712):1098-1101. doi:10.1126/science.1106148

1232. Ran FA, Hsu PD, Wright J, Agarwala V, Scott DA, Zhang F. Genome engineering using the CRISPR-Cas9 system. *Nat Protoc*. 2013;8(11):2281-2308. doi:10.1038/nprot.2013.143

1233. Mutant Mouse Resource & Research Centers supported by NIH (MMRRC) at the University of California. KOMP Repository Collection. Knockout Mouse Project. Accessed November 28, 2020. https://www.komp.org/geneinfo.php?geneid=23923

1234. Savic D, Partridge EC, Newberry KM, et al. CETCh-seq: CRISPR epitope tagging ChIP-seq of DNA-binding proteins. *Genome Res*. 2015;25(10):1581-1589. doi:10.1101/gr.193540.115

8 Publications and congress contributions

8.1 Publications

Szymansky A, Witthauer MJ, Gürgen D, Dorado Garcia H, Ahrens K, Henssen AG, Hertwig F, Toedling J, Eggert A, Schulte JH. Antitumoral activity of the dual PLK1 and PI3K selective inhibitor rigosertib in preclinical neuroblastoma models. *Manuscript in Preparation,* 2020.

Firle KA & **Szymansky A**, Witthauer MJ, Dorado Garcia H, Toedling J, Ahrens K, Henssen AG, Hertwig F, Eggert A, Schulte JH. Preclinical evaluation of BET-bromodomain inhibitor TEN-010 as monotherapy and combination therapy in MYC-driven neuroblastoma. *Manuscript in Preparation,* 2020.

Szymansky A & Becker L-L & Overath MD, Hertwig F, Winkler A, Ahrens K, Dorado Garcia H, Künkele A, Henssen AG, Eggert A, Toedling J, Kaindl AM & Schulte JH, ASPM is a regulator of neuroblastoma cell proliferation and differentiation. *In submission for Annals of Neurology,* 2020.

Szymansky A, Hertwig F, Winkler A, Witthauer MJ, Fuchs S, Chamorro González R, Overath MD, Hero B, Deubzer H, Helmsauer K, Barz MJ, Ahrens K, Heukamp L, Heuckmann JM, Astrahantseff K, Schmelz K, Kuenkele A, Menon R, Hundsdoerfer P, Eggert A, Toedling J, Fischer M & Eckert C & Henssen AG & Schulte JH, Quantitative and sensitive detection of neuroblastoma minimal residual disease based on extrachromosomal DNA breakpoints. *In submission for Journal of Clinical Investigation,* 2020.

Barz MJ, Hof J, Groeneveld-Krentz S, Loh JW, **Szymansky A**, Astrahantseff K, von Stackelberg A, Khiabanian H, Ferrando AA, Eckert C, Kirschner-Schwabe R, Subclonal *NT5C2* mutations are associated with poor outcomes after relapse of pediatric acute lymphoblastic leukemia. *Blood.* 2020 Mar 19;135(12):921-933

Timme N, Han Y, Liu S, Yosief HO, Dorado García H, Bei Y, Klironomos F, MacArthur I, **Szymansky A**, von Stebut J, Bardinet V, Dohna C, Künkele A, Rolff J, Hundsdörfer P, Lissat A, Seifert G, Eggert A, Schulte JH, Zhang W, Henssen AG, Small-Molecule Dual PLK1 and BRD4 Inhibitors are Active Against Preclinical Models of Pediatric Solid Tumors. *Translational Oncology*, 2020, Volume 13, Issue 2, Page 221-232.

Helmsauer K, Valieva M, Ali S, Chamorro González R, Schoepflin R, Roeefzaad C, Bei Y, Dorado Garcia H, Rodriguez-Fos E, Puiggros M, Kasack K, Haase K, Keskeny C, Chen CY, Kuschel LP, Euskirchen P, Heinrich V, Robson M, Rosswog C, Toedling J, **Szymansky A**, Hertwig F, Fischer M, Torrents D, Eggert A, Schulte JH, Mundlos S, Henssen AG & Koche RP, Enhancer hijacking determines extrachromosomal circular *MYCN* amplicon architecture in neuroblastoma. *Nature communications*, 2020, 11, 5823

Koche RP, Rodriguez-Fos E, Helmsauer K, Burkert M, MacArthur IC, Maag J, Chamorro R, Munoz-Perez N, Puiggròs M, Dorado Garcia H, Bei Y, Röefzaad C, Bardinet V, **Szymansky A**, Winkler A, Thole T, Timme N, Kasack K, Fuchs S, Klironomos F, Thiessen N, Blanc E, Schmelz K, Künkele A, Hundsdörfer P, Rosswog C, Theissen J, Beule D, Deubzer H, Sauer S, Toedling J, Fischer M, Hertwig F, Schwarz RF, Eggert A, Torrents D, Schulte JH & Henssen AG, Extrachromosomal circular DNA drives oncogenic genome remodeling in neuroblastoma. *Nature genetics*, 2020 Jan; 52(1): 29–34.

Hoffmann J, Krumbholz M, Pimentel Gutiérrez H, Fillies M, **Szymansky A**, Bleckmann K, zur Stadt U, Köhler R, Kuiper RP, Horstmann M, von Stackelberg A, Eckert C, Metzler M, High sensitivity and clonal stability of the genomic fusion as single marker for response monitoring in ETV6-RUNX1-positive acute lymphoblastic leukemia. *Pediatric blood & cancer*, 2019. Aug;66(8):e27780

Henssen AG, Odersky A, **Szymansky A**, Seiler M, Althoff K, Beckers A, Speleman F, Schaefers S, De Preter K, Astrahanseff K, Struck J, Schramm A, Eggert A, Bergmann A, Schulte JH, Targeting tachykinin receptors in neuroblastoma. *Oncotarget*, 2016. 8.1 (0): 430-443.

8.2 **Congress contributions**

Szymansky A, Becker L-L, Overath MD, Hertwig F, Winkler A, Ahrens K, McGearey A, Dorado García H, Astrahantseff K, Künkele A, Henssen AG, Eggert A, Toedling J, Klose J, Kaindl AM, Schulte JH,. High levels of ASPM alter mitosis of neuroblastomas and regulate cell proliferation and differentiation. *Microtubules: From Atoms to Complex Systems – virtual, EMBL/EMBO Symposium series 2020*: Heidelberg, Germany.

Szymansky A, Hertwig F, Winkler A, Witthauer MJ, Fuchs S, Overath MD, Winter K, Pogodzinski MJ, Schönbeck K, Heukamp L, Heukmann JM, Menon R, Henssen AG, Hundsdoerfer P, Eggert A, Fischer M, Eckert C, Toedling J, Schulte JH. Individualized MRD diagnostics for high-risk neuroblastoma using patient-specific *MYCN* chromosomal breakpoints. *9th Mildred Scheel Cancer Conference 2019*: Bonn, Germany.
Flash Talk, **Poster Prize winner**

Overath MD & **Szymansky A**, Becker L-L, Hartmann B, Schönbeck K, Winkler A, Witthauer MJ, Hertwig F, Toedling J, Eggert A, Klose J, Kaindl AM, Schulte JH, The functional relevance of centrosomal mitotic-spindle protein ASPM as novel risk factor in neuroblastoma. *1. Deutscher Krebsforschungskongress (DKFK), Hopp-Kindertumorzentrum Heidelberg 2019*: Heidelberg, Germany.

Szymansky A, Hertwig F, Witthauer MJ, Winkler A, Fuchs S, Overath MD, Winter K, Pogodzinski MJ, Schönbeck K, Heukamp L, Heukmann JM, Menon R, Hundsdoerfer P, Henssen AG, Eggert A, Fischer M, Eckert C, Toedling J, Schulte JH. Minimal residual disease monitoring in high-risk *MYCN*-amplified neuroblastoma by chromosomal breakpoint recognition. *1. Deutscher Krebsforschungskongress (DKFK), Hopp-Kindertumorzentrum Heidelberg 2019*: Heidelberg, Germany.

Toedling J, Schmelz K, Proba J, **Szymansky A**, Hundsdörfer P, Eggert A, Schulte JH, Multi-region sequencing dissects intratumour heterogeneity in neuroblastoma. *1. Deutscher Krebsforschungskongress (DKFK), Hopp-Kindertumorzentrum Heidelberg 2019*: Heidelberg, Germany.

Szymansky A, Klironomos F, Danßmann C, Toedling J, Winkler A, Luz U, McGearey, Hundsdoerfer P, Hertwig F, Eggert A, Schulte JH, Fuchs S, Circular RNAs contribute to neuroblastoma pathogenesis. *1. Deutscher Krebsforschungskongress (DKFK), Hopp-Kindertumorzentrum Heidelberg 2019*: Heidelberg, Germany.

Szymansky A, Becker L-L, Overath MD, Hartmann B, Winkler A, Witthauer MJ, Hertwig F, Toedling J, Eggert A, Klose J, Kaindl AM, Schulte JH, ASPM is a novel risk factor of aggressive neuroblastoma. *Sozialpädiatrisches Zentrum der Charité – Universitätsmedizin Berlin, Jährliche Postersitzung 2018*: Berlin, Germany.

Pogodzinski MJ, Hof J, Groeneveld-Krentz S, **Szymansky A**, von Stackelberg A, Ferrando AA, Eckert C, Kirschner-Schwabe R, Transient subclones carrying *NT5C2* mutations define a high-risk patient group with poor outcome in pediatric relapsed B-cell precursor acute lymphoblastic leukemia. *European Hematology Association Library* 2019: 267331; S130, Amsterdam, The Netherlands.

Szymansky A, Menon R, Witthauer MJ, Winkler, Pogodzinski MJ, Overath MD, Toedling J, Hertwig F, Klironomos F, Fuchs S, Schönbeck K, Heukamp L, Heukmann JM, Hundsdoerfer P, Eggert A, Fischer M, Eckert C, Schulte JH, Recognition of *MYCN* chromosomal breakpoints for monitoring of minimal residual disease in high-risk neuroblastoma. *E:Med Systems Medicine Meeting* 2018: Berlin, Germany.

Szymansky A, Becker L-L, Overath MD, Hartmann B, Schönbeck K, Winkler A, Witthauer MJ, Hertwig F, Toedling J, Eggert A, Klose J, Kaindl AM, Schulte JH, ASPM is a novel risk factor of aggressive neuroblastoma. *Sozialpädiatrisches Zentrum der Charité – Universitätsmedizin Berlin, Jährliche Postersitzung 2018*: Berlin, Germany.

Firle KA, **Szymansky A**, Witthauer MJ, Dorado Garcia H, Toedling J, Schönbeck K, Henssen AG, Hertwig F, Eggert A, Schulte JH, Preclinical evaluation of BET-inhibition as monotherapy and combination therapy in MYC-driven neuroblastoma. *From Lab to Life – Childhood Cancer Research Initiatives 2018*; Wien, Austria.

Szymansky A, Menon R, Witthauer MJ, Winkler A, Pogodzinski MJ, Overath MD, Toedling J, Hertwig F, Schönbeck K, Heukamp L, Heukmann J, Hundsdoerfer P, Eggert A, Fischer M, Eckert C, Schulte JH, Monitoring of minimal residual disease in *MYCN*-amplified neuroblastoma by chromosomal breakpoint recognition. *Klinische Pädiatrie*, 2018; 230(03): 175. Wilsede, Germany.

Schoenbeck K, Witthauer MJ, Winkler A, **Szymansky A**, Toedling J, Schramm A, Hertwig F, Eggert A, Schulte JH, Hippo-YAP pathway activation favors neuroblastoma progression. *Klinische Pädiatrie* 2018; 230(03): 171. Wilsede, Germany.

Firle KA, **Szymansky A**, Witthauer MJ, Toedling J, Schönbeck K, Hertwig F, Eggert A, Schulte JH, Preclinical evaluation of BET-inhibition as monotherapy and combination therapy in MYC-driven neuroblastoma. *Klinische Pädiatrie* 2018; 230(03): 171. Wilsede, Germany.

Schönbeck K, Winkler A, Witthauer MJ, **Szymansky A**, Toedling J, Schramm A, Hertwig F, Eggert A, Schulte JH, Hippo-YAP pathway activation favors neuroblastoma progression. *Advances in Neuroblastoma Research Conference 2018*: San Francisco, California, USA.

Dorado-García H, Liu S, Yosief HO, Joshi P, MacArthur IC, Klironomos F, Timme N, Han Y, Schoenbeck K, **Szymansky A**, Eggert A, Hundsdoerfer P, Schulte JH, Zhang W, Henssen AG, Dual inhibition of PLK1 and BRD4 for treating high-risk neuroblastoma. *Advances in Neuroblastoma Research Conference 2018*: San Francisco, California, USA.

Szymansky A, Menon R, Witthauer MJ, Winkler A, Pogodzinski MJ, Overath MD, Toedling J, Hertwig F, Klironomos F, Fuchs S, Schönbeck K, Heukamp L, Heukmann J, Hundsdoerfer P, Eggert A, Fischer M, Eckert C, Schulte JH. Monitoring of minimal residual disease in *MYCN*-amplified neuroblastoma by chromosomal breakpoint profiling. *Advances in Neuroblastoma Research Conference 2018*: San Francisco, California, USA.

Szymansky A, Becker L-L, Overath MD, Hartmann B, Schönbeck K, Winkler A, Witthauer MJ, McGearey A, Hertwig F, Toedling J, Klironomos F, Fuchs S, Eggert A, Klose J, Kaindl AM, Schulte JH, ASPM is a novel risk factor of aggressive neuroblastoma. *Advances in Neuroblastoma Research Conference 2018*: San Francisco, California, USA.

Szymansky A, Firle KA, Witthauer MJ, Bock M, Dorado-García H, Toedling J, Klironomos F, Fuchs S, Schönbeck K, Künkele A, Henssen AG, Hertwig F, Eggert A, Schulte JH, Preclinical evaluation of BET-bromodomain inhibitor TEN-010 as monotherapy and combination therapy in MYC-driven neuroblastoma. *Advances in Neuroblastoma Research Conference 2018*: San Francisco, California, USA.

Hertwig F, Menon R, Ackermann S, Peifer M, Toedling J, **Szymansky A**, Engesser A, Bartenhagen C, Theissen J, Klironomos F, Fuchs S, Hundsdoerfer P, Heukmann J, Eggert A, Hero B, Heukamp L, Fischer M, Schulte JH, Neuroblastoma Risk Assessment and Treatment Stratification with Hybrid Capture-based Panel Sequencing. *Advances in Neuroblastoma Research Conference 2018*: San Francisco, California, USA.
Flash Talk speaker as representative of Hertwig F

Timme N, Liu S, Yosief H, Dorado García H, MacArthur I, **Szymansky A**, Dohna C, Seifert G, Hundsdörfer P, Lissat A, Eggert A, Schulte JH, Zhang W, Henssen AG, Dual PLK1 and BRD4 inhibition has synergistic therapeutic effects against high-risk rhabdomyosarcoma. Proceedings: Abstract 2624, AACR Annual Meeting 2018; April 14-18, 2018; Chicago, IL, USA

Dorado García H, von Stebut J, MacArthur I, Imami K, Timme N, Schönbeck K, **Szymansky A**, Seifert G, Hundsdörfer P, Lissat A, Selbach M, Eggert A, Schulte JH, Henssen AG, Synthetic lethal targeting of ATR in alternative lengthening of telomeres-dependent rhabdomyosarcoma. Proceedings: Abstract 2628, *AACR Annual Meeting 2018*; April 14-18, 2018; Chicago, IL, USA

Szymansky A, Witthauer MJ, Firle KA, Overath MD, Schönbeck K, Toedling J, Hertwig F, Eggert A, Schulte JH, Antitumoral activity of the dual PLK1 and PI3K selective inhibitor rigosertib in preclinical neuroblastoma models. *CESAR Jahrestagung / CESAR Annual Meeting 2018*; Berlin, Germany.

Firle KA, **Szymansky A**, Witthauer MJ, Dorado Garcia H, Timme N, Baum C, Overath MD, Schönbeck K, Toedling J, Henssen AG, Hertwig F, Eggert A, Schulte JH, BET-Bromodomain inhibitor TEN-010 displays antitumoral activity in preclinical high-risk neuroblastoma models. *CESAR Jahrestagung / CESAR Annual Meeting 2018*; Berlin, Germany.

Firle KA, **Szymansky A**, Witthauer MJ, Dorado Garcia H, Toedling J, Schönbeck K, Henssen AG, Hertwig F, Eggert A, Schulte JH. Preclinical evaluation of BET-bromodomain inhibitor TEN-010 as monotherapy and combination therapy in MYC-driven neuroblastoma. *Targeted Anticancer Therapies / Annals of Oncology 2018*: Paris, France.

Szymansky A, Toedling J, Hertwig F, Witthauer MJ, Winkler A, Overath MD, Schoenbeck K, Heukamp L, Menon R, Heukmann J, Eggert A, Fischer M, Eckert C, Schulte JH, Development and validation of targeted sequencing and minimal residual disease assays for risk stratification of neuroblastoma patients. *3rd AEK Autumn School: Minimal Residual Disease, Circulating Tumor Cells and Metastasis 2017*: Berlin, Germany.
Flash Talk

Szymansky A, Witthauer MJ, Dorado Garcia H, Schönbeck K, Henssen AG, Hertwig F, Toedling J, Eggert A, Schulte JH. Antitumoral activity of the dual PLK1 and PI3K selective inhibitor rigosertib in preclinical neuroblastoma models. *1st SIOPEN/GPOH Neuroblastoma Research Symposium 2017*: Berlin, Germany.

Szymansky A, Witthauer MJ, Dorado Garcia H, Timme N, Schönbeck K, Henssen AG, Hertwig F, Toedling J, Eggert A, Schulte JH. BET-Bromodomain inhibitor TEN-010 displays antitumoral activity in preclinical high-risk neuroblastoma models. *1st SIOPEN/GPOH Neuroblastoma Research Symposium 2017*: Berlin, Germany.

Szymansky A, Overath MD, Hertwig F, Witthauer MJ, Schönbeck K, Toedling J, Eggert A, Klose J, Kaindl AM, Schulte JH. ASPM is a novel risk factor of aggressive neuroblastoma. *1st SIOPEN/GPOH Neuroblastoma Research Symposium 2017*: Berlin, Germany.

Szymansky A, Winkler A, Witthauer MJ, Schoenbeck K, Eickhoff J, Hertwig F, Eggert A, Schulte JH. Interfering with the LIN28B-let-7-MYCN pathway in neuroblastoma. *Klinische Pädiatrie* 2017; 229(03): 182-195. Wilsede, Germany.

Overath MD, **Szymansky A,** Witthauer MJ, Toedling J, Schönbeck K, Klose J, Kaindl AM, Hertwig F, Eggert A, Schulte JH. ASPM is a novel risk factor of aggressive neuroblastoma. *Klinische Pädiatrie* 2017; 229(03): 182-195. Wilsede, Germany.

Schoenbeck K, Witthauer MJ, Winkler A, **Szymansky A**, Schramm A, Toedling J, Hertwig F, Schulte JH, The Hippo-YAP1-pathway is activated in relapsed and *MYCN*-non-amplified neuroblastoma. *Klinische Pädiatrie* 2017; 229(03): 182-195. Wilsede, Germany.

Szymansky A, Heukamp L, Menon R, Heukmann J, Winkler A, Witthauer M, Schönbeck K, Astrahantseff K, Fischer M, Eckert C, Schulte JH. Development and validation of targeted re-sequencing and minimal residual disease assays for risk stratification of neuroblastoma patients. *E:Med Systems Medicine Meeting* 2016: Kiel, Germany.

Schönbeck, K, Witthauer MJ, Winkler A, **Szymansky A,** Deubzer H, Kuenkele A, Schramm A, Eggert A, Schulte JH. The Hippo-YAP1-pathway is activated in relapsed neuroblastoma. *E:Med Systems Medicine Meeting* 2016: Kiel, Germany.

Szymansky A, Heukamp L, Menon R, Heukmann J, Winkler A, Witthauer M, Schönbeck K, Astrahantseff K, Fischer M, Eckert C, Schulte JH. Development and validation of targeted re-sequencing and minimal residual disease assays for risk stratification of neuroblastoma patients. *3rd Berlin Cancer Retreat - German Consortium for Translational Cancer Research (DKTK).* 2016: Berlin, Germany.

Schönbeck K, Winkler A, Witthauer MJ, **Szymansky A,** Deubzer H, Kuenkele A, Schramm A, Eggert A, Schulte JH. The Hippo-YAP1-pathway is activated in relapsed neuroblastoma. *3rd Berlin Cancer Retreat - German Consortium for Translational Cancer Research (DKTK).* 2016: Berlin, Germany.

Hof J, **Szymansky A**, von Stackelberg A, Eckert C, Kirschner-Schwabe R. Clinical Significance of NT5C2 Mutations in Children with First Relapse of B-Cell Precursor Acute Lymphoblastic Leukemia. *Blood/American Society of Hematology (ASH) 56th Annual Meeting*, 2014. 124(21): p. 3789-3789.

Szymansky A, Groeneveld-Krentz S, Hof J, Krischner-Schwabe R, Eckert C. Improving Diagnostic Methods for Minimal Residual Disease Detection (MRD) in Childhood Acute Lymphoblastic Leukemia (ALL). *Klinische Pädiatrie*, 2014. 226(03): p. A16. Wilsede, Germany.

8.3 **Awards and scholarships**

My curriculum vitae will not be published in the electronic version of my thesis for data protection reasons.

9 Curriculum vitae

My curriculum vitae will not be published in the electronic version of my thesis for data protection reasons.

10 Appendix

10.1 Additional material

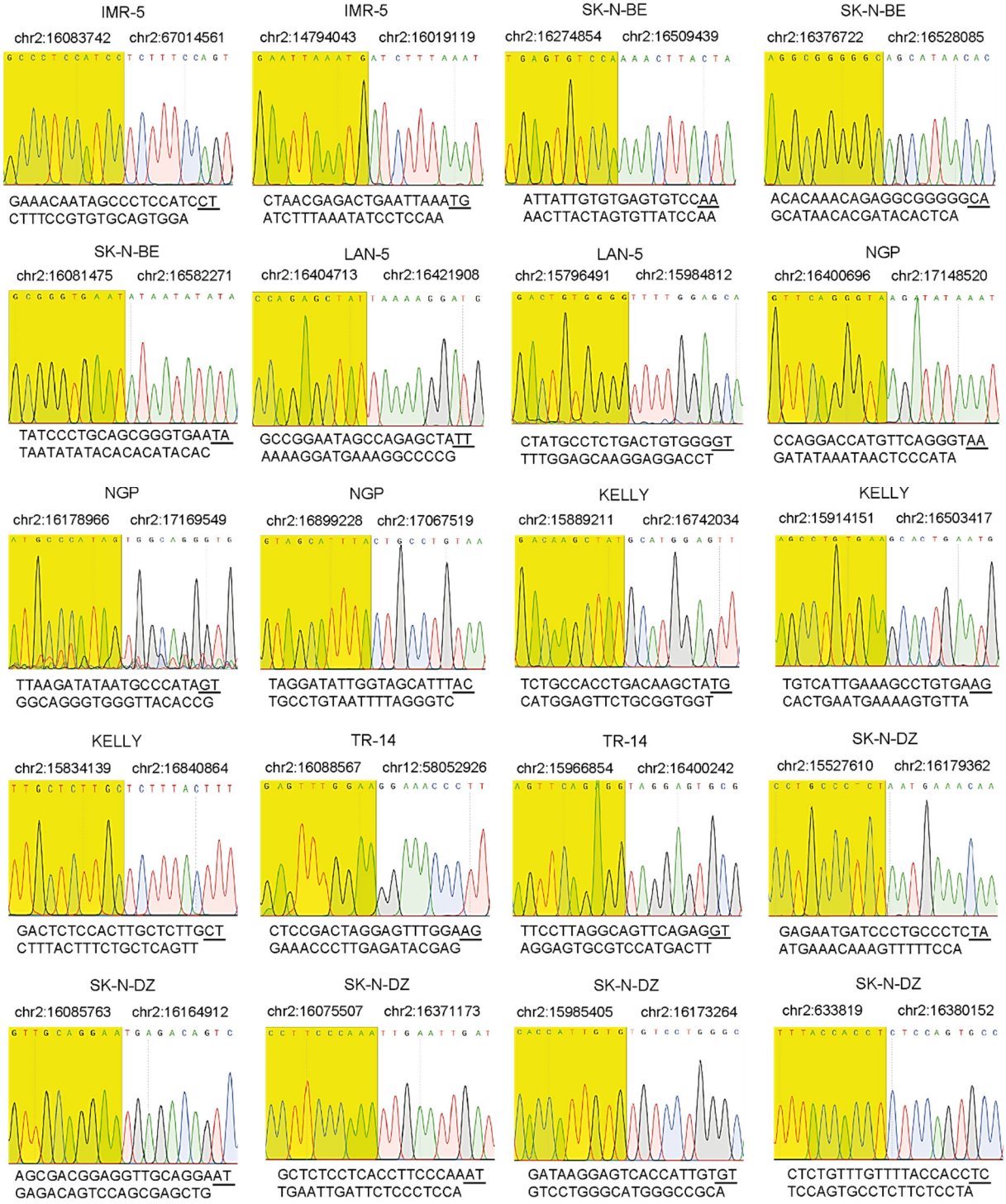

Figure 128: Validation of rearrangements of the *MYCN* locus in neuroblastoma cell lines by Sanger sequencing. Sequencing chromatograms of the breakpoint regions of *MYCN* chr.2p24.3 rearrangements along with their genomic coordinates (GRCh37(hg19)), and the breakpoint-spanning nucleotide sequences. The sequence rearrangement partners are indicated in yellow and white. The breakpoint sequence was determined applying Sanger sequencing from the PCR product with cell line DNA inserted previously. Corresponding PCR assays are listed in Table 15[634]

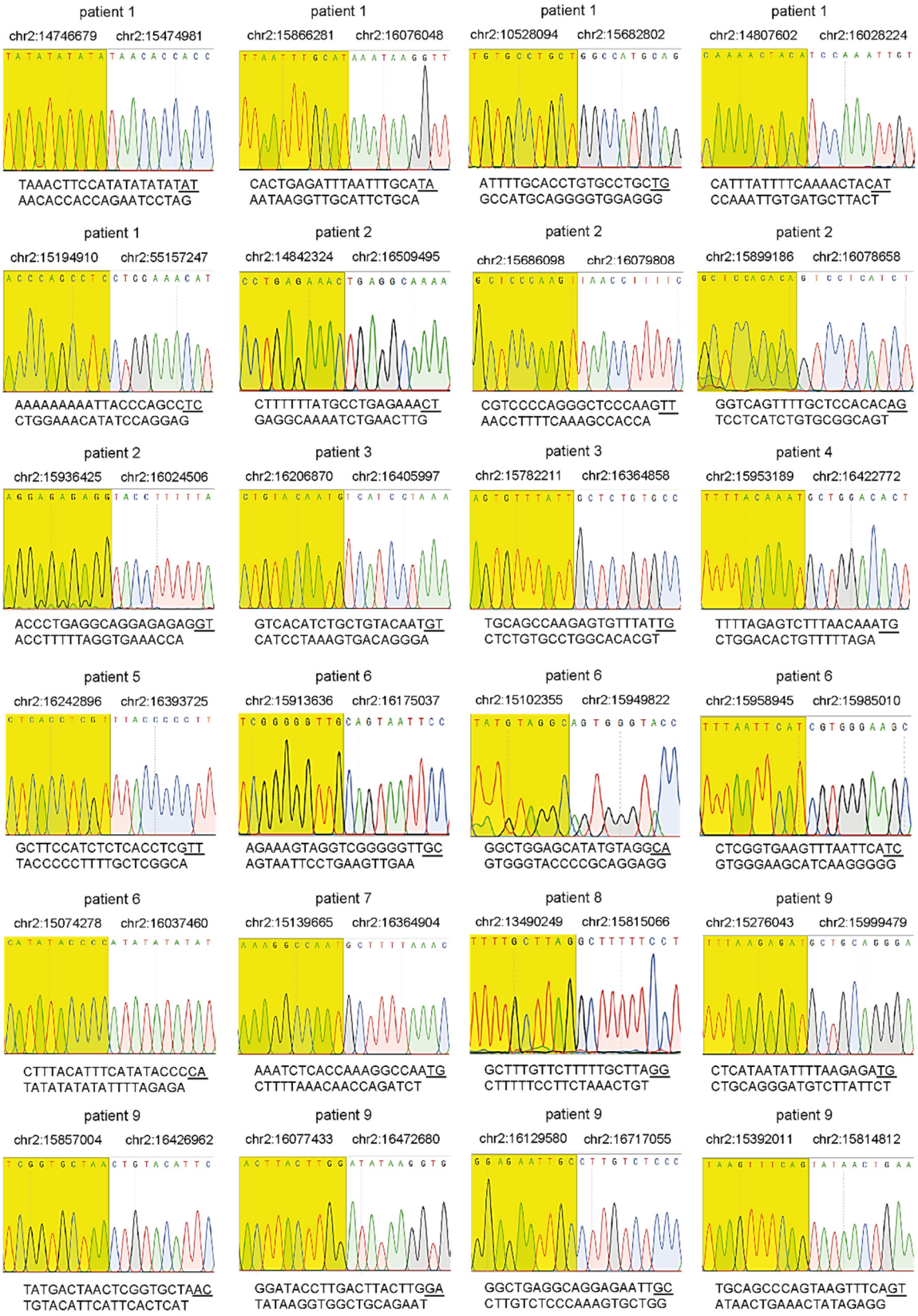

Figure 129: Validation of rearrangements of the *MYCN* locus in neuroblastoma tumors by Sanger sequencing (Part I). Sequencing chromatograms of the breakpoint regions of *MYCN* chr.2p24.3 rearrangements along with their genomic coordinates (GRCh37(hg19)), and the breakpoint-spanning nucleotide sequences. The sequence rearrangement partners are indicated in yellow and white. The breakpoint sequence was determined applying Sanger sequencing from the PCR product with neuroblastoma tumor DNA inserted previously. Corresponding PCR assays are listed in Table 17. The figures run continuously on Figure 130[634]

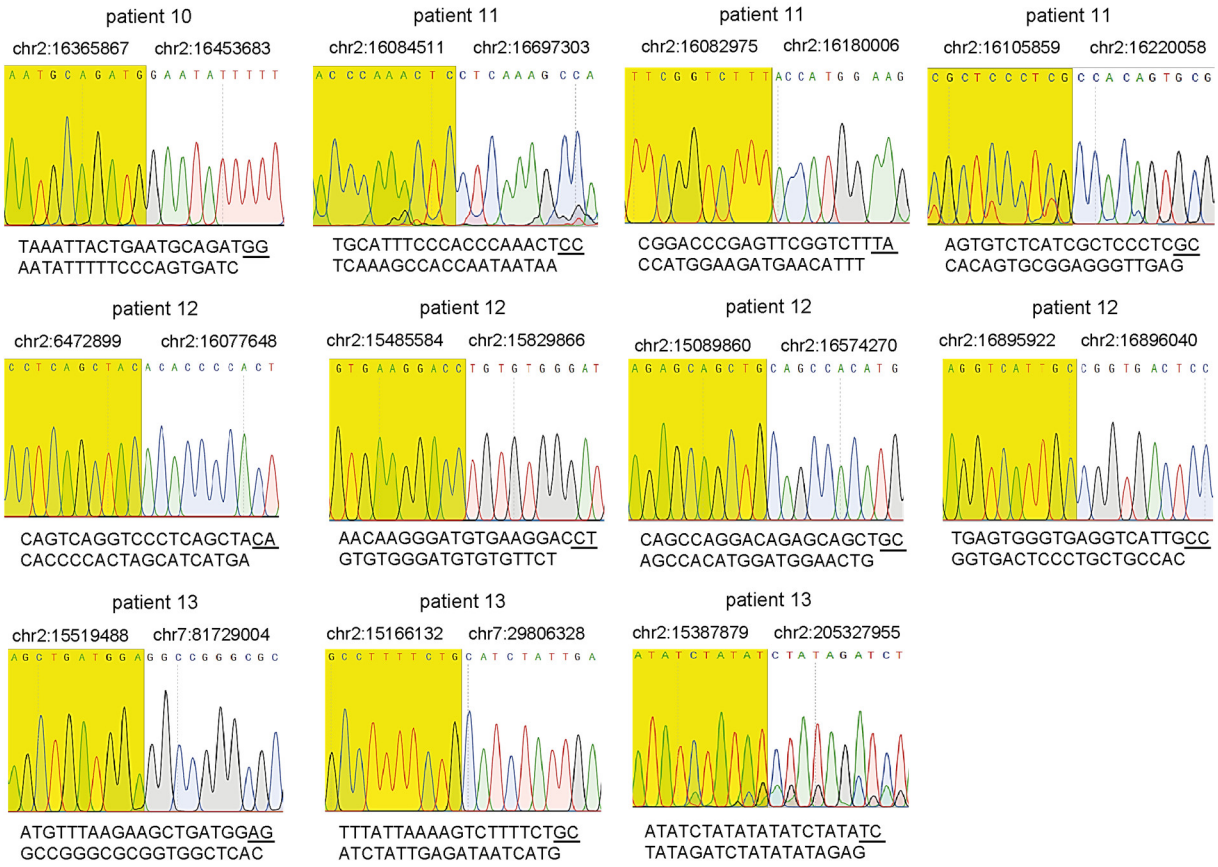

Figure 130: Validation of rearrangements of the *MYCN* locus in neuroblastoma tumors by Sanger sequencing (Part II). Sequencing chromatograms of the breakpoint regions of *MYCN* chr.2p24.3 rearrangements along with their genomic coordinates (GRCh37 (hg19)), and the breakpoint-spanning nucleotide sequences. The sequence rearrangement partners are indicated in yellow and white. The breakpoint sequence was determined applying Sanger sequencing from the PCR product with neuroblastoma tumor DNA inserted previously. Corresponding PCR assays are listed in Table 17. The previous Sanger sequencing results of PCR assays of tumor DNA can be found in Figure 129.[634]

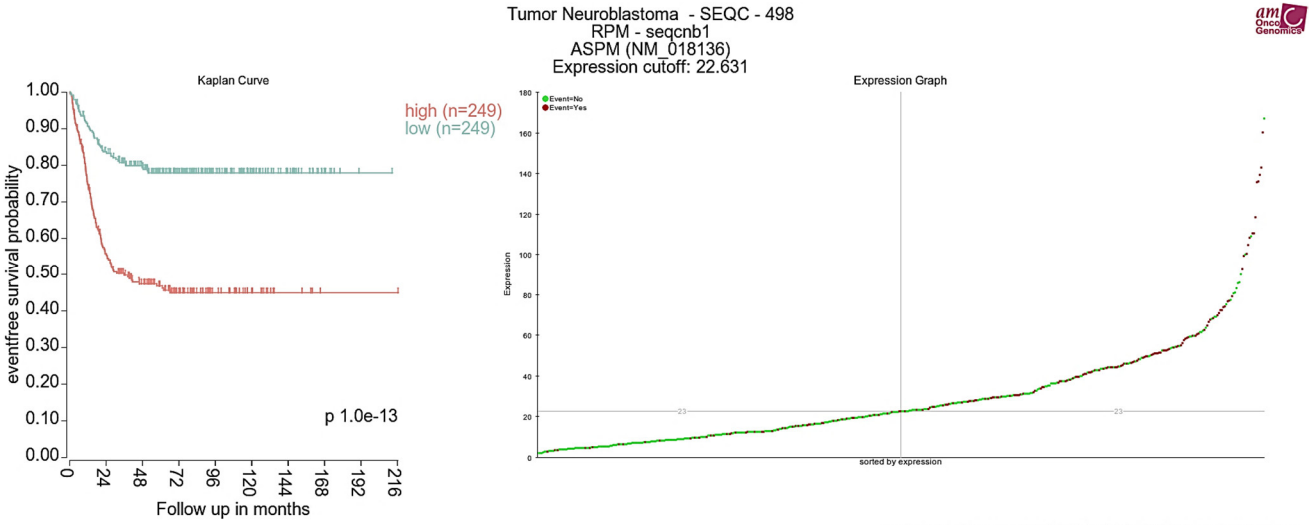

Figure 131: High expression of *ASPM* correlates with a diminished event-free survival probability. Survival analysis of RNA-Sequencing data of neuroblastoma patients (SEQC study[42]) display a correlation between event-free survival probability and *ASPM* expression. A low *ASPM* expression follows a high event-free survival probability, whereas a high expression of *ASPM* lead to a lower event-free survival probability ($p<1.0x10^{-13}$). *Cutoff modus*: median, cutoff: 249 neuroblastoma tumors with high expression of ASPM from expression cutoff 22.631, chi = 55.31, df = 1, high is worse. (Microarray SEQC-498-RPM-seqcnb1 data set; figure was created using the R2 Genomics platform[496,497]).

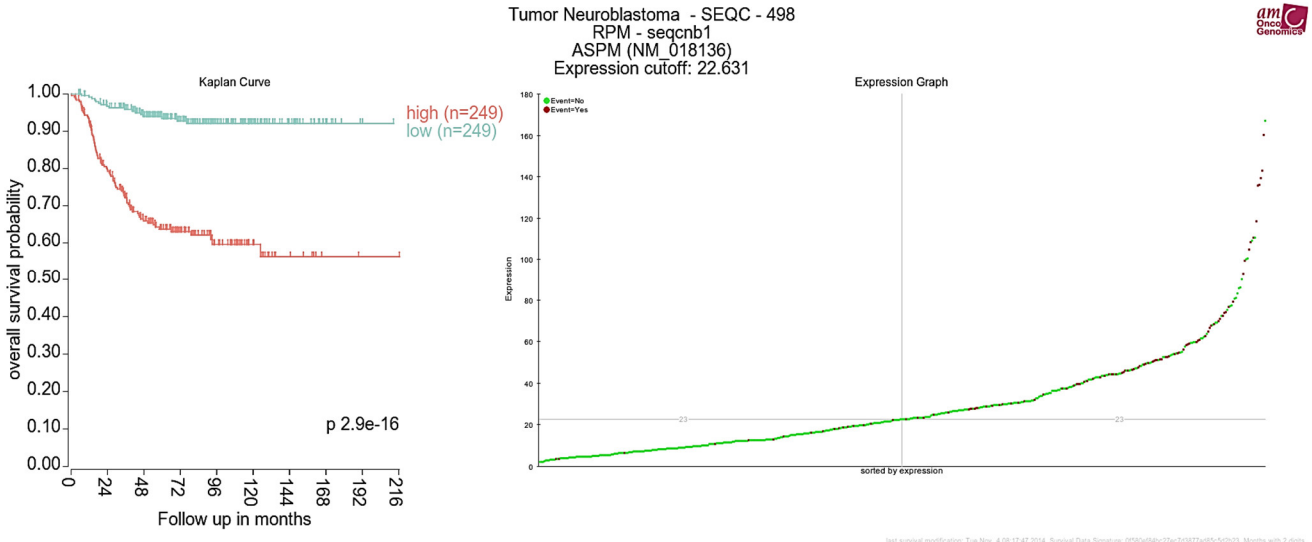

Figure 132: High expression of *ASPM* correlates with a diminished overall survival probability. Survival analysis of RNA-Sequencing data of neuroblastoma patients (SEQC study[42]) display a correlation between overall survival probability and *ASPM* expression. A low *ASPM* expression follows a high overall survival probability, whereas a high expression of *ASPM* lead to a lower overall survival probability ($p<2.9x10^{-16}$). *Cutoff modus*: median, cutoff: 249 neuroblastoma tumors with high expression of *ASPM* from expression cutoff 22.631, chi = 66.88, df = 1, high is worse. (Microarray SEQC-498-RPM-seqcnb1 data set; figure was created using the R2 Genomics platform[496,497]).

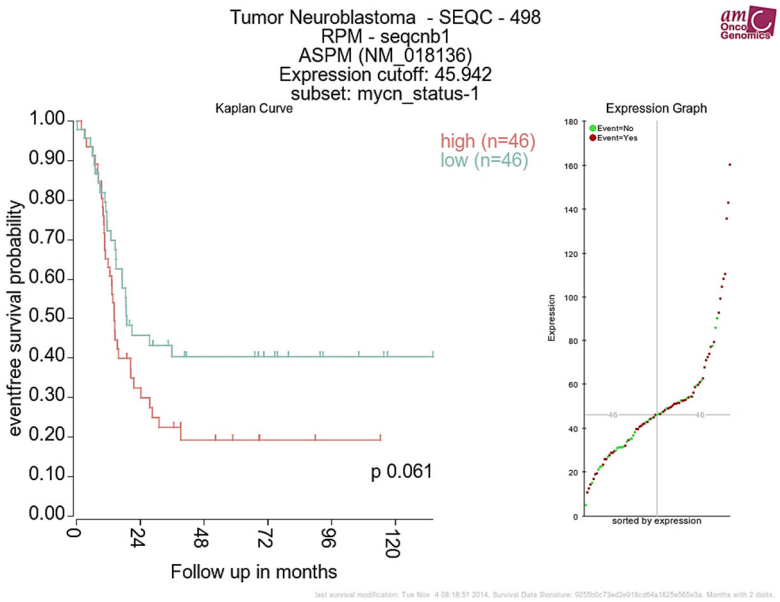

Figure 133: Neuroblastoma subgroup with *MYCN* amplification and high expression of *ASPM* show lower event-free survival probability.
Survival analysis of RNA-Sequencing data of neuroblastoma patients (SEQC study[42]) display a correlation between event-free survival probability, *MYCN* amplification and high *ASPM* expression. Low *ASPM* expression in combination with *MYCN* amplification follows a moderate event-free survival probability, whereas a high expression of *ASPM* in combination with *MYCN* amplification lead to a lower event-free survival probability (p<0.061). *Cutoff modus*: median, cutoff: 46 neuroblastoma tumors with high expression of *ASPM* from expression cutoff 45.942, chi = 3.50, df = 1, high is worse. (Microarray SEQC-498-RPM-seqcnb1 data set; figure was created using the R2 Genomics platform[496,497]).

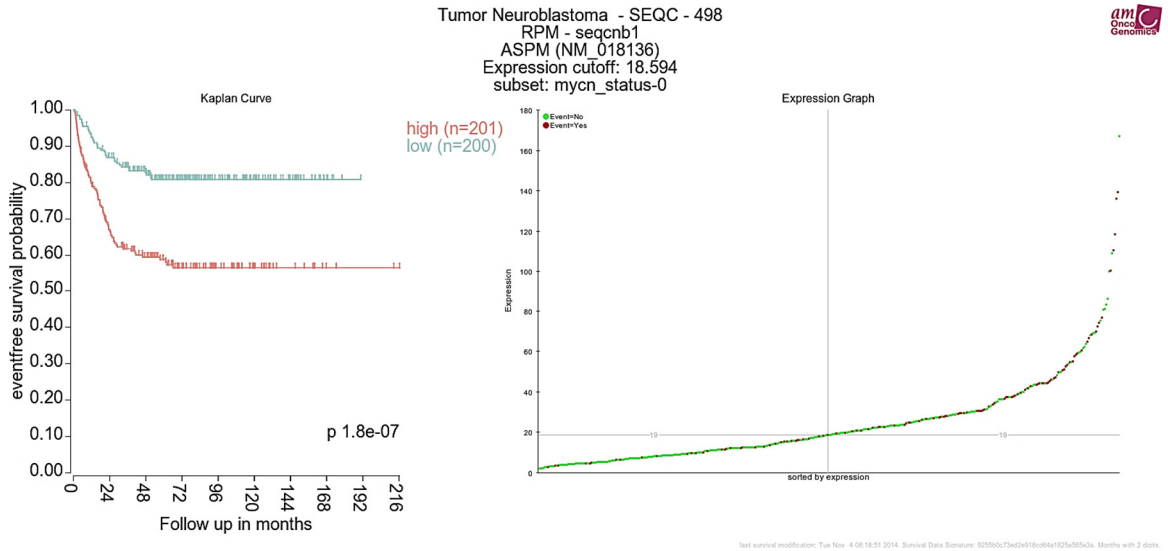

Figure 134: Neuroblastoma subgroup without *MYCN* amplification and high expression of *ASPM* show similar event-free survival probability compared to the total cohort.
Survival analysis of RNA-Sequencing data of neuroblastoma patients (SEQC study[42]) shows event-free survival probability in a subgroup of non-*MYCN* amplification and high *ASPM* expression. Low *ASPM* expression in combination without *MYCN* amplification follows a high event-free survival probability, whereas a high expression of *ASPM* in combination without *MYCN* amplification lead to a lower event-free survival probability (p<1.8x10^{-7}). *Cutoff modus*: median, cutoff: 201 neuroblastoma tumors with high expression of *ASPM* from expression cutoff 18.594, chi = 27.27, df = 1, high is worse. (Microarray SEQC-498-RPM-seqcnb1 data set; figure was created using the R2 Genomics platform[496,497]).

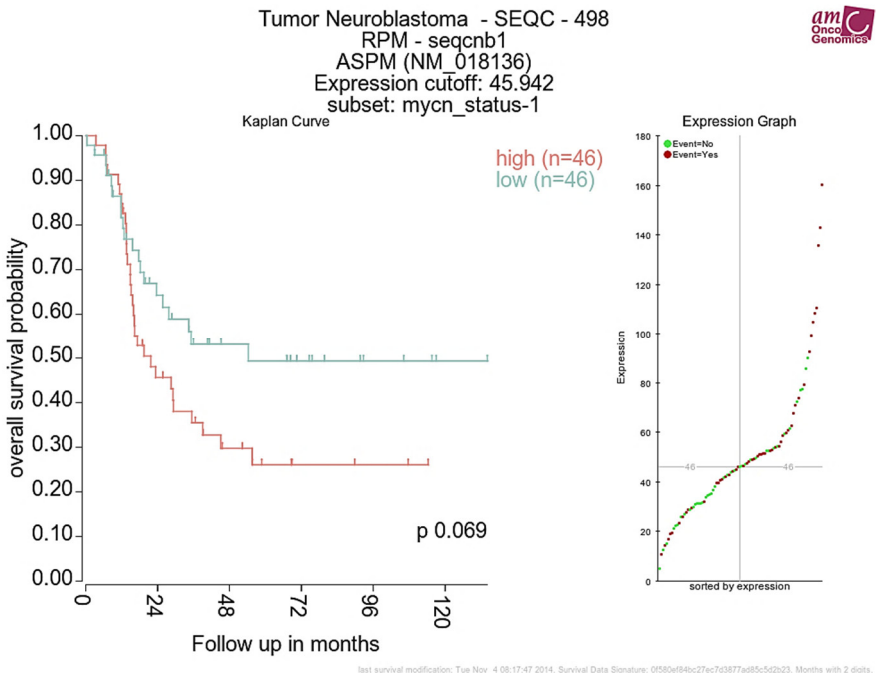

Figure 135: Neuroblastoma subgroup with *MYCN* amplification and high expression of *ASPM* show lower overall survival probability.

Survival analysis of RNA-Sequencing data of neuroblastoma patients (SEQC study[42]) display a correlation between overall survival probability, *MYCN* amplification and high *ASPM* expression. Low *ASPM* expression in combination with *MYCN* amplification follows a moderate overall survival probability, whereas a high expression of *ASPM* in combination with *MYCN* amplification lead to a lower overall survival probability (p<0.069). *Cutoff modus*: median, cutoff: 46 neuroblastoma tumors with high expression of *ASPM* from expression cutoff 45.942, chi = 3.50, df = 1, high is worse. (Microarray SEQC-498-RPM-seqcnb1 data set; figure was created using the R2 Genomics platform[496,497]).

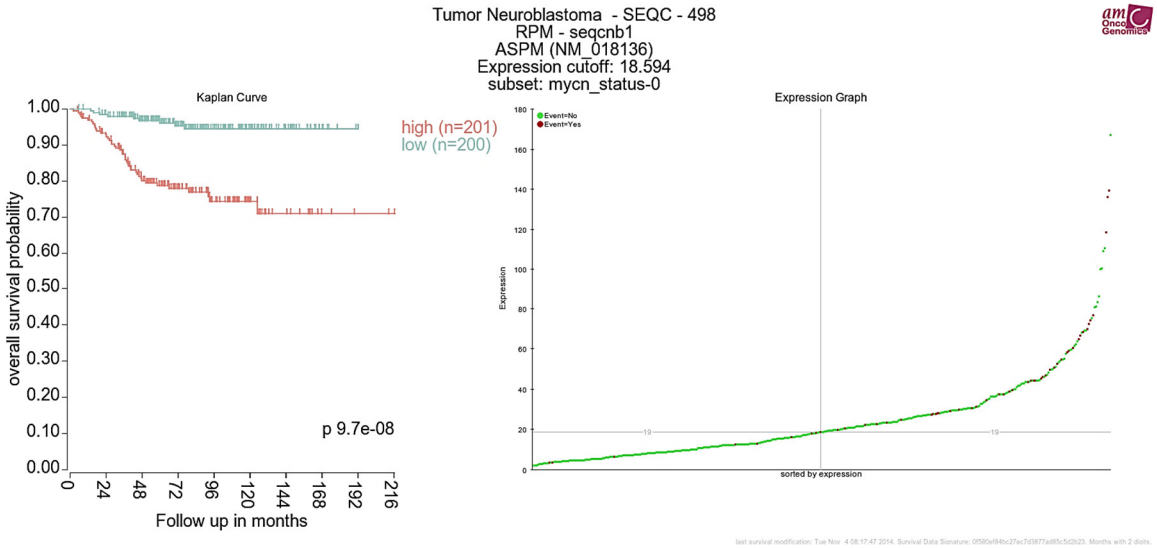

Figure 136: Neuroblastoma subgroup without *MYCN* amplification and high expression of *ASPM* show improved overall survival probability compared to the total cohort.

Survival analysis of RNA-Sequencing data of neuroblastoma patients (SEQC study[42]) shows overall survival probability in a subgroup of non-*MYCN* amplification and high *ASPM* expression. Low *ASPM* expression in combination without *MYCN* amplification follows a high overall survival probability, whereas a high expression of *ASPM* in combination without *MYCN* amplification lead to a lower overall survival probability (p<9.7x10^{-8}). *Cutoff modus*: median, cutoff: 201 neuroblastoma tumors with high expression of *ASPM* from expression cutoff 18.594, chi = 27.27, df = 1, high is worse. (Microarray SEQC-498-RPM-seqcnb1 data set; figure was created using the R2 Genomics platform[496,497]).

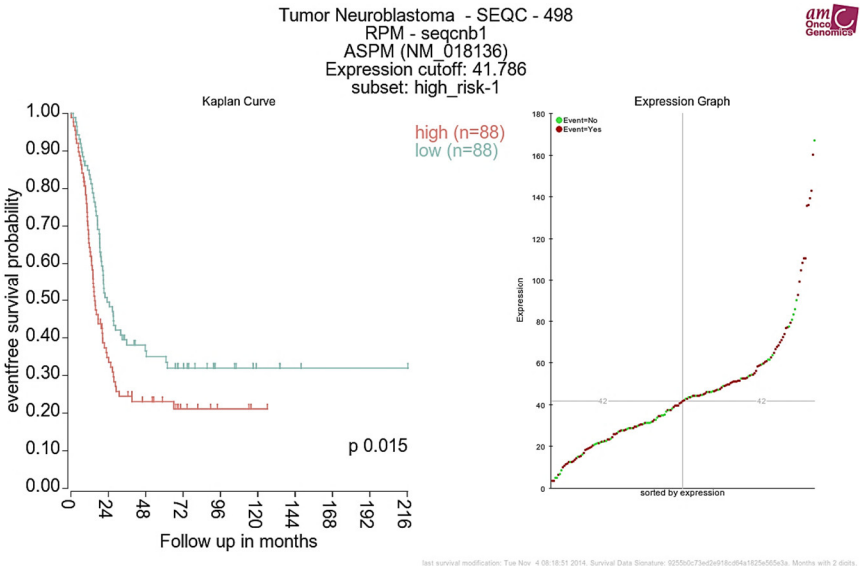

Figure 137: Neuroblastoma high-risk subgroup with high expression of *ASPM* show greatly reduced event-free survival probability.

Survival analysis of RNA-Sequencing data of neuroblastoma patients (SEQC study[42]) display a correlation between event-free survival probability, high-risk stage and high *ASPM* expression. Low *ASPM* expression in combination with high-risk neuroblastomas follows a low event-free survival probability, whereas a high expression of *ASPM* in combination with high-risk neuroblastomas lead to an even lower event-free survival probability (p<0.015). *Cutoff modus*: median, cutoff: 88 neuroblastoma tumors with high expression of *ASPM* from expression cutoff 41.786, chi = 9.56, df = 1, high is worse. (Microarray SEQC-498-RPM-seqcnb1 data set; figure was created using the R2 Genomics platform[496,497]).

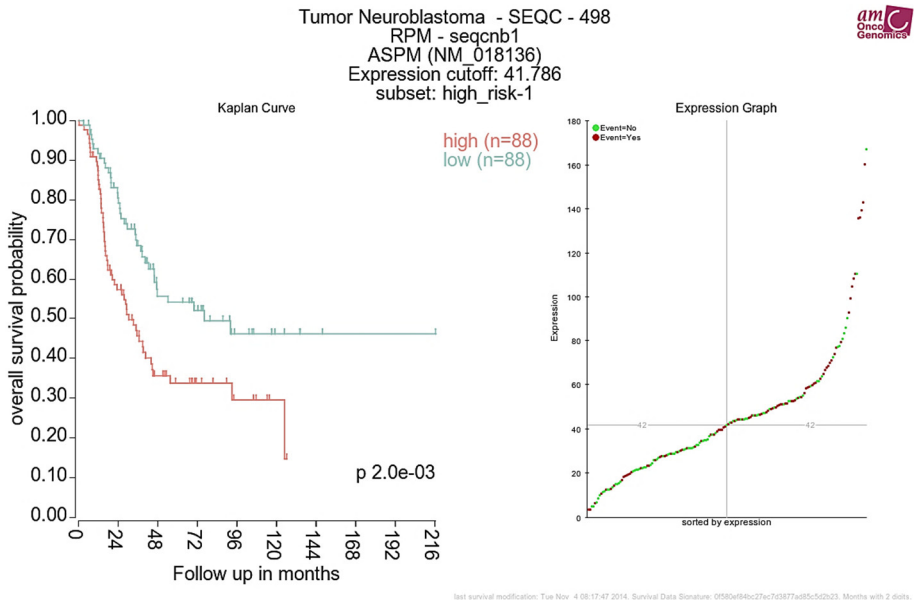

Figure 138: Neuroblastoma high-risk subgroup with high expression of *ASPM* show greatly reduced overall survival probability.

Survival analysis of RNA-Sequencing data of neuroblastoma patients (SEQC study[42]) display a correlation between overall survival probability, high-risk stage and high *ASPM* expression. Low *ASPM* expression in combination with high-risk neuroblastomas follows a moderate overall survival probability, whereas a high expression of *ASPM* in combination with high-risk neuroblastomas lead to a very low overall survival probability (p<2.0x10^{-3}). *Cutoff modus*: median, cutoff: 88 neuroblastoma tumors with high expression of *ASPM* from expression cutoff 41.786, chi = 9.56, df = 1, high is worse. (Microarray SEQC-498-RPM-seqcnb1 data set; figure was created using the R2 Genomics platform[496,497]).

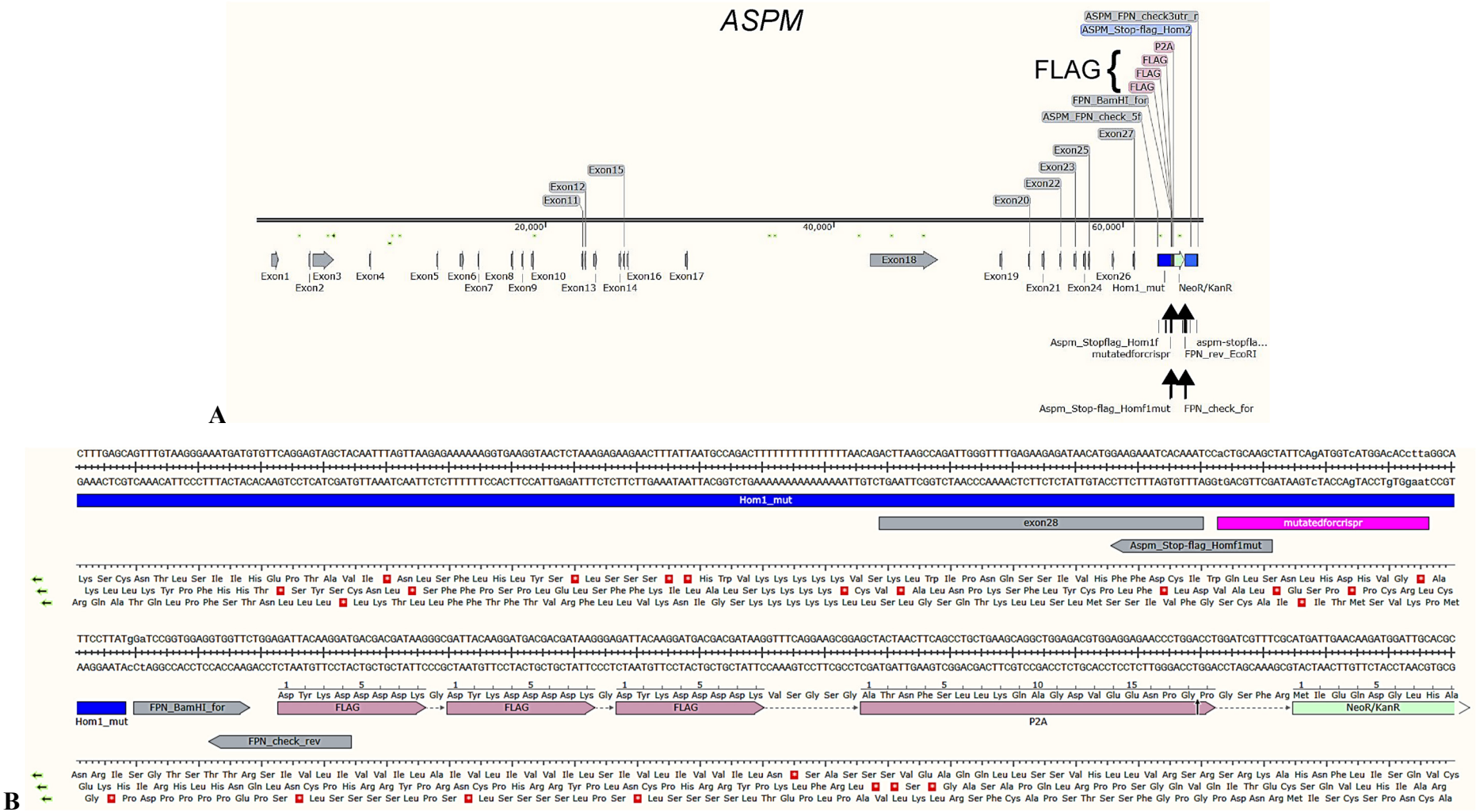

Figure 139: Sequence map of genomic *ASPM* after CRISPR/Cas9 3xFLAG knockin at stop codon site.
Human genomic *ASPM* was endogenously tagged with a 3xFLAG-tag, mediated by a CRISPR/Cas9 knockin. The attachment of a FLAG-tag peptide to ASPM would allow a detection with an anti-FLAG antibody. The knockin was conducted targeting the TAG stop codon in exon 28 of *ASPM*, thereby attaching the FLAG-tag C-terminal. The stop codon region is cleaved by CRISPR/Cas9 and the resulting double-strand break is repaired by HDR at homology arm HA/Hom1 sites. FLAG sequence and NeoR are fused through P2A, which separates the FLAG-tag and the NeoR after translation[544,598,603]. **(A)** Complete genomic *ASPM* with 3xFLAG insert. **(B)** 3xFLAG knockin region in detail.

Table 9: List of human cell lines used in this thesis

Cell line	Cell type	Patient	Site of origin	Therapy time point	*MYCN*	*TP53*	*ALK*	*TERT*	*ATRX*	PubMed ID Reference
BJ1-hTERT	skin fibroblast	♂ <1M	foreskin	not applicable	non-MNA					9454332
CHLA-90	neuroblastoma	♂ 8Y 6M	bone marrow metastasis	after post-chemotherapy (progressive disease), post-bone marrow transplant	non-MNA	wt			mut	9850071
CHP-134	neuroblastoma	♂ 1Y 1M	tumor of the left adrenal area	after polychemotherapy, radiation therapy	MNA					10079
CHP-212	neuroblastoma	♂ 1Y 8M	kidney mass	diagnosis	MNA		c.4164+ 137C>G			7139592
GI-ME-N	neuroblastoma	♀ 3Y 6M	bone marrow metastasis	after six months of chemotherapy	non-MNA	wt	wt	rea		3615018
HEK293	embryonic kidney tissue	♀ 0Y fetus	epithelial	transformed by adenovirus type 5 (Ad 5)	non-MNA	wt	wt	wt	wt	886304
HEK293T	embryonic kidney tissue	♀ 0Y Fetus	epithelial, derivative of HEK293	transformed by adenovirus type 5 (Ad 5); contains SV40 T-antigen	non-MNA	wt	wt	wt	wt	3031469
HeLa	papillomavirus-related endocervical adenocarcinoma	♀ 30Y 6M	cervix	diagnosis	non-MNA	wt p53-null	wt			13052828
hTERT RPE-1	pigment epithelial cells	♀ 1Y	eye retina	not applicable	non-MNA					9454332
IMR-32	neuroblastoma	♂ 1Y 1M	abdominal primary tumor		MNA	wt	wt			5459762
IMR-5	neuroblastoma	♂ 1Y 1M	abdominal primary tumor, sub-clone of IMR-32		MNA	wt	wt			6160155

IMR-5/75	neuroblastoma	♂ 1Y 1M	abdominal primary tumor, sub-clone of IMR-32		MNA	wt	wt			16216448
Kelly	neuroblastoma	♀ 1Y	primary tumor (CNS)		MNA	wt ? tp53: P117T ?	c.3522C>A			7139592
LAN-1	neuroblastoma	♂ 2Y	bone marrow metastasis	after polychemotherapy	MNA		c.3522C>A			856461
LAN-5	neuroblastoma	♂ 4M	bone marrow metastasis	unknown	MNA	wt	c.3824G>A			6172518
LAN-6	neuroblastoma	♂ 6Y	bone marrow metastasis	after treatment	non-MNA	c.455C>T	c.3271G>A			8242562
N206 (Kelly?)	neuroblastoma	♀ 1Y	primary tumor (CNS)		MNA	mut	c.3522C>A			7838528
NB-1643	neuroblastoma	♂ 3Y	primary tumor (retro-peritoneal mass)	diagnosis	MNA		c.3824G>A			9815701
NBL-S	neuroblastoma	♂ 3Y 6M	primary adrenal tumor	diagnosis	non-MNA		wt			11550280
NGP	neuroblastoma	♂ 2Y 6M	lung metastasis	after chemotherapy	MNA	c.423C>G	wt			922665
NGP_ASPM-FPN_87_#1	neuroblastoma	♂ 2Y 6M	lung metastasis; ASPM 3xFLAG 87 knockin clone #1	after chemotherapy	MNA	c.423C>G	wt			Szymansky et al.[543,544,598] (*Manuscript in prep.*)
NGP_ASPM-FPN_87_#7	neuroblastoma	♂ 2Y 6M	lung metastasis; ASPM 3xFLAG 87 knockin clone #7	after chemotherapy	MNA	c.423C>G	wt			Szymansky et al.[543,544,598] (*Manuscript in prep.*)
PLF (Fi301)	primary human embryonic lung fibroblasts		epithelial, embryonal	not applicable	non-MNA					20383190

Rh1	rhabdomyosarcoma (reclassified as Ewing family tumor)[500]	♂ age unk.	bone marrow metastasis	unknown	non-MNA	c.659A>G c.5882G>A	wt	wt	wt	8275086
SK-N-AS	neuroblastoma	♀ 6Y	bone marrow metastasis		non-MNA					2987426
SK-N-BE / SK-N-BE(1)	neuroblastoma	♂ 1Y 8M	bone marrow metastasis	no treatment	MNA			?		29704
SK-N-BE(2)	neuroblastoma	♂ 2Y 2M	bone marrow metastasis, same patient as SK-N-BE(1)	after repeated courses of chemotherapy and radiotherapy	MNA	c.404G>T				62055
SKNBE(2)-C/ BE(2)-C	neuroblastoma	♂ 2Y 2M	bone marrow metastasis, sub-clone of SK-N-BE(2)	after repeated courses of chemotherapy and radiotherapy	MNA	c.404G>T				6582512
SK-N-FI	neuroblastoma	♂ 11Y	bone marrow metastasis	post-chemotherapy (progressive disease)	non-MNA	c.737T>G				2987426
SK-N-DZ	neuroblastoma	♀ 2Y	bone marrow metastasis		MNA					2987426
SK-N-SH	neuroblastoma	♀ 4Y	bone marrow metastasis	after radiation therapy, polychemotherapy	non-MNA	wt	c.3522C>A	wt	wt	4748425
SH-EP	neuroblastoma	♀ 4Y	bone marrow metastasis, sub-clone of SK-N-SH	after radiation therapy, polychemotherapy	non-MNA	wt	c.3522C>A	wt	wt	6137586
SH-SY5Y	neuroblastoma	♀ 4Y	bone marrow metastasis, sub-clone of SK-N-SH	after radiation therapy, polychemotherapy	non-MNA	wt	c.3522C>A	wt	wt	4748425
TR-14	neuroblastoma	♂ 3Y	abdominal primary tumor	after polychemotherapy	MNA					6861117
VH7	skin fibroblast	♂	foreskin	not applicable	non-MNA					8847504

Information about human cell lines was obtained from different publications[1224,1225] and databases[1226–1228]. Abbreviations: ♀ = female, ♂ = male, MNA = MYCN-amplified, non-MNA= non-MYCN-amplified, wt = wildtype, mut = mutated, rea = Rearrangement

Table 10: Cell culture media and supplements used in this study

Cell line	Cell type	Media	Fetal calf serum content	Supplements	Prokaryote Antibiotics	Eukaryote Antibiotics
BJ1-hTERT	skin fibroblast	DMEM	10% FCS Superior		1% penicillin (100U/ml) / 1% streptomycin (100µg/ml)	
CHLA-90	neuroblastoma	DMEM	20% FCS Superior		1% penicillin (100U/ml) / 1% streptomycin (100µg/ml)	
CHP-134	neuroblastoma	RPMI 1640	10-15% FCS Superior		1% penicillin (100U/ml) / 1% streptomycin (100µg/ml)	
CHP-212	neuroblastoma	RPMI 1640	10-15% FCS Superior		1% penicillin (100U/ml) / 1% streptomycin (100µg/ml)	
GI-ME-N	neuroblastoma	RPMI 1640	10% FCS Superior	for shRNA transduction: polybrene (8µg/ml end concentration)	1% penicillin (100U/ml) / 1% streptomycin (100µg/ml)	
HEK293	embryonic kidney tissue	DMEM	10% FCS Superior		1% penicillin (100U/ml) / 1% streptomycin (100µg/ml)	
HEK293T	embryonic kidney tissue	DMEM	10% FCS Superior		1% penicillin (100U/ml) / 1% streptomycin (100µg/ml)	
HEK293T	embryonic kidney tissue during transfection	DMEM	10-20% FCS Superior	for shRNA transfection: + 2% L-Glutamine (200mM) + 2% HEPES 0.5M (10mM) + 1/1000 Chloroquine (25mM) For shRNA transduction: polybrene (10µg/ml end concentration)		for selection: 10mg/ml Puromycin (End concentration 1,000ng/ml)
HeLa	adenocarcinoma	RPMI 1640	10% FCS Superior		1% penicillin (100U/ml) / 1% streptomycin (100µg/ml)	
hTERT RPE-1	pigment epithelial cells	DMEM	10% FCS Superior		1% penicillin (100U/ml) / 1% streptomycin (100µg/ml)	
IMR-32	neuroblastoma	RPMI 1640	10% FCS Superior		1% penicillin (100U/ml) / 1% streptomycin (100µg/ml)	

IMR-5	neuroblastoma	RPMI 1640	10% FCS Superior		1% penicillin (100U/ml) / 1% streptomycin (100µg/ml)	
IMR-5/75	neuroblastoma	RPMI 1640	10% FCS Superior	for shRNA transduction: polybrene (3µg/ml end concentration)	1% penicillin (100U/ml) / 1% streptomycin (100µg/ml)	for selection: 10mg/ml Puromycin (End concentration 300ng/ml)
Kelly	neuroblastoma	RPMI 1640	10% FCS Superior		1% penicillin (100U/ml) / 1% streptomycin (100µg/ml)	for selection: 10mg/ml Puromycin (End concentration 250ng/ml)
LAN-1	neuroblastoma	RPMI 1640	20% FCS Superior	optional: + 1% L-Glutamine (200mM) +1% MEM NEAA (10mM)	1% penicillin (100U/ml) / 1% streptomycin (100µg/ml)	
LAN-5	neuroblastoma	RPMI 1640	10% FCS Superior		1% penicillin (100U/ml) / 1% streptomycin (100µg/ml)	
LAN-6	neuroblastoma	DMEM	20% FCS Superior	Optional: +1% MEM NEAA (10mM)	1% penicillin (100U/ml) / 1% streptomycin (100µg/ml)	
N206	neuroblastoma	DMEM	10% FCS Superior		1% penicillin (100U/ml) / 1% streptomycin (100µg/ml)	
NB-1634	neuroblastoma	RPMI 1640	10% FCS Superior		1% penicillin (100U/ml) / 1% streptomycin (100µg/ml)	
NBL-S	neuroblastoma	RPMI 1640	10% FCS Superior		1% penicillin (100U/ml) / 1% streptomycin (100µg/ml)	
NGP	neuroblastoma	RPMI 1640	10% FCS Superior	for shRNA transduction: Polybrene (6µg/ml end concentration)	1% penicillin (100U/ml) / 1% streptomycin (100µg/ml)	for selection: 10mg/ml Puromycin (End concentration 450ng/ml)
NGP_ASPM-FPN_#1	neuroblastoma, ASPM 3xFLAG knockin clone #1	RPMI 1640	10% FCS Superior		1% penicillin (100U/ml) / 1% streptomycin (100µg/ml)	for selection: Geneticin (G-418; end concentration 800µg/ml)
NGP_ASPM-FPN_#7	neuroblastoma, ASPM 3xFLAG knockin clone #7	RPMI 1640	10% FCS Superior		1% penicillin (100U/ml) / 1% streptomycin (100µg/ml)	for selection: Geneticin (G-418; end concentration 800µg/ml)
PLF (Fi301)	primary human embryonic lung fibroblasts	EMEM	10% FCS Superior	+ 7.5% Sodium Bicarbonat (w/v) + 1mM Sodium Pyruvate (100mM)	1% penicillin (100U/ml) / 1% streptomycin (100µg/ml)	

				+ 2mM L-Glutamine (200mM) +1% MEM NEAA (10mM)		
Rh1	rhabdomyosarcoma (reclassified as Ewing family tumor)[500]	RPMI 1640	10% FCS Superior		1% penicillin (100U/ml) / 1% streptomycin (100µg/ml)	
SK-N-AS	neuroblastoma	RPMI 1640	10% FCS Superior		1% penicillin (100U/ml) / 1% streptomycin (100µg/ml)	
SK-N-BE / SK-N-BE(1)	neuroblastoma	RPMI 1640	10% FCS Superior	for shRNA transduction: Polybrene (8µg/ml end concentration)	1% penicillin (100U/ml) / 1% streptomycin (100µg/ml)	for selection: 10mg/ml Puromycin (End concentration 200ng/ml)
SK-N-BE(2)	neuroblastoma	RPMI 1640	10% FCS Superior		1% penicillin (100U/ml) / 1% streptomycin (100µg/ml)	
SKNBE(2)-C/ BE(2)-C	neuroblastoma	RPMI 1640	10% FCS Superior	for shRNA transduction: Polybrene (8µg/ml end concentration)	1% penicillin (100U/ml) / 1% streptomycin (100µg/ml)	
SK-N-FI	neuroblastoma	RPMI 1640	10-15% FCS Superior		1% penicillin (100U/ml) / 1% streptomycin (100µg/ml)	
SK-N-DZ	neuroblastoma	DMEM	10% FCS Superior	optional: + 1% L-Glutamine (200mM)	1% penicillin (100U/ml) / 1% streptomycin (100µg/ml)	
SK-N-SH	neuroblastoma	RPMI 1640	10% FCS Superior		1% penicillin (100U/ml) / 1% streptomycin (100µg/ml)	
SH-SY5Y	neuroblastoma	RPMI 1640	10% FCS Superior	for shRNA transduction: Polybrene (6µg/ml end concentration)	1% penicillin (100U/ml) / 1% streptomycin (100µg/ml)	for selection: 10mg/ml Puromycin (End concentration 500ng/ml)
SH-EP	neuroblastoma	RPMI 1640	10% FCS Superior		1% penicillin (100U/ml) / 1% streptomycin (100µg/ml)	
TR-14	neuroblastoma	DMEM	10% FCS Superior		1% penicillin (100U/ml) / 1% streptomycin (100µg/ml)	
VH7	skin fibroblast	DMEM	10% FCS Superior		1% penicillin (100U/ml) / 1% streptomycin (100µg/ml)	

Table 11: Clinical data of neuroblastoma patient cohort analyzed with *NB targeted NGS assay* and *NB breakpoint MRD assay*

Patient number	Gender/ Sex	Age at primary diagnosis (days)	Stadium	*MYCN* status	*MYCN* CNV	1p36 status	*ALK* status	Site primary tumor	Metastasis	Primary treatment	EFS (days)	OS (days)	Outcome
8	♂	511	4	MNA	48.25	del	c.3824G>A	right adrenal gland	BM, local LN, pancreas	NB2004-HR (2xN8, 3xN5, 3xN6, autoSCT, 5 cycles dinutuximab beta)	1134	1134	CR1
9	♂	1130	4	MNA	112.53	del	wt	right adrenal gland	BM, pancreas, local + distant LN, orbit, bone,	NB2016	261	261	death of Therapy Tox (VOD/ pulmonary bleeding)
10	♂	103	4	MNA	28.21	del	wt	left adrenal gland	BM, adrenal, liver, skin, bone, left kidney, LN	2xN4 acc. NB2016	N/A	43	death of Therapy Tox (VOD)
11	♂	2909	4	MNA	153.57	del	c.3824G>A	left adrenal gland	BM (sparse), left kidney, local + distant LN,	NB2016	241	327	DOD
12	♀	1395	4	MNA	28.75	del	c.3522C>A	left adrenal gland	BM, bone, local + distant LN	3xN5 and 3xN6 acc. NB2016, haploSCT, dinutuximab beta, ALKi	424	424	CR1
13	♀	443	4	MNA	31.15	del	c.3824G>A	left adrenal gland	BM, bone, local + distant LN, liver, abdomen	NB2016, salvage CTX, ALKi	150	314	DOD

Tumor tissue and bone marrow aspirates were obtained from 6 patients treated at the Charité Department for Pediatric Oncology and Hematology, Berlin, Germany.
Abbreviations: MNA = MYCN-amplified

Table 12: Genes examined in *NB targeted NGS assay*

Gene name (HUGO) or chromosome section	Mutation	Copy Number Change	Fusion Gene
1p36		deletion	
11q		deletion	
17q		gain	
ALK	x	amplification, rearrangement	
ARAF	x		
ATM	x		
ATR	x		
ATRX	x	deletion, rearrangement	
BRAF	x		
BRCA1	x		
BRCA2	x		
CCDN1	x	amplification	
CDK4		amplification	
CDK6		amplification	
CDKN2A	x	deletion	
CDKN2B	x	deletion	
CTNNB1	x		
DDR2	x		
EGFR	x	deletion	
ERBB2	x		
FGFR1	x	including UTR	
FGFR2	x	including UTR	
FGFR3	x	including UTR	
FGFR4	x	including UTR	
HRAS	x		
IDH1	x		

IDH2	x		
JAK2	x		
KIT	x		
KRAS	x		
MAP2K1	x		
MAP2K2	x		
MDM2		amplification	
MDM4		amplification	
MET	x		
mTOR	x		
cMYC	x	amplification	x
MYCL1	x	amplification	
MYCN	x	amplification	x
NF1	x	deletion	
NRAS	x		
NTRK2	x		
PDGFRa	x		
PDGFRb	x		
PIK3CA	x		
PIK3CB	x		
PTCH1	x		
PTEN	x		
PTPN11	x		
RET	x		
RICTOR	x		
ROS1	x		
RPTOR	x		
SMO	x		
TERT		deletion, amplification	x
TP53	x		

TSC1	x		
TSC2	x		

Genes of interest were defined by M. Fischer and J.H. Schulte (includes international consensus from London Conferences[667]).

Table 13: Housekeeping PCR assay for normalization of MRD detection

Gene name	Chromosomal location (GRCh37; hg19)	Sequence	Forward primer (5'-3')	Reverse primer (5'-3')	FAM-BHQ1 probe (5'-3')	annealing temperature (T_a)
ß-globin (hemoglobin subunit beta)	Chr11: 5,246,694-5,250,625 reverse strand	TATTGGTCTCCTTAAACCTGTCTTGTA ACCTTGATACCAACCTGCCCAGGGCC TCACCACCAACTTCATCCACGTTCACC TTGCCCCACAGGGCAGTAACGGCAGA CTTCTCCTCAGGAGTCAGATGCACCAT GGTGTCTGTTTGAGGTTGCTAGTGAAC ACAGTTGTGTCAG	TATTGGTCTCCTTAAA CCTGTCTTG	CTGACACAACTGTGT TCACTAGC	FAM-CCCACAGGGCAGTA ACGGCAGACT-BHQ1	65°C

Table 14: Genomic locations of *MYCN* associated breakpoints within neuroblastoma cell lines

Name of cell line	Breakpoint number	Chromosome Start	Gene Start	Breakpoint Start	Chromosome End	Gene End	Breakpoint End	*MYCN* CNV	Coverage *NB targeted NGS assay*
IMR-5	1	chr2	*MYCN*	16083742	chr2	intergenic	67014561	49.90	1739x
	2	chr2	Intergenic	14794043	chr2	intergenic	16019119		
SK-N-BE	3	chr2	intergenic	16274854	chr2	intergenic	16509439	68.06	1685x
	4	chr2	intergenic	16376722	chr2	intergenic	16528085		
	5	chr2	Intergenic	16081475	chr2	Intergenic	16582271		
LAN-5	6	chr2	intergenic	16404713	chr2	intergenic	16421908	59.50	1726x
	7	chr2	intergenic	15796491	chr2	intergenic	15984812		
NGP	8	chr2	intergenic	16400696	chr2	intergenic	17148520	56.93	1938x
	9	chr2	intergenic	16178966	chr2	intergenic	17169549		
	10	chr2	intergenic	16899228	chr2	intergenic	17067519		
KELLY	11	chr2	intergenic	15889211	chr2	*FAM49A*	16742034	88.00	1534x

	12	chr2	intergenic	15914151	chr2	intergenic	16503417		
	13	chr2	intergenic	15834139	chr2	intergenic	16840864		
TR-14	14	chr2	intergenic	16088567	chr12	intergenic	58052926	57.00	1567x
	15	chr2	intergenic	15966854	chr2	intergenic	16400242		
SK-N-DZ	16	chr2	*NBAS*	15527610	chr2	intergenic	16179362	43.20	2075x
	17	chr2	*MYCN*	16085763	chr2	intergenic	16164912		
	18	chr2	intergenic	16075507	chr2	intergenic	16371173		
	19	chr2	intergenic	15985405	chr2	intergenic	16173264		
	20	chr2	intergenic	633819	chr2	intergenic	16380152		

Table 15: PCR assays of *MYCN* associated breakpoints within neuroblastoma cell lines

Name of cell line	Break-point no.	Chromo-some Start	Gene Start	Break-point Start	Chromo-some End	Gene End	Break-point End	*MYCN* CNV	Coverage *NB targeted NGS assay*	Breakpoint sequence	Forward primer (5'-3')	Reverse primer (5'-3')	FAM-BHQ1 probe (5'-3')	MRD assay sensi-tivity range	MRD assay quanti-tative range
IMR-5	1	chr2	*MYCN*	16083742	chr2	intergenic	67014561	49.90	1739x	CTGGTGTGGATGGCATGGCAGAATGGTAGATACTGCATGGATTAAGACATGCTAGGCTGCAGAAACAATAGCCCTCCATCCTCTTTCAAGTGTGCAGTGGAAACTGGCTGTAGTTTTGTCTTCC	CTGGTGTGGATGGCATGGC	GGAAGACAAAACTACAGCCAG	Not performed	Not performed	Not performed
	2	chr2	Intergenic	14794043	chr2	intergenic	16019119			AGCTAAGGGTGTTCCAGCCAGCACTGTTTGTAATAGCAAAACTGGAAACAACCAAAAGTCCACTAACGAGACTGAATTAAATGATCTTTAAATATCCTCCAAGTTCTAAAAGTCTGTAAGGCCTGTTCC	AGCTAAGGGTGTTCCAGCCA	GGAACAGGCCTTACAGACTTTTA	FAM-GCAAAACTGGAAACAACCAAAAGTCCA-BHQ1	RQ-PCR: 10^{-4} ddPCR: 10^{-4}	RQ-PCR: 10^{-3} ddPCR: 10^{-4}
SK-N-BE	3	chr2	intergenic	16274854	chr2	intergenic	16509439	68.06	1685x	GGACACAAGTTCAGATTTTGCCTCAGAAATATGCAAGGGGTCAGGCAAATCATGAAAATTATTATTGTGTGAGTGTCCAAACTTACTAGTGTTATCCAATGAGGTCAATATTAGC	GGACACAAGTTCAGATTTGC	GCTAATATTGACCTCATTGG	FAM-GAAATATGCAAGGGGTCAGG-BHQ1	RQ-PCR: 10^{-5} ddPCR: 10^{-6}	RQ-PCR: 10^{-4} ddPCR: 10^{-5}
	4	chr2	intergenic	16376722	chr2	intergenic	16528085			CAAGCATTCCAAGTAGGAAGGTGGGGTTGACACAAACAGAGGCGGGGGCAGCATAACACGATACACTCAGGAAG	CAAGCATTCCAAGTAGGAAG	CTTCCTGAGTGTATCGTG	Not performed	Not performed	Not performed
	5	chr2	Intergenic	16081475	chr2	Intergenic	16582271			CTCCCTGGAAGAGGACGTTGTCGTGGGTTTGGAAGAGCAGGGGTGGGCTTAGAGAGCTTCCAATTAAGCTATTGGCAGGAGTATCCCTGCAGCGG	CTCCCTGGAAGAGGACGTTG	TGTACACACTCATATATG	Not performed	Not performed	Not performed

										GTGAATATAATATATA CACACATACACATACA TATATATGAGTGTGTA CA					
LAN-5	6	chr2	intergenic	16404713	chr2	intergenic	16421908	59.50	1726x	CTGAGAATGCCACATC CTTGAGATAGAGAGGA GCTGGCCGGAATAGCC AGAGCTATTAAAAGGA TGAAAGGCCCCGTAAT TATTACCATTCGAAAA CACAGAGACTGTC	CTGAGA ATGCCA CATCCT TG	CGAAAA CACAGA GACTGT C	Not performed	Not performed	Not performed
	7	chr2	intergenic	15796491	chr2	intergenic	15984812			CCATGACCGACTGTTT CCTCTTATAAACTGCG ACGAATATCAGCTATG CCTCTGACTGTGGGGT TTTGGAGCAAGGAGGA CCTGCCCATTCTGATC TGAGGGATG	CCATGA CCGACT GTTTCCT C	CATCCC TCAGAT CAGAAT G	FAM-GCGACG AATATC AGCTAT GC-BHQ-1	RQ-PCR: 10^{-6} ddPCR: 10^{-6}	RQ-PCR: 10^{-5} ddPCR: 10^{-5}
NGP	8	chr2	intergenic	16400696	chr2	intergenic	17148520	56.93	1938x	CATGCTAAGATGGGGT CCCCCAGGACCATGTT CAGGGTAAGATATAAA TAACTCCCATATGCAT AGCATTCC	CATGCT AAGATG GGGTCC	CCCATA TGCATA GCATTC C	Not performed	Not performed	Not performed
	9	chr2	intergenic	16178966	chr2	intergenic	17169549			ATGGTCCTGATGTACT GAGATTTATTGGCCAG TTGAAACACATACTTG CACAATGGACTGGTTT TAAGATATAATGCCCA TAGTGGCAGGGTGGGT TACACCGTGGAAAATG CCTTCCT	ATGGTC CTGATG TACTGA GA	CCGTGG AAAATG CCTTCCT	FAM-CTTGCA CAATGG ACTGGT TTT-BHQ1	RQ-PCR: 10^{-6} ddPCR: 10^{-6}	RQ-PCR: 10^{-5} ddPCR: 10^{-5}
	10	chr2	intergenic	16899228	chr2	intergenic	17067519			GGTATGTGAATCATGT CCCAACAAAGCTATTT AAAAAGATAAAGAAA GTTTTATTCCCTAGGA TATTGGTAGCATTTAC TGCCTGTAATTTTAGG GTCCCCTGGAGACGTA GCTGA	GGTATG TGAATC ATGTCC CAAC	CCCTGG AGACGT AGCTGA	Not performed	Not performed	Not performed
KELLY	11	chr2	intergenic	15889211	chr2	*FAM49A*	16742034	88.00	1534x	GCATCTGTGATCTGAG CCTTGGTTCTGCCACC TGACAAGCTATGCATG GAGTTCTGCGGTGGTT CTTTTCCACAAGACAC CTTGTTTATTATTATAT GCAACTTCATTTTCAT GTCTTTTAATACTTTTC ACAAAGAAAGCTTTTG CAAATTGGAGGAG	GCATCT GTGATC TGAGCC TTG	GCTTTT GCAAAT TGGAGG AG	FAM-TTCTGC CACCTG ACAAGC TA-BHQ1	RQ-PCR: 10^{-4} ddPCR: 10^{-5}	RQ-PCR: 10^{-4} ddPCR: 10^{-5}
	12	chr2	intergenic	15914151	chr2	intergenic	16503417			CAGAGATTTAGGCAGG TAAGGTGACTTGTCCA AGGTAACACCACCTGT AAGTGATGGAACTGGG ATTTGAGCTGAGGCAG TCTGACCGCCTTGCCC TGGGCTTATGCTTCCT	CAGAGA TTTAGG CAGGTA AGGTG	GAATAA AGGAAG CACGTG GC	FAM-GCTGAG GCAGTC TGACCG CC-BHQ1	RQ-PCR: 10^{-4}	RQ-PCR: 10^{-4}

										AACCACTATCCTCTGC TGCCCCTCACTGGATT GTCATTGAAAGCCTGT GAAGCACTGAATGAA AAGTGTTATTTCTGCC TCCATTTTACAGAAGG AGAAGCAAGGGGCTG GAATAAAGGAAGCAC GTGGC				ddPCR: 10^{-6}	ddPCR: 10^{-5}
	13	chr2	intergenic	15834139	chr2	intergenic	16840864			AAATGTTTATCATTGT CCTGCTGACAATACCC TACATGGCTCAGTAGG AACACAAGACTCAGG AGATCGACAGCTTGTC AAAGCCCAGGCTGCTT GTAAGTGGGCAGCGTG ACTACAAGACCCCGGG TCTTCTTGGACTCTCCA CTTGCTCTTGCTCTTTA CTTTCTGCTCAGTTTTG CTGTGAACCTAAAACT ACTGCAAAAAAATAA AAAATAGAAAAGACT CAGACTTTAATTACGG AAGAGAAGCTTTCCCT TACCCCAGCTTG	AAATGT TTATCA TTGTCCT GCTGA	CTTTCCC TTACCC CAGCTT G	Not performed	Not performed	Not performed
TR-14	14	chr2	intergenic	16088567	chr12	intergenic	58052926	57.00	1567x	GGCCACTCTTCTTATC ACCCAATATCAAACTG ATAAGCCTTAAATTTG CCCTCACATGGGCCCC TTCATCTTTAATCCAA CCTCCGACTAGGAGTT TGGAAGGAAACCCTTG AGATACGAGGTTGG	GGCCAC TCTTCTT ATCACC CAATA	ACCCTT GAGATA CGAGGT TGG	Not performed	Not performed	Not performed
	15	chr2	intergenic	15966854	chr2	intergenic	16400242			ACTAGTCTTCCCTGAT TTGCCCCCATCAAGTT TTCTCTCTAGAGTATA CTGGTGCATTTGGCCT TTTCCTTAGGCAGTTC AGAGGTAGGAGTGCGT CCATGACTTTTCAGGC TTTGAGAGTGAAACCA ACCAAACCAGGGATCT GGAGTA	ACTAGT CTTCCCT GATTTG CCC	ACCAAA CCAGGG ATCTGG AGTA	FAM-CTAGAG TATACT GGTGCA TTTGGC-BHQ1	RQ-PCR: 10^{-6} ddPCR: 10^{-6}	RQ-PCR: 10^{-5} ddPCR: 10^{-5}
SK-N-DZ	16	chr2	*NBAS*	15527610	chr2	intergenic	16179362	43.20	2075x	CAATGGTCAGTGTGGC AATGTCAACACCCTGA GCCACTGGCTGTGGCA GGCAGGTGGAAATCCC TTCCAGTCCCACCCTC CAGTCCTGTGAGAATG ATCCCTGCCCTCTAAT GAAACAAAGTTTTTCC AGATTTTTAAAATCTG TCATTATCTTTTCACTC ACTTATTCTCACTTATT CCTTTGAAATGAGT	CAATGG TCAGTG TGGCAA TGT	ACTCAT TTCAAA GGAATA AGTGAG	FAM-GCTGTG GCAGGC AGGTGG AA-BHQ1	RQ-PCR: 10^{-4} ddPCR: 10^{-6}	RQ-PCR: 10^{-4} ddPCR: 10^{-}
	17	chr2	*MYCN*	16085763	chr2	intergenic	16164912			CAGGAATGAGACAGTC CAGCGAGCTGATCCTC AAACGATGCCTTCCCA TCCACCAGCAGCACAA CTATGCCG	CAGGAA TGAGAC AGTCCA GC	CGGCAT AGTTGT GCTGCT	Not performed	Not performed	Not performed
	18	chr2	intergenic	16075507	chr2	intergenic	16371173			CAGTGGCTCTCCTCAC CTTCCCAAATTGAATT GATTCTCCCTCCACCT	CAGTGG CTCTCCT	ACTTTG AAGAAG	Not performed	Not performed	Not performed

										GACTGATTGTCTTCTTCAAAGT	CACCTTC	ACAATCAGTCAGG			
	19	chr2	intergenic	15985405	chr2	intergenic	16173264			GGGAGTGCTTACCTCACTGGATTGCCGGGAGGATTAAATGAGTTGATAGACATAAGTTACTTGGGATAAGGAGTCACCATTGTGTGTCCTGGGCATGGGCCGCAGTTTGACCATGACCTCCTGATAGACTGCAGCTCTGGACACCAGATTTGCCCATACCACTCTTTAGCAGGACCTACCTTTGTCCCTCATAAACTCCCTAGCAGC	GGGAGTGCTTACCTCACTGG	GCTGCTAGGGAGTTTATGAGGG	Not performed	Not performed	Not performed
	20	chr2	intergenic	633819	chr2	intergenic	16380152			GGCCCCGGCTTATTTCTTAGAGAGCTGTCACAATYCGCAGCTACSCTGCTTCATTGTGTTTGTGTGTCTTTATCRTTTAATTCCKTCTTAGAGAAGGTCTGCTCCCAAGGGAGGAAAACATTTTTATTTTTCTTACCTCTGTTTGTTTTACCACCTCTCCAGTGCCTCTTCTCCTAGGAAGAATTTTCCAAACCTTCTAATTAAAAATAATCAACCATCCATGCCTCCC	GGCCCCGGCTTATTTCTTAGA	ATCAACCATCCATGCCTCCC	Not performed	Not performed	Not performed

Table 16: Genomic locations of *MYCN*-associated breakpoints in primary neuroblastoma samples

Patient number	Breakpoint number	Chromosome Start	Gene Start	Breakpoint Start	Chromosome End	Gene End	Breakpoint End	*MYCN* CNV	Coverage *NB targeted NGS assay*
1	1	chr2	intergenic	14746679	chr2	*NBAS*	15474981	61.02	1485x
	2	chr2	intergenic	15866281	chr2	intergenic	16076048		
	3	chr2	intergenic	10528094	chr2	*NBAS*	15682802		
	4	chr2	intergenic	14807602	chr2	intergenic	16028224		
	5	chr2	intergenic	15194910	chr2	*EML6*	55157247		
2	6	chr2	intergenic	14842324	chr2	intergenic	16509495	73.27	1398x
	7	chr2	*NBAS*	15686098	chr2	intergenic	16079808		
	8	chr2	intergenic	15899186	chr2	intergenic	16078658		
	9	chr2	intergenic	15936425	chr2	intergenic	16024506		
3	10	chr2	intergenic	16206870	chr2	intergenic	16405997	47.90	1917x
	11	chr2	intergenic	15782211	chr2	intergenic	16364858		
4	12	chr2	intergenic	15953189	chr2	intergenic	16422772	54.63	1582x

5	13	chr2	intergenic	16242896	chr2	intergenic	16393725	66.11	1554x
6	14	chr2	intergenic	15913636	chr2	intergenic	16175037	44.50	1421x
	15	chr2	intergenic	15102355	chr2	intergenic	15949822		
	16	chr2	intergenic	15958945	chr2	intergenic	15985010		
	17	chr2	intergenic	15074278	chr2	intergenic	16037460		
7	18	chr2	intergenic	15139665	chr2	intergenic	16364904	14.53	2005x
8	19	chr2	intergenic	13490249	chr2	intergenic	15815066	48.25	1190x
9	20	chr2	intergenic	15276043	chr2	intergenic	15999479	31.15	2017x
	21	chr2	intergenic	15857004	chr2	intergenic	16426962		
	22	chr2	intergenic	16077433	chr2	intergenic	16472680		
	23	chr2	intergenic	16129580	chr2	intergenic	16717055		
	24	chr2	*NBAS*	15392011	chr2	intergenic	15814812		
10	25	chr2	intergenic	16365867	chr2	intergenic	16453683	28.21	1777x
11	26	chr2	*MYCN*	16084511	chr2	intergenic	16697303	153.57	1460x
	27	chr2	*MYCN*	16082975	chr2	intergenic	16180006		
	28	chr2	intergenic	16105859	chr2	intergenic	16220058		
12	29	chr2	intergenic	6472899	chr2	intergenic	16077648	28.75	732x
	30	chr2	*NBAS*	15485584	chr2	intergenic	15829866		
	31	chr2	intergenic	15089860	chr2	intergenic	16574270		
	32	chr2	intergenic	16895922	chr2	intergenic	16896040		
13	33	chr2	*NBAS*	15519488	chr7	*CACNA2D1*	81729004	112.53	513x
	34	chr2	intergenic	15166132	chr7	intergenic	29806328		
	35	chr2	*NBAS*	15387879	chr2	intergenic	205327955		

Table 17: PCR assays of *MYCN*-associated breakpoints in primary neuroblastoma samples

Patient no.	**Break-point no.**	**Chromo-some Start**	**Gene Start**	**Break-point Start**	**Chromo-some End**	**Gene End**	**Break-point End**	***MYCN* CNV**	**Coverage *NB targeted NGS assay***	**Breakpoint sequence**	**Forward primer (5'-3')**	**Reverse primer (5'-3')**	**FAM-BHQ1 probe (5'-3')**	**MRD assay sensi-tivity range**	**MRD assay quanti-tative range**
1	1	chr2	intergenic	14746679	chr2	*NBAS*	15474981	61.02	1485x	GTGATTGTGTGAGTTAATACTTAATAAACTTCCATATATATATATAACACCACCAGAATCCTAGAAGCTCCTCTTG	GTGATTGTGTGAGTTAATAC	CAAGAGGAGCTTCTAGGA	Not performed	Not performed	Not performed
	2	chr2	intergenic	15866281	chr2	intergenic	16076048			GCCAGTACTTTGGGCCAATCTGCTAGACCCAAAAATGTTAATCTCACTGAGATTTAATTTGCATAAATAAGGTTGCATTC	GCCAGTACTTTGGGCCAATC	AGAGCACCCCCAAATTCATGT	Not performed	Not performed	Not performed

										TGCATTCCTGGGAAGA ACATGAATTTGGGGGT GCTCT					
	3	chr2	intergenic	10528094	chr2	*NBAS*	15682802			TCACATGGTAGTGTTT CCTTAGCACATAAATA TTTTCAGGGGAAAATT GTCATCTTGCTGGTTTT TATGTAGCATCTGTGC ATATGTCAATTTTTTAT TCTTTTGTTATTTTGCA CCTGTGCCTGCTGGCC ATGCAGGGGTGGAGG GAGGCCTGGATGCTTT TTCTTCCCTGCACTCGC AGGCCCCCCATGGGAC CCTCAGCCCCCAGAGG ACAATTGGAGGCTTCT GGA	TCACAT GGTAGT GTTTCCT TAGC	TCCAGA AGCCTC CAATTG TCC	Not performed	Not performed	Not performed
	4	chr2	intergenic	14807602	chr2	intergenic	16028224			CAGTTCACTACACGTT GCTGTTATATGTGTTTT CATTTCCCATTAATCT GGAATGGGTAATAATT TCATTAAATGACTTCT CATACTTTTTGAGATT ATTAGAAATGTTCCTT CTCTAATACATGAAGA TTTATTAAAATAATAC AACTAATTTTATAACA GCCCTTTATTTCAGGA ATAAAACCGACATAGT CGTAGTATACCAATCT TTAAATACAGTTCTGG ATCTTAATTTCTTGGC ATTTCATAAAGTTTTTC CCATTTATTTTCAAAA CTACATCCAAATTGTG ATGCTTACTGTTACAG GAGGAGCACAGGGGC CCTATTTGGGTAGAGT GGCTGGCAAAGGCCTC TTCGAGAGAGCGACAC TGACTCAGAACGATGA GCGAGCCTCAGGCAGG GTGGGGACAGGCGTG AAGAACACTCCAGGTG GATGGGACAATGACCG CAAAGGCTGT	CAGTTC ACTACA CGTTGC TGTTAT	ACAGC CTTTGC GGTCAT TGT	FAM-ACAGGAGGAGCACAGGGGCC-BHQ1	RQ-PCR: 10^{-5} ddPCR: 10^{-5}	RQ-PCR: 10^{-5} ddPCR: 10^{-4}
	5	chr2	intergenic	15194910	chr2	*EML6*	55157247			CTTGCAACATGGTTTT AAAGTGGCCACAAAC AGAAAATAATTTTTAA AAGTCCTAATTCTAAG AATTAAGGGGAAAAA AGAACCATATGCACAG AAGTGCATGAATAGGC CTCCCACTTAAATAAT CCAATCTAAAAAAATG TTTCACCTGAAGTATT CATTCCTTTGGAAAAA AAAAAATTACCCAGCC TCCTGGAAACATATCC AGGAGGCCCTCATCAT GGGCTGCCTTCCAAAG AGGAGAGCATGTGAC	CTTGCA ACATGG TTTTAA AGTGGC	TCCAGA TCGGGC CAACTG A	Not performed	Not performed	Not performed

										ACATCTGATCAGTTGG CCCGATCTGGA					
2	6	chr2	intergenic	14842324	chr2	intergenic	16509495	73.27	1398x	TGGAAGGAGATGAGT AGATTTGAGATGTACT GGAAAAATGCAAGAG TTTTAAGTCAAATTAA TTAATATTTTGTAGGA CTAACCATGAGCTAGT CTTGGTACAAAGTCTT TTCTGTGTATTACCCCT GTAACAGATTTATGGG GTTGGTACTATTATTG TTTCTTTTTTATGCCTG AGAAACTGAGGCAAA ATCTGAACTTGTGTCC CATAACTAGCTGTTTC TCCTTAGACCTGGATG GTAGGTGGA	TGGAAG GAGATG AGTAGA TTTGAG	TCCACC TACCAT CCAGGT CT	Not performed	Not performed	Not performed
	7	chr2	*NBAS*	15686098	chr2	intergenic	16079808			GATTTTCCCTTGCTGGT GGAATCAAATACAATA TCTAGTGGCTTGCTGC TCATAACTTTTGCAGC CGTCCCCAGGGCTCCC AAGTTAACCTTTTCAA AGCCACCATTCTCCCC AGTTATGGGCAGGCGA ATCTGATTTACCGAGA TGGAAGTGCTGTCCAC ACCTCCTGAGACCCAG CCTCGGCTCAAACAGC TTGA	GATTTT CCCTTG CTGGTG GA	TCAAGC TGTTTG AGCCG AGG	FAM-CGTCCC CAGGGC TCCCAA GT-BHQ1	RQ-PCR: 10^{-6} ddPCR: 10^{-6}	RQ-PCR: 10^{-5} ddPCR: 10^{-5}
	8	chr2	intergenic	15899186	chr2	intergenic	16078658			CCGTGACACTGTGGAA GACAGGCTCAGTCTCC CTCACTAACCTGTGAC CTGGGTCAGTTTTGCT CCACACAGTCCTCATC TGTGCGGCAGTTATTT TAAGAATTAAGTGAGA GACTCTCTGGCTGGCA GGAGATAAGTGCCCAA	CCGTGA CACTGT GGAAGA CA	TTGGGC ACTTAT CTCCTG CC	FAM-CACAGT CCTCAT CTGTGC GGCA-BHQ1	RQ-PCR: 10^{-3} ddPCR: 10^{-6}	RQ-PCR: 10^{-3} ddPCR: 10^{-5}
	9	chr2	intergenic	15936425	chr2	intergenic	16024506			TCAATTGCAACCCTGA GGCAGGAGAGAGGTA CCTTTTTAGGTGAAGA CCACTATCTTTTTATAA ACCAAATGTGTATATC TCATCTTATGAATGGA ATTGAACATCTTTTCC GTGGTATTCATTGGTA TTTCTTTCATATGCAAC TCTTAGTTTTTTGCCCT TTGCTCTTTTTTTTTCA AACAGGATCTCACTCT GTTACCCAGGCTGC	TCAATT GCAACC CTGAGG CA	GCAGC CTGGGT AACAG AGTG	Not performed	Not performed	Not performed
3	10	chr2	intergenic	16206870	chr2	intergenic	16405997	47.90	1917x	TTGCCTGTGTCACATC TGCTGTACAATGTCAT CCTAAAGTGACAGGGA TCAATTTAACCTCCTC ATTTAAAAGATGAGGA GACAGGCTCAAAGGG	TTGCCT GTGTCA CATCTG CT	CCCAG GTGCAT TCCTCT CAG	FAM-GGCTTG CCCTGC ACAGCG TA-BHQ1	RQ-PCR: 10^{-6}	RQ-PCR: 10^{-5}

										CAAAGCCGACTCACCCAGGCTCACACAACCAGAGTGGCAGAGCCTCAGGGCTTGCCCTGCACAGCGTAGCTTCTGTTCTGAGAGGAATGCACCTGGG				ddPCR: 10^{-6}	ddPCR: 10^{-5}
	11	chr2	intergenic	15782211	chr2	intergenic	16364858			GGTGGGAGCCTCAGATGATTCAGGAGGCTCAGAAGGAAGGCATGCTGTACTGCATTGAACATGCCTGCAAAAATTCTCAGCTGAGATGTTTGAGAAAGAGTTAGGGATAACATCTGAACCTCAGTCATTATATGCAGCCAAGAGTGTTTATTGCTCTGTGCCTGGCACACGTAGGGGCTCAGGAAA	GGTGGGAGCCTCAGATTC	TTTCCTGAGCCCCTACGTGT	Not performed	Not performed	Not performed
4	12	chr2	intergenic	15953189	chr2	intergenic	16422772	54.63	1582x	TGTAGGAGACCATTGGAGCATGGGGCCAAAAGGCCTAGGGAGGAGGAGGGGTCCCTCTCTGGGATCAGGCCTCCTCAGCCCAGAGGCAGCAGGTTCTTACCCAGTTAGGATTATTCTAGTTTGTTTTAAATAACTCTGGCTTACTACATTGTTTTTAAGGTCACGTTTGGTAGACTTGATTTTAGAGTCTTTAACAAATGCTGGACACTGTTTTTAGAGAGAAGAATTGGTGG	TGTAGGAGACCATTGGCA	CCACCAATTCTTCTCTCTAAAAACA	FAM-AGGCCTAGGGAGGAGGAGGG-BHQ1	RQ-PCR: 10^{-6} ddPCR: 10^{-6}	RQ-PCR: 10^{-65} ddPCR: 10^{-5}
5	13	chr2	intergenic	16242896	chr2	intergenic	16393725	66.11	1554x	GCCCAGCAGATTCCTGTTCTGCTTCCTCTGTCCCATGCTGAGCACACAGCATGGAGCGCAGCCCTGGGCGCACAGTAGGCGCTCTGCCCTGCTCCCTGAACTAGTGGTCAGGTGAACGAGCCCTGACTTTGCTCTGCCATTGCTGGGCTGTGTCCCTCGGATTGCGCCCCCCGTTCCCACACGCCTGGGCCCATTAAGCTTCCATCTCTCACCTCGTTTACCCCCTTTGCTCGGCATTTCTCCTTGCTGCCGCCATGTGAAGAAGGACGTGTTTGCTTCCCCTTCCATCGT	GCCCAGCAGATTCCTGTT CT	ACGATGGAAGGGGAAGCAAA	FAM-GTGTCCCTCGGATTGCGCCC-BHQ1	RQ-PCR: 10^{-6} ddPCR: 10^{-6}	RQ-PCR: 10^{-5} ddPCR: 10^{-5}
6	14	chr2	intergenic	15913636	chr2	intergenic	16175037	44.50	1421x	TAAGTGCTAACGCATGCCGCAGCGTGGATGGACCTTGAAAACATCATGCTAAGTGAAAGAAGCCAGTCACGAAAGACCACGTAGTGTATGATCTTATTTACACGAAATATCCAGAACAGGCGAAACCAAGAAGACAGAAAGTAGGTCGGGGGTTGCAG	TAAGTGCTAACGCATGCCGC	GTGGAGCTGACTGCAAAGGTT	FAM-AGTAGGTCGGGGGTTGCAGT-BHQ1	RQ-PCR: 10^{-5}	RQ-PCR: 10^{-5}

										TAATTCCTGAAGTTGA ATTACTAAGTCAAAGG GTATGAATAGTTTAAC ATCCTTGATCAATGTG TCCAAACAGCATTCTA ACTATTTAAGCATATT TTAAATATTGACTTAC AGAGTGTCAAATAGGA AGGAACCTTTGCAGTC AGCTCCAC				ddPCR: 10^{-5}	ddPCR: 10^{-4}
	15	chr2	intergenic	15102355	chr2	intergenic	15949822			GCTCCCTGTGTGGGTT GATTTAGGGCAGAAAG AGGGCTGGAGCATATG TAGGCAGTGGGTACCC CGCAGGAGGCGGTGG GAGTCACCTGGGAGTC CTGTC	GCTCCC TGTGTG GGTTGA TT	GACAG GACTCC CAGGT GACT	Not performed	Not performed	Not performed
	16	chr2	intergenic	15958945	chr2	intergenic	15985010			GCCAGATGCTCTCGGT GAAGTTTAATTCATCG TGGGAAGCATCAAGG GGGAGGTGACCCGGA GCTGCCTCCTTTAAGA TCAGAGGATTTTGCCT GGTAGATGAGGTGAG GATGGCACCTGTAAAT ACCAGAAAAAGCATG GTGTGTTCAAAGACCA G	GCCAGA TGCTCT CGGTGA A	CTGGTC TTTGAA CACACC ATGC	Not performed	Not performed	Not performed
	17	chr2	intergenic	15074278	chr2	intergenic	16037460			GAGTGGGACTGGGTGT TGAGAAAATGGGGTG GACTTTACATTTCATA TACCCCATATATATAT ATTTTAGAGACAGGGT CTTGCTCTGTTGCCCA GGCTGAAGTGCAGTGG TGCGATCCTAGCTCAC TGCAGGCTTGAAGTCC TGGGCTCAAGCGATCC TCCCACCTGGCCTCCG AAAATCCAATTACAGG CATGAGCCACTGTGCC CAGCCCACCCAGCTCT TCATGGGCTACACTGC AATCACAGCTCACTGC AC	GAGTGG GACTGG GTGTTG AG	GTGCA GTGAG CTGTGA TTGC	FAM-ACATTT CATATA CCCCAT AT-BHQ1	Not performed, probe used for semi-quanti-tative PCR detection	Not performed, probe used for semi-quanti-tative PCR detection
7	18	chr2	intergenic	15139665	chr2	intergenic	16364904	14.53	2005x	AGATGGTGGGAGCCTC AGATGATTCAGGAGGC TCAGAAGGAAGGCAT GCTGTACTGCATTGAA CATGCCTGCAAAAATT CTCAGCTGAGATGTTT GAGAAAGAGTTAGGG ATAACATCTGAACCTC	AGATGG TGGGAG CCTCAG AT	CCCCCT TGTTGT TCTGGT GA	FAM-GGAGGC TCAGAA GGAAGG CATGC-BHQ1	RQ-PCR: 10^{-4}	RQ-PCR: 10^{-4}

										AGTCATTATATGCAGC CAAGAGTGTTTATTGA AAGAATGAATGGATAT TTTGATTTAAATCTCA CCAAAGGCCAATGCTT TTAAACAACCAGATCT CCTGAGAACTCGTTCA CTATCACCAGAACAAC AAGGGGG				ddPCR: 10^{-6}	ddPCR: 10^{-5}
8	19	chr2	intergenic	13490249	chr2	intergenic	15815066	48.25	1190x	CCTGTAGTATAGTTGG AAGTGAGTTAGCATGA TGCCTCCAGCTTTGTTC TTTTTGCTTAGGCTTTT TCCTTCTAAACTGTCTT GTGTGGATAGTCCCTA GGGCTGAGGTCCAATG GCGACAACGCGAGAA TAATAGGCTGTGGCTA GGGTATTTTGAGTACA AGAGCT	CCTGTA GTATAG TTGGAA GTGAGT T	AGCTCT TGTACT CAAAA TACCCT A	FAM-AGGGCT GAGGTC CAATGG CGA-BHQ1	RQ-PCR: 10^{-6} ddPCR: 10^{-6}	RQ-PCR: 10^{-5} ddPCR: 10^{-5}
9	20	chr2	intergenic	15276043	chr2	intergenic	15999479	31.15	2017x	CCCACCACTTCAGGCC ATAGAAATACACCATC TCCATAGAGCAGGGGT GTCCAATCTTTTGGCTT CCCTGGGACACACTGG AAAAAGAATTGTCTTG GGCCACACATAAAAA AACACAAACCATACCT GATTACCTAAAAAAAA AAAAAAAATCACACA CAGTAAAAAAAAAAA AAAAAAAATCACACA CAGAAAAATCTCATAA TATTTTAAGAGATGCT GCAGGGATGTCTTATT CTACTTTGTACCCCTG GGTCTCA	CCCACC ACTTCA GGCCAT AG	TGAGA CCCAG GGGTA CAAAG	Not performed	Not performed	Not performed
	21	chr2	intergenic	15857004	chr2	intergenic	16426962			TCCCCACATTTTCCATC GTCATAATGAAGGAGA CAGTGACTTAGTTCAT TCACTGACACTTACCT ACTGGGCACATAAGGG CAAGAAGGGGAGATT CTTGTCCTCAAGAATC CTGGAGGCTACGGGAG GAAGCAGATGGTTAAA ATATGACTAACTCGGT GCTAACTGTACATTCA TTCACTCATTCATTTAA TTACTTCAACAAATAT TTAGTGAGTCAACCAC ATGCCAGACGTTTTCC ACCGTCCTTCCCAGCA TATCAATCTCCCGCTTT TGCACAC	TCCCCA CATTTTC CATCGT CA	GTGTGC AAAAG CGGGA GATTG	Not performed	Not performed	Not performed
	22	chr2	intergenic	16077433	chr2	intergenic	16472680			ACCTGCAGACCACTTG TGAGGCCACTGGGAGC CACTAGGAACCTGTAG CCCACACTTGGGGATA CCTTGACTTACTTGGA TATAAGGTGGCTGCAG AATAATAGAAGATTTT GGGCAGCAATTTCACA TGACTAGCAAAAGGA	ACCTGC AGACCA CTTGTG AG	GGGTTC AGTGG GTCTTA GCC	Not performed	Not performed	Not performed

										AACTGTTGAAATGGCT GCAGAGGCCATGGGCT AAGACCGTGAAAAAC AGAGTGTAACCAAGCT GGCTAAGACCCACTGA ACCC					
	23	chr2	intergenic	16129580	chr2	intergenic	16717055			TACTCAGGAGGCTGAG GCAGGAGAATTGCCTT GTCTCCCAAAGTGCTG GGATTACAGCATAAGC CACCACACCCAGCCCC AAGAACCGGAATTTTT ATGGGCGCCCACCATG TGTAGACAG	TACTCA GGAGGC TGAGGC A	CTGTCT ACACAT GGTGG GCG	FAM-ACCCAG CCCCAA GAACCG GA-BHQ1	Not performed, probe used for semi-quanti-tative PCR detection	Not performed, probe used for semi-quanti-tative PCR detection
	24	chr2	*NBAS*	15392011	chr2	intergenic	15814812			TCTTGTGCCGACTTCCT GTCTCATCCTATGACT TAGATTGCCTTAACCT CCTGGGAATGCAGCCC AGTAAGTTTCAGTATA ACTGAAACTATAGAGG CCTTGTACAATGG	TCTTGT GCCGAC TTCCTGT C	CCATTG TACAA GGCCTC TATAGT T	FAM-TTAACC TCCTGG GAATGC AG-BHQ1	RQ-PCR: 10^{-5} ddPCR: 10^{-5}	RQ-PCR: 10^{-5} ddPCR: 10^{-5}
10	25	chr2	intergenic	16365867	chr2	intergenic	16453683	28.21	1777x	GTGGTGGCTTTTCCCC CTTAGTGATAGAAATG CAAGGGAATGAGTACT AATTGTTGAAGGTTTT AAATGTGCTGTACCTT GTTAATGTTTCTAACA TATTGATTCCTATTAAT TAATCTAGTGTAATGG AAAAGTCAATTACGCC ATATTAACACCACTTG TTGTAGAAAAGACTAA ATTACTGAATGCAGAT GGAATATTTTTCCCAG TGATCACAATATTTCA GGTGAGTTTCCCATGG TCTTTGGAGTATGAGA ATAATTTCATAAACAC AGATTTAGGGAGAAA GCACTGCCTGATGCCA GATGCCATTCTAGAGT GTTATTTTATTTAATCT GCAATCAGGAAGGGCT CA	GTGGTG GCTTTTC CCCCTT A	CTGCAA TCAGG AAGGG CTCA	FAM-AGGTGA GTTTCC CATGGT CTTTGG A-BHQ1	RQ-PCR: 10^{-4} ddPCR: 10^{-4}	RQ-PCR: 10^{-3} ddPCR: 10^{-4}
11	26	chr2	*MYCN*	16084511	chr2	intergenic	16697303	153.57	1460x	AAGCTTTCTGTGTGTC CTGCATTTCCCACCCA AACTCCTCAAAGCCAC CAATAATAACAGCAAC AACAGAAACGTGT	AAGCTT TCTGTG TGTCCT GCATT	ACACGT TTCTGT TGTTGC TGTTAT T	Not performed	Not performed	Not performed
	27	chr2	*MYCN*	16082975	chr2	intergenic	16180006			AGCACTAACAAAGGG GACGCGACCCGGGGTC CAGTGCCCCAGGGAGG CAGCCGGACCCGAGTT CGGTCTTTACCATGGA AGATGAACATTTAGCT	AGCACT AACAAA GGGGAC GC	GAAGC CGGGTC TGAGA AGTAG	FAM-CCAGCG CCAGTG CCTGAT CC-BHQ1	RQ-PCR: 10^{-5}	RQ-PCR: 10^{-5}

										TCTTTTATATCGGTCCCTGTCTCAATACCACTGGCGCCAGCGCCAGTGCCTGATCCTGAACTAGTTTTGCTACTTCTCAGACCCGGCTTC				ddPCR: 10^{-6}	ddPCR: 10^{-5}
	28	chr2	intergenic	16105859	chr2	intergenic	16220058			CTGGGGACAGTGTCTCATCGCTCCCTCGCCACAGTGCGGAGGGTTGAGTTACTCTGCAGTTCATGAAACATTACC	CTGGGGACAGTGTCTCATCG	GGTAATGTTTCATGAACTGCAGAGT	Not performed	Not performed	Not performed
12	29	chr2	intergenic	6472899	chr2	intergenic	16077648	28.75	732x	CTAACAGTCAGGTCCCTCAGCTACACACCCCACTAGCATCATGACACTTCCGAGAACACCCATATTTGGT	CTAACAGTCAGGTCCCTCAGC	ACCAAATATGGGTGTTCTCGGA	FAM-ACCCCACTAGCATCATGACAC-BHQ1	RQ-PCR: 10^{-5} ddPCR: 10^{-6}	RQ-PCR: 10^{-5} ddPCR: 10^{-5}
	30	chr2	*NBAS*	15485584	chr2	intergenic	15829866			ACAGTTAACAAGGGATGTGAAGGACCTGTGTGGGATGTGTGTTCTCCCACTTCCTCCTCCTGTGTGGCATGTG	ACAGTTAACAAGGGATGTGAAGG	CACATGCCACACAGGAGGAG	FAM-CTGTGTGGGATGTGTGTTCTCCC-BHQ1	Not performed, probe used for semi-quantitative PCR detection	Not performed, probe used for semi-quantitative PCR detection
	31	chr2	intergenic	15089860	chr2	intergenic	16574270			GGCCTCTGGGCTTTGGTAATTTGGCAATATGCCACTCCCATCAAGCCTCTGCAGTGCTCTGTTGAGCCAGATTCTTCCCAGAGTCCCTGATTCCTGATGCTGAGCCTACCCCATCACCTGCTCTCCAGAGCCAGCCCTTGAAGGCAGCAATTCATCCTCCAGTGGAGCCCTCAGCAGTGACTGGGGAGCCCTAGCCCCTGGGTCAGCCAGGACAGAGCAGCTGCAGCCACATGGATGGAACTGGAGGTCATTTTGTTAAGAGAAATAAGCCAAGTACAGAAAGGCAAATACCACATGTTCTCACTCATATGTAAAGCTTAAAAAGTGGACCTCATGAAGATAGAAAGTAGATTGGTGGCTACCAGAGTCTTGGAAGGGTAGGCAGGA	GGCCTCTGGGCTTTGGTAAT	TCCTGCCTACCCTTCCAAGA	FAM-GGAGCCCTAGCCCCTGGGTC-BHQ1	Not performed, probe used for semi-quantitative PCR detection	Not performed, probe used for semi-quantitative PCR detection

	32	chr2	intergenic	16895922	chr2	intergenic	16896040			GAGGATAAGAGGGTCAGACTGAGTGGGTGAGGTCATTGCCGGTGACTCCCTGCTGCCACCAGAGCTGTATGGGGACCA	GAGGATAAGAGGGTCAGACTGAGTG	TGGTCCCCATACAGCTCTGGT	Not performed	Not performed	Not performed
13	33	chr2	*NBAS*	15519488	chr7	*CACNA2D1*	81729004	112.53	513x	AGCTACATGAACGAGACAGGCATTACCTACGCATGCTGAAAATTTTCAGAACTTGAATTTATAGGCTATCACATGAATCTCTTCCAACAGAAGAGAAATACACAGCCTTATAATCAGCAAAAATGACCATGGGAAAGCGCGCTGGAGAAAAATGTTTAAGAAGCTGATGGAGGCCGGGCGCGGTGGCTCACGCCTGTAATC	AGCTACATGAACGAGACAGGC	GATTACAGGCGTGAGCCACC	FAM-GAAGCTGATGGAGGCCGGGCG-BHQ1	RQ-PCR: 10^{-4} ddPCR: 10^{-4}	RQ-PCR: 10^{-4} ddPCR: 10^{-4}
	34	chr2	intergenic	15166132	chr7	intergenic	29806328			GCTCTGGCCAGGACTTGTAATACCACATTGAATAGGAGTGTTGAGAGTAGACATCCCTGTCTTGTGCCAGTTTTCAGTATGATGCTGGCTGTGGGTTTGTCATAGATGGCCCTTATTATTTTGAAGTATGTTCCTTTGATGCCTAGTTTATTGAGAGTTTTTAACATGAAGGGATGTTGAATTTTATTAAAAGTCTTTTCTGCATCTATTGAGATAATCATGTGGTTTTTGTCTTTGGCTCTGTTTATATGCTGGATTACATTTATTGATTTGCGTATATTGAACCAGCCTTGCATCCCAGGGATGAAGCCCACTTGATCATGGTGG	GCTCTGGCCAGGACTTGTAA	CCACCATGATCAAGTGGGCT	Not performed	Not performed	Not performed
	35	chr2	*NBAS*	15387879	chr2	intergenic	205327955			CAGGGGTTGCAATCCTAGTCTCTGATACAACAGAATTTAAACCAACAAAGATCAAAAGAGACAAAGAAGGGCATTACATAATGGTAAAGGGATCAATGCACCAAGAAGAGCCTACTCTCTCTCTCTCTCTCTATATATATCTATATATCTCTCTATATATCTATATATACCTCTATCTATATCTATATATCTATATCTATAGATCTATATAT	CAGGGGTTGCAATCCTAGTCTC	ATATATAGATCTATAGATATAG	FAM-AGGGATCAATGCACCAAGAAGAGCT-BHQ1	Not performed	Not performed

Table 18: Complete list of TR-14 breakpoints found in the genomic *MYCN* amplicon region on chr.2p24.3-2p24.2.

Chr. Pair1	Min Pos_Pair1	Max Pos_Pair1	Chr. Pair2	Min Pos_Pair2	Max Pos_Pair2	Gene Pair1	Gene Pair2	Repeat Pair1	Repeat Pair2	No. En-compassing	No. Spann-ing	In-version
chr1	88110445	88110508	chr2	15953519	15953524	intergenic	intergenic	no_repeat	no_repeat	3	4	n
chr2	15952511	15953252	chr2	15953212	15954138	intergenic	intergenic	no_repeat	no_repeat	105	0	t
chr2	15966847	15967084	chr2	16399600	16400169	intergenic	intergenic	no_repeat	MIRb_SINE	65	14	n
chr2	15966933	15967559	chr2	15967705	15968245	intergenic	intergenic	no_repeat	AluJb_SINE	92	0	n
chr2	15984120	15985090	chr2	15984862	15985875	intergenic	intergenic	no_repeat	MIR_SINE	135	1	n
chr2	16018809	16019045	chr2	16019442	16019842	intergenic	intergenic	L1ME3D_LINE	L1ME3D_LINE	21	0	n
chr2	16027334	16028089	chr2	16028019	16028831	intergenic	intergenic	MLT1G1_LTR	L2c_LINE	42	0	n
chr2	16060732	16061550	chr2	16061542	16062370	intergenic	intergenic	L2b_LINE	no_repeat	27	0	n
chr2	16074662	16077547	chr2	16075553	16078429	intergenic	intergenic	AluJb_SINE	MSTD_LTR	176	0	n
chr2	16077555	16077899	chr2	16078173	16078506	intergenic	intergenic	MER41E_LTR	no_repeat	22	0	n
chr2	16077760	16080338	chr2	16078556	16080994	intergenic	intergenic	MIR3_SINE	no_repeat	111	1	n
chr2	16080878	16080889	chr2	16081491	16081531	intergenic	intergenic	no_repeat	no_repeat	3	0	n
chr2	16080986	16083613	chr2	16081660	16084458	*MYCN*	*MYCN*	no_repeat	no_repeat	82	2	n
chr2	16083620	16084030	chr2	16084236	16084669	*MYCN*	*MYCN*	no_repeat	no_repeat	137	0	n
chr2	16083802	16086497	chr2	16084673	16087309	*MYCN*	*MYCN*	MIRb_SINE	no_repeat	467	0	n
chr2	16085154	16085566	chr5	95722616	95722619	*MYCN*	intergenic	AluSq_SINE	AluSx1_SINE	7	0	n
chr2	16086429	16086628	chr2	16274661	16274842	intergenic	intergenic	no_repeat	no_repeat	23	10	n
chr2	16086630	16086694	chr2	16274662	16274990	intergenic	intergenic	no_repeat	no_repeat	52	10	n
chr2	16087692	16089638	chr2	16088640	16090501	intergenic	intergenic	no_repeat	no_repeat	333	0	n
chr2	16088566	16088976	chr12	58052920	58053414	intergenic	intergenic	no_repeat	MER57-int_LTR	1018	11	h
chr2	16089704	16090378	chr2	16090332	16091245	intergenic	intergenic	no_repeat	MIR3_SINE	58	1	t
chr2	16102329	16102374	chr2	116349172	116349176	intergenic	*DPP10*	L1PA5_LINE	L1PA5_LINE	3	0	n
chr2	16104968	16105634	chr2	16105656	16106508	intergenic	intergenic	no_repeat	no_repeat	32	0	t
chr2	16164032	16166931	chr2	16164654	16167641	intergenic	intergenic	L2_LINE	L2_LINE	86	0	n
chr2	16166899	16166935	chr2	16167696	16167738	intergenic	intergenic	no_repeat	L1MC5_LINE	3	0	n
chr2	16174160	16175068	chr2	16174910	16176067	intergenic	intergenic	no_repeat	no_repeat	98	0	n
chr2	16178404	16179199	chr2	16179099	16179953	intergenic	intergenic	no_repeat	no_repeat	52	0	n

chr2	16212248	16212296	chr2	16212914	16213018	intergenic	intergenic	L2c_LINE	no_repeat	3	0	n
chr2	16229882	16230909	chr2	16230678	16231712	intergenic	intergenic	no_repeat	no_repeat	71	0	n
chr2	16241754	16243460	chr2	16242444	16244246	intergenic	intergenic	no_repeat	no_repeat	145	0	n
chr2	16354910	16355481	chr2	16355600	16356312	intergenic	intergenic	no_repeat	AluJb_SINE	28	0	n
chr2	16364077	16364605	chr2	16364828	16365454	intergenic	intergenic	L1ME4a_LINE	AluSq_SINE	35	0	n
chr2	16375992	16377213	chr2	16376690	16377878	intergenic	intergenic	no_repeat	MIRb_SINE	119	0	n
chr2	16378899	16379640	chr2	16379672	16380381	intergenic	intergenic	no_repeat	L2c_LINE	41	0	n
chr2	16378940	16379026	chr2	16379596	16379650	intergenic	intergenic	no_repeat	no_repeat	8	0	n
chr2	16394797	16395776	chr2	16395674	16396712	intergenic	intergenic	no_repeat	no_repeat	136	0	n
chr2	16399050	16399777	chr2	16399811	16400422	intergenic	intergenic	AluSq2_SINE	no_repeat	16	0	n
chr2	16405002	16406685	chr2	16405767	16407911	intergenic	intergenic	no_repeat	no_repeat	153	0	n
chr2	16416587	16417334	chr2	16417268	16418147	intergenic	intergenic	no_repeat	no_repeat	88	0	n
chr2	16421516	16422301	chr2	16422294	16423153	intergenic	intergenic	MER70A_LTR	no_repeat	84	0	n
chr2	16432592	16433472	chr2	16433334	16434182	intergenic	intergenic	no_repeat	no_repeat	49	0	n
chr2	16440648	16441531	chr2	16441466	16442178	intergenic	intergenic	MIRb_SINE	no_repeat	54	0	n
chr2	16453023	16453999	chr2	16453891	16454726	intergenic	intergenic	no_repeat	no_repeat	141	0	n
chr2	16599987	16600239	chr2	16600781	16601087	intergenic	intergenic	no_repeat	no_repeat	2	0	n
chr2	17067130	17067421	chr2	17067747	17068256	intergenic	intergenic	no_repeat	L1M4_LINE	3	0	n
chr2	17150863	17150982	chr2	17151627	17151659	intergenic	intergenic	no_repeat	no_repeat	3	0	n
chr2	17527306	17527971	chr2	17528067	17528852	intergenic	intergenic	LTR17_LTR	L3_LINE	14	0	n

The list shows all found and unfiltered breakpoints. Qualitative filtering can be applied as follows: The green highlighted breakpoints are supported by >10 encompassing and spanning reads. The breakpoints marked in yellow are supported by >2 encompassing and spanning reads. The breakpoints marked in red are supported by ≤1 encompassing and spanning read.. Inversion codes: n = head to tail, t = tail to tail, h = head to head.

Table 19: *MYCN* amplicon breakpoints found in matching primary and relapse tumor samples of patient no. #5.

Tumor sample	Break-point number	Chr. Pair1	Exact Pos_Pair1	Chr. Pair2	Exact Pos_Pair2	Gene Pair1	Gene Pair2	Repeat Pair1	Repeat Pair2	No. En-compassing	No.Spann-ing	In-version
Primary	1	chr2	15984734	chr2	33141347	intergenic	intergenic	no_repeat	(G)n_Simple_repeat	173	20	t
Primary	2	chr2	16028210	chr2	33141308	intergenic	intergenic	L2c_LINE	(G)n_Simple_repeat	86	276	h
Primary	3	chr2	16170269	chr2	16178954	intergenic	intergenic	no_repeat	no_repeat	88	14	n
Primary	4	chr2	16242896	chr2	16393725	intergenic	intergenic	no_repeat	THE1C_LTR	477	19	t
Primary	5	chr2	16376997	chr2	33141316	intergenic	intergenic	no_repeat	(G)n_Simple_repeat	299	498	h
Relapse	1	chr2	15984736	chr2	33141310	intergenic	intergenic	no_repeat	(G)n_Simple_repeat	11	3	n
Relapse	2	chr2	16028211	chr2	33141308	intergenic	intergenic	L2c_LINE	(G)n_Simple_repeat	4	186	h
Relapse	3	chr2	16170268	chr2	16178955	intergenic	intergenic	no_repeat	no_repeat	15	4	n
Relapse	4	chr2	16242896	chr2	16393724	intergenic	intergenic	no_repeat	THE1C_LTR	70	16	t
Relapse	5	chr2	16376998	chr2	33141315	intergenic	intergenic	no_repeat	(G)n_Simple_repeat	60	297	h

Overview of the MYCN amplicon breakpoints supported by many covering sequencing reads detected using NB targeted NGS assay of the tumor of patient number 5. All breakpoints with a high number of supporting reads found in the primary tumor sample could be detected in the relapse tumor sample as well. The breakpoint highlighted in green shade displays the breakpoint of highest importance and was therefore used for further PCR and MRD assay detection. The breakpoints are catalogued in order of their genomic localization. Inversion codes: n = head to tail, t = tail to tail, h = head to head.

Table 20: PCR assay of *ATRX*-associated breakpoint in CHLA-90 neuroblastoma cell line

Name of cell line	Chromo - some Start	Gene Start	Break-point Start	Chromo -some End	Gene End	Break-point End	Coverage *NB targeted NGS assay*	Breakpoint sequence	Forward primer (5'-3')	Reverse primer (5'-3')	FAM-BHQ1 probe (5'-3')	MRD assay sensi-tivity range	MRD assay quanti-tative range
CHLA-90	chrX	*ATRX*	76935121	chrX	*ATRX*	76959029	1889x	TCAACATGAGAGGTGC ATAACAGAAACTTTCA TAGGTATCAATAAATC AGGGCCCCAAAGAGG GAGTCACAGCCCTGGC TTGGGGAGCTCCCAGG TCTGGGCTCCCCAGAG GGCTGCAGCTCTTCTT TCCTTCTCTTCACCTGC AACAAGGTGAGCAAG GGGCATGTCTCAGCCC TGTTTGTGTTACAGCT ATTTTAGCCTCATCTG GCAGGTC	TCAACATG AGAGGTG CATAACA G	GACCTGCC AGATGAG GCTAAA	TTCACC TGCAAC AAGGTG AG	RQ-PCR: 10^{-5}	RQ-PCR: 10^{-5}

Table 21: ASQ-PCR assay of *ALK* SNV c.3824G>A in neuroblastoma cell line and tumor

Name of cell line/ patient no.	*ALK* mutation	Coverage *NB targeted NGS assay*	*ALK* c.3824G>A sequence	Forward primer (5'-3')	Reverse primer (5'-3')	FAM/HEX-BHQ1 probe (5'-3')
LAN-5	c.3824G>A	1726x	CTTTACTCACCTGTAGAT GTCTTGGGCCATCCCGAA GTCTCCAATCTTGGCCAC TCTTCCAGGGCCTGGACA GGTCAAGAGGCAGTTTCT GGCAGCAATGTCTCTGGG AAGAAAGGAAATGCATT TCCTAATTTTATCCCTAG GAAGATGAGTGTACAAC GGCCATCACTAGGATTTT ATCTCCAAGCTGAAGTTT AAATAGTTCCTTCCCTTC CCTATATTTCCTTTAGTA TAGTATACTTCAGTGTGA GAGAAACAGCCTTAACA ATTCTAGGCC	CTTTACT CACCTGT AGATGTA TT	GGCCTAG AATTGTT AAGGCT GT	TCCAGGGCCTG GACAGGTCA
8	c.3824G>A	1190x				

The mutated ALK c.3824G>A sequence located on the reverse strand of chromosome 2 is displayed in mirroring sense strand direction.

Table 22: Cell counts used for *in vitro* assays

Cell line	Cell type	One 6-well flat bottom growth area 9.5cm²		One 12-well flat bottom growth area 3.8cm²		One 96-well flat bottom growth area 0.32cm²	
		4 days of growth (3 or 4 days of treatment)	10 days of growth	4 days of growth (3 or 4 days of treatment)	10 days of growth	4 days of growth (3 or 4 days of treatment)	10 days of growth
BJ1-hTERT	skin fibroblast	$8x10^4$ cells/well	$3x10^4$ cells/well	$3.5x10^4$ cells/well	$1.2x10^4$ cells/well	$5x10^3$ cells/well	$1x10^3$ cells/well
CHP-134	neuroblastoma	$1.5x10^5$ cells/well	$1x10^4$ cells/well	$6x10^4$ cells/well	$4x10^3$ cells/well	$5x10^3$ cells/well	$5x10^2$ cells/well
CHP-212	neuroblastoma	Not performed	Not performed	Not performed	Not performed	$1x10^4$ cells/well	Not performed
GI-ME-N	neuroblastoma	$1x10^5$ cells/well	$2x10^4$ cells/well	$4x10^4$ cells/well	$8x10^3$ cells/well	$3x10^3$ cells/well	$7x10^2$ cells/well
IMR-32	neuroblastoma	$7.5x10^4$ cells/well	Not performed	$3x10^4$ cells/well	Not performed	$6x10^3$ cells/well	$4.5x10^3$ cells/well
IMR-5	neuroblastoma	$7.5x10^4$ cells/well	Not performed	$3x10^4$ cells/well	Not performed	$6x10^3$ cells/well	$4.5x10^3$ cells/well
IMR-5/75	neuroblastoma	$7.5x10^4$ cells/well	Not performed	$3x10^4$ cells/well	Not performed	$6x10^3$ cells/well	$4.5x10^3$ cells/well
Kelly	neuroblastoma	Not performed	Not performed	Not performed	Not performed	$1.25x10^4$ cells/well	$15x10^3$ cells/well
NBL-S	neuroblastoma	$1x10^5$ cells/well	Not performed	$4x10^4$ cells/well	Not performed	$4x10^3$ cells/well	Not performed

NGP	neuroblastoma	$8x10^4$ cells/well	$5.4x10^4$ cells/well	$3.2x10^4$ cells/well	$2x10^4$ cells/well	$3x10^3$ cells/well	$1x10^3$ cells/well
NGP_ASPM-FPN_#1	neuroblastoma, ASPM 3xFLAG knockin clone #1	$8x10^4$ cells/well	$5x10^4$ cells/well	$3.2x10^4$ cells/well	$2x10^4$ cells/well	$3x10^3$ cells/well	$1x10^3$ cells/well
NGP_ASPM-FPN_#7	neuroblastoma, ASPM 3xFLAG knockin clone #7	$8x10^4$ cells/well	$5x10^4$ cells/well	$3.2x10^4$ cells/well	$2x10^4$ cells/well	$3x10^3$ cells/well	$1x10^3$ cells/well
PLF (Fi301)	primary human embryonic lung fibroblasts	Not performed	Not performed	Not performed	Not performed	$2x10^3$ cells/well	Not performed
SK-N-AS	neuroblastoma	$1x10^5$ cells/well	Not performed	$4x10^4$ cells/well	Not performed	$4x10^3$ cells/well	Not performed
SK-N-BE(2)	neuroblastoma	$5x10^4$ cells/well	$3x10^4$ cells/well	$2x10^4$ cells/well	$1.2x10^4$ cells/well	$1x10^3$ cells/well	$1x10^2$ cells/well
SKNBE(2)-C/ BE(2)-C	neuroblastoma	Not performed	Not performed	Not performed	Not performed	$3x10^3$ cells/well	Not performed
SK-N-FI	neuroblastoma	Not performed	Not performed	Not performed	Not performed	$1.2x10^3$ cells/well	Not performed
SK-N-DZ	neuroblastoma	Not performed	Not performed	Not performed	Not performed	$1x10^4$ cells/well	Not performed
SK-N-SH	neuroblastoma	Not performed	Not performed	Not performed	Not performed	$2.5x10^3$ cells/well	Not performed
SH-SY5Y	neuroblastoma	$1.5x10^5$ cells/well	$4x10^4$ cells/well	$6x10^4$ cells/well	$1.6x10^4$ cells/well	$3x10^3$ cells/well	$5x10^2$ cells/well
SH-EP	neuroblastoma	Not performed	Not performed	Not performed	Not performed	$3x10^3$ cells/well	Not performed
VH7	skin fibroblast	Not performed	Not performed	Not performed	Not performed	$1x10^3$ cells/well	Not performed

Surface areas for cell culture plates are related to Corning disposable cell culture vessels[1229] used in this thesis.

Table 23: List of PCR primers (except for MRD assays in cell line or patient material*) used in this thesis

Sub-project	Primer name	Specifications	Sequence 5'-3'	Source / Reference	Manufacturer
ASPM	ASPM_Stop_87f	3x FLAG CRISPR/Cas9 knockin	CACCGCAAATGGTGATGGATACGCT		Eurofins Genomics GmbH
ASPM	ASPM_Stop_87r	3x FLAG CRISPR/Cas9 knockin	AAACAGCGTATCCATCACCATTTGC		Eurofins Genomics GmbH
ASPM	ASPM_Stop_75f	3x FLAG CRISPR/Cas9 knockin	CACCGCACCATTTGAATAGCTTGCA		Eurofins Genomics GmbH
ASPM	ASPM_Stop_75r	3x FLAG CRISPR/Cas9 knockin	AAACTGCAAGCTATTCAAATGGTGC		Eurofins Genomics GmbH

ASPM	For_U6_seq	gRNA seq in px459 3x FLAG CRISPR/Cas9 knockin	TAAAATGGACTATCATATGCTTACC		Eurofins Genomics GmbH
ASPM	ASPM_flagcheck_f1	3x FLAG CRISPR/Cas9 knockin	CCCCGAAGCAAAGGAAAGGA		Eurofins Genomics GmbH
ASPM	ASPM_flagcheck_r1	3x FLAG CRISPR/Cas9 knockin	GGCCGGATGCAATCATTCAA		Eurofins Genomics GmbH
ASPM	FLAG_for	3x FLAG CRISPR/Cas9 knockin	ATGGACTACAAGGACGACGATGACAAG		Eurofins Genomics GmbH
ASPM	ASPM_FPN_check3'UTR_r	3x FLAG CRISPR/Cas9 knockin	GAGAAGCAAGGAGTTTAGTGTCTC		Eurofins Genomics GmbH
ASPM	ASPM-stop_T7_f1	3x FLAG CRISPR/Cas9 knockin	ACTTCTTAGTGAGTAGACAGAACTT		Eurofins Genomics GmbH
ASPM	FPN_check_for	3x FLAG CRISPR/Cas9 knockin	TTCTATCGCCTTCTTGACGAG		Eurofins Genomics GmbH
ASPM	FPN_check_rev	3x FLAG CRISPR/Cas9 knockin	ATCCTTGTAATCTCCAGAACCAC		Eurofins Genomics GmbH
ASPM	ASPM-stop_T7_r1	3x FLAG CRISPR/Cas9 knockin	GCTGATGACCAAAAGGCAGTG		Eurofins Genomics GmbH
ASPM	ASPM_FPN_check_5f	3x FLAG CRISPR/Cas9 knockin	AAAATAAAATCAGCTTGGTTGTG		Eurofins Genomics GmbH
ASPM	DCX_F	*DCX* qPCR Primer forward strand	GCTGTGTCCTCTGACCGTTT	K. Ahrens[543,544,598]	Eurofins Genomics GmbH
ASPM	DCX_R	*DCX* qPCR Primer reverse strand	TGACAGACCAGTTGGGAT TG	K. Ahrens[543,544,598]	Eurofins Genomics GmbH
ASPM	MAP2_F	*MAP2* qPCR Primer forward strand	TCTCTTCTTCAGCACGGCG	25312269	Eurofins Genomics GmbH
ASPM	MAP2_R	*MAP2* qPCR Primer reverse strand	GGGTAGTGGGTGTTGAGGTACC	25312269	Eurofins Genomics GmbH
ASPM	TUBB3_F	*TUBB3* qPCR Primer forward strand	ATGAGGGAGATCGTGCACAT	24298367	Eurofins Genomics GmbH
ASPM	TUBB3_R	*TUBB3* qPCR Primer reverse strand	GCCCCTGAGCGGACACTGT	24298367	Eurofins Genomics GmbH
ASPM	CCNB1_F	*CCNB1* qPCR Primer forward strand	AAGAGCTTTAAACTTTGGTCTGGG	15637593	Eurofins Genomics GmbH
ASPM	CCNB1_R	*CCNB1* qPCR Primer reverse strand	CTTTGTAAGTCCTTGATTTACCATG	15637593	Eurofins Genomics GmbH
ASPM	CDK1_F	*CDK1* qPCR Primer forward strand	AAGCTGGCTCTTGGAAATTGA	25016158	Eurofins Genomics GmbH
ASPM	CDK1_R	*CDK1* qPCR Primer reverse strand	ATGGCTACCACTTGACCTGTAGTT	25016158	Eurofins Genomics GmbH
ASPM/ BETi/ rigosertib	MYCN_F	*MYCN* qPCR Primer forward strand	CTCAGTACCTCCGGAGAG	12907629	Eurofins Genomics GmbH
ASPM/ BETi/ rigosertib	MYCN_R	*MYCN* qPCR Primer reverse strand	GGCATCGTTTGAGGATC	12907629	Eurofins Genomics GmbH
MRD	M13 Reverse (-24 mer) M13-24R	Breakpoint PCR product subcloning for sequence validation	CGGATAACAATTTCACACAGG		LGC Genomics GmbH
rigosertib	UBC1_F	*UBC1* qPCR Primer forward strand	ATTTGGGTCGCGGTTCTTG	12184808	Eurofins Genomics GmbH
rigosertib	UBC1_R	*UBC1* qPCR Primer reverse strand	TGCCTTGACATTCTCGATGGT	12184808	Eurofins Genomics GmbH

Table 24: List of small interfering RNAs used in this study

Target	siRNA name	Name abbreviation	siRNA Sequence 5'-3' (Sense strand)	Specifications	Source
ASPM	siASPM genescr 1		(AAGUACUACAAAGCAUAUCUG)TT		GenScript siRNA Target Finder[591]
ASPM	siASPM genescr 3	siRNA1	(AAGCUAGGCGGUUAAUUGUUC)TT		GenScript siRNA Target Finder[591]
ASPM	siASPM IDT front		(GCAUCACUUAUUCAGGGAUAUUGGA)TT		IDT Custom Dicer-Substrate siRNA[592]
ASPM	siASPM siSPOTR1	siRNA2	(CCACUCUCUGUACGUCGAU)TT		siSPOTR[593]
ASPM	Hs_ASPM_1	siRNA3	(GGCGGUUAAUUGUUCGAAA)TT	FlexiTube siRNA Order no. 3157911 Lot no. 210414149	QIAGEN
Non specific background control	Scramble 1	Scr1	(UAAUGUAUUGGAACGCAUA)TT	Non Specific Control 31% GC	Eurofins genomics siMAX siRNA controls
Non specific background control	Scramble 2	Scr2	(AGGUAGUGUAAUCGCCUUG)TT	Non Specific Control 47% GC	Eurofins genomics siMAX siRNA controls

Table 25: List of oligonucleotides (>25 nucleotides; except for MRD project) used in this thesis

Sub-project	Oligo name	Specifications	Sequence 5'-3' (Sense strand)	Manufacturer
ASPM	shScramble1	shScramble P referring to Plasmid #1864 scramble shRNA	Forward: 5´CCGGCCAGTCGCGTTTGCGACTGGTttcaagagaACCAGTCGCAAACGCGACTGTTTTTGGAAAT 3´ 3'GGCCGGTCAGCGCAAACGCTGACCAaagttctctTGGTCAGCGTTTGCGCTGACAAAAACCTTTA 5' Reverse: 5' TAAAGGTTTTTGTCAGCGCAAACGCTGACCAagagaacttTGGTCAGCGTTTGCGCTGACCGGCC 3'	Eurofins Genomics GmbH
ASPM	shScramble2	shScramble W referring to Plasmid pTer_shScr	Forward: 5´CCGGTCCTAAGGTTAAGTCGCCCTCGttcaagagaCGAGGGCGACTTAACCTTAGGTTTTTGGAAAT 3´ 3'GGCCAGGATTCCAATTCAGCGGGAGCaagttctctGCTCCCGCTGAATTGGAATCCAAAAACCTTTA 5' Reverse: 5´ATTTCCAAAAACCTAAGGTTAAGTCGCCCTCGtctcttgaaCGAGGGCGACTTAACCTTAGGACCGG 3´	Eurofins Genomics GmbH
ASPM	shASPM 967 named as shASPM 1	ASPM (2898 bp in NM_018136) targeting shRNA sequence (967)	Forward: 5´GATCCCGCTTTGTCCAAGTTTACATttcaagagaATGTAAACTTGGACAAAGCTTTTTGGAAATTAAT 3´ 3´ GGCGAAACAGGTTCAAATGTAaagttctctTACATTTGAACCTGTTTCGAAAAACCTTTAAT 5´ Reverse: 5´ TAATTTCCAAAAAGCTTTGTCCAAGTTTACATTCTCTTGAAATGTAAACTTGGACAAAGCGG 3´	Eurofins Genomics GmbH

ASPM	shASPM 968 named as shASPM 2	ASPM (5685 bp in NM_018136) targeting shRNA sequence (968)	Forward: 5´GATCCCGCAGCTTACAGAGGTTATAttcaagagaTATAACCTCTGTAAGCTGCTTTTTGGAAATTAAT 3´ 3´GGCGTCGAATGTCTCCAATATaagttctctATATTGGAGACATTCGACGAAAAACCTTTAAT 5´ Reverse: 5´ TAATTTCCAAAAAGCAGCTTACAGAGGTTATATCTCTTGAATATAACCTCTGTAAGCTGCGG 3´	Eurofins Genomics GmbH
ASPM	shASPM 969 named as shASPM 3	ASPM (9315 bp in NM_018136) targeting shRNA sequence (969)	Forward: 5´GATCCCGCTCATGAACACTTCTTAAttcaagagaTTAAGAAGTGTTCATGAGCTTTTTGGAAATTAAT 3´ 3´GGCGAGTACTTGTGAAGAATTaagttctctAATTCTTCACAAGTACTCGAAAAACCTTTAAT 5´ Reverse: 5´ TAATTTCCAAAAAGCTCATGAACACTTCTTAATCTCTTGAATTAAGAAGTGTTCATGAGCGG 3	Eurofins Genomics GmbH
ASPM	sgRNA TAG Stop 75	3x FLAG CRISPR/Cas9 knockin	caccgCACCATTTGAATAGCTTGCA	Eurofins Genomics GmbH
ASPM	sgRNA TAG Stop 87	3x FLAG CRISPR/Cas9 knockin	caccgCAAATGGTGATGGATACGCT	Eurofins Genomics GmbH

Table 26: List of plasmids used in this thesis.

Subproject	Plasmid name	Parental for	Created from	Reference	Source
MRD breakpoint PCR product subcloning	pUC18 control plasmid			Norrander et al.[1230]	Agilent Technologies (#200314)
MRD breakpoint PCR product subcloning	pCR™4-TOPO™ TA				Thermo Fischer Scientific (#450030)
shRNA mediated *ASPM* knockdown	psPAX2 lentiviral packaging vector			Hahne et al.[599]	K. Ahrens and F. Buttgereit (Charité)
shRNA mediated *ASPM* knockdown	pMD2.G lentiviral envelope vector			Henssen et al.[600]	A. G. Henssen (ECRC of the Charité and MDC) and A. Kentsis (Memorial Sloan Kettering Cancer Center)
shRNA mediated *ASPM* knockdown	Plasmid #1864 scramble shRNA (Scramble 1 / Scramble P)	pLKO.1_AXE_Puro-T2A-GFP		Sarbassov et al.[1231]	Addgene (#1864)
shRNA mediated *ASPM* knockdown	pLKO.1_Puro empty vector	pLKO.1_AXE_Puro-T2A-GFP		Molenaar et al.[322]; Vector referring to Stewart et al.[601]	J.J. Molenaar (Princess Máxima Center for Pediatric Oncology)
shRNA mediated *ASPM* knockdown	pLKO.1_AXE_Puro-T2A-GFP	pLKO.1_shScrambleP/ shASPM 967/968/969_Puro-T2A-GFP lentiviral transfer vector	Plasmid #1864 scramble shRNA and pLKO.1_Puro	Szymansky et al.[543,544,598] (*Manuscript in prep.*)	A. Winkler (Charité)

shRNA mediated *ASPM* knockdown	pLKO.1_shScrambleP/ shASPM 967/968/969_Puro-T2A-GFP lentiviral transfer vector		pLKO.1_AXE_Puro-T2A-GFP	Szymansky et al.[543,544,598] (*Manuscript in prep.*)	A. Winkler (Charité)
CRISPR/Cas9 mediated knockin of *ASPM* 3xFLAG	pSpCas9(BB)-2A-Puro (PX459) V2.0	pSpCas9(BB)-2A-Puro (PX459) V2.0_sgRNA-ASPM-Stop		Ran et al.[1232]	Addgene (#62988)
CRISPR/Cas9 mediated knockin of *ASPM* 3xFLAG	pSpCas9(BB)-2A-Puro (PX459) V2.0_sgRNA-ASPM-Stop		Plasmid #62988 pSpCas9(BB)-2A-Puro (PX459) V2.0	Szymansky et al.[543,544,598] (*Manuscript in prep.*)	A. Winkler (Charité)
CRISPR/Cas9 mediated knockin of *ASPM* 3xFLAG	WI2-3482I04 fosmid	pBS_Cas9_3xFLAG_2A Puro-Neo-Hom1mut2		KOMP Repository Collection[1233]	BACPAC Resources Center (BPRC)
CRISPR/Cas9 mediated knockin of *ASPM* 3xFLAG	pETCH_Donor (EMM0021) vector	pBS_Cas9_3xFLAG_2A Puro-Neo-Hom1mut2		Savic et al.[1234]	Addgene (#63934)
CRISPR/Cas9 mediated knockin of *ASPM* 3xFLAG	pBluescript II KS (+)	pBS_Cas9_3xFLAG_2APuro-Neo-Hom1mut2		Savic et al.[1234]	J.H. Schulte (Charité)
CRISPR/Cas9 mediated knockin of *ASPM* 3xFLAG	pBS_Cas9_3xFLAG_2APuro-Neo-Hom1mut2		WI2-3482I04 fosmid and pETCH_Donor (EMM0021) vector and pBluescript II KS (+)	Szymansky et al.[543,544,598] (*Manuscript in prep.*)	A. Winkler (Charité)

Generation of plasmids was performed in cooperation with A. Winkler (Charité).

Table 27: Microarray data sets from adult tumors, pediatric tumors and normal tissue for MCPH gene expression analysis

Specification tumor entity	Specification normal tissue	Age (years)	Adult / Pediatric / Mixed Patient Samples	Sample number	Author of Dataset	GEO DataSet Number
neuroblastoma			pediatric	34	Delattre	GSE14880
neuroblastoma		1 to 9	pediatric	51	Hiyama	GSE16237
neuroblastoma		1 to 10	pediatric	30	Lastowska	GSE13136
neuroblastoma			pediatric	88	Versteeg	GSE16476
	adrenal gland		mixed	13	Various	GSE3526, GSE7307, GSE8514
	brain regions	20 to 99	adult	172	Berchthold	GSE11882
	cerebellum	1 to 53	mixed	9	Roth	GSE3526
	normal Various	20 to 79?	adult	504	Roth	GSE7307
ALL (B)			pediatric	207	Murphy	GSE11877
AML			adult	179	Ley	GSE10358
ATRT		Mean 1	pediatric	18	Birks	GSE 28026
ATRT		0 > 9.5	pediatric	49	Kool	GSE70678

breast			adult	351	Expression Project for Oncology (expO)	GSE2109
CLL			adult	130	Kipps	GSE39671
colon			adult	315	Expression Project for Oncology (expO)	GSE2109
endometrium			adult	209	Expression Project for Oncology (expO)	GSE2109
ependymoma		0.4 > 61	pediatric	83	Gilbertson	Pubmed: 20639864
glioblastoma		26.4 > 70.3	adult	84	Hegi	GSE7696
kidney			adult	261	Expression Project for Oncology (expO)	GSE2109
medulloblastoma			pediatric	76	Gilbertson	GSE37418
myeloma (multiple)			adult	542	Hanamura	GSE2658
ovarian		22 to 79	adult	285	Bowtell	GSE9891
pheochromocytomas		mean 47	adult	188	Favier	Pubmed:22492777
prostate			adult	72	Expression Project for Oncology (expO)	GSE2109
thyroid			adult	34	Expression Project for Oncology (expO)	GSE2109

Preprocessed gene expression data from 25 data sets were downloaded from the R2 Platform[496,497]*. All measurements had been obtained using Affymetrix HG-U133-Plus2 Microarrays and processed using the MAS5.0 method*[639]*. Abbreviation: GEO = Gene Expression Omnibus*[498,499]*.*

Table 28: Mutant genes of the primary MCPH microcephaly, which are the cause of the disease.

MCPH number	Protein name	Gene name	Chromosomal location (GRCh38)	OMIM number	PubMed ID Reference
MCPH1	Microcephalin	*MCPH1*	8p23.1	251200	12046007 9683597
MCPH2	WD repeat-containing protein 62	*WDR62*	19q13.12	604317	10573015 20890279
MCPH3	CDK5 regulatory subunitassociated protein 2	*CDK5RAP2*	9q33.2	604804	10677332 15793586
MCPH4	Cancer susceptibility candidate 5	*CASC5*	15q15.1	604321	10521316 22983954
MCPH5	abnormal spindle-like microcephaly associated protein	*ASPM*	1q31.3	608716	11067780 11078481 12355089

MCPH6	Centromeric protein J	*CENPJ*	13q12.12	608393	15793586 12843329
MCPH7	SCL/TAL1 interrupting locus	*STIL*	1p33	612703	19215732 20978018
MCPH8	Centrosomal protein 135kDa	*CEP135*	4q12	614673	22521416
MCPH9	Centrosomal protein 152kDa	*CEP152*	15q21.1	604852	20598275
MCPH10	Zinc finger protein 335	*ZNF335*	20q13.12	615095	23178126
MCPH11	Polyhomeotic-like protein 1	*PHC1*	12p13.31	615414	23418308
MCPH12	Cyclin-dependent kinase 6	*CDK6*	10q11.23-21.3	616080	23918663
MCPH13	Centromeric protein E	*CENPE*	4q24	616051	24748105
MCPH14	C. elegans homolog of SAS6	*SASS6*	1p21.2	616402	24951542
MCPH15	Major facilitator superfamily domain-containing protein 2A	*MFSD2A*	1p34.2	616486	26005865 26005868
MCPH16	Ankyrin repeat- and LEM domain containing protein 2	*ANKLE2*	12q24.33	616681	25259927 30086807
MCPH17	Citron Rho-Interacting Serine/Threonine Kinase	*CIT*	12q24.23	605629	30086807
MCPH18	Wd Repeat- And Fyve Domain-Containing Protein 3	*WDFY3*	4q21.23	617485	30086807
MCPH19	Coatomer Protein Complex, Subunit Beta-2	*COPB2*	3q23	606990	29036432
MCPH20	Kinesin Family Member 14	*KIF14*	1q32.1	611279	28892560
MCPH21	Non-Smc Condensin I Complex Subunit D2	*NCAPD2*	12p13.31	615638	27737959 31056748
MCPH22	Non-Smc Condensin I Complex Subunit D3	*NCAPD3*	11q25	609276	27737959
MCPH23	Non-Smc Condensin I Complex Subunit H	*NCAPH*	2q11.2	602332	27737959

MCPH genes number 1-16 represent the "classic" MCPH genes, for which several clinical cases have already been identified and several (basic) research publications have been published. MCPH genes number 17-23 represent the more recently known MCPH mutations, for which there have so far been only individual cases reported and rarely basic research published.

Table 29: Gene expression of *ASPM* correlates high with expression of other genes involved in cell division and cell cycle.

Ranked number	Gene name	Spearman correlation coefficient to *ASPM*	MCPH gene number
1	*CENPF*	0.97	
2	*CENPE*	0.96	MCPH13
3	*KIF14*	0.95	MCPH20
4	*CDCA2*	0.94	
5	*BUB1*	0.94	
6	*NUF2*	0.94	
7	*BUB1B*	0.94	
8	*ECT2*	0.93	
9	*ARHGAP11A*	0.93	
10	*KIF11*	0.93	
11	*TPX2*	0,93	
12	*HJURP*	0.93	
13	*NCAPG*	0.93	
14	*CKAP2L*	0.93	
15	*KIF23*	0.93	
16	*NCAPH*	0.93	MCPH23
17	*KIF20A*	0.93	
18	*KIF15*	0.93	
19	*PLK4*	0.93	
20	*DLGAP5*	0.93	

Correlation of ASPM expression to the expression of other MCPH genes in a mRNA sequencing dataset obtained from a representative cohort of 498 primary neuroblastomas (SEQC study[42]). Analysis was performed in cooperation with J. Toedling (Charité).

10.2 List of figures

FIGURE 1: THE PRIMARY DISTRIBUTION OF NEUROBLASTOMAS IN CHILDREN. 18
FIGURE 2: EMBRYONIC DEVELOPMENT OF THE SYMPATHOADRENAL SYSTEM AND MODEL OF NEUROBLASTOMA INITIATION. 20
FIGURE 3: GENOMIC LOCATION AND TRANSCRIPT STRUCTURE OF THE *MYCN* ONCOGENE. 24
FIGURE 4: DIAGNOSTIC IDENTIFICATION OF A NEUROBLASTOMA. 26
FIGURE 5: KAPLAN-MEIER OVERALL SURVIVAL ESTIMATES OF PATIENTS WITH NEUROBLASTOMA ACCORDING TO INSS STAGE, *MYCN* STATUS AND AGE. 29
FIGURE 6: TREATMENT STRATIFICATION OF PATIENTS WITH A NEUROBLASTOMA. 30
FIGURE 7: COMPARISON OF DNA SEQUENCING METHODS, FOCUSING ON THE TARGETED SEQUENCING METHOD. 31
FIGURE 8: SCHEMATIC OF THE MRD CONCEPT WITHIN CELL BURDEN CHANGES OF LEUKEMIA PROGRESSION AND FOLLOWING RELAPSES. 34
FIGURE 9: TIME COURSE OF HIGH-RISK NEUROBLASTOMA TREATMENT PROTOCOLS. 38
FIGURE 10: CHEMOTHERAPEUTICS APPLIED IN NEUROBLASTOMA THERAPY ACT ON DIFFERENT PHASES OF THE CELL CYCLE. 39
FIGURE 11: THERAPEUTIC STRATEGIES TARGETING THE MYCN ONCOPROTEIN IN NEUROBLASTOMA. 42
FIGURE 12: THE BET PROTEIN BRD4 BINDS TO ACETYLATED HISTONE RESIDUES IN OPEN CHROMATIN REGIONS AND PROMOTES THE TRANSCRIPTION OF *MYCN*. 44
FIGURE 13: CHEMICAL STRUCTURES OF THE BET INHIBITORS JQ1, OTX015 AND TEN-010. 45
FIGURE 14: CHEMICAL STRUCTURES OF THE PLK1/PI3K INHIBITORS ALPELISIB, VOLASERTIB AND RIGOSERTIB. 49
FIGURE 15: KINASE INHIBITORS LIKE RIGOSERTIB PREVENT RAS-MEDIATED ERK- AND AKT ACTIVATION IN CANCER CELLS. 50
FIGURE 16: ASPM, A MICROTUBULE-BINDING PROTEIN, IS ASSOCIATED WITH CENTROSOMES (MTOCS). 53
FIGURE 17: ANALYSIS OF WOUND HEALING ASSAY USING IMAGE J. 72
FIGURE 18: BASIC AND CELL-BY-CELL ANALYZER MASKS FOR EXAMINATION OF CELL PROLIFERATION IN LIVE CELL ANALYSIS. 75
FIGURE 19: GATING STRATEGY OF EGFP DETECTION AND DNA CONTENT USING PI STAINING. 77
FIGURE 20: GATING STRATEGY OF CELL CYCLE ANALYSIS BY DNA CONTENT USING PI. 79
FIGURE 21: GATING STRATEGY OF EDU ALEXA FLUOR™ 647 AND 7-AAD DNA STAINING USING THE CLICK-IT™ PLUS ASSAY. 80
FIGURE 22: GATING STRATEGY OF FITC LABELED ANNEXIN V CELL APOPTOSIS ANALYSIS COMBINED WITH 7-AAD DNA STAINING. 82
FIGURE 23: PRINCIPLE OF RQ-PCR DETECTION USING A TAQMAN™ HYDROLYSIS PROBE. 93
FIGURE 24: SEQUENCE MAP OF GENOMIC *ASPM* WITH TARGET SITES OF SIRNA MEDIATED KNOCKDOWN. 96
FIGURE 25: SEQUENCE MAP OF GENOMIC *ASPM* WITH TARGET SITES OF SHRNA SEQUENCES FOR LENTIVIRAL MEDIATED KNOCKDOWN. 97
FIGURE 26: SGRNA BINDING SITES ARE ADJACENT TO THE STOP CODON OF *ASPM*. 100
FIGURE 27: CLONING STRATEGY FOR STOP CODON *FLAG* KNOCKIN AT C-TERMINAL END OF *ASPM* GUIDED BY A DONOR PLASMID. 101
FIGURE 28: SEQUENCE MAP OF GENOMIC *ASPM* AFTER CRISPR/CAS9 3X FLAG KNOCKIN AT TAG STOP CODON SITE. 104
FIGURE 29: SCHEMATIC OF SPANNING AND ENCOMPASSING SEQUENCING READS SUPPORTING A GENOMIC BREAKPOINT. 110
FIGURE 30: FLOW DIAGRAM OF THE ANALYSIS OF *NB TARGETED NGS ASSAY* SEQUENCING RAW DATA. 110
FIGURE 31: IGV BASED DETECTION OF A *MYCN* AMPLICON BREAKPOINT. 112
FIGURE 32: DEFINITIONS FOR ANALYSIS OF RQ-PCR MRD DATA. 118
FIGURE 33: DEFINITION OF POSITIVE, NEGATIVE AND INTERMEDIATE ("RAIN") DROPLETS IN DDPCR ANALYSIS. 119
FIGURE 34: CIRCOS PLOT OF GENOMIC TARGET REGIONS AND SEQUENCING COVERAGE OF THE *NB TARGETED NGS ASSAY*. 123
FIGURE 35: FISH BASED EVIDENCE FOR *MYCN* AMPLIFICATION FOUND IN NEUROBLASTOMA CELL LINE TR-14. 125
FIGURE 36: DETECTION OF TUMOR-SPECIFIC BREAKPOINTS OF THE *MYCN* AMPLICON USING NEXT-GENERATION SEQUENCING DATA. 126
FIGURE 37: GENOMIC REGIONS OF SEQUENCING CAPTURE PROBE HYBRIDIZATIONS IN THE *MYCN* AMPLICON. 127
FIGURE 38: SEQUENCING READ DEPTH DROP OF *MYCN* AMPLICON BREAKPOINT IN NEUROBLASTOMA CELL LINE TR-14. 128
FIGURE 39: *MYCN* COPY NUMBER AND FOCALITY PLOT OF CHROMOSOME 2 FROM NEUROBLASTOMA CELL LINE TR-14. 130
FIGURE 40: PATIENT-INDIVIDUAL DETECTION OF BREAKPOINTS OF THE *MYCN* AMPLICON USING *NB TARGETED NGS ASSAY*. 130
FIGURE 41: IGV BASED DETECTION OF THE TR-14 *MYCN* AMPLICON BREAKPOINT NO.15. 131
FIGURE 42: GENOMIC REARRANGEMENT EVENTS DERIVE *MYCN* AMPLICON BREAKPOINT IN *MYCN*-AMPLIFIED TR-14 CELL LINE. 132
FIGURE 43: JUNCTIONAL MICROHOMOLOGY IN *MYCN* AMPLICON BREAKPOINT OF TR-14 NEUROBLASTOMA CELL LINE. 133
FIGURE 44: *MYCN* COPY NUMBER AND FOCALITY PLOT OF CHROMOSOME 2 FROM MATCHING PRIMARY AND RELAPSE TUMOR SAMPLES. 134

FIGURE 45: DETECTION OF THE SAME BREAKPOINT OF THE *MYCN* AMPLICON IN MATCHING PRIMARY AND RELAPSE TUMOR SAMPLES. 136
FIGURE 46: GENOMIC REARRANGEMENT EVENTS DERIVE *MYCN* AMPLICON BREAKPOINT IN *MYCN*-AMPLIFIED TUMOR OF PATIENT NO.5. 137
FIGURE 47: SCHEME SHOWING DIFFERENT PCR AMPLICON LENGTH APPROACHES WITH DIFFERENT DISTANCES OF THE PRIMER TO THE BREAKPOINT/MICROHOMOLOGY. 138
FIGURE 48: AUTOMATED DNA ELECTROPHORESIS OF CONVENTIONAL PCR ASSAY DESIGNED TO AMPLIFY THE TR-14 BREAKPOINT NO.15 SEQUENCE. 139
FIGURE 49: ELECTROPHEROGRAM OF SANGER SEQUENCING OF THE PCR AMPLICON OF TR-14 CONFIRMED THE EXACT *MYCN* BREAKPOINT SEQUENCE. 140
FIGURE 50: DESIGN OF MRD ASSAY ON SPECIFIC *MYCN* BREAKPOINT IN *MYCN*-AMPLIFIED TR-14 CELL LINE. 141
FIGURE 51: RESULTS OF MRD ASSAY ON A SPECIFIC *MYCN* ASSOCIATED BREAKPOINT IN THE *MYCN*-AMPLIFIED TR-14 CELL LINE. 142
FIGURE 52: COMPARISON OF DETECTION SENSITIVITY FROM RQ-PCR AND DDPCR *NB BREAKPOINT MRD ASSAYS*. 143
FIGURE 53: VALIDATION OF A *MYCN* BREAKPOINT WITHIN PARENTAL CELL LINE IMR-32 AND SUB-CLONES IMR-5 AND IMR5/75 WITH CONVENTIONAL PCR 144
FIGURE 54: VALIDATION OF THE *MYCN* BREAKPOINT SEQUENCE WITHIN PARENTAL CELL LINE IMR-32 AND SUB-CLONES IMR-5 AND IMR5/75 USING SANGER SEQUENCING. 145
FIGURE 55: SCHEME SHOWING *MYCN* BREAKPOINT PCR ASSAY DESIGN AND PREDICTED PCR AMPLICON FOR NEUROBLASTOMA PATIENT NUMBER 5. 146
FIGURE 56: VALIDATION OF THE PATIENT-SPECIFIC *MYCN* ASSOCIATED BREAKPOINT IN THE INITIAL AND RELAPSE TUMOR DNA OF PATIENT NO. 5 WITH CONVENTIONAL PCR AND SANGER SEQUENCING. 147
FIGURE 57: RESULTS OF *MYCN* ASSOCIATED BREAKPOINT MRD DETECTION IN PATIENT PRIMARY AND RELAPSE NEUROBLASTOMA TUMOR MATERIAL. 148
FIGURE 58: *MYCN* AMPLICON BREAKPOINT MRD DETECTION IN COMPARISON TO ESTABLISHED DIAGNOSTICS FOR PATIENT NO. 8. 151
FIGURE 59: *MYCN* AMPLICON BREAKPOINT MRD DETECTION IN COMPARISON TO ESTABLISHED DIAGNOSTICS FOR PATIENT NO. 9. 152
FIGURE 60: *MYCN* AMPLICON BREAKPOINT MRD DETECTION IN COMPARISON TO ESTABLISHED DIAGNOSTICS FOR PATIENT NO. 10.153
FIGURE 61: *MYCN* AMPLICON BREAKPOINT MRD DETECTION IN COMPARISON TO ESTABLISHED DIAGNOSTICS FOR PATIENT NO. 11.154
FIGURE 62: *MYCN* AMPLICON BREAKPOINT MRD DETECTION IN COMPARISON TO ESTABLISHED DIAGNOSTICS FOR PATIENT NO. 12.155
FIGURE 63: *MYCN* AMPLICON BREAKPOINT MRD DETECTION IN COMPARISON TO ESTABLISHED DIAGNOSTICS FOR PATIENT NO. 13.156
FIGURE 64: OUTLINE OF THE CLINICAL IMPLEMENTATION OF *NB BREAKPOINT MRD ASSAY* DETECTION. 158
FIGURE 65: *ATRX* (DELETION) BREAKPOINT NEUROBLASTOMA MRD ASSAY IN CHLA-90 NON-*MYCN*-AMPLIFIED CELL LINE. 161
FIGURE 66: *ALK* SNV C.3824G>A NEUROBLASTOMA MRD ASQ-PCR IN LAN-5 CELL LINE AND SAMPLES OF PATIENT NO. #8. 164
FIGURE 67: (+)-JQ1 DOSE TO CELL VIABILITY RESPONSE RELATIONSHIP IN NEUROBLASTOMA AND FIBROBLAST CELL LINES. 166
FIGURE 68: OTX015 DOSE TO CELL VIABILITY RESPONSE RELATIONSHIP IN NEUROBLASTOMA AND FIBROBLAST CELL LINES. 167
FIGURE 69: TEN-010 DOSE TO CELL VIABILITY RESPONSE RELATIONSHIP IN NEUROBLASTOMA AND FIBROBLAST CELL LINES. 169
FIGURE 70: COMPARISON OF INHIBITORY EFFECTS OF BET INHIBITORS (+)-JQ1, OTX-015 AND TEN-010 ON CELL VIABILITY. 172
FIGURE 71: SINGLE TREATMENT INHIBITORY EFFECTS OF PLK1 / PI3K INHIBITORS RIGOSERTIB, VOLASERTIB AND ALPELISIB ON CELL VIABILITY. 176
FIGURE 72: COMPARISON OF INHIBITORY EFFECTS OF ALPELISIB (PI3KI), VOLASERTIB (PLK1I) AND RIGOSERTIB (PLK1I + PI3KI) ON CELL VIABILITY. 178
FIGURE 73: RIGOSERTIB DOSE TO CELL VIABILITY RESPONSE RELATIONSHIP IN NEUROBLASTOMA CELL LINES AND VH7 FIBROBLAST CELL LINE. 179
FIGURE 74: RIGOSERTIB SHOWS INHIBITORY EFFECTIVENESS IN LOW CONCENTRATIONS AND HIGH MAXIMUM RESPONSE TO CELL VIABILITY 180
FIGURE 75: TREATMENT WITH RIGOSERTIB INHIBITS CELL GROWTH AND DIMINISHES THE CELL POPULATION 24 AND 48H AFTER APPLICATION. 182
FIGURE 76: NEUROBLASTOMA CELLS DISPLAY REDUCED REPRODUCTIVE SURVIVAL AND DECREASED ABILITY TO FORM COLONIES AFTER RIGOSERTIB TREATMENT. 183
FIGURE 77: IMR5/75 NEUROBLASTOMA CELL MIGRATION AND WOUND HEALING IS DISRUPTED AFTER ADMINISTRATION OF RIGOSERTIB. 184
FIGURE 78: TREATMENT WITH THE DUAL PLK1/PI3K INHIBITOR RIGOSERTIB LEADS TO PROGRAMMED CELL DEATH IN IMR5/75 CELLS. 186

FIGURE 79: RIGOSERTIB TREATMENT INDUCES REDUCTION OF *MYCN* MRNA AND PROTEIN LEVELS, AND LEADS TO REPRESSION OF PLK1 AND PI3K FUNCTIONS IN NEUROBLASTOMA CELL. 187
FIGURE 80: RIGOSERTIB SHOWS ANTITUMOR EFFECTS AGAINST A PDX MICE MODEL OF A HIGH-RISK *MYCN*-AMPLIFIED NEUROBLASTOMA. 188
FIGURE 81: RIGOSERTIB SHOWS ANTITUMOR EFFECTS AGAINST A PDX MICE MODEL OF A HIGH-RISK NON-*MYCN*-AMPLIFIED NEUROBLASTOMA. 190
FIGURE 82: RIGOSERTIB SHOWS ANTITUMOR EFFECTS AGAINST A PDX MICE MODEL OF THE *MYCN*-AMPLIFIED IMR5/75 CELL LINE. 191
FIGURE 83: VOLASERTIB DOSE TO CELL VIABILITY RESPONSE RELATIONSHIP IN NEUROBLASTOMA AND FIBROBLAST CELL LINES. 193
FIGURE 84: ANALYSIS OF CELL VIABILITY DOSE-RESPONSE AFTER OTX015 AND VOLASERTIB DRUG COMBINATION IN NEUROBLASTOMA CELLS. 195
FIGURE 85: PRIMARY-MICROCEPHALY ASSOCIATED MCPH GENES ARE HIGHLY EXPRESSED IN PEDIATRIC TUMORS. 196
FIGURE 86: PRIMARY-MICROCEPHALY ASSOCIATED MCPH GENES ARE HIGHLY EXPRESSED IN HIGH-RISK NEUROBLASTOMA. 197
FIGURE 87: THE MICROTUBULE-ASSOCIATED PROTEIN ASPM IS DISTINCT IN NEURO-PEDIATRIC TUMORS. 198
FIGURE 88: HIGH EXPRESSION OF THE MICROTUBULE-ASSOCIATED GENE *ASPM* IN NEUROBLASTOMA CELL LINES. 199
FIGURE 89: HIGH EXPRESSION OF THE MICROTUBULE-ASSOCIATED ASPM PROTEIN CORRELATES WITH AGGRESSIVE NEUROBLASTOMAS. 200
FIGURE 90: HIGH EXPRESSION OF *ASPM* CORRELATES WITH ADVERSE OUTCOME AND IS LINKED TO CELL CYCLE, CELL DIVISION AND DNA REPLICATION. 201
FIGURE 91: EXPRESSION OF *ASPM* IS LINKED TO CELL CYCLE, CELL DIVISION AND DNA REPLICATION. 202
FIGURE 92: EXPRESSION OF *ASPM* IS HIGHLY CORRELATED WITH THE EXPRESSION OF *PLK1*, *FOXM1* AND *MKI67*. 203
FIGURE 93: EXPRESSION OF *ASPM* IS RAISED IN NEUROBLASTOMA CELL LINES. 204
FIGURE 94: CULTURING OF NGP NEUROBLASTOMA CELL LINE UNDER DIFFERENT SERUM CONCENTRATIONS AND CELL DENSITIES. 205
FIGURE 95: EXPRESSION OF *ASPM* IS LARGELY AUTONOMOUS OF SERUM AND CELL DENSITY FACTORS IN NGP NEUROBLASTOMA CELL LINE. 206
FIGURE 96: DIFFERENT SERUM CONCENTRATIONS AND CELL DENSITIES HAVE NO INFLUENCE ON THE CELL CYCLE OF NGP NEUROBLASTOMA CELLS. 207
FIGURE 97: CELL PROLIFERATION AND EXPRESSION OF *ASPM* IS LARGELY AUTONOMOUS OF SERUM AND CELL DENSITY FACTORS IN GI-ME-N AND LAN-5 NEUROBLASTOMA CELL LINES. 208
FIGURE 98: SIRNA KNOCKDOWN OF *ASPM* IN NGP NEUROBLASTOMA CELL LINE RESULTS IN DECREASE OF CELL VIABILITY AND PROLIFERATION AND INCREASE IN CELL DEATH FOUR DAYS AFTER TREATMENT. 209
FIGURE 99: SIRNA KNOCKDOWN OF *ASPM* IN NGP CELLS RESULTS IN DECREASE OF CELL VIABILITY AND PROLIFERATION AND INCREASE IN CELL DEATH AFTER 10 DAYS OF TREATMENT. 210
FIGURE 100: SIRNA KNOCKDOWN OF *ASPM* IN NGP CELLS LEADS TO A REDUCTION OF PROLIFERATION REPRESENTED BY A LOWER CELL CONFLUENCE AND FEWER CELL NUMBERS. 211
FIGURE 101: SIRNA KNOCKDOWN OF *ASPM* IN NEUROBLASTOMA CELLS RESULTS IN A DECREASE OF CELL VIABILITY AFTER FOUR AND 10 DAYS OF TREATMENT, IN CONTRAST ONLY A SLIGHT DECREASE WAS SEEN IN A FIBROBLAST CELL LINE. 212
FIGURE 102: SIRNA KNOCKDOWN OF *ASPM* IN SH-SY5Y CELLS RESULTS IN DECREASE OF CELL PROLIFERATION AFTER FOUR DAYS OF TREATMENT. 213
FIGURE 103: CLICK-IT™ PLUS ASSAY AFTER SIRNA MEDIATED KNOCKDOWN OF *ASPM* IN NGP NEUROBLASTOMA CELL LINE SHOWS REDUCTION OF S-PHASE, INCREASE IN G2/M-PHASE AND INCREASED SUB-G1 APOPTOTIC CELL FRACTIONS. 214
FIGURE 104: NEUROBLASTOMA NGP CELLS PRESENT WITH NEURITE-LIKE SHAPES AND EXPRESS MARKERS OF NEURONAL DIFFERENTIATION FOUR DAYS AFTER SIASPM TREATMENT. 215
FIGURE 105: NEUROBLASTOMA NGP CELLS PRESENT WITH NEURITE-LIKE SHAPES AND EXPRESS MARKERS OF NEURONAL DIFFERENTIATION 10 DAYS AFTER SIASPM TREATMENT. 216
FIGURE 106: PROLONGED SIRNA KNOCKDOWN OF *ASPM* IN NGP CELLS LEADS TO A VISABLE REDUCTION OF PROLIFERATION AND A HIGHER CELL BODY ECCENTRICITY. 217
FIGURE 107: NEUROBLASTOMA CHP-134 CELLS PRESENT WITH NEURITE-LIKE SHAPES AND EXPRESS MARKERS OF NEURONAL DIFFERENTIATION 10 DAYS AFTER SIASPM TREATMENT. 218
FIGURE 108: NEUROBLASTOMA NGP CELLS PRESENT WITH NEURITE-LIKE SHAPES AND EXPRESS MARKERS OF NEURONAL DIFFERENTIATION FOUR DAYS AFTER ATRA TREATMENT. 219
FIGURE 109: NEUROBLASTOMA NGP CELLS SHOW LOW EXPRESSION OF EARLY AND LATE POSITIVE MARKERS FOR NEURONAL DIFFERENTIATION FOUR AND 10 DAYS AFTER SIASPM TREATMENT. 220

FIGURE 110: NEUROBLASTOMA SH-SY5Y AND GI-ME-N CELLS SHOW INCREASED EXPRESSION OF LATE POSITIVE MARKER DCX FOR NEURONAL DIFFERENTIATION 10 DAYS AFTER SIASPM TREATMENT. 221
FIGURE 111: NEUROBLASTOMA NGP CELLS SHOW VARIABLE EXPRESSION OF EARLY AND LATE POSITIVE MARKERS FOR NEURONAL DIFFERENTIATION 10 DAYS AFTER ATRA TREATMENT. 221
FIGURE 112: SHRNA LENTIVIRAL KNOCKDOWN OF *ASPM* IN NGP CELLS RESULTS IN DECREASE OF CELL VIABILITY AND PROLIFERATION. 222
FIGURE 113: NEUROBLASTOMA NGP CELLS PRESENT WITH NEURITE-LIKE SHAPES AND DISPLAY NEURONAL DIFFERENTIATION 10 DAYS AFTER SHASPM TREATMENT. 223
FIGURE 114: NEUROBLASTOMA NGP CELLS SHOW INCREASED EXPRESSION OF EARLY POSITIVE MARKERS FOR NEURONAL DIFFERENTIATION 10 DAYS AFTER SHASPM TREATMENT. 223
FIGURE 115: NGP ASPM-FPN SINGLE CELL CLONES SHOWED POSITIVE DETECTION FOR FLAG PROTEIN AT EXPECTED WEIGHT FOR ASPM-FPN. 225
FIGURE 116: DETECTION OF ASPM-FLAG PROTEIN SIGNAL INCREASES UPON APPLICATION OF NOCODAZOLE WHICH BLOCKS POLYMERIZATION OF MICROTUBULES. 226
FIGURE 117: AFTER TREATMENT WITH NOCODAZOLE, NGP ASPM-FPN CELL LINE EXPRESSES HIGHER LEVELS OF *ASPM* AND CELL CYCLE G2/M-PHASE MARKERS. 226
FIGURE 118: NGP ASPM-FPN CELLS TREATED WITH NOCODAZOLE SHOW INCREASED ASPM-FLAG POSITIVE SIGNALS. 227
FIGURE 119: NGP ASPM-FPN CELLS TREATED WITH SIASPM AND NOCODAZOLE EXHIBIT LESS ASPM-FLAG POSITIVE SIGNALS AS COMPARED TO NOCODAZOLE TREATMENT ALONE. 228
FIGURE 120: NGP ASPM-FPN CELLS TREATED WITH SIASPM AND NOCODAZOLE EXHIBIT A LOWER ASPM-FLAG SIGNAL AS COMPARED TO TREATMENT WITHOUT SIASPM. 229
FIGURE 121: DEFINITION OF THE *MYCN* AMPLICON CONSIDERING *FRA2C* COMMON FRAGILE SITES OF CHROMOSOME 2P AS BOUNDARIES 233
FIGURE 122: RESULTS OF *NB TARGETED NGS ASSAY* SHOWING SEQUENCING COVERAGE OF THE 5' END OF *TERT* IN GI-ME-N. .. 244
FIGURE 123: COMPARISON OF MATCHING RESULTS IN NEUROBLASTOMA FISH ROUTINE DIAGNOSTICS, WGS/WES AND *NB TARGETED NGS ASSAY*. 249
FIGURE 124: SCHEMATIC PRINCIPLE OF THE MEDIATOR PROBE PCR (MP-PCR). 255
FIGURE 125: TREATMENT WITH TEN-010 INHIBITS CELL GROWTH AND REDUCES THE POPULATION OF *MYCN*-AMPLIFIED CELLS 24 AND 48H AFTER APPLICATION. 260
FIGURE 126: TREATMENT WITH THE BET INHIBITOR TEN-010 LEADS TO APOPTOSIS AND CELL DEATH IN NEUROBLASTOMA CELLS. 261
FIGURE 127: TEN-010 TREATMENT INDUCES REDUCTION OF BRD4 AND *MYCN* TRANSCRIPT LEVELS, INCREASES PROTEIN LEVELS OF HEXIM1 AND DOWNREGULATES PROTEIN LEVELS OF MYCN AND P53. 263
FIGURE 128: VALIDATION OF REARRANGEMENTS OF THE *MYCN* LOCUS IN NEUROBLASTOMA CELL LINES BY SANGER SEQUENCING. 359
FIGURE 129: VALIDATION OF REARRANGEMENTS OF THE *MYCN* LOCUS IN NEUROBLASTOMA TUMORS BY SANGER SEQUENCING (PART I). 360
FIGURE 130: VALIDATION OF REARRANGEMENTS OF THE *MYCN* LOCUS IN NEUROBLASTOMA TUMORS BY SANGER SEQUENCING (PART II). 361
FIGURE 131: HIGH EXPRESSION OF *ASPM* CORRELATES WITH A DIMINISHED EVENT-FREE SURVIVAL PROBABILITY. 362
FIGURE 132: HIGH EXPRESSION OF *ASPM* CORRELATES WITH A DIMINISHED OVERALL SURVIVAL PROBABILITY. 362
FIGURE 133: NEUROBLASTOMA SUBGROUP WITH *MYCN* AMPLIFICATION AND HIGH EXPRESSION OF *ASPM* SHOW LOWER EVENT-FREE SURVIVAL PROBABILITY. 363
FIGURE 134: NEUROBLASTOMA SUBGROUP WITHOUT *MYCN* AMPLIFICATION AND HIGH EXPRESSION OF *ASPM* SHOW SIMILAR EVENT-FREE SURVIVAL PROBABILITY COMPARED TO THE TOTAL COHORT. 363
FIGURE 135: NEUROBLASTOMA SUBGROUP WITH *MYCN* AMPLIFICATION AND HIGH EXPRESSION OF *ASPM* SHOW LOWER OVERALL SURVIVAL PROBABILITY. 364
FIGURE 136: NEUROBLASTOMA SUBGROUP WITHOUT *MYCN* AMPLIFICATION AND HIGH EXPRESSION OF *ASPM* SHOW IMPROVED OVERALL SURVIVAL PROBABILITY COMPARED TO THE TOTAL COHORT. 364
FIGURE 137: NEUROBLASTOMA HIGH-RISK SUBGROUP WITH HIGH EXPRESSION OF *ASPM* SHOW GREATLY REDUCED EVENT-FREE SURVIVAL PROBABILITY. 365
FIGURE 138: NEUROBLASTOMA HIGH-RISK SUBGROUP WITH HIGH EXPRESSION OF *ASPM* SHOW GREATLY REDUCED OVERALL SURVIVAL PROBABILITY. 365
FIGURE 139: SEQUENCE MAP OF GENOMIC *ASPM* AFTER CRISPR/CAS9 3XFLAG KNOCKIN AT STOP CODON SITE. 366

10.3 List of tables

TABLE 1: INTERNATIONAL NEUROBLASTOMA STAGING SYSTEM (INSS)[129] AND INTERNATIONAL NEUROBLASTOMA RISK GROUP STAGING SYSTEM (INRGSS)[131]. 28
TABLE 2: MIXING RATIOS FOR PCR PRODUCT LIGATION APPROACH. 89
TABLE 3: OVERVIEW OF 144 SAMPLES PROCESSED WITH THE *NB TARGETED NGS ASSAY* 125
TABLE 4: BREAKPOINTS DETECTED IN THE GENOMIC *MYCN* AMPLICON IN NEUROBLASTOMA CELL LINES. 129
TABLE 5: BREAKPOINTS DETECTED IN THE GENOMIC *MYCN* AMPLICON IN PRIMARY NEUROBLASTOMA TUMOR SAMPLES. 129
TABLE 6: SENSITIVITY OF RQ-PCR AND DDPCR ASSAYS FOR DETECTION OF *MYCN* ASSOCIATED BREAKPOINTS IN NEUROBLASTOMA CELL LINES. 141
TABLE 7: SENSITIVITY OF RQ-PCR AND DDPCR ASSAYS FOR THE DETECTION OF *MYCN* ASSOCIATED BREAKPOINTS IN NEUROBLASTOMA TUMORS. 143
TABLE 8: SUMMARY OF CELL LINE FEATURES POSSIBLY CONTRIBUTING TO BET INHIBITOR SENSITIVITY OR RESISTANCE. 174
TABLE 9: LIST OF HUMAN CELL LINES USED IN THIS THESIS 367
TABLE 10: CELL CULTURE MEDIA AND SUPPLEMENTS USED IN THIS STUDY 370
TABLE 11: CLINICAL DATA OF NEUROBLASTOMA PATIENT COHORT ANALYZED WITH *NB TARGETED NGS ASSAY* AND *NB BREAKPOINT MRD ASSAY* 373
TABLE 12: GENES EXAMINED IN *NB TARGETED NGS ASSAY* 374
TABLE 13: HOUSEKEEPING PCR ASSAY FOR NORMALIZATION OF MRD DETECTION 376
TABLE 14: GENOMIC LOCATIONS OF *MYCN* ASSOCIATED BREAKPOINTS WITHIN NEUROBLASTOMA CELL LINES 376
TABLE 15: PCR ASSAYS OF *MYCN* ASSOCIATED BREAKPOINTS WITHIN NEUROBLASTOMA CELL LINES 377
TABLE 16: GENOMIC LOCATIONS OF *MYCN*-ASSOCIATED BREAKPOINTS IN PRIMARY NEUROBLASTOMA SAMPLES 380
TABLE 17: PCR ASSAYS OF *MYCN*-ASSOCIATED BREAKPOINTS IN PRIMARY NEUROBLASTOMA SAMPLES 381
TABLE 18: COMPLETE LIST OF TR-14 BREAKPOINTS FOUND IN THE GENOMIC *MYCN* AMPLICON REGION ON CHR.2P24.3-2P24.2. .. 390
TABLE 19: *MYCN* AMPLICON BREAKPOINTS FOUND IN MATCHING PRIMARY AND RELAPSE TUMOR SAMPLES OF PATIENT NO. #5. 392
TABLE 20: PCR ASSAY OF *ATRX*-ASSOCIATED BREAKPOINT IN CHLA-90 NEUROBLASTOMA CELL LINE 392
TABLE 21: ASQ-PCR ASSAY OF *ALK* SNV C.3824G>A IN NEUROBLASTOMA CELL LINE AND TUMOR 393
TABLE 22: CELL COUNTS USED FOR *IN VITRO* ASSAYS 393
TABLE 23: LIST OF PCR PRIMERS (EXCEPT FOR MRD ASSAYS IN CELL LINE OR PATIENT MATERIAL*) USED IN THIS THESIS 394
TABLE 24: LIST OF SMALL INTERFERING RNAS USED IN THIS STUDY 396
TABLE 25: LIST OF OLIGONUCLEOTIDES (>25 NUCLEOTIDES; EXCEPT FOR MRD PROJECT) USED IN THIS THESIS 396
TABLE 26: LIST OF PLASMIDS USED IN THIS THESIS. 397
TABLE 27: MICROARRAY DATA SETS FROM ADULT TUMORS, PEDIATRIC TUMORS AND NORMAL TISSUE FOR MCPH GENE EXPRESSION ANALYSIS 398
TABLE 28: MUTANT GENES OF THE PRIMARY MCPH MICROCEPHALY, WHICH ARE THE CAUSE OF THE DISEASE 399
TABLE 29: GENE EXPRESSION OF *ASPM* CORRELATES HIGH WITH EXPRESSION OF OTHER GENES INVOLVED IN CELL DIVISION AND CELL CYCLE. 401
TABLE 30: LIST OF ALL CHEMICALS USED IN THIS WORK. 407
TABLE 31: LIST OF ALL SOLUTIONS USED IN THIS WORK. 408
TABLE 32: LIST OF ALL ASSAYS OR KITS USED IN THIS WORK. 411
TABLE 33: LIST OF ALL ENZYMES USED IN THIS WORK. 412
TABLE 34: LIST OF ALL INHIBITORS / ANTIBIOTICS USED IN THIS WORK. 413
TABLE 35: LIST OF ALL PRE-DESIGNED PRIMER AND OLIGOS "ON-DEMAND" USED IN THIS WORK. 414
TABLE 36: LIST OF ANTIBODIES USED IN THIS THESIS FOR WESTERN BLOT AND/OR IMMUNOFLUORESCENCE DETECTION. 415
TABLE 37: LIST OF ALL CONSUMABLES USED IN THIS WORK. 416
TABLE 38: LIST OF ALL DEVICES USED IN THIS WORK. 420
TABLE 39: LIST OF SOFTWARE USED IN THIS WORK. 423

10.4 List of materials

All buffers and solutions were prepared with de-ionized ultrapure water (aqua valde purificata, Milli-Q® System). Buffers and solutions that should be used under sterile conditions were autoclaved or sterile filtered before use. pH values were set with HCl and NaOH.

10.4.1 Chemicals

Table 30: List of all chemicals used in this work.

Name	Catalog number	Supplier/Company
2-Propanol, ROTIPURAN® min. 99,8%, p.a.	6752.3	Carl Roth GmbH + Co. KG, Karlsruhe, Germany
2-Propanol Suitable for the precipitation of nucleic acids	39559.02	SERVA Electrophoresis GmbH, Heidelberg, Germany
7-AAD ~97% (HPLC), powder	A9400-1MG	Sigma-Aldrich, St.Louis, MO, USA
Agarose Biozym LE	840004	Biozym Scientific GmbH, Hessisch Oldendorf, Germany
Albumin fraction V ≥98%, for biochemistry and molecular biology	8076.3	Carl Roth GmbH + Co. KG, Karlsruhe, Germany
Aprotinin from bovine lung	10236624001	Merck KGaA, Darmstadt, Germany
Bovine serum albumin fraction V powder, pH 7, ≥98%	A9647-50G	Sigma-Aldrich, St.Louis, MO, USA
$CaCl_2*2H_2O$ BioXtra, ≥99.0%	C5080-500G	Sigma-Aldrich, St.Louis, MO, USA
Chloroquine diphosphate salt	C6628-25g	Sigma-Aldrich, St.Louis, MO, USA
Crystal Violet certified by the Biological Stain Commission	C0775-25G	Sigma-Aldrich, St.Louis, MO, USA
D (+) – saccharose ≥99.5% p.a.	4621.1	Carl Roth GmbH + Co. KG, Karlsruhe, Germany
Dimethyl sulphoxide (DMSO) ≥99.5% BioScience-Grade	A994.1	Sigma-Aldrich, St.Louis, MO, USA
EDTA ≥99%	8040.3	Carl Roth GmbH + Co. KG, Karlsruhe, Germany
EGTA for molecular biology, ≥97.0%	E-3889	Sigma-Aldrich, St.Louis, MO, USA
Ethanol, absolut (200 Proof), molecular biological quality	10517694	Fisher Scientific GmbH, Schwerte, Germany
Glycin PUFFERAN® ≥99% p.a.	3908.3	Carl Roth GmbH + Co. KG, Karlsruhe, Germany
HEPES BioXtra, pH 5.0-6.5 (1 M in H2O), ≥99.5% (titration)	H7523-50G	Sigma-Aldrich, St.Louis, MO, USA
Human Laminin (pepsinized) Purified Protein	AG56P	Sigma-Aldrich, St.Louis, MO, USA
IGEPAL® CA-630 for molecular biology	I8896-50ML	Sigma-Aldrich, St.Louis, MO, USA

LB-Agar (Luria/Miller) for molecular biology	X969.2	Carl Roth GmbH + Co. KG, Karlsruhe, Germany
Leupeptin synthetic, ≥85% (HPLC)	L8511-5MG	Sigma-Aldrich, St.Louis, MO, USA
Magnesium chloride		Carl Roth GmbH + Co. KG, Karlsruhe, Germany
Magnesium chloride hexahydrate	1058330250	Supelco, Inc., Bellefonte, PA, USA
Magnesium sulfate heptahydrate Puriss. p.a., ACS Reagent, ≥99.0%	63140-500G-F-D	Honeywell International Inc., Charllotte, NC, USA
Methanol denatured ≥99.8%	K9284	Carl Roth GmbH + Co. KG, Karlsruhe, Germany
Methanol ROTIPURAN® ≥99.9%	4627.6	Carl Roth GmbH + Co. KG, Karlsruhe, Germany
Methanol ROTIPURAN®≥99.8%	9065.4	Carl Roth GmbH + Co. KG, Karlsruhe, Germany
Milk powder Blotting grade, powdered, low-fat	T145.2	Carl Roth GmbH + Co. KG, Karlsruhe, Germany
NaCl BioXtra, ≥99.5% (AT)	S7653-250G	Sigma-Aldrich, St.Louis, MO, USA
Na_2HPO_4 BioXtra, ≥99.0%	S7907-100G	Sigma-Aldrich, St.Louis, MO, USA
PBS dry substance without Ca2+, Mg2+	L182-10	Biochrom GmbH, Berlin, Germany
Phenylmethylsulfonyl fluoride	10837091001	Hoffmann-La Roche, Basel, Switzerland
Polybrene Hexadimethrine bromide >=95%	107689-10G	Sigma-Aldrich, St.Louis, MO, USA
Retinoic acid ≥98% (HPLC), powder	R2625	Sigma-Aldrich, St.Louis, MO, USA
SDS Pellets ≥99%, for biochemistry	CN30.3	Carl Roth GmbH + Co. KG, Karlsruhe, Germany
TEMED ≥99%, p.a., for electrophoresis	2367.1	Carl Roth GmbH + Co. KG, Karlsruhe, Germany
TRIS hydrochloride PUFFERAN® ≥99%, p.a.	9090.3	Carl Roth GmbH + Co. KG, Karlsruhe, Germany
Triton® X 100 extra pure	3051.4	Carl Roth GmbH + Co. KG, Karlsruhe, Germany
Tri-sodium citrate dehydrate ≥99% CELLPURE®	HN12.1	Carl Roth GmbH + Co. KG, Karlsruhe, Germany
TRIS PUFFERAN® ≥99.9% p.a.	4855.5	Carl Roth GmbH + Co. KG, Karlsruhe, Germany
Tween®20 Ph.Eur.	9127.1	Carl Roth GmbH + Co. KG, Karlsruhe, Germany
Tween®80 Ph.Eur.	9139.1	Carl Roth GmbH + Co. KG, Karlsruhe, Germany
Tween®100 Ph.Eur.	3051.4	Carl Roth GmbH + Co. KG, Karlsruhe, Germany

10.4.2 Solutions

Table 31: List of all solutions used in this work.

Name	Catalog number	Supplier/Company
Accutase® solution sterile-filtered, suitable for cell culture	A6964-500ML	Sigma-Aldrich, St.Louis, MO, USA
Biocoll Separating Solution	186-L-6155	Biochrom GmbH, Berlin, Germany

Buffer P1 500ml Resuspension Buffer	19051	QIAGEN N.V., Hilden, Germany
Buffer P2 500ml Lysis Buffer	19052	QIAGEN N.V., Hilden, Germany
Buffer P3 500ml Neutralization Buffer	19053	QIAGEN N.V., Hilden, Germany
CF-1 Calibration Check Fluid NanoDrop™, 0.5ml ampule	11810301	Fisher Scientific GmbH, Schwerte, Germany
cOmplete™, Mini, EDTA-free Protease Inhibitor Cocktail Tablets	11836170001	Hoffmann-La Roche, Basel, Switzerland
CutSmart® Buffer	B7204S	New England Biolabs Inc. (NEB), Ipswich, MA, USA
ddPCR™ Buffer Control for Probes	1863052	Bio-Rad Laboratories, Inc., Hercules, CA, USA
ddPCR™ Droplet Generation Oil for Probes	1863005	Bio-Rad Laboratories, Inc., Hercules, CA, USA
ddPCR™ Droplet Reader Oil	1863004	Bio-Rad Laboratories, Inc., Hercules, CA, USA
DMEM (1x) Dulbecco's Modified Eagle Medium Gibco™	41966-029	Thermo Fisher Scientific Inc., Waltham, MA, USA
DNA AWAY® Nuclease Removal ready-to-use	X996.1	Carl Roth GmbH + Co. KG, Karlsruhe, Germany
dNTP Mix 5 µmol/dNTP my-Budget	80-80010250	Bio-Budget Technologies GmbH, Krefeld, Germany
DPBS (1x) Gibco™	14190-094	Thermo Fisher Scientific Inc., Waltham, MA, USA
EMEM (Eagle's minimal essential medium) Gibco™	31095029	Thermo Fisher Scientific Inc., Waltham, MA, USA
Ethidium bromide solution 0,5% in dropper bottle, 5mg/ml in water	HP46.1	Carl Roth GmbH + Co. KG, Karlsruhe, Germany
Fetal Cow Serum (FCS) Superior	S0615	Merck Millipore, Burlington, MA, USA
Fetal Cow Serum (FCS) Tetracycline negative	Order no.: TZN-FCS 0.500 Lot no.: BS.045627TZN	Bio&SELL GmbH, Feucht/Nürnberg, Germany
Formaldehyde solution 4% phosphate buffered for histology	LC64701	neoLab Migge GmbH, Heidelberg, Germany
FlowClean Cleaning Agent 500 mL	A64669	Becton Dickinson BD Biosciences, Franklin Lakes, NJ, USA
GeneRuler 100 bp DNA Ladder	SM0241	Thermo Fisher Scientific Inc., Waltham, MA, USA
GeneRuler 1 kb DNA Ladder	SM0311	Thermo Fisher Scientific Inc., Waltham, MA, USA
Glycerol anhydrous pure	1.04093.1000	Merck Millipore, Burlington, MA, USA
HiMark™ Pre-stained Protein Standard	LC5699	Thermo Fisher Scientific Inc., Waltham, MA, USA
Laemmli Protein Sample Buffer fo SDS-PAGE 4x	1610747	Bio-Rad Laboratories, Inc., Hercules, CA, USA
L-Glutamine (200mM) Gibco™	25030081	Thermo Fisher Scientific Inc., Waltham, MA, USA
Lipofectamine™ RNAiMAX Transfection Reagent	13778075	Thermo Fisher Scientific Inc., Waltham, MA, USA

MEM non-essential amino acid solution (10mM, 100X stock) Lonza	882031	Biozym Scientific GmbH, Hessisch Oldendorf, Germany
NaCl (5 M), RNase-free	AM9759	Thermo Fisher Scientific Inc., Waltham, MA, USA
NaOH 10M in H_2O BioUltra, for molecular biology	72068-100ML	Sigma-Aldrich, St.Louis, MO, USA
NEBuffer™ 1.1 10x	B7201S	New England Biolabs Inc. (NEB), Ipswich, MA, USA
NEBuffer™ 2.1 10x	B7202S	New England Biolabs Inc. (NEB), Ipswich, MA, USA
NEBuffer™ 3.1 10x	B7203S	New England Biolabs Inc. (NEB), Ipswich, MA, USA
NEBuffer™ Set (EcoRI, DpnII) 10x	B7006S	New England Biolabs Inc. (NEB), Ipswich, MA, USA
Nuclease-Free Water (not DEPC-Treated), Ambion	AM9937	Thermo Fisher Scientific Inc., Waltham, MA, USA
NuPAGE™ Tris-Acetate SDS Running Buffer (20X)	LA0041	Thermo Fisher Scientific Inc., Waltham, MA, USA
NuPAGE™ Sample Reducing Agent (10X)	NP0004	Thermo Fisher Scientific Inc., Waltham, MA, USA
NuPAGE™ LDS Sample Buffer (4X)	NP0007	Thermo Fisher Scientific Inc., Waltham, MA, USA
NuPAGE™ Antioxidant	NP0005	Thermo Fisher Scientific Inc., Waltham, MA, USA
Opti-MEM™ I (1x) Gibco™ Reduced Serum Medium, no phenol red	11058021 or 31985-062	Thermo Fisher Scientific Inc., Waltham, MA, USA
Orange G (C.I. 16230) for microscopy and electrophoresis	0318.1	Carl Roth GmbH + Co. KG, Karlsruhe, Germany
PBS pH 7.4 (1x) Gibco™	10010-015	Thermo Fisher Scientific Inc., Waltham, MA, USA
Phenylmethanesulfonyl fluoride solution ~0.1 M in EtOH (T)	93482-50ML-F	Sigma-Aldrich, St.Louis, MO, USA
ROTIPHORESE®Gel 30 (37,5:1), ready-to-use, gas-stabilized, Polyacrylamid	3029-1	Carl Roth GmbH + Co. KG, Karlsruhe, Germany
Poly-L-lysine solution 0.01%, sterile-filtered, BioReagent	P4707-50ML	Sigma-Aldrich, St.Louis, MO, USA
ProLong™ Gold Antifade Mountant	P10144	Thermo Fisher Scientific Inc., Waltham, MA, USA
Protein Ladder HiMark™ Pre-stained Protein Standard	LC5699	Thermo Fisher Scientific Inc., Waltham, MA, USA
Protein Ladder PageRuler™ Prestained, 10 to 180kDa	26616	Thermo Fisher Scientific Inc., Waltham, MA, USA
Protein Ladder Precision Plus Protein™ Dual Color Standards	1610374	Bio-Rad Laboratories, Inc., Hercules, CA, USA
QX Alignment Marker 15 bp/3 kb QIAxcel®	929522	QIAGEN N.V., Hilden, Germany
QX DNA Size Marker 25–500bp v2.0 QIAxcel®	929560	QIAGEN N.V., Hilden, Germany
QX Nitrogen Cylinder (6) QIAxcel®	929705	QIAGEN N.V., Hilden, Germany
RNase AWAY® Nuclease Removal ready-to-use	A998.1	Carl Roth GmbH + Co. KG, Karlsruhe, Germany

Recombinant Posi-Tag Epitope Tag Protein, contains FLAG™ tag	BLD-931301	BioLegend, San Diego, CA, USA
RPMI Medium 1640 (1x) (Roswell Park Memorial Institute media), Gibco™	21875-034	Thermo Fisher Scientific Inc., Waltham, MA, USA
ROTIPHORESE® Gel 30 Aqueous acrylamide, bisacrylamide stock solution	3029.1	Carl Roth GmbH + Co. KG, Karlsruhe, Germany
Sheath Fluid BD FACSFlow™	342003	Becton Dickinson BD Biosciences, Franklin Lakes, NJ, USA
Sodium Bicarbonate 7.5% solution Gibco™	25080094	Thermo Fisher Scientific Inc., Waltham, MA, USA
Sodium Pyruvate (100mM) Gibco™	11360070	Thermo Fisher Scientific Inc., Waltham, MA, USA
T4 DNA Ligase Reaction Buffer	B0202S	New England Biolabs Inc. (NEB), Ipswich, MA, USA
TE buffer solution (TRIS-EDTA buffer) pH 8.0 for biotechnology	E112-100ML	VWR International, Randor, PA, USA
Trypan Blue Solution 0.4% Gibco™	15250061	Thermo Fisher Scientific Inc., Waltham, MA, USA
Trypsin-EDTA (0.05%) 1x phenol red Gibco™	25300054	Thermo Fisher Scientific Inc., Waltham, MA, USA
Trizma® hydrochloride buffer solution, BioUltra, for mol. bio., pH 7.4	93313-1L	Supelco Inc., Bellefonte, PA, USA
Vectashield® Antifade Mounting Medium with DAPI	H-1200	VECTOR LABORATORIES, INC., Burlingame, CA, USA
Water DEPC (0.1%) treated, sterile, molecular biology grade	39798.03	SERVA Electrophoresis GmbH, Heidelberg, Germany
Western Blotting Luminol Reagent	sc-2048	Santa Cruz Biotechnology, Inc., Santa Cruz, CA, USA

10.4.3 Ready-to-use assays or kits

Table 32: List of all assays or kits used in this work.

Name	Catalog number	Supplier/Company
BCA Protein Assay Kit	sc-202389	Santa Cruz Biotechnology, Inc., Dallas, TX, USA
Cell Death Detection ELISA^{PLUS}	11774425001	Hoffmann-La Roche, Basel, Switzerland
Cell Proliferation ELISA, BrdU (colorimetric)	11647229001	Hoffmann-La Roche, Basel, Switzerland
CellTiter-Glo® Luminescent Cell Viability Assay	G7570	Promega Corporation, Madison, WI, USA
Click-iT™ Plus EdU Alexa Fluor™ 647 flow cytometry Assay Kit	C10634	Thermo Fisher Scientific Inc., Waltham, MA, USA
ddPCR™ Buffer Control for Probes	1863052	Bio-Rad Laboratories, Inc., Hercules, CA, USA
Dead Cell Apoptosis Kit with Annexin V FITC & Propidium Iodide (PI)	V13242	Thermo Fisher Scientific Inc., Waltham, MA, USA
FastStart Essential DNA Green Master SYBR	6402712001	Hoffmann-La Roche, Basel, Switzerland
Genomic DNA ScreenTape Analysis	5067-5365	Agilent Technologies, Inc., Santa Clara, CA, USA
MycoAlert^{TM} Mycoplasma Detection Kit	LT07-318	Lonza Group Ltd., Basel, Switzerland

NucleoBond® Xtra Midi	740410.100	Macherey-Nagel GmbH & Co. KG, Düren, Germany
NucleoSpin® Tissue purification of total DNA	740952.50	Macherey-Nagel GmbH & Co. KG, Düren, Germany
QIAamp DNA FFPE Tissue Kit	56404	QIAGEN N.V., Hilden, Germany
QIAquick® Gel Extraction Kit	28706	QIAGEN N.V., Hilden, Germany
QIAquick® PCR Purification Kit	28106	QIAGEN N.V., Hilden, Germany
QIAxcel® DNA High Resolution Kit (1200), incl. gel cartridge	929002	QIAGEN N.V., Hilden, Germany
REPLI-g UltraFast Mini Kit (25)	150033	QIAGEN N.V., Hilden, Germany
RNeasy Micro Kit	74004	QIAGEN N.V., Hilden, Germany
RNeasy Mini Kit	74106	QIAGEN N.V., Hilden, Germany
StepOnePlus™ Real-Time PCR System Spectral Calibration Kit (96 well)	4371435	Thermo Fisher Scientific Inc., Waltham, MA, USA
TOPO™ TA Cloning™ Kit for Sequencing	450030	Thermo Fisher Scientific Inc., Waltham, MA, USA
Transcriptor First Strand cDNA Synthesis Kit	4897030001	Hoffmann-La Roche, Basel, Switzerland

10.4.4 Enzymes

Table 33: List of all enzymes used in this work.

Name	Catalog number	Supplier/Company
Acc65I 10,000 units/ml	R0599S	New England Biolabs Inc. (NEB), Ipswich, MA, USA
AgeI 5,000 units/ml	R0552S	New England Biolabs Inc. (NEB), Ipswich, MA, USA
Alkaline Phosphatase rAPid	4898133001	Hoffmann-La Roche, Basel, Switzerland
BamHI 20,000 units/ml	R0136S	New England Biolabs Inc. (NEB), Ipswich, MA, USA
BbsI 10,000 units/ml	R0539S	New England Biolabs Inc. (NEB), Ipswich, MA, USA
BglII 10,000 units/ml	R0144S	New England Biolabs Inc. (NEB), Ipswich, MA, USA
ddPCR™ Supermix for Probes (No dUTP)	1863024	Bio-Rad Laboratories, Inc., Hercules, CA, USA
DpnI, recombinant 20,000 units/ml	R0176L	New England Biolabs Inc. (NEB), Ipswich, MA, USA
EcoRI, recombinant 20,000 units/ml	R0101S	New England Biolabs Inc. (NEB), Ipswich, MA, USA
Go*Taq*® Hot Start Polymerase kit 5 u/µl	M5001	Promega Corporation, Madison, WI, USA
HindIII 20,000 units/ml	R0104S	New England Biolabs Inc. (NEB), Ipswich, MA, USA
KAPA2G Fast HotStart ReadyMix 5 U/µL	KK5601	Hoffmann-La Roche, Basel, Switzerland
Phusion® High-Fidelity DNA Polymerase 2,000 units/ml	M0530 S	New England Biolabs Inc. (NEB), Ipswich, MA, USA
Platinum™ *Taq* Green Hot Start DNA Polymerase	10966034	Thermo Fisher Scientific Inc., Waltham, MA, USA
Q5® High-Fidelity DNA Polymerase, 2,000 units/ml	M0491S	New England Biolabs Inc. (NEB), Ipswich, MA, USA
RNase-Free DNase Set 1500 Kunitz units RNase-free DNase I	79254	QIAGEN N.V., Hilden, Germany

SalI 20,000 units/ml	R0138S	New England Biolabs Inc. (NEB), Ipswich, MA, USA
T4 DNA Ligase 400,000 units/ml	M0202S	New England Biolabs Inc. (NEB), Ipswich, MA, USA
T7 DNA Endonuclease I 10,000 units/ml	M0302S	New England Biolabs Inc. (NEB), Ipswich, MA, USA
XbaI 20,000 units/ml	R0145S	New England Biolabs Inc. (NEB), Ipswich, MA, USA
XhoI 20,000 units/ml	R0146S	New England Biolabs Inc. (NEB), Ipswich, MA, USA

10.4.5 Inhibitors

Table 34: List of all inhibitors / antibiotics used in this work.

Name	Catalog number	Supplier/Company
(+)-JQ1 BET bromodomain inhibitor	S7110-0010	Selleckchem, Houston, TX, USA
Alpelisib (BYL-719) PI3Kα inhibitor	HY-15244-5	Hycultec GmbH, Beutelsbach, Germany
Ampicillin sodium salt, ≥97%, for molecular biology	K029.2	Carl Roth GmbH + Co. KG, Karlsruhe, Germany
Blasticidin S HCl 50mg	R21001	Thermo Fisher Scientific Inc., Waltham, MA, USA
Chloramphenicol (Chloromycetin) CAM	C4350.25	Biomol GmbH, Hamburg, Germany
G418-BC, Geneticin® 30.000U/ml in WFI sterile	A2912	Merck Millipore, Burlington, MA, USA
Nocodazole ≥99% (TLC), powder	M1404-2MG	Sigma-Aldrich, St.Louis, MO, USA
OTX015 (MK 8628/Birabresib) BET bromodomain inhibitor	S7360	Selleckchem, Houston, TX, USA
Penicillin-Streptomycin (10,000 U/mL), Gibco™	15140122	Thermo Fisher Scientific Inc., Waltham, MA, USA
PhosSTOP™ Phosphatase Inhibitor tablets	4906837001	Hoffmann-La Roche, Basel, Switzerland
Propidium iodide solution (1.0mg/ml in water)	P4864-10ML	Sigma-Aldrich, St.Louis, MO, USA
Puromycin dihydrochloride (from *Streptomyces alboniger*) powder, for cell culture	P8833	Sigma-Aldrich, St.Louis, MO, USA
Rigosertib (ON-01910) for *in vitro* experiments	S1362 - 5MG	Selleckchem, Houston, TX, USA
Rigosertib sodium - ON01910 sodium – Estybon for *in vivo* experiments	2950, Batch 4 [592542-60-4]	Axon Medchem LLC, Reston, VA, USA
TEN-010 (RG6146) BET bromodomain inhibitor	DTP07 ELN024588-197-2 RO870810-000 Thema 70151	Hoffmann-La Roche, Basel, Switzerland
Tetracycline hydrochloride ≥95% HPLC	T3383-25G	Sigma-Aldrich, St.Louis, MO, USA
Volasertib (BI 6727) Plk1 inhibitor	S2235	Selleckchem, Houston, TX, USA

10.4.6 Pre-designed oligonucleotides

Table 35: List of all pre-designed primer and oligos "on-demand" used in this work.

Name	Catalog number	Supplier/Company
FISH probes N-MYC SpectrumGreen/CEP 2 SpectrumOrange Probes Vysis LSI	07J72-001	Abbott Laboratories, Chicago, IL, USA
Hs_ASPM_1 FlexiTube siRNA 5nM	3157911	QIAGEN N.V., Hilden, Germany
Hs_ASPM_va.1_SG QuantiTect Primer Assay 10x	Product no.: 249900 Catalogue no.: QT0244181	QIAGEN N.V., Hilden, Germany
Hs_B2M_1_SG QuantiTect Primer Assay 10x	Product no.: 249900 Catalogue no.: QT00088935	QIAGEN N.V., Hilden, Germany

10.4.7 Antibodies

Table 36: List of antibodies used in this thesis for Western blot and/or Immunofluorescence detection.

Antibody name	Target (protein or primary antibody)	Primary / secondary antibody	Species	Conjugated to a dye	Dilution	Catalog number	Supplier/Company
ß-Actin (C4)	Human ß-Actin	primary unconjugated	Chicken mAb	unconjugated	1:200 WB	sc-47778	Santa Cruz Biotechnology, Dallas, TX, USA
β3-Tubulin (D71G9) XP®	Human β3-Tubulin	primary unconjugated	Rabbit mAb	unconjugated	1:200 IF	#5568	Cell Signaling Technology, Danvers, MA, USA
ANTI-FLAG® clone M2	FLAG-Tag	primary unconjugated	Mouse mAb	unconjugated	1:1000	F3165-.2MG F1804-50UG ?	Sigma-Aldrich, St.Louis, MO, USA
ASPM IHC	Human ASPM	primary unconjugated	Rabbit pAb	unconjugated	1:100	IHC-00058	Bethyl Laboratories, Inc., Montgomery, TX, USA
DCX	Human DCX	primary unconjugated	Rabbit mAb	unconjugated	1:200 IF	#4604	Cell Signaling Technology, Danvers, MA, USA
GAPDH (FL-335)	Human GAPDH	primary unconjugated	Rabbit pAb	unconjugated	1:1000	sc-25778	Santa Cruz Biotechnology, Dallas, TX, USA
IgG (H+L)	Mouse IgG	secondary unconjugated	Goat anti-mouse	unconjugated	1:5000	SKU: 115-035-146	DIANOVA GmbH, Hamburg, Germany
IgG (H+L)	Rabbit IgG	secondary unconjugated	Goat anti-rabbit	unconjugated	1:5000	SKU: 111-035-003	DIANOVA GmbH, Hamburg, Germany
IgG (H+L)	Mouse IgG	secondary conjugated	Goat anti-mouse	Alexa Fluor™ 488	1:500 IF	# A-11029	Thermo Fisher Scientific Inc., Waltham, MA, USA
IgG (H+L)	Rabbit IgG	secondary conjugated	Goat anti-rabbit	Alexa Fluor™ 488	1:500 IF	#A-11034	Thermo Fisher Scientific Inc., Waltham, MA, USA
MAP2 (D5G1) XP®	Human MAP2	primary unconjugated	Rabbit mAb	unconjugated	1:200 IF	#8707	Cell Signaling Technology, Danvers, MA, USA
MST1	Human MST1	primary unconjugated	Rabbit mAb	unconjugated	1:1000	#3682	Cell Signaling Technology, Danvers, MA, USA
N-Myc (B8.4B)	Human MYCN	primary unconjugated	Mouse mAb	unconjugated	1:200	sc-53993	Santa Cruz Biotechnology, Dallas, TX, USA
Phalloidin (rhodamine)	Human F-actin	primary conjugated		Alexa Fluor™ 555	1:20 IF	#8953	Cell Signaling Technology, Danvers, MA, USA
WEE1	Human WEE1	primary unconjugated	Mouse mAb	unconjugated	1:200	sc-5285	Santa Cruz Biotechnology, Dallas, TX, USA

10.4.8 Consumables

Table 37: List of all consumables used in this work.

Name	Catalog number	Supplier/Company
96well FrameStar® PCR Platte ABi FAST PCR	4Ti-0910	4 Titude Ltd, Surrey, UK
Adhesive slides SuperFrost® plus matt edge white	03-0060	R. Langenbrinck GmbH, Emmendingen, Germany
Amicon® Ultra-15, PLHK Ultracel-PL Membran, 100kDa	UFC910024	Merck Millipore, Burlington, MA, USA
Bags autoclavable large, 610x910 mm	129-0019	VWR International, Radnor, PA, USA
Bags Disposable 300x200mm, 40ym	E706.1	Carl Roth GmbH + Co. KG, Karlsruhe, Germany
Blotting papers ROTILABO® thickness 0.35 mm, 13 x 10cm	CL64.1	Carl Roth GmbH + Co. KG, Karlsruhe, Germany
Campingaz Easy Click gas cartridge; Butane / propane gas mixture in the ratio 80/20	cv 470 Plus	Campingaz, France
Cell Culture Assay Plate 96 well, flat bottom Sterile, Costar™	white: 3917 clear: 3628	Corning, Inc., Corning, NY, USA
Cell Culture Dish Tissue, Falcon™, Sterile, polystrene	100x20 mm: 353003 150x25 mm: 353025	Corning, Inc., Corning, NY, USA
Cell Culture Flask Tissue, Falcon™, Sterile, polystrene	25cm²: 353108 75cm²: 353110 175cm²: 353112	Corning, Inc., Corning, NY, USA
Cell Culture Multiwell Plate CELLSTAR® clear Sterile, F-bottom	6 well: 657 160 12 well: 665 180 24 well: 662 160 48 well: 677 180 96 well: 655 180	Greiner Bio-One International, Kremsmünster, Austria
Cell Culture Tube (for Ficoll) CELLSTAR® clear	12ml: 64 160	Greiner Bio-One International, Kremsmünster, Austria
Culture-Inserts 2 Well for self-insertion	80209	ibidi GmbH, Martinsried, Germany
Cell Scraper blade L 1.8cm, handle L 25cm, sterile	CLS3010	Corning, Inc., Corning, NY, USA
Combitips advanced® Eppendorf Biopur®, colorless tips	0.1ml 0030089618 0.5ml 0030089634 1.0ml 0030089642 5.0ml 0030089669 25ml 0030089685	Eppendorf AG, Hamburg, Germany
Counting chamber Neubauer 0.100 mm depth, 0.0025 mm² BLAUBRAND®	718605	BRAND GMBH + CO KG, Wertheim, Germany
Counting Slides for TC10™/TC20™ Cell Counter, Dual-Chamber	145-0011	Bio-Rad Laboratories, Inc., Hercules, CA, USA
Cover glasses for hemacytometer 20 * 26mm	HECH40415710	VWR International, Radnor, PA, USA
Cryoboxes (PC) plastic 81 spaces, 53 mm high	78031	neoLab Migge GmbH, Heidelberg, Germany
Cryo-Safe™ -1˚C Freeze Controller Scienceware™	F18844-0000	Bel-Art Products, Inc., South Wayne, NJ, USA

Cryogenic storage boxes, cardboard, ultra-low temperature, with grid insets	FB71211	Thermo Fisher Scientific Inc., Waltham, MA, USA
Cryo Vial 2ml CryoPure internal yellow cap	72.380.004	Sarstedt AG & Co. KG, Nümbrecht, Germany
DG8 Cartridges, QX100/QX200™	1864008	Bio-Rad Laboratories, Inc., Hercules, CA, USA
DG8 Gaskets, QX100/QX200™	1863009	Bio-Rad Laboratories, Inc., Hercules, CA, USA
Dispensehead cassettes HP T8 PLUS 20PC	30097370	Tecan Group AG, Männedorf, Switzerland
Dispensehead cassettes HP D4 PLUS 20PC	30097371	Tecan Group AG, Männedorf, Switzerland
Disposable syringes PP 2ml Luer	1799	Semadeni AG, Ostermundigen, Switzerland
Disposable wipes KIMTECH® Science precision wipes, 7551	AA63.1	Carl Roth GmbH + Co. KG, Karlsruhe, Germany
Dymo Label Cassette D1 Tape 19mm x 7m Black on White	S0720830 / 45803	Dymo Corporation, Berkeley, CA, USA
EDTA-anticoagulated tubes BD Vacutainer® blood collection tube	4.0ml: 367862 6.0ml: 367863	BD Biosciences, Franklin Lanes, IN, USA
Eppendorf Combitips advanced®, Biopur®, 10 mL, orange, colorless tips	30089677	Eppendorf AG, Hamburg, Germany
Eppendorf twin.tec® PCR Plates	30128575	Eppendorf AG, Hamburg, Germany
Erlenmeyer flask, DURAN® wide neck	25ml: C144.1 250ml: C137.1 500ml: C139.1	Carl Roth GmbH + Co. KG, Karlsruhe, Germany
ExactaCruz® Round Gel Loading Tips in Sterile Rack	sc-201732	Santa Cruz Biotechnology, Dallas, TX, USA
Falcon™ Round-Bottom Polystyrene Tubes for FACS	VE125 352054	Corning, Inc., Corning, NY, USA
Falcon™ 15 mL High Clarity PP Centrifuge Tube, Conical Bottom, Sterile	352096	Corning, Inc., Corning, NY, USA
Falcon™ 50 mL High Clarity PP Centrifuge Tube, Conical Bottom, Sterile	352070	Corning, Inc., Corning, NY, USA
Floating stands for reagent and sample tubes	212-9125	VWR International, Radnor, PA, USA
Forceps Dumont Style 5, Polished, Dumostar®	11295-10	Fine Science Tools (FST) Group, North Vancouver, B.C., Canada
Glass beads diam. ~5 mm	18406-500G	Sigma-Aldrich, St.Louis, MO, USA
Gene Pulser®/MicroPulser™ Electroporation Cuvettes, 0.4cm gap	165-2088	Bio-Rad Laboratories, Inc., Hercules, CA, USA
Gloves Nitra-Touch™ Powder-free PPE made of nitrile	4400053	Ansell, Richmond, Australia
Gloves Vasco ® Guard long S Nitril Butadien	9205518	B. Braun Melsungen AG, Melsungen, Germany
Immersion oil for microscopy, fluorescence tested	X899.2	Carl Roth GmbH + Co. KG, Karlsruhe, Germany
Inoculation loop with aluminum coated handle, 3 mm	612-2675	VWR International, Radnor, PA, USA
Loading Tips, 1 Pk for TapeStation	5067-5153	Agilent Technologies, Inc., Santa Clara, CA, USA
Marking tape ROTI®Tape range, 12.7 m x 13.0 mm	AK66.1	Carl Roth GmbH + Co. KG, Karlsruhe, Germany

Mini cooler for 12 tubes (4 x 3) - Temp.: - 20 ° C - yellow - without gel	KR-MC-12-Y	Kisker Biotech GmbH & Co. KG, Steinfurt, Germany
Microscope Slide Boxes 100-Place	HS15994D	VWR International, Radnor, PA, USA
Mini-PROTEAN® Empty Cassettes for Western blot	4560006	Bio-Rad Laboratories, Inc., Hercules, CA, USA
Mini-PROTEAN® Comb, 12-well, 20 µl for Western blot	4560015	Bio-Rad Laboratories, Inc., Hercules, CA, USA
Multiply®-µStrip 0.2ml chain 8-tube PCR chain	72.985.002	Sarstedt AG & Co. KG, Nümbrecht, Germany
Nail polish clear trend it up, double volume & shine	010	dm-drogerie markt GmbH + Co. KG, Karlsruhe, Germany
Nitrocellulose membrane, 0.45 µm	162-0115	Bio-Rad Laboratories, Inc., Hercules, CA, USA
Nunc® Lab-Tek® II Chamber Slide™ system 4 wells, glass slide, 1.7cm2/well, sterile	C6807-1PAK	Sigma-Aldrich, St.Louis, MO, USA
NuPAGE™ 3-8% Tris-Acetate Protein Gels, 1.0 mm, 10-well	EA0375BOX	Thermo Fisher Scientific Inc., Waltham, MA, USA
NuPAGE™ LDS Sample Buffer (4X)	NP0007	Thermo Fisher Scientific Inc., Waltham, MA, USA
NuPAGE™ Sample Reducing Agent (10X)	NP0009	Thermo Fisher Scientific Inc., Waltham, MA, USA
Optical adhesive film for qPCR	4Ti-0560	4 Titude Ltd, Surrey, UK
Optical tube strips (8x Strip) for TapeStation	401428	Agilent Technologies, Inc., Santa Clara, CA, USA
Optical tube strip caps (8x Strip) for TapeStation	401425	Agilent Technologies, Inc., Santa Clara, CA, USA
Pasteur pipettes without cotton plug, 2ml, 150 mm, tip length: 60 mm	4518.1	Carl Roth GmbH + Co. KG, Karlsruhe, Germany
Parafilm™ M Sealing Film	PM-999	Bemis Company, Inc, Neenah, Wi, USA
PCR-Cooler 0.2ml Starter-Set	3881000015	Eppendorf AG, Hamburg, Germany
PCR Plate Heat Seal, foil, pierceable	1814040	Bio-Rad Laboratories, Inc., Hercules, CA, USA
PCR tube lids 8-lid PCR chain	65.1998.400	Sarstedt AG & Co. KG, Nümbrecht, Germany
Plastic tube 13ml 100 x 16 mm PP	62515006	Sarstedt AG & Co. KG, Nümbrecht, Germany
PVDF Western Blotting Membrane 0,45 µm	3010040001	Hoffmann-La Roche, Basel, Switzerland
Reaction tubes Micro tube clear Safe Seal	0.5ml: 72.704 1.5ml: 72.706.400 2.0ml: 72.691	Sarstedt AG & Co. KG, Nümbrecht, Germany
Reaction tubes ROTILABO® 1.5ml black	AA80.1	Sarstedt AG & Co. KG, Nümbrecht, Germany
Respiratory mask with valve covered 3M ™ Aura ™ 1883+	3M-ID 7000088733	3M (Minnesota Mining and Manufacturing Company), Maplewood, MN, USA
Round coverslips Microscope 22mm , Karl Hecht ™	10063691 - 1001/0022	Fisher Scientific GmbH, Schwerte, Germany
Scalpels sterile, disposable	0570	Swann Morton Ltd, Sheffield, UK
Serological pipettes Costar® Stripette®, polystyrene, individually wrapped, sterile	2ml: 4486	Corning, Inc., Corning, NY, USA

Serological pipettes Falcon™ polystyrene, individually wrapped, sterile	5ml: 357543 10ml: 357551	Corning, Inc., Corning, NY, USA
Serological pipettes CELLSTAR®, polystyrene, individually wrapped, sterile	25ml: 760 180	Greiner Bio-One International, Kremsmünster, Austria
Sharps Container Sharpsafe® discharge bin	12.000.04.110	Dahlhausen Medizintechnik & Co. GmbH, Cologne, Germany
Spray bottle LaboPlast® 500ml	215-6511	VWR International, Radnor, PA, USA
Sterillium® classic pure hands disinfectant	975512	Bode Chemie GmbH, Hamburg, Germany
Syringe 10ml Injekt® Luer Lock Solo	4606728V	B. Braun Melsungen AG, Melsungen, Germany
Syringe filter ROTILABO® cellulose acetate (CA), 25 mm, sterile	Pore size 0.20µM: KC70.1 Pore size 0.45µM: KC71.1	Carl Roth GmbH + Co. KG, Karlsruhe, Germany
Tips, filter SafeSeal SurPhob sterile, low binding	10µl: VT0200 100µl: VT0230 1200µl: VT0270	Biozym Scientific GmbH, Hessisch Oldendorf, Germany
Tips, SafeSeal SurPhob Reload, low binding	10µl: VT0103 100µl: VT0143 1200µl: VT0173	Biozym Scientific GmbH, Hessisch Oldendorf, Germany
Tips, filter for PCR Biosphere®	0.1-10µl: 70.1130.210 0.5-10µl: 70.1115.210 0.5-20µl: 70.1116.210 2-20µl; 70.760.213 2-200µl: 70.760.211	Sarstedt AG & Co. KG, Nümbrecht, Germany
Tips, filter for PCR FlexTop Ultrafine Tip Extended-Length Filtered Racked Sterile ZAP™	ZP1250S	Alpha Laboratories Eastleigh, Hampshire, UK
Tissue culture Dish 100 mm TC-treated Falcon™	353003	Corning, Inc., Corning, NY, USA
Tissue culture Dish 150 mm with 20 mm Grid TC-treated Falcon™	353025	Corning, Inc., Corning, NY, USA
Transfer pipette drop size: 35 - 55 µl, sterile,	86.1171.001	Sarstedt AG & Co. KG, Nümbrecht, Germany
Tube racks (for Falcon tubes)	18 x 15ml / 10 x 50ml = 99017 30 x 15ml / 20 x 50ml = 99019	TPP Techno Plastic Products AG, Trasadingen, Switzerland
UV face shield RELRSI	KP10.1	Carl Roth GmbH + Co. KG, Karlsruhe, Germany
Water bath stabilizer neoLab Bad Stabil® 100ml	1-6095 / 100-500	neoLab Migge GmbH, Heidelberg, Germany
Weighing dishes ROTILABO® white, antistatic, 330ml, 140 mm, 140 mm	0875.2	Carl Roth GmbH + Co. KG, Karlsruhe, Germany
Wipes ECO Fleece cloths and impregnation with suitable surface disinfectants	00-915-REW10006-01	Dr. Schumacher GmbH, Malsfeld, Germany

10.4.9 Devices

Table 38: List of all devices used in this work.

Name	Catalog number	Supplier/Company
4200 TapeStation System	G2991AA	Agilent Technologies, Inc., Santa Clara, CA, USA
C1000 Touch™ Thermal Cycler with Dual 48/48 Fast Reaction Module	1851148	Bio-Rad Laboratories, Inc., Hercules, CA, USA
APC Smart-UPS, 1000 VA, LCD, 230 V, for IncuCyte®	SMT1000I	American Power Conversion, West Kingston, RI, USA
Apple iMac 7,1 (20" Year of construction mid 2007)	A1224	Apple Inc., Cupertino, CA, USA
Color camera XC10 CCD U-TV1XC Fluorescence microscopy	XC10	Olympus, Shinjuku, Prefecture Tokio, Japan
Centrifuge 5415 D with rotor 13200 1/min centrifugation	556954240/ 33617	Eppendorf AG, Hamburg, Germany
Centrifuge 5424 R, cooled, with rotor FA-45-24-11, membrane keyboard, 230 V / 50–60 Hz	5404000010 and 5404000410	Eppendorf AG, Hamburg, Germany
Centrifuge 5427 R, cooled, with rotor FA-45-48-11, knobs, 230 V / 50–60 Hz	5409000530	Eppendorf AG, Hamburg, Germany
Centrifuge 5810 R, cooled, with rotor A-4-62, Adapters 15/50 mL tubes, 230 V / 50–60 Hz	5811000325	Eppendorf AG, Hamburg, Germany
Centrifuge Sorvall® Evolution™ RC Superspeed Centrifuge	Evolution 32	Thermo Fisher Scientific Inc., Waltham, MA, USA
Centrifuge Heraeus™ Primo™ R	75005440	Thermo Fisher Scientific Inc., Waltham, MA, USA
Centrifuge Heraeus™ Megafuge 1.0R	75003060	Thermo Fisher Scientific Inc., Waltham, MA, USA
Centrifuge Heraeus™ function line Labofuge™ 400	75008150	Thermo Fisher Scientific Inc., Waltham, MA, USA
Centrifuge MiniStar Silverline Microcentrifuge 8x0,2ml 6000rpm	461	VWR International, Radnor, PA, USA
Centrifuge PerfectSpin Mini	PEQL91-PSPIN-M	VWR International, Radnor, PA, USA
Centrifuge Sorvall™ LYNX 4000 superspeed centrifuge Used with the F14-6x250y rotor	75006580	Thermo Fisher Scientific Inc., Waltham, MA, USA
Centrifuge Universal 320 R	1406	Hettich Unternehmensgruppe, Kirchlengern, Germany
Charge-coupled device Camera DP-CF-011.C with TV Zoom Lens	DP-CF-011.C	Vilber Lourmat, Collégien, France
Conductivity pH meter FE30 FiveEasy™	51302912	Mettler-Toledo, Columbus, OH, USA
Consort Doc Print VX5 1100 Imaging System	VLDP11-26M	Vilber Lourmat, Collégien, France
Cryogenic Storage 24K System	10-033-01-0111	Worthington Cylinders (Worthington Industries), Columbus, OH, USA
Digital Dispenser D300E	30100152	Tecan Group AG, Männedorf, Switzerland
Dymo LabelManager™ 420P labeling device	S0915440	Dymo Corporation, Berkeley, CA, USA
Epoch™ Microplate Spectrophotometer	6283693 / EPOCH	BioTek Instruments Inc., Winooski, VT, USA

Eppendorf ThermoMixer® C 220–240 V / 50–60 Hz	5382000015	Eppendorf AG, Hamburg, Germany
Flow Cytometer BD LSRFortessa™ X-20 Cell Analyzer	657669	Becton Dickinson BD Biosciences, Franklin Lakes, NJ, USA
Fluorescence Lamp Illuminator X-Cite® Series 120PC Q	120PC Q	Excelitas Technologies Corp., Waltham, MA, USA
Fridge FKUv 1610 Index 21J/001 , +4°C	FKUv 160-22Q	Liebherr, Bulle FR, Switzerland
Freezer LCv4010eez MediLine -20°C	LCv 4010-23C	Liebherr, Bulle FR, Switzerland
Freezer LKexv 3910 MediLine +4°C	LTM Liebherr	Liebherr, Bulle FR, Switzerland
Freezer HERAfreeze™ HFU T series -86 ° C ultra-low freezers HFU400TV63	11650823	Thermo Fisher Scientific Inc., Waltham, MA, USA
Freezer Innova U725-G ULT ultra-low freezer -86°C 725L, New Brunswick Scientific	11389884 U9440-0005	Eppendorf AG, Hamburg, Germany
Gene Pulser Xcell Electroporation Eukaryotic System, 100/240 V, 50/60 Hz	1652661	Bio-Rad Laboratories, Inc., Hercules, CA, USA
GloMax®-Multi+ Microplate Multimode Reader	SA3030	Promega Corporation, Madison, WI, USA
Horizontal Mini Gel System chamber, PerfectBlue™	40-1214	VWR International, Randor, PA, USA
Ice Flaker Scotsman AF 80	AF 80	Scotsman Ice Machines, Vernon Hills, IL, USA
Ice machine Manitowoc UFP0399A	Man-UFP0399A	Manitowoc Cranes, Manitowoc, WI, USA
Incubator Heratherm™ Compact Microbiological Incubator	50125882	Thermo Fisher Scientific Inc., Waltham, MA, USA
Incubator Heracell™ 240i CO_2 with Stainless-Steel Chambers for human cell culture	51026331	Thermo Fisher Scientific Inc., Waltham, MA, USA
Incubator Midi 40 CO_2 with Stainless-Steel Chambers for human cell culture	3403	Thermo Fisher Scientific Inc., Waltham, MA, USA
IncuCyte® S3 Live-Cell Analysis System	4647 no. of IncuCyte®: 10.43.144.105	Essen BioScience, Ann Arbor, MI, USA
IncuStore® S Storage Unit, expansion data storage for IncuCyte® S3	4689	Essen BioScience, Ann Arbor, MI, USA
Liquid nitrogen storage tank LD, Type series XL240	000016	Taylor-Wharton®, Baytown, TX, USA
Magnetic stirrer IKA RH basic	0005019700	IKA-Werke, Staufen im Breisgau, Germany
MCO-230AIC IncuSafe CO2 Incubato, for IncuCyte®	MCO-230AICUV-PE	PHC Corporation (PHCBI), Tokio, Japan
Microdissection Leica LMD 6500	LMD6500	Leica Camera, Wetzlar, Germany
Microscope inverted Axio Vert.A1	491237	Carl Zeiss AG, Oberkochen, Germany
Microscope Axiovert 40 CFL, transmitted light, bright field, phase difference	491202-0002-001	Carl Zeiss AG, Oberkochen, Germany
Microscope BX43 Olympus Fluorescence microscope	BX43	Olympus, Shinjuku, Prefecture Tokio, Japan

Microscope Leica DMRA with JVC KY F-75 digital camera Fluorescence microscope	27170	Leica Camera, Wetzlar, Germany
Microwave Bosch Home, white 800 W	HMT72M420	Robert Bosch GmbH, Gerlingen, Germany
Mini-PROTEAN® Tetra Cell 4-gel vertical electrophoresis system, 0.75 mm gel	1658000	Bio-Rad Laboratories, Inc., Hercules, CA, USA
Mini Trans-Blot® Electrophoretic Transfer Cell	1703930	Bio-Rad Laboratories, Inc., Hercules, CA, USA
Multipette® Xstream	4987000380	Eppendorf AG, Hamburg, Germany
NanoDrop™ 2000 Microvolume Spectrophotometer	ND-2000 ND2000LAPTOP	Thermo Fisher Scientific Inc., Waltham, MA, USA
PCR Workstation Pro PEQLAB Biotechnologie GmbH	732-2840DE	VWR International, Randor, PA, USA
Photometer BioPhotometer® 6131230 V/50 – 60 Hz	613101964 / 6133000001	Eppendorf AG, Hamburg, Germany
Pipettes, Research® plus	0.1 – 2.5µl 3123000012 0.5 – 10µl 3123000020 10 – 100µl 3123000047 20 – 200µl 3123000055 100 – 1000µl 3123000063	Eppendorf AG, Hamburg, Germany
Pipetus® 100-240 Volt	9907200	Hirschmann Laborgeräte GmbH & Co. KG, Eberstadt, Germany
PowerPac™ Basic Electrophoresis Power Supply	1645050	Bio-Rad Laboratories, Inc., Hercules, CA, USA
PowerPac™ 300 Electrophoresis Power Supply	165-5050	Bio-Rad Laboratories, Inc., Hercules, CA, USA
QIAxcel® Advanced Instrument	9001941	QIAGEN N.V., Hilden, Germany
Reax top Mechanical shaker 0 – 2.500rpm	541-10000-00	Heidolph Instruments GmbH & Co. KG, Schwabach, Germany
Roll Mixer analog *RS*-TR 5	RS-TR 5	Phoenix Instrument GmbH, Garbsen, Germany
Safety cabinet Safe 2020 1.8 Laminar airflow bench class II	51026637	Thermo Fisher Scientific Inc., Waltham, MA, USA
Scale precision EW-N Readability 0.001 g	EW 620-3NM	KERN & SOHN GmbH, Balingen, Germany
Scale precision ABS Readability 0.001 g	ABS 80-4N	KERN & SOHN GmbH, Balingen, Germany
Scanner Epson Perfection V700 Photo	B11B178023	Seiko Epson K.K., Suwa, Prefecture Nagano, Japan
Shaker G24 Environmental Incubator, New Brunswick Scientific		Eppendorf AG, Hamburg, Germany
Shaker Innova™ 4300 incubator, New Brunswick Scientific		Eppendorf AG, Hamburg, Germany
Shaker IKA KS 4000 i control	0003510000	IKA-Werke, Staufen im Breisgau, Germany
Shaker Gyratoral / Orbital Rotamax 120 20 - 300 U/min	544-41200-00	Heidolph Instruments GmbH & Co. KG, Schwabach, Germany
Shaker Rocker Duomax 1030 (5° inclination)	543-32205-00	Heidolph Instruments GmbH & Co. KG, Schwabach, Germany
StepOnePlus™ Real-Time PCR System	4376600	Thermo Fisher Scientific Inc., Waltham, MA, USA
TC20™ Automated Cell Counter	145-010	Bio-Rad Laboratories, Inc., Hercules, CA, USA

Thermal Cycler T100™	1861096	Bio-Rad Laboratories, Inc., Hercules, CA, USA
ThermoMixer® C with thermoblock for 1.5 or 2ml tubes	5382000015	Eppendorf AG, Hamburg, Germany
Timer ROTILABO®	A802.1	Carl Roth GmbH + Co. KG, Karlsruhe, Germany
Trans-Blot® Turbo™ Western blot Transfer System	1704150	Bio-Rad Laboratories, Inc., Hercules, CA, USA
Transilluminator Fusion-FX7-826.WL Superbright	151115241	Vilber Lourmat, Collégien, France
UV table ECX-F20.C V1	ECX-F20.C V1	Vilber Lourmat, Collégien, France
Vacuum Safety Suction System, pump 15 l/min, AC02	981423101	Hettich Unternehmensgruppe, Kirchlengern, Germany
Vortexer Minishaker MS1		IKA-Werke, Staufen im Breisgau, Germany
Waterbath shaking	1086	GFL Gesellschaft für Labortechnik mbH, Burgwedel, Germany
Waterbath WNB 7	8419 8998	Memmert GmbH + Co. KG, 6 Schwabach, Germany
XCell SureLock® Mini-Cell Electrophoresis System	EI0002	Thermo Fisher Scientific Inc., Waltham, MA, USA

10.4.10 Software

Table 39: List of software used in this work.

Name	Download source	Supplier/Company
Adobe® Acrobat Reader DC Version 2019.021.20058	https://get.adobe.com/de/reader/	Adobe Inc., San José, CA, USA
Adobe® Illustrator® version CS6 (64 Bit)	http://www.adobe.com/de/creativecloud/plans.html?filter=design	Adobe Inc., San José, CA, USA
Adobe® Photoshop® CS6 (64 Bit)	http://www.adobe.com/de/creativecloud/plans.html?filter=design	Adobe Inc., San José, CA, USA
Agilent TapeStation Software Download Revision 3.2	https://www.agilent.com/en/promotions/tapestation-sw?productURL=https%3A%2F%2Fwww.agilent.com%2Fen%2Fproduct%2Fautomated-electrophoresis%2Ftapestation-systems%2Ftapestation-software%2Ftapestation-software-379381	Agilent Technologies, Inc., Santa Clara, CA, USA
BD FACSDiva™ Software v8.0.2	http://www.bdbiosciences.com/us/instruments/research/software/flow-cytometry-acquisition/bd-facsdiva-software/m/111112/features	Becton Dickinson BD Biosciences, Franklin Lakes, NJ, USA
cellSens Dimension	https://www.olympus-lifescience.com/de/software/cellsens/#!cms[tab]=%2Fsoftware%2Fcellsens%2Fdownloads	Olympus, Shinjuku, Prefecture Tokio, Japan
D300eControl Tecan version 3.2.5	https://lifesciences.tecan.com/products/liquid_handling_and_aut	Tecan Group AG, Männedorf, Switzerland

	omation/tecan_d300e_digital_dispenser?p=tab--2	
Diskus Viewer software	https://diskus-viewer.software.informer.com/4.8/	Hilgers Technisches Buero e.K., Koenigswinter, Germany
DOC-PRINT VX	http://www.vilber.de/produkte/analysesoftware/	Vilber Lourmat, Collégien, France
Epson Scan (Version 5.1.1f2) Mac OS X	https://www.epson.co.uk/support#drivers_and_manuals	Seiko Epson K.K., Suwa, Prefecture Nagano, Japan
Excel 2016 Microsoft Office Professional Plus 2016	https://products.office.com/de-de/compare-all-microsoft-office-products?&market=de&activetab=tab:primaryr1	Microsoft Corporation, Redmond, WA, USA
FlowJo™ v10.6.1	https://www.flowjo.com/solutions/flowjo/downloads	FlowJo LLC Becton Dickinson, Ashland, OR, USA
FusionCapt Advance FX7	http://www.vilber.de/produkte/analysesoftware/capt-softwares/	Vilber Lourmat, Collégien, France
Gen5™ Data Analysis Software 2.04.11.0	https://www.biotek.de/de/products/software-robotics-software/gen5-microplate-reader-and-imager-software/	BioTek Instruments Inc., Winooski, VT, USA
GloMax®-Multi+ Detection System with Instinct™ Software Firmware (version 04.15) and Software (version 3.1.3)	https://www.promega.de/resources/software-firmware/glomax-systems/detection-instruments-software/promega-branded-instruments/glomax-multi-plus-detection-system-instinct/	Promega Corporation, Madison, WI, USA
GraphPad Prism® v7.03.	https://www.graphpad.com/how-to-buy/	Graphpad Software, Inc., San Diego, CA, USA
ImageJ version 1.8.0_112	https://imagej.nih.gov/ij/download.html	Wayne Rasband (National Institutes of Health (NIH)), Bethesda, MD, USA
Integrative Genomics Viewer (IGV) version 2.8.0	https://software.broadinstitute.org/software/igv/download	Broad Institute, Cambridge, MA, USA
IncuCyte® Software (version 2019B) Rev2	https://www.essenbioscience.com/en/products/software/incucyte-software-v2019b/	Essen BioScience, Ann Arbor, MI, USA
MendeleyDesktop Version 1.19.4	https://www.mendeley.com/download-desktop/	Mendeley, London, UK
NanoDrop™ 2000 Version 1.4.0.1	https://www.thermofisher.com/content/dam/tfs/ATG/CAD/CAD%20Documents/Software/Molecular%20Spectroscopy/Spectrophotometer-Systems/nanodrop-software/NanoDropOnePCViewer%20software%20v1.4.exe	Thermo Fisher Scientific Inc., Waltham, MA, USA
PowerPoint 2016 Microsoft Office Professional Plus 2016	https://products.office.com/de-de/compare-all-microsoft-office-products?&market=de&activetab=tab:primaryr1	Microsoft Corporation, Redmond, WA, USA
QIAxcel® ScreenGel Software version 1.4.0 9021163	https://www.qiagen.com/fi/products/instruments-and-automation/analytics-software/qiaxcel-screengel-software/#orderinginformation	QIAGEN N.V., Hilden, Germany

QuantaSoft™ Software, Regulatory Edition version 1.7.4.0917	https://www.bio-rad.com/de-de/sku/1864011-quantasoft-software-regulatory-edition?ID=1864011	Bio-Rad Laboratories, Inc., Hercules, CA, USA
QuantaSoft™ Analysis Pro version 1.0.596	https://www.bio-rad.com/de-de/product/qx200-droplet-digital-pcr-system?ID=MPOQQE4VY	Bio-Rad Laboratories, Inc., Hercules, CA, USA
RStudio version 1.0.143.0	https://rstudio.com/products/rstudio/download/	RStudio, Inc., Boston, MA, USA
XV-Imaging; Olympus-Soft-Imaging-Solutions Version 3.15	https://www.olympus-sis.com/corp/2417.htm	Olympus, Shinjuku, Prefecture Tokio, Japan
SnapGene version 5.0.1.	https://www.snapgene.com/buy-snapgene/academic/	GSL Biotech LLC, Chicago, IL USA
SnapGene Viewer version 1.4.0.	https://www.snapgene.com/snapgene-viewer/	GSL Biotech LLC, Chicago, IL USA
StepOnePlus™ software version 2.2.2. / 2.3	http://www.thermofisher.com/de/en/home/technical-resources/software-downloads/StepOne-and-StepOnePlus-Real-Time-PCR-System.html	Thermo Fisher Scientific Inc., Waltham, MA, USA
VisionCapt™ software version	http://www.analis.be/bin/site/render.cgi?id=0074231_item_to_sell&ln=	ANALIS, Suarlée, Belgium
Word 2016 Microsoft Office Professional Plus 2016	https://products.office.com/de-de/compare-all-microsoft-office-products?&market=de&activetab=tab:primaryr1	Microsoft Corporation, Redmond, WA, USA
Zen 2012 (blue edition), version 1.1.0.0	http://www.zeiss.de/mikroskopie/produkte/mikroskopsoftware/zen-lite.html#downloads	Carl Zeiss AG, Oberkochen, Germany
Zen version 2.3 lite	http://www.zeiss.de/mikroskopie/produkte/mikroskopsoftware/zen-lite.html#zen-lite	Carl Zeiss AG, Oberkochen, Germany

10.5 Buffers and solutions recipes

All buffers and solutions were prepared with de-ionized ultrapure water (aqua valde purificata, Milli-Q® System). Buffers and solutions that should be used under sterile conditions were autoclaved or sterile filtered before use. pH values were set with HCl and NaOH.

10.5.1 *NB targeted NGS assay* and *NB breakpoint MRD assay*

Phosphate-buffered saline (PBS) (10x) pH 7.0	
Na_2HPO_4	11.6 g
KH_2PO_4	2 g
NaCl	80 g
KCl	2 g
Adjust final volume to 10 l with dH_2O	

Erylysis buffer (10x) pH 7.3	
NH_4Cl	89,9 g
$KHCO_3$	10.0 g
Na4-EDTA	3.72 g
Adjust final volume to 1 l with dH_2O	

0.5 M EDTA buffer pH 8.0	
EDTA	93.06 g
Adjust final volume to 500ml with dH_2O	

1 M TRIS-HCl buffer pH 7.4	
Trizma-base powder	121.14 g
Adjust final volume to 1 l with dH_2O	

Gel loading dye with Orange G (10x)	
Ficol powder	7.5 g
Orange G	100mg
TE buffer (1x)	50ml

TRIS-EDTA (TE) buffer (1x)	
TRIS-HCl pH 7.5	1mM
EDTA pH 8	0.1mM
Adjust final volume to 10ml with dH_2O	

2% Agarosis gel	
Agarosis powder	2 g
TAE buffer (1x)	100ml

Tris-acetate-EDTA (TAE) buffer (50 x)	
Trizma-base powder	242 g
Acetate (100% acetic acid)	57.1ml
Sodium EDTA (0.5 M)	100ml
Adjust final volume to 1 l with dH_2O	

10.5.2 Molecular cloning

Luria-Bertani (LB) broth-agar	
LB powder	35 g
NaCl	10 g
Tryptone	10 g
Yeast extract	5 g
Agar	20 g
Adjust final volume to 1 l with dH_2O	

Luria-Bertani (LB) broth-medium	
LB powder	1mM
EDTA pH 8	0.1mM
Adjust final volume to 1 l with dH_2O	

Luria-Bertani (LB) broth-MDC medium	
LB powder	35 g
NaCl	10 g
Tryptone	10 g
Yeast extract	5 g
Adjust final volume to 1 l with dH_2O	

Transformation buffer	
$MgCl_2$	10mM
$MgSO_4$	10mM
DMSO	5%
PEG 3000	10% (v/m)
Adjust final volume with LB-medium	

Super Optimal broth (SOC) medium	
Tryptone	20 g
Yeast extract	5 g
NaCl	0.5 g
Adjust final volume to 1 l with dH_2O, autoclave	
$MgCl_2$ (1 M)	10ml
$MgSO_4$ (1 M)	10ml
Glucose solution 20% in dH_2O	20ml

10.5.3 Flow cytometry

FACS buffer	
PBS 1x	99%
FCS	1%

PI staining solution	
DNase buffer	1ml
RNase A 100mg/mL	2.5µl
Incubate at 95°C for 10 min, cool down on ice	
Add 40µl PI stock solution (1mg/mL)	

DNase buffer	
NaCl (5 M)	150µl
$MgCl_2$ (1 M)	20µl
dH_2O	4.83ml

10.5.4 Clonogenic 2D assay with crystal violet staining

1% Crystal violet solution	
Crystal violet powder	0.5 g
EtOH	5ml
dH_2O	45ml

10.5.5 Calcium phosphate transfection of HEK-293T

2.5mM HEPES	
HEPES (0.5 M)	83µl
dH_2O	16.6µl

25mM Choloroquine	
Choloroquine	0.51586 g
dH_2O	40ml

Transfection medium	
DMEM medium	50ml
FCS 10%	5ml
Glutamine 2%	1ml
HEPES 0.5 M (10mM)	1ml
1/1000 Chloroquine 25mM	50µl

2x HEPES-buffered saline (HeBS) solution pH 7.00	
HEPES (50mM)	5.96 g
NaCl (280mM)	8.18 g
Na_2HPO_4 (1.5mM)	0.106 g
Dissolve chemicals in 400ml dH_2O, adjust pH, adjust to final volume to 500ml with dH_2O	

2.5 M $CaCl_2$*$2H_2O$	
$CaCl_2$*$2H_2O$	3675 g
dH_2O	10ml

15% Glycerol solution	
2x HeBS buffer	5ml
Glycerol	1.5ml
dH_2O	3.5ml

10.5.6 SDS-PAGE and semi-dry protein transfer

Protein lysis buffer I	
HEPES	15mM
NaCl	150mM
EGTA	10mM
Triton X-100	2%
Add 1 tablet cOmpleteMini per 400µl before Add 1 tablet PhosSTOP in 1ml ddH_2O before	

SDS-Electrophoresis running buffer (10x)	
Trizma-base powder	30.3 g
Glycine	144 g
SDS 20% (w/w) SDS pellets	50ml (10 g)
Adjust final volume to 1 l with dH_2O	

Stacking gel buffer pH 6.8	
TRIS-HCl pH 7.5	1 M

Separation gel buffer pH 8.8	
TRIS-HCl pH 7.5	1.5 M

SDS-polyacrylamide stacking gel	
Polyacrylamide (30%)	330µl
Stacking Gel Buffer	250µl
dH_2O	1.4ml
20% SDS	10µl
10% APS	20µl
TEMED	2µl

10% SDS-polyacrylamide separation gel	
Polyacrylamide (30%)	3.3ml
Separation gel buffer	2.5ml
dH_2O	4ml
SDS 20%	50ml
APS 10%	100µl
TEMED	4µl

SDS-transfer buffer (10x)	
Trizma-base powder	30.3 g
Glycine	144 g
Adjust final volume to 1 l with dH_2O	

SDS-transfer buffer (1x)	
MeOH	200ml
SDS-transfer buffer 10x	100ml
Adjust final volume to 1 l with dH_2O	

Blocking buffer	
Low fat milk powder	10%
Adjust final volume with TBS-T buffer	

Phosphate-buffered saline (TBS) (10x) pH 7.4	
NaCl 1.5 M	87.66 g
Trizma-base 0.1 M	15.76 g
Adjust final volume to 1 l with dH_2O	

Phosphate-buffered saline (TBS)-T (1x) pH 7.4	
10x TBS-buffer	100ml
Tween-20	0.5ml
Adjust final volume to 1 l with dH_2O	

10.5.7 NuPAGE™ system and wet protein transfer

Protein lysis buffer II	
Triton X-100	1%
TRIS (1 M, pH 7.4)	1%
EDTA	0.2%
IGEPAL	0.5%
NaCl	8.76 g/l
PMSF	1%
Leupeptin	0.1%
Aprotinin	1%
Adjust final volume with dH_2O	

SDS-transfer buffer (10x)	
Trizma-base powder	30.3 g
Glycine	144 g
Adjust final volume to 1 l with dH_2O	

SDS-transfer buffer (1x)	
MeOH	200ml
SDS-transfer buffer 10x	100ml
Adjust final volume to 1 l with dH_2O	

10.5.8 Immunofluorescence staining

30% Sucrose solution	
PBS 1x	500ml
Sucrose	150mg

Blocking buffer	
PBS 1x	100ml
Triton X-100	0.3%
FCS (freshly added)	5%